Edited by Bruno Pignataro

WILEY-VCH

Ideas in Chemistry and Molecular Sciences

Advances in Nanotechnology, Materials and Devices

Ideas in Chemistry and Molecular Sciences

Edited by
Bruno Pignataro

Related Titles

Pagliaro, Mario

Nano-Age
How Nanotechnology Changes our Future

2010
ISBN: 978-3-527-32676-1

Garcia-Martinez, Javier (ed.)

Nanotechnology for the Energy Challenge

2010
ISBN: 978-3-527-32401-9

Pignataro, Bruno (ed.)

Ideas in Chemistry and Molecular Sciences
Advances in Synthetic Chemistry

2010
ISBN: 978-3-527-32539-9

Pignataro, Bruno (ed.)

Ideas in Chemistry and Molecular Sciences
Where Chemistry Meets Life

2010
ISBN: 978-3-527-32541-2

Pignataro, Bruno (ed.)

Tomorrow's Chemistry Today
Concepts in Nanoscience, Organic Materials and Environmental Chemistry
Second edition

2009
ISBN: 978-3-527-32623-5

Cademartiri, Ludovico/Ozin, Geoffrey A.

Concepts of Nanochemistry

2009
ISBN: 978-3-527-32626-6 (Hardcover)
ISBN: 978-3-527-32597-9 (Softcover)

Ideas in Chemistry and Molecular Sciences

Advances in Nanotechnology, Materials and Devices

Edited by
Bruno Pignataro

WILEY-VCH Verlag GmbH & Co. KGaA

The Editor

Prof. Bruno Pignataro
University of Palermo
Department of Physical Chemistry
Viale delle Scienze
90128 Palermo
Italy

Cover

We would like to thank Dr. Frank Hauke and Mrs. Cordula Schmidt (both Friedrich-Alexander University Erlangen-Nuremberg) for providing us with the graphic material used in the cover illustration.

Library of Congress Card No.: applied for

British Library Cataloguing-in-Publication Data
A catalogue record for this book is available from the British Library.

Bibliographic information published by the Deutsche Nationalbibliothek
The Deutsche Nationalbibliothek lists this publication in the Deutsche Nationalbibliografie; detailed bibliographic data are available on the Internet at <http://dnb.d-nb.de>.

Cover Design Adam Design, Weinheim
Typesetting Laserwords Private Limited, Chennai, India
Printing and Binding betz-druck GmbH, Darmstadt

Printed in the Federal Republic of Germany
Printed on acid-free paper

ISBN: 978-3-527-32543-6

Set ISBN: 978-3-527-32875-8

Contents

Ideas in Chemistry and Molecular Sciences: Advances in Nanotechnology, Materials and Devices.
Edited by Bruno Pignataro

ISBN: 978-3-527-32543-6

Preface

The idea of publishing books based on contributions given by emerging young chemists arose during the preparations of the first EuCheMs (European Association for Chemical and Molecular Sciences) Conference in Budapest. In this conference, I cochaired the competition for the first European Young Chemist Award aimed at showcasing and recognizing the excellent research being carried out by young scientists working in the field of chemical sciences. I then proposed to collect in a book the best contributions from researchers competing for the Award.

This was further encouraged by EuCheMs, SCI (Italian Chemical Society), RSC (Royal Society of Chemistry), GDCh (Gesellschaft Deutscher Chemiker), and Wiley-VCH and brought out in the book ''Tomorrow's Chemistry Today'' edited by myself and published by Wiley-VCH.

The motivation gained by the organization from the above initiatives was, to me, the trampoline for co-organizing the second edition of the award during the second EuCheMs Conference in Torino. Under the patronage of EuCheMs, SCI, RSC, GDCh, the Consiglio Nazionale dei Chimici (CNC), and the European Young Chemists Network (EYCN), the European Young Chemist Award 2008 was again funded by the Italian Chemical Society.

In Torino, once again, I personally learned a lot and received important inputs from the participants about how this event can serve as a source of new ideas and innovations for the research work of many scientists. This is also related to the fact that the areas of interest for the applicants cover many of the frontier issues of chemistry and molecular sciences (see also *Chem. Eur. J.* 2008, **14**, 11252–11256). But, more importantly, I was left with the increasing feeling that our future needs for new concepts and new technologies should be largely in the hands of the new scientific generation of chemists.

In Torino, we received about 90 applications from scientists (22 to 35 years old) from 30 different countries all around the world (*Chem. Eur. J.* 2008, **14**, 11252–11256).

Most of the applicants were from Spain, Italy, and Germany (about 15 from each of these countries). United Kingdom, Japan, Australia, United States, Brazil, Morocco, Vietnam, as well as Macedonia, Rumania, Slovenia, Russia, Ukraine, and most of the other European countries were also represented. In terms of applicants, 63% were male and about 35% were PhD students; the number of

Ideas in Chemistry and Molecular Sciences: Advances in Nanotechnology, Materials and Devices.
Edited by Bruno Pignataro

ISBN: 978-3-527-32543-6

postdoctoral researchers was only a small percentage, and only a couple of them came from industry. Among the oldest participants, mainly born between 1974 and 1975, several were associate professors or researchers at universities or research institutes and others were lecturers, assistant professors, or research assistants.

The scientific standing of the applicants was undoubtedly very high and many of them made important contributions to the various symposia of the 2nd EuCheMs Congress. A few figures help to substantiate this point. The, let me say, ''*h* index'' of the competitors was 20, in the sense that more than 20 applicants coauthored more than 20 publications. Some patents were also presented. Five participants had more than 35 publications, and, *h* indexes, average number of citations per publication, and number of citations, were as high as 16, 35.6, and 549, respectively. Several of the papers achieved further recognition as they were quoted in the reference lists of the young chemists who were featured on the covers of top journals. The publication lists of most applicants proudly noted the appearance of their work in the leading general chemistry journals such as *Science*, *Nature*, *Angewandte Chemie*, *Journal of the American Chemical Society*, or the best niche journals of organic, inorganic, organometallic, physical, analytical, environmental, and medicinal chemistry.

All of this supported the idea of publishing a second book with the contributions of these talented chemists.

However, in order to have more homogeneous publications and in connection with the great number of interesting papers presented during the competition, we decided to publish three volumes.

This volume represents indeed one of the three edited by inviting a selection of young researchers who participated in the European Young Chemist Award 2008. The other two volumes concern the different areas of synthetic chemistry and life sciences and are entitled ''Ideas in Chemistry and Molecular Sciences: Advances in Synthetic Chemistry'' and ''Ideas in Chemistry and Molecular Sciences: Where Chemistry Meets Life,'' respectively.

It is important to mention that the contents of the books are a result of the work carried out in several topmost laboratories around the world both by researchers who already lead their own group and by researchers who worked under a supervisor. I would like to take this occasion to acknowledge all the supervisors of the invited young researchers for their implicit or explicit support to this initiative that I hope could also serve to highlight the important results of their research groups.

The prospect of excellence of the authors was evident from the very effusive recommendation letters sent by top scientists supporting the applicants for the Award.

A flavor of these letters is given by the extracts from some of the sentences below:

''The original studies of the candidate shed light on extremely important fundamental facets of the chemistry and physics of inorganic materials, such as the hitherto unknown relationship between their structure and their chemical and physical properties. The candidate outstanding contribution in this field is testified by the extraordinary level of publication.'' ''I am particularly glad to express my esteem for this candidate and for the scientific work has performed during the PHD in my Lab.'' ''A first-rate and enthusiastic young chemist with a strong

publication record.'' ''This candidate has a great scientific creativity.'' ''I write in the strongest possible support of candidate nomination. He was without doubt the most productive coworker I have ever had the pleasure of working with. The candidate intense curiosity about chemical reactivity, the fierce determination to make projects succeed, the matchless skill at the bench, and the sharp eye for opportunities across boundaries allowed candidate to pioneer several new areas of investigation.'' ''Pioneering work sparked intense interest worldwide. More than 500 papers have been published in the area in just the past four years.'' ''Extraordinarily careful, very well documented, and utterly reliable.'' ''A revolution enabled by the candidate pioneering work.'' ''The candidate career trajectory is clearly on a very steep incline.'' He is an emerging leader in chemistry.'' ''He is one of the finest scientists I have ever been associated with.'' ''I was always impressed by the candidate enthusiasm in dreaming and doing chemistry.'' ''He is a hard working researcher and intellectually sharp.'' ''I had a very positive impression of the candidate ability to enter new fields, to grab the essential from the very beginning and develop own ideas.'' ''The candidate intellectual and scientific abilities are at the highest possible level. Has established scientific collaboration with various research groups around the world. (15 countries mentioned). '' ''I was always impressed because candidate idea was very clear and the design was beautiful.'' ''As a PhD student the candidate has shown tremendous intellectual capacity. He has been determined and thorough in his pursuit of research goals, and has shown great maturity and responsibility in working with a number of collaborators and in leading experimental teams working at major facilities. Throughout the work candidate has shown great capacity for independent thought and has strongly influenced the development of a highly successful and multifaceted project.'' ''The candidate has made vital and highly significant contributions to projects being undertaken by other members of my research group. In summary this researcher has accomplished a very significant body of first-rate work.'' ''The candidate has been at the forefront of all the projects not only in the amount of work undertaken but in providing and developing ideas.'' ''The candidate has been very much an exemplary example of a European chemist, studying and working in different countries.'' ''He has extra-ordinary intelligence and hard-working nature. This helps him very much to solve most of the issues emerging during the research work in a self-reliant way.''

The contributions of various young scientists, which have been collected in this volume, range from the preparation of new materials to the description of new characterization methods, to the understanding of properties and functions of the materials including simulation of the properties of materials by advanced computational analysis, to materials and materials application in advanced devices. The authors have been stimulated to present the state of the art of their particular fields of research, to describe some highlights of their work and, most importantly, to provide a glimpse into the future by giving their views about future scenarios.

With regard to the area of preparation, the first chapter, by Brea *et al.*, is dedicated to the illustration of aspects of the supramolecular chemistry of cyclic peptides, which, under appropriate conditions, stack through hydrogen bonds to form nanotubes. These nanostructures are being actively investigated because of

their potential applications in different fields such as chemistry, medicine, biology, pharmacology, and materials science. Future research work will be directed to the preparation of self-assembling α,γ-peptide nanotubes with desirable tunable properties employing the methodology described in the chapter. One of the main interests of the authors is the use of these nanotubes in potential applications such as in storage of gases and liquids, selective transport of a wide variety of molecules, energy conversion, and catalysis. The authors also envisage the use of larger diameter nanotubes as novel drug delivery systems.

The second chapter (Luque) in this section describes the preparation of nanoparticles and the application of supported metal nanoparticles on porous materials mainly for the production of catalysts and biofuels. A variety of such systems can now be synthesized through different preparation routes and supports with tailored size and distribution, thus overcoming the limitations of traditional synthetic methodologies.

Another chapter (Diaz-Diaz) deals with click chemistry and suggests that this practice should be helpful at least to create stronger adhesives for both metal and nonmetal surfaces, to enhance the stability of a number of industrial viscoelastic soft materials to great levels while keeping their functional integrity, as well as to fabricate optoelectronic devices. The same chapter suggests the expansion of the click-chemistry toolbox with the use of alternative reactions that could overcome the limitations of those based on the traditional CuAAC process.

Supramolecular receptors for fullurenes is the theme of the next chapter by Fernandez Gustavo *et al*. The authors show that an alternative to classic flexible hosts such as calixarenes or cyclodestrins can be the planar recognition motifs, whose foremost exponents are the porphyrins, while curved and, in most cases, electroactive recognition motifs like 2-[9- (1,3-dithiol-2-ylidene)antracen-10(9H)-ylidene]-1,3-dithiole (exTTF)or truxene TTF-based receptors fulfill the advantages of both classic and planar receptors. The properties of these TTF derivatives are such that they can be considered as optimal candidates in the design of valuable materials for optoelectronics.

The contribution on interaction and reactions of halogens (Espallargas) falls in the same area of supramolecular approach. The chapter summarizes the potentiality of halogen atoms to act as either nucleophiles or electrophiles depending on their coordination environment.

C–X$\cdots$X′–M halogen bonds find interest in the creation of smart materials based on supramolecular architectures. In particular, the application of these concepts to gas sorption is reported.

The second section of the book deals with new tools in the characterization area of materials and nanomaterials. In the first contribution, Baccile discusses the applications of advanced solid-state NMR techniques in the study of surface, interfaces, and structural features of the nanomaterials themselves. Then, the chapter by Gruene *et al*. focuses on the infrared multiple-photon dissociation spectroscopy, which is shown to be particularly effective for the study of the geometries of bare silicon and doped silicon free nanoparticles through the study

of their complexes with loosely bound rare-gas atoms. This study, in particular, reports on the possibility to influence the geometry of silicon-based nanoparticles.

The potentiality of the recently introduced X-ray magnetic circular dichroism technique in the area of single-molecule magnets is underlined in the following chapter by Mannini.

This section finally deals with evolving analytical techniques based on the usage of tools not commercially available such as the X-ray diffraction method (Naumov), which can provide invaluable information on dynamic processes in the bulk state of ordered solid materials. The same contribution underlines the importance of other X-ray-based methods to study processes in the time domain, both in solid-state and in solution such as X-ray scattering at picoseconds scale and X-ray absorption spectroscopy.

The third section, Understanding properties and function of materials, begins with the chapter (Reitmeir *et al.*) dealing with transport in an important class of materials such as zeolites. This contribution fills the gaps in the understanding of diffusion and sorption on zeolites and the origin of shape selectivity.

Taking into account the important contribution of supercomputing in the understanding of the behavior and properties of the materials, a contribution also in this area was considered a must. The specific contribution by Greenwell refers to the modeling of organic–mineral interaction. The chapter deals in particular with some interesting properties of layered structures and their intercalation, as well as with the possible applications. Electronic structure calculations or large-scale molecular dynamics simulations on these systems are expected to contribute to a vast spectrum of areas such as those of petroleum-forming conditions, biofuel green diesel, origin of life, as well as biodegradable packaging design.

The final section of this book deals more with applications including the area of innovative devices. This section contains a specific contribution by Baglio *et al.* on the direct methanol fuel cells (DMFC). In this chapter, the status of the technology and perspectives for portable applications of this type of device are reviewed. The contribution underlines that applications of DMFC in portable power sources cover the spectrum of cellular phones, personal organizers, laptop computers, military back power packs, and so on, and that for some applications, this tool may be very competitive with respect to the most advanced type of rechargeable batteries based on lithium ion.

The following chapter by Sommer *et al.* describes new strategies to direct the nanomorphology of bulk-heterojunctionsolar cells. In this regard, they propose a block copolymers approach, which is very promising in the design of new materials and material combinations for the next generation of organic solar cells as also in improving the energy conversion efficiency of these devices.

Some other contributions refer to materials that are suggested in order to improve performances of present devices. In one of these (Gil Ibanez, Draper), copper complexes are suggested as materials of interest in the solar-energy conversion area. The problem of improving the current lifetimes, intensities, and emission quantum yields of Cu complexes is underlined. Furthermore, device stability and light output are still issues that need to be addressed in order to fully exploit these

low-cost systems. In spite of this, the authors believe that there is the ''the need to turn from oil and to switch on The Copper Age!'' Besides this, the potentiality of single-molecule magnets as potential memory elements organized on well-suited surfaces is explored in the above-mentioned chapter by Mannini. The area of spintronics might receive a fresh impetus by research of the type reported therein. The last chapter highlights, in particular, the prospects for developing fundamental research on single-molecule magnets for single-molecule devices in a bottom-up approach.

On the other hand, the top-down approach is used in another contribution (Nunes). This approach faces the very important problem of sculpturing nanometric patterns. Some suggestions are given on what to do in order to take lithography beyond the 22-nm node for the future device fabrication.

Probably, all those who read this book will have their own opinions on what is relevant for the future of materials chemistry and nanotechnology, and, in this regard, I would like to clarify that, owing to its peculiar genesis, this book reflects the opinions of a select group of young chemists and does not pretend to cover the whole area of emerging materials chemistry and nanotechnology.

The main aim is just to offer a variety of individual, though-provoking views that will possibly provide attractive insights into the minds and research ideas of the next generation of chemical and molecular scientists.

Starting from this point, I hope that the many ideas that can be grasped from the various contributions by the young authors of the book should be very useful in helping the chemistry and molecular science take several steps forward in increasing our knowledge of the molecular world and for better exploiting such knowledge in present and future applications.

I cannot end this preface without acknowledging all the authors and the persons who helped me in the book project together with all the societies (see the book cover) that motivated and sponsored the book. I'm personally grateful to Professors Giovanni Natile, Francesco De Angelis and Luigi Campanella for their motivation and support in this activity.

Palermo, October 2009 *Bruno Pignataro*

List of Contributors

Vincenzo Antonucci
CNR-Istituto di Tecnologie
Avanzate per l'Energia
''Nicola Giordano'' (ITAE)
Via Salita S. Lucia sopra
Contesse 5
I-98126 Messina
Italy

Antonino S. Aricò
CNR-Istituto di Tecnologie
Avanzate per l'Energia
''Nicola Giordano'' (ITAE)
Via Salita S. Lucia sopra
Contesse 5
I-98126 Messina
Italy

Niki Baccile
Collège de France
Laboratoire de Chimie de la
Matière Condensée de Paris
11 Place Marcelin Berthelot
75005 Paris
France

Vincenzo Baglio
CNR-Istituto di Tecnologie
Avanzate per l'Energia
''Nicola Giordano'' (ITAE)
Via Salita S. Lucia sopra
Contesse 5
I-98126 Messina
Italy

Roberto J. Brea
Universidad de Santiago de
Compostela
Departamento de Química
Orgánica, Facultad de Química
Avenida de las Ciencias
s/n, 15782–Santiago de
Compostela, A Coruña
Spain

David DíazDíaz
Dow Europe GmbH Dow
Chemical Company
Bachtobelstr. 3
CH 8810 Horgen
Switzerland

Sylvia M. Draper
University of Dublin
Trinity College
School of Chemistry
Dublin 2
Ireland

Ideas in Chemistry and Molecular Sciences: Advances in Nanotechnology, Materials and Devices.
Edited by Bruno Pignataro

ISBN: 978-3-527-32543-6

Gustavo Fernández
Departamento de Química Orgánica
Facultad de Ciencias Químicas
Avenida Complutense s/n
E-28040-Ciudad Universitaria-Madrid
Spain

and

Ciudad Universitaria de Cantoblanco
IMDEA-Nanociencia, Faculted de Ciencias
Módulo C-IX, 3ª planta, Avenida Francisco Tomás y Valiente, 7
E-28049 Madrid
Spain

André Fielicke
Fritz-Haber-Institut der Max-Planck-Gesellschaft
Faradayweg 4-6
D-14195 Berlin
Germany

Hugh Christopher Greenwell
Durham University
Department of Chemistry
Addison Wheeler Fellow
South Road, Durham DH1 3LE
UK

Belén Gil
University of Dublin
Trinity College
School of Chemistry
Dublin 2
Ireland

Philipp Gruene
Fritz-Haber-Institut der Max-Planck-Gesellschaft
Faradayweg 4-6
D-14195 Berlin
Germany

Sven Hüttner
Universität Bayreuth
Angewandte Funktionspolymere
Universitätsstrasse 30
95440 Bayreuth
Deutschland

and

University of Cambridge
Department of Physics
Cavendish Laboratory
11 J.J. Thomson Avenue
Cambridge CB3 0HE
United Kingdom

Andreas Jentys
TU München, Technische Chemie 2
Lichtenbergstrasse 4
D-85747 Garching
Germany

Johannes A. Lercher
TU München, Technische Chemie 2
Lichtenbergstrasse 4
D-85747 Garching
Germany

Peter Lievens
Katholieke Universiteit Leuven
Laboratorium voor
Vaste-Stoffysica en Magnetisme &
INPAC-Institute for Nanoscale
Physics and Chemistry
Celestijnenlaan 200D
B-3001 Leuven
Belgium

Rafael Luque
The University of York
Green Chemistry Centre of
Excellence, YO10 5DD
Heslington, York,
UK

and

Universidad de Córdoba
Departamento de Química
Orgánica
Campus de Rabanales, Edificio
Marie Curie (C-3), Ctra Nnal IV-A
14014 km 396
Córdoba
Spain

Jonathan T. Lyon
Fritz-Haber-Institut der
Max-Planck-Gesellschaft
Faradayweg 4-6
D-14195 Berlin
Germany

Matteo Mannini
Università degli Studi di Firenze
Dipartimento di Chimica
Laboratory for Molecular
Magnetism–LAMM
Florence INSTM Research Unit
Florence ISTM-CNR Territorial
Research Unit
Lastruccia 3
I-50019 Sesto Fiorentino, Firenze
Italy

Nazario Martán
Departmento de Química
Orgánica
Faculated de Ciencias Químicas
Avenida Complutense s/n
E-28040- Ciudad Universitaria-
Madrid
Spain

and

Ciudad Universitaria de
Cantoblanco
IMDEA-Nanociencia, Facultad de
Ciencias
Módulo C-IX, 3ª planta, Avenida
Francisco Tomás y Valiente, 7
E-28049 Madrid
Spain

Gerard Meijer
Fritz-Haber-Institut der
Max-Planck-Gesellschaft
Faradayweg 4-6
D-14195 Berlin
Germany

Guillermo Mínguez Espallargas
Universidad de Valencia
Instituto de Ciencia Molecular
Poligono de la Coma s/n
46980, Paterna
Spain

Pančе Naumov
Osaka University
Graduate School of Engineering
Department of Material and Life Science
2-1 Yamada-oka
Suita, Osaka
Japan

and

Institute of Chemistry
Faculty of Science
SSCyril and Method ius University
Arhimedova 5
PO Box 162
HK-1000 Skopje
Macedonia

Rui M. D. Nunes
University of Coimbra
Chemistry Department
Rua Larga 3049-535, Coimbra
Portugal

Stephan J. Reitmeier
TU München,
Department für chemie
Lehrstuhl für
Technische Chemie 2
Lichtenbergstrasse 4
D-85747 Garching
Germany

Luis Sánchez
Departmento de Química Orgánica
Faculated de Ciencias Químicas
Avenida Complutense s/n
E-28040- Ciudad Universitaria-Madrid
Spain

and

Ciudad Universitaria de Cantoblanco
IMDEA-Nanociencia, Facultad de Ciencias
Módulo C-IX, 3ª planta, Avenida Francisco Tomás y Valiente, 7
E-28049 Madrid
Spain

Michael Sommer
Universität Bayreuth
Angewandte Funktionspolymere
Universitätsstrasse 30
95440 Bayreuth
Deutschland

Mukundan Thelakkat
Universität Bayreuth
Angewandte Funktionspolymere
Universitätsstrasse 30
95440 Bayreuth
Deutschland

Part I
Preparation of New Materials and Nanomaterials

Ideas in Chemistry and Molecular Sciences: Advances in Nanotechnology, Materials and Devices.
Edited by Bruno Pignataro

ISBN: 978-3-527-32543-6

1
Self-Assembling Cyclic Peptide-Based Nanomaterials

Roberto J. Brea

1.1
Introduction

Over the last years, considerable efforts have been devoted to the design, preparation, and characterization of structures on the sub-100 nanometer scale, and their use as novel functional materials and devices [1]. Nanotubes are extremely attractive as potential building blocks for various applications – sometimes inspired by the remarkable functions of natural tubular structures – in fields including catalysis, drug delivery, optics, electronics, chemotherapy, and transmembrane transport, because their physical and chemical properties are tunable via control of their size and shape [2].

Although great advances have been made in the area of covalently bonded nanostructures [3], noncovalently bonded nanotubes offer significant advantages, including high synthetic convergence, built-in error correction, control through unit design, and self-organization [4]. Self-assembling peptide nanotubes (SPNs) [5] formed by stacking cyclic peptides stabilized by hydrogen bonds have attracted special attention because of the probable ease with which they may be endowed with structural and functional properties (Figure 1.1). Suitable peptides are those in which the cyclic unit can adopt a flat conformation with all the amino side chains having a pseudo-equatorial outward-pointing orientation and the carbonyl and amino groups of the peptide bonds oriented perpendicular to the ring. This approach has two crucial advantages over all others that have so far been tried: first, the size of the polypeptide units, and hence the internal diameter of the nanotube, is easily controlled by varying the number of amino acid residues in each ring; and secondly, the external properties of the peptide nanotube can easily be modified by varying the amino acid side chains. Appropriate design of the cyclic unit and optimization of conditions for self-association allow the properties of the resulting tubular nanostructures to be tailored for specific applications.

Ideas in Chemistry and Molecular Sciences: Advances in Nanotechnology, Materials and Devices.
Edited by Bruno Pignataro

ISBN: 978-3-527-32543-6

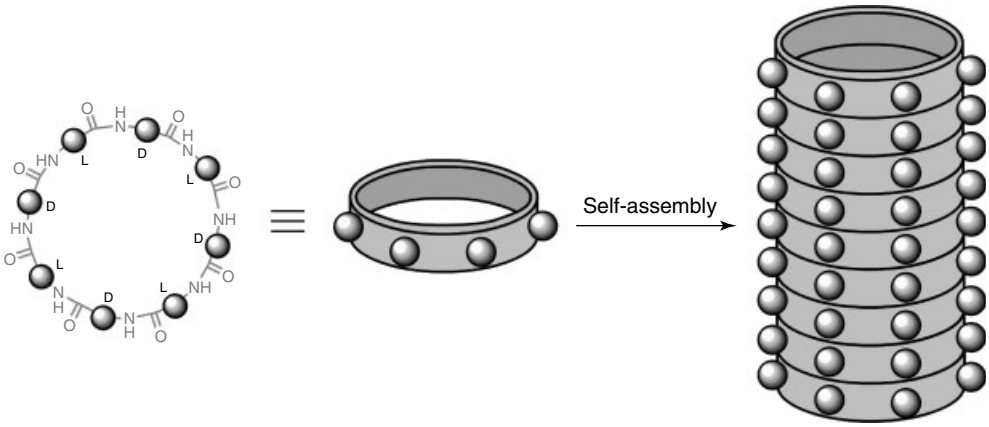

Figure 1.1 Schematic representation of nanotube assembly from cyclic peptides.

1.2
Types of Self-Assembling Cyclic Peptide Nanotubes

1.2.1
Nanotubular Assemblies from Cyclic D,L-α-Peptides

In 1974, within the context of a theoretical analysis of regular enantiomeric peptide sequences, De Santis *et al*. concluded that peptides comprised of an even number of alternating D- and L-amino acids would form closed rings capable of stacking through backbone–backbone hydrogen bonding [6]. Initial attempts to experimentally demonstrate this type of tubular construct were inconclusive because of the poor solubility of the peptides employed [7]. However, in 1993, Ghadiri and coworkers took advantage of a strategy based on pH-variation to control the nanotube formation [8].

1.2.1.1 Solid-State Ensembles: Microcrystalline Cyclic Peptide Nanotubes

The first well-characterized peptide nanotube was prepared using the sequence of octapeptide *cyclo*-[(L-Gln-D-Ala-L-Glu-D-Ala)$_2$], which was chosen to impart solubility in basic aqueous solution, where coulombic repulsion among its negatively charged carboxylate side chains would prevent premature subunit association [8]. Controlled acidification produced microcrystalline aggregates that were fully characterized by transmission electron microscopy (TEM), Fourier transform infrared (FT-IR) spectroscopy, electron diffraction, and molecular modeling. These analyses convincingly established the expected structure in which the ring-shaped subunits stack through antiparallel β-sheet hydrogen bonding to form ordered hollow tubes with internal diameters of 7.5 Å and distances of 4.73 Å between ring-shaped subunits (Figure 1.2).

Proton-triggered self-assembly described above also allowed the preparation of microcrystalline aggregates of nanotubular structures with an internal diameter of 13 Å composed of dodecapeptide *cyclo*-[(L-Gln-D-Ala-L-Glu-D-Ala-)$_3$] units, which

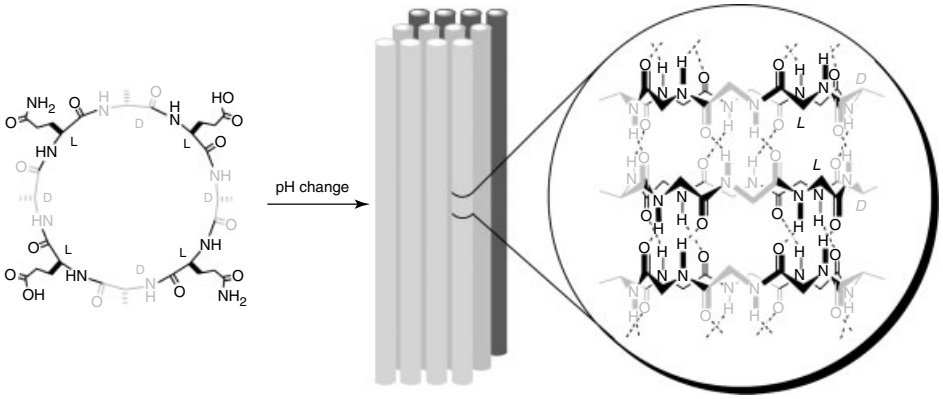

Figure 1.2 Proton-controlled self-assembly process for the preparation of cyclic D,L-α-peptide microcrystals.

confirmed that the internal diameter of the nanotube could be controlled just by varying the number of amino acid residues in the peptide ring [9]. More recently, Lambert *et al*. have employed an analogous pH-controlled self-assembly strategy to synthesize microcrystalline nanotubular structures from a cyclic D,L-α-octapeptide containing bis-aspartic acid units [10].

Ghadiri and coworkers have also prepared solid-state assemblies using various uncharged cyclic D,L-α-octapeptides to explore the effects of intertubular hydrophobic packing interactions on crystal formation [11]. Cryoelectron microscopy, FT-IR spectroscopy, and electron diffraction analyses have shown the expected nanocylindrical ensembles with all the characteristic features of an antiparallel β-sheet-type structure and intersubunit distances of about 4.8 Å.

1.2.1.2 Solution Phase Studies of Dimerization

The association of cyclic peptides has been recently investigated in water by Karlström and Undén using fluorescence-quenching methods, which confirmed that such ring–ring association also occurs in solution and is not just a consequence of crystallization [12]. In order to obtain a better understanding of these stacking interactions, dimeric motifs were designed and studied in which complications associated with unlimited stacking are avoided by allowing only the formation of the corresponding two-ring structures (Figure 1.3). Such minimal models have been achieved by selective backbone N-alkylation of one face of the peptide ring. In 1994, Lorenzi *et al*. reported a crystallographic study of the hemi-N-methylated hexapeptide *cyclo*-[(D-Leu-L-^{Me}N-Leu-)$_3$], providing the expected dimeric antiparallel β-sheet structure in the solid state, while nuclear magnetic resonance (NMR) investigations revealed that the peptide dimerized in deuterochloroform with an association constant (Ka) of 80 M^{-1} [13]. Independent work carried out by Ghadiri and coworkers demonstrated analogous dimerization results by octapeptide *cyclo*-[(L-Phe-D-^{Me}N-Ala-)$_4$], but in this case the association constant values were higher (2540 M^{-1}) [14]. Additionally, they establish that cyclic

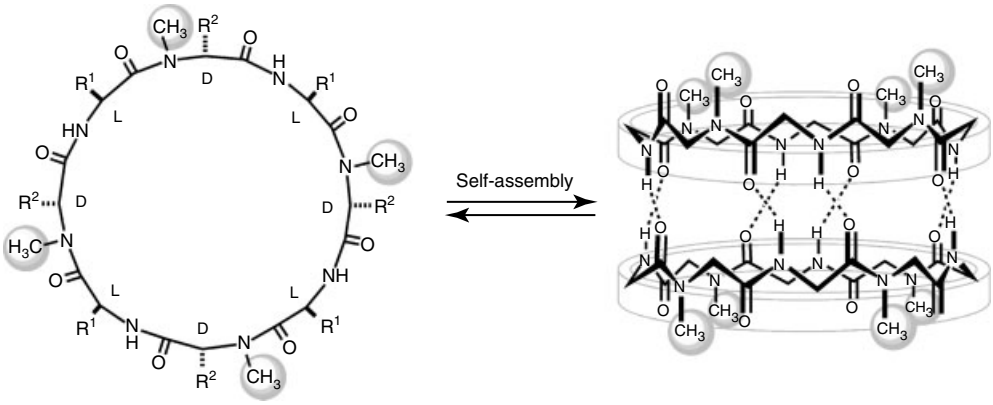

Figure 1.3 Schematic illustration of a dimeric structure composed of cyclic D,L-α-octapeptides.

octapeptides exhibit optimal rigidity and predisposition for nanotube assembly. However, cyclic D,L-α-deca- and -dodecapeptides fail to dimerize because of the difficulty in adopting the required flat conformation [12, 14].

Studies of side chain–side chain interactions have shown that cyclic peptides containing branched side chains are more favorable for dimerization than unbranched chains, presumably by predisposing the peptide backbone for β-sheet adoption. Additionally, aromatic side chain–side chain interactions in cyclic peptide units containing homophenylalanine residues were used to induce crystal growth through the prevalent effect of dimer formation [15]. Dimeric structures have also provided the first experimental model system for evaluation of the relative stability of parallel and antiparallel β-sheet structures [16]. Measurement of solution equilibrium constants using the enantiomeric cyclic peptides *cyclo*-[(L-Phe-D-^{Me}N-Ala-)$_4$] and *cyclo*-[(D-Phe-L-^{Me}N-Ala-)$_4$] revealed that antiparallel orientation is favored over parallel orientation by 0.8 kcal·mol^{-1}. Further confirmation of β-sheet-type hydrogen bonding was obtained by covalent consolidation of noncovalently constituted cyclic peptide dimers [17, 18].

1.2.2
Nanotubular Assemblies from Cyclic β-Peptides

The first designs of peptide nanotubes composed of all β-amino acids were developed by Seebach [19]. Molecular modeling and X-ray analysis showed that in the solid state, cyclic tetrapeptides composed of chiral β^3-amino acids can adopt flat-ring conformations and stack to form nanotubular structures in the same way as previously described for cyclic D,L-α-peptides (Figure 1.4). In the case of β-peptides, such conformation can be achieved with cyclic peptide units composed of homochiral β-amino acid residues as well as with rings of residues of alternating chirality. Extensive studies demonstrated that *cyclo*[(β^3-HAla)$_4$] adopted

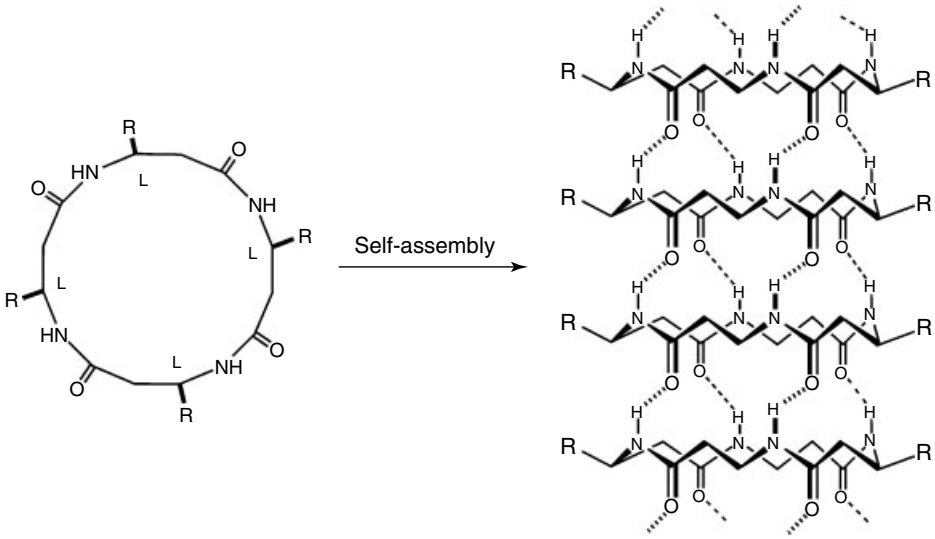

Figure 1.4 Self-assembly of cyclic β-peptides as a nanotube.

a flat conformation and each subunit stacked through four hydrogen-bonding interactions, presenting an inner pore with a diameter of approximately 2.6 Å.

Ghadiri *et al*. also studied the self-assembly process of several cyclic β^3-peptides, especially due to their application in lipid bilayers to form efficient ion channels [20]. More recently, Kimura and coworkers have reported the design, synthesis, and conformation of a novel class of cyclic β-peptides constituted by sugar units [21].

1.2.3
Nanotubular Assemblies from Other Cyclic Peptides

Over the last few years, several cyclic peptide rings composed of novel unnatural amino acid residues have been developed as potential basic units for nanotube construction. Dory *et al*. have recently synthesized a cyclic tripeptide that crystallized as bundles of nanotubes [22]. This unit is composed of α,β-unsaturated δ-amino acid residues that, because of the trans geometry of the vinyl group, adopt the flat conformation required for self-assembly (Figure 1.5). As the peptide backbone has an even number of atoms between the carbonyl and amino groups of each residue, all the carbonyl groups are oriented in the same direction (as in the β-peptide-based nanotubes), which gives the nanotubular structure a large dipole moment that results in highly anisotropic crystals.

Ghadiri and coworkers reported the design, preparation, and full characterization of a new member of peptide-based macrocycle that incorporates 1,2,3-triazole ε-amino acids in the backbone (Figure 1.5) [23]. The resulting open-ended hollow tubular ensemble combines the structural aspects and capacity for outside surface functionalization and the heterocyclic alterations introduced to modify the physical properties of the inner pore.

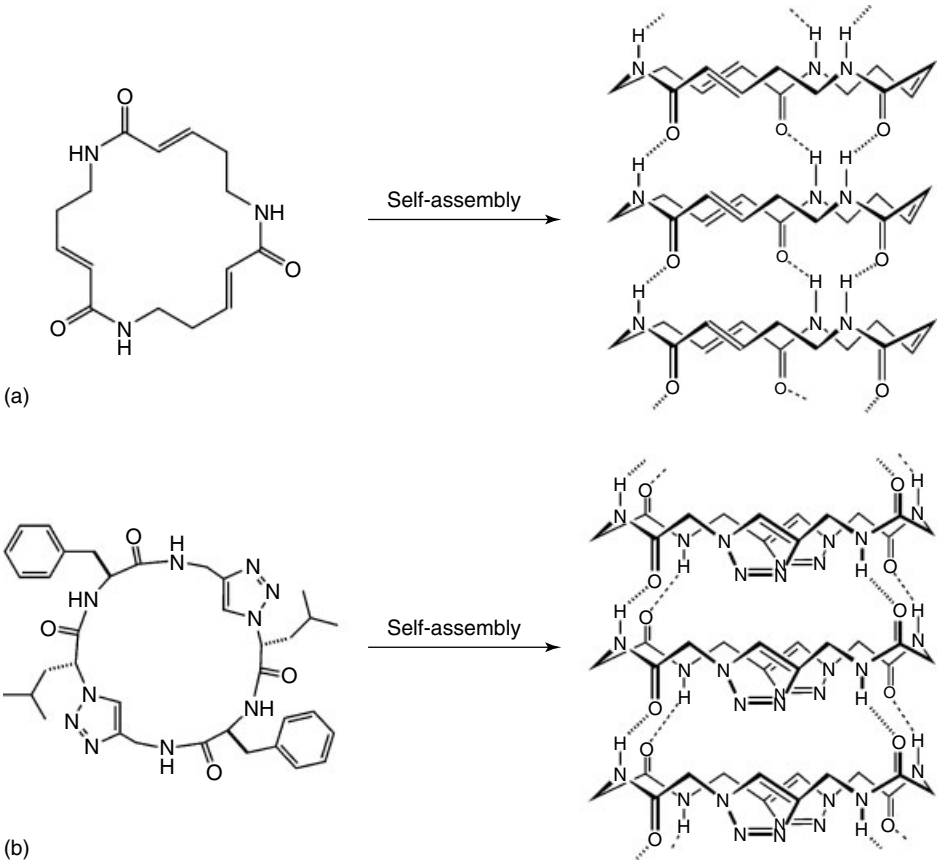

Figure 1.5 Schematic representation of nanotubular structures formed by self-assembly from cyclic δ- and α,ε-peptide units ((a) and (b), respectively).

1.3 Applications of Cyclic Peptide Nanotubes

1.3.1 Antimicrobials

The proliferation of antibiotic-resistant bacteria has intensified the quest for new antibiotics with novel modes of action [24]. Recent approaches include the use of peptide rings capable of stacking in the membrane to form transmembrane pores. In particular, amphipathic cyclic hexa- and octapeptides have been shown to infiltrate the bacterial membrane and associate as nanotubes oriented at an angle of 20° to the membrane plane, causing extensive membrane damage through a carpet-like nanotube formation mechanism (Figure 1.6) [25, 26]. In this model, hydrophobic side chains are inserted into the lipidic

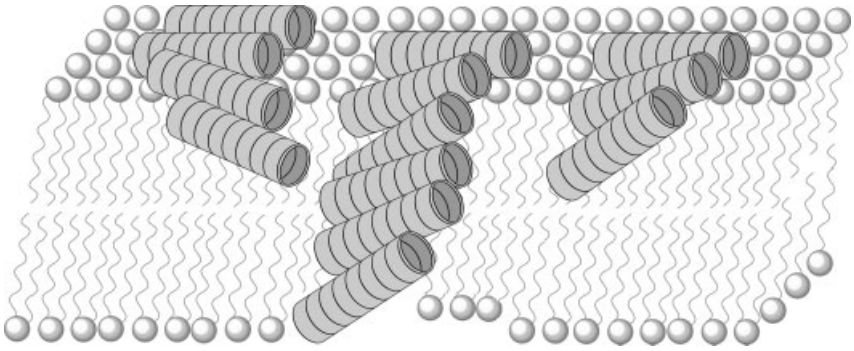

Figure 1.6 Carpet-like mode of action of lethal ion channels based on cyclic peptide nanotubes.

components of the membrane and the hydrophilic residues remain exposed to the hydrophilic components of the cell membrane. An important aspect of this strategy is that cyclic units can be designed to associate as nanotubular structures selectively in bacterial rather than in mammalian membranes. Such peptides exhibit significant antibacterial activity in vitro, and their preferential action against bacterial cells has been demonstrated in mice, which exhibit activity against a broad spectrum of bacteria, including methicillin-resistant *Staphylococcus aureus* (MRSA).

Ghadiri *et al*. also demonstrated that membrane-associating cyclic peptide units effectively block key steps involved in virus entry or escape from endosomes. Toward this goal, these authors developed a directed combinatorial approach to select potentially membrane-active amphiphilic cyclic D,L-α-peptides, exploring their utility in inhibiting adenovirus (Ad) infections in mammalian cells [27]. Their studies also suggested that use of self-assembling cyclic D,L-α-peptides holds considerable potential as a novel rational supramolecular approach toward the design and discovery of broad-spectrum antiviral agents.

1.3.2 Biosensors

Cyclic D,L-α-octapeptide-based nanotubes inserted into organosulfur monolayers supported on gold films have shown the feasibility of diffusion-limited size-selective ion sensing (Figure 1.7) [28]. The functional properties of this nanotubular arrangement were studied by impedance spectroscopy and cyclic voltammetry, showing that small electroactive anions and cations such as $[Fe(CN)_6]^{3-}$ and $[Ru(NH3)_6]^{3+}$ had access to the gold surface, while large ions, such as $[Mo(CN)_8]$,$^{4-}$ did not. Modifications in the cyclic peptide unit, along with the variations in the organosulfur adsorbates, are expected to increase the repertoire of the sensor applications.

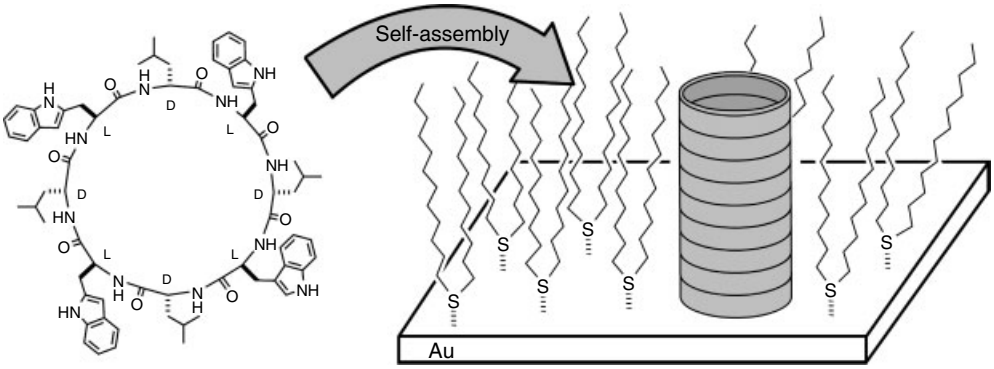

Figure 1.7 Schematic representation of a cyclic peptide-based biosensor inserted into self-assembled organosulfur monolayers supported on gold.

1.3.3 Biomaterials

Biesalski and coworkers recently developed a novel approach to prepare nanometer-sized peptide–polymer hybrid nanostructures, using peptide nanotubes as structurally defined templates (Figure 1.8) [29]. This methodology is based on the self-assembly of cyclic peptides with polymerization initiator groups on distinct side chains to form a nanotubular structure that has the initiator groups exclusively on the outer surface. A subsequent surface-initiated polymerization coats the peptide core with a covalently bound polymer shell. An interesting aspect of this strategy is that defined structural information can be transferred from the peptide nanostructure to the synthetic polymer (and vice versa). Additionally,

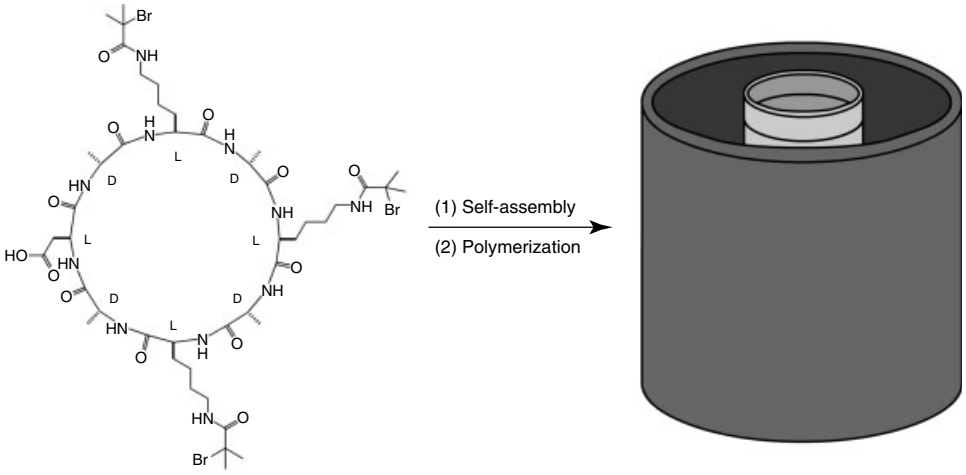

Figure 1.8 Peptide-polymer hybrid nanostructures from cyclic units.

preparation of a large number of shape-persistent hybrid materials that are not easily accessed by any other technique can be easily achieved.

1.3.4
Electronic Devices

The fabrication of nanoscale functional wires by self-assembly has attracted considerable attention in recent years for possible applications to nanoelectronics [30]. In this regard, cyclic peptide nanotubes are one of the most suitable molecular objects because they allow optimal size and length control. Ghadiri and coworkers have recently described a wide collection of eight-residue cyclic D,L-α-peptide units bearing 1,4,5,8-naphthalenetetracarboxylic diimide (NDI) side chains to evaluate their application in the construction of electronic systems [31, 32]. Structural and photoluminescence studies have showed that the hydrogen bond-directed self-assembly of the peptide backbone promotes intermolecular NDI excimer formation, favoring the efficiency of the charge transfer [31]. Additionally, they have also investigated the redox-promoted self-assembly of cyclic octapeptides bearing four cationic NDI residues, obtaining electronically delocalized peptide nanotubes that are hundreds of nanometers in length (Figure 1.9) [32]. This supramolecular approach provides a rational approach for the design and fabrication of electronically active one-dimensional biomaterials with potential utility in optical and electronic devices.

1.3.5
Photoswitchable Materials

Molecules whose physical properties can be reversibly switched using light have been extensively studied because of their great utility in the development of novel

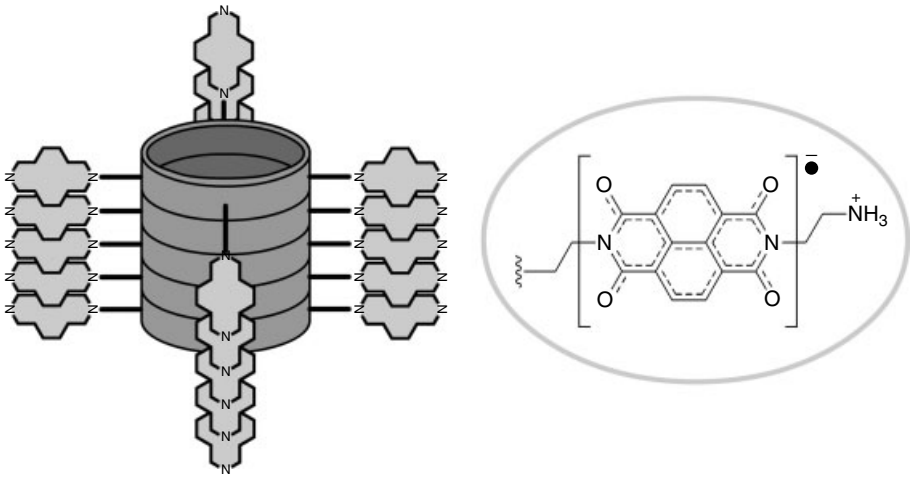

Figure 1.9 Schematic illustration of electronically delocalized cyclic peptide nanotubes.

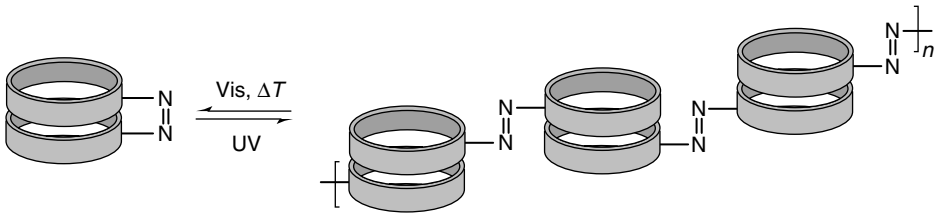

Figure 1.10 Reversible switch system based on azo-linked cyclic peptides.

electronic and/or optical data storage devices [33]. Ghadiri and coworkers recently reported a novel azo-peptide system, in which cyclic D,L-peptide dimers can be *E*/*Z* isomerizated between one state in which the two rings in each dimer are connected covalently by an azobenzene link in the *Z* conformation and another in which the *E* conformation of this link connects neighboring dimers (Figure 1.10) [34, 35]. As expected, reversible switching between inter- and intramolecular hydrogen bonds are permitted both in solution and in thin films at the air–water interface. Intramolecular hydrogen bonding enhanced the stability of the *Z* form, which reveals that the $E \rightarrow Z$ isomerization is the faster process. Further development may lead to smart nanomaterials that could change their macroscopic properties in response to light.

1.3.6
Transmembrane Transport Channels

Naturally occurring transmembrane channels can be mimicked by synthetic peptide nanotubes that are internally hydrophilic and externally endowed with appropriate characteristics [36]. In 1994, Ghadiri and coworkers synthesized *cyclo*-[L-Gln-(D-Leu-L-Trp)$_3$-D-Leu-] units to explore the possibility of self-association in lipid bilayers. Spontaneous assembly into hydrogen-bonded nanotubes was shown by FT-IR spectroscopy, while patch clamp techniques found transport activities for K^+ and Na^+ greater than 10^7 ions/s [37]. Liposome-based proton transport assays, grazing-angle reflection/absorption, and polarized attenuated total reflectance (ATR) analysis of complexes formed from multiple lipid bilayers and peptides have shown that the resulting nanotubes are oriented nearly parallel to the lipid alkyl chains, which supports the model of the peptide nanotubes as the active channel species [38].

These artificial peptide transmembrane channels are naturally size selective. Exhaustive studies have shown that the passage of glucose, which is estimated to require a pore diameter larger than 9 Å, is not allowed by the octapeptide nanotubes described above (internal diameter of approximately 7 Å), while nanotubes composed of decapeptide [L-Gln-(D-Leu-L-Trp)$_4$-D-Leu-] units (internal diameter of 10 Å) display efficient glucose and glutamic acid transport activity [39, 40]. These findings suggest that even larger cyclic peptides may prove useful in the size-selective molecular delivery of pharmacologically active agents.

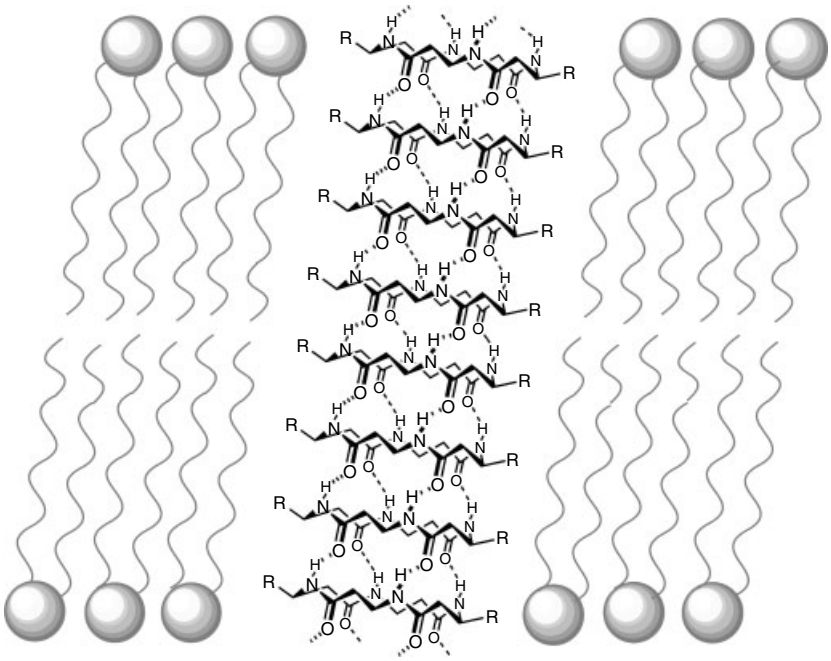

Figure 1.11 Schematic illustration of a cyclic β-peptide nanotube self-assembled in a lipid bilayer.

Like their D,L-α-counterparts, cyclic β^3-peptides can also associate tubewise in lipid bilayers to form channels with K^+ transport rates of 1.9×10^7 ions/s (Figure 1.11) [20]. These channels are anisotropic because all the component subunits of β-peptide nanotubes stack with the same orientation. Application of an electric field should cause all the peptide rings to adopt the correct orientation for stacking into nanotubes.

1.4 Nanotubular Assemblies from Cyclic α, γ-Peptides

SPNs previously described display a wide range of structural and functional capabilities that have enabled their application in biological as well as materials science [5]. Some of their properties depend on the hydrophilic character of the inner pore, which unfortunately is not possible to modify by introducing functional groups on the inner face, because all amino acid side chains pointing outward and additional modification in C_α or C_β would disrupt the nanotube formation process. However, this shortcoming disappears if cyclic α, γ-peptides are used as the basic units for nanotubular assembly.

With a view to favoring adoption of the required all-trans flat conformation, our group have recently been working on the design, synthesis, characterization, and

application of a new class of cyclic peptides in which α-amino acid residues alternate with *cis*-3 aminocycloalkanecarboxylic acids (γ-Acas) [41–49]. The cycloalkane rings of these peptide units not only direct a hydrophobic, functionalizable methylene toward the interior of the cyclic peptide ring (thus allowing manipulation of the behavior of the inner cavity of the corresponding nanotubular structure) but also ensure the flatness and rigidity of the cycloalkane segments of the peptide backbone.

1.4.1 Design

Cyclic peptides in which L-γ-Aca residues alternate with D-α-amino acids adopt a conformation in which the peptide backbone is essentially flat and the carbonyl and amine groups are oriented roughly perpendicular to the plane of the ring (Figure 1.12). This flat ring-shaped conformation facilitates antiparallel β-sheetlike hydrogen bonding between oppositely oriented rings and the formation of hydrogen-bonded nanotubes composed of rings of alternating orientation, in which one face of each ring is hydrogen-bonded via γ-Aca C = O and N–H groups (γ-face) to the similar face of the neighbor ($\gamma-\gamma$ interaction), while the other face is hydrogen-bonded via C = O and N–H groups of the α-amino acid (α-face) to the similar face of the other neighbor ($\alpha-\alpha$ interaction). In such structures, the β-methylene moiety of each cycloalkane is projected into the lumen of the cylinder, creating a partial hydrophobic cavity. In order to establish and evaluate the feasibility and the thermodynamic properties of the corresponding SPNs, dimeric models were prepared.

1.4.2 Homodimers Formation

Hydrogen-bonded homodimers of each of the two types required for nanotubular construction were obtained from cyclic units in which hydrogen bond donation was blocked by selective N-methylation on one face of the ring, preventing the formation of the corresponding peptide nanotubes (Figure 1.12). For this purpose, Granja and coworkers initially synthesized two different patterns of N-methylated cyclic hexapeptides, in which the requisite all-trans conformation is achieved by the alternation of α-amino acids with *cis*-3-aminocyclohexanecarboxylic acid (γ-Ach). First, the authors employed cyclic units with all the α-amino acids N-methylated to study the $\gamma-\gamma$ interaction, showing association constant values of 230 M^{-1}, and establishing that the homodimerization process is enthalpy-driven with a contribution of 2.20 $kJ \cdot mol^{-1}$ per hydrogen bond, which is a value similar to those found for D,L-α-cyclic octapeptides [41]. Secondly, the $\alpha-\alpha$ interaction was analyzed from N-methylated γ-residue-based peptide rings, obtaining high-affinity association (Ka larger than 10^5 M^{-1}) in nonpolar solvents [41]. Crystallographic data of the homodimeric ensemble have corroborated the nanotubular structure. Additionally, the cylindrical cavity presents one molecule of chloroform, confirming

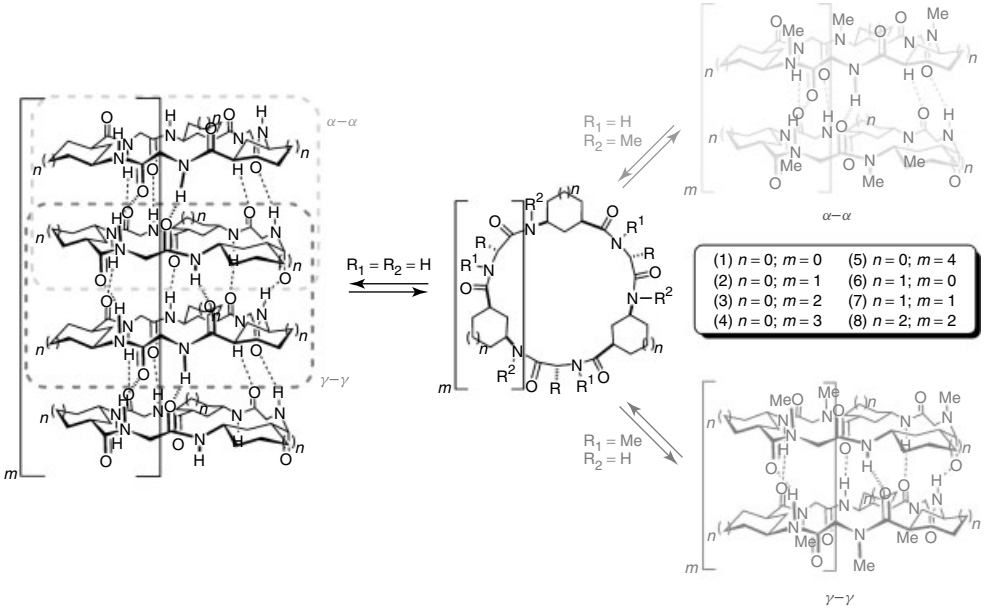

Figure 1.12 Design for self-assembling α, γ-cyclic peptide nanotubes. The two types of hydrogen-bonded patterns involved in nanotube formation are remarked and their corresponding *N*-methylated dimeric models are also shown.

the proposed partial hydrophobic character of the lumen. NMR, FT-IR spectroscopy, and X-ray diffraction studies conclusively confirmed the formation of both these homodimers.

Exhaustive studies were carried out with other rings that differ in the number of amino acids and hence in the internal diameter of the nanotube. Cyclic octapeptides presented similar properties as hexapeptide homologs, showing association constant values of 340 M^{-1} for the $\gamma-\gamma$ interaction and high-affinity association (Ka larger than 10^5 M^{-1}) for the $\alpha-\alpha$ interaction [42]. On the other hand, cyclic tetrapeptides do not self-assemble through their γ-face, and present small association constant values (Ka = 15 M^{-1}) for $\alpha-\alpha$ interaction, suggesting that the rigidity of the 24-membered ring precludes the cyclic unit from adopting the flat conformation required for the self-assembly, which was confirmed by analysis of the corresponding X-ray structure [43, 44].

We recently extended these studies to other γ-Aca by synthesizing *cis*-3-aminocyclopentanecarboxylic acid (γ-Acp) [45] and *cis*-4-aminocyclopent-2-enecarboxylic acid (γ-Ace) [46] from Vince's lactam. Although we initially worked with γ-Ach-based α, γ-cyclic units, we began to use their γ-Acp analogs when we realized that such amino acids can be easily obtained, and more importantly, that the angle defined in the plane of the peptide ring by the C–N and C–C(O) bonds radiating from the cycloalkane ring is wider for γ-Acp than for γ-Ach (147° as

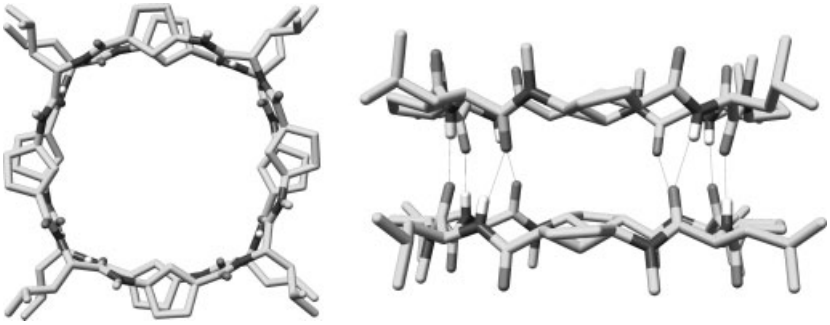

Figure 1.13 Top (a) and side view (b) of the homodimeric supramolecular crystal structure composed of cyclo-[(L-Leu-D-^{Me}*N*-γ-Acp-)$_4$] units.

against 162°). All these features make γ-Acp more suitable for the construction of large self-assembling α,γ-cyclic peptide nanotubes.

Seeking to control the internal diameter of the corresponding nanotubular structures, we have performed the synthesis of tetra- [43, 44], hexa- [45], octa- [47], deca- [47], and dodecapeptides [47] made of alternating α-amino acid and *N*-methyl γ-Acp residues with backbones containing between 16 and 48 atoms and diameter ranging from 4 to 17 Å. All the cyclic units form the expected dimers through their α-face with high-affinity association ($Ka > 10^5\ M^{-1}$) in nonpolar solvents, except for the four-residue γ-Acp-based cyclic peptide in which the association constant was estimated to be 47 M^{-1} [43, 44]. The ability of this kind of peptide rings to form stable nanocylindrical homodimers was confirmed by NMR, FT-IR spectroscopy, and X-ray diffraction data (Figure 1.13).

1.4.3 Heterodimers Formation

Recently, our group reported a novel approach for the design and fabrication of highly stable heterodimeric assemblies based on α,γ-cyclic peptides [45]. The possibility of heterodimer formation was confirmed upon the addition of a cyclic α,γ(Acp)-based peptide to a cyclic α,γ(Ach)-based peptide, which resulted in the appearance in the NMR of a new class of signals corresponding with the heterodimer, which was the most abundant specie in the equilibrium, being about 30 times more stable than the possible homodimers. Conclusive evidence of heterodimerization in the solid state was obtained by X-ray crystallography, showing the expected heterodimeric structure in which the two essentially flat antiparallel peptide subunits are connected in β-sheet fashion through hydrogen bonds (Figure 1.14).

Exhaustive studies also demonstrated that selective formation of the heterodimer is driven mainly by backbone-to-backbone hydrogen-bonded interactions, being

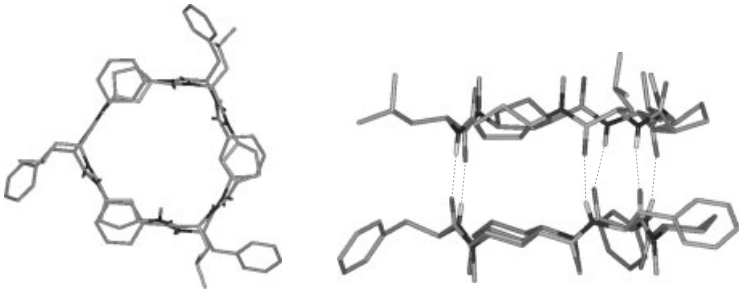

Figure 1.14 Top (a) and side view (b) of the heterodimeric crystal structure obtained from combination of α,γ(Acp)- and α,γ(Ach)-cyclic hexapeptides.

independent of the side chains used. In this regard, the introduction of different functionalities could allow the development of new applications without affecting the self-assembly properties and the heterodimeric structures.

1.4.4 Applications

1.4.4.1 Artificial Photosystems

The design of highly efficient and highly directional electron transfer devices is extremely important for the preparation and development of mimics of the photosynthetic systems of plants and bacteria. In principle, self-assembled peptide nanostructures bearing an appropriate array of photoactive and electroactive units might achieve this goal. In this context, our group described the synthesis and physicochemical properties of a novel class of nanotubular heterodimers in which a cyclic peptide bearing an electron-donor unit (extended tetrathiafulvalene (exTTF)) is coupled by a β-sheet-like hydrogen-bond system to another bearing a photoactive electron-acceptor unit (C_{60}) (Figure 1.15) [48]. Photoexcitation of the fullerene moieties to their 1.76 eV excited state is followed by a charge separation process generating a 1.15 eV radical ion pair state. On average, this state perdures for at least 1.5 μs, which is superior to that of typical covalent C_{60}-exTTF conjugates. These peptide templates can be successfully used to form light-harvesting/light-converting hybrid ensembles with a distinctive organization of donor and acceptor units able to act as efficient artificial photosystems, optical devices, and/or molecular switches.

1.4.4.2 Multicomponent Networks: New Biosensors

One of the most fundamental problems in the field of supramolecular chemistry is the control of self-assembly processes through the design of the molecular components and the practical application at the macromolecular level of such supramolecular associations. In this regard, our group recently reported the design, preparation, and characterization of a novel multicomponent network of pyrene and dapoxyl-derivatized cyclic peptides that display controlled fluorescent

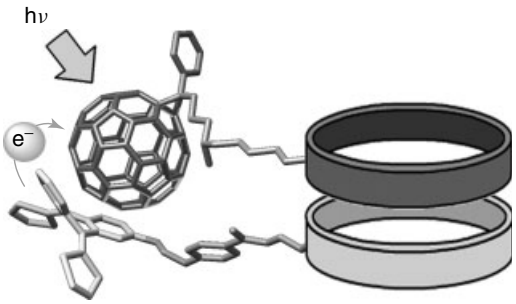

Figure 1.15 Electron transfer nanohybrid system based on α,γ-cyclic peptides.

signal output (Figure 1.16) [49]. The network takes advantage of the large association constant of α,γ-cyclic peptides and the controlled formation of homo- and heterodimers, and makes use of excimer/fluorescence resonance energy transfer (FRET) effects in conjunction to study complex interaction networks. Full characterization of the dynamic processes was achieved using steady-state and time-resolved fluorescence techniques. The first equilibrium studied was the homodimerization of pyrene derivatives, obtaining association constant values of 2.1×10^6 M^{-1}. Additionally, the preference for heterodimer formation between Acp-based and Ach-based cyclic peptides rather than homodimerization was also exploited for the construction of highly efficient FRET systems. This energy transfer is possible because the spectral overlap between dapoxyl absorption and pyrene emission is almost complete, which ensures efficient transfer between the two fluorophores. These preliminary studies are particularly relevant for the development of a new class of biosensors and optical devices, specifically tailored for studying systems involving homo- and heterodimerization processes.

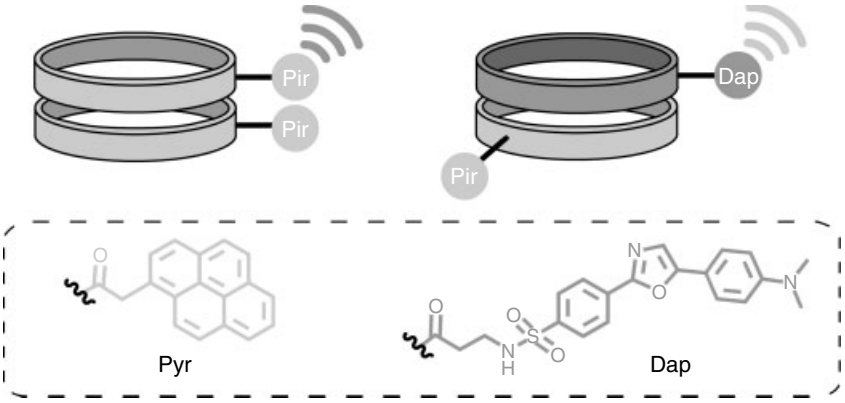

Figure 1.16 Homo- and heterodimeric biosensors from fluorescently derivatized α,γ-cyclic peptides.

1.4.4.3 Other Applications

Cyclic hybrid α,γ-peptide nanotubes are being currently studied because of their ability to modify their inner face properties, which suggests the application of such nanostructures as catalysts, selective ion channels, molecular inclusion devices, and/or porous materials.

1.5 Summary and Outlook

This chapter has fundamentally illustrated various aspects of the supramolecular chemistry of cyclic peptides, which, under appropriate conditions, stack through hydrogen bonds to form nanotubes. Crucial for this interaction is the adoption of a flat conformation in which all the amino acid side chains pointing outward and the carbonyl and amino groups of the peptide bonds are oriented perpendicular to the ring. This conformation can be achieved by peptide rings with a wide variety of residues, paying special attention to cyclic γ-amino acids. In all cases, the corresponding nanotubular ensembles have uniform internal diameters and external surfaces that can be easily endowed with specific properties by side chain modifications. These nanostructures are being actively investigated because of their potential applications in different fields such as chemistry, medicine, biology, pharmacology, and materials science.

Future research work will be directed to the preparation of self-assembling α,γ-peptide nanotubes with desirable tunable properties employing the methodology described above. One of our main interests is the use of those nanotubes in potential applications such as the storage of gases and liquids, selective transport of a wide variety of molecules, energy conversion, and catalysis. We also envisage the use of larger diameter nanotubes as novel drug delivery systems.

References

1. Whitesides, G.M. (2005) Nanoscience, nanotechnology, and chemistry. *Small*, **1** (2), 172–179.
2. Martin, C.R. and Kohli, P. (2003) The emerging field of nanotube biotechnology. *Nat. Rev.*, **2** (1), 29–37.
3. Bong, D.T., Clark, T.D., Granja, J.R., and Ghadiri, M.R. (2001) Self-assembling organic nanotubes. *Angew. Chem. Int. Ed.*, **40** (6), 988–1011.
4. Special issue (2002) Supramolecular chemistry and self-assembly. *Science*, **295** (5564), 2395–2421.
5. Brea, R.J. and Granja, J.R. (2004) Self-assembly of cyclic peptides in hydrogen-bonded nanotubes, in *Dekker Encyclopedia of Nanoscience and Nanotechnology*, 1st edn (eds J.A.Schwarz, C.I. Contescu, and K. Putyera), Marcel Dekker, Inc., New York, pp. 3439–3457.
6. De Santis, P., Morosetti, S., and Rizzo, R. (1974) Conformational analysis of regular enantiomeric sequences. *Macromolecules*, **7** (1), 52–58.
7. Tomasic, L. and Lorenzi, G.P. (1987) Some cyclic oligopeptides with S2n symmetry. *Helv. Chim. Acta*, **70** (4), 1012–1016.
8. Ghadiri, M.R., Granja, J.R., Milligan, R.A., McRee, D.E., and Khazanovich, N. (1993) Self-assembling organic

nanotubes based on a cyclic peptide architecture. *Nature*, **366** (6453), 324–327.
9. Khazanovich, N., Granja, J.R., Milligan, R.A., McRee, D.E., and Ghadiri, M.R. (1994) Nanoscale tubular ensembles with specified internal diameters. Design of a self-assembled nanotube with a 13 Å pore. *J. Am. Chem. Soc.*, **116** (13), 6011–6012.
10. Polaskova, M.E., Ede, N.J. and Lambert, J.N. (1998) Synthesis of nanotube-forming cyclic octapeptides via an Fmoc strategy. *Aust. J. Chem.*, **51** (7), 535–540.
11. Hartgerink, J., Granja, J.R., Milligan, R.A., and Ghadiri, M.R. (1996) Self-assembling peptide nanotubes. *J. Am. Chem. Soc.*, **118** (1), 43–50.
12. Karlström, A. and Undén, A. (1997) Association of cyclic peptides in aqueous solution measured by fluorescence quenching. *Biopolymers*, **41** (1), 1–4.
13. Sun, X.C. and Lorenzi, G.P. (1994) On the stacking of β-rings: the solution self-association behavior of two partially N-methylated cyclo(hexaleucines). *Helv. Chim. Acta*, **77** (6), 1520–1526.
14. Clark, T.D., Buriak, J.M., Kobayashi, K., Isler, M.P., McRee, D.E., and Ghadiri, M.R. (1998) Cylindrical β-sheet peptide assemblies. *J. Am. Chem. Soc.*, **120** (35), 8949–8962.
15. Bong, D.T. and Ghadiri, M.R. (2001) Self-assembling cyclic peptide cylinders as nuclei for crystal engineering. *Angew. Chem. Int. Ed.*, **40** (11), 2163–2166.
16. Kobayashi, K., Granja, J.R., and Ghadiri, M.R. (1995) β -Sheet peptide architecture: measuring the relative stability of parallel vs. antiparallel β-sheets. *Angew. Chem. Int. Ed.*, **34** (1), 95–98.
17. Clark, T.D. and Ghadiri, M.R. (1995) Supramolecular design by covalent capture. Design of a peptide cylinder via hydrogen-bond-promoted intermolecular olefin metathesis. *J. Am. Chem. Soc.*, **117** (49), 12364–12365.
18. Clark, T.D., Kobayashi, K., and Ghadiri, M.R. (1999) Covalent capture and stabilization of cylindrical β-sheet peptide assemblies. *Chem. Eur. J.*, **5** (2), 782–792.
19. Seebach, D., Mathews, J.L., Meden, A., Wessels, T., Baerlocher, C., and McCusker, L.B. (1997) Cyclo-β-peptides. Structure and tubular stacking of cyclic tetramers of 3-aminobutanoic acid as determined from powder diffraction data. *Helv. Chim. Acta*, **80** (1), 173–182.
20. Clark, T.D., Buehler, L.K., and Ghadiri, M.R. (1998) Self-assembling cyclic β3-peptide nanotubes as artificial transmembrane ion channels. *J. Am. Chem. Soc.*, **120** (4), 651–656.
21. Fujimura, F., Horikawa, Y., Morita, T., Sugiyama, J., and Kimura, S. (2007) Double assembly composed of lectin association with columnar molecular assembly of cyclic tri-β-peptide having sugar units. *Biomacromolecules*, **8** (2), 611–616.
22. Gauthier, D., Baillargeon, P., Drouin, M., and Dory, Y.L. (2001) Self-assembly of cyclic peptides into nanotubes and then into highly anisotropic crystalline materials. *Angew. Chem. Int. Ed.*, **40** (24), 4635–4638.
23. Horne, W.S., Stout, C.D., and Ghadiri, M.R. (2003) A heterocyclic peptide nanotube. *J. Am. Chem. Soc.*, **125** (31), 9372–9376.
24. Coates, A., Hu, Y., Bax, R., and Paged, C. (2002) The future challenges facing the development of new antimicrobial drugs. *Nat. Rev. Drug Discov.*, **1**, 895–910.
25. Fernández-López, S., Kim, H.-S., Choi, E.C., Delgado, M., Granja, J.R., Khasanov, A., Kraehenbuehl, K., Long, G., Weinberger, D.A., Wilcoxen, K.M., and Ghadiri, M.R. (2001) Antibacterial agents based on the cyclic D,L-peptide architecture. *Nature*, **412** (6845), 452–455.
26. Fletcher, J.T., Finlay, J.A., Callow, M.E., Callow, J.A., and Ghadiri, M.R. (2007) A combinatorial approach to the discovery of biocidal six-residue cyclic D,L-α-peptides against the bacteria methicillin-resistant Staphylococcus aureus (MRSA) and E. coli and the biofouling algae Ulva linza and Navicula perminuta. *Chem. Eur. J.*, **13** (14), 4008–4013.
27. Horne, W.S., Wiethoff, C.M., Cui, C., Wilcoxen, K.M., Amorín, M., Ghadiri, M.R., and Nemerow, G.R. (2005) Antiviral cyclic D,L-α-peptides: targeting a

general biochemical pathway in virus infections. *Bioorg. Med. Chem.*, **13** (17), 5145–5153.

28. Motesharei, K. and Ghadiri, M.R. (1997) Diffusion-limited size-selective ion sensing based on SAM-supported peptide nanotubes. *J. Am. Chem. Soc.*, **119** (46), 11306–11312.

29. Couet, J., Samuel, J.D.J.S., Kopyshev, A., Santer, S., and Biesalski, M. (2005) Peptide-polymer hybrid nanotubes. *Angew. Chem. Int. Ed.*, **44** (21), 3297–3301.

30. Shimizu, T., Masuda, M., and Minamikawa, H. (2005) Supramolecular nanotube architectures based on amphiphilic molecules. *Chem. Rev.*, **105** (4), 1401–1444.

31. Horne, W.S., Ashkenasy, N., and Ghadiri, M.R. (2005) Modulating charge transfer through cyclic D,L-α-peptide self-assembly. *Chem. Eur. J.*, **11** (4), 1137–1144.

32. Ashkenasy, N., Horne, W.S., and Ghadiri, M.R. (2006) Design of self-assembling peptide nanotubes with delocalized electronic states. *Small*, **2** (1), 99–102.

33. Delaire, J.A. and Nakatani, K. (2000) Linear and nonlinear properties of photochromic molecules and materials. *Chem. Rev.*, **100** (5), 1817–1845.

34. Vollmer, M.S., Clark, T.D., Steinem, C., and Ghadiri, M.R. (1999) Photoswitchable hydrogen-bonding in self-organized cylindrical peptide systems. *Angew. Chem. Int. Ed.*, **38** (11), 1598–1601.

35. Steinem, C., Janshoff, A., Vollmer, M.S., and Ghadiri, M.R. (1999) Reversible photoisomerization of self-organized cylindrical peptide assemblies at air-water and solid interfaces. *Langmuir*, **15** (11), 3956–3964.

36. Bailey, H. (1999) Designed membrane channels and pores. *Curr. Opin. Biotechnol.*, **10** (1), 94–103.

37. Ghadiri, M.R., Granja, J.R., and Buehler, L.K. (1994) Artificial transmembrane ion channels from self-assembling peptide nanotubes. *Nature*, **369** (6478), 301–304.

38. Kim, H.S., Hartgerink, J.D., and Ghadiri, M.R. (1998) Oriented self-assembly of cyclic peptide nanotubes in lipid membranes. *J. Am. Chem. Soc.*, **120** (18), 4417–4424.

39. Granja, J.R. and Ghadiri, M.R. (1994) Channel-mediated transport of glucose across lipid bilayers. *J. Am. Chem. Soc.*, **116** (23), 10785–10786.

40. Sánchez-Quesada, J., Kim, H.S., and Ghadiri, M.R. (2001) A synthetic pore-mediated transmembrane transport of glutamic acid. *Angew. Chem. Int. Ed.*, **40** (13), 2503–2506.

41. Amorín, M., Castedo, L., and Granja, J.R. (2003) New cyclic peptide assemblies with hydrophobic cavities: the structural and thermodynamic basis of a new class of peptide nanotubes. *J. Am. Chem. Soc.*, **125** (10), 2844–2845.

42. Amorín, M., Castedo, L., and Granja, J.R. (2005) Self-assembled peptide tubelets with 7 Å pores. *Chem. Eur. J.*, **11** (22), 6543–6551.

43. Amorín, M., Brea, R.J., Castedo, L., and Granja, J.R. (2006) Self-assembling cyclic α,γ-tetrapeptides. *Heterocycles*, **67** (2), 574–583.

44. Amorín, M., Brea, R.J., Castedo, L., and Granja, J.R. (2005) The smallest α,γ-peptide nanotubulet segments: cyclic α,γ-tetrapeptide dimers. *Org. Lett.*, **7** (21), 4681–4684.

45. Brea, R.J., Amorín, M., Castedo, L., and Granja, J.R. (2005) Methyl-blocked dimeric α,γ-peptide nanotube segments: formation of a peptide heterodimer through backbone-backbone interactions. *Angew. Chem. Int. Ed.*, **44** (35), 5710–5713.

46. Reiriz, C., Castedo, L., and Granja, J.R. (2008) New α,γ-cyclic peptides-nanotube molecular caps using α,α-dialkylated α-amino acids. *J. Pept. Sci.*, **14** (2), 241–249.

47. Brea, R.J., Castedo, L., and Granja, J.R. (2007) Large-diameter self-assembled dimers of α,γ-cyclic peptides, with the nanotubular solid-state structure of cyclo-[(L-Leu-D-MeN-γ-Acp)4]·4CHC2-COOH. *Chem. Commun.*, **31**, 3267–3269.

48. Brea, R.J., Herranz, M.A., Sánchez, L., Castedo, L., Seitz, W., Guldi, D.M., Martín, N., and Granja, J.R. (2007) Electron transfer in Me-blocked heterodimeric α,γ-peptide nanotubular

C_{60}-TTF dyads. *Proc. Natl. Acad. Sci. U.S.A.*, **104** (13), 5291–5294.

49. Brea, R.J., Vázquez, M.E., Mosquera, M., Castedo, L., and Granja, J.R. (2007) Controlling multiple fluorescent signal output in cyclic peptide-based supramolecular systems. *J. Am. Chem. Soc.*, **129** (6), 1653–1657.

2
Designer Nanomaterials for the Production of Energy and High Value-Added Chemicals

Rafael Luque

2.1
Introduction

We are entering what can be described as the *nano* age, where the scientific revolution has nanoscience at the core of future technological progress, provided by the increasing ability to manipulate matter at an ultrasmall scale (i.e., within the nanometer range) [1, 2]. The potential benefits and consequences of controlling matter at the nanoscale are yet to be fully realized. Nevertheless, the ability to directly work and control systems at the same scale as nature (e.g., mitochondria, DNA, cells) can potentially provide a very efficient approach to the production of chemicals, energy, and materials (Figure 2.1). Over a billion years, natural systems have evolved nanoscale biological entities for the efficient production of materials (i.e., enzymes) and energy (i.e., chlorophyll). By mimicking these systems, scientists may be able to reach the aims of a future sustainable society.

The interest in nanoscale materials has recently received tremendous attention (Figure 2.2) and will continue to do so in the future years. Nanoscale forms of carbon (i.e., fullerenes and nanotubes) and inorganic materials provide the building blocks for the assembly of the nanoscale machines.

Nanomaterials have therefore been regarded as a major step forward to miniaturization and nanoscaling with various subfields that have been developed to study such materials. Every different subdiscipline has a role in modern nanoscience and technology [2]. The nanotechnology field is highly multidisciplinary, where inputs from physicists, biologists, chemists, and engineers are required for the advancement of the understanding in the preparation, application, and impact of the new nanotechnologies.

A *nanomaterial* can be defined as a material that has a structure in which at least one of its phases has one or more dimensions in the nanometer size range (1–100 nm, Figure 2.1). Such materials include polycrystalline materials with nanometer-sized crystallites, materials with surface protrusions spatially separated by distances on the order of nanometers, porous materials with particle sizes in the nanometer range, or nanometer-sized metallic clusters dispersed within a porous matrix (supported metal nanoparticles (SMNPs). Among them, metal nanoparticles

Ideas in Chemistry and Molecular Sciences: Advances in Nanotechnology, Materials and Devices.
Edited by Bruno Pignataro

ISBN: 978-3-527-32543-6

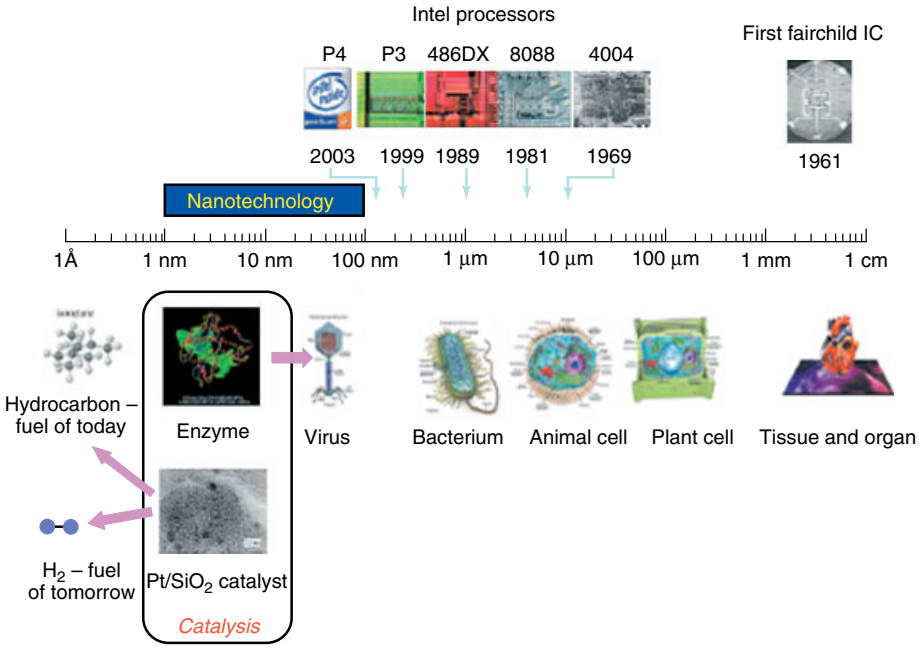

Figure 2.1 Catalysts and the nanometer regime [2b]. Reproduced by permission of the Royal Society of Chemistry.

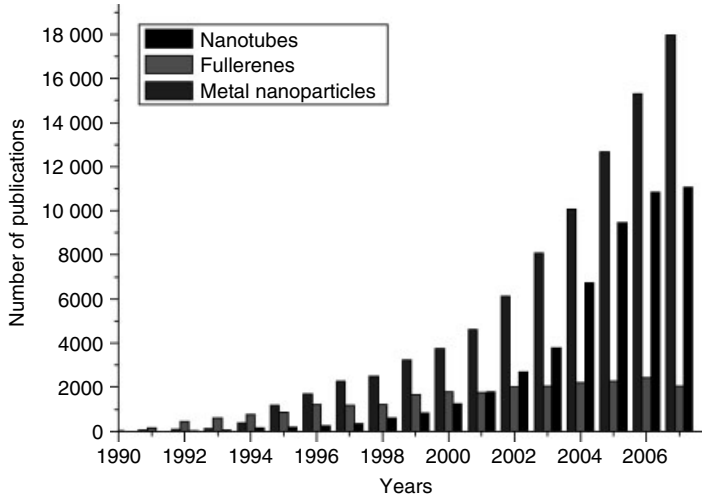

Figure 2.2 Growth in interest of metal nanoparticles (as determined by the number of citations) compared to nanotubes and fullerenes. (Source: ISI Web of Science.) Reproduced by permission of the Royal Society of Chemistry.

(MNPs) have attracted much attention over the last decade compared to their nano-organic counterparts, because of their relatively higher chemical activity and specificity of interaction. Furthermore, MNPs have extremely different properties as compared to their bulk equivalents that mainly include a large surface to volume ratio and sizes in the nanometer scale [1–3]. With all the briefly mentioned advantages and outstanding features of MNPs, it is not surprising that the publications around MNPs have increased almost exponentially over the last few years with over 8000 publications in 2008. The amplitude of research efforts is expected to continue increasing as application benefits of the chemical properties achieved at the nano level become increasingly apparent.

One of the key driving forces for the rapidly developing field of nanoparticle synthesis is the already mentioned distinctly differing physicochemical properties presented by metal nanoparticles as compared to their bulk counterparts. Among these remarkable properties, nanoparticles typically provide highly active centers but they are very small and not at a thermodynamic stable state. Structures at this size regime are indeed unstable due to their high surface energies and large surfaces [1, 3]. To produce stable particles, it is necessary to terminate the particle growth reaction, and there are a number of methods by which this has been achieved. The addition of organic ligands, inorganic capping materials, or other metal salts, creating core shell-type particle morphology as well as colloids and soluble polymers, is one such method [4, 5]. These materials can be grouped in the so-called ''unsupported'' MNPs. However, the nanoparticles may undergo aggregation and suffer from poisoning under the reaction conditions, resulting in deactivation and loss of catalytic activity.

A significant volume of research has been published with the expressed aim of inhibiting aggregation and producing highly active nanoparticles with homogeneous size dispersity [6–8]. The control of nanoparticle size, shape, and dispersity is the key to selectivity and enhanced activity. A mechanism to achieve this control is to utilize another nanotechnology, that of (nano)porous supports.

A *porous material* is normally a solid comprising an interconnected network of pores (voids). Many natural substances such as rocks, clays, biological tissues (e.g., bones), and synthetic materials including ceramics, metal oxides, carbonaceous materials, and membranes can be considered as porous media. A porous medium is characterized by its porosity (e.g., macro-, meso-, microporosity, or combinations of them) as well its textural and physical properties that are dependent on its constituents. These nanomaterials can be grouped into the so-called SMNPs. The unique properties of SMNPs are directly related to the specific particle morphology (size and shape), metal dispersion, concentration, and the electronic properties of the metal within their host environment (Figure 2.3) [1, 2, 9–11].

The fusion between porous materials and nanoparticle technology is potentially one of the most interesting and fruitful areas of this nano-interdisciplinary research. The use of porous environments with defined pore sizes and characteristics as supports for nanoparticles allows the generation of specific adsorption sites, creating a partition between the exterior and the interior pore structure. It also has the added advantage of inhibiting particle growth to a particular size

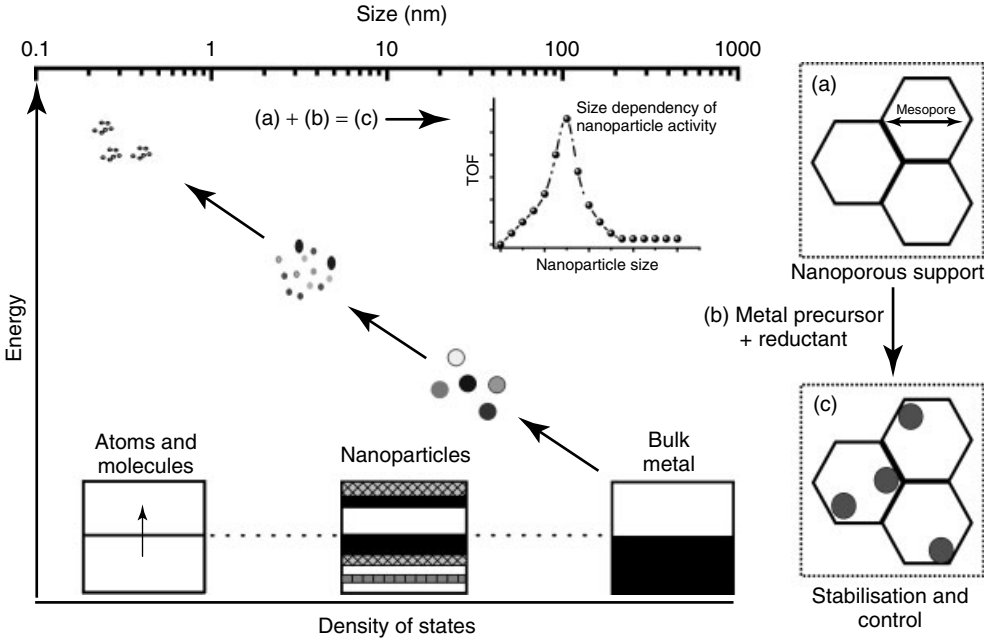

Figure 2.3 Relationship between nanoparticle size, energy, and the principle of density of states. Stabilization and control of nanoparticle size can be achieved by selecting a nanoporous support, potentially leading to enhanced catalytic activity and selectivity, and ultimately designer catalysts [10]. Reproduced by permission of The Royal Society of Chemistry.

regime as well as reducing particle aggregation. Furthermore, by selecting and manipulating the textural properties of the porous support (sometimes in unison with a reduction step), it should be possible to control the size and shape of the resulting nanoparticles. This leads to the possibility of size-selective and reusable heterogeneous catalysts based on nanoparticle size rather than on the pore size. Potential for increased efficiency from nanoparticle catalysts, in combination with the advantages of heterogeneous supports, increases the ''green'' credentials of the process, with higher selectivity, conversion, yield, and catalyst recovery being the proposed advantages and targets. This provides the opportunity to develop specific devices with applications in various fields including medicine [12], sensors [13], and catalysis for the production of chemicals and energy [10, 11, 14, 15].

In parallel to the nanorevolution, environmental issues, growing demand for energy, political concerns, and medium-term depletion of petroleum have created the need to develop sustainable technologies based on renewable raw materials. The term *biorefinery* is used to describe the future manufacturing paradigm for converting biomass to valuable products [16–18]. The biorefinery is analogous to the petroleum refinery, in that here the biomass is ''cracked'' into separate components that are then converted into marketed products. It is important to note that this definition of a biorefinery does not limit the method of conversion of

crops to ''bioconversion'' alone. The biorefinery of the future is likely to integrate both bioconversion and appropriate chemical technologies [16]. It is however essential that for truly sustainable production the technologies that are used have a low environmental impact. In the case of chemical technologies and chemical production, this means the use of green chemistry methods such as heterogeneous catalysis [19] and the application of green chemistry principles [20]. ''Sustainable chemical products'' means sustainable production routes and green lifecycles that encompass feedstocks and processing as well as product fate.

An increasing interest in the use of alternatives to conventional fuels including diesel and gasolines that have been employed over the last 50 plus years have led to the development of the so-called *biofuels* that have the potential to help meet future energy supply demands, particularly for transport fuels, as well as potentially contributing to a reduction of greenhouse gas (GHG) emissions and increase in new agricultural products for stimulating rural economies [21]. Biodiesel and bioethanol are currently available and have become increasingly important over the last few years, with a number of related biofuels being currently developed [21].

This work is intended to be a contribution toward the state of the art and future of the designer nanomaterials (metal and metal oxide nanoparticles) in the production of energy and chemicals. It aims to provide an overview of the recently reported key preparation protocols and applications of such nanomaterials. Because of the rapidly expanding nature of this field, it is hoped that this chapter will be a helpful overview and introduction to the readers in this exciting research area.

2.2
State of the Art in the Preparation of Designer Nanomaterials for the Production of Energy and Chemicals

2.2.1
Preparation of Nanomaterials

Currently, the state of the art in the preparation of SMNPs follows the directions of more efficient and sustainable routes. These can be subdivided into physical (e.g., sonication, microwaves, UV), chemical (e.g., impregnation, photochemistry), and physicochemical routes. The aim of this section is to revise some of the characteristic reported methodologies as well as other related protocols reported up to date.

2.2.1.1 Physical Routes

SMNPs have been prepared using a wide range of trendy physical routes including sonication, microwave irradiation (MWI), laser, supercritical fluids (SCFs), and plasma. Examples of reported protocols will now be examined.

Sonication Sonochemistry deals with understanding the effect of sonic waves and wave properties on chemical systems. There are several interesting features of

sonication. Ultrasounds (USs) remarkably enhance mass transport, reducing the diffusion layer thickness and also affect the surface morphology of the treated materials, normally enhancing the surface contact area [22]. Deposition and reduction of the particles (favored by ultrasonic radiation) takes place almost consecutively, so that the heating step normally employed in other protocols can be avoided [23]. These advantages are related to the acoustic cavitation phenomena, that is, the formation, growth, and collapse of the generated bubbles in a liquid medium. The extremely high temperatures (>5000 °C), pressure (>20 MPa) and cooling rates ($>10^{10}$ °C s^{-1}) lead to many unique properties in the irradiated solution [22]. The SMNPs preparation is usually performed using a conventional ultrasonic cleaning bath or a high power probe. Although, a more controllable NPs size distribution can be achieved with this methodology, these ultrasonic-assisted protocols sometimes require the additional use of a reductant including sodium borohydride [24], hydrogen [23], and hydrogen + polyalcohols [25], to further ensure the reduction of NPs on the supports.

Microwave Irradiation (MWI) Microwaves have been recently demonstrated to be a very effective technology in applied chemistry. Several reports of microwave-assisted reactions have been reported, mainly employing solutions of metal salts as precursors.

MWI has several advantages over conventional methods, including short reaction time, small particle size, narrow size distribution, and high purity [10, 11]. El-Shall *et al*. have extensively investigated the use of MWI for the preparation of a range of SMNPs including Au and Pd [26]. They have also prepared capped Au and Pd NPs on metal oxides using polyethylene glycol (PEG) and poly(*N*-vinyl-2-pyrrolidone) (PVP) as protective polymers prior to microwaving in order to further stabilize the NPs from agglomeration. In this way, the obtained SMNPs were found to have a better dispersion and a narrower particle size distribution, which in turn increased their activity for the investigated application (oxidation of CO). They claimed that fast and uniform heating (due to PEG and PVP) high dielectric constants) achieved under MWI allows a quicker reduction of the metal precursor on the support [26, 27].

Pulsed Laser Ablation (PLA) The laser approach involves the vaporization of metals of mixtures by employing a pulsed laser (e.g., Nd–YAG) and subsequent controlled deposition on the surface of the support under well-defined conditions of temperature and pressure [27, 28]. The method has several advantages for the synthesis of SMNPs. Firstly, it does not usually involve the use of any chemical precursors or solvents and therefore it provides a simple and effective synthetic route for supported contamination-free crystalline MNPs [27]. Secondly, virtually any metal or mixtures in any composition and form (e.g., sheets, films, and powders) can be turned into MNPs. Thirdly, MNPs can directly be supported on catalysts as they are created with a significant number of dangling bonds and they are strongly adsorbed on supports becoming anchored. Fourthly, and most importantly, no side products are created and the technique can be scaled up for

industrial applications [29]. The sizes and compositions of the generated MNPs can be adjusted to generate materials for specific catalytic applications [29, 30].

Supercritical Fluids (SCF) Another efficient and environmentally friendly alternative to prepare SMNPs has been the use of SCF. A very good revision on the subject has been recently prepared by Zhang *et al.* [31]. The conventional procedure involves the dissolution of a metallic precursor in an SCF (e.g., supercritical CO_2) and subsequent incorporation on a substrate/support under various conditions (Figure 2.4) [31, 32]. The impregnated metallic precursor can be reduced to its elemental form by three different approaches:

1) Chemical reduction in the SCF (using a reducing agent such as H_2 or ethanol).
2) Thermal reduction in the SCF.
3) Thermal decomposition (in an inert gas) or chemical reduction with hydrogen or air after depressurization.

SCFs offer several advantages compared to traditional methods. Firstly, they can provide enhanced mass-transfer properties because of their higher diffusivities compared to liquids and lower viscosities. Secondly, the lower surface tension allows a better penetration and wetting avoiding problems related to partial structure shrinkage or pore collapse on certain materials (e.g., silica aerogels) that are present in the conventional chemical methodologies. Thirdly, it is possible to control the particle dispersion and morphology on various supports employing different metal precursors, metal content, and reduction temperatures and chemistries [31]. $ScCO_2$ has been widely employed for the preparation of SMNPs as it is abundant,

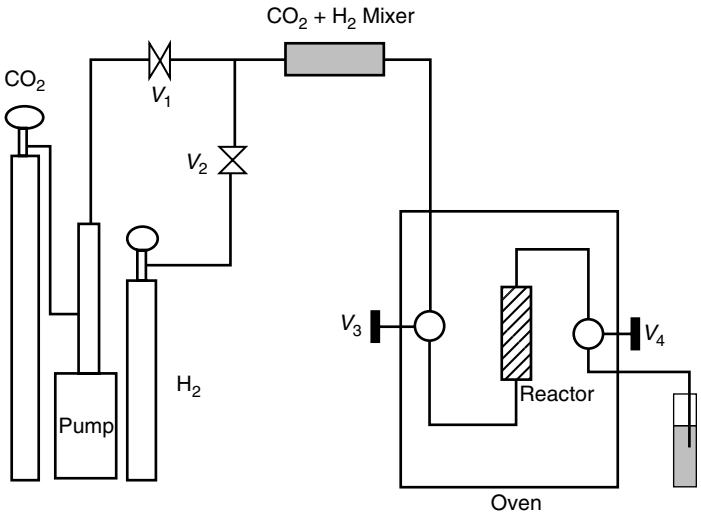

Figure 2.4 Supercritical CO_2 experimental setup for the decoration of multiwalled carbon nanotubes with Pd nanoparticles, as reported by Wai *et al.* [32b]. Reproduced by permission of The Royal Society of Chemistry.

inexpensive, nonflammable, and nontoxic [31–33]. However, more studies are needed in terms of the solubility of the organic precursors into the SCF and the reduction step in order to further develop this technique. Another major issue in its widespread use is the cost of the SCF equipment.

Plasma A novel plasma reduction method at room temperature has been reported to prepare SMNPs. Legrand *et al*. employed dihydrogen microwave plasma to reduce various metal solutions (Au, Pt, and Pt–Au) on zeolites [34]. The afterglow of such a microwave plasma (2.45 Ghz) was found to contain hydrogen atoms at a sufficiently low temperature to effectively reduce the metal ions in solution to small NPs (less than 5 nm) on NaY and HY zeolites. The SMNPs were found to be very stable to thermal treatment. Ar glow discharged plasma has also been employed to support Pt, Pd, Ag, and Au NPs on a range of supports including nonporous TiO_2, γ-alumina, and H–ZSM-5 [35]. NPs were found to be homogeneously distributed on the surface of the support, being in the nanoscale range. Oxygen glow discharge plasma allowed the preparation of SMNPs but small quantities of metal oxides were also found in their preparation. This technique is a very promising and straightforward way to prepare NPs as it may be an environmentally friendly, fast, and simple methodology and also a promising alternative to hydrogen reduction at high temperatures. However, the specialized equipment needed makes its widespread use difficult.

2.2.1.2 Chemical Routes

The classical coprecipitation, impregnation, and deposition–precipitation synthesis methods have been recently predated by novel preparation routes including the precipitation from reverse micelle (water-in-oil) emulsions, photochemistry, chemical vapor impregnation, and electrochemical reduction.

Traditional Methods (Impregnation, Coprecipitation, and Precipitation/Deposition) *Impregnation*. This methodology entails the ''wetting'' of the solid support with a solution containing the metal precursor. The common method of chemical impregnation is the so-called wetness impregnation. In this method, the metal nanoparticle precursor, which is normally a salt (e.g., metal nitrate, chloride, etc.), is dissolved in the minimum quantity of solvent to afford its complete dissolution. The resulting metal salt solution is then added to the porous support filling its pores so that a thick paste is formed. The solvent is then removed in a rotary evaporator and the final solid is oven dried and subsequently calcined and reduced (if needed) before being tested as a catalyst [14, 36]. SMNPs obtained by this methodology have been reported to have various loadings, being differently dispersed depending on the metal, support, and loading of the final solid [14, 36, 37].

Coprecipitation. The coprecipitation method involves the simultaneous precipitation of the metal and the support [38]. In this way, MNPs can be incorporated and/or encapsulated into the structure of various mesoporous materials (Figure 2.5) [2b, 38, 39]. However, the presence of the metallic precursors in solution interferes with the polymerization chemistry of the material, often resulting in samples

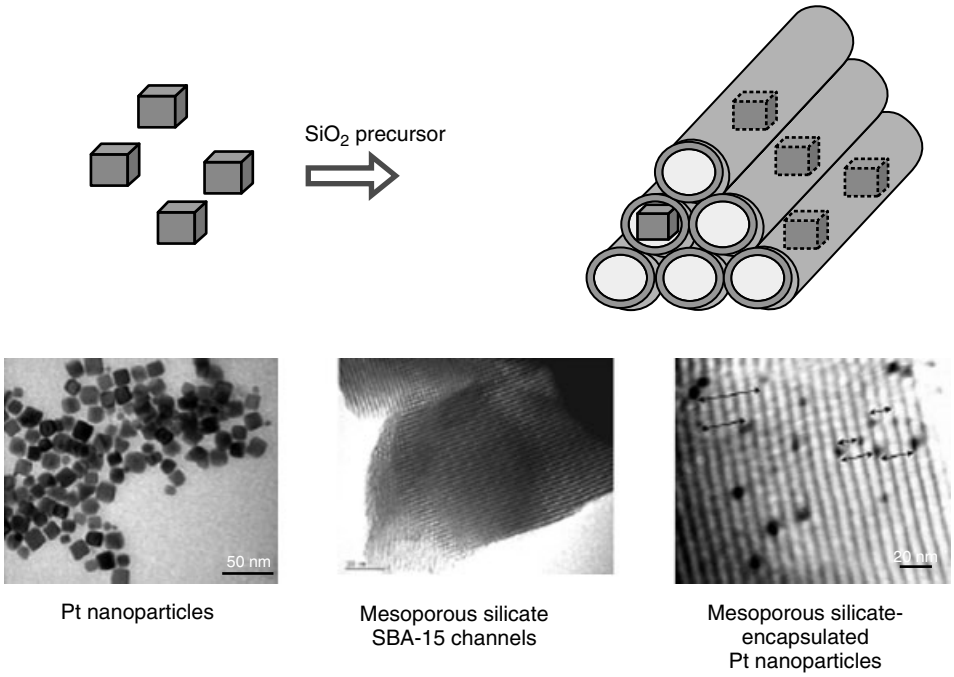

Figure 2.5 Pt-encapsulated nanoparticles using a solgel co-precipitation approach [2b]. Reproduced by permission of the Royal Society of Chemistry.

with undesirable properties. The solgel technology also cannot be easily applied to polymeric substrates [31].

Precipitation–Deposition. This method was initially reported by Haruta *et al*. [40]. It involves the dissolution of the metal precursor followed by adjustment of the pH (i.e., 5–10) to achieve a complete precipitation of the metal hydroxide (e.g., $Au(OH)_3$) that is deposited on the surface of the support. The hydroxide formed is subsequently calcined and reduced to elemental metal [39, 41].

In general, these methodologies often provide a broad nanoparticle size distribution. It is difficult to tune the particle size for a particular application because of poor control over the NP size, which also affects the dispersion and NPs sizes at increasing metal loadings. Particle agglomeration is quite a common phenomena and the use of liquid solutions has been reported to originate a collapse of fragile supports (e.g., organic or silica aerogels) due to the high surface tension of the liquid solution [42]. Furthermore, many of the reported protocols require the use of an excess of external reductant (e.g., $NaBH_4$, H_2, hydrazine), to ensure the complete formation of the SMNPs, which needs to be removed after the reaction.

Microemulsions Microemulsions can be described as homogeneous-like combinations of water, oils, and/or surfactants (often in the presence of alcohol- or

amine-based compounds). The formation of reverse micelles was proved as an interesting alternative to the preparation of SMNPs. Thus, a solid support is impregnated with a microemulsion containing a dissolved metal salt precursor in a similar way to that of the previously described traditional chemical impregnation [42, 43]. SMNPs obtained using this methodology have been reported to have a more controllable, narrow crystallite distribution compared to the traditional impregnation, coprecipitation, and precipitation–deposition methods [43]. This has been attributed to the confined location of a limited amount of metal salt in the micelles that are subsequently taken up upon interaction with the support [7, 42, 43].

The interaction microemulsion support has been proved to be enhanced by increasing the hydrophobicity of the support (e.g., silylation of hydroxyl rich surfaces), making it more chemically compatible with the microemulsion during the deposition step [44]. Wang *et al.* [45] have also recently reported another interesting approach of this methodology employing a water–liquid CO_2 (as oil phase) microemulsion stabilized by a surfactant (sodium bis(2-ethylhexyl)sulfosuccinate) and hexane. In this way, Pd, Rh, and Pd–Rh NPs with sizes ranging from 2 to 10 nm could be homogeneously deposited on the surface of multiwalled carbon nanotubes (MWCNTs) [45].

Photochemistry Only a few reports can be found on photochemical protocols to prepare SMNPs. Kohsuke *et al.* have recently reported a photoassisted deposition method that allows the formation of Pt and Pd NPs on the photoexcited tetrahedrally coordinated titanium species within the framework [46]. Similarly, He *et al.* demonstrated that Au NPs could be supported on a TiO_2 support via decomposition and photochemical deposition of a gold precursor ($HAuCl_4$) employing a 125-W high-pressure mercury lamp [47]. This procedure minimizes the use of chemicals and solvents and is more environmentally friendly than many of the reported protocols. However, it is still not clear how controllable the NP size and distribution on a solid support can be.

Chemical Vapor Deposition (CVD) CVD has been reported as another promising route to the preparation of SMNPs. It has been regarded as a powerful method to generate highly dispersed metal catalysts in a controlled and reproducible manner [48]. This procedure involves the vaporization (sublimation) of metals and growth of NPs under high vacuum in the presence of an excess of stabilizing organic solvents (e.g., aromatic hydrocarbons, alkenes, THF) and/or reducing agent (e.g., H_2) [48, 49]. The reported NPs have a relatively narrow particle size distribution (2–8 nm). CVD is claimed to allow the preparation of SMNPs on a wide range of organic and inorganic supports under very mild conditions ($<50\ ^{\circ}C$) affording highly active heterogeneous catalysts [50], avoiding the formation of large agglomerated NPs from other protocols (Figure 2.6). Nevertheless, the method is often limited by the vapor pressure of the precursor and mass-transfer-limited kinetics.

Electrochemical Reduction Although the method is not widely employed, the electrochemical deposition of NPs on supports has also been reported, mainly

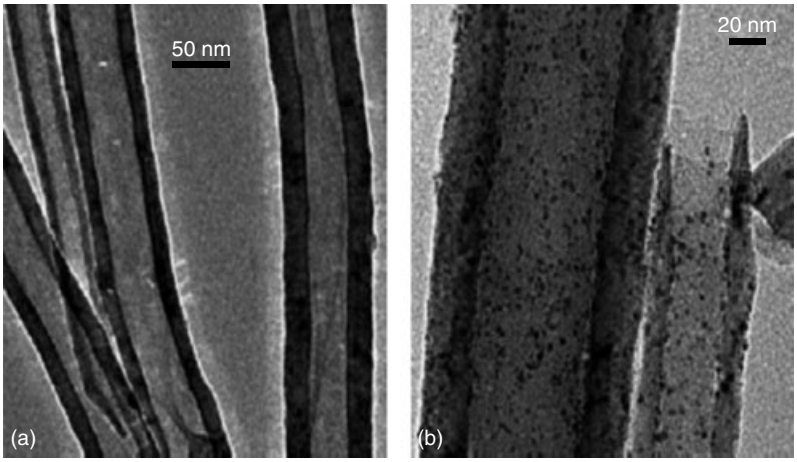

Figure 2.6 TEM images of untreated (left) and functionalized carbon nanofibers (right, 2.04 wt% Pd) with Pd metal nanoparticles via CVD [50]. Reproduced by permission of The Royal Society of Chemistry.

for carbonaceous related supports [51]. The electrodeposition of Pt NPs under potentiostatic conditions takes place from acidic aqueous solutions of H_2PtCl_6. The use of stabilizers (e.g., tetralkylamonium salts) is needed to prevent the particles deposition at the cathode's surface [42].

2.2.1.3 Physicochemical Routes

A few examples of combined efficient physicochemical routes have been reported till date. The most common ones are sonoelectrochemistry and flame spray pyrolysis.

Sonoelectrochemistry This approach is a combination of US waves and electrochemistry. USs have beneficial effects on electrochemistry. They enhance mass transport, thereby altering the rate and sometimes the mechanism of the electrochemical reaction [52]. USs also affect surface morphology through cavitation jets at the electrode–electrolyte interface, increasing the surface area [52]. Finally, USs reduce the diffusion layer thickness and therefore ion depletion.

Flame Spray Pyrolysis This alternative method of preparation was initially reported by Madler *et al.* [53] and further reports on the technique have been recently reported [54]. The liquid precursor mixture was fed in the center of a methane/oxygen flame by a syringe pump and dispersed by oxygen, forming a fine spray. The spray flame was surrounded and ignited by a small flame ring issuing from an annular gap (0.15 mm spacing, at a radius of 6 mm). Product particles were then collected on a glass fiber filter (Whatmann GF/D, 25.7 cm in diameter) with the aid of a vacuum pump. The technique afforded highly stable

supported Pd NPs with small particle size (< 5 nm) that were proved to be very suitable for various applications [53, 54].

2.2.2 Production of Energy and Chemicals: the Biorefinery Concept

The sustainable production of energy and high value-added chemicals through the application of the biorefinery concept has been highlighted as one of the most important challenges of the twenty-first century in order to switch from the current petrol-based industry to a more sustainable renewable-based one [16, 55]. In this regard, there are several examples that can well illustrate the recent state of the art in the production of energy (e.g., biofuels) and fine chemicals utilizing a variety of designer nanomaterials including supported metal and metal oxide NPs, nanocrystals, and related nanomaterials.

The aim of this section is to review some of the most commonly reported applications of SMNPs related to the production of energy and chemicals. These have been grouped into three areas: energy, catalysis, and other applications. This section, far from providing a comprehensive revision of all the reported applications of SMNPs, aims to give an introduction to some of their most interesting applications.

2.2.2.1 Energy

The search for alternative energies to meet the future energy demands (in particular for the transport sector) has prompted scientists to come up with ideas for the preparation of a range of alternative fuels to gasoline and diesel. These alternative fuels are the so-called biofuels that can be simply divided into crop-based fuels (biodiesel and bioethanol, first generation) and non-crop-based biofuels (e.g., biofuels from thermochemical processes, catalytic cracking, etc.) [21]. Although this is in reality a very complex classification which includes a wide range of possibilities, the aim of the next few sections is to provide a very simple overview of the state of the art in the production of some of these biofuels using SMNPs and different nanomaterials.

Biodiesel Biodiesel is a nontoxic, sulfur-free, and biodegradable biofuel that can be used in unmodified diesel engines pure or as a blend [21]. It also has a significant added value compared to petrol-diesel because of its higher lubricity, flash point, and lower aromatic content which extend engine life and reduce maintenance costs.

The conventional methodology for the production of biodiesel involves the transesterification of triglycerides (TGs) from vegetable oils (e.g., palm, corn, soybean, rapeseed, and sunflower) with short chain alcohols including methanol and ethanol to yield fatty acid (m)ethyl esters (FAM/EE) and glycerol as by-products (Scheme 2.1).

Several reviews on the preparation of biodiesel using different feedstocks and catalytic processes can be found in the literature [21, 56]. The methods of preparation

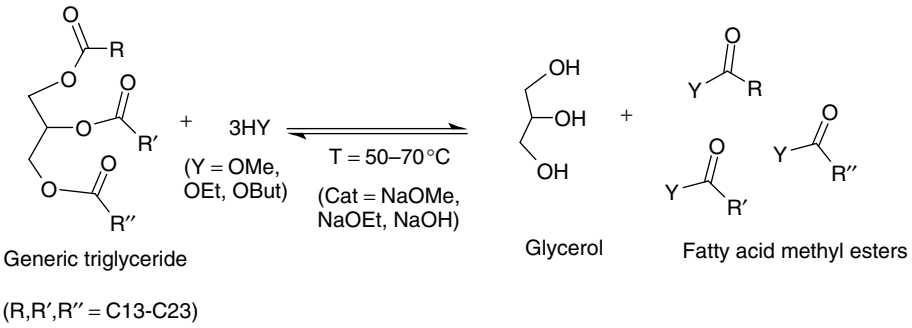

Scheme 2.1 Conventional transesterification of TG for the production of biodiesel [21]. Reproduced by permission of the Royal Society of Chemistry.

of biodiesel can be classified as chemical catalytic (base or acid catalysis under homogeneous and/or heterogeneous conditions), biocatalytic (enzyme catalysis), and noncatalytic processes. Lee *et al.* have recently reported the simple preparation of size-controlled MgO NPs via thermal treatment of a parent nanocrystalline $Mg(OH)(OCH_3)$ precursor for the transesterification of glyceryl tributyrate [57]. Nanomaterials treated at temperatures lower than 600 °C were found to have high surface areas (>200 $m^2\ g^{-1}$) and a narrow particle size distribution of small NPs (2–8 nm). Interestingly, the small, cubic MgO single crystals generated at low-temperature processing (<400 °C) terminate in high coordination (100) facets that were found to exhibit a weak polarizability and a poor activity in the transesterification reaction. Comparatively, the calcination of the materials at higher temperatures (>400 °C) rendered large, cuboidal particles of periclase MgO which terminate in more basic (110) and (111) surfaces that provided good conversions in the production of methyl butyrate under mild conditions (Figure 2.7). These promising findings should be considered as very interesting as they may pave the way to the rapid screening of novel nanostructured basic oxides for biodiesel preparation.

Biofuels Prepared via Selective Hydrogenation Zaccheria *et al.* have very recently demonstrated the selective hydrogenation of nonfood oil methylesters using supported Cu NPs on silica and this has opened up the market for the preparation of novel biofuels suitable for biodiesel formulations [58]. Mixtures of relatively homogeneous compositions could be obtained starting from methylesters with a very different unsaturation degree and acidic distribution (from linseed to tobacco seed oil methyl esters) by means of a 8% Cu/SiO_2 catalyst prepared by a simple impregnation/reduction method. The highly active and selective, cheap, and benign catalyst (compared to other toxic or pyrogenic such as Ni-and Pd-based materials) could also potentially offer the possibility to control the hydrogenation reaction depending on needs by simply following the hydrogen consumption in the system. This smart approach provides a versatile methodology for the production

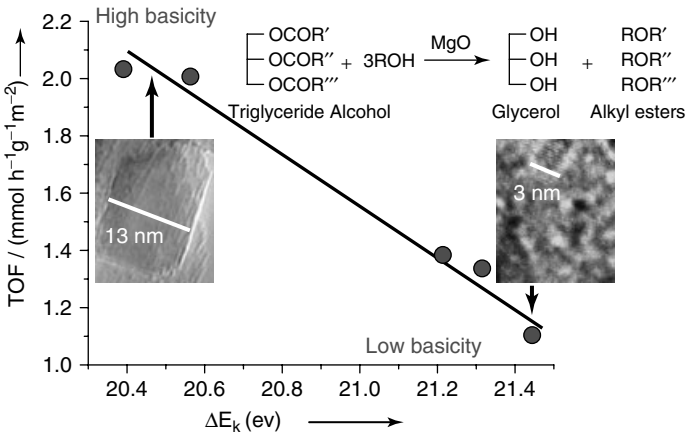

Figure 2.7 Surface area normalized turnover frequency for glyceryl tributyrate conversion as a function of surface polarizability. Top: high basicity, nano-MgO-700; bottom:low basicity, nano-MgO [57]. Reproduced by permission of The Royal Society of Chemistry.

of biofuels depending on feedstocks availability, climate, and regions, thus offering a wide range of alternative biofuels that do not compete with the food market (food vs fuel issue).

Fuels Prepared via Thermochemical Processes Significant research efforts have been devoted to investigate the preparation of biofuels via thermochemical processes (e.g., catalytic cracking, pyrolysis, hydrothermal treatment, gasification + Fischer–Tropsch synthesis(FTS). Chen *et al*. have reported the tailoring of carbon nanotubes (CNT) to confine/encapsulate metal oxide nanoparticles (e.g., Fe_2O_3) [59]. In their work, they have demonstrated that such confinement confers them particular properties compared to those of the nanoparticles located on the outer walls, including enhanced redox properties that can be modified for an optimum performance in catalysis [59]. Fe_2O_3 nanoparticles confined on CNTs were then investigated in the FTS process of converting syngas to synthetic biofuels. Interestingly, the yield of C_{5+} products of the Fe_2O_3 confined within CNTs was found to be twice as much compared to that observed for wall-supported Fe_2O_3 (Table 2.1) despite both having similar iron particle sizes (4–8 nm). H_2 and CO–TPR experiments point to the modification of the redox properties with improved reducibilities in the encapsulated catalysts. Furthermore, the trapping of the reaction intermediates within the CNT channels has been proposed to extend their contact time with the active species, therefore favoring the formation of longer chain hydrocarbons and higher FTS activities.

Another important example for the production of enhanced fuels is the hydroisomerization of *n*-alkanes. Light isoalkanes are required for the production of more environmentally friendly and high-octane number gasolines. Thus, *n*-alkanes are

Table 2.1 Comparison of FTS activities and product selectivities of different Fe materials at 51 bar.

catalyst	CO conversion (%)	CO_2 selectivity (%)	Hydrocarbon selectivities (%)		
			CH_4	C_2-C_4	C_{5+}
Fe-*in*-CNT	40	18	12	41	29
Fe-*out*-CNT	29	12	15	54	19
Fe–AC	17	5	15	71	9

Adapted from [59].

isomerized to increase the octane number in the naphtha (transformation of linear chain paraffins to branched isomers with high-octane numbers) as well as to induce significant improvements in several physical properties of the gasoline, including the pour point and viscosity [60].

The conversion of C_{6+} alkanes has two different and competitive pathways: isomerization and cracking. Alkanes are dehydrogenated on the metallic phase and the alkenes generated are protonated on the acid sites to form alkylcarbenium ions. The reaction (either isomerization or cracking of the alkane) then takes place on the acid sites and the alkene generated in the process is hydrogenated in the metallic sites nearby, affording the isomerized-fragmented *n*-alkane (Scheme 2.2).

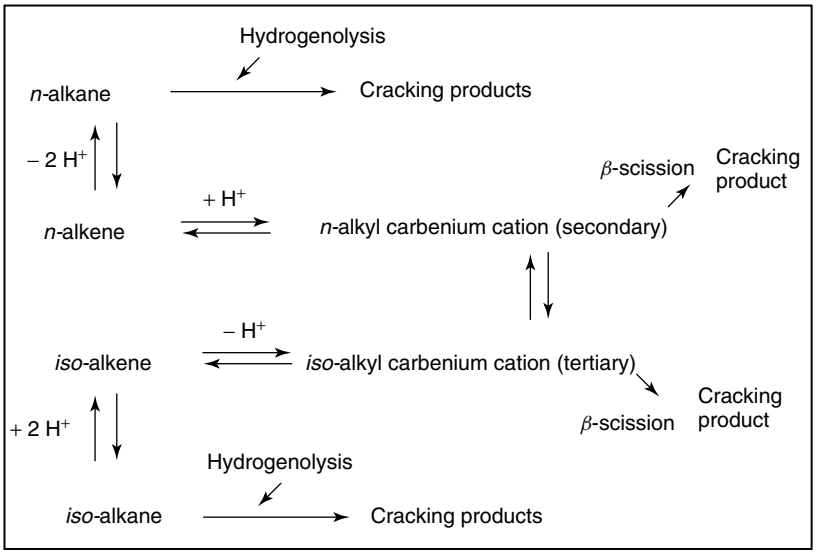

Scheme 2.2 Reaction mechanism of the hydroisomerization of *n*- alkanes [61]. Copyright Wiley-VCH Verlag GmbH & Co.KGaA. Reproduced with permission.

Thus, it is rather complicated to obtain high selectivities to branched isomers without an appreciable selectivity to cracking due to the β-scission of long-chain paraffins [60]. Consequently, the preparation of materials with improved activities and selectivities to the isomerization of long-chain paraffins is highly desirable. The hydroisomerization reactions are generally performed on bifunctional materials having a noble-metal function, usually involved in hydrogenation–dehydrogenation processes, and acidic sites (C–C skeleton rearrangements). The major parameters influencing the reaction selectivity are the pore structure and the acidity [60, 62]. The key to the successful preparation of active and selective catalysts lies in the selection of mild acidity (to minimize the production of cracking products) together with a high active metallic function (e.g., Pt, Pd, and Ni) that improves the selectivity to isomerization and gives high conversion to alkyl branched alkanes. Various catalysts have been reported to be active in the hydroisomerization of C_6 and longer C_7 chain *n*-alkanes, including materials based on MoO_3 [60], Pt–WO_3–ZrO_2 [60, 63], Al–MCM-[60], zeolite-supported Pt [60], and Pt-silicoaluminophosphates (SAPOs) materials [62] as alternatives to the traditional Pt and Re/Al_2O_3 catalysts.

2.2.2.2 Catalysis

Several reports can be found on a wide range of applications of various SMNPs in catalysis including Au, Ag, Pd, and Pt. The key applications of the most commonly employed metals are now briefly reviewed, based on the number of publications. Astruc *et al.* have recently reviewed the applications of metal nanoparticles in catalysis [14, 64]. Tables 2.2–2.5 summarize some of the most reported applications of SMNPs in catalysis.

Oxidations SMNPs have been extensively investigated in the oxidation of a wide range of substrates (Table 2.2), Au being the most employed metal for such catalytic applications. Pd NPs and, to a smaller extent, Pt and Ag NPs, have also been reported to be active and selective in oxidation processes.

The most studied oxidation carried out by SMNPs is the oxidation of CO [65, 66]. The reason for this interest is because of CO oxidation in fuel cells, where residual traces of CO have to be removed from the hydrogen used as fuel source. Au NPs are

Table 2.2 Selected applications of SMNPs in oxidation reactions.

	Metal nanoparticle (references)				
Oxidations	**Au**	**Pd**	**Rh**	**Ag**	**Ru**
CO	[14, 23, 26, 27, 36, 41, 65, 66]	[14, 27]	–	–	–
Alcohols	[14, 65–67]	[14, 67, 68]	–	[67]	–
Amines	[65, 66]	–	–	[14]	–
H_2O_2 synthesis	[66]	[66]	–	–	–
Alkenes	[65–67]	[67]	[29]	[67]	–
Alkanes	–	–	–	–	[25]

Table 2.3 Applications of SMNPs in hydrogenations.

	Metal nanoparticle (references)			
Hydrogenations	**Au**	**Pd**	**Pt**	**Rh**
Alkenes and dienes	[65, 69]	[14, 33, 64, 70–72]	–	[72]
Alkynes	[8e, 65]	[14, 64]	[14, 64]	–
Aromatics	–	[14, 64, 70]	[14, 64]	[70–72]
Allylic alcohols	–	[14, 64]	–	–

the most popularly employed NPs in this oxidative transformation because of the higher selectivity and activity than can be achieved by variation in nanoparticle size as initially reported by Haruta *et al.* [65]. The activities of SMNPs in the oxidation of CO were found to follow the order:

$$Au > Pd \sim Rh > Pt > Ir \gg Ru \gg Ag$$

The optimum nanoparticle size was found to be around 3 nm for Au. The supports employed, mostly metal oxides, can be ordered relative to their efficacy in the oxidation reaction (from best to worst) as follows:

$$CeO_2 > ZrO_2 > AI_2O_3 > SiO_2$$

The catalysts were prepared using a deposition–precipitation method [65].

Among the other reported examples, the oxidation of alcohols is of great importance as a key transformation in organic synthesis. Many reports can be found on the use of supported Au and Pd NPs (Table 2.2) using a wide range of oxidants. Recent research efforts have focused on the oxidation of glycerol, a widely available chemical that is currently obtained as a by-product of biodiesel production. Various reports indicate that the reaction has a selectivity issue [66], although Au NPs on ceria and titania gave very good selectivities to glyceric acid.

Table 2.4 Selected applications of SMNPs in C–C coupling reactions.

	Metal nanoparticle (references)		
Reaction	**Pd**	**Ni**	**Ru**
Heck ArX + alkene → aryl alkenes	[14, 37, 73]	–	[14]
Suzuki ArX + $Ar'B(OH)_2$ → Ar–Ar′	[14, 73]	–	[14]
Sonogashira ArX + alkyne → arylalkyne	[14, 73]	–	–
Negishi ArCl + RZnX → Ar–R	–	[14]	–
Kumada ArCl + RMgX → Ar–R	–	[14]	–

Table 2.5 Various applications of different SMNPs in catalysis.

Reaction	Metal nanoparticle (references)				
	Au	Pd	Pt	Rh	Co
Water–gas shift	[42]	–	–	–	–
Hydroisomerization of *n*-octane	–	–	[61, 62]	–	–
Hydrochlorination	[66]	–	–	–	–
NO_x remediation	–	–	[30]	[30]	–
Cyclization of 7-octen-1-ynes	–	[49]	–	–	–
Formylation of 1-octene	–	–	–	–	[71]

The supports investigated in the reaction (from best to worst) followed the order:

$$CeO_2 > TiO_2 > Fe_2O_3 > C$$

Hydrogenations Hydrogenations are key transformations and SMNPs have been extensively employed for this purpose over the last few decades. Pt, Rh, Pd and Ru, Ni, and Au to a lesser extent have been reported to be very effective in the hydrogenation of a wide range of substrates including alkenes, alkynes, aromatics, and alcohols (Table 2.3).

Of particular interest is the hydrogenation of aromatic compounds catalyzed by SMNPs. The hydrogenation of aromatic compounds is an important reaction used to reduce aromatic content in petroleum. Furthermore, it is also considered a route to obtain high-value commercial chemicals [14, 70]. Silica-supported Ni NPs were found to be relatively active and selective in the hydrogenation of methylbenzene despite the low surface area of the porous silica (15 $m^2\ g^{-1}$). Ni NPs prepared using a conventional impregnation/reduction route were found to be relatively small (<10 nm) and well dispersed on the silica surface, providing interesting activities that were dependent on the preparation of thermal pretreatment step in such a way that the presence of NiO particles was found to influence the hydrogenation process [74].

C–C Coupling Reactions C–C bond forming reactions are among the most interesting and important synthetic transformations in organic chemistry. A summary of the main reported examples of the use of SMNPs in C–C coupling reactions has been included in Table 2.4. Pd is probably the most versatile metal in promoting or catalyzing these reactions, many of which are not easily achieved in good yields and selectivities using other transition metals.

Au and Ru have also been employed in Heck and Suzuki couplings while Ni nanoparticles supported on C catalysts have been reported to be active in Negishi and Kumada couplings [14].

Other Reactions A range of various catalytic applications of SMNPs have also been included in Table 2.5.

2.2.2.3 Other Applications

SMNPs have also been employed in a variety of related applications including hydrogen sorption to be employed as fuel cells in cars [71] (Pd/Pt on carbonaceous materials) and environmental remediation (Fe NPs supported on chitosan and silica [75]). These promising applications will be discussed in more detail in the future prospects section as they may have an important contribution in our future society.

2.3 Highlights of Own Research

This section summarizes some of the most important research studies the author has reported over the last few years in the field of designer nanomaterials for the preparation of high value-added chemicals and some of the recent work on the use of designer materials for the production of biofuels.

2.3.1 Sustainable Preparation of SMNP and Catalytic Activities in the Production of Fine Chemicals

2.3.1.1 Supported Metallic Nanoparticles: Preparation and Catalytic Activities

Over the last few years, the main aim of our research has been the preparation of SMNPs in view of their applications in catalysis. A significant number of publications in the area have dealt with the synthesis of noble-metal nanoparticles (e.g., Pt, Pd, Ag, Au).

A methodology to prepare Pd NPs on mesoporous materials derived from starch at room temperature [73] and silica [37] supports using a conventional impregnation protocol was recently developed. Materials with a bimodal metal particle size distribution (2–4 nm, respectively, Figure 2.8), were found to be very active and selective in microwave-assisted C–C coupling reactions including the Heck, Suzuki, and Sonogashira couplings in very short times of reaction (<30 minutes), showing good reusability under the conditions employed.

Along these lines, the preparation of Pd metal nanoparticles supported on organically modified thin films has also been investigated [76]. The hybrid films containing low loadings of Pd (0.5–1%) were prepared using a modified solgel approach using methyl triethoxy silane (MeTES) with or without the addition of a stabilizing/capping agent (e.g., mercaptopropyl trimethoxysilane, MPTMS) to study the effect of this modifier in the activity of the metal nanoparticles in the Heck coupling of iodobenzene with methyl acrylate (Table 2.6). Pd NPs were found to be highly dispersed on the thin films with particle sizes ranging from 7 to 10 nm. The catalytic hybrid films containing Pd NPs (with and without

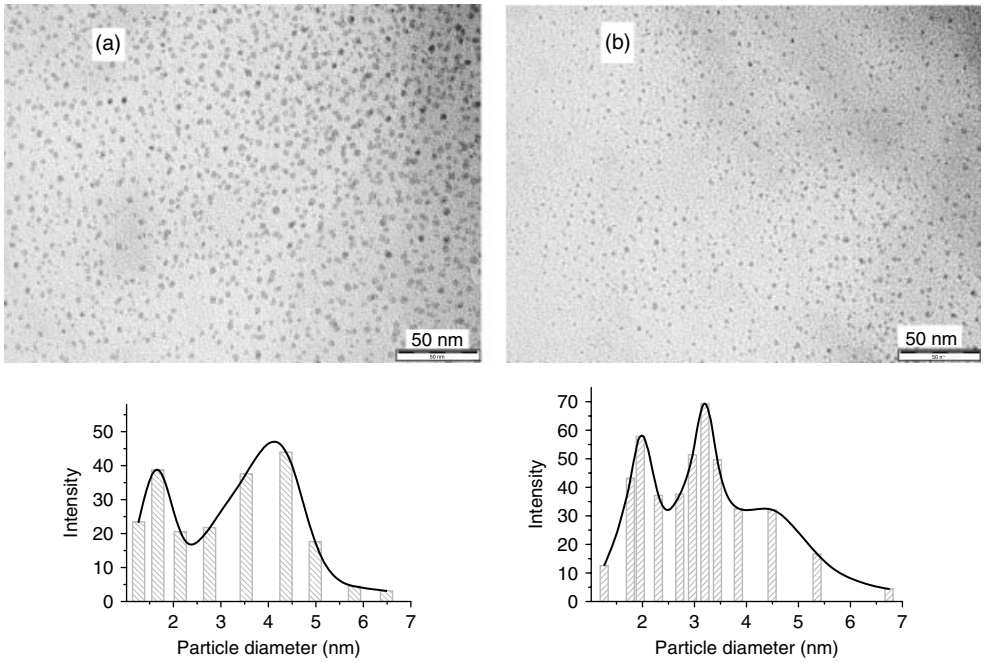

Figure 2.8 TEM micrographs and nanoparticle size distribution (calculated from TEM) of Pd–starch materials (5 wt% Pd) prepared in (a) acetone and (b) ethanol [73]. Reproduced by permission of The Royal Society of Chemistry.

Table 2.6 Catalytic activity (conversion and selectivity to methyl cinnamate) of supported Pd NPs on hybrid films in the Heck coupling of iodobenzene and methyl acrylate[a].

Material	T (°C)	Conversion (mol%)	Selectivity (mol%)
MeTES film (no Pd)	106	– [b]	–
0.5%Pd–MeTES	109	>99	>99
1%Pd–MeTES	90	>99	>99
MeTES/MPTMS film (no Pd)	102	– [b]	–
0.5%Pd–MeTES/MPTMS	101	>99	>99
1%Pd–MeTES/MPTMS	106	>99	>99

[a] Reaction conditions: 8 mmol iodobenzene, 8 mmol methyl acrylate, 5 mmol triethylamine, 0.05 g catalyst, microwave irradiation, 300 W, 90–115 °C, 15 minutes.
[b] No reaction.

MPTMS) gave quantitative conversion and complete selectivity to the targeted product (methyl cinnamate) in a short time of reaction (<15 minutes) under MWI. While Pd containing films without MPTMS were highly active and reusable after three runs, MPTMS containing films were found to be inactive after the first use [76].

Such phenomenon was correlated to the steric hindrance round the Pd NPs due to the adsorption of species on the surface that rendered the catalysts inactive, ruling out the leaching of Pd species as no Pd was found in solution [76]. This protocol has been currently extended to the preparation of highly active Ag NPs in oxidation reactions [77].

A range of SMNPs (Au, Ag, Pd) on ordered mesoporous silica SBA-12 structure have been also recently synthesized using MWI [67]. The Au, Ag, and Pd NPs were prepared in a very short time (<2 minutes) under MWI of a solution of the metal salt precursor in ethanol/water or ethanol/acetone mixture without the need for additional reductant. Both the ethanol and the hydroxyl-rich silica surface facilitate the reduction of the NPs on the support as previously reported [69, 73]. The microwave protocol afforded highly dispersed and relatively small NPs (2, 3.8, and 11.3 nm average particle size for Au, Ag, and Pd, respectively) (Figure 2.9)

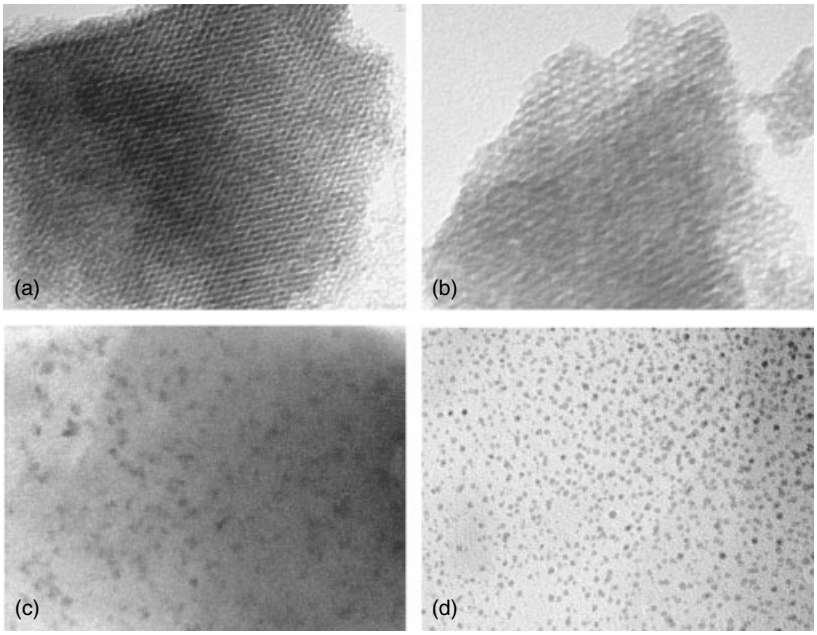

Figure 2.9 Transmission electron microscopy (TEM) micrographs of SBA-12 material ((a) ×160 000 and (b) ×300 000) and (c) Ag and (d) Au MNP on SBA-12 at the same magnification (×300 000, 50 nm) prepared in a domestic microwave oven [67]. Reproduced by permission of the Royal Society of Chemistry.

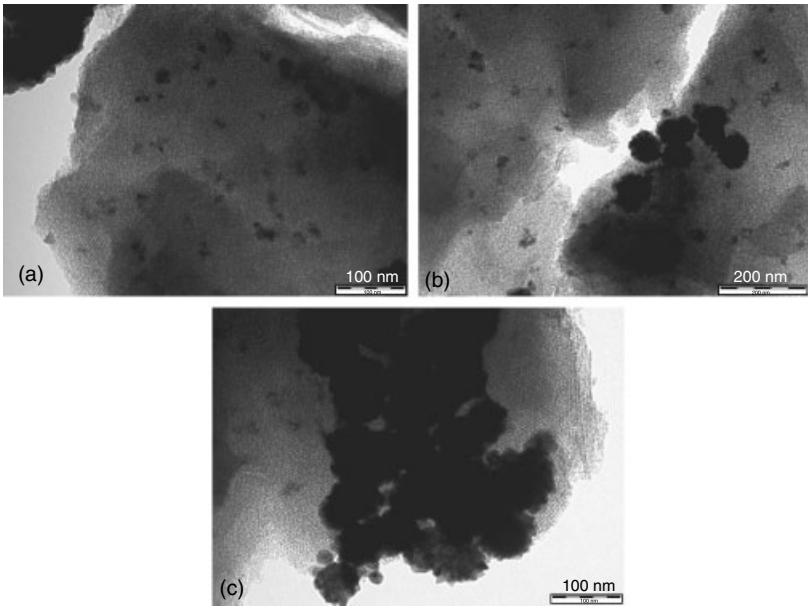

Figure 2.10 TEM micrographs of Pd–SBA-12 materials prepared in a domestic microwave oven at different times: (a) 2 minutes; (b) 10 minutes; and (c) 20 minutes [67]. Reproduced by permission of the Royal Society of Chemistry.

and highly active and selective materials in the oxidation of alcohols (e.g., benzyl alcohol) and alkenes (e.g., styrene).

The time of MWI is a critical parameter to control in the preparation of such materials, as longer reaction times lead to substantial particle agglomeration (Figure 2.10). Our recent studies were in good agreement with findings by El-Shall *et al.* [26]. This methodology has, in general, difficulties to control the particle size and distribution of the NPs on the support. However, the polyalcohols added as stabilizers/capping agents will help to achieve a more homogeneous and narrow particle size distribution. The preparation of the materials was highly reproducible, with different batches of the materials providing similar activities in the oxidation reactions, and the SMNPs were also found to be reusable in the process.

Similarly, a 9.2 wt% Pd supported on a carbonaceous polysaccharide-derived mesoporous material (Starbon®) prepared employing the same MWI methodology was also employed in the oxidation of glycerol (Scheme 2.3) [68]. The material provided high conversions of starting material with unusual selectivities to glycolic acid (following oxidation and decarboxylation) and eventually to oxalic acid (Table 2.7).

2.3.1.2 **Supported Metal Oxide Nanoparticles: Preparation and Catalytic Activities**

Similarly, the use of related nanomaterials containing metal and metal oxide nanoparticles (e.g., Cu, Fe, Ru) and prepared following an MWI protocol in

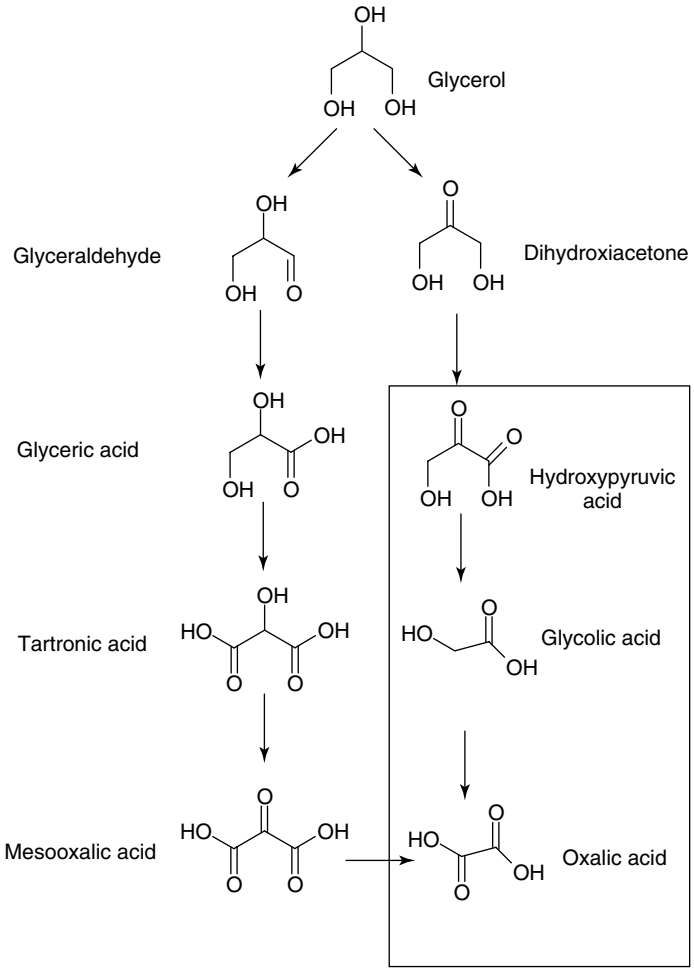

Scheme 2.3 Reaction pathway in the oxidation of glycerol using 9.2% Pd/Starbon® with products obtained marked inside a box [68].

oxidations [78] and oxidative couplings (e.g., C–S arylation) [79] has also been recently reported.

Iron and iron oxide nanoparticles supported on MCM-41 were found to be highly active and selective in the oxidation of alcohols and alkenes, providing turnover numbers (TONs) and turnover frequencies (TOFs) significantly superior to any previously reported similar catalysts (Table 2.8 and Figure 2.11). These supported NPs were also highly reusable in the oxidation reaction, giving even slightly improved results after a few cycles with the support playing a critical role in the stability and reusability of the materials. Comparatively, Fe on starch, cellulose, and even related silica supports was not stable under the reaction conditions

Table 2.7 Catalytic activity of 9.2% Pd–Starbon®-400 tested in the oxidation of glycerol with hydrogen peroxide [a].

Reaction conditions		Conversion (mol%)	Selectivity glycolic acid (mol%)	Selectivity oxalic acid (mol%)
No catalyst 300 W, 100 °C, 30 min		<10	10[b]	–
Effect of power (W)	100	70	90	<5
	200	88	80	16
	300	>95	75	22
Effect of time of reaction (min)	5	58	80	20
	15	>95	75	22
	30	>95	30	60

Adapted from [68].
[a] Reaction conditions: 1 mmol glycerol, 4 mmol H_2O_2, 0.1 g catalyst, 80–100 °C (maximum temperature reached), 300 W (maximum power output) and 15 minute time of reaction, unless otherwise stated; the difference to 100 in selectivities is due to glyceric acid and tartronic acids.
[b] Glyceric acid was obtained as a major product.

and a complete deactivation of the catalysts was observed after two to three cycles (Figure 2.11). The protocol could also be extended to a range of substituted alcohols. Further work carried out to unravel the species involved in the oxidation point to the formation of highly reactive hydroperoxide species on the surface of the catalyst upon contact with H_2O_2 that speed up the rates of reaction in the process (unpublished work).

The most recent work has dealt with the preparation of supported Cu and Fe oxides NP on silica following coprecipitation MWI and conventional heating protocols [79]. These materials were reported, for the first time, in the heterogeneously catalyzed C–S coupling of thiols with aryl iodides (Table 2.9, reaction scheme).

Materials had a very narrow particle size distribution (2–3 nm) and were found to be highly dispersed on the porous support. Cu and Fe materials were found to be differently active and selective in the coupling reaction.

While poor to moderate conversions with complete selectivities to the homocoupling product (B, disulfides) were found for Fe-based nanomaterials, the supported Cu nanoparticles provided complete conversions of starting material and very high selectivities to the cross-coupling product (A) in short times of reaction under MWI. The S-arylation was also found to be amenable to a wide range of substrates and susbtituents (Table 2.9) and the catalysts were reusable under the reaction conditions, preserving almost their initial catalytic activity after three reuses.

2.3.1.3 Other Related Nanomaterials

Further, latest research efforts have been focused on a wider range of nanomaterials including nanotubes, nanocubes, and nanoprisms [80]. The major outbreak in this field firstly came in an attempt to alternatively prepare supported NPs using a

Table 2.8 Efficient and selective oxidation of alcohols (conversion of starting material, conv, mol%; selectivity to the targeted product, select., % and turnover number, TON) using Fe/MCM-41 as catalysts [a].

Entry	Substrate	Product	TON[b]	Conversion (%)	Selectivity (%)[c]
1	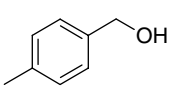	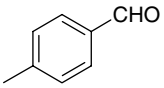	170	31	> 90
2	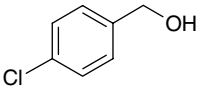	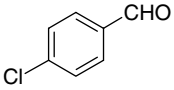	294	60	> 95
3	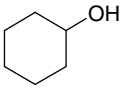	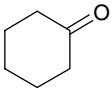	162	38	> 99
4	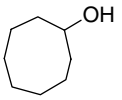	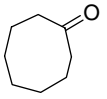	290	54	> 99
5	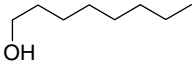	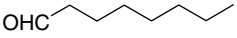	46	< 99	> 99

Adapted from [78]. Copyright Wiley-VCH Verlag GmbH & Co.KGaA. Reproduced with permission.
[a] 0.2 g substrate, 4 mmol H_2O_2 (0.4 ml, 30 wt% in water), 2 ml acetonitrile, 0.050 g catalyst, microwave irradiation, 200 W, 70–90 °C, 1 hour.
[b] Number of moles of product produced per mole of catalyst.
[c] Selectivity based on alcohol conversion.

one-pot step process by coprecipitation of the metal precursor and a gel of the support in solution following a similar protocol to that employed in [79].

Apart from the expected formation of silver nanoparticles on the eventual porous material, the formation of distinctive nanotubular networks self-assembled from the original *n*-dodecylamine/TEOS/water/ACN mixtures was unexpectedly observed [[80]a. Scanning electron microscopy (SEM) and transmission electron microscopy (TEM) images of these materials included in Figure 2.12 proved the formation of characteristic nanotubular-like domains of several micrometers long with diameters typically between 0.1 and 5 μm. These materials, not observed in the absence of metal precursor in solution, could facilely be extended to a range of precursors including Ni, Cu, Fe, Ru, and Co with a satisfactory degree of nanotube formation.

The most plausible explanation for the self-assembly of such mixtures into nanotubes, which was found to be highly dependent on the metal and precursor, may be related to two different effects: the generation of metallic nanoparticles that act as *in situ* generated catalytic seeds to build up the nanotube network and the

Table 2.9 Catalytic activity of Cu–MW–HMS in the S-arylation of aryl iodides with thiols under microwave irradiation [79][a].

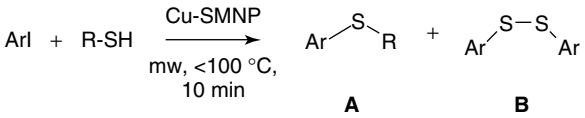

A **B**

Entry	Aryl iodide	Thiol	Conversion (mol%)	Selectivity (A : B ratio)
1	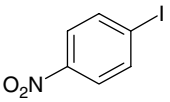	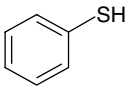	> 99	30 : 1
2	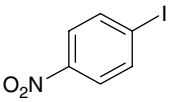	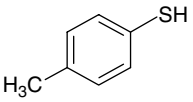	> 99	25 : 1
3	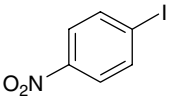	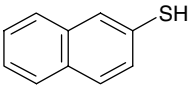	90	40 : 1
4	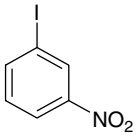	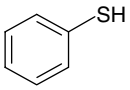	95	18 : 1
5	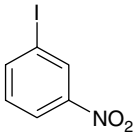	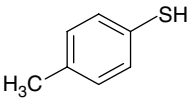	82	25 : 1
6	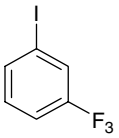	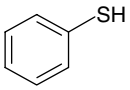	> 99	21 : 1
7	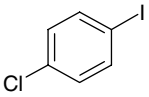	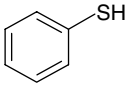	> 99	25 : 1
8	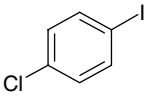	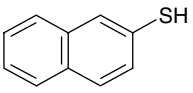	89	42 : 1

Table 2.9 (*Continued*)

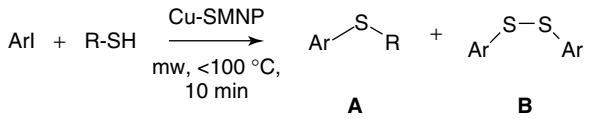

Entry	Aryl iodide	Thiol	Conversion (mol%)	Selectivity (A : B ratio)
9	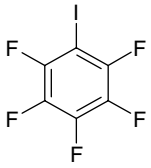	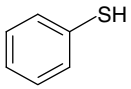	86	33 : 1
10	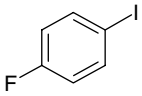	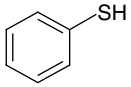	96	20 : 1

Reproduced by permission of the Royal Society of Chemistry.
[a] 1 mmol thiol, 0.5 mmol aryl iodide, 1 mmol K_2CO_3, 2 ml acetonitrile, 0.05 g catalyst, microwaves, 80 W (60–100 °C maximum temperature reached), 10 minutes. Conversion values were based; on the consumption of aryl iodide in the coupling reaction.

anions from the metal precursor. The well-developed nanotubes in Cu–MWNT compared to Cu–NT correlate well with the remarkably superior proportion of metallic copper in the materials while the relatively similar content of metallic Fe in both Fe–MWNT and Fe–NT was in good agreement with a comparable degree of nanotubular arrangement (Figure 2.13). These results will support the hypothesis of the generation of nanotubes mediated/promoted by metal nanoparticles as catalytic seeds [81]. The fast and homogeneous heating achieved under MWI [82] and its reducing properties on solution containing metals [83], compared to conventional heating, are believed to be responsible of the differences found between both types of materials.

2.3.2
Preparation of Designer Nanomaterials for the Production of Energy

2.3.2.1 Biodiesel Preparation Using Metal Oxide Nanoparticles

Following the recent interesting work by Lee *et al.* in the preparation of MgO nanoparticles for the transesterification of glyceryl tributyrate [57], further work related to the preparation of metal oxide heterogeneous catalysts for the transesterification of sunflower oil is ongoing (unpublished work). A range of mixed solid bases including Ca, Mg, and SrO nanoparticles have been prepared following a simple hydrothermal protocol [84] and their activities have been

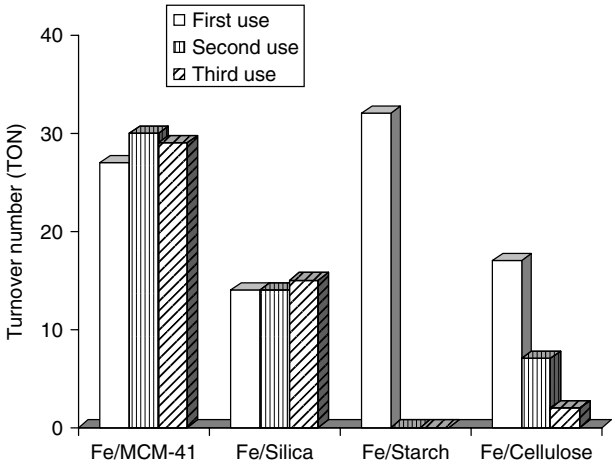

Figure 2.11 Reuse of the supported iron catalysts in the oxidation of benzyl alcohol. Reaction conditions (each run): 0.2 g benzyl alcohol, 0.4 ml H_2O_2, 0.05 g catalyst, microwave irradiation, 200 W, 70 °C, 1 hour [78]. Copyright Wiley-VCH Verlag GmbH & Co.KGaA. Reproduced with permission.

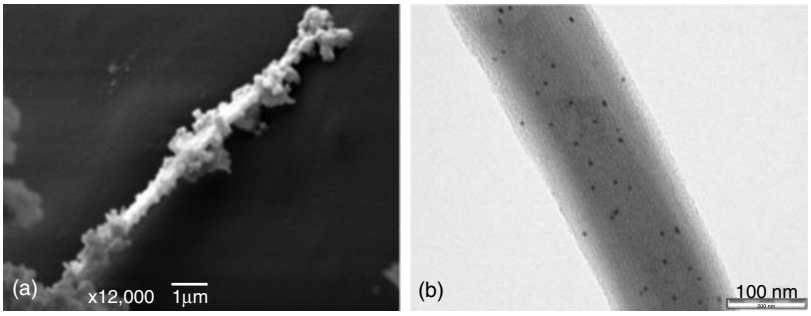

Figure 2.12 (a) SEM and (b) TEM micrographs of nanotubular structures containing metal nanoparticles prepared under microwave irradiation using metal chlorides as precursors [80a]. Reproduced by permission of the Royal Society of Chemistry.

tested in the production of FAME of sunflower oil. Initial results may point to Mg–Sr mixed oxides providing the best FAME profiles in the preparation of biodiesel.

2.3.2.2 **Fuels Prepared via Thermochemical Processes**

The preparation of platinum nanoparticles supported on Al–MCM-48 following a simple impregnation/reduction methodology and their use in the hydroisomerization of *n*-alkanes (*n*-octane) was recently reported [61]. In this work, Pt NPs were found to be evenly dispersed on the mesoporous materials

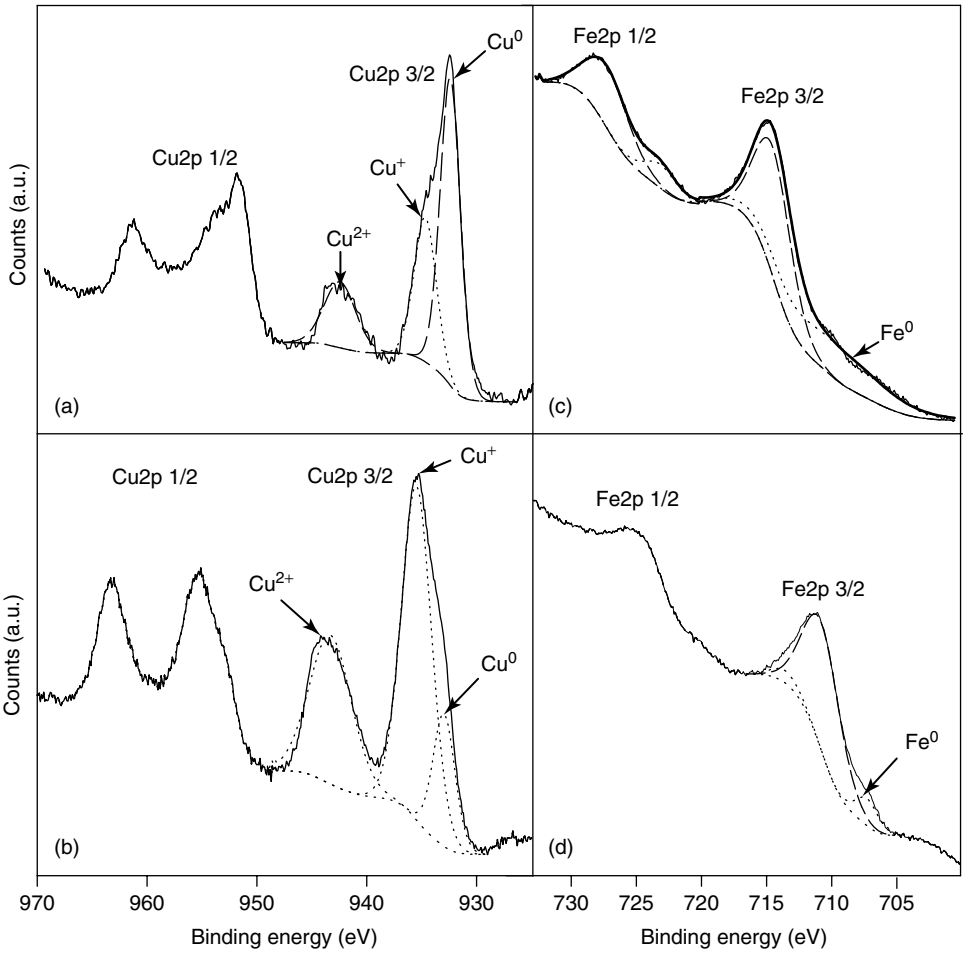

Figure 2.13 Cu (left) and Fe (right) 2p XPS spectra of (a) Cu–MWNT and (b) Cu–NT showed the remarkable differences in the Cu oxidation states that correlate well with the developed nanotubular arrays in Cu–MWNT for a higher content in metallic copper (60% Cu_0) compared to the heterogeneous and poor developed nanotubes in Cu–NT with low Cu_0 content (15% Cu_0). Fe 2p XPS spectra of (c) Fe–MWNT and (d) Fe–NT showing relatively similar Fe_0 content in the materials (slightly lower in Fe–NT 6% compared to a 14% in Fe–MWNT) that correlate well with the comparably developed nanotubes in both Fe materials. Reproduced by permission of the Royal Society of Chemistry.

with particle sizes in the 4–6- nm range (Figure 2.14). The activity of the nanoparticles was tested in the hydroisomerization of *n*-octane to increase the octane number of gasolines as a way to improve the performance of fuels for transport (see Section 2.2.1.3). The catalytic activities were typically over 50% conversion of *n*-octane, with selectivities to the isomerization process higher than 70%, favoring the formation of the 3-methyl-heptane isomer with respect to the 2- and 4-methyl-heptanes (Table 2.10). Materials were found

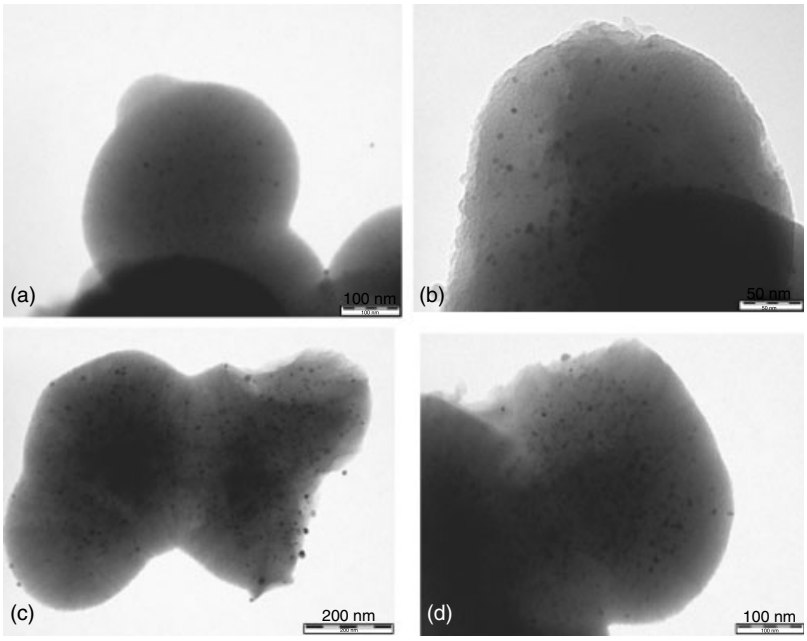

Figure 2.14 TEM micrographs of Pt/Al–MCM-48 materials with different loadings prepared via conventional impregnation/reduction method. (a) 0.5 wt% Pt; (b) 1 wt% Pt; (c) 3 wt% Pt; and (d) 5 wt% Pt [61]. Copyright Wiley-VCH Verlag GmbH & Co.KGaA. Reproduced with permission.

Table 2.10 Total conversion (X_T, mol%) and selectivities to cracking (S_{CK}, mol%) and isomerization to methyl-heptanes (S_{MH}, mol%), including 2, 3, and 4methylheptanes, of different materials in the hydroisomerization of *n*-octane[a].

Catalyst	4 h reaction			12 h reaction			20 h reaction		
	X_T	S_{CK}	S_{MH}	X_T	S_{CK}	S_{MH}	X_T	S_{CK}	S_{MH}
0.5%Pt–40Al	50	18	75	48	17	77	48	18	79
0.5%Pt–30Al	52	28	69	49	27	70	48	19	73
0.5%Pt–20Al	44	17	75	36	14	80	35	14	81
0.5%Pt–15Al	54	26	70	52	21	72	51	15	80
0.5%Pt–SAPO5	50	79	21	45	76	24	41	65	35
0.5%Pt–SAPO11	28	33	59	25	29	64	21	26	74

Adapted from [61]. Copyright Wiley-VCH Verlag GmbH & Co.KGaA. Reproduced with permission.
[a] $T = 375\,^{\circ}C$, $P = 5$ bar, 0.1 g catalyst, Weight hourly space velocity $= 12.7\ h^{-1}$; the difference to 100 in selectivity was due to toluene (ethyl benzene was also obtained in small quantities).

to have activities comparable to those of Pt NPs on SAPOs and commercial zeolites.

Latest research effort has also been devoted to the search of supported Fe and Cu metal oxide nanoparticles supported on a variety of porous materials for the preparation of different synthetic biofuels. Further work in this field is currently ongoing and some interesting results are expected fairly soon in FTS and related processes.

2.4 Future Prospects

2.4.1 Future of the Preparation of SMNPs

The preparation of SMNPs for a wide range of applications has been well developed over the last few years. However, with sustainability as an emerging design criterion in nanoparticle synthesis and applications since the mid 1990s, there is still room for improvement in the methodologies employed for this purpose. In the nanomaterials context, the sustainability concept is reflected in many of the green chemistry principles [20]. Ideally, NPs should be prepared with less toxic precursors, in water or more environmentally benign solvents (e.g., ethanol) using the least number of reagents and a reaction temperature close to RT [20, 85] with as few synthetic steps as possible (one-pot reaction), as well as minimizing the quantities of generated by-products and waste. NPs should also be well dispersed on the support surface and highly active in their catalytic applications. The use of less toxic precursors in benign solvents (e.g., metal acetate or nitrate solutions in water and/or ethanol) [67] using more environmentally friendly supports (e.g., biopolymers and biomaterials) [75, 86] and less energy-intensive protocols [67, 78–80, 85, 87] has been the subject of many recent reports.

Bioreducing agents including sugars, glutathione, starch, and a range of plant and algal extracts have also been employed in the preparation of Au, Ag, and Ni NPs with reasonable good control over particle size and, in some cases, shape [87]. These NPs have been proved to have exceptional catalytic activities in a large range of reactions [10, 11, 67, 88].

Despite their high activities and selectivities in catalysis, the toxicity issue associated with engineered SMNPs also needs to be addressed. It is not clear whether the highly active and dispersed SMNPs desired for catalytic applications are hazardous in contact with human tissues (specially as a result of prolonged exposure) as a consequence of their unique physicochemical properties and the chemical nature of the NP and/or support surfaces [89]. Therefore, more innocuous groups (e.g. hydroxyls) have been explored to replace and/or cover up potentially toxic surface groups in order to improve the biocompability of such nanomaterials [87, 90].

2.4.2 Applications of SMNPs for the Future

Some of the most interesting catalytic trends and future prospects for SMNPs including applications in fuel cells, transformation of platform molecules, environmental remediation, and more recently NMR imaging are highlighted in this section. These only reflect the vision of the author for the future in the research of SMNPs on porous materials.

2.4.2.1 Fuel Cells

Pd/Pt NPs supported on carbonaceous materials (CNTs) have been reported as promising materials to be employed in fuel cells for automotive applications [71]. However, there is still quite a long way to go for the full implementation of such systems, as recent studies by Shao-Horn *et al.* have demonstrated that the stabilities of supported Pt NPs in lowtemperature fuel cells were compromised by the degradation of the electrochemically active surface area in the material through Pt loss from fuel cell electrodes and coarsening of Pt NPs [91]. Manipulation of the surface structure [92] and chemistry (via deposition of Au clusters on Pt NPs) [93] of the SMNPs can improve durability.

2.4.2.2 Catalysis of Platform Molecules

Transformations of platform molecules (e.g., 1, 4 diacids, glycerol) are another interesting research avenue for SMNPs. The US department of energy (USDOE) defined a list of the so-called 12 top sugar-derived main platform molecules (aka building blocks) to be focused on in the next few years [94] (Table 2.11). These platform molecules are generally compounds with various functionalities that can be turned into a plethora of chemicals and high value-added products through different catalytic transformations including oxidations, hydrogenations, amidations, and esterifications. Glycerol and succinic acid are two examples of such platform molecules.

Glycerol is a well-known compound that has recently attracted a great deal of attention, as it is produced in large quantities as by-product in the preparation of biodiesel. The glycerol surplus has challenged both industry and organic chemists to come up with potential routes to obtain high value-added products from glycerol [95]. The oxidation and hydrogenolysis of glycerol has been extensively investigated in a wide range of Pt, Pd, and Au NPs supported on carbonaceous materials [68, 95].

Succinic acid (1, 4, dibutanoic acid) is another important platform molecule. The preparation of high value-added products from succinic acid via different transformations has been recently reported [55, 96] and further investigations are ongoing using supported noble NPs (Pt, Pd, Rh, Ru) in the hydrogenation of succinic acid.

Table 2.11 Top 12 sugar-derived platform molecules (from USDOE report) [11].

1,4-Diacids (succinic, fumaric, and malic acids)	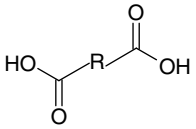
2,5-Furan dicarboxylic acid	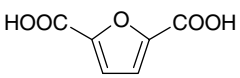
3-Hydroxypropionic acid	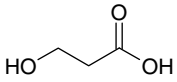
Aspartic acid	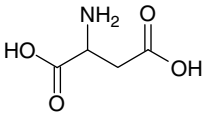
Glucaric acid	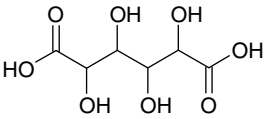
Glutamic acid	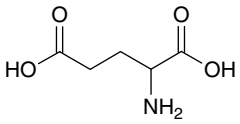
Itaconic acid	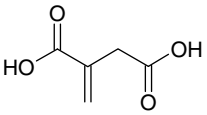
Levulinic acid	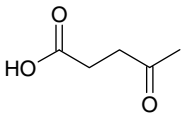
3-Hydroxybutyrolactone	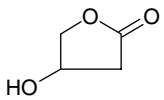
Glycerol	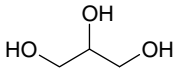

Table 2.11 (*Continued*)

Sorbitol	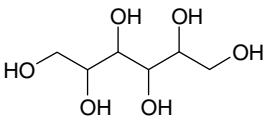
Xylitol/arabinitol	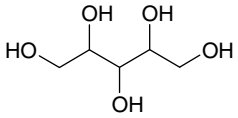

2.4.2.3 **Environmental Remediation**

SMNPs also have a great future in a truly sustainable application: environmental remediation. Fe NPs supported on chitosan and silica [75] and Fe and Ni–cellulose acetate materials [97] were employed in the removal of chlorinated compounds in water. Fe NPs on anionic hydrophilic carbon (Fe/C) and polyacrylic acid (Fe/PAA), with a particle size ranging between 20–100 nm, were also employed in the remediation of soil and groundwater through the dehalogenation of chlorinated hydrocarbons [98] and the remediation of metal ions such as Cr (VI) and As(V) [75, 99]. Both trichloroethylene and metal ions [Cr(VI) and As(V)] were effectively and rapidly reduced under the reaction conditions.

2.4.2.4 **Advanced NMR Applications**

More recently, supported Pt and Pd NPs on Al_2O_3 were reported to provide *para*-hydrogen induced polarization (PHIP) signals in heterogeneous catalyzed hydrogenations [100]. PHIP can improve the NMR signals of reaction intermediates and products by several orders of magnitude providing a high sensitivity that is ideal for following reaction mechanisms. Furthermore, the combination of *para*-hydrogen with SMNPs in hydrogenations will be able to develop new research tools for fundamental and practical applications including kinetics and mechanistic studies and the production of polarized fluids for advanced magnetic resonance imaging (MRI) [101]. MRI techniques suffer from a low intrinsic sensitivity and much effort has been devoted to the use of homogeneous hydrogenations with *para*-hydrogen to produce hyperpolarized contrast agents for biomedical and related applications [101, 102]. In this context, the use of active and reusable heterogeneous catalyzed processes will enable the production of catalyst-free polarized fluids (after separation of the catalyst from the reaction products) and also polarized gases. MRI has also been employed to study catalyst morphologies and synthesis techniques [103, 104].

2.5 Conclusions

The twenty-first century heralds the dawn of a new age in materials science, where the scientist no longer observes the behavior of matter but with the advent of nanoparticles, materials, and technology, is able to predict and manipulate matter for specific applications, with sensitivity and efficiency far surpassing previous systems. This is possible in part due to the ''density of states'' phenomena that exists at the nanometer scale. This idea has sparked tremendous interest and research efforts in the field of nanoparticles. The fusion of the nanoporous and nanoparticles represents one of the most interesting and fruitful areas in the rapidly expanding ''nano'' field, and may ultimately lead to the synthesis of designer catalysts and materials with enormous possibilities in terms of applications. The ideas of sustainable and green chemistry overlap with the core ideas of the SMNP research field. The optimization and use of highly active materials for the preparation of commodity chemicals, in the most efficient manner possible, presents a driving force behind research in both areas. The ''green'' and the ''nano,'' particularly when considering the biorefinery concept, coincide with the desire to carry out transformations under ambient and benign aqueous conditions, with the use of SMNPs potentially offering the most efficient routes to achieving this aim.

Recent advances in the design and preparation of nanomaterials have proved that a numerous variety of them can nowadays be synthesized through different preparation routes and supports with tailored size and distribution, overcoming the limitations of traditional synthetic methodologies. Such designer materials will have significant impact in many areas including increasing applications in industrial catalytic processes. However, the implementation of such nanomaterials may not come without a price and the environmental impact associated with the preparation of SMNPs must be assessed from as many different points of views as possible (e.g., transport, waste, food chain biomagnification, and potential toxicity).

Acknowledgments

The author is very grateful to Prof. Clark and Profs Marinas and Campelo, from the Green Chemistry Centre of Excellence at the University of York and Departamento de Química Orgánica, Universidad de Córdoba, respectively, for their help and support during his stay over the last few years with these two groups. Support and help from Dr. Antonio Romero, Dr. Duncan J. Macquarrie, Dr. Vitaly Budarin, Dr. Camino Gonzalez-Arellano, Alina Balu, and all my coworkers over the last few years is also gratefully acknowledged.

The author would also like to thank Ministerio de Ciencia e Innovación, Gobierno de España, for the provision of a Ramon y Cajal (RyC) fellowship and Dr. Camino Gonzalez-Arellano for her assistance and patience in the revision of the manuscript.

References

1. Ozin, G.A., Arsenault, A.C., and Cademartiri, L. (2009) *Nanochemistry: A Chemical Approach to Nanomaterials*, Royal Society of Chemistry, Cambridge.
2. (a) Mirkin, C.A. (2005) The beginning of a small revolution. *Small*, **1**, 14–16; (b) Grunes, J., Zhu, J., and Somorjai, G.A. (2003) Catalysis and nanoscience. *Chem. Commun.*, 2257–2258.
3. Chen, M., Cai, Y., Yan, Z., and Goodman, D.W. (2006) On the origin of unique properties of supported Au nanoparticles. *J. Am. Chem. Soc.*, **128** (19), 6341–6346.
4. (a) Schmid, G., Maihack, V., Lantermann, F., and Peschel, S. (1996) Ligand-stabilized metal clusters and colloids: properties and applications. *J. Chem. Soc. Dalton Trans.*, 589–595; (b) Doyle, A.M., Shaikhutdinov, S.K., Jackson, S.D., and Freund, H.J. (2003) Hydrogenation on metal surfaces: why are nanoparticles more active than single crystals? *Angew. Chem. Int. Ed.*, **42**, 5240–5243.
5. (a) Luo, X.L., Morrin, A., Killard, A.J., and Smyth, M.R. (2006) Applications of nanoparticles in electrochemical sensors and biosensors. *Electroanalysis*, **18**, 319–326; (b) Shen, Y.C., Tang, Z., Gui, M., Cheng, J.Q., Wang, X., and Lu, Z.H. (2000) Nonlinear optical response of colloidal gold nanoparticles studied by hyper-rayleigh scattering technique. *Chem. Lett.*, 1140–1141; (c) Harada, M., Asakura, K., and Toshima, N. (1993) Catalytic activity and structural analysis of polymer-protected gold/palladium bimetallic clusters prepared by the successive reduction of hydrogen tetrachloroaurate(III) and palladium dichloride. *J. Phys. Chem.*, **97**, 5103–5114.
6. Boudart, M. (1969) Catalysis by supported metals. *Adv. Catal.*, **20**, 153–166.
7. Barkhuizen, D., Mabaso, I., Viljoen, E., Welker, C., Claeys, M., van Steen, E., and Fletcher, J.C.Q. (2006) Experimental approaches to the preparation of supported metal nanoparticles. *Pure Appl. Chem.*, **78**, 1759–1769.
8. (a) Valden, M., Lai, X., and Goodman, D.W. (1998) Onset of catalytic activity of gold clusters on titania with the appearance of non-metallic properties. *Science*, **281**, 1647–1650; (b) Sakurai, H. and Haruta, M. (1996) Synergism in methanol synthesis from CO over gold catalysts supported on metal oxides. *Catal. Today*, **29**, 361–365; (c) Jia, J.F., Haraki, K., Kondo, J.N., Domen, K., and Tamaru, K. (2000) Selective hydrogenation of acetylene over Au/Al_2O_3 catalyst. *J. Phys. Chem. B*, **104**, 11153–11156.
9. (a) Grunes, J., Zhu, J., and Somorjai, G.A. (2003) Catalysis and nanoscience. *Chem. Commun.*, 2257–2258; (b) ColeHamilton, D.J. (2003) Homogeneous catalysis-new approaches to catalysts separation, recovery and recycling. *Science*, **299**, 1702–1706.
10. White, R.J., Luque, R., Budarin, V., Clark, J.H., and Macquarrie, D.J. (2009) Supported metal nanoparticles on porous materials. Methods and applications. *Chem. Soc. Rev.*, **38**, 481–494.
11. Campelo, J.M., Luna, D., Luque, R., Marinas, J.M., and Romero, A.A. (2009) Sustainable preparation of supported metal nanoparticles on porous materials and their applications in catalysis. *ChemSusChem*, **2**, 18–45.
12. (a) Yang, H. and Xia, Y. (2007) Bionanotechnology: enabling biomedical research with nanomaterials. *Adv. Mater.*, **19**, 3085–3087; (b) Huh, Y.M., Lee, E.S., Lee, J.H., Jun, Y.W., Kim, P.H., Yun, C.O., Kim, J.H., Suh, J.S., and Cheon, J. (2007) Hybrid nanoparticles for magnetic resonance imaging of target-specific viral gene delivery. *Adv. Mater*, **19**, 3109–3112.
13. Hu, X. and Dong, S. (2008) Metal nanomaterials and carbon nanotubes-synthesis, functionalization and potential applications towards electrochemistry. *J. Mater. Chem.*, **18**, 1279–1295.

14. Astruc, D., Lu, F., and Aranzaes, J.R. (2005) Nanoparticles as recyclable catalysts: the frontier between homogeneous and heterogeneous catalysis. *Angew. Chem. Int. Ed.*, **44**, 7852–7872.
15. Luque, R. (2008)Supported metal nanoparticles in catalysis, in *Progress in Heterogeneous Catalysis*, 1st edn (ed. D.L.Marmaduke), Nova Publishers, Inc., San Diego.
16. Clark, J.H., Budarin, V., Deswarte, F.E.I., Hardy, J.J.E., Kerton, F.M., Hunt, A.J., Luque, R., Macquarrie, D.J., Milkowski, K., Rodriguez, A., Samuel, O.J., Tavener, S.J., White, R.J., and Wilson, A.J. (2006) Green chemistry and the biorefinery: a partnership for a sustainable future. *Green Chem.*, **8** (10), 853–860.
17. Deswarte, F.E.I., Clark, J.H., Wilson, A.J., Hardy, J.J.E., Marriott, R., Chahal, S.P., Jackson, C., Heslop, G., Birkett, M., Bruce, T.J., and Whiteley, G. (2007) Toward an integrated straw-based biorefinery. *Biofuels Bioprod. Bioref.*, **1** (4), 245–254.
18. Stevens, C.V. and Verhe, R.V. (2004) *Renewable Resources*, Wiley-VCH Verlag GmbH, Chichester.
19. Clark, J.H. (2002) Solid acids for green chemistry. *Acc. Chem. Res.*, **35**, 791–797.
20. Anastas, P. and Warner, J.C. (1998) *Green Chemistry, Theory and Practice*, Oxford University Press, Oxford.
21. Luque, R., Herrero-Davila, L., Campelo, J.M., Clark, J.H., Hidalgo, J.M., Luna, D., Marinas, J.M., and Romero, A.A. (2008) Biofuels: a technological perspective. *Energy Environ. Sci.*, **1**, 542–564.
22. Gedanken, A. (2004) Using sonochemistry for the fabrication of nanomaterials. *Ultrason. Sonochem.*, **11**, 47–55.
23. Perkas, N., Zhong, Z., Grinblat, J., and Gedanken, A. (2008) Deposition of gold particles on mesoporous catalyst supports by sonochemical method, and their catalytic performance for CO oxidation. *Catal. Lett.*, **120**, 19–24.
24. Nagao, D., Shimazaki, Y., Saeki, S., Kobayashi, Y., and Konno, M. (2007) Effect of ultrasonic irradiation on carbon-supported Pt-Ru nanoparticles prepared at high metal concentration. *Colloids Surf. A: Physicochem. Eng. Aspects*, **302** (1-3), 623–627.
25. (a) Perkas, N., Zhong, Z., Chen, L., Besson, A., and Gedanken, A. (2005) Sonochemically prepared high dispersed Ru/TiO_2 mesoporous catalyst for partial oxidation of methane to syngas. *Catal. Lett.*, **103**, 9–14; (b) Li, H., Wang, R., Hong, Q., Chen, L., Zhong, Z., Koltypin, Y., Calderon-Moreno, J., and Gedanken, A. (2004) Ultrasound-assisted polyol method for the preparation of SBA-15-supported ruthenium nanoparticles and the study of their catalytic activity on the partial oxidation of methane. *Langmuir*, **20** (19), 8352–8356.
26. Glaspell, G., Fuoco, L., and El-Shall, M.S. (2005) Microwave synthesis of supported Au and Pd nanoparticle catalysts for CO oxidation. *J. Phys. Chem. B*, **109**, 17350–17355.
27. Glaspell, G., Hassan, H.M.A., Elzatahry, A., Abdalsayed, V., and El-Shall, M.S. (2008) Nanocatalysis on supported oxides for CO oxidation. *Topics Catal.*, **47**, 22–31.
28. Liu, B., Hu, Z., and Che, Y. (2008) US Patent Applications US 2008006524 A1 20080110.
29. Senkan, S., Kahn, M., Duan, S., Ly, A., and Leidholm, C. (2006) High-throughput metal nanoparticle catalysis by pulsed laser ablation. *Catal. Today*, **117**, 291–296.
30. Savastenko, N., Volpp, H.R., Gerlach, O., and Strehlau, W. (2008) Synthesis of nanostructured lean-NO_x catalysts by direct laser deposition of monometallic Pt-, Rh- and bimetallic PtRh-nanoparticles on SiO_2 support. *J. Nanopart. Res.*, **10**, 277–287.
31. Zhang, Y. and Erkey, C. (2006) Preparation of supported nanoparticles using supercritical fluids: a review. *J. Supercrit. Fluids*, **38**, 252–267.
32. (a) Zhang, Y., Kang, D., Saquing, C., Aindow, M., and Erkey, C. (2005) Supported platinum nanoparticles by supercritical deposition. *Ind. Eng. Chem. Res.*, **44**, 4161–4164;

(b) Ye, X.R., Lin, Y., and Wai, C.M. (2003) Decorating catalytic palladium nanoparticles on carbon nanotubes in supercritical carbon dioxide. *Chem Commun*., 642–643.

33. Lee, S.S., Park, B.K., Byoung, S.H., Chang, F., and Kim, H. (2006) Mesoporous silica-supported Pd nanoparticles; highly selective catalyst for hydrogenation of olefins in supercritical carbon dioxide. *Chem. Mater*., **18**, 5631–5633.
34. Legrand, J.C., Diamy, A.M., Riahi, G., Randriamanantenasoa, Z., Polisset–Thfoin, M., and Fraissard, J. (2004) Application of a dihydrogen afterglow to the preparation of zeolite-supported metallic nanoparticles. *Catal. Today*, **89** (1-2), 177–182.
35. Zou, J.J., Zhang, Y.P., and Liu, C.J. (2006) Reduction of supported noble-metal ions using glow discharge plasma. *Langmuir*, **22** (26), 11388–11394.
36. Chiang, C.W., Wang, A., and Mou, C.Y. (2006) CO oxidation catalysed by gold nanoparticles confined in mesoporous aluminosilicate Al-SBA-15: pre-treatment methods. *Catal. Today*, **117**, 220–227.
37. Barau, A., Budarin, V., Caragheorgheopol, A., Luque, R., Macquarrie, D.J., Prelle, A., Teodorescu, V.S., and Zaharescu, M. (2008) A simple and efficient route to active and dispersed silica supported palladium nanoparticles. *Catal. Lett*., **109**, 204–214.
38. Tsubota, S., Haruta, M., Kobayashi, T., Ueda, A., Nakahara, Y., Poncelet, G., Grange, P., and Jacobs, P.A. (1991) *Preparation of Catalysts V*, Elsevier Science B.V., p. 695.
39. Akolekar, D.B., Bhargava, S.K., Foran, G., and Takahashi, M. (2005) Studies of gold nanoparticles supported on iron, cobalt, manganese, and cerium oxide catalytic materials. *J. Mol. Catal. A*, **238**, 78–87.
40. (a) Haruta, M., Tsubota, S., Kobayashi, T., Kageyama, H., Genet, M.J., and Delmon, B. (1993) Low-temperature oxidation of carbon monoxide over gold supported on titanium dioxide, α -ferric oxide, and cobalt tetraoxide. *J. Catal*., **144**, 175–192; (b) Tsubota, S., Cunningham, D.A., Bando, Y., Haruta, M., Poncelet, G., Grange, P., and Jacobs, P.A. (eds) (1995) *Preparation of Catalysts VI*, Elsevier Science B.V., Amsterdam.
41. Centeno, M.A., Portales, C., Carrizosa, I., and Odriozola, J.A. (2005) Gold supported CeO_2/Al_2O_3 catalysts for CO oxidation: influence of the ceria phase. *Catal. Lett*., **102**, 289–297.
42. Cushing, B.L., Kolesnichenko, V.L., and O'Connor, C.J. (2004) Recent advances in the liquid-phase syntheses of inorganic nanoparticles. *Chem. Rev*., **104**, 3893–3946.
43. Eriksson, S., Nylen, U., Rojas, S., and Boutonnet, M. (2004) Preparation of catalysts from microemulsions and their applications in heterogeneous catalysis. *Appl. Catal. A*, **265**, 207–219.
44. Martinez, A. and Prieto, G. (2007) The key role of support-surface tuning during the preparation of catalysts from reverse micellar-synthesized metal nanoparticles. *Catal. Commun*., **8**, 1479–1486.
45. Wang, J.S., Pan, H.B., and Wai, C.M. (2006) Deposition of metal nanoparticles on carbon nanotubes via hexane modified water-in-CO_2 microemulsion at room temperature. *J. Nanosci. Nanotechnol*., **6**, 2025–2030.
46. Kohsuke, M., Miura, Y., Shironita, S., Tomonari, M., Mimura, N., and Yamashita, H. (2007) Preparation and catalysis of nano-sized metal (Pd,Pt) catalysts deposited on Ti-containing zeolite materials by a photo-assisted deposition (PAD) method. *Stud. Surf. Sci. Catal*., **170B**, 1319–1324.
47. He, P., Zhang, M., Yang, D., and Yang, J. (2006) Preparation of Au-Loaded TiO_2 by photochemical deposition and ozone photocatalytic decomposition. *Surf. Rev. Lett*., **13**, 51–55.
48. Serp, P., Kalck, P., and Feurer, R. (2002) Chemical vapor deposition methods for the controlled preparation of supported catalytic materials. *Chem. Rev*., **102**, 3085–3128.
49. Panziera, N., Pertici, P., Barazzone, L., Caporusso, A.M., Vitulli, G., Salvadori,

P., Borsacchi, S., Geppi, M., Veracini, C.A., Martra, G., and Bertinetti, L. (2007) Supported Rh nanoparticles obtained by metal vapour synthesis as catalysts in the preparation of valuable organic compounds. *J. Catal.*, **246**, 351–361.

50. Liang, C., Xia, W., Soltani-Ahmadi, H., Shlueter, O., Fischer, R.A., and Muhler, M. (2005) The two-step chemical vapor deposition of Pd(allyl)Cp as an atom-efficient route to synthesize highly dispersed palladium nanoparticles on carbon nanofibers. *Chem. Commun.*, 282–284.

51. (a) Dominguez-Dominguez, S., Arias-Pardilla, J., Berenguer-Murcia, A., Morallon, E., and Cazorla-Amoros, D. (2008) Electrochemical deposition of platinum nanoparticles on different carbon supports and conducting polymers. *J. Appl. Electrochem.*, **38**, 259–268; (b) Kim, S., Jung, Y., Lee, Y.S., and Park, S. (2007) Electrochemical characteristics of carbon-supported metal nanoparticles catalysts prepared by electrical deposition methods. *J. Diffus. Defect Data-Solid State Data B: Solid State Phenom.*, **124-126**, 1821–1824.

52. Haas, I. and Gedanken, A. (2008) Synthesis of metallic magnesium nanoparticles by sonoelectrochemistry. *Chem Commun.*, 1795–1797.

53. Madler, L., Stark, W.J., and Pratsinis, S.E. (2002) Flame-made ceria nanoparticles. *J. Mater. Res.*, **17**, 1356–1362.

54. Strobel, R. and Pratsinis, S.E. (2007) Flame aerosol synthesis of smart nanostructured materials. *J. Mater. Chem.*, **17**, 4743–4756.

55. Budarin, V., Luque, R., Macquarrie, D.J., and Clark, J.H. (2007) Towards a bio-based industry: benign catalytic esterifications of succinic acid in the presence of water. *Chem. Eur. J.*, **13**, 6914–6919.

56. (a) Marchetti, J.M., Miguel, V.U., and Errazu, A.F. (2007) Possible methods for biodiesel production. *Renew. Sustainable Energy Rev.*, **11**, 1300–1311; (b) Al-Zuhair, S. (2007) Production of biodiesel: possibilities and challenges. *Biofuels Bioprod. Biorefin.*, **1**, 57–66; (c) Mittelbach, M. and Remschmidt, C. (2005) *Biodiesel, the Comprehensive Handbook*, 2nd edn, Graz, Austria.

57. Montero, J.M., Gai, P., Wilson, K., and Lee, A.F. (2009) Structure-sensitive biodiesel synthesis over MgO nanocrystals. *Green Chem.*, **11**, 265–268.

58. Zaccheria, F., Psaro, R., and Ravasio, N. (2009) Selective hydrogenation of alternative oils: a useful tool for the production of biofuels. *Green Chem.*, doi: 10.1039/b817625f.

59. Chen, W., Fan, Z., Pan, X., and Bao, X. (2008) Effect of confinement in carbon nanotubes on the activity of Fischer-Tropsch iron catalyst. *J. Am. Chem. Soc.*, **130**, 9414–9419.

60. Akhmedov, V.M. and Al-Khowaiter, S.H. (2007) Recent advances and future aspects in the selective isomerization of high n-alkanes. *Catal. Rev.*, **49**, 33–109.

61. Campelo, J.M., Lee, A.F., Luna, D., Luque, R., Marinas, J.M., and Romero, A.A. (2008) Preparation of highly active and dispersed platinum nanoparticles on mesoporous Al-MCM-48 and their activity in the hydroisomerisation of n octane. *Chem. Eur. J.*, **14** (19), 5988–5995.

62. (a) Campelo, J.M., Lafont, F., and Marinas, J.M. (1995) Pt/SAPO-5 and Pt/SAPO-11 as catalysts for the hydroisomerization and hydrocracking of n-octane. *J. Chem. Soc. Faraday Trans.*, **91**, 1551–1555; (b) Campelo, J.M., Lafont, F., and Marinas, J.M. (1995) Catalytic properties of the silicoaluminophosphates SAPO-5 and SAPO-11 in n-octane and isooctane hydroconversion. *J. Chem. Soc. Faraday Trans.*, **91**, 4171–4177.

63. Iglesia, E., Barton, D.G., Soled, S.L., Miseo, S., Baumgartner, J.E., Gates, W.E., Fuentes, G.A., and Meitzner, G.D. (1996) Selective isomerization of alkanes on supported tungsten oxide acids. *Stud. Surf. Sci. Catal.*, **101**, 533–540.

64. Astruc, D. (ed.) (2008) *Nanoparticles and Catalysis*, Wiley-VCH Verlag GmbH & Co. KGaA, Weinheim, Germany.

65. Haruta, M. (2003) When gold is not noble: catalysis by nanoparticles. *Chem. Rec.*, **3**, 75–87.
66. Hutchings, G.J. (2008) Nanocrystalline gold and gold palladium alloy catalysts for chemical synthesis. *Chem. Commun.*, 1148–1164.
67. Campelo, J.M., Conesa, T.D., Gracia, M.J., Jurado, M.J., Luque, R., Marinas, J.M., and Romero, A.A. (2008) Microwave facile preparation of highly active and dispersed SBA-12 supported metal nanoparticles. *Green Chem.*, **10**, 853–858.
68. Luque, R., Budarin, V., Clark, J.H., and Macquarrie, D.J. (2008) Glycerol transformations on polysaccharide-derived mesoporous materials. *Appl. Catal. B: Environ.*, **82**, 157–162.
69. Mukherjee, P., Patra, C.R., Ghosh, A., Kumar, R., and Sastry, M. (2002) Characterisation and catalytic activity of gold nanoparticles synthesized by autoreduction of aqueous chloroaurate ions with fumed silica. *Chem. Mater.*, **14**, 1678–1684.
70. Ye, X.R., Lin, Y., Wang, C., Engelhard, M., Wang, Y., and Wai, C.M. (2004) Supercritical fluid synthesis and characterisation of catalytic metal nanoparticles on carbon nanotubes. *J. Mater. Chem.*, **14**, 908–913.
71. Wildgoose, G.G., Banks, C.E., and Compton, R.G. (2006) Metal nanoparticles and related materials supported on carbon nanotubes: methods and applications. *Small*, **2**, 182–193.
72. Jacinto, M.J., Kiyohara, P.K., Masunaga, S.H., Jardim, R.F., and Rossi, L.M. (2008) Recoverable rhodium nanoparticles: synthesis, characterization and catalytic performance in hydrogenation reactions. *Appl. Catal. A: Gen.*, **338**, 52–57.
73. Budarin, V., Clark, J.H., Luque, R., Macquarrie, D.J., and White, R.J. (2008) Palladium nanoparticles on polysaccharide-derived mesoporous materials and their catalytic performance in C-C coupling reactions. *Green Chem.*, **10**, 382–387.
74. Boudjahem, A.G., Monteverdi, S., Mercy, M., and Bettahar, M.M. (2004) Study of nickel catalysts supported on silica of low surface area and prepared by reduction of nickel acetate in aqueous hydrazine. *J. Catal.*, **221**, 325–334.
75. Zhu, B.W., Lim, T.T., and Feng, J. (2006) Reductive dechlorination of 1,2,4-trichlorobenzene with palladized nanoscale Fe^0 particles supported on chitosan and silica. *Chemosphere*, **65** (7), 1137–1145.
76. Purcar, V., Donescu, D., Petcu, C., Luque, R., and Macquarrie, D.J. (2009) Palladium metal nanoparticles on organically modified thin hybrid films. *Catal. Commun.*, **10** (4), 395–400.
77. Purcar, V., Donescu, D., Petcu, C., Luque, R., and Macquarrie, D.J. (2009) Efficient preparation of silver nanoparticles supported on hybrid films and their activity in the oxidation of styrene under microwave irradiation. *Appl. Catal. A: Gen.*, doi: 10.1016/j.apcata.2009.05.003.
78. Gonzalez-Arellano, C., Campelo, J.M., Macquarrie, D.J., Marinas, A.A., Romero, A.A., and Luque, R. (2008) Efficient microwave oxidation of alcohols using low-loaded supported metallic iron nanoparticles. *ChemSusChem.*, **1**, 743–750.
79. Gonzalez-Arellano, C., Luque, R., and Macquarrie, D.J. (2009) Microwave efficient S-Arylation of thiols with aryl iodides using supported metal nanoparticles. *Chem. Commun.*, 1410–1412.
80. (a) Gonzalez-Arellano, C., Luque, R., and Macquarrie, D.J. (2009) Nanotubular self-assembly of n dodecylamine/TEOS/water/acetonitrile mixtures. *Chem. Commun.*, doi: 10.1030.b903368h; (b) Luque, R., Balu, A.M., Campelo, J.M., Gonzalez-Arellano, C., Gracia, M.J., Luna, D., Marinas, J.M., and Romero, A.A. (2009) Tunable shapes in supported metal nanoparticles: from nanoflowers to nanocubes. *Mater. Chem. Phys.*, doi: 10.1016/j.matchemphys.2009.06.010.
81. Tuan, H.Y., Ghezelbash, A., and Korgel, B.A. (2008) Silicon nanowires and silica nanotubes seeded by copper nanoparticles in an organic solvent. *Chem. Mater.*, **20**, 2306–2313.

82. Kappe, C.O. (2008) Microwave dielectric heating in synthetic organic chemistry. *Chem. Soc. Rev.*, **37**, 1127–1139.
83. Tuval, T. and Gedanken, A. (2007) A microwave-assisted polyol method for the deposition of silver nanoparticles on silica spheres. *Nanotechnology*, **18**, 255601/1–255601/7.
84. Utamapanya, S., Klabunde, K.J., and Schlup, J.R. (1991) Nanoscale metal oxide particles/clusters as chemical reagents. Synthesis and properties of ultrahigh surface area magnesium hydroxide and magnesium oxide. *Chem. Mater.*, **3**, 175–181.
85. Dahl, J.A., Maddux, B.L.S., and Hutchinson, J.E. (2007) Toward greener nanosynthesis. *Chem. Rev.*, **107**, 2228–2269.
86. Reddy, K.R., Kumar, N.S., Reddy, P.S., Sreedhar, B., and Kantam, M.L. (2006) Cellulose-supported palladium(0) catalyst for Heck and Sonogashira coupling reactions. *J. Mol. Catal. A: Chem.*, **252**, 12–16.
87. Murphy, C.J. (2008) Sustainability as an emerging design criterion in nanoparticle synthesis and applications. *J. Mater. Chem.*, **18**, 2173–2176.
88. Zheng, N. and Stucky, G.D. (2006) A general synthetic strategy for oxide-supported metal nanoparticle catalysts. *J. Am. Chem. Soc.*, **128**, 14278–14280.
89. Elder, A., Yang, H., Gwiazda, R., Teng, X., Thurston, S., He, H., and Oberdorster, G. (2007) Testing nanomaterials of unknown toxicity: an example based on platinum nanoparticles of different shapes. *Adv. Mater.*, **19**, 3124–3129.
90. (a) Gerion, D., Pinaud, F., Williams, S.C., Parak, W.J., Zanchet, D., Weiss, S., and Alivisatos, P.A. (2001) Synthesis and properties of biocompatible water-soluble silica-coated CdSe/ZnS semiconductor quantum dots. *J. Phys. Chem. B*, **105**, 8861–8871; (b) Hunyadi, S.E. and Murphy, C.J. (2006) Tunable one-dimensional silver-silica nanopeapod architectures. *J. Phys. Chem. B*, **110**, 7226–7231.
91. Shao-Horn, Y., Sheng, W.C., Chen, S., Ferreira, P.J., Holby, E.F., and Morgan, D. (2007) Instability of supported platinum nanoparticles in low-temperature fuel cells. *Topics Catal.*, **46** (3-4), 285–305.
92. Komanicky, V., Chang, K.C., Menzel, A., Markovic, N.M., You, H., Wang, X., and Myers, D. (2006) Stability and dissolution of platinum surfaces in perchloric acid. *J. Electrochem. Soc.*, **153** (10), B446–B451.
93. Zhang, J., Sasaki, K., Sutter, E., and Adzic, R.R. (2007) Stabilisation of platinum oxygen-reduction electrocatalysts using gold clusters. *Science*, **315**, 220–222.
94. Werpy, T. and Pedersen, G. (2004) Top Value Chemicals from Biomass, May 2009. *http://www1.eere.energy.gov/biomass/pdfs/35523.pdf*.
95. Pagliaro, M., Ciriminna, R., Kimura, H., Rossi, M., and Della Pina, C. (2007) From glycerol to value-added products. *Angew. Chem. Int. Ed.*, **46**, 4434–4440.
96. (a) Budarin, V., Clark, J.H., Luque, R., Macquarrie, D.J., Koutinas, A., and Webb, C. (2007) Tunable mesoporous materials optimised for aqueous phase esterifications. *Green Chem.*, **9**, 992–995; (b) Budarin, V., Clark, J.H., Luque, R., and Macquarrie, D.J. (2007) Versatile mesoporous carbonaceous materials for acid catalysis. *Chem. Commun.*, 634–636.
97. Linfeng, W. and Ritchie, S.M.C. (2006) Removal of trichloroethylene from water by cellulose acetate supported bimetallic Ni/Fe nanoparticles. *Chemosphere*, **63**, 285–292.
98. Schrick, B., Hydutsky, B.W., Blough, J.L., and Mallouk, T.E. (2004) Delivery vehicles for zerovalent metal nanoparticles in soil and groundwater. *Chem. Mater.*, **16** (11), 2187–2193.
99. Hoch, L.B., Mack, E.J., Hydutsky, B.W., Hershman, J.M., Skluzacek, J.M., and Mallouk, T.E. (2008) Carbothermal synthesis of carbon-supported zero-valent iron particles for the remediation of hexavalent chromium. *Environ. Sci. Technol.*, **42**, 2600–2605.

100. Kovtunov, K.V., Beck, I.E., Bukhtiyarov, V.I., and Koptyug, I.V. (2008) Observation of para-hydrogen induced polarisations in heterogeneous hydrogenation on supported metal catalysts. *Angew. Chem. Int. Ed.*, **47**, 1492–1495.

101. Bouchard, L.S., Burt, S.R., Anwar, M.S., Kovtunov, K.V., Koptyug, I.V., and Pines, A. (2008) NMR imaging of catalytic hydrogenation in microreactors with the use of para-hydrogen. *Science*, **319**, 442–445.

102. Mansson, S., Johansson, E., Magnusson, P., Chai, C.M., Hansson, G., Petersson, J.S., Stahlberg, F., and Golman, K. (2006) 13C imaging: a new diagnostic platform. *Eur. Radiol.*, **16**, 57–67.

103. Koptyug, I.V., Sagdeev, D.R., Gerkema, E., Van As, H., and Sagdeev, R.Z. (2005) Solid State 27Al MRI and NMR thermometry for catalytic applications with conventional (liquids) MRI instrumentation and techniques. *J. Mag. Res.*, **175** (1), 21–29.

104. Lysova, A.A., Koptyug, I.V., Sagdeev, R.Z., Parmon, V.N., Bergwerff, J.A., and Weckhuysen, B.M. (2005) Non-invasive in situ visualisation of supported catalyst preparation using multinuclear magnetic resonance imaging. *J. Am. Chem. Soc.*, **127** (34), 11916–11917.

3
Supramolecular Receptors for Fullerenes

Gustavo Fernández, Luis Sánchez, and Nazario Martín

3.1
Introduction

Since the extraction of fullerenes from the carbon soot using aromatic solvents [1], the interaction between the convex surface of fullerenes and the flat π surface of aromatic moieties has received increasing attention [2]. Fullerene [3] is a polyenic structure constituted by 12 pentagonal and 20 hexagonal rings, in which each carbon atom possess $sp^{2,3}$ hybridization [4]. The existence of pentagonal rings provokes a curvature and, therefore, a weak polarization on its surface between the 5 : 6 ring junctions, which represent centers of positive charge, and the negatively charged 6 : 6 fusions [5, 6]. This anisotropic distribution of the electronic charge is the basis to determine the interactions with other substrates.

There are two main driving forces to design supramolecular receptors for fullerenes: on one hand, it would be feasible for an effective purification from their natural extraction sources, mainly carbon soot and fullerite. On the other hand, in combination with electron donor receptors, we could design highly organized architectures that can find application in optoelectronics, where the organization of the active materials plays a crucial role in the improvement and precise operation of the devices.

In the design of supramolecular receptors for fullerenes we have to consider the neutral features of fullerenes. Therefore, there are some energetic factors to take into account that will determine the final properties and the nature of the interactions involved in the supramolecular complexes: (i) van der Waals forces, (ii) electrostatic interactions, (iii) induction energy, (iv) charge-transfer, and (v) desolvation [7, 8].

Considering the nature of all of these noncovalent forces and the geometry and electronic features of C_{60} and its higher congeners, van der Waals and solvophobic interactions should be decisive in the stability of the C_{60}-receptor complexes [9]. The large global area of fullerenes, consequence of their spherical geometry, and their nonpolar character make these noncovalent effects key factors to attain highly stabilized complexes. Thus, the direct strategy consists in increasing the aromatic

Ideas in Chemistry and Molecular Sciences: Advances in Nanotechnology, Materials and Devices.
Edited by Bruno Pignataro

ISBN: 978-3-527-32543-6

surface of the receptor in short contact with the fullerene guest, where van der Waals forces would be maximized and fullerenes can find refuge from the solvent.

Taking these factors into consideration, we will revise those receptors for fullerenes described up to now, including (i) the earlier and most significant examples of classic receptors, (ii) flat receptors – primarily based on porphyrins as recognizing elements – and (iii) the most recent examples based on curved aromatic scaffolds.

3.2
Classic Receptors for Fullerenes Based on Curved Recognizing Units

Host–guest chemistry of fullerenes with traditional or classic host molecules, calix[*n*]arenes, calix[*n*]resorcinarenes, and cyclotriveratrylenes (CTVs) has been widely used with the main goal of separating fullerenes from their natural sources. The first receptor for [60] fullerene was serendipitously described in 1992. Wennerström and coworkers observed that β-cyclodextrins (β-CDs) formed water-soluble complexes of 2 : 1 stoichiometry with C_{60}. Shortly after this discovery, Diederich *et al.* described the first purposely designed receptor capable of forming stable complexes with fullerenes in solution [11]. These authors demonstrated that a set of azacrown ether-derived macrocycles decorated in their periphery with lipophilic chains (**1**–**2**) were capable of effectively binding C_{60} and C_{70} in solution (Scheme 3.1).

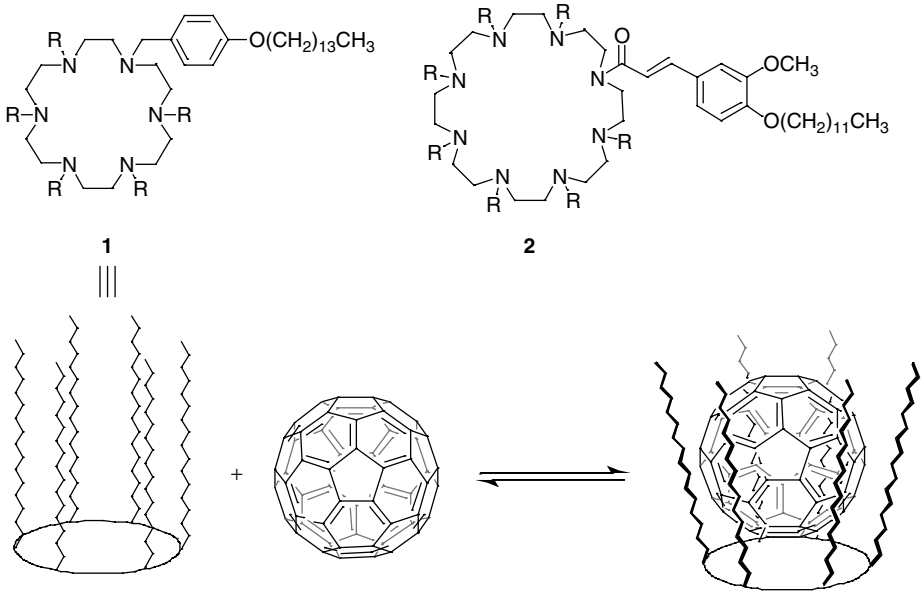

Scheme 3.1 Chemical structure of the receptors reported by Diederich, Ringsdorf, and coworkers and cartoon representation showing their binding stoichiometry.

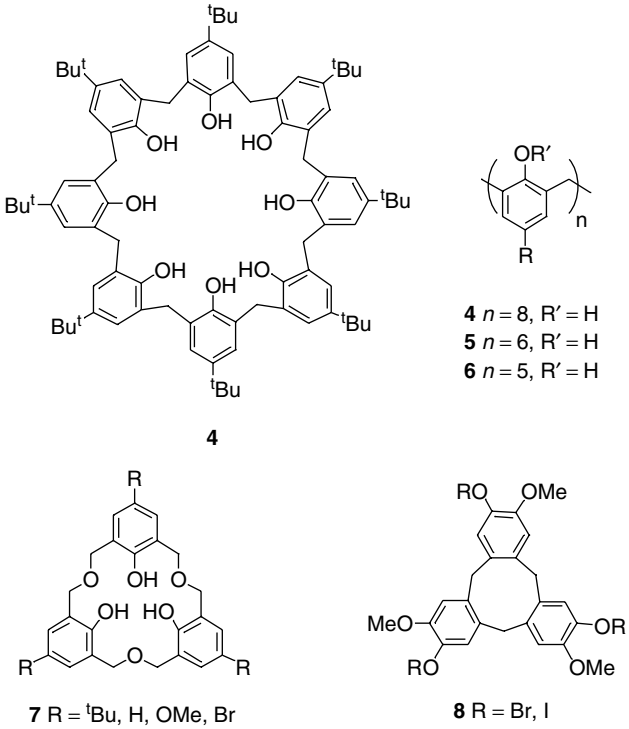

Figure 3.1 Chemical structure of different classic curved receptors for fullerenes.

In 1994, Atwood [12] and Shinkai [13], independently, found out that *p*-tert-butylcalix[8]arene (**3**, Figure 3.1) selectively precipitated with C_{60} from a mixture of fullerite, thus giving rise to an effective purification of C_{60}. These authors demonstrated that the complexation of C_{60} depends fundamentally on the size cavity as well as the functional groups present in the upper rim of the calixarene. This discovery motivated several research groups to design different calixarene-based receptors for fullerenes. Calix[8]-, [6]-, y [5]arenes (**4** [14], **5** [15], and **6** [16], Figure 3.1), and oxacalix[3]arenes (**7**) [17] have been demonstrated to form a large variety of inclusion complexes with fullerenes, in which the guest is located in the inner cavity of the calixarene (Figure 3.1).

At the same time, Atwood and coworkers reported that cyclotriveratrilene (CTV) derivatives (**8**) were capable of effectively binding C_{60} in the solid state, yielding a ''ball-and-socket'' nanostructure [18]. Fukazawa and coworkers described for the first time that unsubstituted OH–calix[5]arenes (compounds **9–11** in Figure 3.2) form stable complexes with C_{60} in solution [19]. UV–Vis titration experiments demonstrated the appearance of a new transition with an isosbestic point at 478 nm upon addition of C_{60} to a solution of receptors **9** and **10** in different solvents (toluene, *o*-DCB, CS_2, benzene). The binding constants extracted from titration experiments were determined to be highly solvent dependent. Thus, receptor

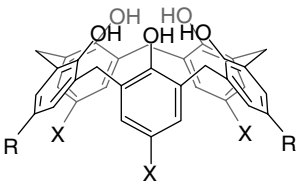

9 : R = I, X = CH_3
10 : R, X = CH_3
11 : R = H, X = CH_3
12 : R, X = Ph

Figure 3.2 Chemical structures of hydroxycalixarene-based receptors.

9 showed a binding constant (K_a) of 308 M^{-1} in *o*-DCB, 660 M^{-1} in CS_2, 1840 M^{-1} in benzene, and 2120 M^{-1} in toluene. Consequently, the binding constant increases as the solubility of C_{60} decreases, a fact that clearly demonstrates the crucial role that solvophobic forces play in this interaction. Likewise, the K_a resulted to be dependent on the nature of the peripheral substituents of the receptors. Thus, receptor **9**, substituted in its periphery with two iodine atoms, showed the highest stability for all complexes described therein, affording a K_a of $\sim$ 2120 M^{-1} in toluene, whereas receptors **10** and **11**, endowed with smaller substituents, showed a lower ability ($K_a \sim 1670$ and 590 M^{-1}, respectively) to bind C_{60}. These results also prove the great contribution of van der Waals forces in the final interaction.

Shortly after, Fukazawa and coworkers found that calix[5]arene **11** forms a 1 : 1 complex in solution. This behavior is completely different to that observed in the solid state [20]. The X-ray crystalline structure of complex **12**-C_{60} revealed that one C_{60} molecule is sandwiched between two units of calixarene, affording a complex with 2 : 1 stoichiometry. This apparent contradiction in the complex stoichiometry when comparing solution and solid state was later observed in several supramolecular fullerene assemblies [21]. On the basis of these findings, it seems reasonable to attribute a lower complexation stoichiometry in solution, where molecules are more disordered due to solvent and thermal vibration effects, in comparison with the regularly packed arrangements of solid-state structures (Figure 3.3).

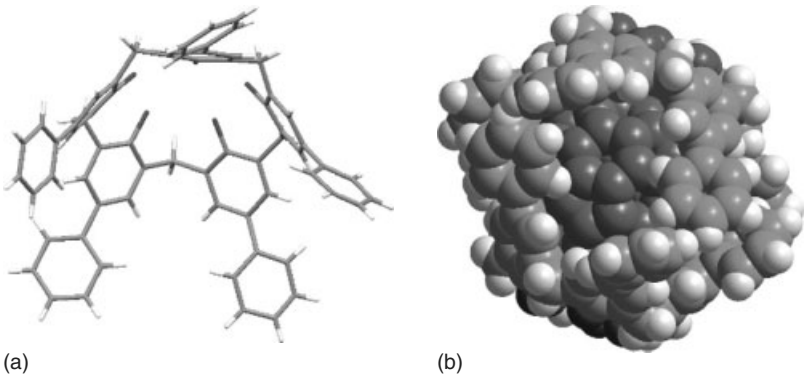

(a) (b)

Figure 3.3 (a) X-ray structure of receptor **12**. (b) Optimized geometry of complex [**12**]$_2$·C_{60}.

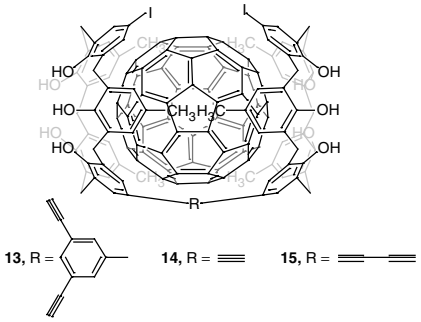

Figure 3.4 Chemical structure of complexes **13–15** and C_{60}.

The discovery of a 2 : 1 supramolecular complex in the solid state led Fukazawa and coworkers to design novel bis-calix[5]arene receptors in which two units of calixarene were covalently attached through different spacers [22]. Three new receptors were synthesized with well-defined cavities with the aim to cover the maximum available surface of C_{60} (Figure 3.4). As expected, the use of receptors that effectively match the convex surface of C_{60} provokes a dramatic increase in the binding constants. Thus, the 1 : 1 complex between receptor **13** and C_{60} afforded a K_a of 76000 M^{-1} in toluene. The values of K_a followed a similar pattern than that observed for receptors **9–12**. Moreover, receptors **13–15** were demonstrated to bind C_{70} even more selectively than C_{60}, affording a K_a of 163 000 M^{-1} for the complex **13** · C_{70}, a significantly higher value than that observed in the complex **13** · C_{60} under similar conditions. Later on, other similar dimeric receptors with comparable binding constants have also been described [23].

Mendoza and coworkers described a calix[4]arene dimer with a high affinity for C_{70} (Figure 3.5), affording a calculated K_a of 15 000 M^{-1} in toluene [24]. The formation of a smaller cavity in comparison with calix[5]arene derivatives makes the

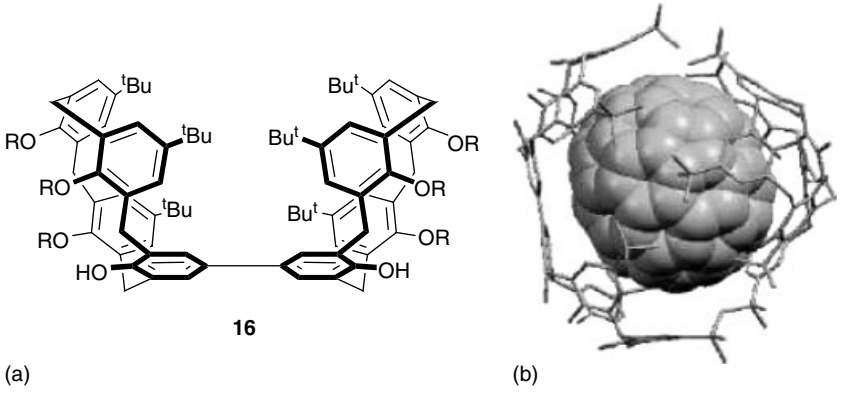

Figure 3.5 (a) Chemical structure of receptor **16**, formed by two calix[4]arene units. (b) Optimized geometry of [**16**]$_2$·C_{70}.

participation of two units of receptor **16** to complex C_{70} necessary, thus generating a dimeric capsule (Figure 3.5). Recently, these authors have reported the synthesis and complexation of two CTV-based derivatives, decorated in their periphery with three self-complementary ureido pyrimidinone (UPy) units [25]. In the presence of C_{60} and/or C_{70}, receptors **17** and **18** were capable to encapsulate C_{60} and C_{70} through a combination of self-complementary hydrogen bonds between UPy units and π-stacking of CTVs in nonpolar solvents, similar to that observed for receptor **16** (Figure 3.6). These receptors were proved to bind C_{70} with higher affinity than C_{60}, and by means of solid–liquid extraction techniques, these authors succeeded in the selective purification of C_{70} from carbon soot and fullerite.

Some cage-shaped host molecules constructed by metal-assisted coordination have been examined for the encapsulation of [60]fullerene. Shinkai and coworkers first reported a C_{60} complex with a self-assembled cage, the oxacalix[3]arene dimer, functionalized with three pyridine moieties. The introduction of Pd (II) centers allows the coordination of the peripheral pyridine units of two complementary fragments of oxacalixarene and yields a dimeric capsule (**19**, Figure 3.7). NMR studies demonstrated the inclusion of C_{60} inside the cavity generated by two units of oxacalixarene. ^{1}H NMR studies showed the shielding of most aromatic resonances corresponding to the receptor upon addition of ^{13}C-enriched C_{60}, which demonstrates the interaction between the aromatic rings of the receptor and C_{60}. Furthermore, ^{13}C NMR experiments showed the presence of a new downfield resonance (140.9 ppm) besides the typical signal at ~142.8 ppm of free fullerene. This new resonance was assigned to the inclusion complex formed between the dimeric capsule **19** and C_{60} [26].

Recently, Wang, and coworkers described a set of receptors (**20**–**21**, Figure 3.8) based on calix[5] pyridines and calix [10] pyridines as recognizing elements [27]. Unlike calix[5]arenes, which adopt a cone conformation, X-ray structures revealed that calix[5]pyridines show a distorted 1,3-alternate conformation with one pyridine ring oriented inward in which all bridging nitrogen atoms have nearly sp^2 character,

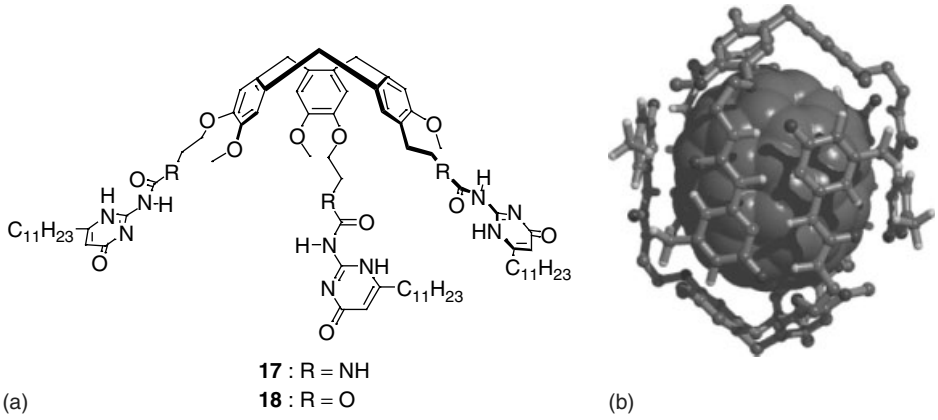

Figure 3.6 Chemical structure and molecular modeling of $[17]_2 \cdot C_{70}$.

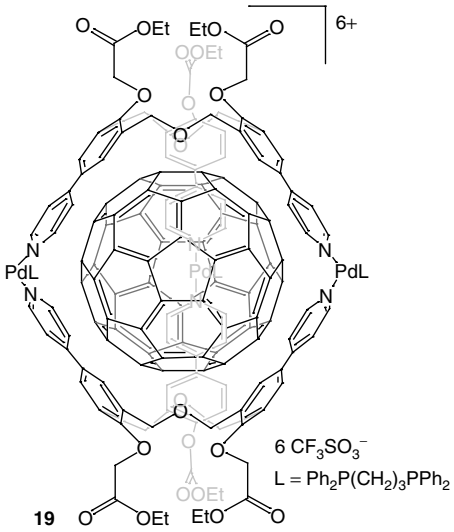

Figure 3.7 Inclusion complex formed between dimeric capsule **19** and C_{60}.

giving rise to a partial conjugated system in combination with pyridine rings (Figure 3.8). On the other hand, calix[10]pyridines present a parallelogram structure in the solid state with the four corner pyridine atoms pointing inward (Figure 3.8). UV–Vis titration experiments of both receptors with C_{60} in toluene revealed a ~20 nm red shifting in the electronic transition at 452 nm upon addition of increasing amounts of fullerene. Moreover, fluorescence titration experiments shed K_a values of 2.6×10^5 and 3.0×10^5 M^{-1} for **20** and **21**, respectively. Remarkably, receptors **20** and **21** showed a similar binding ability to form 1 : 1 complexes with C_{70}, affording K_a values of 1.2×10^5 and 1.3×10^5 M^{-1}, respectively.

3.3
Receptors for Fullerenes Based on Planar Recognizing Units

Porphyrins are widely known to interact favorably with fullerenes in solution and in the solid state, which has been exploited to design a variety of receptors for C_{60} and higher fullerenes [28]. In principle, the planar surface of porphyrins would serve as a primary recognizing element to increase $\pi-\pi$ and van der Waals interactions with fullerene surface.

The association between C_{60} and a porphyrin was firstly observed in the solid state by Boyd, Reed, and coworkers [29]. The short distance observed (2.75 Å) between the free-base porphyrin and C_{60} in the crystalline structure of dyad **22** (Figure 3.9) points out to a strong $\pi-\pi$ interaction.

However, different examples described in the literature demonstrate that the presence of only one planar recognizing unit is not sufficient to complex fullerenes in solution [28]. Therefore, at least two recognizing moieties are necessary to bind

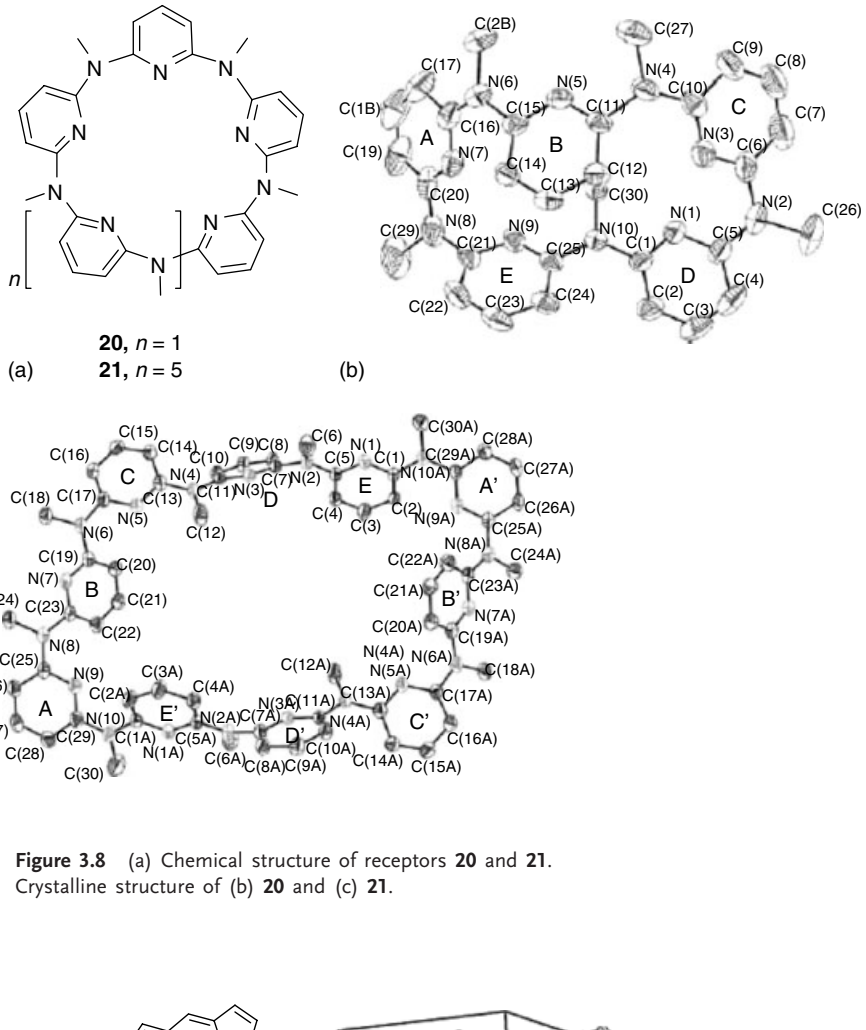

Figure 3.8 (a) Chemical structure of receptors **20** and **21**. Crystalline structure of (b) **20** and (c) **21**.

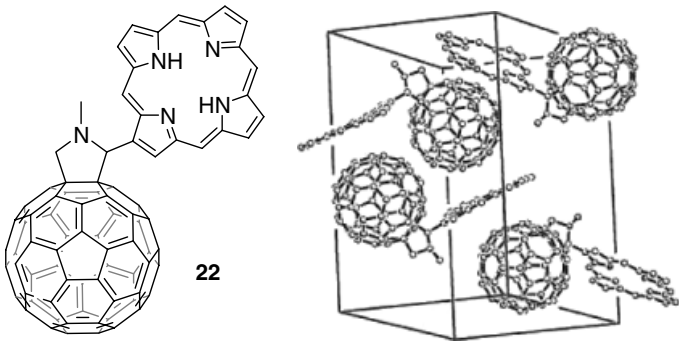

Figure 3.9 Chemical structure and crystalline packing of dyad **22**.

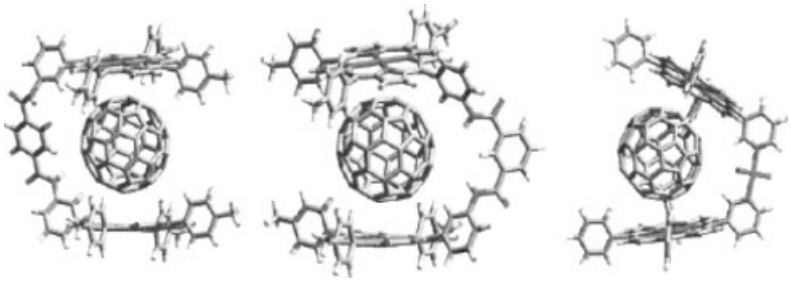

Figure 3.10 Supramolecular complexes formed by bisporphyrins **23**–**25** and C_{60}.

C_{60} efficiently, what has been achieved through suitable spacers and leads to bi- and polyvalent receptors.

Boyd *et al.* prepared a series of porphyrin-based tweezer-like receptors (**23**–**25**) capable to complex C_{60} in solution [30]. X-ray structures of their corresponding complexes revealed that the electron-rich 6 : 6 fusions of fullerene rings were in close contact with porphyrin planes (Figure 3.10). Furthermore, it was demonstrated that the substitution pattern of the metallomacrocycle rings strongly influences the association of these receptors. Thus, the binding constants in toluene varied from 490 M^{-1} for Fe–porphyrin to 5200 M^{-1} for the free-base porphyrin. The higher K_a observed for the free-base porphyrin accounts for the participation of electrostatic forces that strengthens the initial π-stacking. It is also suggested that solvation effects could reinforce the sum of electrostatic and π-stacking interactions involved in the complexation.

In a recent example, Sanders and coworkers described the synthesis and fullerene complexation of two different tripodal porphyrin hosts (**26**–**27**) by means of X-ray crystallography, and NMR and fluorescence titrations [31]. Surprisingly, the binding of C_{60} resulted to be completely different in solution and in the solid state. Whereas ^{1}H NMR titration and Job plot analysis demonstrated the formation of supramolecular complexes with 1 : 1 stoichiometry for both receptors, crystallographic analysis showed a rather complex packing of fullerene and porphyrin units. For receptor **26**, two of the porphyrins intercalate a C_{60} molecule in a tweezer-like arrangement, whereas the remaining porphyrin unit bends to one side relative to the tweezer motif (Figure 3.11). The resulting solid-state packing is composed by a dimer of trimers in which four C_{60} fragments are intercalated both intra- and intermolecularly. On the other hand, the asymmetric unit in **27** contains one porphyrin trimer and two crystallographically unique C_{60} molecules. The small trimer in the unit cell is arranged in such a way that binding cavities suitable for two intermolecularly bound fullerene are created (Figure 3.11). Two fullerene molecules are accommodated in binding pockets composed of two tilted porphyrins, belonging to the neighboring trimeric units. The resulting structure revealed that all fullerene molecules are surrounded by two porphyrins in an inclined fashion, consequently, leaving no unbound C_{60} in the structure.

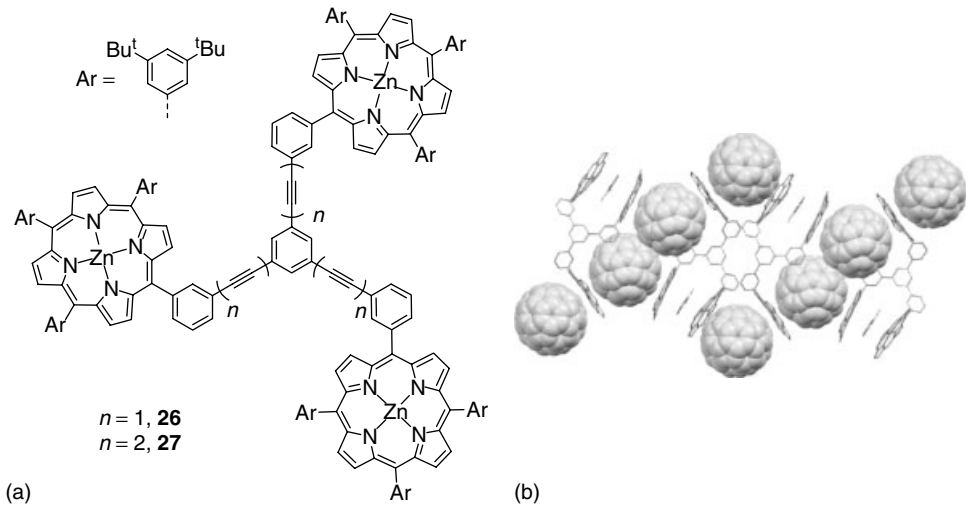

Figure 3.11 (a) Chemical structure of the porphyrin-based tripodal receptors. (b) Crystalline structure of the complex formed from **27** and C_{60}.

The binding constants extracted from NMR and fluorescence studies were found to be ~2500 M^{-1}, which is in the range of the affinities of previously reported related systems under similar conditions [32]. This markedly different behavior in solution and in the solid state is attributed to the large entropic penalty associated with solvated molecules, which prevents the formation of supramolecular networks, yet observed in the solid state.

In 1999, Aida reported for the first time the formation of highly stable inclusion complexes between fullerenes and a dimeric porphyrin in which two porphyrins are covalently attached by flexible alkyl chains (**28**–**30**, Figure 3.12) [33]. Structural variations on this design, either introducing different substituents on the porphyrin rings or exchanging the metal center, have led to one of the richest collection of receptors for fullerenes up to now [34]. It is also worth noting that the flexible linkers have a decisive influence on the stability of the complexes. When the alkyl linkers were substituted by more rigid unsaturated hydrocarbon chains of approximately equivalent length, the dimeric receptor completely loses the capability to bind C_{60}. Moreover, the solid-state structure of the inclusion complexes shows the alkyl spacers folded in order to maximize van der Waals contacts with fullerenes, once more highlighting the important contribution of the alkyl chains to the stabilization of the complexes.

The nature of the metal center also affects the K_a values to a great extent. Binding constants of 7.9×10^5 M^{-1} for the free-base porphyrin, 1.8×10^6 for Co (II) porphyrin, and 2.5×10^7 for the case of Rh (II) porphyrin were calculated, using toluene as solvent. Recently, it was found that Ir (II) porphyrin showed remarkably high values of association constant, affording a maximum value for

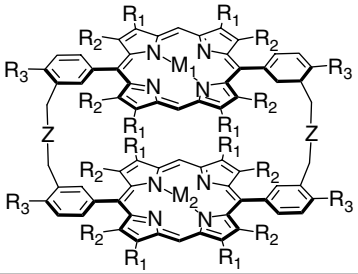

Receptor	Z	R_1	R_2	R_3	M1	M_2
28	$(CH_2)_6$	Hex	Hex	H	Zn (II)	Zn (II)
29	$(CH_2)_6$	Me	Hex	H	Ir (II)	Ir (II)
30	$(CH_2)_6$	H	H	^{t}Bu	Me, H	Rh (III)

Figure 3.12 General structure and substitution pattern of the bisporphyrin receptors **28–30**.

29 of $\sim 1.3 \times 10^8$ M^{-1} in o-DCB. This example is, up to now, the receptor with highest ability to complex C_{70} in solution [35]. Nevertheless, the most significant feature in all these complexes is the shape of porphyrins in the solid state, since all of them adopt a nonplanar concave conformation to maximize the positive contacts with C_{60} and C_{70}. These findings again demonstrate the key role that van der Waals interactions play in the formation of supramolecular complexes with fullerenes.

3.4
Concave Receptors for Fullerenes

Curved molecules are tensioned structures with bond lengths and angles away from the preferred ones, and therefore, their synthetic methodology is not a simple task. This circumstance explains why the number of receptors described in the literature is scarce in comparison with planar ones [36].

Corannulene, a large aromatic system composed of a five-membered central ring fused to five benzene rings (**31**, Figure 3.13) was the first bowl-shaped molecule reported in literature [37]. Theoretical calculations predicted that the curvature of corannulene would favor a concave–convex stacking with the outer surface of fullerenes [36]. However, X-ray studies showed the lack of interaction with C_{60} in the solid state [38]. On the other hand, it was proved that corannulene forms a stable complex with C_{60} in the gas phase [39], which demonstrates the geometrical complementarity between concave corannulene and the convex surface of C_{60} in the gas phase.

On the basis of this early observation, several corannulene-based receptors have been reported. Receptors **32** [40] and **33** [41] feature five additional aromatic rings on their periphery, what is expected to increase the cavity size and, consequently,

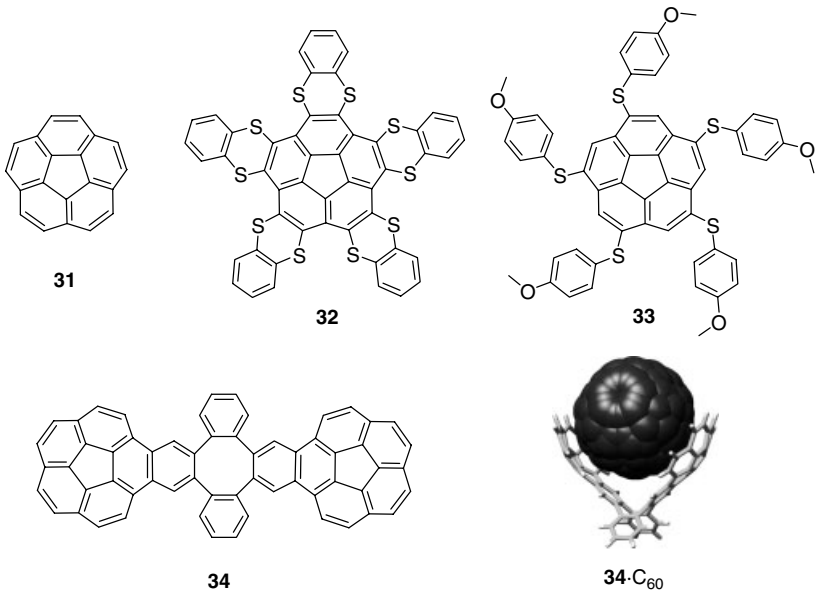

Figure 3.13 Chemical structure of receptors based on corannulene (**31**) as recognizing element.

the affinity for fullerenes (Figure 3.13). The calculated binding constants were found to be 3.0×10^2 M^{-1} for receptor **32** and 1.4×10^3 M^{-1} for **33** in toluene and CS_2, respectively. The higher value for **33** was attributed to the increase in electronic density due to the methoxy-substituted rings.

Recently, Sygula *et al.* reported receptor **34** in which two corannulene units were connected through a rigid aromatic spacer to give rise to a tweezer-like bivalent receptor [42]. X-ray diffraction studies of mixtures of ''buckycatcher'' **34** and C_{60} allowed the determination of the solid-state structure of the complex (Figure 3.13), where two corannulene units cover great part of the convex surface of C_{60}. The K_a values extracted from UV–Vis titrations in toluene shed values of 8.6×10^3 M^{-1}, which is slightly higher than that for receptor **33**. This fact reveals the strong influence of the enhancement of the curved surface in the design of suitable receptors for fullerenes.

Subphthalocyanines (SubPcs) are curved molecules that can behave as weak electron donors or acceptors, depending on the nature of their peripheral and axial substituents [43]. Unlike porphyrins, SubPcs feature an aromatic and concave surface which is expected to interact favorably with C_{60}, essentially by means of van der Waals and $\pi-\pi$ stacking interactions. Torres and coworkers were the first to harness the curved surface of SubPcs to complex fullerenes [44]. These authors described a 3-ethynylpyridyl-based subphthalocyanine coordination cage (**35**) capable of encapsulating C_{60} in solution. By means of ^1H and ^{13}C NMR and

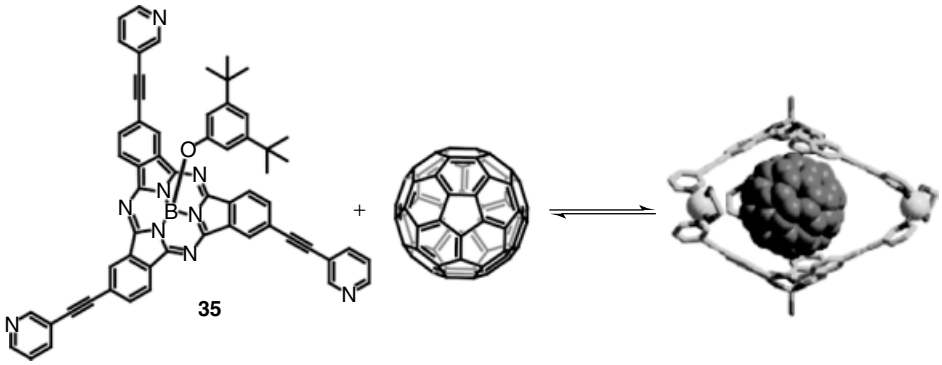

Scheme 3.2 Chemical structure of the subphthalocyanine-based capsule **35** and schematic representation of its complexation with C_{60}.

MALDI-TOF experiments, the encapsulation of C_{60} inside the cavity of the dimeric capsule **35** (Scheme 3.2) was demonstrated.

One of the most remarkable contributions in the field of macrocyclic concave receptors comes from the research group of Kawase, and makes use of cyclic oligophenyleneethynylene (OPE) derivatives. In 1996, this group described the first example of a OPE-based receptor for fullerenes [45]. This example reports a series of macrocyclic [*n*]-paraphenyl acetylenes (**36**–**39**) called *nanorings* (Figure 3.14). The diameter of the cavity of **36** extracted from its solid-state structure was found to be 1.33 nm, which, taking into consideration the dimensions of C_{60} and C_{70}, would be a perfect cavity to host fullerenes. Therefore, Kawase *et al.* investigated the ability of this receptor to bind fullerenes. As revealed by UV–Vis titrations, **36** is able to host C_{60} with a binding constant of 1.6×10^4 M^{-1} in benzene and a value of free energy associated to complex formation ($\Delta G_{binding}$) of 9.9 kcal mol^{-1}.

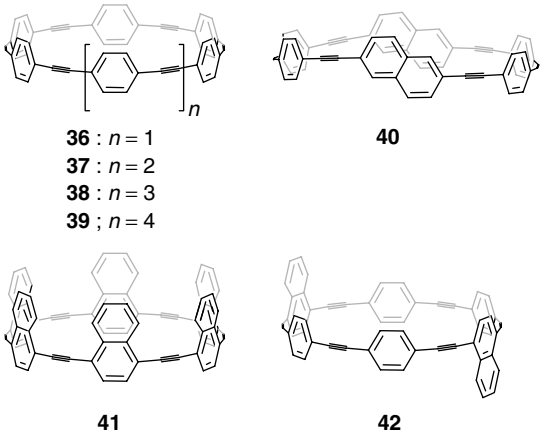

Figure 3.14 Chemical structure of different rigid carbon nanorings **36**–**42**.

On the basis of the structural design of nanorings **36**–**39**, other different OPE-derived macrocycles were later synthesized in which some benzene units were exchanged by naphthalene rings (**40**–**42**, Figure 3.14) [46]. The association between these macrocycles and the convex surface of C_{60} and C_{70} is particularly favored, taking into account the sum of different van der Waals and aromatic concave–convex interactions. Whereas C_{60} fits well in the cavity of the receptors, C_{70} can adopt different conformations, thus favoring a higher overlap with the orbitals of the receptor.

The complexation of nanoring **36** with a more soluble Bingel-type fullerene derivative (**43**) has also been explored. Variable temperature (VT) NMR experiments allowed the determination of the complex stability and values of free energy $\Delta G_{binding} = 9.4$ kcal mol^{-1}, revealing that this complex is less stable than **36**-C_{60}. X-ray structure of the complex **36**–**43** showed that the Bingel-type fullerene adduct did not reside in the center of the cavity, but slightly above, forcing the aromatic rings of **36** to tilt to maximize the contact with this fullerene derivative and adopting a bowl shape (Figure 3.15).

Furthermore, Kawase serendipitously observed the formation of double inclusion complexes between previously described nanorings **36** and **39** together with C_{60} [47]. In this complex structure, C_{60} was accommodated inside the smaller cycle **36**, which, at the same time, was included in the larger cavity of the ring **39**. This rather peculiar double complexation was termed as *nano-onions* by the authors. Surprisingly, in the purification of **36** and **39**, both nanorings co-precipitated in a 1 : 1 ratio. Subsequent theoretical calculations revealed that **39** has a cavity diameter of 1.98 nm, in which **36** (1.33-nm diameter) perfectly fits (Figure 3.16). VT-NMR experiments unambiguously demonstrated the formation of inclusion complexes between **36** and **39**. In addition, the cavity left by **36** can be exploited to host a molecule of C_{60}, which was further proved by NMR titrations between the inclusion complex **36**–**39** and C_{60}. The binding constant extracted from NMR titrations was calculated to be ~470 M^{-1} in chloroform (Figure 3.16).

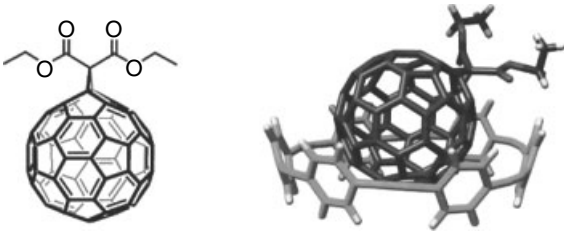

43 **36–43**

Figure 3.15 Chemical structure of **43** and X-ray of its supramolecular complex with nanoring **36**.

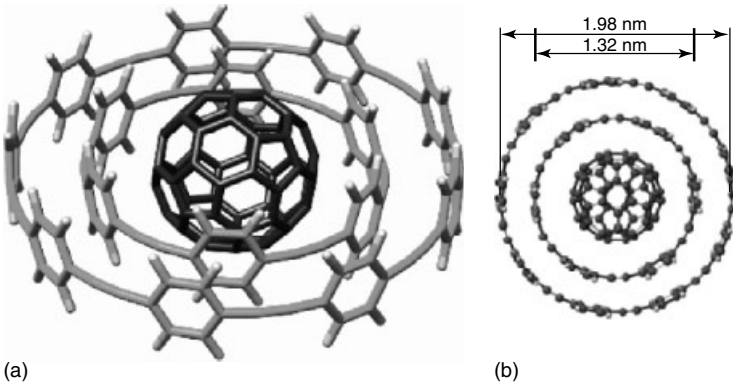

Figure 3.16 Cartoon representation of the onion-type **36**—**39**·C_{60} complex.

3.5
Concave Electroactive Receptors for Fullerenes

In comparison with neutral or weakly electroactive curved receptors for fullerenes, highly electroactive concave receptors for fullerene are relatively scarce in literature. The usage of an effective electron donor and concave receptor in combination with the electron-poor character of fullerenes would arise as a completely new approach to control the morphology of the electroactive materials in the solid state, which, as previously explained, is a key factor to ensure the precise operation of optoelectronic devices [48].

In this regard, tetrathiafulvalene (TTF) is an outstanding electron donor fragment and has been exploited to construct a wide variety of molecular devices [49], including photo- and electroactive donor–acceptor dyads and triads [50], organic field-effect transistors (OFETs) [51], cation sensors and bistable molecular shuttles, and catenanes [52]. The corresponding π-extended analogs, in which the 1,3-dithiole rings are covalently connected to a π-conjugated core, have been primarily utilized as electron donor units covalently attached to fullerenes to give rise to a number of donor–acceptor conjugates [50]. Therefore, although the covalent chemistry of TTF and π-extended analogs has been deeply investigated by several research groups, their supramolecular aspects are yet to be explored. In this regard, we now briefly describe the recent advances carried out by our research group in the development of TTF and π-extended derivatives to construct supramolecular receptors for fullerenes and, in a final part, we also make use of structurally related electron-deficient fragments to achieve suitable fullerene receptors.

Recently, we noticed that the concave curved shape of the electron donor 2-[9-(1,3-dithiol-2-ylidene)antracen-10(9*H*)-ylidene]-1,3-dithiole (exTTF, Figure 3.17) would be a perfect match for the convex surface of fullerenes. Moreover, exTTF is capable of aromatizing upon a two-electron oxidation process, giving rise to a dication with a planar geometry, unlike the concave shape of the neutral molecule (Figure 3.17).

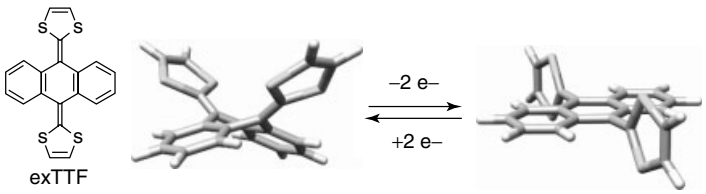

Figure 3.17 Chemical structure of exTTF and molecular modeling of its neutral and oxidized forms.

Theoretical calculations (DFT) predicted binding energies up to 7.00 kcal mol^{-1} between a single unit of exTTF and C_{60} (Unpublished results in collaboration with E. Ortí (Universidad de Valencia). Calculations carried out at the BH&H/6−31 + G^{**} level; $\Delta G_{binding} = 9.47$ kcal mol^{-1} which is reduced to 7.00 kcal mol^{-1} after BSSE correction.) However, we have not observed conclusive experimental evidence of association in either UV–Vis or NMR titrations.

Thus, preliminary molecular-modeling studies suggested that an isophthalic ester would be well suited as a spacer between two exTTF fragments. Receptor **44** was synthesized in excellent yield in only five steps from easily available exTTF methyl alcohol and commercially available isophthaloyl dichloride [53]. To evaluate the ability of our receptor to host [60] fullerene, we performed UV–Vis titrations of **44** upon addition of increasing amounts of C_{60} in chlorobenzene. The depletion of the absorption band characteristic of exTTF ($\lambda_{max} = 434$ nm) was accompanied by the appearance of a new transition centered at 482 nm, which we attributed to a charge-transfer band. Fitting the spectral changes to the binding isotherm displayed a hyperbolic binding curve, affording a binding constant of 3.0×10^3 M^{-1} in chlorobenzene at room temperature. The emergence of one isosbestic point suggests the formation of only one kind of supramolecular complex, which was further confirmed by Job Plot analysis by the appearance of a maximum at molar ratio of 0.5. These combined results demonstrate the formation of a 1 : 1 stoichiometry complex. The considerable stability of **44** · C_{60} complex – given the lack of preorganization of **44** – demonstrates the validity of exTTF as a building block to design efficient fullerene receptors. Surprisingly, the complexation behavior of **44** with C_{60} in $CHCl_3/CS_2$ mixtures proved to be significantly different. Similar to that observed in chlorobenzene, the maximum at 434 nm decreases as a new band ($\lambda_{max} = 482$ nm) increases, forming a distinctly clear isosbestic point at 451 nm, which points to the formation of a 1 : 1 complex in this system, too. The binding stoichiometry was further supported by Job Plot analysis, in which a maximum at molar ratio of 0.5 is again noticeable. However, in this case, the binding isotherm turned to be sigmoidal in shape, which is generally regarded as the criterion of cooperativity [54]. Indeed, the binding isotherm fitted well to the Hill equation [54], yielding a Hill coefficient (n_H) of 2.7 and an apparent binding constant of 3.56×10^3 M^{-1}. Although it is considered a direct indication of the number of available binding sites on the receptor, the Hill coefficient also reflects the degree of the cooperativity of the system, with a maximum value equal to the maximum number of binding sites. Therefore, a value of $n_H > 2$ rules out the formation of

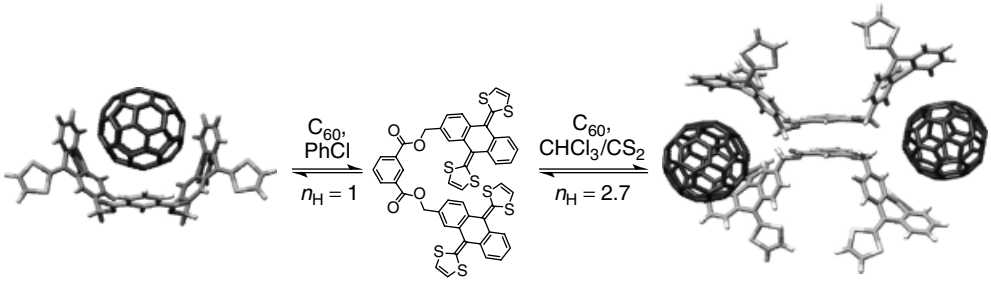

Scheme 3.3 Chemical structure of exTTF-based receptor **44** and scheme showing its different binding modes with C_{60}.

the expected pincer-like complex **44** · C_{60} since it features two binding sites only. This, together with the 1 : 1 stoichiometry, strongly suggests the formation of a supramolecular tetramer in which two units of C_{60} are sandwiched between two molecules of receptor **44**, as depicted in Scheme 3.3.

Photophysical studies carried out on complex **44** · $\mathbf{C}_{60}$ in solution demonstrate the formation of a supramolecularly bound radical-pair with lifetimes in the range of ∼12 ns. The short lifetime values are indeed an indirect proof of the orbital overlapping between both electroactive species that experience a fast recombination in solution [55]. Time-dependent DFT theoretical calculations (B3LYP/6−31 G^{**}) predict that the lower energetic transitions (∼480 nm) occur between the HOMO and HOMO+1 levels, located on the exTTF receptor, and the LUMO+4 which spreads on the whole C_{60} molecule. The HOMO → LUMO + 4 and HOMO−1 → LUMO + 4 transitions generates new excited electronic states in which the exTTF moieties accumulate a positive charge of +1 electron and a negative charge of −1 electron on the C_{60} unit (Figure 3.18).

The great capability of our tweezer-like receptor **44** to bind fullerenes and give rise to stable charge-transfer complexes encouraged us to design highly organized self-assembled architectures to the basis of these recognition elements. These two prerequisites are essential for the successful design of optoelectronic devices. We first designed a linear monomer **45** composed of a tweezer-like recognition fragment covalently attached to a PCBA-derived fullerene-containing fragment (Scheme 3.4) [56].

The introduction of two connected complementary binding motifs, namely, exTTF-based tweezer and fullerene fragment, would ensure the self-organization of our system in a head-to-tail fashion. A comprehensive collection of experiments, including variable concentration and temperature NMR, PFG-NMR, MALDI-TOF-MS, dynamic light scattering (DLS), and atomic force microscopy (AFM) demonstrated that **45** forms linear and/or cyclic multimeric supramolecular aggregates, in solution, gas, and solid phase. Moreover, cyclic voltammetry (CV) and UV−Vis experiments demonstrated a great electronic communication between both electroactive fragments. We are currently investigating the photophysical features and the applicability of this linear monomer **45** in the construction of efficient optoelectronic devices.

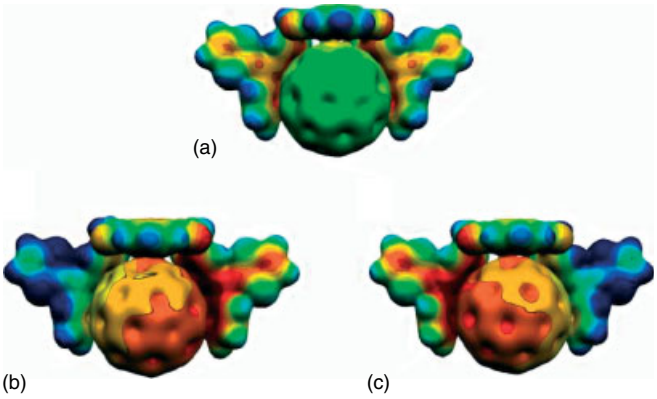

Figure 3.18 Electrostatic potential (B3LYP/6−31 *G***) calculated for the complex **44**·C_{60} in (a) the ground electronic state and (b) the charge-separated HOMO → LUMO + 4 and (c) HOMO−1 → LUMO + 4 excited states.

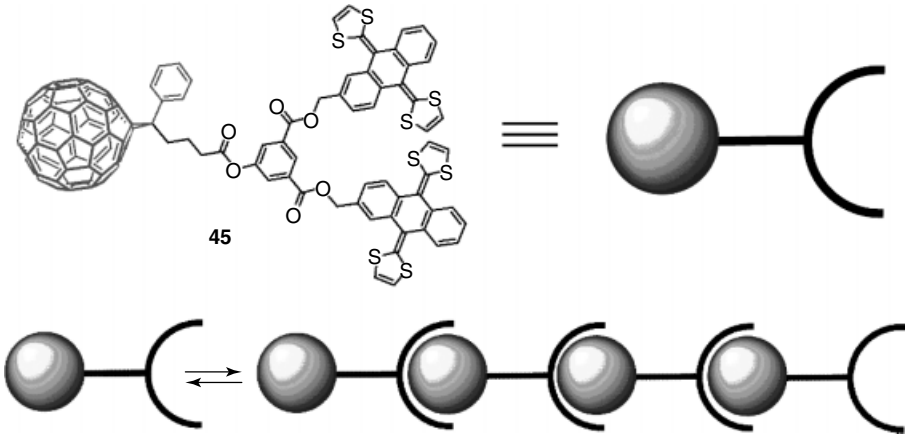

Scheme 3.4 Chemical structure of monomer **45** and scheme showing its self-organization into linear polymers.

On the basis of our research on electroactive supramolecular dendrimers, we began to investigate the possibility of constructing polydisperse supramolecular dendrimers, with the aim of exploring a new type of organization that would lie at the interface between dendrimers and supramolecular polymers. We synthesized a branched monomer **46** composed of two units of our tweezer-like receptor and a C_{60} derivative as recognizing units [57]. The bifurcated nature of **46** would be expected to drive the self-assembly into arborescent, dynamically polydisperse aggregates (Scheme 3.5).

A thorough set of experiments in solution, in particular variable temperature ^{1}H NMR experiments, suggests that binding primarily occurred inside the cavity of

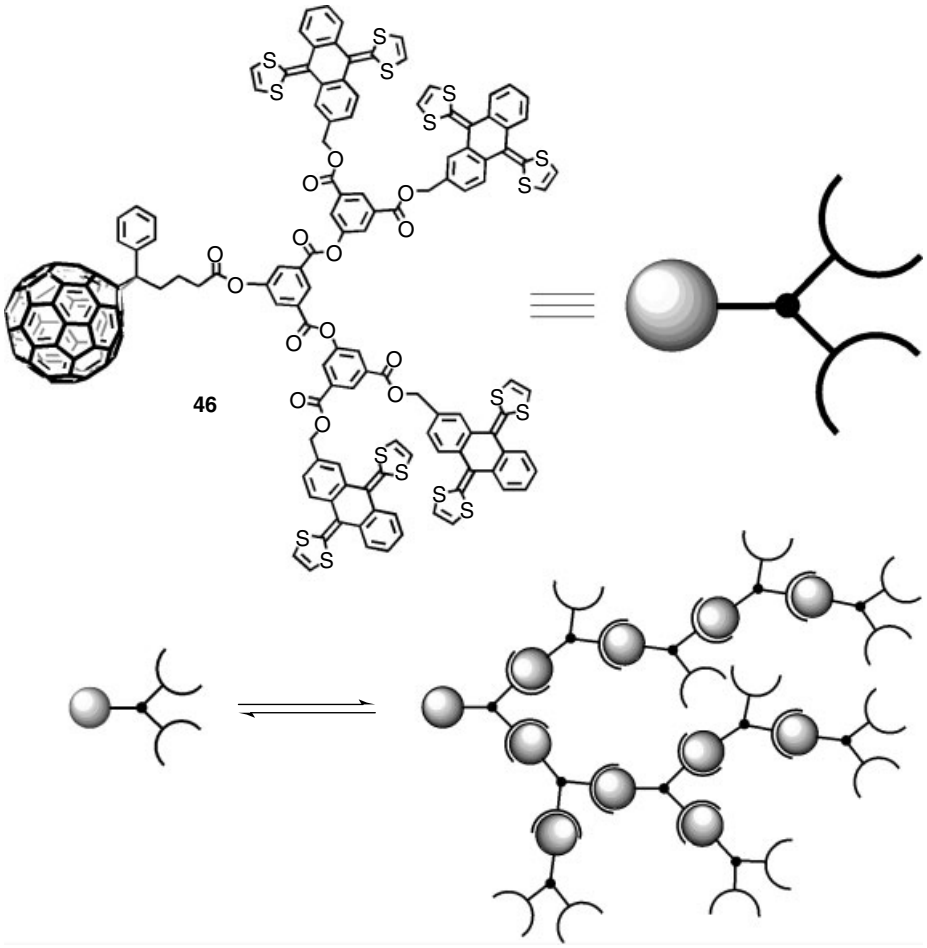

Scheme 3.5 Chemical structure of bifurcated monomer **46** and scheme showing its self-organization into supramolecular dendrimers.

the receptor, as previously anticipated. AFM images provided evidence on the size and shape of the aggregates formed on solid substrates. Most of the aggregates of **46** show a triangular or pseudocircular form in which two of the vertices are rounded off, reminiscent of a bunch of grapes with average sizes of 0.9–1.1 nm in height and 60–80 nm in length. These dimensions match with those expected for branched, flattened oligomers of **46**, since it is well understood that dendrimers tend to adopt planar structures when cast on surfaces.

The relatively high association constant of receptor **44** in combination with C_{60}, despite its inherent lack of preorganization, prompted us to investigate the specific contribution of the different noncovalent forces involved in the binding to the overall stabilization of the complexes formed in solution. In this regard, the group

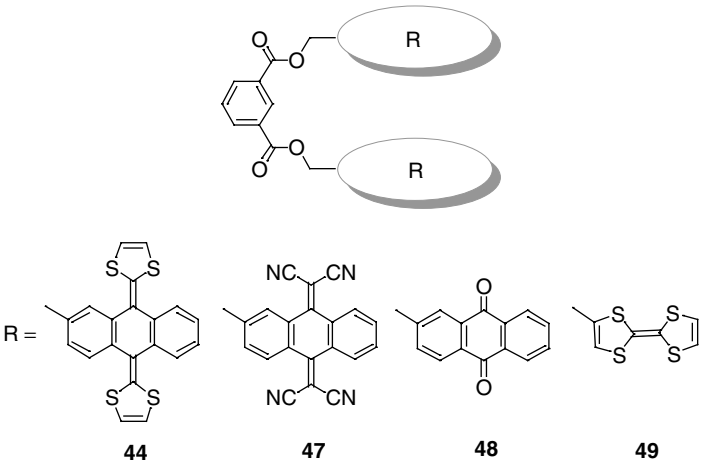

Scheme 3.6 Chemical structure of receptors **44**–**49**.

of Kawase recently introduced the term *concave–convex* interactions to define the noncovalent interactions between curved and concave aromatic hosts and convex guests. These authors also suggest that these ''concave–convex'' interactions have their own contribution to the stability of the complexes and serve to reinforce other noncovalent forces involved in the complexation [2, 45–47]. To have some insight whether or not these concave–convex forces have their own contribution to the global stability of the complexes formed from **44** and C_{60}, we designed and synthesized a new collection of structurally related receptors **47**–**49** (Scheme 3.6) [58].

In combination with receptor **44**, these provided a full collection of receptors in which we modulated the size, shape, and electronic character of the recognizing motifs. In this case, the binding constants were extracted from ^{1}H NMR titrations. The solubility of receptors **44**–**49** at the concentrations employed in titration experiments ($\leq$1 mM) is sufficient to discard solvophobic effects as a major factor in the stability of the complexes.

Receptor **44** incorporates five aromatic rings – two per recognizing unit plus the isophthalic spacer, a large and concave surface – and is electronically complementary to C_{60}. As expected, **44** is the receptor with highest affinity for C_{60}, with a $K_a = 3.00 \times 10^3$ M^{-1} ($CDCl_3/CS_2$). Receptor **47** utilizes 11,11,12,12-tetracyano-9,10-anthraquinodimethane (TCAQ) as the recognizing element [58]. Thus, as compared to **44**, it presents equal number of aromatic rings and surface available for recognition, with close to identical curvature (dihedral angle $C_a-C_b-C_c-C_d = 144.7^\circ$ for **44** · C_{60}, 146.1° for **47** · C_{60}, averaged values), but electron-poor character. The change in electronic nature results in a decrease of K_a to 1.54×10^3 M^{-1}. Although with small differences, this trend is reproduced by DFT calculations (Figure 3.19). A similar drop-off in the association constant is observed when moving from **47** to **48**. In this case, the surface available for van der Waals interactions is similar to that of **44** and **47**, but **48** lacks both the

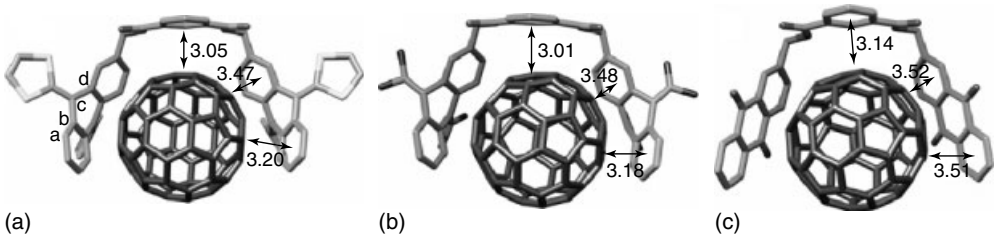

Figure 3.19 Structures of (a) **44**·C_{60}, (b) **47**·C_{60}, and (c) **48**·C_{60} complexes calculated at the BH&H/6−31 G^{**} level. The distances shown are given in angstroms. The $C_a-C_b-C_c-C_d$ dihedral angle is taken as a measure of the curvature of the anthracene units.

concave–convex and the electronic complementarity. This results in a binding constant of 0.79×10^3 M^{-1}. In this case, DFT calculations seem to overestimate noncovalent interactions and predict a slightly more stable complex for **48**·C_{60} compared to **47**·C_{60}. It should, however, be noted that calculations were performed in gas phase without taking solvent effects into account. Finally, no sign of association with C_{60} was observed in either the ^{1}H NMR or the electronic absorption spectra of receptor **49**, which is decorated with the electron rich, small, and nonaromatic TTF unit.

Therefore, comparison of the binding constants of **44** and **47** toward C_{60} suggests a perceptible contribution of electrostatic interactions, which is in agreement with previous observations on related systems. However, receptor **49** showed no sign of complexation toward C_{60}, which implies that this contribution is not quantitatively comparable to those of $\pi-\pi$ and van der Waals interactions. Remarkably, we observed for the first time that concave–convex complementarity does make its own contribution, as was shortly before anticipated by Kawase, although the contribution is relatively small. Despite the more electron-poor character of **47** in comparison with **48**, its binding constant toward C_{60} was considerably higher. This observation can only be justified by the concave shape of the TCAQ fragments.

On the basis of the principle of concave–convex complementarity, π-extended derivatives of TTF in which the dithioles are connected to a π-conjugated core have been shown to exhibit improved photophysical properties. We noticed that a truxene core [3, 59] would be particularly well suited as a scaffold, as its π-delocalized system should result in a significant shift of the electronic absorption spectrum toward the visible region and at the same time provide a large aromatic surface with which fullerenes might establish favorable noncovalent interactions. Thus, we designed three truxene TTF′s with variable substituents (**50**–**52**, Figure 3.20) in which three dithiole units were connected to a truxene core [60].

The association of **50** in solution and fullerenes was investigated by ^{1}H NMR titrations in 1 : 1 $CDCl_3/CS_2$ mixtures. The progressive shielding of the aromatic protons of **50** upon addition of fullerene guests fitted well to a 1 : 1 binding

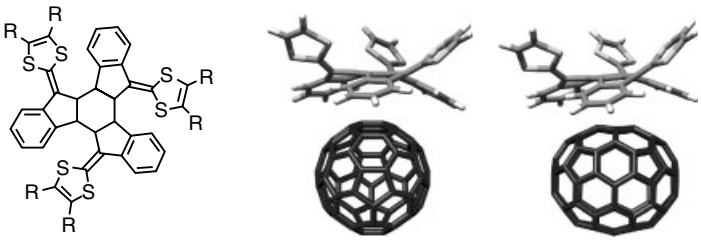

50 : R = H
51 : R = SCH_3
52 : R = $(SCH_3)_2$

Figure 3.20 Chemical structure of receptors **50**–**52** and structures of the complexes **50**·C_{60} and **50**·C_{70} calculated at MPWB1K/6–31 G^{**} level.

isotherm, which was further demonstrated by Job Plot analysis, affording binding constants of 1.2×10^3 M^{-1} and 8×10^3 M^{-1}($CDCl_3/CS_2$) for C_{60} and C_{70}, respectively. A slight deshielding of the dithiole resonances owing to charge-transfer interactions between the electron-rich receptor and the electron-poor fullerenes was also observed, suggesting that binding occurs preferentially on the aromatic face of **50**. To gain some insight on the complex stability, we also studied theoretically the complexes formed at DFT level using the MPWB1K density functional. These calculations afforded a binding energy for the complexes of 8.98 and 9.94 kcal mol^{-1} for **50**·C_{60} and **50**·C_{70}, respectively (Figure 3.20).

Single crystals suitable for X-ray diffraction were obtained by slow diffusion of cyclohexane into a solution of **50** in chloroform. As illustrated in Figure 3.21, the truxene core breaks down its planar structure to accommodate the dithioles and adopts an all-cis spherelike geometry with the three dithiole rings protruding outside. This arrangement results in the generation of a molecule with threefold helical chirality of which only the *P, P, P/ M, M, M* enantiomeric pair can be found in the crystal structure. Interestingly, each enantiomer appears forming homochiral dimers in the unit cell (Figure 3.21). The concave bowl-shaped configuration adopted by the truxene core perfectly mirrors the convex surface of fullerenes, as has already been demonstrated by complexation studies.

3.6 Conclusions and Future Perspectives

The search for supramolecular receptors for fullerenes continues to be a very active field of research. The earlier receptors, primarily based on classic and flexible aromatic scaffolds such as calixarenes, cyclotriveratrilenes, and cyclodextrins have been widely demonstrated to form highly stable complexes with fullerenes in

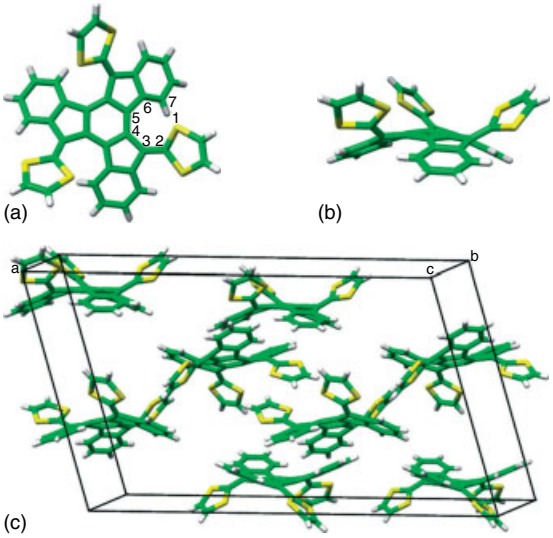

Figure 3.21 X-ray crystal structure of **50**. (a) (*P*, *P*, *P*) top view, (b) side view, and (c) unit cell showing the racemic mixture. S yellow, C green, H white.

solution and in the solid state. An alternative to classic flexible hosts are planar recognition motifs, whose foremost exponents are porphyrins. The planar surface of porphyrins serves as a primary recognizing element to increase $\pi-\pi$ and van der Waals interactions with fullerene surface. The most recent approaches for the design of efficient receptors for fullerenes make use of curved and, in most cases, electroactive recognition motifs. Among them, exTTF- or truxeneTTF-based receptors have been demonstrated to fulfill the advantages of both classic and planar receptors: (i) they harvest light efficiently in the visible region, (ii) possess electron-donating character, and (iii) are capable of effectively binding fullerenes in solution, solid state, and in the gas phase. These properties make TTF derivatives optimal candidates to design valuable materials for optoelectronics, where the absorption of light, generation of free charges upon electron transfer processes, and the morphology between donor and acceptor are essential prerequisites for their precise operation [48, 61].

Acknowledgments

Financial support by the MEC of Spain (projects CTQ2005-02609/BQU and Consolider-Ingenio 2010C-07-25200) and the CAM (MADRISOLAR project P-PPQ-000225-0505). G. F. thanks the MEC of Spain for a research grant. We are thankful to Dr E. M. Pérez who has actively participated in the exTTF-based receptor part.

References

1. Krätchmer, W., Lamb, L.D., Fostiropoulos, K., and Huffman, D.R. (1990) Solid C60: a new form of carbon. *Nature*, **347**, 354–358.
2. (a) Beck, M.T. (1998) Solubility and molecular state of C60 and C70 in solvents and solvent mixtures. *Pure Appl. Chem.*, **70**, 1881–1889; (b) Korobov, M.V. and Smith, A.L. (2000) in *Fullerenes Chemistry, Physics, and Technology* (eds K.M.Kadish and R.S. Ruoff), Wiley-Interscience, New York, p. 53.
3. (a) Sun, Y., Xiao, K., Liu, Y., Wang, J., Pei, J., Yu, G., and Zhu, D. (2005) Oligothiophene-functionalized truxene: star-shaped compounds for organic field-effect transistors. *Adv. Funct. Mater.*, **15**, 818–822; (b) Kanibolotsky, A.L., Berridge, R., Skabara, P.J., Perepichka, I.F., Bradley, D.D.C., and Koeberg, M. (2004) Synthesis and properties of monodisperse oligofluorene-functionalized truxenes: highly fluorescent star-shaped architectures. *J. Am. Chem. Soc.*, **126**, 13695–13702; (c) De Frutos, O., Gómez-Lor, B., Granier, T., Monge, M.A., Gutiérrez-Puebla, E., and Echavarren, A.M. (1999) syn-trialkylated truxenes: building blocks that self-associate by arene stacking. *Angew. Chem. Int. Ed.*, **38**, 204–207.
4. Haddon, R.C. (1993) Chemistry of the fullerenes: the manifestation of strain in a class of continuous aromatic molecules. *Science*, **261**, 1545–1550.
5. (a) Kroto, H.W., Heath, J.R., O'Brien, S.C., Curl, R.F., and Smalley, R.E. (1995) C60: Buckminsterfullerene. *Nature*, **318**, 162–163; (b) Hirsch, A. and Bettreich, M. (eds) (2005) *Fullerenes*, Wiley-VCH Verlag GmbH & Co. KGaA, Weinheim; (c) Martín, N. (2006) New challenges in fullerene chemistry. *Chem. Commun.*, 2093–2104.
6. (a) Bürgi, H.-B., Blanc, E., Schwarzenbach, D., Lui, S., Lu, Y.-J., Kappes, M.M., and Ibers, J.A. (1992) The structure of C60: orientational disorder in the low-temperature modification of C60. *Angew. Chem. Int. Ed. Engl.*, **31**, 640–643; (b) Meidine, M.F., Hitchcock, P.B., Kroto, H.W., Taylor, and Walton, D.R.M. (1992) Single crystal X-ray structure of benzene-solvated C60. *J. Chem. Soc., Chem. Commun.*, 1534–1537; (c) Balch, A.L., Catalano, V.J., Lee, J.W., and Olmstead, M.M. (1992) Supramolecular aggregation of an (.eta.2-C60) iridium complex involving phenyl chelation of the fullerene. *J. Am. Chem. Soc.*, **114**, 5455–5457.
7. Steed, J.W. and Atwood, J.L. (eds) (2001) *Supramolecular Chemistry*, John Wiley & Sons, Inc., New York.
8. (a) Hunter, C.A. and Sanders, J.K.M. (1990) The nature of pi-pi interactions. *J. Am. Chem. Soc.*, **112**, 5525–5534; (b) Hunter, C.A., Lawson, K.R., Perkins, J., and Urch, J.C. (2001) Aromatic interactions. *J. Chem. Soc., Perkin Trans. 2*, 651–669; (c) Hunter, C.A. (2004) Quantifying intermolecular interactions: guidelines for the molecular recognition toolbox. *Angew. Chem. Int. Ed.*, **43**, 5310–5324.
9. Kawase, T. and Kurata, H. (2006) Ball-, Bowl-, and belt-shaped conjugated systems and their complexing abilities: exploration of the Concave-convex$\pi-\pi$interaction. *Chem. Rev.*, **106**, 5250–5273.
10. Andersson, T., Nilsson, K., Sundahl, M., Westman, G., and Wennerstroem, O. (1992) C60 embedded in γ-cyclodextrin: a water-soluble fullerene. *J. Chem. Soc., Chem. Commun.*, 604–606.
11. Diederich, F., Effing, J., Jonas, L., Jullien, L., Plesnivy, T., Ringsdorf, H., Thilgen, C., and Weinstein, D. (1992) C60 and C70 in a basket? – Investigations of Mono-and multilayers from azacrown compounds and fullerenes. *Angew. Chem., Int. Ed. Engl.*, **31**, 1599–1602.
12. Atwood, J.L., Koutsantonis, G.A., and Raston, C.L. (1994) Purification of C60 and C70 by selective complexation with calixarenes. *Nature*, **368**, 229–231.
13. Suzuki, T., Nakashima, K., and Shinkai, S. (1994) Very convenient and efficient purification method for fullerene (C60) with

5,11,17,23,29,35,41,47-Octa-tert-butylcalix[8]arene-49,50,51,52,53,54,55,56--octol. *Chem. Lett.*, **23**, 699–671.

14. Raston, C.L., Atwood, J.L., Nichols, P.J., and Sudria, I.B.N. (1996) Supramolecular encapsulation of aggregates of C60. *Chem. Commun.*, 2615–2616.
15. Atwood, J.L., Barbour, L.J., Raston, C.L., and Sudria, I.B.N. (1998) C60 and C70 compounds in the pincerlike jaws of calix[6]arene. *Angew. Chem. Int. Ed.*, **37**, 981–983.
16. (a) Haino, T., Yanase, M., and Fukazawa, Y. (1997) Crystalline supramolecular complexes of C60 with calix[5]arenes. *Tetrahedron Lett.*, **38**, 3739–3742; (b) Atwood, J.L., Barbour, L.J., Heaven, M.W., and Raston, C.L. (2003) Association and orientation of C70 on complexation with calix[5]arene. *Chem. Commun.*, 2270–2271; (c) Atwood, J.L., Barbour, L.J., Heaven, M.W., and Raston, C.L. (2003) Controlling van der Waals contacts in complexes of fullerene C60. *Angew. Chem. Int. Ed.*, **42**, 3254–3257.
17. (a) Tsubaki, K., Tanaka, K., Kinoshita, T., and Fuji, K. (1998) Complexation of C60 with hexahomooxacalix[3]arenes and supramolecular structures of complexes in the solid state. *Chem. Commun.*, 895–896; (b) Komatsu, N. (2001) New synthetic route to homooxacalix[n]arenes via reductive coupling of diformylphenols. *Tetrahedron Lett.*, **42**, 1733–1736.
18. (a) Steed, J.W., Junk, P.C., Atwood, J.L., Barnes, M.J., Raston, C.L., and Burkhalter, R.S. (1994) Ball and socket nanostructures: new supramolecular chemistry based on cyclotriveratrylene. *J. Am. Chem. Soc.*, **116**, 10346–10347; (b) Atwood, J.L., Barnes, M.J., Gardiner, M.G., and Raston, C.L. (1996) Cyclotriveratrylene polarisation assisted aggregation of C60. *Chem. Commun.*, 1449–1450; (c) Konarev, D.V., Khasanov, S.S., Vorontsov, I.I., Saito, G., Antipin, M.Y., Otsuka, A., and Lyubovskaya, R.N. (2002) The formation of a single-bonded (C70–)2 dimer in a new ionic multicomponent complex of cyclotriveratrylene: (Cs+)2(C70–)2·CTV·(DMF)7(C6H6)0.75. *Chem. Commun.*, 2548–2549.
19. Haino, T., Yanase, M., and Fukazawa, Y. (1997) New supramolecular complex of C60 based on calix[5]arene – its structure in the crystal and in solution. *Angew. Chem. Int. Ed. Engl.*, **36**, 259–260.
20. Haino, T., Yanase, M., and Fukazawa, Y. (1997) Crystalline supramolecular complexes of C60 with calix[5]arenes. *Tetrahedron Lett.*, **38**, 3739–3742.
21. (a) Mizyed, A., Ashram, M., Miller, D.O., and Georghiou, P.E. (2001) Supramolecular complexation of [60]fullerene with hexahomotrioxacalix[3]naphthalenes: a new class of naphthalene-based calixarenes. *J. Chem. Soc., Perkin Trans. 2*, 1916–1919; (b) Felder, D., Heinrich, B., Guillon, D., Nicoud, J.-F., and Nierengarten, J.-F. (2000) A liquid crystalline supramolecular complex of C60 with a cyclotriveratrylene derivative. *Chem. Eur. J.*, **6**, 3501–3507; (c) Rio, Y., and Nierengarten, J.-F. (2002) Water soluble supramolecular cyclotriveratrylene–[60]fullerene complexes with potential for biological applications. *Tetrahedron Lett.*, **43**, 4321–4324.
22. Haino, T., Yanase, M., and Fukazawa, Y. (1998) Fullerenes enclosed in bridged calix[5]arenas. *Angew. Chem. Int. Ed.*, **37**, 997–998.
23. (a) Wang, J. and Gutsche, C.D. (1998) Complexation of fullerenes with bis-calix[n]arenes Synthesized by tandem Claisen rearrangement. *J. Am. Chem. Soc.*, **120**, 12226–12231; (b) Wang, J., Bodige, S.G., Watson, W.H., and Gutsche, C.D. (2000) Complexation of fullerenes with 5,5′-biscalix[5]arene. *J. Org. Chem.*, **65**, 8260–8263; (c) Van, Y., Mitkin, O., Barnhurst, L., Kurchan, A., and Katateladze, A. (2000) Molecular assembly and disassembly: novel photolabile molecular hosts. *Org. Lett.*, **2**, 3817–3819.
24. Iglesias-Sánchez, J.C., Fragoso, A., de Mendoza, J., and Prados, P. (2006) Aryl-aryl linked bi-5,5′- p-tert-butylcalix[4]arene tweezer for fullerene complexation. *Org. Lett.*, **8**, 2571–2574.
25. Huerta, E., Metselaar, G.A., Fragoso, A., Santos, E., Bo, C., and de Mendoza, J.

(2007) Selective binding and easy separation of C70 by nanoscale self-assembled capsules. *Angew. Chem. Int. Ed.*, **46**, 202–205.

26. (a) Ikeda, A., Yoshimura, M., Udzu, H., Fukuhara, C., and Shinkai, S. (1999) Inclusion of [60]fullerene in a homooxacalix[3]arene-based dimeric capsule cross-linked by a PdII – pyridine interaction. *J. Am. Chem. Soc.*, **121**, 4296–4297; (b) Ikeda, A., Udzu, H., Yoshimura, M., and Shinkai, S. (2000) Inclusion of [60]fullerene in a self-assembled homooxacalix[3]arene-based dimeric capsule constructed by a PdII – pyridine Interaction. The Li+-binding to the lower rims can improve the inclusion ability. *Tetrahedron*, **56**, 1825–1832.

27. Liu, S.-Q., Wang, D.-X., Zheng, Q.-Y., and Wang, M.-X. (2007) Synthesis and structure of nitrogen bridged calix[5]- and -[10]-pyridines and their complexation with fullerenes. *Chem. Commun.*, 3856–3857.

28. Boyd, P.D.W. and Reed, C.A. (2005) Fullerene-porphyrin constructs. *Acc. Chem. Res.*, **38**, 235–242.

29. Sun, Y., Drovetskaya, T., Bolskar, R.D., Bau, R., Boyd, P.D.W., and Reed, C.A. (1997) Fullerides of pyrrolidine-functionalized C60. *J. Org. Chem.*, **62**, 3642–3649.

30. Sun, D., Tham, F.S., Reed, C.A., Chaker, L., and Boyd, P.D.W. (2002) Supramolecular fullerene-porphyrin chemistry. Fullerene complexation by metalated ''Jaws Porphyrin'' hosts. *J. Am. Chem. Soc.*, **124**, 6604–6612.

31. Tong, L.H., Wietor, J.-L., Clegg, W., Raithby, P.R., Pascu, S.I., and Sanders, J.K.M. (2008) Supramolecular assemblies of tripodal porphyrin hosts and C60. *Chem. Eur. J.*, **14**, 3035–3044.

32. (a) Ayabe, M., Ikeda, A., Kubo, Y., Takeuchi, M., and Shinkai, S. (2002) A dendritic porphyrin receptor for C60 which features a profound positive allosteric effect.*Angew. Chem. Int. Ed.*, **41**, 2790–2792; (b) Yamaguchi, T., Ishii, N., Tashiro, K., and Aida, T. (2003) Supramolecular peapods composed of a metalloporphyrin nanotube and fullerenes. *J. Am. Chem. Soc.*, **125**, 13934–13935.

33. Tashiro, K., Aida, T., Zheng, J.-Y., Kinbara, K., Saigo, K., Sakamoto, S., and Yamaguchi, K. (1999) A cyclic dimer of metalloporphyrin forms a highly stable inclusion complex with C60. *J. Am. Chem. Soc.*, **121**, 9477–9478.

34. Tashiro, K. and Aida, T. (2007) Metalloporphyrin hosts for supramolecular chemistry of fullerenes. *Chem. Soc. Rev.*, **36**, 189–201.

35. Yanagisawa, M., Tashiro, K., Yamasaki, M., and Aida, T. (2007) Hosting fullerenes by dynamic bond formation with an iridium porphyrin cyclic dimer: a ''chemical friction'' for rotary guest motions. *J. Am. Chem. Soc.*, **129**, 11912–11913.

36. Pérez, E.M. and Martín, N. (2008) Curves ahead: molecular receptors for fullerenes based on concave–convex complementarity. *Chem. Soc. Rev.*, **37**, 1512–1519.

37. Barth, W.E. and Lawton, R.G. (1966) Dibenzo[ghi,mno]fluoranthene. *J. Am. Chem. Soc.*, **88**, 380–381.

38. (a) Hanson, J.C. and Nordman, C.E. (1976) The crystal and molecular structure of corannulene, C20H10. *Acta Crystallogr. B*, **32**, 1147; (b) Petrukhina, M.A., Andreini, K.W., Mack, J., and Scott, L.T. (2005) X-ray quality geometries of geodesic polyarenes from theoretical calculations: what levels of theory are reliable? *J. Org. Chem.*, **70**, 5713–5716.

39. Becker, H., Javahery, G., Petrie, S., Cheng, P.C., Schwarz, H., Scott, L.T., and Bohme, D.K. (1993) Gas-phase ion/molecule reactions of corannulene, a fullerene subunit. *J. Am. Chem. Soc.*, **115**, 11636–11637.

40. Myzed, S., Georghiou, P., Bancu, M., Cuadra, B., Rai, A.K., Cheng, P., and Scott, L.T. (2001) Embracing C60 with multiarmed geodesic partners. *J. Am. Chem. Soc.*, **123**, 12770–12774.

41. Georghiou, P.E., Tran, A.H., Myzyed, S., Bancu, M., and Scott, L.T. (2005) Concave polyarenes with sulfide-linked flaps and tentacles: new electron-rich hosts for fullerenes. *J. Org. Chem.*, **70**, 6158–6162.

42. Sygula, A., Fronczek, F.R., Sygula, R., Rabideau, P.W., and Olmstead, M.M. (2007) A double concave hydrocarbon buckycatcher. *J. Am. Chem. Soc.*, **129**, 3842–3843.
43. Claessens, C.G., González-Rodríguez, D., and Torres, T. (2002) Subphthalocyanines: singular nonplanar aromatic compounds – synthesis, reactivity, and physical properties. *Chem. Rev.*, **102**, 835–854.
44. Claessens, C.G. and Torres, T. (2004) Inclusion of C60 fullerene in a M3L2 subphthalocyanine cage. *Chem. Commun.*, 1298–1299.
45. Kawase, T., Darabi, H.R., and Oda, M. (1996) Cyclic [6]- and [8]paraphenylacetylenes. *Angew. Chem. Int. Ed.*, **35**, 2664–2666.
46. (a) Kawase, T., Tanaka, K., Seirai, Y., Shiono, N., and Oda, M. (2003) Complexation of carbon nanorings with fullerenes: supramolecular dynamics and structural tuning for a fullerene sensor. *Angew. Chem. Int. Ed.*, **42**, 5597–5600; (b) Kawase, T., Fujiwara, N., Tsutumi, M., Oda, M., Maeda, Y., Wakahara, T., and Akasaka, T. (2004) Supramolecular dynamics of cyclic [6]paraphenyleneacetylene complexes with [60]- and [70]fullerene derivatives: electronic and structural effects on complexation. *Angew. Chem. Int. Ed.*, **43**, 5060–5062.
47. Kawase, T., Tanaka, K., Shiono, N., Seirai, Y., and Oda, M. (2004) Onion-type complexation based on carbon nanorings and a buckminsterfullerene. *Angew. Chem. Int. Ed.*, **43**, 1722–1724.
48. Thompson, B.C. and Fréchet, J.M.J. (2008) Polymer-fullerene composite solar cells. *Angew. Chem. Int. Ed.*, **47**, 58–77.
49. Segura, J.L. and Martín, N. (2001) New concepts in tetrathiafulvalene chemistry. *Angew. Chem. Int. Ed.*, **40**, 1372–1409.
50. Martín, N., Sánchez, L., Herranz, M.A., Illescas, B., and Guldi, D.M. (2007) Electronic communication in tetrathiafulvalene (TTF)/C60 systems: toward molecular solar energy conversion materials? *Acc. Chem. Res.*, **40**, 1015–1024.
51. Mas-Torrent, M. and Rovira, C. (2006) Tetrathiafulvalene derivatives for organic field effect transistors. *J. Mater. Chem.*, **1**, 433–436.
52. (a) Kay, E.R., Leigh, D.A., and Zerbetto, F. (2007) Synthetic molecular motors and mechanical machines. *Angew. Chem. Int. Ed.*, **46**, 72–191; (b) Saha, S., Flood, A.H., Stoddart, J.F., Impellizzeri, S., Silvi, S., Venturi, M., and Credi, A. (2007) A redox-driven multicomponent molecular shuttle. *J. Am. Chem. Soc.*, **129**, 12159–12171; (c) Tomcsi, M.R. and Stoddart, J.F. (2007) Bispyrrolotetrathiafulvalene-containing [2]catenanes. *J. Org. Chem.*, **72**, 9335–9338.
53. Pérez, E.M., Sánchez, L., Fernández, G., and Martín, N. (2006) exTTF as building block for fullerene receptors. Unexpected solvent-dependent positive homotropic cooperativity. *J. Am. Chem. Soc.*, **128**, 7172–7173.
54. (a) Takeuchi, M., Ikeda, M., Sugasaki, A., and Shinkai, S. (2001) Molecular design of artificial molecular and ion recognition systems with allosteric guest responses. *Acc. Chem. Res.*, **34**, 865–873; (b) Shinkai, S., Ikeda, M., Sugasaki, A., and Takeuchi, M. (2001) Positive allosteric systems designed on dynamic supramolecular scaffolds: toward switching and amplification of guest affinity and selectivity. *Acc. Chem. Res.*, **34**, 494–503.
55. Gayathri, S.S., Wielopolski, M., Pérez, E.M., Fernández, G., Sánchez, L., Viruela, R., Ortí, E., Guldi, D.M., and Martín, N. (2009) Discrete supramolecular donor-acceptor complexes. *Angew. Chem. Int. Ed.*, **48**, 815–819.
56. Fernández, G., Pérez, E.M., Sánchez, L., and Martín, N. (2008) Self-organization of electroactive materials : a head-to-tail donor-acceptor supramolecular polymer. *Angew. Chem. Int. Ed.*, **47**, 1094–1097.
57. Fernández, G., Pérez, E.M., Sánchez, L., and Martín, N. (2008) An electroactive dynamically polydisperse supramolecular dendrimer. *J. Am. Chem. Soc.*, **130**, 2410–2411.
58. Pérez, E.M., Capodilupo, A.L., Fernández, G., Sánchez, L., Viruela, P.M., Viruela, R., Ortí, E., Bietti, M., and Martín, N. (2008) Weighting

non-covalent forces in the molecular recognition of C60. Relevance of concave-convex complementarity. *Chem. Commun.*, 4567–4569.

59. (a) Yamaguchi, S., Tatemitsu, H., Sakata, Y., and Misumi, S. (1983) Synthesis of two isomeric tetracyanoanthraquinodimethanes. *Chem. Lett.*, 1229–1230; (b) Kini, A.M., Cowan, D.O., Gerson, F., and Möckel, R. (1985) New synthesis and properties of 11,11,12,12-tetracyano-9,10-anthraquinodimethane: an electron acceptor displaying a single-wave, two-electron reduction and a coproportionation pathway to the radical anion. *J. Am. Chem. Soc.*, **107**, 556–557; (c) Martín, N. and Seoane, C. (1997) in *Handbook of Organic Conductive Molecules and Polymers* (ed. H.S. Nalwa), John Wiley & Sons, Ltd, Chichester, pp. 1–86; Martín, N., (d) Segura, J.L., and Seoane, C. (1997) Design and synthesis of TCNQ and DCNQI type electron acceptor molecules as precursors for organic metals. *J. Mater. Chem.*, **7**, 1661–1676; Gómez, R.,; (e) Seoane, C., and Segura, J.L. (2007) The first two decades of a versatile electron acceptor building block: 11,11,12,12-tetracyano-9,10-anthraquinodimethane (TCAQ). *Chem. Soc. Rev.*, **36**, 1305–1322.

60. Pérez, E.M., Sierra, M., Sánchez, L., Torres, M.R., Viruela, R., Viruela, P.M., Ortí, E., and Martín, N. (2007) Concave tetrathiafulvalene-type donors as supramolecular partners for fullerenes. *Angew. Chem. Int. Ed.*, **46**, 1847–1851.

61. (a) Forrest, S.R. and Thompson, M.E. (2007) Introduction: organic electronics and optoelectronics. *Chem. Rev.*, **107**, 923–925; (b) Samuel, I.D.W. and Turnbull, G.A. (2007) Organic semiconductor lasers. *Chem. Rev.*, **107**, 1272–1295; (c) Günes, S., Neugebauer, H., and Sariciftci, N.S. (2007) Conjugated polymer-based organic solar cells. *Chem. Rev.*, **107**, 1324–1338.

4
Click Chemistry: A Quote for Function

David Díaz Díaz

4.1
Introduction

In the 1960s, Huisgen presented, to the scientific community, the wide scope of the 1,3-dipolar cycloaddition between azides and alkynes (AAC) to give 1,2,3-triazoles [1]. Over 40 years later, the Cu^{I}-catalyzed variant of this reaction (CuAAC) became the prototype of a new synthetic philosophy inspired by the simplicity and efficiency of the processes that take place in nature. Such modular synthetic approach was designated as "*Click Chemistry*" by Sharpless and coworkers, who published a first analysis of the most efficient chemical reactions that can be used to stitch organic fragments together to make complex functional molecules [2]. Since then, more than 1000 citations for this work have been reported. In general, click chemistry encourages a number of criteria, such as modular application, wide scope, large thermodynamic enthalpy force (>20 kcal mol^{-1}), formation of a stable linkage via carbon–heteroatom bond formation, minimal cross-reactivity with other functional groups (maximum orthogonality), high atom economy, quantitative conversions with high yields, stereospecificity, simple reaction conditions, involvement of no solvent or a benign solvent (preferably water), no or inoffensive by-products, easy product isolation and purification (e.g., crystallization, distillation), production of a physiologically stable product, and use of readily available starting materials and reagents. Despite the intrinsic subjectivity of some of these criteria, several reactions has been already identified as potential candidates to fit the requirements of a click process: (i) cycloaddition reactions (e.g., 1,3-dipolar cycloadditions, hetero Diels–Alder reactions); (ii) nucleophilic ring-opening reactions, especially of small strained rings (e.g., epoxy, aziridine, cyclic sulfates); (iii) carbonyl-chemistry of the nonaldol type (e.g., formation of ureas, oxime ethers, hydrazones); and (iv) addition reactions to carbon–carbon multiple bonds (e.g., epoxidation, dihydroxylation, and aziridination).

One of the most interesting examples within the above groups of reactions is the 1,3-dipolar cycloaddition of azides and alkynes, which, under thermal conditions, affords an equimolar mixture of the 1,4- and 1,5-disubstituted regioisomers of

Ideas in Chemistry and Molecular Sciences: Advances in Nanotechnology, Materials and Devices.
Edited by Bruno Pignataro

ISBN: 978-3-527-32543-6

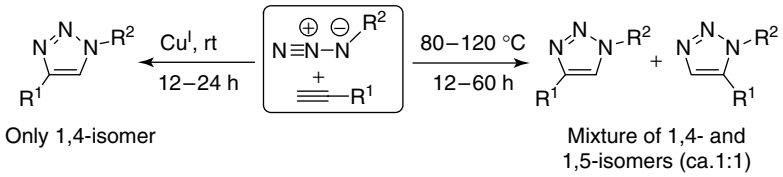

Scheme 4.1 Huisgen 1,3-dipolar AAC under general thermal and Cu^{I}-catalyzed conditions.

1,2,3-triazoles (Scheme 4.1, on the right). In 2002, the regioselective Cu^{I}-catalyzed cycloaddition at room temperature of organic azides and terminal alkynes to exclusively give the 1,4-regioisomers of 1,2,3-triazoles (Scheme 4.1, on the left) was reported independently by the groups of Sharpless [3] and Meldal [4], the former working under solid-phase conditions. This catalytic process was soon referred as "*the cream of the crop*" of click chemistry by Sharpless and coworkers, due to its unprecedented level of selectivity, reliability, and scope for those organic synthesis endeavors which depend on the creation of covalent links between diverse building blocks. Cu^{I} catalysts bind to terminal alkynes to form copper acetylides, the key intermediate for the triazole formation [5], and accelerate the process by factors up to 10^7 while preserving the inertness of both azides and alkynes toward the vast majority of functional groups and conditions that are typical of the terrestrial environment.

More recently, Sharpless and his group have also reported the ruthenium-catalyzed version of this reaction to form the complementary 1,5-disubstituted triazoles [6]. Among several ruthenium complexes, $Cp^*RuCl(PPh_3)_2$ (Cp^* = pentamethylcyclopentadienyl) provide the best results. Remarkably, although the Cu^{I}-catalyzed reaction is limited to terminal alkynes, the Ru^{II}-catalyzed reaction is active with internal alkynes as well.

From an experimental point of view, CuAAC can be performed using commercial sources of Cu^{I} (e.g., CuBr, CuI), although the Cu^{I} catalyst is usually generated *in situ* by a mixture of a Cu^{II} salt (e.g., Cu_2SO_4) and a reducing agent (e.g., sodium ascorbate). As Cu^{I} is unstable in aqueous solvents, stabilizing ligands have been proved to be effective for improving the reaction outcome (e.g., tris-(benzyltriazolylmethyl)amine (TBTA), benzimidazole-based ligands) [7, 8]. The reaction can be run in both solution and solid phase, and in a variety of solvents including mixtures of water with a number of (partially) miscible organic solvents (e.g., alcohols, DMSO, DMF, *t*-BuOH, acetone). Significantly, the starting reagents need not be completely soluble for the reaction to be successful, and usually the product can be simply filtered from the solution as the only purification step required [3]. It is worth mentioning that the use of microwave irradiation can significantly shorten reaction times of CuAAC, while keeping excellent yields, purity, and selectivity [9].

The click nature of the CuAAC has propelled it as the most versatile example for molecular connections in organic synthesis, but especially for biological molecules [10–12] and for the discovery of biologically active compounds [13, 14], principally in

combination with combinatorial chemistry, by making each reaction in a multistep synthesis fast, efficient, and predictable. Undeniably, the practical importance of this reaction is derived from the easy introduction of azides and alkynes functionalities into organic molecules. The reaction is useful in biological settings for two main reasons: (i) the azide and alkyne components are largely unreactive with biological molecules (and therefore selectively reactive with each other) and (ii) the product triazole can interact with biological structures in several noncovalent ways while being, at the same time, extraordinarily stable. In addition, CuAAC has also rapidly captured the attention of researchers in material and surface sciences by allowing more efficient synthetic routes to functional materials [15–25]. After all, the use of a limited number of supremely reliable bond-forming methods to easily achieve sophisticated functions is indeed the foundation of polymer science [26]. It is under this concept where click chemistry should serve as a guiding principle in the quest for function.

This chapter is not intended to be a comprehensive survey of the subject, which has been already the aim of many previous review articles [27–33]. The objective is instead to review several new applications of the CuAAC in the synthesis of well-defined multifunctional materials, derived from our research activities during the last few years, and give a brief perspective of the future direction in this field.

4.2
New Applications in Materials Synthesis

4.2.1
Metal Adhesives

Adhesive connections between metallic surfaces are important in a variety of applications, but perhaps most notably in electronics where conductive, semiconducting, or insulating properties may be required. The range of available metal adhesives is rather limited especially when conducting connections are desired, as ductile solders containing lead have become recognized as environmental issues [34]. In particular, polymers incorporating 1,2,4-triazoles are widely used in corrosion inhibitors and adhesion promoters on copper or copper-based products, which act as a stabilizing inert film by covering the vulnerable oxide layer [35]. With the exception of benzotriazoles, the 1,2,3-triazole isomer is poorly represented in the adhesives and coatings literature probably due to the difficulty of its synthesis prior to the development of the CuAAC.

Taking advantage of the anticipated affinity of triazoles for metal surfaces, Finn, Díaz and coworkers reported, in 2004, the use of the CuAAC in fast cure adhesive applications [36], which indeed constitutes the first example of this reaction for networks synthesis. A first approach to generate polymeric structures via CuAAC was developed in solution using bivalent azides and bivalent acetylenes (i.e., **1** + **2**) in the presence of Cu_2SO_4 and sodium ascorbate in a *t*-butyl alcohol/water mixture

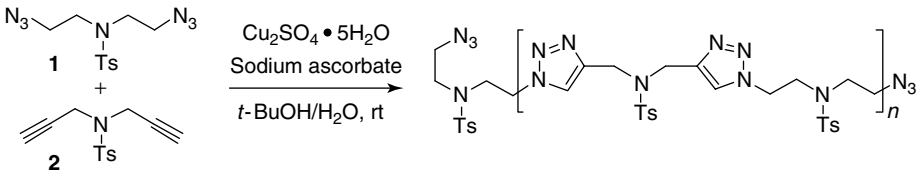

Scheme 4.2 Solution-phase polymerization of diazide **1** and dialkyne **2** by CuAAC (Ts = Tosyl). Adapted from [36] with permission from John Wiley & Sons.

(Scheme 4.2). This methodology allows the synthesis of linear polycondensates with molecular weights up to about 12 000 g mol^{-1}.

The success of the polymerization reaction was taken as a starting point to prepare *in situ* resin-type structures derived from polyvalent azides and alkynes on copper and brass plates (Figure 4.1). The general experimental procedure consists of spreading a mixture of monomers dissolved in the minimum amount of a volatile solvent (e.g., THF) over the surface of two metal plates, and pressing the crossed plates together after evaporation of the solvent, under defined conditions of pressure, temperature, and time. These adhesives usually show cohesive failure with extensive crack propagation, which is in agreement with the brittle nature of these materials.

Herein, polyvalency and flexibility of the monomeric units constitute critical factors in determining the power of azide/alkyne adhesive mixtures. Thus, combinations of diazides with dialkynes provide poor results, since such reactions should produce linear, rather than covalently cross-linked networks. Control experiments has established that no adhesion is obtained with monodentate azides and polyalkynes (i.e., **3** + **19**), nor with polydentate azide or alkyne alone (Figure 4.2).

Since Cu^{II} or Cu^{0} are unable to promote the AAC, the Cu^{0} surface must act to reduce the Cu^{II} species, formed by air oxidation, into diffusible Cu^{I} available to both the metal surface and the developing polymer matrix. Indeed, adhesion to Cu surfaces requires oxygen at approximately the level of atmospheric composition [37]. From a mechanistic point of view, despite the necessary oxidation for such comproportionation equilibrium [38], too much oxygen would be expected to be deleterious to the reaction, since active Cu^{I} centers could be oxidized before engaging in CuAAC catalysis. Nevertheless, samples prepared in the absence of oxygen have shown adhesive strengths near but slightly below than those of the samples prepared in air, showing that the surface Cu^{I} atoms are all that are required to get the reaction going [37]. The metal adhesion takes place by the binding of the surface to the growing polymer, by virtue of σ- or π-interactions with multiple triazoles and perhaps dangling alkynes (Figure 4.3). Interestingly, when no additional Cu^{I} catalyst is used in this process, the final cross-linking products usually contains between 2 and 5 wt% of copper indicating that the triazole products efficiently leach copper ions from the surface [36], creating a surface binding region with a blurred boundary between the various copper species and the triazole backbone.

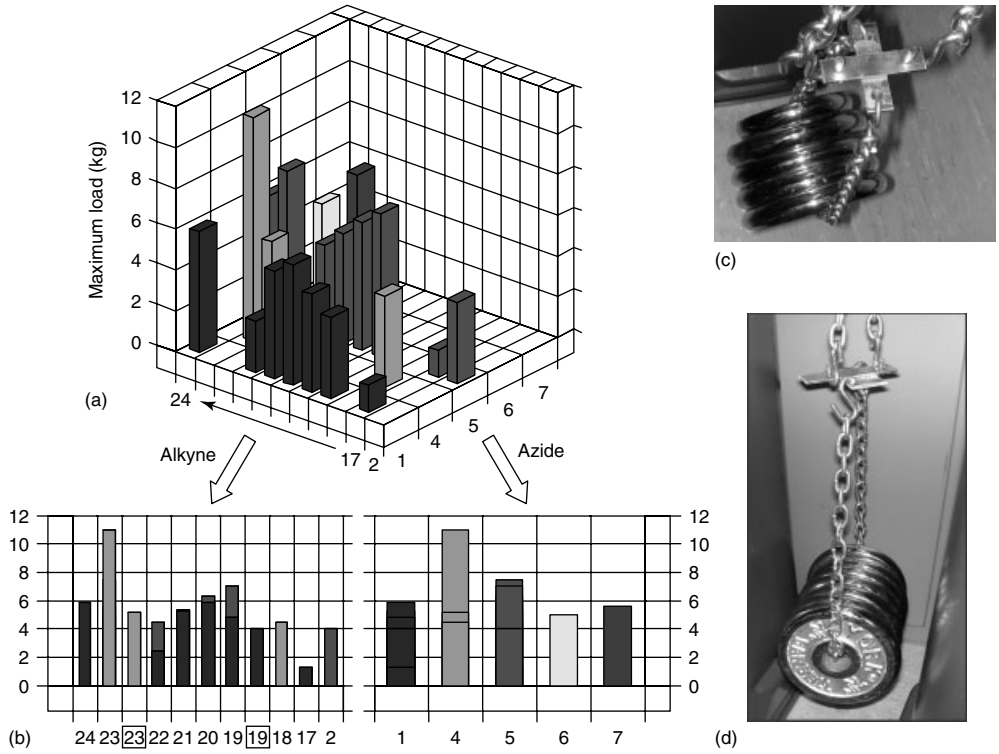

Figure 4.1 (a)Three-dimensional (3D) plot and (b) axes projection of adhesive strength on Cu for a series of azides and alkynes (see Figure 4.2). Alkynes designations marked with boxes denote the use of a 1 : 1.5 ratio of total azide groups to alkyne groups in the mixture instead of the usual 1 : 1 ratio. The bonded area was the same in each case (0.001 m^2). Conversion units: 1 kg = 9.81 N; 1 Pa = 1 N m^{-2}. The photographs (c and d) illustrate a simple peel test with crossed (c) Cu and (d) Zn plates for the determination of load-bearing capacity of adhesives by measuring the force normal to the surface required to separate the adhered plates. Adapted from [36] with permission from John Wiley & Sons.

As polytriazoles bind to metals of various kinds, the addition of Cu^{I} or Cu^{II} salts to the monomers mixture promotes also the formation of adhesive materials with other metal surfaces (i.e., Zn), which do not mediate the AAC [36]. On the other hand, it has been found that the formation of a uniform oxide layer (e.g., by etching) on Al surfaces is likely to promote adhesion, albeit not as effective as Cu surfaces, which requires no such pretreatment, since its surface (including the surface oxide) is already etched by the oxidative generation of Cu^{I} ions and their participation in the AAC process [37]. Several factors that affect the adhesive strength of these materials are listed below:

- **Effect of amine-containing Monomers:** The use of amine-containing monomers (i.e., **18**, **23**) are beneficial to the Cu-catalyzed process because they assist in the production of Cu-acetylide intermediates and contribute to productive

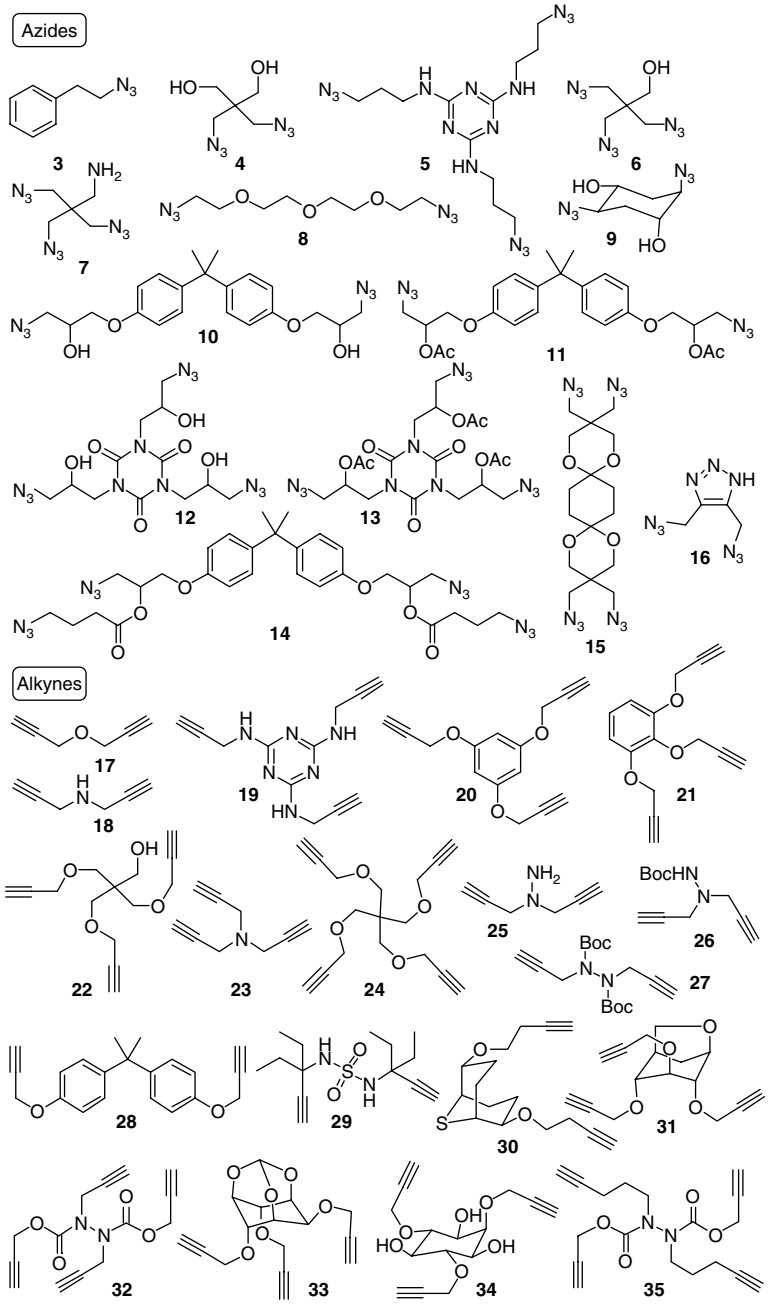

Figure 4.2 Series of azides and alkynes tested for the fabrication of metal adhesives. Adapted from [39] with permission from John Wiley & Sons.

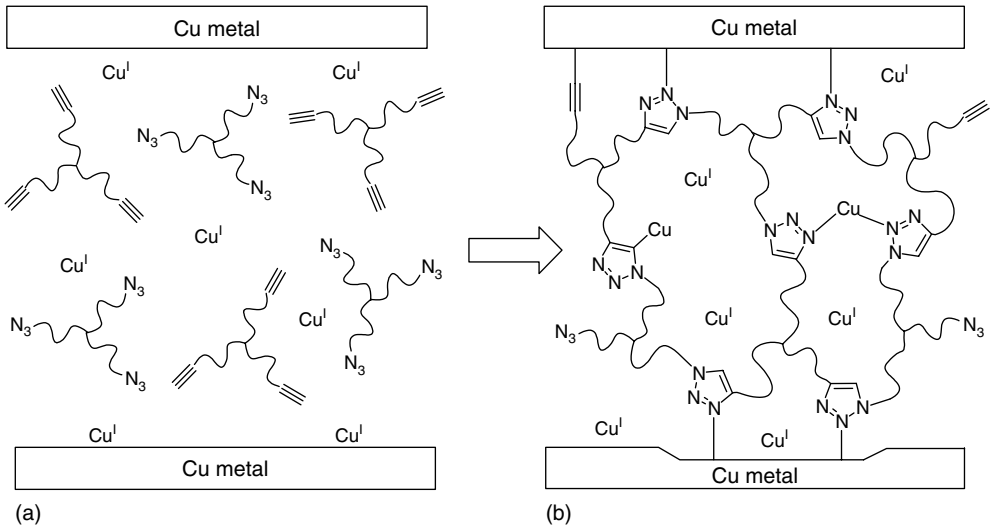

Figure 4.3 Proposed copper adhesion mechanism by formation of networked triazoles: (a) azide and alkyne monomers in the presence of Cu^{I} ions generated from, and/or stabilized by, the Cu^{0} surface; (b) Cu-mediated cycloaddition near the metal surface, where Cu^{I} concentration is presumed to be highest; and later polymer cross-linking by triazole formation. Potential Cu-acetylide and Cu-triazole interactions are shown. Adapted from [36] with permission from John Wiley & Sons.

chelating interactions with the metal center [36–39]. Indeed, the Cu^{I} complexes of tris (triazolylamine) compounds derived from **23** are highly active catalysts in solution-phase triazole-forming reactions as mentioned earlier [7].

- **Addition of Cu^{I} Catalyst:** The addition of Cu^{I} catalyst has been also found to be important for the synthesis of stronger adhesive polymers when cured at room temperature by speeding the polymerization of the preadhesive [37, 39]. For instance, the addition of $CuPF_6$4MeCNprovides uniform adhesive strength improvements.
- **Addition of Accelerating Ligands:** The use of adhesive mixtures having accelerating ligands (e.g., TBTA, benzimidazole-based ligands) can enhance the average maximum load strength, at least one-third. Nevertheless, the right amount of the specific ligand must be used (i.e., [ligand] = 50 mM; [total azide or alkyne functional groups] = 1 M), since it is necessary to reach a balance between competing factors of cross-link density and brittleness, and/or different CuAAC reaction rates at different ligand : metal ratios [39].
- **Effect of Temperature:** In general, the reactions between the metal plates are slow, requiring curing for several hours under pressure to achieve the maximum adhesive strength. However, heating at about 70 °C also accelerates curing rates, although the maximum adhesive strengths achieved at both room temperature and high temperature are very similar, suggesting that cross-linking reaches the same advanced point in any case. Under these conditions, enough Cu^{I} is

apparently made available from the metallic surface (without additional catalyst or precatalyst) to achieve full adhesive strength [37].

- **Other Minor Effects:** Other factors like adsorbed water, annealing pressure, or the addition of a dendrimeric poly(alkyne) has been also explored, each having only a modest effect on the outcome when the adhesive material is formed in a thin layer between two metal surfaces.

Figure 4.4 summarizes the results of a survey of adhesive mixtures along with 2 mol% $CuPF_6$4MeCN catalyst at room temperature. Among the alkynes, all distinguished by their branched nature, **31**–**34** provide the strongest adhesion. For azides, tripodal connections are also more effective than dipodal ones, the triazide **5** and the triol **12** being the most effective. Acetates **11** or **13** give weaker adhesives than their corresponding free-hydroxyl derivatives **10** or **12** respectively. Although it seems that hydroxyl versus acetate substitution makes little difference in the extent of triazole formation in the CuAAC, it is possible that additional hydrogen bonding of the OH groups favors the formation of a more effective network in terms of both cross-linking and flexibility. On the other hand, long flexible alkyl chains seem to have an adverse effect on the adhesion strength (i.e., tetraacetylene **35** vs **32**). This screening has allowed to identify a particularly effective tetravalent alkyne **5** and

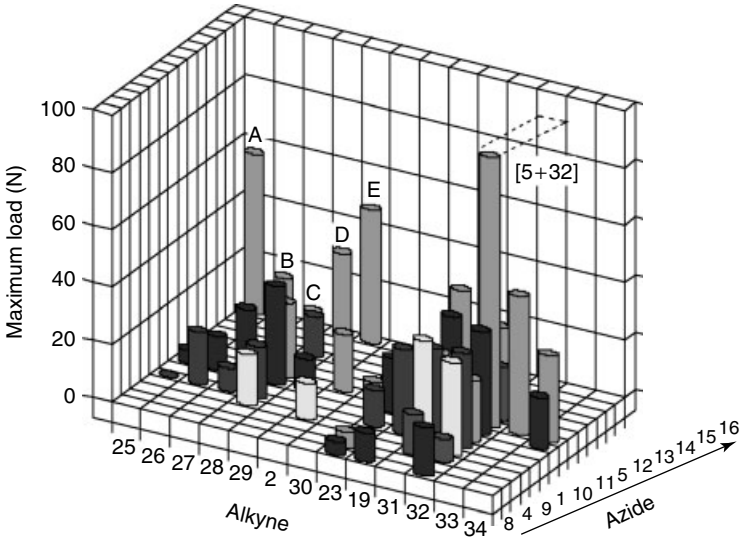

Figure 4.4 Adhesive strength given my maximum load for combinations of multivalent azides and alkynes (see Figure 4.2) in the presence of 2 mol% $CuPF_6$4MeCN (ratio azide : alkyne groups = 1 : 1, curing time = three days, RT). Commercial adhesives: A = J-B Weld, B = crazy glue, C = amazing goop, D = metal epoxy, E = copper bond. Estimated values error = 5–20%. The bonded area was the same in each case (2.0×10^{-5} m^2). Conversion units: 1 kg = 9.81 N; 1 Pa = 1 N m^{-2}. The failure load tests were performed by a customized prototype instrument designed to mimic the standard Instron® machine in a shear lap configuration. Adapted from [39] with permission from John Wiley & Sons.

trivalent azide **32** combination, which provides exceptional strength (32.8 ± 4.9 N) that matches or exceeds twice the load of the best commercial products, either made at room temperature in the presence of 2% Cu^{II} salt or at 70 °C without additives.

Finn and coworkers recently demonstrated that the strength of these adhesives can be even further improved by the incorporation of amine functionality into the monomers and/or the addition of CuAAC-accelerating ligands, which is in agreement with previous observations [39]. Very interestingly, the use of some divalent alkynes and azides as additives can also considerably improve the strength of the materials. In general, additional 3D branching from the additives is helpful in preventing the aggregation of flat triazole components into phase-separated brittle domains [39]. The most impressive strength improvement so far (twice as strong as the mixture **5** + **32**) has been reached by the incorporation of flexibility-inducing polyethylene glycol (PEG)-based difunctionalized additives in optimized proportions (i.e., 4% of the total amount of reactive groups). The most advantageous PEG-containing components were found to be divalent azides or alkynes having 24 units of ethyleneglycol, which corresponds to an optimized chain length to keep the right dilution of the cross-linked matrix.

In order to understand the physical properties of these polymers, several cross-linked polymers analogous to the adhesive materials have been prepared in bulk via CuAAC and characterized by standard techniques such as modulated differential scanning calorimetry (MDSC) and dynamic mechanical analysis (DMA) [40]. Interestingly, these materials present the remarkable glass transition temperatures (T_g) (up to 200 °C), which are time-dependent and usually up to 60 °C higher than the curing temperatures (T_{cure}) employed. This value is well above the normal range of 10–25 °C seen in step-growth polymerization systems [41]. This finding indicates a high degree of cross-linking even in the diffusion-restricted glassy state. As the G′ and tan δ peaks are not unusually wide for these polymers, the inhomogeneity of the network is unlikely responsible of the large difference between T_{cure} and T_g, as it happens in other materials [42]. A plausible explanation for this observation considers as potential contributing factors: (i) the high mobility of catalytic Cu^{I} centers and (ii) the intrinsic thermodynamic properties of the CuAAC. In this sense, triazoles have good thermodynamic affinity for Cu^{I} ions and yet the Cu-triazole interaction is kinetically labile. Therefore, Cu ions should be able to move readily from one triazole binding site in the developing network to another, even when the network is in the glassy state, in a similar way to radical diffusion in addition to polymerizations. Besides, the fact that Cu-triazole complexes are also good catalysts for the AAC [7, 8] enables the Cu ions to migrate through the structure to create local hot spots of catalytic reactivity, especially in areas of the polymer matrix in which multiple triazoles have already been formed. The exothermic nature of the AAC (about 50 kcal mol^{-1}) may also induce increased local motion of polymer chains in the vicinity of the catalytic hot spots. In addition, the large dipole moments, good hydrogen-bond accepting capability, and pseudoaromatic nature of 1,2,3-triazoles [2, 3] allows for π-stacking, which can also contribute to strong

noncovalent interactions facilitating the easy formation of associated domains in cross-linked polymers.

4.2.2 Synthesis and Stabilization of Gels

4.2.2.1 Strength Enhancement of Nanostructured Organogels

Low molecular weight organogelators (LMWOGs) represent remarkable examples of molecular self-assembly [43]. Such compounds make networks of fibers that can immobilize up to 10^5 liquid molecules per gelator and increase the viscosity of organic media by factors up to 10^{10}, with the potential to respond to a variety of external stimuli. The aggregation of gelator molecules into fibrous networks is driven by multiple low-energy interactions, such as dipole–dipole, van der Waals, and hydrogen bonding. However, the stability of this assembly is associated with a certain range of physico-chemical conditions (pH, monomer concentration, temperature, solvent quality, ionic force, etc.), outside of which the gel becomes a solution again. The solution/gel transition is therefore reversible by these so-called physical gels [44, 45]. Therefore, they are different from chemical or polymer gels, which have 3D structures created by cross-linked covalent bonds [46]. One of the biggest challenges in this field is the development of new methods to increase the thermo-mechanical stability of the gels with the minimum disruption of their functional properties. Several methods for *in situ* enhancement of gel thermostability have been reported, including post-polymerization of gel fibers, addition of polymers, use of host–guest interactions, and use of metal ion coordination [47]. However, some of these methods turn the physical gels into chemical gels with a consequent loss of their thermoreversibility.

In this context, the first practical use of the CuAAC in a supramolecular environment was reported in 2006 by Finn, Díaz and coworkers for the stabilization of gels via the introduction of azide or alkyne groups into organogelator compounds and subsequent cross-linking of their noncovalent networks by CuAAC [48]. In this approach, the small and nonprotic azides and alkynes groups are placed at the end of the hydrophobic chains of the gelator molecule to avoid a major disruption of the intermolecular interactions that lead to gelation. The concept has been tested using the LMWOG based on the undecylamide of *trans*-1,2-diaminocyclohexane, **36**, and its ''clickable'' analogs **37** and **38** (Figure 4.5).

In general, gels made from **37** or **38** have been found to be strengthened by the incorporation of an equimolar amount of **36** into the mixture, The introduction of Cu^I and cross-linkers (optimized ratio gelator : cross-linker = 10 : 1) into these samples afforded brittle gels with even much greater thermostability, as confirmed by oscillatory rheological measurements (storage moduli (G') > loss moduli G''; frequency range = 0.1–100 rad s^{-1}; <1% strain). It is important to note that the direct triazole cross-linking of azide and alkyne gelators (i.e., **37** + **38**) provides weaker materials relative to those produced by the addition of aliphatic cross-linkers (i.e., **39** + **37**, **40** + **38**). Herein, Cu^I catalyst can be introduced into the materials by (i) direct addition to the isotropic solution of the components or (ii) by layering

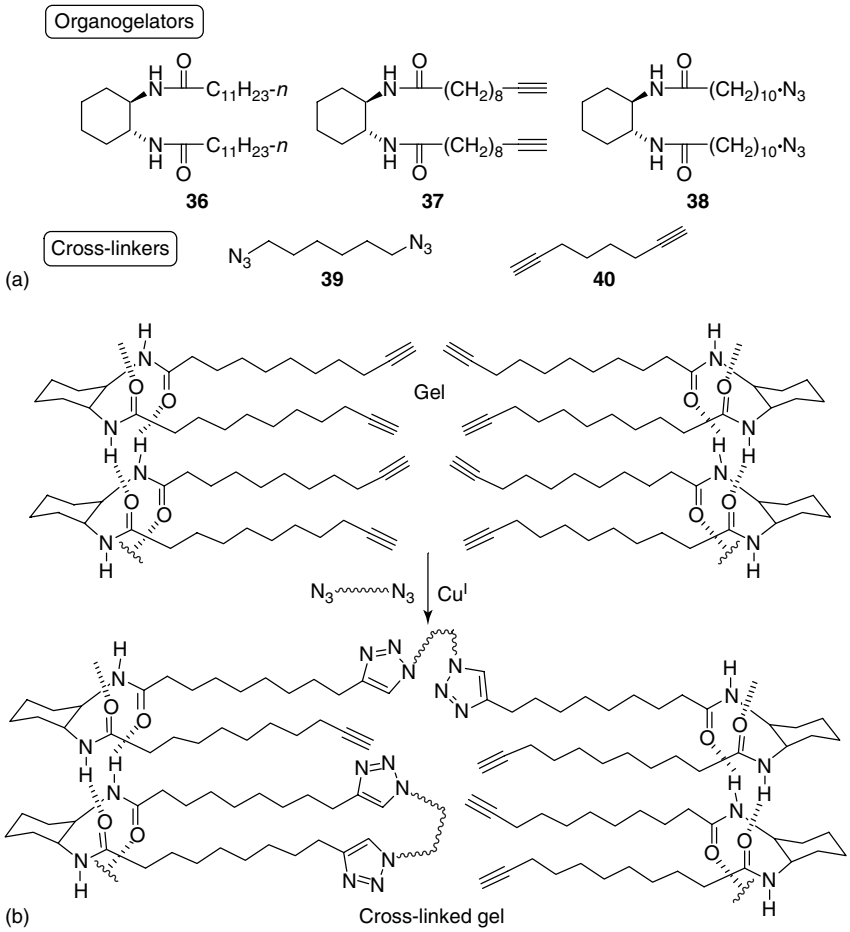

Figure 4.5 (a) Organogelators (**36**–**38**) and linear divalent cross-linkers (**39**–**40**). (b) Proposed hydrogen-bond pattern for gelation by **37** and Cu^{I}-catalyzed cross-linking with a linear diazide. The presence of triazole moieties in cross-linked materials can be confirmed by NMR analysis. Adapted from [48] with permission from the American Chemical Society.

a solution of the catalyst after gel formation with further diffusion into the matrix. Control experiments has demonstrated that enhancement of gel thermostability upon cross-linking is dependent upon the simultaneous presence of the metal in the active Cu^{I} oxidation state and the appropriate bivalent additive, as opposed to the use of monovalent capping reagents such as 1-heptyne or 1-azidooctano [48]. The expected Cu–triazole interactions seem not to be imperative to the stabilization of these materials, and the low concentration of click connectivity in the cross-linked gels allows the preservation of the thermoreversible function. Indeed, Fourier transform infrared (FT-IR) spectroscopy has showed the same

characteristic evidence for amide H-bond participation in the gelled state of both noncross-linked and cross-linked materials, which also present a similar morphology under transmission electron microscopy (TEM), suggesting that the enhanced stabilities are not the result of gross changes in structure.

Such *in situ* cross-linking process has been later applied for the stability enhancement (including thermoresistance, mechanical strength, and temporal stability under storage conditions) of photoactive organogels [47]. Thus, stable photoactive organogels can be successfully prepared by a two-step sequence involving (i) formation of thermoreversible organogels by use of a combination of LMWOGs (i.e., **41**) and ZnPc moieties containing complementary organogelator structures (i.e., **42**) and (ii) strength enhancement of the gels by *in situ* cross-linking via CuAAC (Figure 4.6) making use of a flexible C6 aliphatic diazide (i.e., **39**) and a suitable complementary diacetylene (i.e., **43**) (molar ratio 1 : 1, and 5 mol% with respect to the organogelator system [LMOG + ZnPc]). Emission of a red luminescence from the dry nanoscale fibrous structure due to the self-assembly of the phthalocyanine (Pc)-containing compounds in the organogel fibers can be directly observed by confocal laser scanning microscopy (CLSM). On the other hand, the dialkyne unit incorporated into the system for the stabilization process should resemble the LMWOGs structure in such a way that it could also participate in the self-assembly of [LMWOG + ZnPc].

It is important to note that the CuAAC here represent a much more challenging process than that in the previous case [48], since the cycloaddition must occur in an already multicomponent preformed organic gel, in which the appropriate

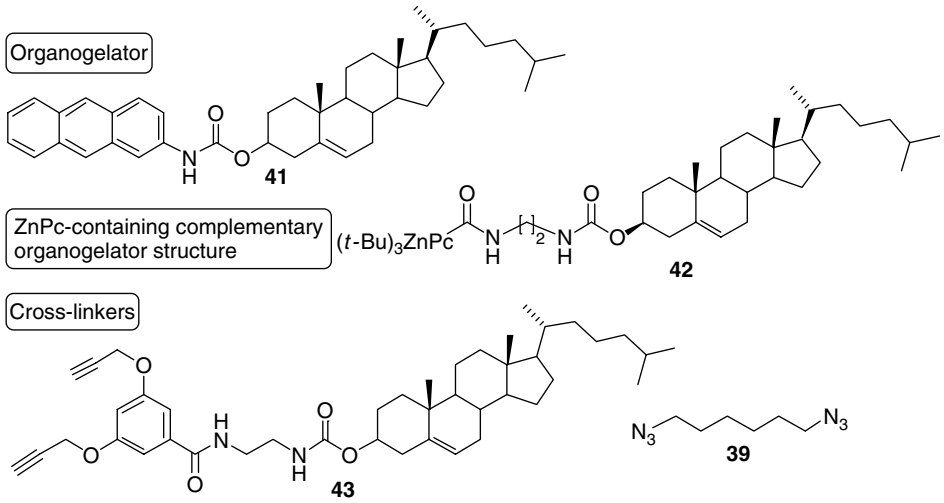

Figure 4.6 Organogelator **41**, ZnPc-containing complementary organogelator molecule **42**, and azide/alkyne-containing cross-linkers (**43**, **39**) used to prepared stable photoactive organogels.

"clickable" acetylene monomer should be at least partially associated with the gel fibers by virtue of multiple noncovalent interactions.

In this example, FT-IR studies have indicated that the greater part of the original noncovalent pattern is still retained upon stabilization, whereas UV/Vis and fluorescence spectroscopic evidences pointed to a preservation of the optical properties and a certain agglomeration degree of the Pc moieties upon CuAAC [47].

Figure 4.7 provides an overview of the procedure developed for the preparation of standard functional organogels and their further stabilization by *in situ* cross-linking through CuAAC. System 4 represents a standard organogel formed upon cooling of the isotropic solution of the appropriate LMWOG (system 2). If further strength

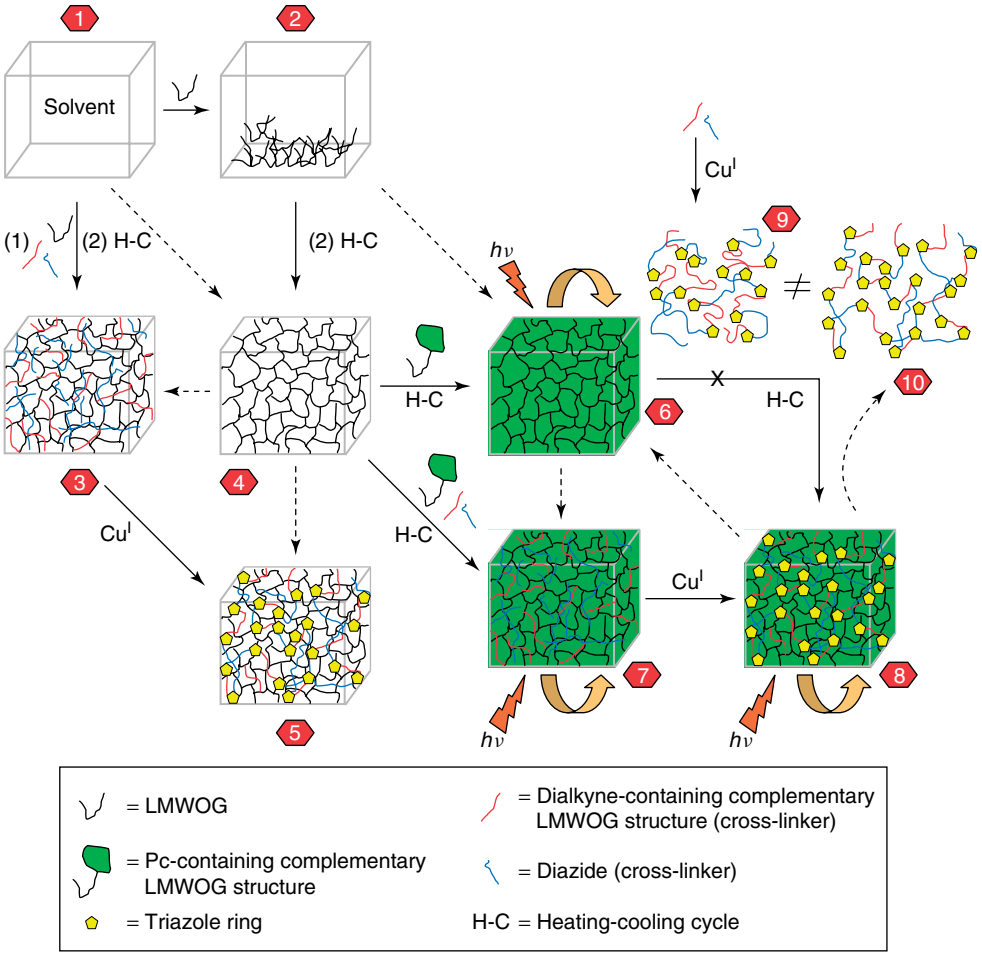

Figure 4.7 Strategy for the synthesis and stabilization of standard and Pc-based photoactive organogels. Reprinted from [47] with permission from Wiley-VCH.

enhancement of the material is required, a well-defined concentration of a suitable diacetylene-containing complementary LMWOG structure, linear diazide, and Cu^{I} catalyst can be swollen into the organogel network or premixed with the LMWOG prior to gel formation (system 3) in the heating–cooling process. The subsequent cross-linking reaction should enhance the thermostability of the organogel while preserving its thermoreversibility (system 5). On the other hand, organogel 4 may be prepared in the presence, for instance, of the appropriate Pc-containing complementary organogelator structures to afford a multicomponent photoactive viscoelastic material (system 6). Also in this case, suitably designed clickable monomers (diacetylene-containing complementary LMWOG structure and linear diazide) and the Cu^{I} catalyst can be incorporated into the gel network (system 7) in order to achieve further cross-linking to generate a new photoactive organogel with enhanced thermostability and mechanical properties. Nevertheless, the structural differences between a preformed [1,3,5]-triazole-based polymer (system 9) –made by CuAAC of the appropriate monomers in solution- and the cross-linked material (system 10) –obtained by *in situ* CuAAC of the clickable monomers-, induce a fast-phase separation process when the former is incorporated into the photoactive organogels.

4.2.2.2 **Synthesis of Polymer Thermoreversible Gels**

Selective [1,2,3]-triazole-based polymeric organogelators can be also prepared via CuAAC [49]. As demonstrated by rheological experiments, from a series of synthesized click polymers (Figure 4.8), those of the type $\{(\mathbf{44a–b})_x(\mathbf{45e–f})_y\}$, having at least a sulfonyl group in the polymer backbone, exhibit a discriminating gelling ability for DMSO and organic solvent mixtures containing at least 80% DMSO by volume, with minimum gelator concentrations in the range 3–5 wt %. Surprisingly, the $\{(\mathbf{44a–b})_x(\mathbf{45e–f})_y\}$ macromonomers (MACs) did not yield supramolecular aggregates in any solvent upon treatment either with 0.1 M EDTA aqueous solution for 24 hours at 65 °C or with coppersorb, remove effectively all the Cu ions associated to the polymer backbone. These results might suggest the importance of Cu ions interactions with the polymer backbone (typically with triazole rings) in forming these gels. In this sense, the Cu ions could probably help the cross-linking between the supramolecular polymers and play a critical role in the formation of a closely packed 3D-network, as no gelation was either observed by using the materials obtained under thermal conditions (absence of copper catalyst).

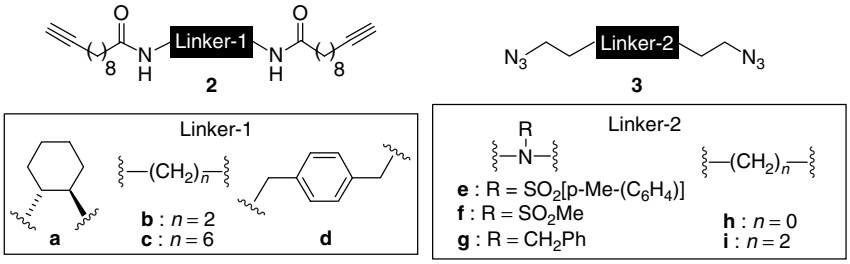

Figure 4.8 Alkyne and azide-containing divalent monomers. Adapted from [49] with permission from Elsevier.

From a morphological point of view, these organogels are formed by fibers of about 150–200 nm diameters and lengths in the micron scale, intertwined through numerous junction zones. They typically show broad endotherms with onset temperatures ascertained in the range 41–63 °C, and a T_{gel} which rises in an approximately linear manner as the concentration of the polymers increase, indicating that the polymer organogelators form more closely packed 3D-networks at high concentrations [49].

It is important to note that the gelation property here refers to well-defined [1,2,3]-triazole based polymers, in contrast to the previously discussed strategy to improve the thermal stability of the organogels [48], where the same or similar monomers are used only to induce cross-linking between the organogels fibers formed by an LMWOG without the formation of polymers in the gel phase.

4.2.2.3 Synthesis of Degradable Model Networks

The structurally simplest polymer networks are termed *model networks* (MNs) and are typically comprised of MACs, which are linear telechelic polymers cocovalently cross-linked through their end groups with multifunctional small molecules [50]. MNs are unique because their cross-link functionality is constant and predetermined, so that the molecular weight between cross-links is defined by that of the MAC, and the material is homogeneous with respect to cross-link density [50]. Despite the practical well-defined pore sizes of MNs [51] they are not considered ''ideal'' in a theoretical sense because (i) they unavoidably contain some number of unreacted functionalities, chain entanglements, and inelastic loops, (ii) the inherent polydispersity polydispersity index, (PDI) of the MAC precursor leads to a corresponding dispersity of pore sizes, and (iii) their intrinsic insolubility in many solvents makes them difficult to characterize by common analytical techniques.

In 2006, Finn, Turro, and coworkers envisioned a new way to prepare MNs easy to characterize [52]. The synthetic strategy is based on the reaction of an azide-containing MAC of low PDI (i.e., α,ω-azido-poly(*tert*-butyl acrylate), **46**), previously prepared by atom transfer radical polymerization (ATRP) [53], and a small polyalkyne (i.e., **24**) (Scheme 4.3). The MAC has a cleavable functionality at its center, which allows the preparation of degradable MNs via ozonolysis. Such process can yield soluble products that are easily analyzable by size-exclusion chromatography (SEC) in order to confirm the well-defined MN between cross-links.

Interestingly, when an approximately 2 : 1 ratio of azide to alkyne is used, the FT-IR spectrum still displays an azide resonance. The remaining azides and the olefin moiety can potentially be functionalized after cross-linking, providing another means of tailoring the properties of these materials.

4.2.3 Functionalization of SWNTs with Phthalocyanines

The electrical conductivity, morphology, and good chemical stability of single-wall carbon nanotubes (SWNTs) are promising features that stimulate their integration into photovoltaic systems or electronic devices [54]. In fact, the attachment of

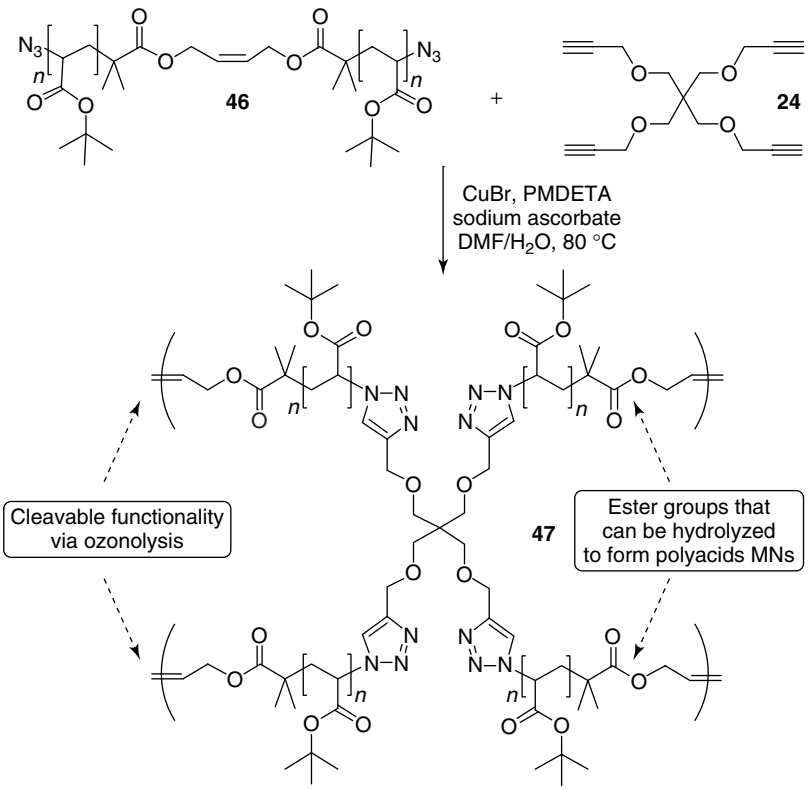

Scheme 4.3 Synthesis of the MN **47** via CuAAC of diazide **46** and tetraalkyne **24**. PMDETA = *N*,*N*,*N*′,*N*′′,*N*′′-pentamethyldiethylenetriamine. Adapted from [52] with permission from the American Chemical Society.

exceptional donor/antenna building blocks such as Pcs [55, 56] to nanotubes and fullerenes has recently emerged as an excellent approach to carbon nanostructure Pc-based photovoltaic and other electronic devices [57]. However, the fabrication of nanotube-based molecular assemblies is still limited mainly because of the difficulty to incorporate highly engineered molecules on the nanotube surfaces. This problematic issue can have mainly two origins: (i) the incompatibility between the functionality on the molecules and the conditions required for nanotube functionalization and/or (ii) the fact that nanotube functionalization usually requires a large excess of reagent, which is difficult or impossible to recycle and cannot be envisioned with high added value molecules such as Pcs. For instance, functionalization of carbon nanotubes with diazonium derivatives requires at least 4 equiv. of amine precursor or diazonium salt per carbon atom.

CuAAC has proved to overcome these problems and allowed the effective functionalization of alkyne-containing SWNTs **49** with an azido-containing ZnPc derivative **48** [58]. The synthetic strategy (Scheme 4.4) involves a first functionalization

of the SWNTs with 4-(trimethylsilyl)ethynylaniline and a subsequent Cu^{I}-catalyzed click attachment of an azide-containing ZnPc derivative [59, 60].

The physico-chemical characterization of the so prepared nanohybrids **50** [58] have showed a series of remarkable features, which are summarized as follows:

- The addition of Pc does not modify the linkage on the nanotube carbon lattice and the sp^2/sp^3 ratio, as established by Raman spectroscopy.
- Thermogravimetric have demonstrated the successful reaction of all the acetylenic groups (estimated loading = 1 phenylacetylene per 165 carbon atoms in *f*-SWNTs **49**) with azido-Pc moieties (estimated loading = 1 Pc per 155 carbon atoms in SWNT-ZnPc **50**).

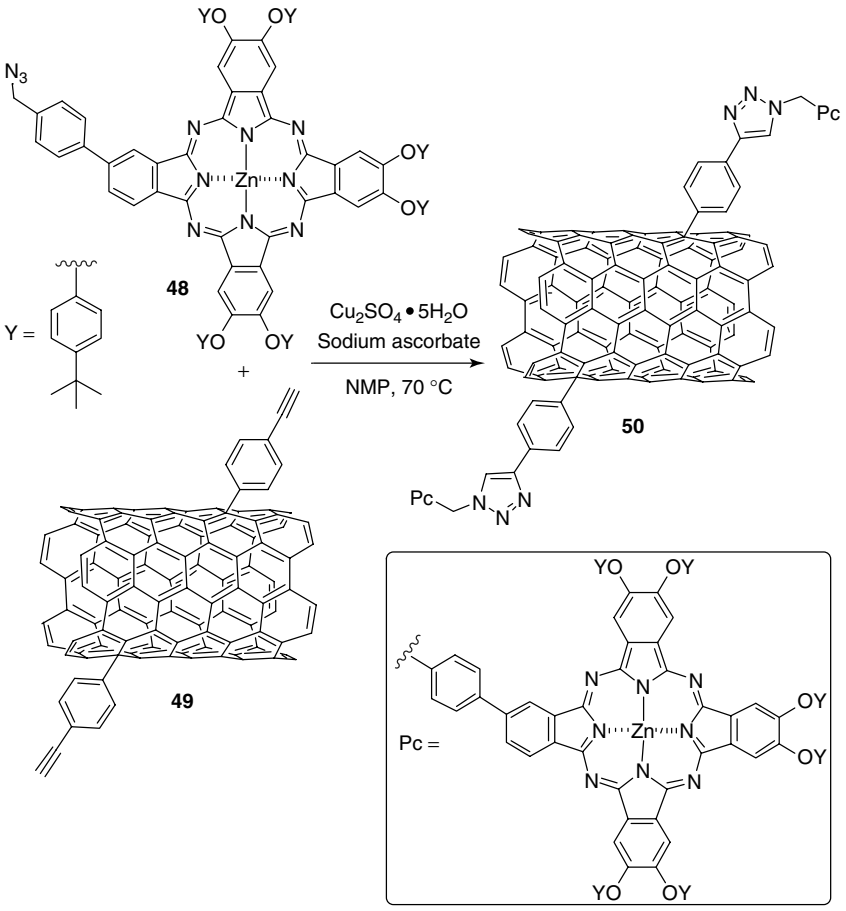

Scheme 4.4 Functionalization of alkyne-containing SWNTs **49** with azide-containing ZnPc **48** via CuAAC. Adapted from [58] with permission from the American Chemical Society.

- The typical lengths of both *f*-SWNTs **49** and SWNT-ZnPc **50** are about 500 nm to 1.5 μm with diameters of about 1–3 nm in the form of individual or bundles of nanotubes as showed by atomic force microscope (AFM).
- Despite being linked to SWNTs, the ZnPcs keep their electronic integrity as demonstrated by fluorescence and transient absorption measurements.
- A series of steady-state and time-resolved spectroscopy experiments have also demonstrated an impressive photoinduced communication between the two photoactive components of the nanoconjugate **50** (incident monochromatic photon to current conversion (IPCE) = 17.3%) when tested as a photoactive component in an indium tin oxide (ITO) photoanode in a photoelectrochemical cell at + 0.6 V and ascorbic acid as sacrificial electron donor.

4.3 Perspective

Our research during the last few years has convinced us that the click chemistry philosophy will afford the development of new ways to create stronger adhesive systems for both metal and nonmetal surfaces, to enhance the stability of a number of industrial viscoelastic soft materials to great levels while keeping their functional integrity, and to fabricate optoelectronic devices based on functionalized carbon nanotube field effect transistors. From a more general standpoint, the scientific community has been gifted, in less than a decade, with an impressive number of articles related to the synthetic aspects and applications of click chemistry in important research fields such as drug discovery and materials synthesis. Although most of these contributions are based on the use of the CuAAC as a key process, they have also assisted in a slow identification of some of its limitations. For instance, current shortcomings in materials synthesis indicate the participation of terminal alkynes in free radical polymerizations, which may require the use of protection–deprotection strategies in some applications. In this context, a general aqueous protocol for performing the cycloaddition with free radical polymers would be highly desirable. On the other hand, the use of Cu-based catalysts remains a drawback in some biomedical applications, in which a great level of nontoxicity is required. Thus, the development of more metal-free methods (e.g., a photochemically activated AAC) or other catalytic systems based on more biocompatible catalysts should be in the line of fire of future investigations. In this sense, a first breakthrough has been made by Bertozzi and coworkers, who employed a difluorinated cyclooctyne instead of the usual terminal alkyne to carry out copper-free click chemistry [61, 62]. Here, the ring strain and the electron-withdrawing difluoro group activate the alkyne toward the cycloaddition, allowing the use of this reagent attach fluorescent labels to cells with azide-containing sialic acid in their surface glycans.

Above all, the learning from the CuAAC should encourage chemists to expand the click-chemistry toolbox with alternative reactions that could overcome the limitations of their predecessors, especially in industrial environments. Without

doubt, this exercise will be driven by the permanent need of achieving specific and sophisticated molecular functions. A dose of motivation has been given already by the successful use of the thiol-ene click reactions in the modification of polymer multilayers [22]. With all the success associated so far to the use of the versatile click chemistry so far, it is easy to imagine that much more applications may appear by understanding the full spectrum of capabilities of any named click reaction. In the particular case of the CuAAC, the general vision of the triazole, only as a very stable and innocuous heterocyclic linkage, should also undergo an expansion by sharply looking at new opportunities where its other inherent and unique physicochemical properties [2, 3] could play a key functional role.

Acknowledgments

The author is deeply indebted to Profs M.G. Finn, K. Barry Sharpless, Valery V. Fokin, and Craig J. Hawker for their continuous support and guidance. Special thanks to Prof. T. Torres and coworkers for their work related to the functionalization of SWNTs. The great effort of all individual co-authors of the key papers cited in Section 4.3 is also deeply acknowledged.

References

1. Huisgen, R. (1961) Cenetary lecture–1,3-dipolar cycloadditions. *Proc. Chem. Soc. Lond*, 357–396.
2. Kolb, H.C., Finn, M.G., and Sharpless, K.B. (2001) Click chemistry: diverse chemical function from a few good reactions. *Angew. Chem. Int. Ed*, **40**, 2004–2021.
3. Rostovtsev, V.V., Green, L.G., Fokin, V.V., and Sharpless, K.B. (2002) A stepwise huisgen cycloaddition process: copper(I)-catalyzed regioselective ligation of azides and terminal alkynes. *Angew. Chem. Int. Ed*, **41**, 2569–2599.
4. Tornøe, C.W., Christensen, C., and Meldal, M. (2002) Peptidotriazoles on solid phase: [1,2,3-triazoles by regiospecific copper(I)-catalyzed 1,3-dipolar cycloadditions of terminal alkynes to azides]. *J. Org. Chem*, **67**, 3057–3064.
5. Rodionov, V.O., Presolski, S., Díaz, D.D., Fokin, V.V., and Finn, M.G. (2007) Ligand-accelerated cu-catalyzed azide-alkyne cycloaddition: a mechanistic report. *J. Am. Chem. Soc*, **129**, 12705–12712.
6. Zhang, L., Chen, X., Xue, P., Sun, H.H.Y., Williams, I.D., Sharpless, K.B., Fokin, V.V., and Jia, G. (2005) Ruthenium-catalyzed cycloaddition of alkynes and organic azides. *J. Am. Chem. Soc*, **127**, 15998–15999.
7. Chan, T.R., Hilgraf, R., Sharpless, K.B., and Fokin, V.V. (2004) Polytriazoles as copper(I)-stabilizing ligands in catalysis. *Org. Lett*, **6**, 2853–2855.
8. Rodionov, V.O., Presolski, S.I., Gardinier, S., Lim, Y.-H., and Finn, M.G. (2007) Benzimidazole and related ligands for cu-catalyzed azide-alkyne cycloaddition. *J. Am. Chem. Soc*, **129**, 12696–12704.
9. Appukkuttan, P., Dehaen, W., Fokin, V.V., and Van der Eycken, E. (2004) A microwave-assisted click chemistry synthesis of 1,4-disubstituted 1,2,3-triazoles via a copper(I)-catalyzed three-component reaction. *Org. Lett*, **6**, 4223–4225.
10. Beatty, K.E., Xie, F., Wang, Q., and Tirrell, D.A. (2005) Selective dye-labeling

of newly synthesized proteins in bacterial cells. *J. Am. Chem. Soc*, **127**, 14150–14151, and references therein.

11. Klok, H.A. (2005) Biological-synthetic hybrid block copolymers: Combining the best from two worlds. *J. Polym. Sci., Part A: Polym. Chem*, **43**, 1–17.
12. Kele, P., Mezo, G., Achatz, D., and Wolfdeis, O.S. (2009) Dual labeling of biomolecules by using click chemistry: a sequential approach. *Angew. Chem. Int. Ed*, **48**, 344–347.
13. Kolb, H.C. and Sharpless, K.B. (2003) The growing impact of click chemistry on drug discovery. *Drug Discov. Today*, **8**, 1128–1137, and references therein.
14. Fu, X., Albermann, C., Zhang, C., and Thorson, J.S. (2005) Diversifying vancomycin via chemoenzymatic strategies. *Org. Lett*, **7**, 1513–1515.
15. Evans, R.A. (2007) The rise of azide–alkyne 1,3-dipolar 'click' cycloaddition and its application to polymer science and surface modification. *Aust. J. Chem*, **60**, 384–395, and references therein.
16. Lutz, J.-F. (2007) 1,3-dipolar cycloadditions of azides and alkynes: a universal ligation tool in polymer and materials science. *Angew. Chem. Int. Ed*, **46**, 1018–1025.
17. Nandivala, H., Jiang, X., and Lahann, J. (2007) Click chemistry: versatility and control in the hands of materials scientists. *Adv. Mater*, **19**, 2197–2208.
18. Binder, W.H. and Sachsenhofer, R. (2007) 'Click' chemistry in polymer and materials science. *Macroml. Rapid Commun*, **28**, 15–54.
19. See articles references published at the special issue 'Click' chemistry in polymer science. Binder, W.H. (ed.) *Macroml. Rapid Commun*, **29**, 952–1185.
20. Carlmark, A., Hawker, C., Hult, A., and Malkoch, M. (2009) New methodologies in the construction of dendritic materials. *Chem. Soc. Rev*, **38**, 352–362.
21. Fokin, V.V., Finn, M.G., and Sharpless, K.B. (2006) Polymeric materials via click chemistry. US Patent WO/2006/012569, filed Jul. 22, 2005 and issued Feb. 2, 2006.
22. Connal, L.A., Kinnane, C.R., Zelikin, A.N., and Caruso, F. (2009) Stabilization and functionalization of polymer multilayers and capsules via thiol-ene click chemistry. *Chem. Mater*, **21**, 576–578, and references therein.
23. Kohman, R.E. and Zimmerman, S.C. (2009) Degradable dendrimers divergently synthesized via click chemistry. *Chem. Commun*, 794–796.
24. Nagao, Y. and Takasu, A. (2009) Click polyester: synthesis of polyesters containing triazole units in the main chain by click chemistry and improved thermal property. *Macroml. Rapid Commun*, **30**, 199–203.
25. Xu, X.-D., Chen, C.-S., Lu, B., Wang, Z.-C., Cheng, S.-X., Zhang, X.-Z., and Zhuo, R.-X. (2009) Modular synthesis of thermosensitive P(NIPAAm-co-HEMA)/β-CD based hydrogels via click chemistry. *Macroml. Rapid Commun*, **30**, 157–164.
26. Hawker, C.J., Fokin, V.V., Finn, M.G., and Sharpless, K.B. (2007) Bringing efficiency to materials synthesis: the philosophy of click chemistry. *Aust. J. Chem*, **60**, 381–383.
27. Wang, Q., Chittaboina, S., and Barnhill, H.N. (2005) Advances in 1,3-dipolar cycloaddition reaction of azides and alkynes–a prototype of "click" chemistry. *Lett. Org. Chem*, **2**, 136–138.
28. Bock, V.D., Hiemstra, H., and van Maarseveen, J.H. (2006) CuI-catalyzed alkyne-azide "click" cycloadditions from a mechanistic and synthetic perspective. *Eur. J. Org. Chem*, 51–68.
29. Wu, P. and Fokin, V.V. (2007) Catalytic azide-alkyne cycloaddition: reactivity and applications. *Aldrichchim. Acta*, **40**, 7–17.
30. Meldal, M. and Tornøe, C.W. (2008) Cu-catalyzed azide-alkyne cycloaddition. *Chem. Rev*, **108**, 2952–3015.
31. (2009) *http://clickchemicals.com/Click_Chemicals.html* (accessed 8 March 2009).
32. (2009) *http://www.sigmaaldrich.com/chemistry/chemical-synthesis/technology-spotlights/click.html* (accessed 8 March 2009).

33. (2009) *http://www.scripps.edu/chem/sharpless/click.html* (accessed 8 March 2009).
34. Rovner, S.L. (2007) Stopping the tin whisker stalkers. *Chem. Eng. News*, **85**, 30–33.
35. Trachli, B., Keddam, M., Takenouti, H., and Srhiri, A. (2002) Protective effect of electropolymerized 3-amino 1,2,4-triazole towards corrosion of copper in 0.5 M NaCl. *Corros. Sci*, **44**, 997–1011, and references therein.
36. Díaz, D.D., Punna, S., Holzer, P., McPherson, A.K., Sharpless, K.B., Fokin, V.V., and Finn, M.G. (2004) Click chemistry in materials synthesis. 1. Adhesive polymers from copper-catalyzed azide-alkyne cycloaddition. *J. Polym. Sci., Part A: Polym. Chem*, **42**, 4392–4403.
37. Accurso, A.A., Díaz, D.D., and Finn, M.G. (2009) Click chemistry in materials synthesis. IV. Improved metal-adhesive polymers by cui-catalyzed azide-alkyne cycloaddition, submitted.
38. For an application of this phenomenon in microcontact printing, see: Spruell, J.M., Sheriff, B.A., Rozkiewicz, D.I., Dichtel, W.R., Rohde, R.D., Reinhoudt, D.N., Stoddart, J.F., and Heath, J.R. (2008) Heterogeneous catalysis through microcontact printing. *Angew. Chem. Int. Ed*, **47**, 9927–9932.
39. Liu, Y., Díaz, D., Sharpless, K.B., Fokin, V.V., and Finn, M.G. (2007) Metal-adhesive polymers from cu(I)-catalyzed azide-alkyne cycloaddition. *J. Polym. Sci., Part A: Polym. Chem*, **45**, 5182–5189.
40. Le Baut, N., Díaz, D.D., Punna, S., Finn, M.G., and Brown, H.R. (2007) Study of high glass transition temperature thermosets made from the copper(I)-catalyzed azide-alkyne cycloaddition reaction. *Polymer*, **48**, 239–244.
41. Rozenberg, B.A. (1986) Kinetics, thermodynamics and mechanism of reactions of epoxy oligomers with amines. *Adv. Polym. Sci*, **75**, 113–165.
42. Lu, H., Lovell, L.G., and Bowman, C.N. (2001) Exploiting the heterogeneity of cross-linked photopolymers to create high-Tg polymers from polymerizations performed at ambient conditions. *Macromolecules*, **34**, 8021–8025, and references therein.
43. Gronwald, O., Snip, E., and Shinkai, S. (2002) Gelators for organic liquids based on self-assembly: a new facet of supramolecular and combinatorial chemistry. *Curr. Opin. Colloid Interface Sci*, **7**, 148–156, and references therein.
44. George, M. and Weiss, R.G. (2006) Molecular organogels. Soft matter comprised of low-molecular-mass organic gelators and organic liquids. *Acc. Chem. Res*, **39**, 489–497.
45. Ajayaghosh, A., Praveen, V.K., and Vijayakumar, C. (2008) Organogels as scaffolds for excitation energy transfer and light harvesting. *Chem. Soc. Rev*, **37**, 109–122, and references therein.
46. Bohidar, H.B., Dubin, P., and Osada, Y. (2003) *Polymer Gels: Fundamentals and Applications*, American Chemical Society Symposium Series, Vol. **833**, Washington, DC.
47. A detailed collection of references in this aspect can be found in: Díaz, D.D., Cid, J.J., Vázquez, P., and Torres, T. (2008) Strength enhancement of nanostructured organogels through inclusion of phthalocyanine-containing complementary organogelator structures and in situ cross-linking by click chemistry. *Chem. Eur. J*, **14**, 9261–9273.
48. Díaz, D.D., Rajagopal, K., Strable, E., Schneider, J., and Finn, M.G. (2006) "Click" chemistry in a supramolecular environment: stabilization of organogels by copper(I)-catalyzed azide-alkyne [3 + 2] cycloaddition. *J. Am. Chem. Soc*, **128**, 6056–6057.
49. Díaz, D.D., Marrero-Tellado, J.J., Velázquez, D.G., and Ravelo, A.G. (2008) Polymer thermoreversible gels from organogelators enabled by 'click' chemistry. *Tetrahedron Lett*, **49**, 1340–1343.
50. Hild, G. (1998) Model networks based on 'endlinking' processes: synthesis, structure and properties. *Prog. Polym. Sci*, **23**, 1019–1149.
51. Hoffman, A.S. (2002) Polysaccharide colloidal particles as delivery systems for macromolecules. *Adv. Drug Deliv. Rev*, **54**, 3–12, and references therein.

52. Johnson, J.A., Lewis, D.R., Díaz, D.D., Finn, M.G., Koberstein, J.T., and Turro, N.J. (2006) Synthesis of degradable model networks via ATRP and click chemistry. *J. Am. Chem. Soc*, **128**, 6564–6565.

53. Tsarevsky, N.V., Sumerlin, B.S., and Matyjaszewski, K. (2005) Step-Growth "Click" coupling of telechelic polymers prepared by atom transfer radical polymerization. *Macromolecules*, **38**, 3558–3561.

54. O'Connell, M.J. (2006) *Carbon Nanotubes: Properties and Applications*, CRC Press, Boca Raton.

55. de la Torre, G., Vázquez, P., Agulló-López, F., and Torres, T. (2004) Role of structural factors in the nonlinear optical properties of phthalocyanines and related compounds. *Chem. Rev*, **104**, 3723–3750.

56. O'Regan, B.C., Lopez-Duarte, I., Martinez-Diaz, M.V., Forneli, A., Albero, J., Morandeira, A., Palomares, E., Torres, T., and Durrant, J.R. (2008) Catalysis of recombination and its limitation on open circuit voltage for dye sensitized photovoltaic cells using phthalocyanine dyes. *J. Am. Chem. Soc*, **130**, 2906–2907, and references therein.

57. Ballesteros, B., Campidelli, S., de la Torre, G., Ehli, C., Guldi, D.M., Prato, M., and Torres, T. (2007) Synthesis, characterization and photophysical properties of a SWNT-phthalocyanine hybrid. *Chem. Commun*, 2950–2952, and references therein.

58. Campidelli, S., Ballesteros, B., Filoramo, A., Díaz, D.D., de la Torre, G., Torres, T., Rahman, G.M.A., Ehli, C., Kiessling, D., Werner, F., Sgobba, V., Guldi, D.M., Cioffi, C., Prato, M., and Bourgoin, J.-P. (2008) Facile decoration of functionalized single-wall carbon nanotubes with phthalocyanines via "click chemistry". *J. Am. Chem. Soc*, **130**, 11504–11509.

59. For the functionalization of SWNTs with polystyrene via CuAAC, see: Li, H., Cheng, F., Duft, A.M., and Adranov, A. (2005) Funtionalization of single-walled carbon nanotubes with well-defined polystyrene by "click" coupling. *J. Am. Chem. Soc*, **127**, 14518–14524.

60. Juricek, M., Kouwer, P.H.J., Rehak, J., Sly, J., and Rowan, A.E. (2009) A novel modular approach to triazole-functionalized phthalocyanines using click chemistry. *J. Org. Chem*, **74**, 21–25.

61. Baskin, J.M., Prescher, J.A., Laughlin, S.T., Agard, N.J., Chang, P.V., Miller, I.A., Lo, A., Codelli, J.A., and Bertozzi, C.R. (2007) Copper-free click chemistry for dynamic in vivo imaging. *Proc. Natl. Acad. Sci. U.S.A*, **104**, 16793–16797.

62. Johnson, J.A., Baskin, J.M., Bertozzi, C.R., Koberstein, J.T., and Turro, N.J. (2008) Copper-free click chemistry for the in situ crosslinking of photodegradable star polymers. *Chem. Commun*, 3064–3066.

5
Supramolecular Interactions and Smart Materials: C–X···X′–M Halogen Bonds and Gas Sorption in Molecular Solids

Guillermo Mínguez Espallargas

5.1
Introduction

The ultimate goal of a solid-state chemist is the rational design and synthesis of crystalline materials with the presence of specific and tunable chemical or physical properties, the so-called "*smart materials*." Porosity, magnetism, chirality, conductivity, superconductivity, spin-transition, optical, and photophysical properties can be exploited for a wide variety of applications including gas storage, separations, electronic, catalysis, nonlinear optics, or drug delivery, and are therefore the objectives of intense research activity. The occurrence of these properties in crystalline materials[1)] results from the combination of two aspects: (i) the molecular units (building blocks) that compose the crystal and (ii) the arrangement of these building blocks in the crystal. Controlling the former is relatively simple, and essentially it is only limited to the imagination and creativity of the researcher, since molecular chemistry has, over about two centuries, developed a wide range of very powerful procedures for creating even more sophisticated molecules from atoms linked by covalent bonds. On the contrary, organizing the molecules, or building blocks, in a predetermined manner is difficult to accomplish given that the structure of crystalline solids results from a delicate balance between all the intermolecular interactions present in the crystal, maximizing the attractive ones and minimizing the repulsive ones while, although not always, adopting the densest packing [1]. When a single strong interaction dominates in the system other weak intermolecular interactions normally play a secondary role in the crystal packing, providing support to the stronger interactions. In this situation, control over the molecular packing can successfully be achieved [2], although the presence of numerous weak interactions can in some cases overwhelm much stronger interactions as a result of their abundance [3]. Further difficulties can be encountered if the building blocks are

1) It should of course be acknowledged that crystalline products might not always represent the most desirable form of a material with respect to a given application.

Ideas in Chemistry and Molecular Sciences: Advances in Nanotechnology, Materials and Devices.
Edited by Bruno Pignataro

ISBN: 978-3-527-32543-6

potentially able to associate by utilizing more than one type of strong noncovalent interactions: competition and cooperativity between them becomes crucial and nontrivial. A design strategy incorporating intermolecular interaction hierarchies has been recently successfully applied using strong hydrogen bonds and halogen bonds [4], although in other cases unexpected results are obtained as a consequence of the competition between intermolecular interactions [5]. Thus, the recognition and understanding of the nature of (potential) intermolecular interactions are of paramount importance for the deliberate organization of molecules.

Control on the arrangement of molecules in the solid state permits the rational design of ''smart materials.'' Among these materials, those suitable for gas sorption present an ample variety which range from porous materials to nonporous materials. In addition, the gas molecules can be sorbed either via weak interactions (physisorption process) or by forming chemical bonds (chemisorption), which provide great versatility to this type of materials.

The first part of this chapter focuses on the study of intermolecular interactions involving halogen atoms, which are very abundant within many molecules, and can act principally as either nucleophiles or electrophiles depending on their coordination environment. Special attention will be given to their role as electrophiles, which might appear at first surprising and counterintuitive given that halogen atoms are typically viewed as being negatively charged. The second part of the chapter presents one type of ''smart materials,'' those suitable for gas sorption, a topic of current interest, and will focus on the unusual uptake of gases by nonporous crystals involving cleavage and formation of covalent bonds of the gas molecules and the framework. In these systems not only the gas molecules ''enter'' the crystal without disrupting the internal order despite the lack of channels, but a chemical reaction also occurs in the interior of the crystal in the absence of the solvents.

5.2
Interactions Involving Halogens: Nucleophiles versus Electrophiles

Halogen atoms are most frequently terminally bonded, and consequently, they are normally located at the periphery of the molecules. Thus, they are ideally positioned to be involved in intermolecular interactions and, therefore, they can play a fundamental role in the aggregation of molecules into solids, similar to the importance of hydrogen bonds due to the almost ubiquitous presence of hydrogen atoms on molecular surfaces in condensed phases. In addition, halogen atoms are common constituents in inorganic and organic molecules, and are present in a wide range of materials. Understanding their behavior is accordingly a crucial aspect in the rational design of halogen-containing materials; in fact, as will be detailed below, the properties of halogens atoms vary greatly with their coordination environment and differ enormously between metal-bound halogens, M–X (hereafter called *inorganic halogens*), and carbon-bound halogens, C–X (hereafter called *organic halogens*). Clear understanding of the nature of the type of interactions in which

halogens can be involved is essential not only because they may interfere with other noncovalent interactions but also because they can wisely be exploited to direct the aggregation of molecular units for the design of materials with desirable properties.

5.2.1 Halogens as Nucleophiles

Terminally bound halogen atoms exhibit a markedly anisotropic charge density distribution around the halogen as a consequence of the involvement in the M–X or C–X covalent bond of the halogen p-orbital that is coaxial with the bond and the noninvolvement of the two orthogonal p-orbitals [6]. Examination of the electrostatic potential in the vicinity of terminal halogens illustrates this point and shows the presence of a belt located at 100–130° to the M–X or C–X covalent bond where the negative electrostatic potential is minimum (Figure 5.1). The magnitude of the negative electrostatic potential around the halogen depends on the bond polarity. Thus, there is a more negative potential associated with inorganic halogens since

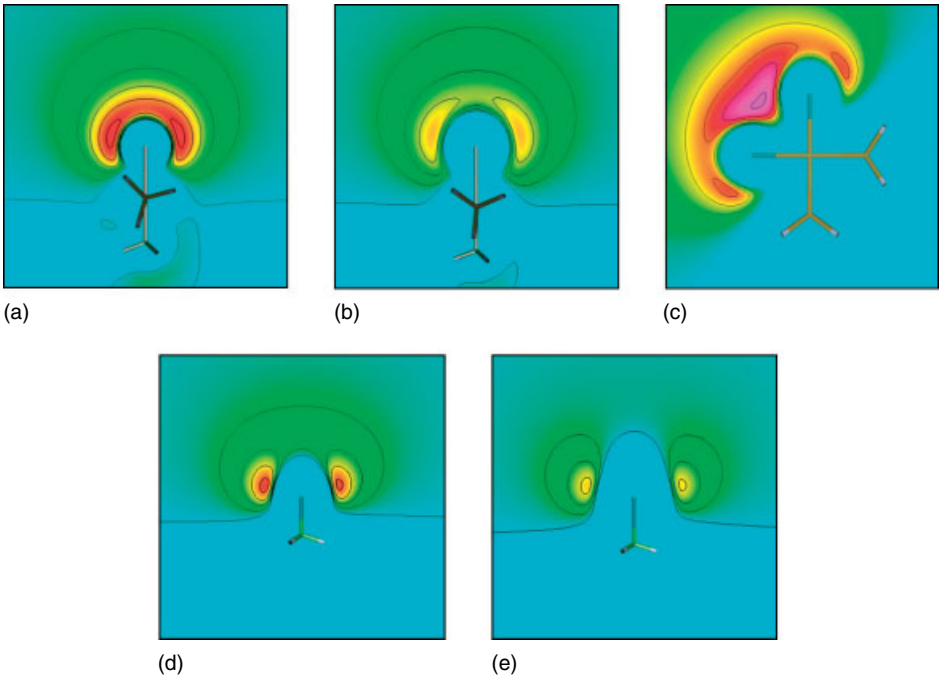

Figure 5.1 Calculated negative electrostatic potentials for model compounds (a) *trans*-[PdCl(Me)$(PH_3)_2$], (b) *trans*-[PdI(Me)$(PH_3)_2$], (c) *cis*-[$PdCl_2(PH_3)_2$], (d) CH_3Cl, and (e) CH_3I, contoured at intervals of 10 kcal mol^{-1} for inorganic halogens (a–c) and 4 kcal mol^{-1} for organic halogens (d,e). The calculations are presented and described in full in [6, 8]. Figures are adapted from [6, 8] with permission of the American Chemical Society and the National Academy of Science, USA.

the M–X bond is more polar than the C–X bond; similarly, lighter terminal halides, which are more electronegative, present a more pronounced minimum than heavier halides. Therefore, metal halides, especially fluorides and chlorides, can serve as potent and directional nucleophiles, as was first pointed out by Brammer, Orpen, and coworkers for the case of metal chlorides [7] and later generalized for all inorganic halogens through statistical and computational studies based upon data from thousands of interactions involving halogens [6]. These results were extended focusing on the cooperative effects of neighboring halide ligands in square planar, tetrahedral, and octahedral metal halides [8]. Examination of the electrostatic potential in the vicinity of a model *cis*-dichloride complex (Figure 5.1c) illustrates that a cooperative effect between neighboring halides arises because of overlap of the regions of negative electrostatic potential from the individual halide ligands, thus creating a binding pocket for electrophiles [9].

Novel hybrid organic–inorganic materials with appealing properties can be designed using perhalometallate anions as potent and directional hydrogen-bond acceptors with suitable organic molecules as hydrogen-bond donors [10]. For example, organic–inorganic layered perovskites that exhibit interesting electrical (semiconducting) [11] and optical [12] properties have been synthesized [13]. Magnetic [14] and nonlinear optical [15] hybrid materials have also been designed exploiting the nucleophilic character of perhalometallates, and the judicious design of a multiple hydrogen-bond donor ligand which can encapsulate perhalometallates has been employed for the recovery of metal salts [16]. Recently, some studies on hydrogen bonded salts have demonstrated that N–H···X–M hydrogen bonds permit the formation of N–M bonds in the solid state by the elimination of gaseous HX, which will be discussed in detail in Section 5.4.5 [17, 18].

5.2.2
Halogens as Electrophiles

In contrast to the strong nucleophilic behavior of inorganic halogens, organic halogens are at best very weak hydrogen-bond acceptors [19]. However, the most relevant difference between both types of halogens can be understood by close examination of the (anisotropic) calculated electrostatic potential around the organic halogens of the model molecules from Figure 5.1d and e, which shows the presence of a discontinuity in the negative potential in the region *trans* to the C–X bond. This electron-deficient region, which is more pronounced for heavier halogens (less electronegative), can be enhanced by the use of electron-withdrawing groups attached to the carbon atom or by the use of positively charged molecules [20], thus making plausible the attractive interaction of halogens with nucleophiles, which was first recognized by Hassel 40 years ago [21]. The term "*halogen bond*" refers to this type of interaction and can be defined as a directional (almost linear) attractive noncovalent interaction involving halogens as electron acceptors [22]. For a given nucleophile, halogen bonds are stronger for I > Br > Cl, due to the difference in electronegativity, and are absent for F, whose electrostatic potential remains negative all around the atom [23].

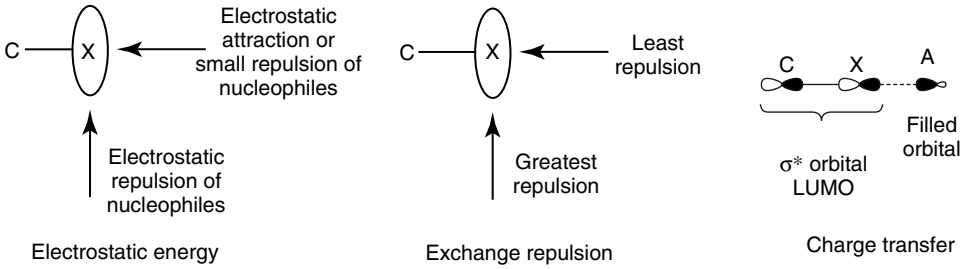

Scheme 5.1 Schematic representation of the contributions to the C–X···A interaction energy from electrostatic energy, exchange repulsion and (n → σ^*) charge transfer.

To emphasize the similarities with the D–H···A hydrogen bonds, with which they share numerous properties [22a], the general description D–X···A can be applied to halogen bonds, where D is the (hydrogen or halogen bond) donor and A is the (hydrogen or halogen bond) acceptor.[2)] The same acceptors used for hydrogen bonds are found as halogen bond acceptors; however, in the case of hydrogen bonds typical donors are nitrogen or oxygen atoms whereas, in the case of halogen bonds the donor is typically a carbon atom or another halogen. The main difference between hydrogen bonds and halogen bonds, which imparts more versatility to the latter regarding tuning the strength of the interaction, is the possibility of using different halogens which offer distinct capabilities for the interaction with Lewis bases, as will be discussed in later sections.

The nature of C–X···A halogen bonds is not fully established and is still under debate. They have been the focus of many theoretical investigations which concentrate on the relative roles of electrostatic forces, polarization, dispersion, and charge transfer in determining the geometry and stability of such complexes [24]. In small molecules, Allen, Taylor and coworkers, through combination of database studies with *ab inito* calculations, have characterized the geometry of C–Cl···O halogen bonds and show that the interaction is primarily electrostatic, with minor contributions from the other terms (Scheme 5.1) [24a]. However, halogen bonds are often discussed in terms of a charge transfer between the Lewis base and the C–X σ^* orbital [25] by analogy to halogen bonds involving dihalogen molecules, for example X–X···N [26], where the lengthening of the X–X bond is a clear indication of the charge transfer to an antibonding orbital.

Halogen bonds have been the focus of studies in the gas phase involving dihalogen molecules [27], but more recently they have become the subject of many investigations in the solid state, with a major emphasis on organic materials [22a–c]. However, the use of halogen bonds in metal-containing materials is also

2) Note that the halogen bond (or hydrogen bond) donor is the electron (density) acceptor, and the halogen bond (or hydrogen bond) acceptor is the electron (density) donor in these interactions.

developing quite rapidly, mainly motivated by the variety of properties that metal atoms provide [22d]. The strength of halogen bonds can be comparable to that of hydrogen bonds [28], and in fact in some cases there is preference on halogen bond formation over hydrogen-bond formation [29].

Iodo- and bromoperfluorocarbon moieties have been proved to form reliable halogen bonds in condensed phases with a number of bases. The presence of the electron-withdrawing fluorines strongly enhances the electron acceptor ability of the organic iodine and in addition minimizes the interferences from the other weak interactions, the C–F groups being very insensitive to the interaction with other functional groups. This has permitted their application to dictate the arrangement of molecules for topological reactions in the solid state [30], for the creation of binding sites in crosslinked polymers [31], for layer-by-layer assembly of two polymers [32], for the design nonlinear optical materials [33] and liquid crystals [34], as anion receptors [35], for chiral resolution [36], for complex radicals to tune the magnetic interactions [37], and also for the controlled growth of thin films [38]. Nevertheless, the effectiveness of halogen bonds are not restricted to the use of haloperfluorocarbons; activation of the halogens can also be achieved by other means, such as sp hybridization of the carbon atom attached to the halogen or use of positively charged molecules, leading to novel materials with interesting properties. Examples of these include structural control of polyoxometallates [39], polymerization [40], or design of conducting [41], magnetic [42], and luminescent [43] molecular materials. Functionalization of porous materials with substituents capable of halogen bonding is an interesting feature that can lead to many applications, although competition with the formation of the network has yet to be overcome [44]. Furthermore, it has also been recognized that halogen bonds play an important role in fields different from materials chemistry, such as structural biology, where they can direct the molecular folding of macromolecules such as proteins or DNA [45].

5.3
Combining Complementary Environments: C–X···X′–M Halogen Bonds

As shown in Section 5.2, halogen atoms can exhibit either nucleophilic or electrophilic character depending upon their coordination environment, with the formation of strong and directional D–H···X–M hydrogen bonds and C–X···A halogen bonds, respectively. Thus, one could envisage the combination of these two contrasting but complementary environments to create a new type of supramolecular synthon [46], C–X···X′–M, that could be used in the supramolecular construction of hybrid organic–inorganic systems given the abundance of halogen atoms in organic and inorganic species, and has the potential to yield applications in the control of conformations in metal complexes, and of substrate binding in catalysis (Scheme 5.2).

The formation of such interactions was clearly demonstrated in the preparation of neutral [47] and ionic crystalline materials [17, 48–50] using as halogen bond

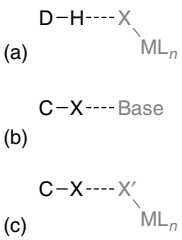

Scheme 5.2 (a) M–X groups are directional Lewis bases that act as nucleophiles, typically as hydrogen-bond acceptors; (b) C–X groups are directional Lewis acids that act as electrophiles; and (c) formation of directional C–X···X′–M halogen bonds by combination of the two complementary environments of inorganic and organic halogens.

donors halogenated pyridines or pyridinium cations, respectively, and different metal halides as halogen bond acceptors, thereby showing the applicability of the C–X···X′–M halogen bonds as an effective driving interaction for supramolecular construction from neutral or ionic building blocks. In all cases, the halogen bond geometry (linear interactions at the organic halogen and markedly bent interaction at the inorganic halogen) suggests an interaction within which the organic and inorganic halogens function as electrophile and nucleophile, respectively. Nevertheless, a clear understanding of the nature of C–X···X′–M halogen bonds would be necessary to provide a successful application of this synthon for materials design.

Zordan *et al.* synthesized a series of molecular crystals of general formula *trans*-[MCl_2(3-Xpy)$_2$] (M = Pd, Pt; 3-Xpy = 3-halopyridine; X = F, Cl, Br, I) which are propagated solely via C–X···Cl–M halogen bonds (X ≠ F) (Figure 5.2) [47a]. The halogen bonds were observed to be stronger for heavier organic halogens (I > Br > Cl) and absent when X = F, consistent with both a charge transfer and an electrostatic model for this interaction. The calculated electrostatic potential of the series of compounds *trans*-[$PdCl_2$(3-Xpy)$_2$] shows a positive potential associated with the heavy organic halogens (I > Br > Cl), whereas the potential remains negative for X = F. Thus, this suggests that the electrostatic contribution to a putative C–F···Cl–M interaction would be repulsive [23]. Therefore, in that study it was concluded that an electrostatic component to C–X···X′–M interactions may be quite important, although the use of only one type of inorganic halogen and the adoption of five separate C–X···Cl–M propagated networks limited the extent to which the importance of the electrostatic contribution could be assessed relative to other contributors, notably charge transfer.

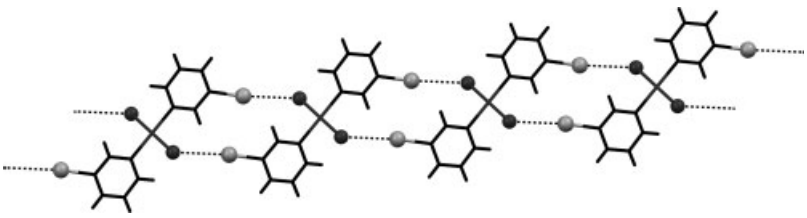

Figure 5.2 1D tape formed in *trans*-[$PdCl_2$(3-Ipy)$_2$]. Palladium and chloride ligands shown in dark gray, carbon-bound iodine in light gray, and all other atoms in black (C, H, N). Black dotted lines represent C–I···Cl–Pd halogen bonds. Halogen atoms are represented as spheres.

These limitations for the correct establishment of the nature of the C–X···X′–M were overcome in a subsequent study on a series of isostructural networks $(4\text{-XpyH})_2[CoX'_4]$ (X = Cl, Br; X′ = Cl, Br, I) which permit the systematic variation of both the organic and the inorganic halogens without structural changes, including doping to give mixed halide sites [49]. Correlation of intermolecular interaction geometries with their strength in the solid state is often problematic, even in chemically related compounds, because of large differences between the crystal structures of the compounds, which can have a profound effect on the metrics of a given intermolecular interaction. However, this family of compounds overcomes this difficulty due to the isostructurality of all the members. This allows the relative importance of electrostatic and charge transfer contribution to be evaluated since other interactions remain effectively constant within the series. As shown in Figure 5.3a, the compounds form one-dimensional tapes propagated via bifurcated N–H···X_2Co hydrogen bonds and C–X···X′–Co halogen bonds. Figure 5.3b presents the interhalogen X···X′ distance normalized to account for differences in

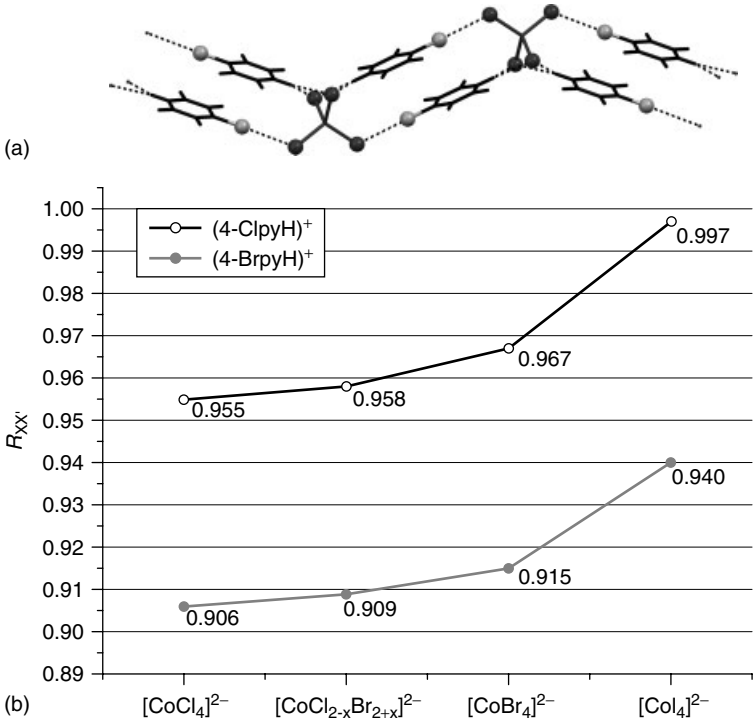

Figure 5.3 (a) Network formed in crystal structures of $(4\text{-XpyH})_2[CoX'_4]$. Cobalt and halide ligands shown in dark gray, organic halogens in light gray, and all other atoms in black (C, H, N). Black dotted lines represent N–H···X_2Co hydrogen bonds and C–X···X′–Co halogen bonds. Halogen atoms are represented as spheres and (b) variation of C–X···X′–Co halogen bond distances with change of halogen. Distances, $R_{XX'}$, are normalized to account for differences in van der Waals radii of the different halogens [51].

the van der Waals radii of the different halogen atom, $R_{xx'}$ [51]. This normalization permits the comparison of halogen bond distances for the different compounds using a common scale, and it is clear that the halogen bonds are shorter, and by implication stronger, for the heavier organic halogen species (C–X), but weaker for the heavier inorganic halogen species (Co–X). This result is consistent with a dominant contribution of electrostatics in the C–X···X′–M halogen bonds. The opposite trend upon changing the inorganic halogen would be expected if the $n \rightarrow \sigma^*$ charge transfer were the dominant contributor to the halogen bond (requiring a stronger halogen bond for Co–I > Co–Br > Co–Cl). This structural study was combined with DFT calculations of electrostatic potentials, which gave theoretical confirmation of the trends in C–X···X′–M halogen bond geometry observed across the series [52].

Two members of the previous series of isostructural compounds, $(4\text{-ClpyH})_2[CoCl_4]$ and $(4\text{-ClpyH})_2[CoBr_4]$, were further investigated at extreme conditions [50]. Specifically, structural changes were studied by single crystal X-ray diffraction at nine temperatures (from 300 to 30 K) and nine pressures (from atmospheric pressure to about 4 GPa) in order to gather information on the compressibility of the different types of noncovalent interactions. Interestingly, the reduction in unit cell volume is more pronounced with the application of pressure than with the reduction of temperature (about 18% vs. about 5%). In addition, this compression is not isotropic but varies with the type of interactions in each direction. For instance, the direction in which N–H···X_2Co hydrogen bonds and C–X···X′–Co halogen bonds are present is only reduced to about 3%, while the orthogonal directions are compressed more than 10%. This demonstrates that these two types of interactions possess a deep potential well, typical of strong attractive interactions, which are difficult to deform. The electrostatic nature of these strong attractive interactions was further confirmed by the study of the ''internal'' or ''chemical'' pressure exerted upon changing the larger $[CoBr_4]^{2-}$ anion for a smaller $[CoCl_4]^{2-}$ anion, which has an effect on the unit cell volume similar to the application of an external pressure of about 1 GPa, thus affording comparison of isovolumetric (and isostructural) compounds which are chemically different. This chemical pressure is quite anisotropic. Comparison of pairs of structures with equivalent volumes shows a compression along the direction of the tapes for the compound containing $[CoCl_4]^{2-}$ anions and a corresponding expansion in the other directions. This clearly implies that the N–H···X_2Co and C–Cl···X–Co interactions that propagate the tape are more attractive for X = Cl than for X = Br, consistent with an electrostatic model for the N–H···X_2Co hydrogen bonds and C–Cl···X–Co halogen bonds.

Because of the ubiquity of halogen atoms in both organic and inorganic compounds the establishment of the nature of the C–X···X′–M halogen bond provides an impetus for a wide range of applications to supramolecular construction of organic–inorganic hybrid materials. Furthermore, the strength of C–X···X′–M halogen bonds can be easily tuned through the choice of halogen and the electronic environment of both the organic and inorganic components. This strong and directional interaction has been used in the crystallization of a very large linear

halocuprate anion [53], in the synthesis of three-dimensional hybrid networks propagated solely via this interaction [54], in the design of molecular conductors [55], and, as will be detailed in Section 5.4.5, in developing materials that undergo solid–gas reactions with HCl gas [17].

5.4
Smart Materials for Gas Sorption

The previous sections have presented the understanding of noncovalent interactions involving halogen atoms and have also introduced some of the areas where they have been applied in order to control the arrangement of molecules in the solid state. This control on the assemblage of building blocks is essential for the design of smart materials, such as those suitable for gas sorption, where the positioning of the molecules can permit (or prevent) the appearance of the property of interest.

Gas sorption by designed porous crystalline materials is a topic of intense current interest [56] with a number of potential applications including gas storage, separations, and molecular sensing [57]. However, sorption of gases is not restricted to the presence of pores in the materials since it is also possible for gas molecules to ''enter'' a crystal without disrupting its crystallinity in the absence of channels [58]. Reviewing the literature on gas sorption shows that these processes are normally classified depending on the *nature* of the absorbing material, that is, porous or nonporous. However, three general major differences can be encountered looking instead at the *process* of the gas uptake, which are common for both porous and nonporous materials: (i) the binding interaction of the gas molecules with the framework ranges from weak dispersion interactions (physisorption) to strong covalent bonds (chemisorption); (ii) the sorbed gas molecules can either be located in voids of the material or be incorporated into the framework; and (iii) cleavage of covalent bonds of the gas molecules may occur as a result of the sorption process. Thus, taking into account these observations gas–solid reactions can be classified into five separate categories each enclosing both porous and nonporous materials (Scheme 5.3).

5.4.1
Physisorption of Gases (Type I)

Zeolites are the traditional rigid porous materials suitable for gas and solvent uptake [59]. Their robust framework does not collapse with guest removal, thus permitting reversible uptake and removal, which facilitates a wide variety of applications including petrochemical cracking, ion exchange, separations, and extraction. More recently, a specific class of porous materials known as *metal-organic framework*s (MOFs) have shown particular efficacy in the sorption of gases such as H_2, CH_4, and CO_2, which are important for future developments in the energy and transportation sectors of the economy, and are nowadays undoubtedly the most studied class of porous materials [56]. The pore walls of MOFs most commonly

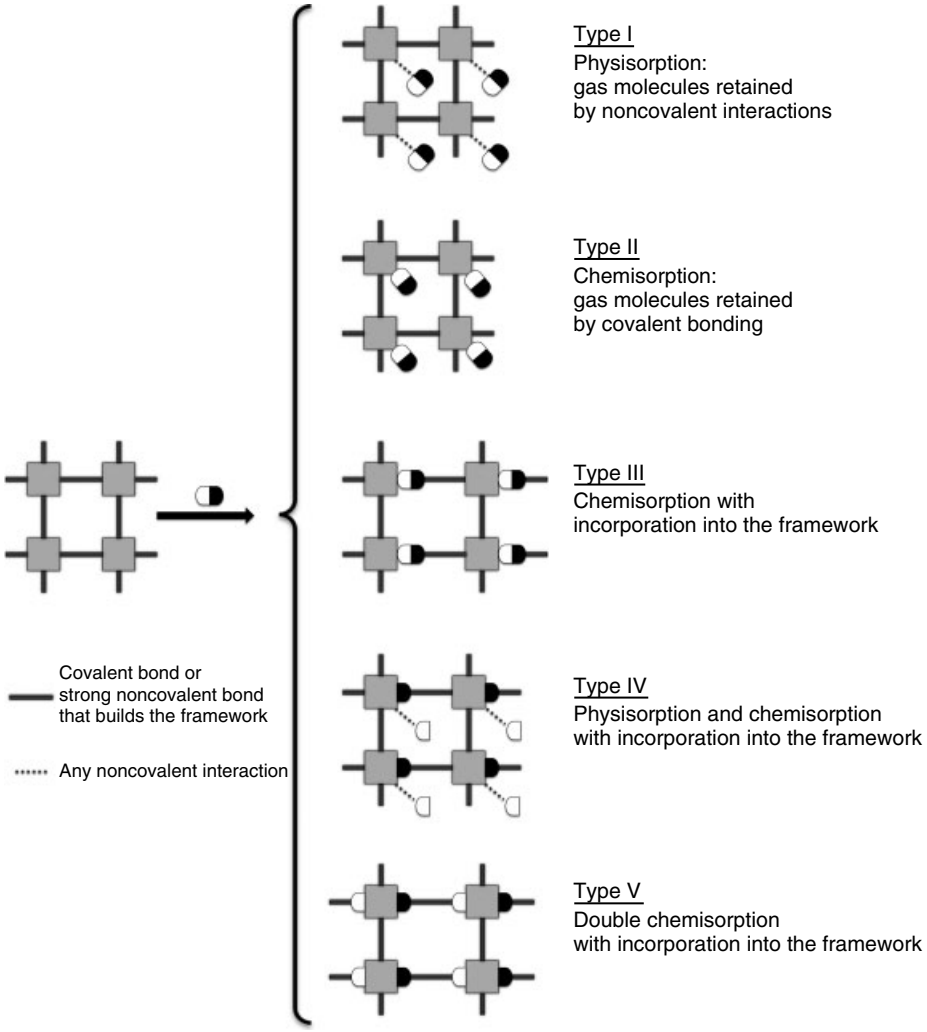

Scheme 5.3 Classification of the different types of gas–solid reactions in porous and nonporous materials.

comprise hydrocarbon moieties arising from the use of organic ligands to link between metal sites. Such materials often provide only dispersion forces as a means of containing guest molecules. Thus, gas molecules are typically physisorbed and therefore rather weakly bound to the interior surfaces of the pores [60], although recent developments have shown that binding of gas molecules may be feasible through strong noncovalent interactions, for example, hydrogen bonding, within the pores [61]. Crystallinity of the solid may be retained in many cases after sorption or desorption [62], but often this is not the case [63]. In general, the pores formed in crystals are uniform and therefore inclusion phenomena in all the channels

are identical. However, if two (or more) distinct channels exist in a crystal, they may take up two (or more) guests independently. Such biporous materials make, for example, the simultaneous isolation or transportation of two different guests possible, and are extremely rare [64].

Physisorption of gases can also occur in nonporous materials, as was reported by Atwood *et al.* in the gas uptake by crystalline *p*-^{t}Bu-calix[4]arene in one of its polymorphs [65]. This organic system, although nonporous, possesses void spaces accessible to guest molecules which are then confined by dispersion forces. The proposed mechanism for the gas uptake in this system involves cooperative alkyl group motions that permit the gas molecules to ''enter'' the crystal without disrupting its crystallinity. Since the discovery of this unusual behavior, many other related organic compounds possessing ''porosity without pores'' [66] have been reported which are not only interesting for the uptake of H_2, CH_4, and acetylene, but also for many technological applications [58].

5.4.2
Chemisorption of Gases (Type II)

Physisorption of gases has been studied extensively for storage and catalysis applications, but reversible gas incorporation can also involve covalent bond formation in what is known as *chemisorption*. Although maintaining the crystallinity of the solid in this type of process is a much rarer phenomenon than in the physisorption of gases, there are a few reports both in porous [67] and nonporous materials [68]. Chemisorption is an attractive process for gas sorption which overcomes the limitation of the low temperature needed for physisorption due to the low heat of adsorption of the process. This may have potential for the development of materials for gas storage at room temperature. In addition, where a change in the coordination environment of the metal center is involved can lead to changes in physical properties which make such materials suitable for sensing devices.

Most common are reactions that involve solvent-molecule coordination upon uptake by an evacuated framework in a porous transition metal coordination framework compound. Typically, a single metal–ligand bond is formed, and transport of the solvent (ligand) molecule through the crystal is relatively facile owing to the available channels [67]. Zur Loye and coworkers present the change in coordination environment in the mixed-metal 3D porous MOF $[Co_2(ppca)_2(V_4O_{12})_{0.5}]$ (ppca = 4-(pyridin-4-yl)pyridine-2-carboxylate) from five (distorted trigonal bypiramidal) to six (distorted octahedral) upon water chemisorption (Figure 5.4) [67a]. Surprisingly, this causes an expansion of the channels of the framework from about 6–15% of the crystal volume, although they are partially filled with noncoordinated water. Interestingly, the process is accompanied by a change of color of the crystals from brown to red.

An early example of chemisorption involving a nonporous crystalline material reported by van Koten and coworkers involves the reaction an organoplatinum complex with SO_2 gas, and might find use as a gas sensor or even as an

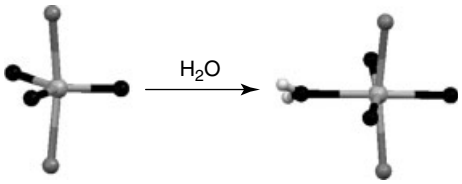

Figure 5.4 Change in the Co coordination sphere in $[Co_2(ppca)_2(V_4O_{12})_{0.5}]$ upon chemisorption of water. Co is shown in dark gray, N in dark gray, O in black, and H in white.

optical switch [68a]. In this reversible reaction, the coordination geometry at the platinum center is converted from square planar to square pyramidal and requires the formation of only an axial Pt–S bond enabling SO_2 to be bound upon its uptake by these crystals. When crystalline $[PtCl(C_6H_2(CH_2NMe_2)_2\text{-}2,6\text{-}OH\text{-}4)]$ is exposed to an atmosphere of SO_2, absorption of the gas by the platinum sites is indicated by a dramatic color change of the material from colorless to deep orange. Surprisingly, this process occurs without the loss of crystallinity, despite the change in the geometry around the platinum center. Part of the reason for this remarkable behavior is that the crystalline framework is held together by O–H···Cl–Pt hydrogen bonds which can easily tolerate the deformation.

5.4.3
Chemisorption of Gases with Incorporation into the Framework (Type III)

Very recent studies show the chemisorption of gas molecules by molecular crystals where the gas molecules are not only covalently bound upon absorption but also incorporated into the framework, involving processes akin to intercalation [69, 70].

An unusual example of gas insertion was recently reported by Rosseinsky *et al.* [69a]. Porous crystalline $[Co_2(\mu_2\text{-bipy})_3(\mu_1\text{-bipy})(SO_4)_2(CH_3OH)]$ (bipy = 4,4′-bipyridine) possesses two distinct octahedral Co centers which differ in two of the coordination sites: in one case, they are occupied by terminal bipy ligands and in the other case by two methanol molecules. This compound is able to reversibly sorb 2 mol of water per formula unit at ambient conditions provoking a substitution reaction at the two independent Co centers. The water molecules displace the monocoordinated bipy ligand and the coordinated methanol molecule, resulting in the complex $[Co_2(bipy)_3(SO_4)_2(H_2O)_2](bipy)(CH_3OH)$, where the Co centers have equivalent environments. One of the inserted water molecules hydrogen-bond to the leaving bipy, which serve as bridges between Co centers.

Brammer and coworkers have synthesized a nonporous coordination network based upon silver carboxylate dimer units linked via neutral tetramethylpyrazine ligands, $[Ag_4(TMP)_3\{O_2C(CF_2)_3CF_3\}_4]$ (TMP = tetramethylpyrazine). This material reacts with vapors of ethanol resulting in $[Ag_4(TMP)_3\{O_2C(CF_2)_3CF_3\}_4(EtOH)_2]$, where the $Ag_2(O_2CR)_2$ dimer is expanded due to the insertion of an EtOH molecule into one of the Ag–O bonds (Scheme 5.4) [70a]. This reaction requires

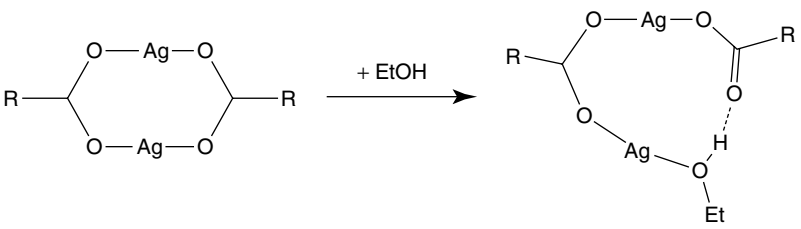

Scheme 5.4 Expansion of the $Ag_2(O_2CR)_2$ dimer upon ethanol uptake [70a]. The coordination spheres of the Ag atoms are completed with tetramethylpyrazine ligands (not shown for clarity).

a rearrangement of the coordination sphere of the metal center in addition to substantial ligand motions, but nevertheless crystallinity is maintained. Because of the lack of channels for the alcohol molecules to enter the crystal, the authors propose a mechanism where a cooperative motion of the flexible fluoroalkyl chains allow the ethanol molecules to reach the metal centers for the chemical reaction.

5.4.4
Combined Physisorption and Chemisorption of Gases with Incorporation into the Framework (Type IV)

A remarkable type of solid–gas reactions with profound structural changes involves, typically, the uptake of volatile acids via cleavage of covalent bonds of the gas molecules (normally H–A) with the generation of two fragments, one that is chemisorbed and incorporated into the framework (H^+) and the other which is physisorbed in voids of the materials (A^-). These reactions have been extensively studied in organic systems [71], although more recently Braga *et al.* have demonstrated that the uptake of volatile acids by organometallic compounds is also feasible [72]. They have shown that the organometallic zwitterion $[Co(\eta^5 - C_5H_4CO_2H)(\eta^5 - C_5H_4CO_2)]$ reacts with aqueous HX vapor to form crystalline $[Co(\eta^5 - C_5H_4CO_2H)_2]X \cdot nH_2O$ ($X = Cl^-$, BF_4^-, CF_3COO^-, CHF_2COO^-, CH_2ClCOO^-), a reaction which is also reversible upon thermal treatment of the resultant salts under low pressure. Formation and cleavage of hydrogen bonds as well as protonation of the carboxylate groups is required in order to accommodate the gas molecules in the solid. The incorporation of H_2O molecules in some cases and the use of wet vapors suggest that water may be important in this type of reactions, and the gas sorption could even occur via microscopic recrystallization.

5.4.5
Double Chemisorption of Gases with Incorporation into the Framework (Type V)

An extremely uncommon situation is the sorption of gases involving cleavage of a covalent bond followed by the chemisorption of both fragments, in what can be

called *double chemisorption*. This situation has only been reported for the sorption of HCl, where the covalent bond is broken with the formation of a H^+ and a Cl^- fragment. The proton coordinates a pyridine derivative, while the chloride coordinates a metal center [17, 18b].

Some of the hybrid organic–inorganic materials presented in Section 5.3 which form N–H···Cl–M hydrogen bonds are able to extrude HCl gas molecules generated *in situ* inside the crystal. This remarkable process is analogous to the elimination of gaseous H_2 from N–H···H–E dihydrogen bonds (E = B, Ga) reported by the groups of Jackson and Gladfelter for the preparation of covalently bonded systems inaccessible by other means [73]. The resultant compounds from the HCl extrusion are nonporous solids that are able to reabsorb HCl involving multiple structural changes while keeping their crystallinity. More specifically, $(3\text{-XpyH})_2[CuCl_4]$ (3-XpyH = 3-halopyridinium; X = Cl, Br) were found to release HCl gas leading to conversion into *trans*-$[CuCl_2(3\text{-Xpy})_2]$ (Figure 5.5) [17]. The original compounds are a yellow crystalline material in which halopyridinium cations are linked to the distorted tetrahedral $[CuCl_4]^{2-}$ anions via a series of bifurcated N–H···Cl_2Cu hydrogen bonds and C–X···Cl–Cu halogen bonds (see Section 5.3 for a complete description of this interaction). The products of HCl loss are blue molecular crystalline materials in which the copper center has square planar coordination and molecules are linked solely via C–X···Cl–Cu halogen bonds. Although the yellow salts can be prepared as single crystals their conversion

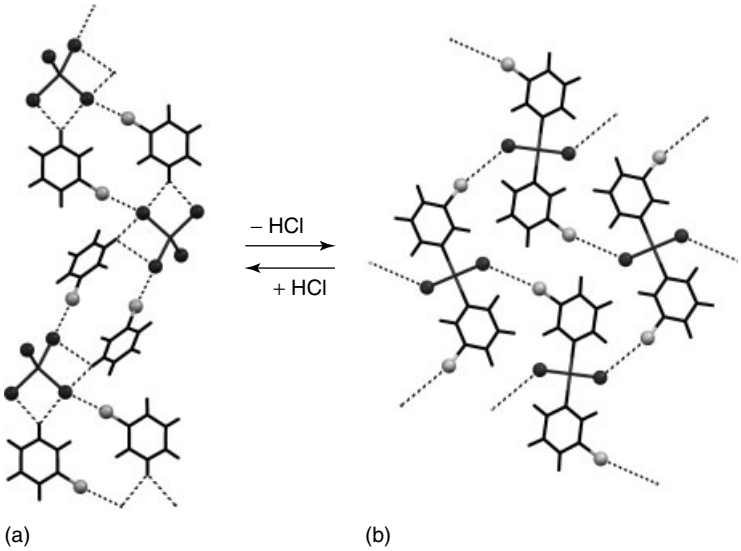

Figure 5.5 Interconversion of $(3\text{-XpyH})_2[CuCl_4]$ (a) and *trans*-$[CuCl_2(3\text{-Xpy})_2]$ (b) showing crystal structures [17]. (a) 1D network propagated via N–H···Cl_2Cu hydrogen bonds and C–X···Cl–Cu halogen bonds, indicated as black dotted lines and (b) 2D network propagated via C–X···Cl–Cu halogen bonds represented as black dotted lines. Halogen atoms are represented as spheres.

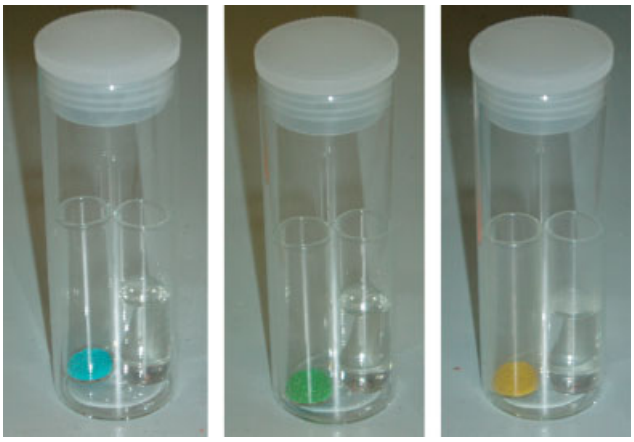

Figure 5.6 Reaction of *trans*-$[CuCl_2(3\text{-Clpy})_2] \rightarrow (3\text{-ClpyH})_2[CuCl_4]$ in the presence of vapor HCl after (a) 0 hour; (b) 2 hours; and (c) two days. Note that intermediate color green is a mixture of *trans*-$[CuCl_2(3\text{-Clpy})_2]$ (blue) and $(3\text{-ClpyH})_2[CuCl_4]$ (yellow). Reproduced from [17a] with permission of the American Chemical Society.

to the blue coordination compound results in a polycrystalline powder. Thus, X-ray powder diffraction data was used to solve the structures of *trans*-$[CuCl_2(3\text{-Xpy})_2]$ and obtain a good fit in structure refinement by Rietveld methods. Remarkably, upon exposure to vapor from concentrated aqueous HCl the blue material becomes yellow (Figure 5.6) and the resulting crystalline product was confirmed to be the original salt using powder diffraction. Similar studies carried out by Orpen and coworkers have also shown that salts of the form $(bipyH_2)[MCl_4]$ (bipy = 4,4′-bipyridine; M = Co, Zn) and coordination polymers *trans*-$[MCl_2(bipy)]$ can be interconverted by heating or treatment with aqueous vapors of HCl [18b]. These studies clearly demonstrate a new applicability of solid–gas reactions as a novel route for covalent materials.

The mechanism of the gas uptake by nonporous materials is unclear. As mentioned before, the most plausible mechanism for such reactions seems to be one involving a water-assisted microscopic recrystallization, analogous to that demonstrated for some anion exchange reactions involving crystalline network solids [74]. However, the possibility of this mechanism was very recently ruled out by carrying out the HCl gas uptake by crystalline *trans*-$[CuCl_2(3\text{-Clpy})_2]$ under anhydrous conditions. The reaction proceeds in the absence of solvent or water vapor, that is a *direct* solid–gas reaction, which is remarkable given the many structural changes that take place [17b].

In addition, this solid–gas reaction has been established to be an equilibrium process. In a closed system no release of HCl (no change of color) takes place when the crystalline yellow material (with HCl) is placed on its own. However, HCl release can be promoted in a closed system by trapping the HCl with Ag^+

ions (with the formation of AgCl). This solid–gas reaction was confirmed to be an equilibrium process by following the release of HCl gas by time-resolved gas phase IR spectroscopy. In a closed system where all gases have been previously evacuated, the HCl pressure was monitored and found to increase rapidly with time at the outset and reached a maximum pressure, indicating the establishment of the

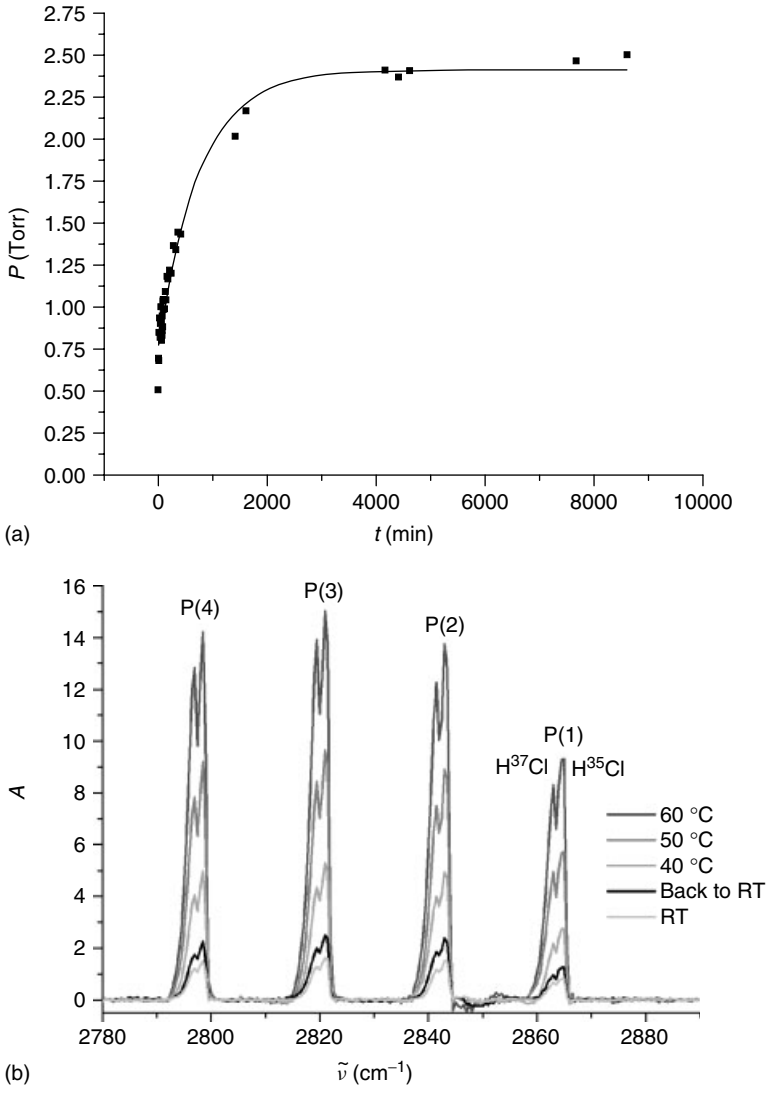

Figure 5.7 (a) Pressure increase of HCl gas release by $(3\text{-ClpyH})_2[CuCl_4]$ at 35 °C (derived from IR absorbance measurements) versus time (exponential fit) and (b) variation with temperature of the IR absorbance for HCl at equilibrium, showing the bands P(1), P(2), P(3), and P(4). Figures are adapted from [17b] with permission of the American Chemical Society.

equilibrium (Figure 5.7a). The solid–gas equilibrium constant was determined at $1.03(5) \times 10^{-5}$ [$\Delta G^{\circ} = 29.5(1)$ kJ mol^{-1}], indicating good sensitivity (in the range 200–20 000 ppm) of the blue nonporous material to HCl gas. Further confirmation of the solid–gas equilibrium was obtained by displacing the equilibrium position by changing temperature (Figure 5.7b). Specifically, the equilibrium pressure of HCl increases with increase in temperature, indicating HCl extrusion is endothermic. Importantly, a reduction in temperature returns the equilibrium pressure to its original lower value thereby confirming the ability of the blue coordination compound to react directly with gaseous HCl in the absence of water.

To better understand the mechanism of this type of reaction, which still remains unknown, a series of time-resolved *in situ* and *ex situ* structural studies of a range of molecular crystals were undertaken under temperature control to direct the elimination of HCl [17b]. A plausible mechanism could involve stepwise loss of the two equivalents of HCl, requiring the formation of an intermediate phase resulting from the loss of one molecule of HCl per formula unit of the ionic compound. Rietveld analysis revealed an excellent fit to a two-phase model for each pattern indicating the absence of a detectable intermediate crystalline phase in the reaction, with no evidence for formation of an amorphous phase during the reaction. Furthermore, the rate constant of the reaction was determined as 1.1×10^{-3} s^{-1}.

5.5 Conclusions

An important group of atoms normally involved in noncovalent interactions are halogens, not only due to their ubiquitous presence at the periphery of molecules, but also because of their amphiphilic character: halogen atoms can interact with either nucleophiles or electrophiles. This chapter has presented recent studies on the reliability of M–X and C–X groups to act as nucleophiles and electrophiles, respectively. The combination of both environments can be exploited in the formation of the supramolecular synthon C–X$\cdots$X′–M, which has proved to be robust and reliable. The strength of this synthon can be tuned by choice of the halogens involved to be comparable to strong hydrogen bonds. Thus, this adaptable interaction shows promise as an alternative or complement to hydrogen bonds and provides a valuable synthetic tool for supramolecular chemistry.

The second part of this chapter focuses on gas sorption materials. Since this process involves the cooperative movement of atoms in solid state, it is the porous crystalline compounds that comprise the major category of this type of reactions, although it has been shown that nonporous materials can also sorb gases. A novel classification for gas sorption is proposed on the basis of the process of the gas uptake instead of on the nature of the absorbing material, illustrated with recent examples from the literature. An attractive goal in this area is the intentional assemblage of molecules that are capable of absorbing molecules from the gas

phase *and* react, which could be exploited to produce new materials in crystalline form otherwise not achievable.

Acknowledgments

The work presented here was conducted in the context of the author's PhD thesis at the University of Sheffield (UK), under the supervision of Prof. Lee Brammer, to whom I am greatly indebted for all his support, encouragement, and valuable discussions.

Financial support for the author's PhD from the Cambridge Crystallographic Data Centre and the Centre for Molecular Structure and Dynamics of the Science and Technology Funding Council is gratefully acknowledged. The author also thanks the Spanish Ministerio de Ciencia e Innovacion for a current research contract (Programa Juan de la Cierva).

References

1. (a) Kitaigorodskii, A.I. (1961) *Organic Chemical Crystallography*, Consultants Bureau, New York; (b) Kitaigorodskii, A.I. (1973) *Molecular Crystals and Molecules*, Academic Press, New York; (c) Pidcock, E. and Motherwell, W.D.S. (2004) *Cryst. Growth. Des.*, **4**, 611; (d) Pidcock, E. and Motherwell, W.D.S. (2004) *Acta Crystallogr.*, **B60**, 725; (e) Pidcock, E. and Motherwell, W.D.S. (2005) *Cryst. Growth Des.*, **5**, 2322; (f) Pidcock, E. and Motherwell, W.D.S. (2003) *Chem. Commun.*, 3028.
2. Etter, M.C. (1990) *Acc. Chem. Res.*, **23**, 120.
3. Mareque Rivas, J.C. and Brammer, L. (1999) *Coord. Chem. Rev.*, **183**, 43.
4. (a) Saha, B.K., Nangia, A., and Jaskólski, M. (2005) *CrystEngComm*, **7**, 355; (b) Aakeröy, C.B., Desper, J., Helfrich, B.A., Metrangolo, P., Pilati, T., Resnati, G., and Stevenazzi, A. (2007) *Chem. Commun.*, 4236; (c) Bouchmella, K., Boury, B., Dutremez, S.G., van der Lee, A. (2007) *Chem. Eur. J.*, **13**, 6130; (d) Aakeröy, C.B., Hussain, I., Forbesa, S., and Desper, J. (2007) *CrystEngComm*, **9**, 46.
5. (a) Zordan, F., Mínguez Espallargas, G., and Brammer, L. (2006) *CrystEngComm*, **8**, 425; (b) Aakeröy, C.B., Schultheiss, N., Desper, J., and Moore, C. (2007) *CrystEngComm*, **9**, 420; (c) Reddy, L.S., Chandran, S.K., George, S., Babu, N.J., and Nangia, A. (2007) *Cryst. Growth Des.*, **7**, 2675.
6. Brammer, L., Bruton, E.A., and Sherwood, P. (2001) *Cryst. Growth Des.*, **1**, 277.
7. (a) Aullon, G., Bellamy, D., Orpen, A.G., Brammer, L., and Bruton, E.A. (1998) *Chem. Commun.*, 653; (b) Mareque Rivas, J.C. and Brammer, L. (1998) *Inorg. Chem.*, **37**, 4756; (c) Lewis, G.R. and Orpen, A.G. (1998) *Chem. Commun.*, 1873; (d) Brammer, L., Bruton, E.A., and Sherwood, P. (1999) *New J. Chem.*, **23**, 965.
8. Brammer, L., Swearingen, J.K., Bruton, E.A., and Sherwood, P. (2002) *Proc. Nat. Acad. Sci. U.S.A.*, **99**, 4956.
9. Similar effects are also observed for octahedral and tetrahedral metal halide complexes; see ref. 8 for details.
10. (a) Brammer, L. (2003) Hydrogen bonds in inorganic chemistry: application to crystal design, in *Perspectives in Supramolecular Chemistry*, Crystal Design–Structure and Function, Vol. 7 (ed. G.R.Desiraju), John Wiley & Sons, Ltd, Chichester, pp. 1–75; (b) Brammer, L. (2003) *Dalton Trans.*, 3145.

11. (a) Mitzi, D.B., Feild, C.A., Harrison, W.T.A., and Guloy, A.M. (1994) *Nature*, **369**, 467; (b) Mitzi, D.B., Wang, S., Feild, C.A., Chess, C.A., and Guloy, A.M. (1995) *Science*, **267**, 1473; (c) Kagan, C.R., Mitzi, D.B., and Dimitrakopoulos, C.D. (1999) *Science*, **286**, 945; (d) Mitzi, D.B., Chondroudis, K., and Kagan, C.R. (2001) *IBM J. Res. Dev.*, **45**, 29; (e) Sourisseau, S., Louvain, N., Bi, W., Mercier, N., Rondeau, D., Boucher, F., Buzaré, J.Y., and Legein, C. (2007) *Chem. Mater.*, **19**, 600; (f) Takahashi, Y., Obara, R., Nakagawa, K., Nakano, M., Tokita, J., and Inabe, T. (2007) *Chem. Mater.*, **19**, 6312.
12. Mitzi, D.B. (1996) *Chem. Mater.*, **8**, 791.
13. Mitzi, D.B. (2001) *J. Chem. Soc., Dalton Trans.*, 1, and references therein.
14. (a) Bonamartini-Corradi, A., Battaglia, L.P., Rubenacker, J., Willett, R.D., Grigereit, T.E., Zhou, P., and Drumheller, J.E. (1992) *Inorg. Chem.*, **31**, 3859; (b) Willett, R.D., Place, H., and Middleton, M. (1988) *J. Am. Chem. Soc.*, **110**, 8639; (c) Rubenacker, G.V., Haines, D.N., Drumheller, J.E., and Emerson, K. (1984) *J. Magn. Magn. Mater.*, **43**, 238.
15. Maggard, P.A., Kopf, A.L., Sternb, C.L., and Poeppelmeier, K.R. (2004) *CrystEngComm*, **6**, 451.
16. (a) Bell, K.J., Westra, A.N., Warr, R.J., Chartres, J., Ellis, R., Tong, C.C., Blake, A.J., Tasker, P.A., and Schröder, M. (2008) *Angew. Chem. Int. Ed.*, **47**, 1745; (b) Ellis, R.J., Chartres, J., Sole, K.C., Simmance, T.G., Tong, C.C., White, F.J., Schröder, M., and Tasker, P.A. (2009) *Chem. Commun.*, 583.
17. (a) Mínguez Espallargas, G., Brammer, L., van de Streek, J., Shankland, K., Florence, A.J., and Adams, H. (2006) *J. Am. Chem. Soc.*, **128**, 9584; (b) Mínguez Espallargas, G., Hippler, M., Florence, A.J., Fernandes, P., van de Streek, J., Brunelli, M., David, W.I.F., Shankland, K., and Brammer, L. *J. Am. Chem. Soc.*, **129**, 15606.
18. (a) Adams, C.J., Crawford, P.C., Orpen, A.G., Podesta, T.J., and Salt, B. (2005) *Chem. Commun.*, 2457; (b) Adams, C.J., Colquhoun, H.M., Crawford, P.C., Lusi, M., and Orpen, A.G. (2007) *Angew. Chem. Int. Ed.*, **46**, 1124; (c) Adams, C.J., Kurawa, M.A., Lusi, M., and Orpen, A.G. (2008) *CrystEngComm*, **10**, 1790.
19. Some examples of organic halogens acting as hydrogen bond acceptors can be found in: (a) Thalladi, V.R., Weiss, H.-C., Bläser, D., Boese, R., Nangia, A., and Desiraju, G.R. (1998) *J. Am. Chem. Soc.*, **120**, 8702; (b) McBride, M.T., Luo, T.-J.M., and Palmore, G.T.R. (2001) *Cryst. Growth Des.*, **1**, 39.
20. (a) Riley, K.E., Murray, J.S., Politzer, P., Concha, M.C., and Hobza, P. (2009) *J. Chem. Theory Comput.*, **5**, 155; (b) Politzer, P., Lane, P., Concha, M.C., Ma, Y., and Murray, J.S. (2007) *J. Mol. Model.*, **13**, 305; (c) Valerio, G., Raos, G., Meille, S.V., Metrangolo, P., and Resnati, G. (2000) *J. Phys. Chem. A*, **104**, 1617.
21. Hassel, O. (1970) *Science*, **170**, 497.
22. (a) Metrangolo, P., Neukirch, H., Pilati, T., and Resnati, G. (2005) *Acc. Chem. Res.*, **38**, 386; (b) Metrangolo, P., Meyer, F., Pilati, T., Resnati, G., and Terraneo, G. (2008) *Angew. Chem. Int. Ed.*, **47**, 6114; (c) Rissanen, K. (2008) *CrystEngComm*, **10**, 1107; (d) Brammer, L., Mínguez Espallargas, G., and Libri, S. (2008) *CrystEngComm*, **10**, 1712; (e) Metrangolo, P. and Resnati, G. (ed.) (2007) *Halogen Bonding: Fundamentals and Applications, Structure and Bonding*, Springer, Berlin; (f) Metrangolo, P., Resnati, G., Pilati, T., Liantonio, R., and Meyer, F. (2007) *J. Polymer Chem. A*, **45**, 1.
23. (a) Fluorine atoms do not normally participate in halogen bonding with nucleophiles, although recent theoretical studies have shown that the fluorine atom has the capability of forming halogen bonds if the group bound to F is very strongly electron withdrawing [23b-d]; (b) Lu, Y.-X., Zou, J.-W., Yu, Q.-S., Jiang, Y.-J., and Zhao, W.-N. (2007) *Chem. Phys. Lett.*, **449**, 6; (c) Alkorta, I., Solimannejad, M., Provasi, P., and Elguero, J. (2007) *J. Phys. Chem. A*, **111**, 7154;

(d) Politzer, P., Murray, J.S., and Concha, M.C. (2007) *J. Mol. Model.*, **13**, 643.

24. (a) Lommerse, J.P.M., Stone, A.J., Taylor, R., and Allen, F.H. (1996) *J. Am. Chem. Soc.*, **118**, 3108; (b) Glaser, R., Chen, N., Wu, H., Knotts, N., and Kaupp, M. (2004) *J. Am. Chem. Soc.*, **126**, 4412; (c) Zou, J.-W., Jiang, Y.-J., Guo, M., Hu, G.-X., Zhang, B., Liu, H.-C. and Yu, Q.-S. (2005) *Chem. Eur. J.*, **11**, 740; (d) Poleshchuk, O.K. Branchadell, V., Brycki, B., Fateev, A.V., and Legon, A.C. (2006) *J. Mol. Struct. Theochem*, **760**, 175; (e) Lu, Y.X., Zou, J.W., Wang, Y.H., and Yu, Q.S. (2006) *J. Mol. Struct. Theochem*, **767**, 139; (f) Clark, T., Hennemann, M., Murray, J.S., and Politzer, P. (2007) *J. Mol. Model.*, **13**, 291; (g) Riley, K.E. and Merz, K.M. (2007) *J. Phys. Chem. A*, **111**, 1688; (h) Riley, K.E. and Hobza, P. (2008) *J. Chem. Theory Comput.*, **4**, 232; (i) Lu, Y.-X., Zou, J.-W., Wang, Y.-H., Jiang, Y.-J., and Yu, Q.-S. (2007) *J. Phys. Chem. A*, **111**, 10781; (j) Lu, Y.-X., Zou, J.-W., Wang, Y.-H., and Yu, Q.-S. (2006) *J. Mol. Struct. Theochem*, **776**, 83.
25. Rosokha, S.V., Neretin, I.S., Rosokha, T.Y., Hecht, J., and Kochi, J.K. (2006) *Heteroatom Chem.*, **17**, 449.
26. Bailey, R.D., Grabarczyk, M.R., Hanks, T.W., Newton, E.M., and Pennington, W.T. (1997) *J. Chem. Soc., Perkin Trans. 2*, 2781.
27. Legon, A.C. (1999) *Angew. Chem. Int. Ed.*, **38**, 2687.
28. Libri, S., Jasim, N.A., Perutz, R.N., and Brammer, L. (2008) *J. Am. Chem. Soc.*, **130**, 7842.
29. (a) Corradi, E., Meille, S.V., Messina, M.T., Metrangolo, P., and Resnati, G. (2000) *Angew. Chem. Int. Ed.*, **39**, 1782; (b) Alkorta, I., Blanco, F., Solimannejad, M., and Elguero, J. (2008) *J. Phys. Chem. A*, **112**, 10856.
30. (a) Caronna, T., Liantonio, R., Logothetis, T.A., Metrangolo, P., Pilati, T., and Resnati, G. (2004) *J. Am. Chem. Soc.*, **126**, 4500.
31. Takeuchi, T., Minato, Y., Takase, M., and Shinmori, H. (2005) *Tet. Lett.*, **46**, 9025.
32. Wang, F., Ma, N., Chen, Q., Wang, W., and Wang, L. (2007) *Langmuir*, **23**, 9540.
33. Cariati, E., Forni, A., Biella, S., Metrangolo, P., Meyer, F., Resnati, G., Righetto, S., Tordin, E., and Ugo, R. (2007) *Chem. Commun.*, 2590.
34. (a) Nguyen, H.L., Horton, P.N., Hursthouse, M.B., Legon, A.C., and Bruce, D.W. (2004) *J. Am. Chem. Soc.*, **126**, 16; (b) Metrangolo, P., Präsang, C., Resnati, G., Liantonio, R., Whitwood, A.C., and Bruce, D.W. (2006) *Chem. Commun.*, 3290; (c) Bruce, W.D., Metrangolo, P., Meyer, F., Präsang, C., Resnati, G., Terraneo, G., and Whitwood, A.C. (2008) *New J. Chem.*, **32**, 477.
35. Mele, A., Metrangolo, P., Neukirch, H., Pilati, T., and Resnati, G. (2005) *J. Am. Chem. Soc.*, **127**, 14972.
36. Farina, A., Meille, S.V., Messina, M.T., Metrangolo, P., Resnati, G., and Vecchio, G. (1999) *Angew. Chem. Int. Ed.*, **38**, 2433.
37. Boubekeur, K., Syssa-Magalé, J.-L., Palvadeau, P., and Schöllhorn, B. (2006) *Tetrahedron Lett.*, **47**, 1249.
38. Shirman, T., Freeman, D., Diskin Posner, Y., Feldman, I., Facchetti, A., and van der Boom, M.E. (2008) *J. Am. Chem. Soc.*, **130**, 8162.
39. (a) Han, Z., Ahao, Y., Peng, J., Tian, A., Liu, Q., Ma, J., Wang, E., and Hu, N. (2005) *CrystEngComm*, **7**, 380; (b) Wei, Y., Xu, B., Barnes, C.L., and Peng, Z. (2001) *J. Am. Chem. Soc.*, **123**, 4083; (c) He, J.-H., Yu, J.-H., Pan, Q.-H., Chen, P., and Xu, R.-R. (2005) *Chem J. Chin. Univ. (Chinese edition)*, **26**, 797; (d) Han, Z., Gao, Y., Zhai, X., Peng, J., Tian, A., Zhao, Y., and Hu, C. (2009) *Cryst. Growth Des.*, **9**, 1225.
40. (a) Sun, A., Lauher, J.W., and Goroff, N.S. (2006) *Science*, **312**, 1030; (b) Luo, L., Wilhem, C., Sun, A., Grey, C.P., Lauher, J.W., and Goroff, N.S. (2008) *J. Am. Chem. Soc.*, **130**, 7702; (c) Wilhelm, C., Boyd, S.A., Chawda, S., Fowler, F.W., Goroff, N.S., Halada, G.P., Grey, C.P., Lauher, J.W., Luo, L., Martin, C.D., Parise, J.B., Tarabrella,

C., and Webb, J.A. (2008) *J. Am. Chem. Soc.*, **130**, 4415.

41. (a) Fourmigué, M., and Batail, P. (2004) *Chem. Rev.*, **104**, 5379, and references therein; (b) Imakubo, T. (2004) *TTF Chemistry–Fundamentals and Applications of Tetrathiafulvalene: Halogenated TTFs*, Chapter 3, (eds J. Yamada and T. Sugimoto), Kodansha & Springer, Tokyo, and references therein.
42. (a) Masciocchi, N., Galli, S., Sironi, A., Cariati, E., Galindo, M.A., Barea, E., Romero, M.A., Salas, J.M., Navarro, J.A.R., and Santoyo-González, F. (2006) *Inorg. Chem.*, **45**, 7612; (b) Ranganathan, A., El-Ghayoury, A., Mézière, C., Harté, E., Clérac, R., and Batail, P. (2006) *Chem. Commun.*, 2878.
43. Derossi, S., Brammer, L., Hunter, C.A., and Ward, M.D. (2009) *Inorg. Chem.*, **48**, 1666.
44. Smart, P., Mínguez Espallargas, G., and Brammer, L. (2008) *CrystEngComm*, **10**, 1335.
45. (a) Auffinger, P., Hays, F.A., Westhof, E., and Ho, P.S. (2004) *Proc. Natl. Acad. Sci. U.S.A.*, **101**, 16789; (b) Regier Voth, A., Hays, F.A., and Ho, P.S. (2007) *Proc. Nat. Acad. Sci. U.S.A.*, **104**, 6188; (c) Muzet, N., Guillot, B., Jelsch, C., Howard, E., and Lecomte, C. (2003) *Proc. Nat. Acad. Sci. U.S.A.*, **100**, 8742; (d) Regier Voth, A. and Ho, P.S. (2007) *Curr. Top. Med. Chem.*, **7**, 1336; (e) Hays, F.A., Vargason, J.M., and Ho, P.S. (2003) *Biochemistry*, **42**, 9586.
46. Desiraju, G.R. (1995) *Angew Chem. Int. Ed.*, **34**, 2311.
47. (a) Zordan, F., Brammer, L., and Sherwood, P. (2005) *J. Am. Chem. Soc.*, **127**, 5979; (b) Zordan, F. and Brammer, L. (2006) *Cryst. Growth Des.*, **6**, 1374; (c) Awwadi, F.F., Willett, R.D., Haddad, S.F., and Twamley, B. (2006) *Cryst. Growth Des.*, **6**, 1833.
48. (a) Brammer, L., Mínguez Espallargas, G., and Adams, H. (2003) *CrystEngComm*, **5**, 343; (b) Zordan, F. and Brammer, L. (2004) *Acta Crystallogr.*, **B60**, 512; (c) Zordan, F., Purver, S.L., Adams, H., and Brammer, L. (2005) *CrystEngComm*, **7**, 350; (d) Willett, R.D., Awwadi, F., and Butcher, R. (2003) *Cryst. Growth Des.*, **3**, 301; (e) Awwadi, F.F., Willett, R.D., and Twamley, B. (2007) *Cryst. Growth Des.*, **7**, 624.
49. Mínguez Espallargas, G., Brammer, L., and Sherwood, P. (2006) *Angew. Chem. Int. Ed.*, **45**, 435.
50. Mínguez Espallargas, G., Brammer, L., Allan, D.R., Pulham, C.R., Robertson, N., and Warren, J.E. (2008) *J. Am. Chem. Soc.*, **130**, 9058.
51. (a) $R_{XX'}=d(X\cdots X')/(r_X+r_{X'})$ are, respectively, the van der Waals radii[51b] of halogens X and X′ (following the definition of Lommerse *et al.* [24a]; (b) Bondi, A.J. (1964) *J. Chem. Phys.*, **68**, 441.
52. (a) Very recently, it has also been established that $C–X\cdots X^-$ halogen bonds are also dominated by electrostatic effects;[52b]; (b) Awwadi, F.F., Willett, R.D., Peterson, K.A., and Twamley, B. (2007) *J. Phys. Chem. A*, **111**, 2319.
53. Haddad, S., Awwadi, F., and Willett, R.D. (2003) *Cryst. Growth Des.*, **3**, 501.
54. Rosokha, S.V., Lu, J., Rosokha, T.Y., and Kochi, J.K. (2007) *Chem. Commun.*, 3383.
55. (a) Shirahata, T., Kibune, M., Maesato, M., Kawashima, T., Saito, G., and Imakubo, T. (2006) *J. Mater. Chem.*, **16**, 3381; (b) Miyazaki, A., Yamazaki, H., Aimatsu, M., Enoke, T., Watanabe, R., Ogura, E., Kuwatani, Y., and Iyoda, M. (2007) *Inorg. Chem.*, **46**, 3353; (c) Alberola, A., Fourmigué, M., Gómez-García, C.J., Llusar, R., and Triguero, S. (2008) *New J. Chem.*, **32**, 1103.
56. (a) Férey, G. (2008) *Chem. Soc. Rev.*, **37**, 197; (b) Kitagawa, S., Kitaura, R., and Noro, S.-I. (2004) *Angew. Chem. Int. Ed.*, **43**, 2334; (c) Eddaoudi, M., Kim, J., Rosi, N., Vodak, D., Wachter, J., O'Keeffe, M., and Yaghi, O.M. (2002) *Science*, **295**, 469; (d) Zhao, X., Xiao, B., Fletcher, A.J., Thomas, K.M., Bradshaw, D., and Rosseinsky, M.J. (2004) *Science*, **306**, 1012; (e) Forster, P.M., Eckert, J., Chang, J.-S., Park, S.-E., Férey, G., and Cheetham, A.K. (2003) *J. Am. Chem. Soc.*, **125**, 1309; (f) Lin, X., Blake, A.J., Wilson, C., Sun, X.Z., Champness, N.R., George, M.W., Hubberstey, P., Mokaya, R., and Schröder, M. (2006) *J. Am. Chem. Soc.*,

128, 10745; (g) Thomas, K.M. (2009) *Dalton Trans.*, 1487.

57. (a) Kesanli, B. and Lin, W. (2003) *Coord. Chem. Rev.*, **246**, 305; (b) James, S.L. (2003) *Chem. Soc. Rev.*, **32**, 276; (c) Chen, B., Liang, C., Yang, J., Contreras, D.S., Clancy, Y.L., Lobkovsky, E.B., Yaghi, O.M., and Dai, S. (2006) *Angew. Chem. Int. Ed.*, **45**, 1390; (d) Halder, G.J., Kepert, C.J., Moubraki, B., Murray, K.S., and Cashion, J.D. (2002) *Science*, **298**, 1762; (e) Janiak, C. (2003) *Dalton. Trans.*, 2781; (f) Morris, R.E., and Wheatley, P.S. (2008) *Angew. Chem. Int. Ed.*, **47**, 4966.

58. Dalgarno, S.J., Thallapally, P.K., Barbour, L.J., and Atwood, J.L. (2007) *Chem. Soc. Rev.*, **37**, 236.

59. *http://www.bza.org/zeolites.html* (last accessed 27 January 2010).

60. Rowsell, J.L.C., Spencer, E.C., Eckert, J., Howard, J.A.K., and Yaghi, O.M. (2005) *Science*, **309**, 1350.

61. Matsuda, R. Kitaura, R., Kitagawa, S., Kubota, Y., Belosludov, R.V., Kobayashi, T.C., Sakamoto, H., Chiba, T., Takata, M., Kawazoe, Y., and Mita, Y. (2005) *Nature*, **436**, 238.

62. (a) Serre, C., Millange, F., Thouvenot, C., Nogués, M., Marsolier, G., Louer, D., and Feréy, G. (2002) *J. Am. Chem. Soc.*, **124**, 13519; (b) Kitaura, R., Seki, K., Akiyama, G., and Kitagawa, S. (2003) *Angew. Chem. Int. Ed.*, **42**, 428.

63. (a) Rosi, N., Eddaoudi, M., Kim, J., O'Keeffe, M., and Yaghi, O.M. (2002) *Angew. Chem. Int. Ed.*, **41**, 284; (b) Sun, J., Weng, L., Zhou, Y., Chen, J., Chen, Z., Liu, Z., and Zhao, D. (2002) *Angew. Chem. Int. Ed.*, **41**, 4471.

64. (a) Ohmori, O., Kawano, M., and Fujita, M. (2005) *Angew. Chem. Int. Ed.*, **44**, 1962; (b) Price, D.J., Tripp, S., Powell, A.K., and Wood, P.T. (2001) *Chem. Eur. J.*, **7**, 200; (c) Carlucci, L., Cozzi, N., Ciani, G., Moret, M., Proserpio, D.M., and Rizzato, S. (2002) *Chem. Commun.*, 1354; (d) Abrahams, B.F., Moylan, M., Orchard, S.D., and Robson, R. (2003) *Angew. Chem. Int. Ed.*, **42**, 1848; (e) Li, G., Shi, Z., Liu, X., Dai, Z., Gao, L., and Feng, S. (2004) *Inorg. Chem.*, **43**, 8224; (f) Monge, A., Snejko, N., Gutiérrez-Puebla, E., Medina, M., Cascales, C., Ruiz-Valero, C., Iglesias, M., and Gómez-Lor, B. (2005) *Chem. Commun.*, 1291; (g) Ohmori, O., Kawano, M., and Fujita, M. (2005) *CrystEngComm*, **7**, 255.

65. Atwood, J.L., Barbour, L.J., Jerga, A., and Schottel, B.L. (2002) *Science*, **298**, 1000.

66. Barbour, L.J. (2006) *Chem. Commun.*, 1163.

67. (a) Chen, C.-L., Goforth, A.M., Smith, M.D., Su, C.-Y., and Zur Loye, H.-C. (2005) *Angew. Chem. Int. Ed.*, **44**, 6673; (b) Beauvais, L.G., Shores, M.P., and Long, J.R. (2000) *J. Am. Chem. Soc.*, **122**, 2763; (c) Suh, M.P., Cheon, Y.E., and Lee, E.Y. (2007) *Chem. Eur. J.*, **13**, 4208; (d) Moon, H.R., Kobayashi, N., and Suh, M.P. (2006) *Inorg. Chem.*, **45**, 8672; (e) Chen, B., Eddaoudi, M., Reineke, T.M., Kampf, J.W., O'Keeffe, M., and Yaghi, O.M. (2000) *J. Am. Chem. Soc.*, **122**, 11559; (f) Wang, X.-Y., Scancella, M., and Sevov, S.C. (2007) *Chem. Mater.*, **19**, 4506.

68. (a) Albrecht, M., Lutz, M., Spek, A.L., and van Koten, G. (2000) *Nature*, **406**, 970; (b) Supriya, S. and Das, S.K. (2007) *J. Am. Chem. Soc.*, **129**, 3464; (c) Lennartson, A., Håkansson, M., and Jagner, S. (2007) *New J. Chem.*, **31**, 344; (d) Benito-Garagorri, D., Puchberger, M., Mereiter, K., and Kirchner, K. (2008) *Angew. Chem. Int. Ed.*, **47**, 9142.

69. (a) Bradshaw, D., Warren, J.E., and Rosseinsky, M.J. (2007) *Science*, **315**, 977; (b) Chen, C.-L. and Beatty, A.M. (2008) *J. Am. Chem. Soc.*, **130**, 17222; (c) Kaneko, W., Ohba, M., and Kitagawa, S. (2007) *J. Am. Chem. Soc.*, **129**, 13706; (d) Aslani, A., Morsali, A., and Zeller, M. (2008) *Dalton Trans.*, 5173.

70. (a) Libri, S., Mahler, M., Mínguez Espallargas, G., Singh, D.C.N.G., Soleimannejad, J., Adams, H., Burgard, M.D., Rath, N.P., Brunelli, M., and Brammer, L. (2008) *Angew. Chem. Int. Ed.*, **47**, 1693; (b) Campo, J., Falvello, L.R., Mayoral, I., Palacio, F., Soler, T., and Tomás, M. (2008) *J. Am. Chem. Soc.*, **130**, 2932.

71. Paul, I.C. and Curtin, D.Y. (1973) *Acc. Chem. Res.*, **6**, 217.

72. (a) Braga, D., Cojazzi, G., Emiliani, D., Maini, L., and Grepioni, F. (2001) *Chem. Commun.*, 2272; (b) Braga, D., Cojazzi, G., Emiliani, D., Maini, L., and Grepioni, F. (2002) *Organometallics*, **21**, 1315; (c) Braga, D., Maini, L., Mazzotti, M., Rubini, K., and Grepioni, F. (2003) *CrystEngComm*, **5**, 154.

73. (a) Custelcean, R. and Jackson, J.E. (1998) *J. Am. Chem. Soc.*, **120**, 12935; (b) Custelcean, R. and Jackson, J.E. (1999) *Angew. Chem. Int. Ed.*, **38**, 1661; (c) Custelcean, R. and Jackson, J.E. (2000) *J. Am. Chem. Soc.*, **122**, 5251; (d) Custelcean, R., Vlassa, M., and Jackson, J.E. (2000) *Angew. Chem. Int. Ed.*, **39**, 3299; (e) Custelcean, R. and Jackson, J.E. (2002) *Thermochim. Acta*, **388**, 143; (f) Hwang, J.-W., Campbell, J.P., Kozubowski, J., Hanson, S.A., Evans, J.F., and Gladfelter, W.L. (1995) *Chem. Mater.*, **7**, 517.

74. (a) Khlobystov, A.N., Champness, N.R., Roberts, C.J., Tendler, S.J.B., Thomson, C., and Schröder, M. (2002) *CrystEngComm*, **4**, 426; (b) Thompson, C., Champness, N.R., Khlobystov, A.N., Roberts, C.J., Schröder, M., Tendler, S.J.B., and Wilkinson, M.J. (2004) *J. Micros.*, **214**, 261.

Part II
Innovative Characterization Methods

Ideas in Chemistry and Molecular Sciences: Advances in Nanotechnology, Materials and Devices.
Edited by Bruno Pignataro

ISBN: 978-3-527-32543-6

6
Application of Advanced Solid-State NMR Techniques to the Characterization of Nanomaterials: A Focus on Interfaces and Structure

Niki Baccile

6.1
Introduction

This chapter illustrates the use of solid-state NMR spectroscopy for the characterization of some examples of engineered nanomaterials. The chapter is structured as three main sections: the first one provides a short introduction to NMR methods keeping the main focus on the practical tools which are exploited in the wide bibliography on nanomaterials; the second one presents a broad review of solid-state NMR studies to selected examples of nanomaterials (nanocarbons, nanoparticles, quantum dots (QDs), self-assembled, and mesostructured solids); and the last one provides an overview of some work by the author, mainly concentrating on the characterization of organic/inorganic interfaces of mesostructured solids and on the amorphous structures of carbon spheres.

The ultimate goal is to show how solid-state NMR can be used in the study of surface, interfacial, and structural features of nanomaterials (Scheme 6.1), to provide information on what has been mainly achieved so far, and to direct attention toward more specific sources to carry on similar studies.

6.2
Solid-State NMR Tools

In the past 25 years, solid-state NMR experienced many technical and theoretical developments, which allowed recording of extremely well-resolved spectra, hence overcoming the problems of lack of resolution, which are intrinsic to this technique. In fact, the absence of Brownian motion, which generally averages out interactions like dipolar coupling (DC) in solution NMR, contributes to their introduction in the solid state. The most relevant NMR interactions in solid state are chemical shift anisotropy (CSA), which is directly related to the chemical environment of the nuclei; DC, which is a through-space interaction and directly related to the internuclear distance; quadrupolar coupling which corresponds to the interaction between the quadrupolar moment of a given nucleus and the local electric field

Ideas in Chemistry and Molecular Sciences: Advances in Nanotechnology, Materials and Devices.
Edited by Bruno Pignataro

ISBN: 978-3-527-32543-6

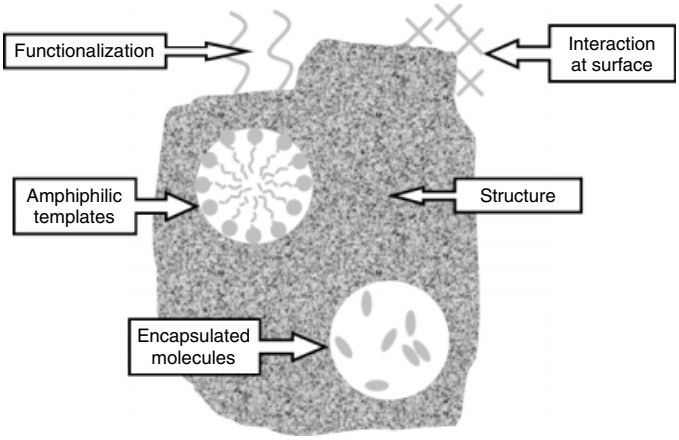

Scheme 6.1 Schematic view of several aspects belonging to nanomaterials which can be studied using solid-state NMR: structure, self-assembling/templating, functionalization, confinement, interfaces.

gradient. Finally, J-coupling, which is often neglected in solid state, is characteristic of chemical bonding between nuclei. These interactions may be extremely strong (up to megahertz) and the lack of resolution in the final NMR spectra can limit the application of the technique unless several tools, listed below, are used to enhance spectral resolution. Some typical pulse sequences as well as their practical applications are also reported for convenience. For an overview on NMR, one could refer to [1], while for more insights on solid-state NMR one could refer to [2–4]. For fairly explanatory descriptions of basic NMR principles and their application in chemistry, one could refer to Andrew and Szczesniak [5], Blanc *et al.* [6] and, in particular, to Laws *et al.* [7]. We begin with a brief description of the main tools used for spectral resolution and information extraction as directly related to what is presented in the next sections.

- **Chemical shift anisotropy**: CSA is a factor responsible for large broadening in solid-state NMR of powders. It can be efficiently removed by spinning the sample holder (zirconia rotor) around its axis which forms a 54.74° angle with the external magnetic field. This is generally termed as magic-angle spinning (MAS) and it only refers to a mechanical treatment of the sample. In some occasions, CSA can be efficiently exploited to recover valuable information on the local symmetry of the nucleus. For more information, the reader can refer to paragraph 4.4 of [7].
- **J-coupling**: This is a scalar through-bond interaction whose values are relatively weak (10–150 Hz) when compared with other interactions (e.g., CSA or DC) in solids and it is generally not observed. Nevertheless, provided all other interactions averaged (through MAS, radio frequency – RF- pulse sequences, or local mobility), it is possible in some cases to exploit J-coupling interactions in solids (both homonuclear and heteronuclear) via RF pulse sequences which use either single quantum (SQ) (INEPT (insensitive nuclei enhanced by polarization

transfer) [8], HSQC (heteronuclear single-quantum correlation) [9]) or double quantum (DQ) SQ (heteronuclear multiple-quantum correlation (HMQC) [10], INADEQUATE (Incredible Natural Abundance DoublE QUAntum Transfer Experiment) [11]) coherences excitation. In general, J-resolved techniques can be edited via two-dimensional correlation maps allowing a clear and direct way of interpretation of the internuclei interactions via correlation cross-peaks.

- **Dipolar coupling (DC, I=1/2)**: This interaction depends on the internuclear distance ($\sim 1/r^3$) and it can be a source of extreme line broadening for rigid solids. Two main ways exist to average the dipolar interaction and recover resolution: either via MAS or via RF pulse sequences.[1)] In both cases, the characteristic frequency associated to MAS or RF pulses must be larger than the characteristic frequency of the interaction, knowing that the homonuclear ^{1}H–^{1}H DC is by far the strongest interaction in spin-1/2 solids (up to 100 kHz according to internuclear distance). In general, in solid state (where some local motion may nevertheless occur and which contributes to reduce the intensity of the interaction), DC is not completely averaged out but it can actually be exploited for a number of informative experiments which bring valuable internuclear information. DC can even be reintroduced via RF pulse schemes in order to excite multiple-quantum coherences, which can be selected to provide unique information on through-space coupled spin pairs. Since DC depends on coupled spins, it is possible to put in evidence direct correlations between them via easy-to-read two-dimensional maps. Table 6.1 summarizes some of the main techniques used to reduce, and exploit at the same time, the dipolar interaction in the most informative possible way. This is not meant to be an exhaustive list but rather a guideline used in conjunction with Table 6.2 with respect to the NMR work presented in the rest of the chapter. For additional information and more recent insights on these topics together with some examples, one can refer to [7, 12–14]. A special, very important, mention concerns the cross-polarization (CP) technique highlighted on purpose in Table 6.1. CP consists in a transfer of magnetization between abundant (I) and dilute (S) dipolar coupled nuclear spins and, together with MAS, CP is routinely used to enhance the sensitivity of rare low-γ (S) nuclei (e.g., ^{13}C, ^{29}Si) using, most commonly, the magnetization transfer from abundant nuclei, like ^{1}H. This has several benefits: (i) long spin–lattice relaxation times (T_1) are lowered consequently reducing the overall acquisition times of the experiment; (ii) sensitivity is increased; (iii) the characteristic time of the S–I interaction can be manually tuned via the adjustment of the CP contact time (t_{CP}); and (iv) valuable information on the structure and chemistry of the sample (sensitivity to a protic environment, molecular mobility) can be extracted by manipulating the t_{CP} time.
- **Quadrupolar coupling (I>1/2)**: Quadrupolar nuclei have spin quantum number larger than 1/2; they experience a strong coupling between the nuclear spin and

1) In this case, a number of homonuclear (mainly ^{1}H–^{1}H) and heteronuclear decoupling pulse schemes exist.

Table 6.1 Nonexhaustive summary of the main techniques and pulse schemes used to gain in sensitivity, resolution, and spatial information in solid-state NMR provided magic-angle spinning of the sample.

	Heteronuclear		**Homonuclear**	
	1D	2D	1D	2D
DEC	CW [16], TPPM [17]		CRAMPS [18], LG [19], FSLG [20], PMLG [21], DUMBO [22]	
MAS	CP [23]	WISE [24], HETCOR [25]	NOESY/EXSY [13]	NOESY/EXSY
MAS+REC	TRAPDOR [26], REDOR [27]	TRAPDOR, REDOR	DRAMA* [28], RR [29], RFDR [30], C7* [31], SC14* [32], BABA* [33]	

Asterisk (*) indicates pulse schemes based on double quantum coherence excitation. The terminology ''spin diffusion'' may also be employed by some authors. The TRAPDOR pulse scheme is used between a spin-1/2 and quadrupolar nuclei.

the electric field gradients around the nucleus due to the nonspherical charge distribution. Direct consequences are a higher number of transitions between spin states and complex broad lineshapes, which MAS only partially averages in some favorable cases. Half-integer spins constitute the most abundant category and the main approach to their study involves the use of multiple-quantum techniques combined with magic-angle spinning (MQMAS [15]), which allow the identification of nonequivalent quadrupolar sites via a two-dimensional correlation map [3]. Spins with integer values, and, in particular, those with $I = 1$ (e.g., ^{2}H, ^{14}N), do not have a central transition ($1/2/ - 1/2$) and a doublet of peaks (or horns) is generally observed; the width between the two peaks is a way of measuring the nuclear electric quadrupolar moment and it is very sensitive to molecular motion. For this reason, acquisition under static conditions is a widely used strategy to study the dynamics of molecules having nuclear probes with $I = 1$.

Table 6.2 couples the main techniques introduced in Table 6.1 to a series of practical issues that can be addressed during a typical study on materials in general and nanomaterials in particular. The acronyms are outlined below while the corresponding reference papers have been provided in the text and in Table 6.1. In both Tables 6.1 and 6.2, the heteronuclear (e.g., $^{1}H-^{13}C$, $^{1}H-^{31}P$) and homonuclear (e.g., $^{1}H-^{1}H$, $^{31}P-^{31}P$) character of the pulse sequence is clearly addressed as well as the possibility of performing one-dimensional or two-dimensional NMR experiments, where, in the last case, typical 2D maps giving access to a direct interpretation of interactions can be obtained. For more information on multidimensional NMR techniques, the reader can refer to [3].

Table 6.2 Summary of some of the main techniques introduced above and listed as a function of their practical/potential use.

	Heteronuclear		**Homonuclear**	
	1D	2D	1D	2D
Chemical shift			MAS	
Resolution/sensitivity/reduction in acquisition time (≡ routine experiments)	CP + MAS (TPPM, CW)	–	MAS + (LG, FSLG, PMLG, DUMBO)	MQMAS ($I = n/2$, $n = 3$, 5, 7, 9)
Through-bond correlations/proximities (SQ)	INEPT	INEPT, HSQC	–	
Through-bond correlations/proximities (DQ)	–	HMQC	–	INADEQUATE
Through-space correlations/proximities (SQ)	TRAPDOR, REDOR	CP-HETCOR	NOESY/EXSY	NOESY/EXSY
Through-space correlations/proximities (DQ)	–	–	–	DRAMA, C7, SC14, BABA
Internuclear distance measurements	REDOR, REAPDOR ($I > 1/2$)	–	NOESY/EXSY	NOESY/EXSY

(*continued overleaf*)

Table 6.2 {continued}

	Heteronuclear		Homonuclear	
	1D	2D	1D	2D
Chemical shift			MAS	
Dynamics/local mobility	t_{CP}, relaxation times measurements (T_1, $T_{1\rho}$, $T_{2'}$)	WISE	Static ($I = 1$), relaxation times measurements (T_1, $T_{1\rho}$, $T_{2'}$)	Static ($I = 1$)
Local molecular symmetries	Static (or variable MAS)	–	Static (or variable MAS), Spinning side-band analysis	Anisotropic/isotropic chemical shift correlation

Notes: T_1 = spin–lattice relaxation time; t_{CP} = contact time in cross-polarization experiments; $T_{1\rho}$ = relaxation time in the rotating frame (typical in CP experiments); $T_{2'}$ = spin–spin relaxation time as measured with a Hahn echo pulse sequence. Unless specifically indicated, MAS is generally combined to all these techniques. SQ = single quantum; DQ = double quantum.
BABA, BAck-to-Back; CP, cross polarization; CSA, chemical shift anisotropy; CRAMPS, combined rotation and multiple-pulse spectroscopy; CW, continuous wave; DQ, double quantum; DRAMA, dipolar recoupling at the magic angle; DUMBO, decoupling using mind-boggling optimization; EXSY, EXchange SpectroscopY; FSLG, frequency-switched Lee Goldburg; HETCOR, HETeronuclear CORrelation; HMQC, heteronuclear multiple-quantum correlation; HORROR, HOmonucleaR ROtary Resonance; HSQC, heteronuclear single-quantum correlation; INADEQUATE, Incredible Natural Abundance DoublE QUAntum Transfer Experiment; INEPT, insensitive nuclei enhanced by polarization transfer; LG, Lee-Goldberg MAS, magic-angle spinning; MQMAS, multiple-quantum magic-angle spinning; NOESY, Nuclear Overhauser Effect SpectroscopY; PMLG, phase-modulated Lee Goldburg; REDOR, Rotational Echo DOuble Resonance; RFDR, radio frequency dipolar recoupling; RR, rotational resonance; SQ, single quantum; TPPM, two-pulse phase modulation; TRAPDOR, TRAnsfer of Population in DOuble Resonance; WISE, WIdeline SpEctroscopy.

6.3 Nanocarbons

6.3.1 Fullerenes

Fullerene, discovered in 1985 [34], is a family of carbon allotropes, molecules composed entirely of carbon, in the form of a hollow sphere, ellipsoid, tube, or plane. Spherical fullerenes are also called *buckyballs*, and cylindrical ones are called *carbon nanotubes* (CNTs) or *buckytubes*. Graphene is an example of a planar fullerene sheet. Fullerenes are similar in structure to graphite, which is composed of stacked sheets of linked hexagonal rings, but may also contain pentagonal (or sometimes heptagonal) rings that would prevent a sheet from being planar. Applications vary from medicinal use to heat resistance devices and superconductivity.

Solid-state ^{13}C NMR studies have been accomplished on fullerenes since early 1990s, and confirmed the chemical homogeneity of the 60 carbon atoms [35] and the expected inhomogeneity for the C_{70} material [35]; a solution INADEQUATE [36] experiment provided the exact connectivity among the five carbon resonances characteristic of the C_{70}. Since 1991, solid-state NMR has been used for different tasks in the study of fullerenes. Generally speaking, initial structural studies (bond length calculation, molecular motion) [37–40] including spin relaxation dynamics of C_{60} under different external conditions (pressure, temperature) [41–44] were followed by more detailed studies on the interactions between fullerene and intercalation compounds, focusing on molecular mobility and van der Waals interactions [45–50]. Finally, recent works directed more efforts in the understanding of molecular entrapping within fullerene cages [51, 52]. Recent review papers [53–56] have shown some of these aspects already and for this reason we limit ourselves here to a short, broad description for each category outlined above.

Most of the structural studies have been performed using ^{13}C NMR under both static and MAS conditions. Owing to the high molecular mobility of the fullerene C_{60} cage in solid state at ambient conditions, static NMR is sufficient to show the characteristic isotropic peak at 143 ppm. At low temperature, on the contrary, part of the CSA is reintroduced, as expected, but a small fraction of a mobile phase is kept at temperatures as low as 100 K [39]. Spin–lattice T_1 relaxation times have been largely investigated under different conditions. The first study done by Tycko [41] revealed discontinuous values of T_1 as a function of temperature. This is due to a phase transition from FCC (face centered cubic) to SC (simple cubic) phase, which was already seen from differential calorimetry and X-ray powder diffraction experiments at 250 K. Similar conclusions were drawn in a T_1 study as a function of pressure [44].

Mechanisms of relaxation were mainly attributed to CSA in the low temperature range while the interaction between nuclear spins and molecular rotation was invoked to explain the T_1 behavior at high temperature values, above 400 K [42].

Studies concerning intercalated compounds or physical mixtures of fullerenes with atoms, molecules, or polymers are abundant because of the possible formation

of conducting and superconducting systems [55, 57], for intermolecular interaction studies [47–49], solubility properties [45], or conception of strong composite materials [50]. The most common solid-state NMR techniques used are ^{13}C static NMR, MAS, and CP-MAS, but other nuclei can also be investigated. He *et al*. have nicely shown that, in a stable benzene/C_{60} solvate, the van der Waals interaction between two aromatic compounds does not reduce the molecular mobility of C_{60} and benzene, which are found to be in three relative positions: in two of them, they are nearly freely mobile while in the third one benzene occupies lattice defects of the C_{60}/C_6H_6 crystal. In this case, $^{1}H-^{13}C$ CP-MAS experiments were inefficient and ^{2}H spectra of enriched d_6-benzene only display an isotropic peak under static and MAS conditions for each molecular environment of benzene.

Finally, endohedral encapsulation of atomic or molecular species was deeply investigated using solid-state NMR [56]. We report here an example of endohedral hydrogen/fullerene complexes, which were also recently reviewed [54]. An example worth some attention is the use of $^{1}H-^{1}H$ DQ excitation to prove the existence of a dihydrogen molecule trapped inside an azo-thio-open-cage fullerene (ATOCF) [52] to form the H_2@ATOCF complex (Figure 6.2). Figure 6.1 shows the ^{1}H spectra of H_2@ATOCF acquired under static, MAS (2.0, 4.0, 10.0 kHz) and DQ filtering (MAS = 10.0 kHz). The usual effect of applying MAS to the sample results in a better overall resolution of the complex (aromatic + H_2 protons, Figure 6.1a–d) with respect to acquisition under static conditions; on the contrary, when the DQ filter [58, 59] is applied, H_2 signal (narrow centerband at −7.5 ppm) is enhanced with respect to aromatic protons (large band at 6 ppm), as expected, because the H–H distance is smaller in a H_2 molecule. Unfortunately, due to rapid tumbling of H_2 inside the cage, DC is partially averaged resulting in a reduced intensity of the H_2 signal under DQ filtering with respect to ^{1}H single pulse (SP) MAS.

6.3.2
Nanotubes

CNTs are allotropes of carbon and members of the fullerene structural family having the diameter of few nanometers, while they can be up to several millimeters in length. Nanotubes, categorized as single-walled nanotubes (SWNTs) and multiwalled nanotubes (MWNTs), are entirely composed of C-sp^2 bonds, similar to those of graphite, providing the molecules with their unique strength. Under high pressure, nanotubes can merge together, trading some sp^2 bonds for sp^3 bonds, giving the possibility of producing strong, ''unlimited-length'' wires through high-pressure nanotube linking. These cylindrical carbon molecules exhibit extraordinary strength and unique electrical properties, and are efficient heat conductors that make them potentially useful in many applications in nanotechnology, electronics, optics, and other fields of materials science, as well as potential uses in structural materials.

Solid-state NMR of nanotubes revealed to be very challenging, as already pointed out in [53], until the work of Tang *et al.* [60] and due to some intrinsic problems in the production procedure, which allowed relatively small and polluted (with

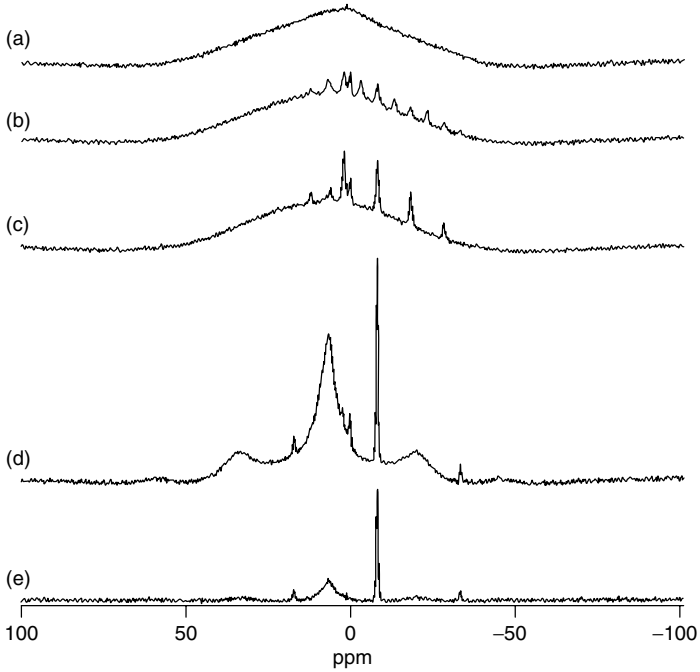

Figure 6.1 ^{1}H spectra of a powder sample of H_2@ATOCF at a field of 9.4 T. Spectra in (a)–(d) were acquired using a simple 90° pulse to excite transverse ^{1}H magnetization. (a) No sample rotation; (b) MAS at 2.0 kHz; (c) MAS at 4.0 kHz; (d) MAS at 10.0 kHz; and (e) DQ-filtered spectrum recorded at 10.0 kHz MAS. (Reprinted with permission from [52]. Copyright 2004 American Chemical Society.)

paramagnetic species from metal catalysts) samples of CNTs. Initial data reported static and MAS NMR spectra, where the first one showed the nonisotropic and nonplanar behaviors of the chemical shift tensor while the second one resulted in a single, multicomposite, peak centered at 124 ppm, whose chemical shift suggests a metallic and semiconducting character of the material. Confirmation for the existence of the electron-conducting behavior is also provided by the linear

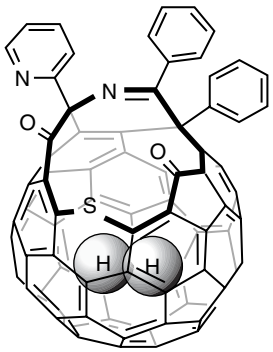

Figure 6.2 Molecular structure of H_2@ATOCF. (Reprinted with permission from [52]. Copyright 2004 American Chemical Society.)

relationship between the spin–lattice T_1 relaxation time and temperature, and described by the Korringa relationship [61].

After this pioneering study, several others started to appear and focused their interest toward a better characterization of the magnetic properties of the CNTs as a result of their metallic behavior. ^{13}C NMR under both static and MAS conditions and T_1 analysis constitute the main tools for investigating the precise nature of the metallic and semiconducting properties of CNTs. More details on this topic have been already reviewed and can be found in [62]. The characterization of confined molecules [63] and gases [64] inside nanotubes also started to be commonly performed. For example, it was observed that two types of molecular regimes exist for adsorbed C_2H_6 inside a SWCNT at $P = 0.093$ MPa [64]. ^1H spin–spin relaxation time (T_2) was measured with the classical Hahn Echo pulse sequence [61] and the variation of the echo height with dephasing time clearly shows the existence of two components in the exponential decay, suggesting that part of the ethane is adsorbed onto the surface while the rest of it is in a free gas state. This was confirmed by the T_1 study as a function of ethane pressure: T_1 value decreases with pressure for adsorbed molecules while it increases for free gas molecules. Finally, the authors found that ^{13}C T_1 values of CNTs vary according to the type of molecule introduced inside the tube. Oxygen, probably due to its paramagnetic properties, was found

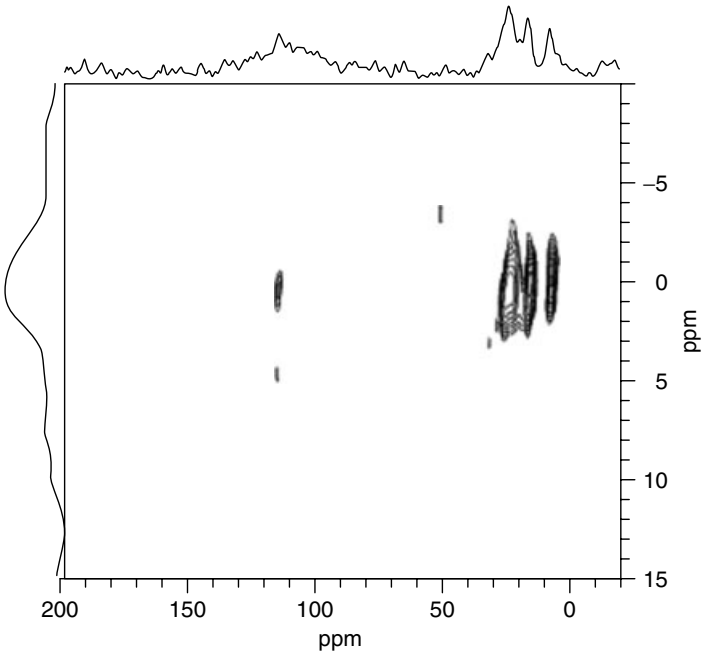

Figure 6.3 ^1H–^{13}C 2D correlation spectra of PMMA-NT. (Reprinted with permission from [68]. Copyright 2004 American Chemical Society.)

to enhance spin–lattice relaxation with respect to He, CO_2, or H_2, whose presence does not affect relaxation times with respect to vacuum conditions.

Functionalization of SWCNTs constitute the third main domain in which solid-state NMR was successfully employed. A number of studies report on oxidation [65], fluorination [66], protonation [67], and grafting of large polymeric moieties [68] on the surface of CNTs but the potential of NMR is not fully exploited, for example, lack of protons generally prevents the use of CP-based techniques. Engtrakul *et al.* [67] used $^{1}H-^{13}C$ CP to show protonation of CNTs after a liquid (sulfuric acid) and solid-state (sulfonated polymers, Nafion, and AQ-55 were used) acidic treatment. Reversibility was proved after a second treatment under basic conditions. Cahill [68] performed a nice study on poly(methyl methacrylate)-functionalized CNTs in which both ^{1}H and ^{13}C nuclei were studied using homonuclear and heteronuclear correlation (HETCOR) experiments. Figure 6.3 shows the $^{1}H-^{13}C$ 2D correlation map of polymethyl methacrylate-carbon nanotube (PMMA-CNT) recorded using the DC-based TEDOR (Transferred-Echo-Double Resonance) pulse sequence [69]. The low-intensity cross-peak centered at $\delta(^{13}\,C) = 121$ ppm and $\delta(^{1}\,H) = 0.5$ ppm shows the existence of a spatial proximity between the aliphatic protons of PMMA and the nanotube ^{13}C signal; even if this does not prove the direct functionalization between PMMA and CNTs, it strongly suggests that part of the PMMA is very close to the surface of the CNTs.

6.4 Nanoparticles

In nanotechnology, a *particle* is defined as a small object that behaves as a whole unit in terms of its transport and properties. It is further classified according to size: in terms of diameter, fine particles cover a range between 100 and 2500 nm, while ultrafine particles, on the other hand, are sized between 1 and 100 nm. Similar to ultrafine particles, nanoparticles are sized between 1 and 100 nm, though the size limitation can be restricted to two dimensions. Nanoparticles may or may not exhibit size-related properties that differ significantly from those observed in fine particles or bulk materials. Nanoparticles are of great scientific interest as they are effectively a bridge between bulk materials and atomic or molecular structures. A bulk material should have constant physical properties regardless of its size, but at the nanoscale this is often not the case. The properties of materials change as their size approaches the nanoscale and as the percentage of atoms at the surface of a material becomes significant. The interesting and sometimes unexpected properties of nanoparticles are partly due to the aspects of the surface of the material dominating the properties in lieu of the bulk properties. Size-dependent properties are observed such as quantum confinement in semiconductor particles, surface plasmon resonance in some metal particles and superparamagnetism in magnetic materials. Nanospheres, nanorods, nanofibers, and nanocups are just a few of the shapes in which nanoparticles have been grown while at the lower end of the size range, they are often referred to as *clusters*. Metal, dielectric, and

semiconductor nanoparticles have been formed, as well as hybrid structures (e.g., core-shell nanoparticles). Nanoparticles made of semiconducting material may also be labeled QDs (see the following section) if they are small enough (typically <10 nm) for quantization of electronic energy levels to occur. Such nanoscale particles are used in biomedical applications as drug carriers or imaging agents.

Solid-state NMR is probably not the most used technique to characterize such small objects since very often the resolution is affected by the heterogeneous dispersion in chemical shifts, which is due to a continuous variation of chemical sites from core to surface. Nevertheless, a combination of NMR methods can be of great help to perform structural investigation as well as studies of interaction between the particle surface and ligands and reactants in case of catalytic applications. The materials under study may be very large: nanoparticles from natural sources [70–72], silicon-based compounds [73, 74], metals [75–80], metal oxides [81–86], and other systems [87–89]. The surface chemistry and the nanoparticle/ligand interaction attracted most attention. Owing to the high reactivity of nanoparticles, much effort is spent in surface passivation and particle dispersion. Mayeri *et al.* [73] have investigated the surface chemistry of butyl-capped silicon nanoclusters obtained after reacting a Zintl salt, NaSi, with silicon tetrachloride and subsequent reaction with butyllithium to introduce the passivating butyl function. A combination of ^{29}Si SP and CP-MAS experiments on all intermediates allows a partial identification of bulk and surface species. After chlorination and passivation, all NaSi sites had reacted and new species were formed. Nevertheless, the exact nature of some of them is still unclear. A recurrent problem concerns the large dispersion in chemical shifts due to structural defects both in the core and surface of chlorinated silicon nanoparticles. After passivation, three specific silicon sites were attributed to silicon-butyl bonds. In no case, peaks in the $-90/-110$ ppm region were observed, as no SiOH and SiO_2 bonds were formed. On the contrary, exposure to water of the chlorinated silicon nanoparticles resulted in an extended oxidation of the particle surface. The study clearly indicates the high reactivity of intermediates and formation of Si–C bonds. Similar conclusions were drawn by Giuliani *et al.* [74], who demonstrated the formation of a silicon-(dimethylamino)propyl bond at the surface of silicon nanoparticles using chemical shifts and spin–lattice relaxation times arguments obtained from ^{29}Si SP and CP-MAS experiments.

Several works exist on the functionalization of gold nanoparticles using alkylthiol compounds. Badia *et al.* [77] demonstrated, using ^{13}C chemical shift and ^{1}H linewidth arguments, that self-assembled monolayers (SAMs) of alkylthiols are formed on the surface of spherical gold nanoparticles via thiolate instead of disulfide bonds; in addition, the broad signals detected suggest the existence of different adsorption sites. A carboxy-functionalized alkylthiolate group was used to cap gold nanoparticles and interact with a peptide for bioanalytical application [78]. An LK-based (leucine–L-, lycine–K-) ^{13}C and ^{15}N-enriched peptide was used for this purpose and, based on their study on variation of chemical shift values, CSA and DQ filtering for internuclear distance measurement, authors found that (i) the peptide covalently binds to the hydrophilic surface of gold nanoparticles; (ii) a secondary helical structure is maintained; and (iii) peptide side chains (from the same particle

or from two adjacent particles) interact with one another (this is apparently due to the molecular mobility which was found to be quite low). Similar issues were addressed in [79]. Phosphonic and sulfonic alkyl thiols were used to functionalize gold nanoparticles. Chemical shifts and relaxation measurements data on ^{13}C and ^{31}P nuclei were used to demonstrate that (i) an SAM forms at the gold nanoparticle surface, despite the high curvature of the particle (diameter = 2–3 nm), and that (ii) polar terminal groups of functionalized alkanethiols self-interact within the monolayer. ^{13}C CP-MAS experiments as a function of temperature coupled to DSC (Differential Scanning Calorimetry) experiments showed that phosphonic acid contributes to a much higher thermal resistance with respect to sulfonic end-functionalization, where, in the last case, progressive disassembly occurs before thermal decomposition of the organic function. ^{31}P chemical shift coupled to CSA values were used to support the formation of intramonolayer and, possibly, intraparticle hydrogen bonding among phosphate groups. Similar results were observed by Pawsey [86], who found that a carboxy-containing alkylphosphonic acid (C_n: n = 11, 15) is much strongly bound onto ZrO_2 nanoparticles than only pure zirconia powder, as observed by ^{13}C and ^{31}P chemical shift and linewidth analysis at room temperature and up to 80 °C. In all cases, a clear particle size effect is systematically observed in the ligand/surface interaction: the smaller the nanoparticle size, the stronger the interaction.

The problem of particle size and surface heterogeneity in metal oxides was addressed by Scolan *et al.* [84]. The authors performed a ^{17}O MAS NMR study on three model titanium oxo-organo clusters {$[Ti_{12}O_{16}(OPr^i)_{16}]$, $[Ti_{16}O_{16}(OEt)_{32}]$, and $[Ti_{18}O_{22}(OBu^n)_{26}(acac)_2]$} and monodisperse titania nanoparticles having 2- and 3-nm core diameters. Model compounds were characterized and showed sharp resonances which were identified for each oxo-bridge. These data are finally used for comparison with those obtained from the ^{17}O NMR spectra of nanoparticles, which exhibit a broad spectrum mainly due to superposition of chemical shifts. Keeping in mind that ^{17}O is a quadrupolar nucleus ($I = 5/2$) and that quadrupolar interaction is partly averaged by MAS or by strong RF decoupling, the MQMAS technique was found necessary to resolve the spectrum. A 3Q-MAS experiment on the nanoparticles allowed identification of four different oxygen signals, which were attributed to a bulk anatase phase, a surface coordination site (acac ligand), and two surface oxo bridges, whose nature is identified after comparison with results obtained from model compounds. The Ti atoms at the nanoparticle surface were also addressed as being Ti–OH and coordinated by water. Titania nanoparticles have also been studied by Gervais *et al.* [83], who used ^{47}Ti ($I = 5/2$) and ^{49}Ti ($I = 7/2$) static NMR in combination with X-ray diffraction (XRD) to identify the percentage of anatase and rutile phase formation when the material undergoes annealing up to 850 °C.

Another interesting way to use NMR consists in the *in situ* detection of adsorbed organic molecules at the surface of nanoparticles [80, 81]. Nicholas *et al.* [81] showed combined *in situ* ^{13}C CP-MAS NMR and density functional theory (DFT) calculation to prove that an edge Mg-acetylide bond occurs with respect to a vinylidene one when acetylene reacts on nanosized MgO and that at least 25% of

ethoxide is also formed in coexistence of the acetylide groups. On the contrary, the formation of methylene groups was observed after the reaction of ethylene with ruthenium hydride nanoparticles [80] at room temperature using ^{13}C MAS and CP-MAS NMR. Even though the reaction mechanism was not completely understood, authors proposed the formation of an intermediate vinylidene bond formed onto the Ru atom, an assumption which needs further verification.

Finally, when nanoparticles are embedded in a matrix [72, 85], interface interaction can be studied using several methods. Rawal *et al.* [85] showed a multimethod NMR study to characterize a dispersion of silicates in a phosphate matrix focusing on ^{29}Si and ^{31}P nuclei, after isotopic ^{29}Si enrichment. In this study, mainly chemical shift, T_1 (spin–lattice) and T_2 (spin–spin) relaxation times and J-filtering via DQ coherences excitation (an INADEQUATE pulse sequence was used) were exploited to show silicate species[2)] and short-range connections among them. Finally, dipolar-based Rotational Echo DOuble Resonance (REDOR) experiments have been used to determine the distance between ^{31}P and ^{29}Si-containing species, the dimension of silicate nanoparticles, and the distance between them. The authors were able to determine a homogeneous distribution of phosphate-free amorphous silicate nanoparticles of about 8 nm in diameter and about 5-nm apart. Additionally, they showed the existence of silicate ions SiO_4^{4-} and a crystalline silica-rich phase was also observed and attributed to cristobalite, formed after sample heat treatment.

6.5 Quantum Dots

A QD is a colloidal semiconductor nanocrystal whose excitons are confined in all three spatial dimensions. As a result, they have properties that are between those of bulk semiconductors and discrete molecules. There are colloidal methods to produce many different semiconductors, including cadmium selenide, cadmium sulfide, indium arsenide, and indium phosphide. These QDs can contain as few as 100–100 000 atoms within their volume. This corresponds to about 2–10 nm. Application of QD can take place in transistors, solar cells, light-emitting diodes (LEDs), and diode lasers; they have also investigated QDs as agents for medical imaging and hope to use them as qbits.

Solid-state NMR studies on QD are being performed since 1988 [90], when ^{77}Se was used to discriminate various Se sites mainly using chemical shift values in CdSe QD of different sizes. It was found that the bulk-like behavior of the Se atoms increases with nanoparticle size. The smaller the CdSe QD size, the higher the number of site heterogeneity, mainly located at the particle surface. This approach, in which chemical shift values are mainly used to compare bulk semiconductor materials with their corresponding QD, is of common use [91–93]. The ^{113}Cd, ^{31}P ^{77}Se chemical shifts obtained from SP MAS or spin-echo experiments performed

2) $Qx = Si(OH)_{(4-x)}OSi_x$, $(0 < X < 4)$.

on the bulk semiconducting material was compared to the respective CdS, CdSe, CdTe, and InP QDs with similar conclusions. In addition, it was proved that in the case of CdS_xSe_{x-1} and $CdSe_xTe_{x-1}$ alloys, ^{113}Cd chemical shift varies between the pure binary compounds both in their bulk and QD form [93]. This is not the case when a physical mixture of CdSe and CdTe is prepared, because two distinct ^{113}Cd chemical shifts are clearly observed, each one corresponding to its specific phase.

Generally speaking, NMR studies on QD mainly concentrate on discrimination between surface and bulk atomic sites, interaction between capping/stabilizing agents and surface and structural identification. The most common atoms under study are ^{113}Cd, ^{77}Se, ^{31}P and, in some cases, ^{13}C and ^{1}H. The first, despite the intrinsic experimental difficulties which require long acquisition times for SP experiments, provide direct access to local structure homogeneity as a function of composition, temperature, and aging. The others generally provide information on surface adsorbed species like organic capping agents or water. In addition, surface versus bulk recognition can only be done by mean of CP-MAS experiments. ^{1}H sources originate from OH groups, water, or organic molecules at the surface. CP-filtered experiments are only sensitive to protonated species and for this reason they discriminate surface with respect to bulk atoms. The first example of surface site discrimination was proposed by Becerra *et al.* [94] using ^{31}P–^{77}Se REDOR experiments in CdSe QD, where phosphorus atoms originate from the commonly used capping agent tri-*n*-octylphosphine oxide (TOPO). Authors found that TOPO molecules are closely packed to the surface, which is rich in Cd rather than in Se atoms. More recent studies have mainly used CP-MAS as the preferred technique to enhance ^{113}Cd [95, 96], ^{31}P [92], and ^{77}Se [97] nuclei. Only in one case [39], CP-MAS experiments were unsuccessful, due to very weak dipolar interactions between surface agents and QD. Deep surface analysis has required dipolar driven 2D homonuclear and heteronuclear techniques, which allow direct visualization of close spin neighbors. This approach is particularly useful in the study of interfaces. Spin-diffusion experiments were successfully employed in the study of InP QD [92]. The material was first investigated by CP which enhanced only surface sites with respect to bulk ones, as evidenced by the increasing ^{1}H–^{31}P CP-MAS signal between 0 and 100 ppm, which is otherwise too low to be detected by SP. Then, ^{31}P–^{31}P spin-diffusion experiments at various mixing times revealed the existence of two main phosphorus sites: sites likely situated within the particle core and sites likely located at the surface and experiencing a more heterogeneous environment. Berrettini *et al.* [97] have used 2D ^{1}H–^{13}C, ^{1}H–^{113}Cd, and ^{1}H–^{77}Se CP HETCOR experiments to characterize the surface of hexadecylamine (HAD) and thiophenol-capped CdSe QD. Despite the long acquisition times (504 hours for the ^{1}H–^{77}Se CP HETCOR), the authors were able to propose a structural model of HAD and thiophenol adsorption at the surface (Figure 6.4), where nitrogen binds to Cd atoms while methylene protons from the HAD chain interact with Se sites. On the contrary, when HAD is replaced by thiophenol, sulfur atom seems to preferentially interact with a Cd or Se-vacant site.

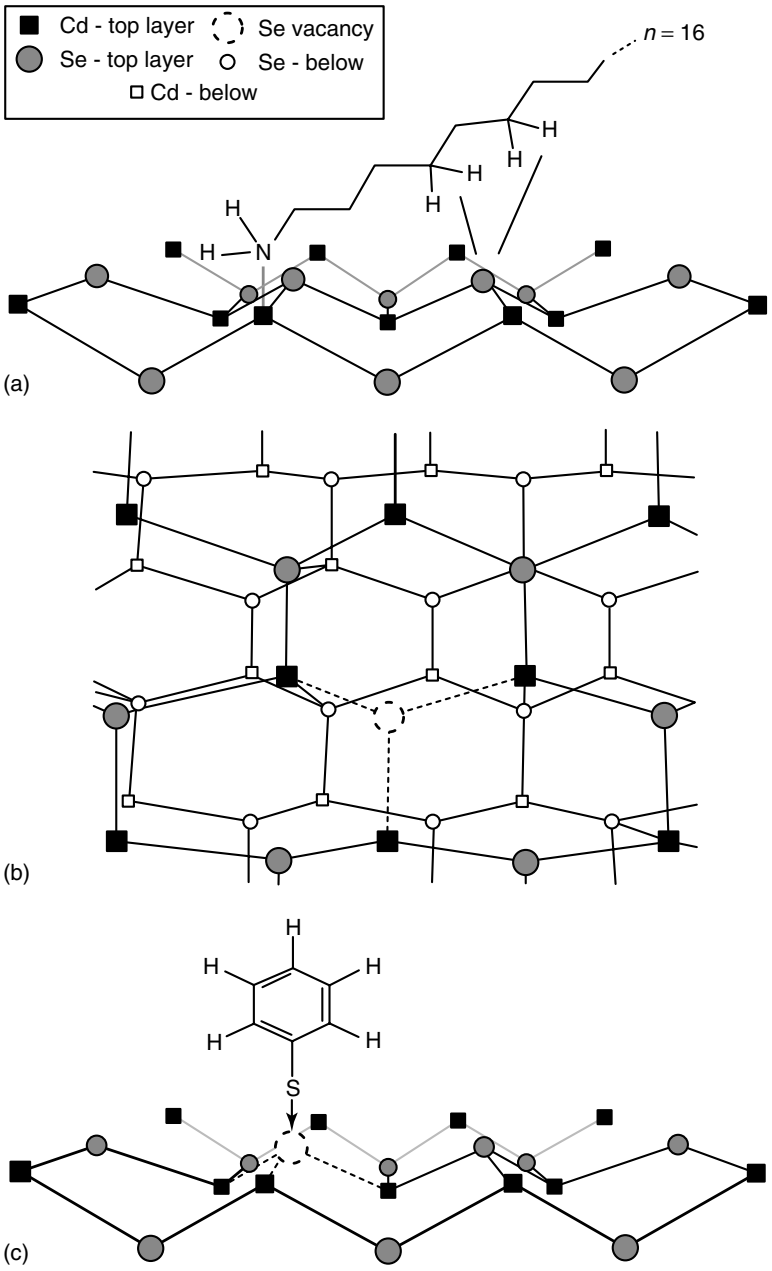

Figure 6.4 (a) Chain tilt of HDA to the surface of the particle. (b) Selenium vacancy on the surface of a CdSe nanocrystal. (c) A thiophenol molecule filling a selenium vacancy. (Reprinted with permission from [97]. Copyright 2004 American Chemical Society.)

Specific studies were dedicated to noncapped, water-containing, CdS QD [90, 98]. 1D ^{1}H SP MAS experiment recorded with decoupling (using the Lee–Goldberg (LG) pulse scheme) and 2D ^{1}H–^{1}H spin-diffusion experiments were crucial to identify the existence of different types of protons at the nanoparticle surface as well as within particle pores. Isolated OH groups are carried both by Cd (1.9 ppm) and S (2.8 ppm) atoms while water molecules exist under different forms, either bound to Cd (6.1 ppm) and S (4.2 ppm) or in exchange. The authors have observed that part of the molecular water is strongly adsorbed, probably within the interparticle nanopores, after the sample was treated under vacuum.

Finally, solid-state NMR is also used for simple ''quality check'' of the as-synthesized or postsynthesis treated materials, as observed after annealing (under air, nitrogen atmospheres, and vacuum at 300 °C) $Cd(SR)_2$ ($R=(CH_2)_{11}CH_3$) particles dispersed in a polystyrene matrix [95]. ^{13}C and ^{113}Cd CP-MAS NMR analysis were used to demonstrate that the annealing under vaccum produced very good quality nanocomposites with a low content of undesired impurities.

6.6 Self-Assembly

The domain of self-assembly offers a very large variety of examples in which solid-state NMR is efficiently used as a selective technique to probe intermolecular proximities. The nature itself of self-assembly processes based on weak intermolecular forces allows a very nice exploitation of dipolar coupling to probe through-space interactions in solids. The domain of self-assembly is very large and only two types of processes are described here.

The first concerns molecular recognition mainly via hydrogen bonding, which provides extended supramolecular solids. Application of advanced solid-state NMR techniques to supramolecular systems has recently been reviewed [12, 13]. Here, spin diffusion, ^{1}H double and triple quantum and HETCOR experiments are exploited to study different types of interactions, such as hydrogen bonding in benzoxazine oligomers, π-stacking between alkyl-substituted hexabenzocoronenes, host–guest interactions in molecular complexes like poly(dimethylsiloxane) inside γ-cyclodextrin, and so on. Some more examples that are not discussed in the cited review papers follow. Cyanuric acid (CA) and melamine (MA) are used as DNA nucleobase mimics, and Damodaran *et al.* [99] have used a multinuclear (^{13}C, ^{15}N, and ^{2}H) NMR approach to show the formation of H-bonding driven CA/MA dimer basing their analysis on variations of chemical shift (^{13}C, ^{15}N, and ^{2}H) and in quadrupole constant and asymmetry parameter (^{2}H) in the 1 : 1 mixture complex with respect to the pure systems. The group of Brown has studied the hydrogen-bonded N–H···N connectivity [100] in alkyl-modified deoxyguanosines via DQ INADEQUATE pulse scheme and it was able, via ^{15}N CP-MAS spin-echo experiments, to measure intra and intermolecular $^{2}J_{NN}$ couplings [101]. This was possible using a low-power (22.5 kHz) ^{1}H decoupling scheme RS-HEPT, Rotor synchronised Hahn-echo pulse train during the spin-echo evolution periods.

This strategy, with respect to classical high-power decoupling, was necessary to probe long echo times and, consequently, small, long-range, J-coupling constants, avoiding, at the same time, high-power loads on the probe.

Self-assembly of hybrid organic–inorganic species is the object of a recent work by Arrachart *et al.* [102].

Hybrid materials were made from sililated base pairs, in which adenine (A) or thymine (T) was modified with triethoxysilyl groups. Individual precursors, Si–A and Si–T as well as the hybrid self-assembled material Si–A···T–Si, in which hydrolysis and condensation of alkoxysilanes occurred, were characterized using 2D ^{1}H–^{1}H DQ experiments with the BAck-to-Back (BABA) pulse sequence. In particular, the authors proved the existence of direct interaction of A–T base pairs via N–H···N hydrogen bonds: a clear cross-peak connecting the NH group of thymine (13.9 ppm) to the NH_2 group of adenine (8.3 ppm) is observed in the hybrid Si–A···T–Si material, as shown in Figure 6.5.

The second important domain concerns self-assembled monolayers (SAMs), which was largely studied by the group of Raven. A review of their works on this topic and, in particular, on the use of solid-state NMR applied to the study of SAM both on gold and metal oxide nanoparticles was recently published [103]. Two issues are mainly addressed: conformation and mobility of the alkyl chains away from the particle surface, usually complexed by means of a thiol, carboxylate, or phosphonate group according to the nature of the particle itself. Nuclei under investigation are ^{1}H, ^{2}H, and ^{13}C while direct SP excitation under MAS, CP and

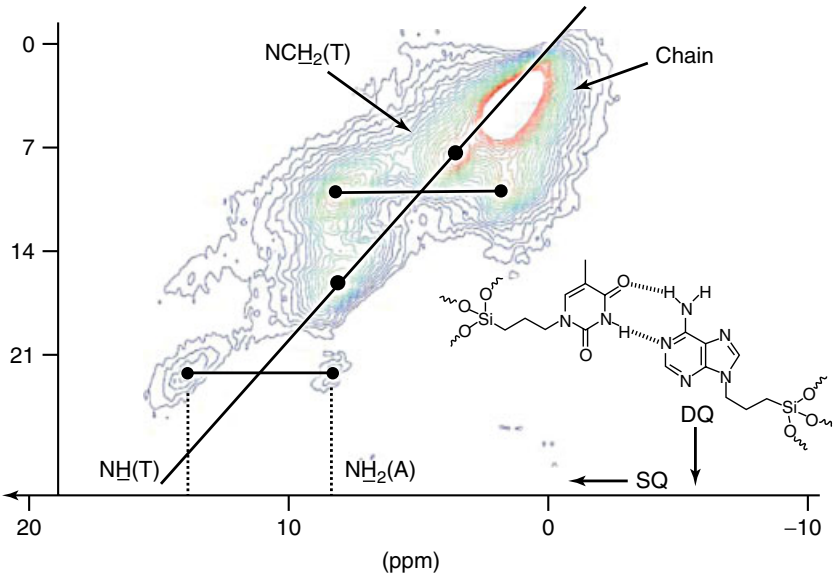

Figure 6.5 ^{1}H–^{1}H DQ BABA MAS of hybrid Si–A···T–Si material. (Reference [102] Reproduced by permission of The Royal Society of Chemistry – RSC – *www.rsc.org*.)

study of relaxation times are the most common employed approaches. ^{13}C chemical shift of methylene groups is very sensitive to the mobile *gauche* (31 ppm) or rigid all-trans (33 ppm) conformation of the backbone alkyl chains. As an example, in the octadecanethiol-complexed gold nanoparticles, a total population of 12% gauche bonds exists at 25 °C indicating a low degree of order in the chain packing. In addition, ^{13}C chemical shifts can be edited in a 2D HETCOR map via ^{1}H spectra ((WIdeline SpEctroscopy) WISE NMR), whose full width at half maximum provides information on the mobility of the specific carbon species. This approach showed that interchain interaction among octadecylphosphonic acid molecules is much stronger when its adsorption occurs on γ-Al_2O_3 with respect to ZrO_2 and TiO_2; this suggests the existence of a rigid aluminophosphonate lamellar phase where the organic solid forms a crystalline bilayer. Following similar working lines, ^{13}C CP-MAS spin-diffusion studies using a ^{1}H dipolar filter which eliminates DCs between protons in the mobile phase were performed on C_{30}-organo-modified silica surfaces; magnetization transfer from rigid all-trans to mobile *gauche* conformers was followed at increasing contact times (1μ s to 500 ms) at 312 K [104]. The purpose of the study was to determine whether the long alkyl chains settled parallel to the silica surface or whether they formed assembled monolayers perpendicular to it, provided a Si–C chemical bond was present. They found that the alkyl chains form two families of assembled monolayers perpendicular to the silica surface: one with short length (32 Å) containing domains of rigid conformers and an extended one (112 Å) containing mobile aliphatic chains.

6.7
Mesostructured Materials

Mesostructured materials[3)] (MMs) are part of the recent development in nanoscience and are the result of a combination of self-assembly of surface active molecules (surfactants) and inorganic polymerization of molecular compounds (sol-gel chemistry) in aqueous solution. Originally, silica-based highly porous powders were first synthesized in 1992 by researchers working for the Mobil Corporation [105], who were able to organize an inorganic (silica) porous network around a uniform hexagonal array of pores whose size varied between 1.5 and 10 nm and, consequently, with very high specific surface areas (up to 1000 $m^2\ g^{-1}$). This material was named MCM-41. Six years later, researchers at the University of California at Santa Barbara announced that they had produced silica nanoparticles with much larger pores (4.6–30 nm), but still in hexagonal array, and named it SBA-15 [106]. The initial intended use of these materials was molecular sieving for molecules of larger dimension than those filtered by zeolites. Currently, the

3) For convenience we used the acronym MM standing for mesostructured materials. Nevertheless, one should be aware of the fact that once the template is removed, the notation mesoporous materials is commonly used. In this case, we consider that MM refers to these materials in a much broader sense, including template-containing and template-free materials.

research on mesoporous materials (where silica constitutes the main material under study) has extended to other domains of application, including medicine, biofuels, and imaging. Shaping of the material went much further as membranes, thin films, or microspheres can be easily processed and the inorganic source is no longer restricted to silica, as many metal (Ti, Al, V, Zr, etc.) oxides can be synthesized as well under similar conditions.

Solid-state NMR has been extensively used in the characterization of MMs and some recent review articles have already dedicated some relative attention to this topic [14, 107–109]. Generally speaking, the domain of MM is very broad and many NMR studies have investigated specific aspects such as structure [110–124], interactions at interfaces [8, 125–144], confinement of organic molecules within nanopores [145–159], surface and bulk functionalization [160–170]. Each of these is addressed in the following text.

6.7.1 Structure

NMR is largely used to investigate structural features of the amorphous inorganic framework of MM.[4] ^{29}Si, ^{27}Al, and ^{31}P are the most frequently investigated nuclei but more rare ones, like ^{11}B and ^{17}O [121, 123], can be looked at, as well. By far, ^{29}Si is considered as being a ''routine'' nucleus and since 1995, three years after the discovery of MM, several studies exploit SP acquisition (SP) and CP-MAS to have an idea of the type of Si sites present within the framework of MM [111, 112, 115]. Steel *et al.* [111] compared ^{29}Si relaxation (spin–lattice, relaxation under spin-lock) and contact time studies on mesostructured silica with different mesophases and submitted to various temperature treatments. For example, Q_4 (SiO_2) sites in hexagonal structures (for uncalcined materials) seem to have longer (120 seconds) T_1 spin–lattice relaxation times with respect to lamellar (69 seconds) and cubic structures (106 seconds) and to amorphous silica gels (20–50 seconds). As for Q_3 (Si–OH) sites, differences are much less marked among all uncalcined materials. This study is the first to provide an overview on the dynamic relaxation parameters for several, silica-based, MM. The same approach is used for Al–Si [110], B–Si [113], Al–P–B [114] MM. In all cases, chemical shift of ^{29}Si, ^{27}Al, ^{11}B, and ^{31}P under CP-MAS is simply used to verify the incorporation and the coordination of the corresponding element. As an example, ^{11}B MAS and ^{1}H–^{11}B CP-MAS NMR show that boron is mainly incorporated into mesoporous aluminophosphates in its tetrahedral coordination form while ^{31}P MAS NMR shows at the same time that inclusion of boron reduced the degree of condensation of the inorganic framework.

In addition to chemical shift and CP-MAS-based studies (some additional ones can be found in [120, 121]), more advanced NMR techniques started to

4) On the contrary, XRD is a key technique for these systems to study the long-range order of the porous network.

be exploited for structural elucidation only after 2004: HETCOR [117, 118, 124], DQ excitation [116, 118], rotor-synchronized double resonance (TRAnsfer of Population in DOuble Resonance (TRAPDOR), REDOR, REAPDOR) [117, 119, 122, 123], and J-derived [116, 131] experiments became unique investigation tools that allowed direct proof for spatial proximities and direct network connectivities. An example of each is detailed below.

- **HETCOR:** The problems of boron-containing Al–P MM (BAPO) have been thoroughly studied by Huang *et al*. [117], who used multinuclear and multitechnique approaches to prove the proximities between Al/P, P/B, and Al/B atom pairs. After identifying one octahedral (−8 ppm) and one tetrahedral (+42 ppm) aluminum site and two separate phosphorus sites (−13 and −3 ppm) via classical SP MAS experiments, they were able to unambiguously identify a close proximity between the −3 ppm ^{31}P site only to the octahedral aluminum site, while the −13 ppm phosphorus site is close to both aluminum sites.
- **DQ-SQ experiments**: The group of Chmelka [116, 131] was able to synthesize, for the first time, a lamellar MM with inorganic crystalline walls using a cationic surfactant with a nonsymmetric polar head, $C_{16}NMe_2Et^+$. Using through-space dipolar-based DQ–SQ excitation/reconversion and J-resolved DQ–SQ INADEQUATE pulse schemes, they were able to identify each silicon site and depict its nearest neighbor connectivity (Figure 6.6). Then, using quantum chemical modeling they could obtain an energy-minimized silicate framework structure [116] that satisfies ^{29}Si interconnectivity and XRD data.

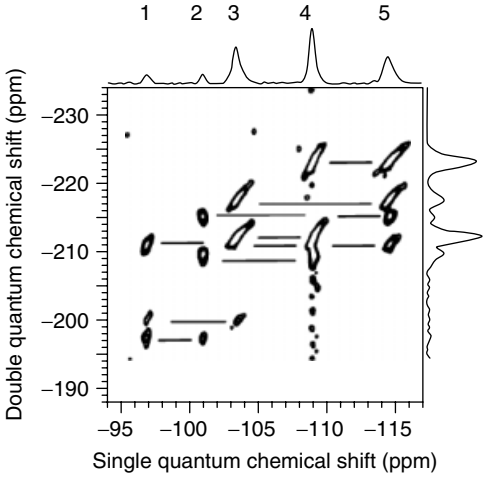

Figure 6.6 ^{29}Si–^{29}Si Double quantum single quantum INADEQUATE experiment probing atomic bonding in a ^{29}Si-enriched lamellar silica network with crystalline walls. (Reprinted with permission from [116]. Copyright 2004 American Chemical Society.)

- **Double resonance experiments**: TRAPDOR and REDOR experiments exploit DCs between close nuclei. The first is designed to probe the heteronuclear dipolar interactions involving at least one quadrupolar nucleus, which constitute the irradiated spin bath. The second is generally used to measure heteronuclear DCs and, therefore, internuclear distances. Hu *et al.* [119] used a $^{1}H/^{27}Al$ TRAPDOR experiment in Al-SBA-15 material to show that no proximity exists between hydroxyl protons and aluminum sites, meaning that Brönsted acid sites, expected to be in the form of Si–O(H)–Al form, detected in the ^{1}H MAS spectrum and whose presence was indirectly confirmed by the adsorption of molecules with a basic character like trimethylphosphine (TMP) oxide, are actually in the form of Si–OH or Al–OH (1.9 ppm) rather than in a bridging Si–O(H)–Al fashion.

6.7.2 Interaction at Interfaces

The study of interfaces in MM received wide attention and the actual knowledge has advanced mainly because of the number of through-space correlation experiments involving the inorganic framework and the organic templating agent. One of the recurrent questions is, where are the surfactant molecules exactly located? How do they influence the structuring process? How do they behave in a confined cavity after templating the inorganic matter? Many studies presented here use the HETCOR experiment as the main tool to directly visualize the proximity between the inorganic network (probed by ^{29}Si or ^{27}Al nuclei) and the organic matter (probed via ^{1}H, ^{13}C, or ^{31}P).

The first work (followed by similar experiments by Simonutti *et al.* [133] in 2001) on this topic appeared in 1996, in which Wang *et al.* [125] reported the chemical shifts and relaxation times (T_1, t_{CP}, and $t_{1\rho}$) related to the spin dynamics for the CTAC (cetyltrimethylammonium chloride) structuring agent in typical ordered and disordered mesostructured silica materials. They found that the surfactant molecule is highly mobile with an exception made for the methyl carbon atoms near the ammonium polar head, whose chemical shift experienced a 1-ppm downfield shift with respect to solution measurements and lineshape revealed an increase in broadness. The authors attributed these unusual features to the restraint mobility of the polar head due to the electrostatic interactions with the silicate surface. Nevertheless, no direct proof was provided.

One had to wait for a series of works from the group of Chmelka [12, 128, 129] who used, for the first time, HETCOR experiments to detect the proximity between the trimethylammonium polar head of CTAB and the inorganic framework. They repeated the same experiment in block-copolymer-derived alumino-silicates (poly-(ethylene oxide-*b*-propylene oxide-*b*-ethylene oxide)-PEO–PPO–PEO was used as structuring agent). In general, a first $^{1}H–^{13}C$ HETCOR is used to unambiguously attribute all proton signals. Then, $^{1}H–^{27}Al$ or $^{1}H–^{29}Si$ HETCOR experiments proved the direct interaction between the surfactant headgroup with SiOH (Q_3 sites at $\delta = 100$ ppm) or tetrahedral ^{27}Al (resonating at 50 ppm) groups within the inorganic framework. Materials under study were either

pure silica monoliths [86] or Al-MCM-[128, 129] powders. Similar approaches were used by Jones *et al.* [134] to prove the embedding of a Pd/Ru-based cation in a MCM-41 material. Trebosc *et al.* [137] performed a systematic study of hydrated and dehydrated MCM-41 type of materials, where additional 2D $^{1}H-^{1}H$ homonuclear DQ–SQ and exchange experiments helped to focus on proton–proton interaction at the silica interface. Baccile *et al.* [141] used double CP experiments $^{1}H \rightarrow {}^{29}Si \rightarrow {}^{1}H$ to edit only those protons close to the silica surface via a variation of the $^{29}Si \rightarrow {}^{1}H$ contact time in a comparison between acid and basic catalyzed CTAB-containing mesostructured silica.

In the remaining studies on the inorganic/organic interfaces, one should mention the use of $^{1}H-^{13}C$ 2D-WISE by De Paul *et al.* [127] and Khimyak *et al.* [132], who observed an increased rigidity of the surfactant moiety close to the inorganic wall (poly-(isoprene-*b*-ethylene-oxide)-PI-*b*-PEO-aluminosilicate in [127] and CTAC-aluminophosphate system in [132]). Complementary tools inspired by liquid-state NMR methods were introduced in the domain of MM by Sizun *et al.* [135] and Alonso *et al.* [8]. The first author showed the possibility of increasing the ^{1}H resolution using a small amount of methanol directly added in the rotor, while the second author showed that surfactant-containing MM have long-enough spin–spin relaxation times to apply $^{1}H-^{13}C$ through-bond filtering (INEPT), typical for liquid systems. Homonuclear $^{1}H-^{1}H$ correlation methods have also been used either exploiting spin diffusion [135, 137, 138] or DQ–SQ excitation [136, 137]. Spin diffusion showed the existence of unreacted ethoxy moieties [138] at the pore surface in spray-dried mesostructured silica spheres and the authors were able to correlate their presence to the increasing long-range disorder of the mesophase. The existence of PEO/silica interface in thin films was shown for the first time using ^{1}H DQ–SQ (BABA) experiments [136]. Finally, at least two works focusing on organic/titania interface were recently reported [140, 142], as well as a very nice study by Cadars *et al.* [143] on the influence of a dissymmetric cationic surfactant on the order/disorder transition in a lamellar silicate using a detailed cross-peak analysis of $^{29}Si-^{29}Si$ DQ–SQ INADEQUATE experiments.

6.7.3
Confinement of Organic Molecules within Nanopores

The previous sections mainly dealt with structural analysis of MM and surface/template interactions. Here, the focus shifts toward the template-free material and, given the high specific surface area (up to 1000 $m^2\,g^{-1}$ for silica), several groups studied the behavior, and therefore the interactions, of encapsulated molecules. Three domains can be identified: polar and nonpolar organic molecules, water, and molecules with a specific function.

- **Polar and nonpolar organic molecules**: Many contributions to this topic come from the group of Buntkowsky [145, 147, 150, 155–157], who studied d_6-benzene [145, 150], ^{15}N-pyridine [147, 157], and d_6-isobutyric acid [155] adsorbed on mesoporous materials (SBA-15 and MCM-41 mainly). Recently, a short review article on this topic was published by the same group [156]. The NMR strategy

all along their studies is to use isotopically enriched (^{2}H and ^{15}N) molecules and follow their behavior and possible surface interactions in a confined environment. Information on the molecular state and the surface functions and defects are then provided. Deuterium NMR is very sensitive to the molecular mobility and phase transitions (liquid–solid or solid–solid) can be easily observed as a function of temperature just by looking at the variations of lineshape and linewidth of ^{2}H NMR signal, whose simulation and quantification provides the amount of freely rotating or rigid molecules. Studies performed on benzene confined in 30-nm pores of a SBA-15 sample showed the existence of an amorphous benzene layer coexisting with a crystalline phase located at the pore center. The same approach was exploited by other groups who used ^{2}H NMR to investigate the adsorption of *tert*-butyl chloride [146], *p*-nitroaniline [149], and tetraalanine [153]. Surface studies at nanoscale can be done using external molecules as surface probes. In this case, the focus is on the surface itself and not on the dynamics of the adsorbent. Shenderovich *et al.* [157] outlined the existence of surface defects in MCM-41 and SBA-15 and this was related to the amount of Q_2 species, as observed after pyridine adsorption; trimethylphosphine (TMP) was instead used by Luo *et al.* [148] to probe the surface of Al-MCM-41. ^{31}P, ^{1}H, and ^{27}Al NMR responses were investigated via CP-MAS and TRAPDOR experiments to probe the proximity of TMP to acidic surface sites. The authors could obtain fairly sensitive, CP-filtered (^{1}H $\rightarrow$ ^{27}Al),^{27}Al–^{31}P TRAPDOR spectra that proved the existence of bridging Brönsted Si–O(H)–Al sites. It is important to note that in one of the aforementioned studies [11], the authors could not clearly detect these particular sites.

- **Water**: The number of studies concerning water adsorption, as seen by solid-state NMR, is limited. One of them [151] mainly concentrates on chemical shift analysis of water adsorbed on MCM-41 and SBA-15, where the pore-filling mechanism seems to vary as a function of the pore size and another [158] is mainly focused on the adsorption and NMR signal detection procedure; a glass capillary is filled with water, which is then inserted into the NMR rotor together with the sample. During rotation, the capillary breaks and water vapor is diffused; meanwhile, fast ^{1}H spectra acquisition allows time-resolved *in situ* study of water adsorption.
- **Molecules with specific function**: Mesoporous materials can act as molecular sieves and also as supports for drug delivery purposes. Few NMR studies have used ^{1}H, ^{13}C CP, ^{1}H–^{13}C, and ^{1}H–^{29}Si HETCOR experiments to investigate the interactions between drugs [152, 154] or pollutants [159] with mesoporous materials. Baccile *et al.* [159] used organic functionalized mesoporous silica materials to adsorb chlorophenyl pollutants. Despite the better retention performance of the functionalized samples with respect to the nonfunctionalized ones undoubtedly depending on short-range dispersion forces, the molecular mobility at room temperature of the pollutant was still very high and a liquid-like behavior was found. In all cases, owing to the high molecular mobility, HETCOR experiments at room temperature did not provide clear-cut answers about the interactions between the molecules and the surface. Similar results were found on ibuprofen-impregnated mesoporous silicas for drug release control [154].

6.7.4
Surface and Bulk Functionalization

Functionalization of MM can occur via different strategies, mainly via postfunctionalization and co-condensation pathways. There are two issues that generally need a clear answer from NMR experiments: Did functionalization occur? Where are the functional groups exactly located (in the bulk or at the surface)?

In all silica-based materials, it is quite easy to prove the existence of a Si–C bond because of its clear chemical shift signature between −50 and 10 ppm [160, 164]. Nevertheless, it is trickier to prove that a homogeneous functionalization occurred at the pore surface. The group of Pruski demonstrated functionalization of organic compounds at silica surface mainly via $^{1}H-^{13}C$ and $^{1}H-^{29}Si$ HETCOR experiments [161, 163, 165, 166]. In all cases, a big effort was put into the development of robust and adapted pulse sequences, which could provide unambiguous (e.g., use of LG homonuclear decoupling to prevent ^{1}H spin diffusion) and high-quality data (e.g., sensitivity enhancement via very fast MAS or Carr-Purcell-Meiboom-Gill (CPMG) pulse sequences). Similar studies were realized by Morales *et al.* [167] who showed the incorporation of arene sulfonic acid species in silica containing ethane bridging groups (−OSi–CH_2–CH_2–SiO–), Tsai *et al.* [169] who were able to synthesize COOH-containing mesoporous silica in a one-step reaction via the hydrolysis of the initially grafted –CN group and the group of Babonneau [14, 161] which demonstrated (confirmed by Kao *et al.* [170] in 2008) the proximity between the surfactant polar head and grafted phenyl (and vinyl) groups pending from the silica surface toward the pore center. Finally, with the purpose of making Ag^{+} adsorbents, Melnyk *et al.* [168] used proton spin diffusion to probe the functionalization of spray-dried mesoporous silica particles with mercaptopropyl functions.

6.8
Study of Interfaces and Structure by Solid State NMR

This section illustrates through some examples the research domains in which the author of this chapter is actively involved. Most of the work deals with the characterization of inorganic/organic interfaces in MMs. Four examples are proposed.

The first couple of studies were carried on MMs. Synthesis procedures and a general overview of these works are detailed in [141, 161]. The first one concerns the study of silica/CTAB (cetyltrimethylammonium bromide) surfactant interaction in a mesostructured hexagonal powder, while the second one deals with phenyl-functionalized mesostructured silica materials. The third example is more focused on the bioactivity of mesoporous silica/calcium phosphate composite, while the last one shows an example of structural resolution of amorphous carbon microspheres. For some background information about these two last works, please refer to [171, 172].

6.8.1 Double Cross-Polarization Experiments to Probe the Silica/CTAB Interface

The importance of solid-state NMR to probe the silica/surfactant interface should be evident from the number of examples provided on MMs. It is of general acceptance that the synthesis conditions, in particular pH, influence the type of interactions between the organic template (CTAB, a common structuring agent), and silica. In fact, at low pH one would expect a counterion-mediated charge matching model between the positively charged alkylammonium polar head of the surfactant and silica moieties (which also possess a positive surface charge). On the contrary, when synthesis is carried out under basic pH conditions, one would expect a direct electrostatic attraction between the surfactant and silica, which under such a condition possesses a negative charge (point of zero charge for silica is at pH = 2). How can we explain such a difference? How can we prove the type of interaction between silica and the polar head of CTAB?

First of all, one can make the assumption that the distance between the silica surface and the organic template within the hexagonal mesostructure strongly depends on the type of interaction. One could expect that a direct $Si{-}O^{-}/N^{+}$ interaction (under basic pH conditions) would result in a shorter distance with respect to a counterion-mediated, $Si{-}O^{+}\cdots Cl^{-}\cdots N^{+}$, interaction (under acidic pH conditions). Qualitative NMR measurements (no absolute distance values could be provided) using DC between ^{1}H and ^{29}Si via CP-based techniques can be performed, considering that ^{29}Si nuclei only exist in silica while ^{1}H nuclei exist both in silica (Si–OH), CTAB ($(CH_3)_3N^{+}C_{16}H_{33}$), and interstitial water. $^{1}H \rightarrow {}^{29}Si$ HETCOR experiments at different contact times (for short contact times, shorter distances are explored) allowed us to show that trimethylammonium groups from CTAB are in close contact with surface silanols (Q_3 sites) only when synthesis pH is acidic (pH < 1) while a strong interaction between $-N^{+}(CH_3)_3$ groups and the inner silica wall (Q_4 sites) occurs in those materials obtained at high synthesis pH (pH > 10). These results were confirmed by a double CP approach in which all ^{29}Si atoms were first polarized by an optimized CP transfer from all surrounding protons while a second transfer occurs from ^{29}Si to ^{1}H. This second step can be tuned by adjusting the contact time meaning that all protons close to the silica surface are detected in advance over protons far from it. Figure 6.7a–c shows the 2D $^{1}H{-}^{1}H$ EXSY (EXchange SpectroscopY) NMR experiment after filtering with a double CP $^{1}H{-}^{29}Si{-}^{1}H$ step. At short mixing times (Figure 6.7a), magnetization is mainly settled on the silanol (7 ppm) and methyl groups (3.3 ppm) and only in part on the chain.

At longer evolution times, magnetization transfers from the silanols toward the surfactant polar head (Figure 6.7b) and chain (Figure 6.7c), as shown by the increasing intensity of the off-diagonal cross-peaks A, B, and C. The EXSY map is clearly not symmetric, as one would expect because of the unidirectional transfer of the magnetization (from silanol to surfactant) which originates from the double CP step. Schemes next to each 2D map help the reader in visualizing the direction of the magnetization transfer at each mixing time.

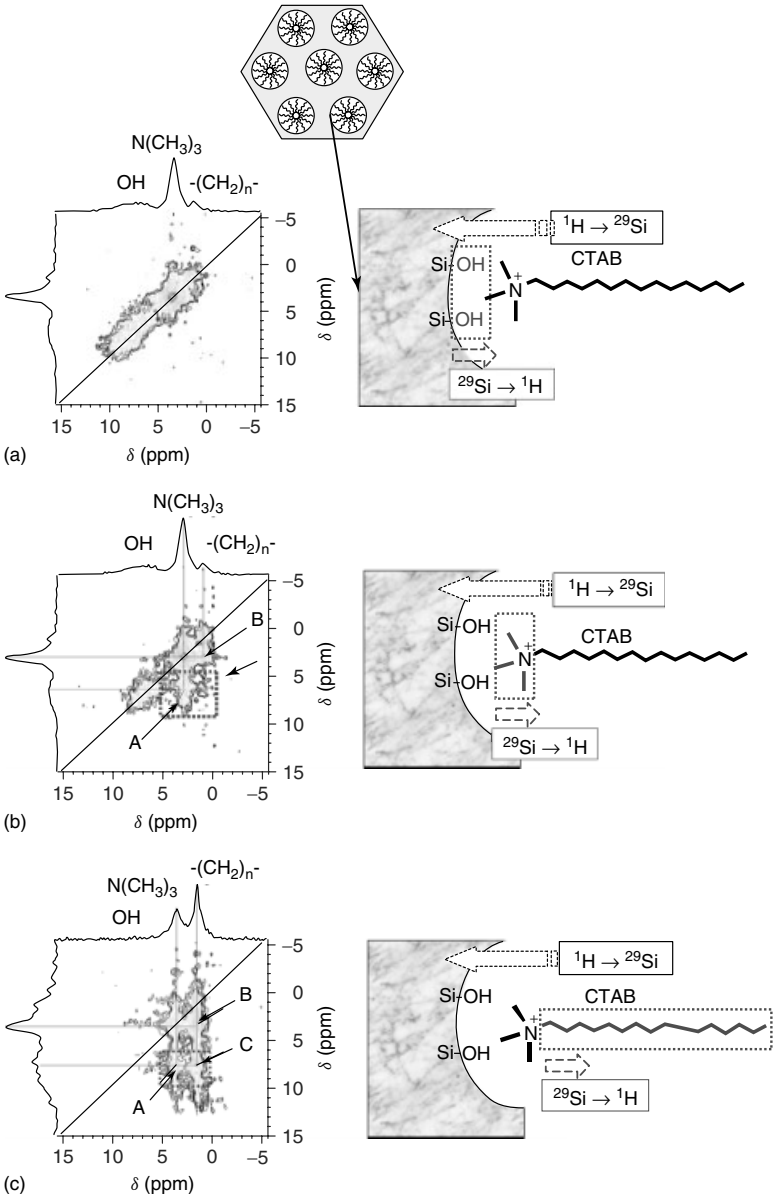

Figure 6.7 Use of CP-filtered ^{1}H spin diffusion experiments at different mixing times are helpful to identify atoms located at various distances from the silica surface. First, (a) the surface atoms (here, ^{29}Si) can be polarized via a standard optimized CP experiment; then, (b) polarization back-transfer to protons can be optimized as well and, finally, (c) evolution of magnetization via spin diffusion identifies both close and distant proton sites. (Partly reprinted with permission from [141]. Copyright 2007 American Chemical Society.)

6.8.2
Heteronuclear Correlation Experiments to Probe the Phenyl Functionalization in Silica/CTAB Interface

In Section 6.7.4, it was shown that HETCOR experiments are extremely useful to prove surface functionalization and they constitute a unique way to show the exact localization of organic functions in MMs (generally, the inorganic/template interface). The co-condensation of tetraethoxysilane with phenyltriethoxysilane in the presence of CTAB produces a hybrid mesostructured solid with a cubic phase (*Pm3n* space group). A time-resolved *in situ* study of the formation of this material using small-angle X-ray scattering under synchrotron radiation (Figure 6.8a) shows that the cubic mesophase actually forms after a typical epitaxial growth from a 2D hexagonal phase (*p6m* space group), which is observed in the first minutes of the reaction. One of the reasons for such a phase transition in this specific system could be the evolution from a low to a high micellar curvature due to the presence of the phenyl ring, which is known, from previous studies [161, 170], to be located at the silica/micellar palisade. Typically, a hexagonal phase is composed of hexagonal close-packed cylindrical micelles while spherical micelles are the building blocks of a typical (*Pm3n*) cubic phase. In the hexagonal to cubic phase transition, the (10) reflection transforms into the (211) reflection of the cubic phase (Figure 6.8a) and, consequently, the curvature of cylindrical micelles increases to form spherical aggregates. This assumption was addressed by means of $^{1}H-^{1}H$ DQ (BABA) correlation experiments, which were run on lyophilized powder samples extracted at short (2 minutes) and long (11 minutes) reaction times, the last one presenting a clear cubic Pm3n structure while the first one had a more disordered, probably

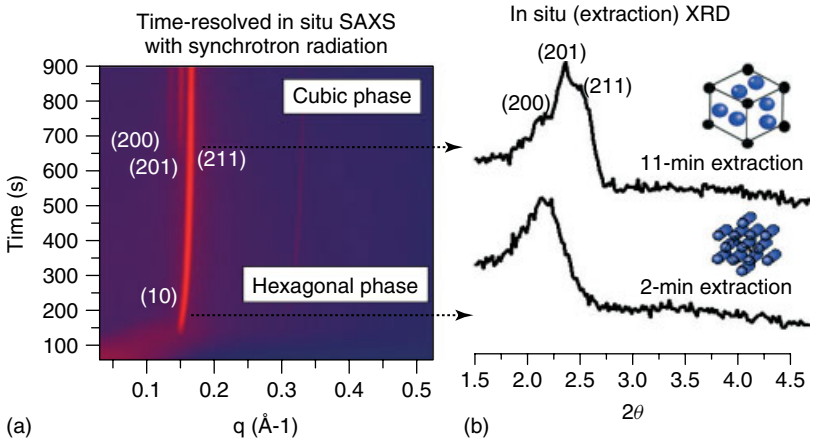

Figure 6.8 Small angle X-ray scattering experiments can be used to follow the formation of a mesophase as a function of time, as shown in (a) for phenyl-functionalized mesostructured silica. This is necessary to have a clear view of the dynamics of mesophase formation and evolution and, if needed, to extract and isolate a fraction of the sample having the desired mesophase (b) for additional studies.

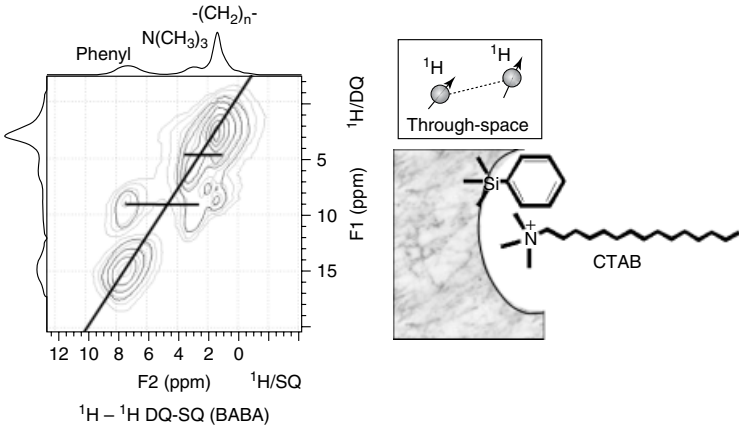

Figure 6.9 $^{1}H-^{1}H$ double quantum single quantum experiments are an extremely powerful tool to probe (through space) close proximities (<0.5 nm) between protons, as shown here for the cubic and hexagonal phenyl-containing mesostructured silica powders. This technique allows a clear discrimination between equivalent (on-diagonal cross-peaks) and nonequivalent (off-diagonal cross-peaks) proton sites, making it much more efficient and selective than spin diffusion-driven experiments, as shown in the sample of Figure 6.7.

hexagonal, mesophase (Figure 6.8b). Figure 6.9 shows the comparison between the 2D DQ–SQ $^{1}H-^{1}H$ BABA experiments run on both hexagonal (light gray) and cubic (dark gray) phases. The signal at 7.0 ppm indicates the presence of phenyl protons while peaks at 3.3 and 1.5 ppm refer to, respectively, the $N(CH_3)_3$ polar head and alkyl chain of the surfactant. According to the specificity of DQ–SQ experiments, all diagonal peaks demonstrate the interactions among equivalent protons, as expected here for all multiproton sources. In addition, two off-diagonal cross-peaks show that the phenyl group (7.0 ppm) and the polar head (3.3 ppm) are correlated indicating the close proximity between these species. Given the choice of short excitation and refocusing times in the BABA pulse sequence, sensitivity for H–H bonds is lower than 5 Å. Both experiments can be superimposed without particularly evident discrepancies showing that (i) the phenyl group has entered the mesophase since the early stages of the material formation and (ii) a clear difference between the hexagonal and cubic phases cannot be made on the sole assumption of close proximity between the phenyl group and the surfactant polar head. Further investigations to better understand the origin of the phase transition are still ongoing.

6.8.3
Structural Study of Mesoporous Silica/Calcium Phosphate Composite Materials for Bone Regeneration via TRAPDOR Experiments

Bone regeneration is an intense field of research and several strategies are followed to favor the formation of hydroxyapatite on biocompatible supports. Generally,

Hydroxyapatite HAP – $Ca_{10}(PO_4)_6(OH)_2$ – is used as a main bone substituent despite its very low solubility. Other materials, like calcium-deficient hydroxyapatites – β-tricalcium phosphate, β-TCP – may be preferred even if, in general, a mixture of HAP and β-TCP shows higher bioactivity in human plasma. In addition, it was shown that a mixture of silica/HAP composite also has a very good bioactivity. Using an engineered material science approach, it is possible to synthesize, in a one-step process, a HAP/silica composite with two functions: bioactivity and hierarchical macro/meso porosity, the last one needed for drug encapsulation and delivery purposes in a possible pain relief goal. Structural identification of SiO_2 and HAP phases is performed via ^{29}Si and ^{31}P MAS, where ^{31}P SP NMR experiments actually revealed a HAP structure (^{31}P broad resonance at 0 ppm referenced with respect to KH_2PO_4) and, under some specific synthesis conditions, the existence of a second phase, correlated to the ^{31}P peak at −1.95 ppm. Identification of this peak could be done with TRAPDOR experiments, where the evolution of ^{31}P peak intensities was monitored in the presence (and in absence) of ^{23}Na irradiation at different times. If ^{31}P signal intensity at −1.95 ppm would be affected by ^{23}Na irradiation, then a clear proximity between phosphorus and sodium is established indicating the existence of a calcium deficient, $NaCaPO_4$, phase, as it is actually observed, as shown in Figure 6.10.

6.8.4
Structural Resolution of Amorphous Carbon Microspheres via 2D ^{13}C–^{13}C Double Quantum NMR Experiments

Determination of the structure of amorphous materials is discussed here in a very specific case. Hydrothermal treatment in water at temperature below 200 °C of mono and polysaccharides gives micrometer-sized particles having a carbonaceous

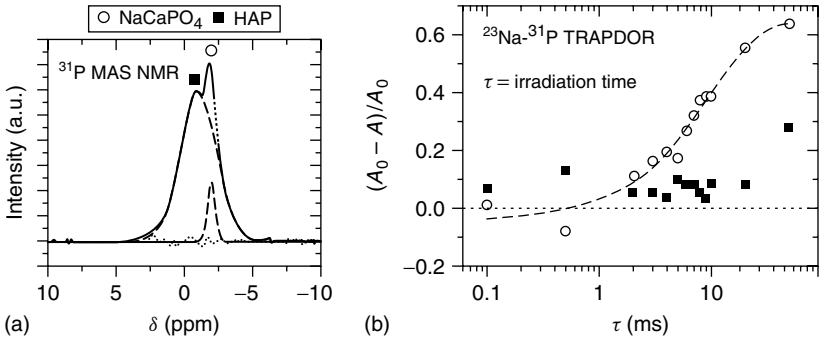

Figure 6.10 TRAPDOR experiments are used to reveal spatial proximities between dipolar (here ^{31}P) and quadrupolar (here ^{23}Na) nuclei. In this case, the ^{31}P signal peak at −1.95 ppm is clearly affected while the sodium atom is irradiated as its intensity varies with irradiation time. (Reference [171] – Reproduced by permission of The Royal Society of Chemistry – RSC – *www.rsc.org*.)

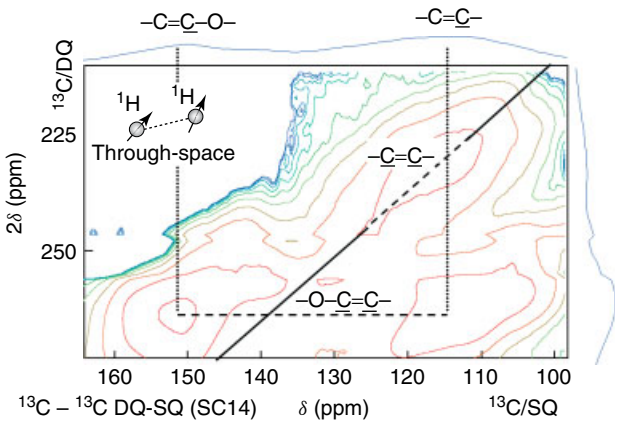

Figure 6.11 The 2D representation of the $^{13}C-^{13}C$ DQ–SQ experiment (SC14 pulse sequence) provides a clear-cut picture of the interior core of carbon spheres obtained via a hydrothermal treatment of glucose. The material is composed of furane moieties, as seen by the off-diagonal cross-peaks at 115 and 150 ppm.

scaffold. This process attracts much interest worldwide because of the possibility of using both pure saccharides and raw biomass under mild conditions when compared to the standard temperatures used to convert biomass into carbon. This is important both from sustainable development (cheap carbon reservoir) and application (chromatography, adsorbents, energy storage) points of view. The final material has an average composition of matter of about 65 wt% carbon, 30 wt% oxygen, and 5 wt% hydrogen and interesting adsorptive properties because of carboxylic acid sites, as shown by FTIR and ^{13}C solid-state MAS NMR techniques. Under these conditions, a clear structural resolution is extremely challenging and up to now no study describes the core structure of these carbonaceous powders. Our approach consisted of isotopic (^{13}C) enrichment of the carbonaceous scaffold via the introduction of fully ^{13}C-enriched glucose at the early stages of the material synthesis. This allows very fast signal recording and opens up several possibilities to deep structural studies using advanced NMR techniques, which would otherwise be impossible to exploit under natural isotopic abundance conditions.

The carbonaceous structure of the carbon spheres is generally interpreted as complex graphene-like material with a polyaromatic core and oxygenated (OH, COOH, COH) surface functions. This picture was highly incorrect, as proved by our 2D $^{13}C-^{13}C$ DQ– SQ experiments[5] and partly shown here (Figure 6.11). Two main signals at 115 and 150 ppm are clearly distinguished, the first corresponding

5) The SC14 pulse program, based on DQ excitation between (through space) dipolar coupled nuclei (see introduction), was used and optimized to detect only next neighbors (one carbon–carbon bond).

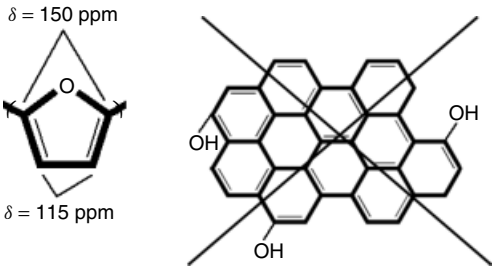

Scheme 6.2 The core of the carbon spheres is composed of a furane-based network instead of a graphene-like network.

to –C=C– and the second to –C=C–O– groups. The on-diagonal cross-peak at 115 ppm exactly indicates the existence of –C=C– bonds while the off-diagonal cross-peaks at 115 and 150 ppm show –C=C–O– proximities. Interestingly, the analysis of the intensities shows that equivalent amount of –C=C– and –C=C–O– exist and are very close (one atom bond) to each other. This excludes the existence of a wide aromatic core (Scheme 6.2b) with external oxygenated functions and it strongly suggests the existence of a furane-based network instead (see Scheme 6.2a). This conclusion is highly unexpected both for these hydrothermally synthesized and for typical pyrolized carbons at $T < 350\,^{\circ}C$, but it is further confirmed by complementary ^{13}C NMR experiments [173].

6.9 Conclusion

This chapter has shown a number of application of solid-state NMR in the field of nanomaterials.

In particular, the structure and surface properties of fullerenes, nanotubes and quantum dots, the self-assembly process in the solid-state, the interactions at the inorganic/organic interfaces are all samples that prove the utility and necessity of solid-state NMR in the characterization of more and more complex materials. In more specific cases, like amorphous materials (silica, carbon), this is the only technique which highlights the short-range structural features.

It is clear that continuous advances in the NMR technique (stronger NMR magnetic field, better performing homonuclear decoupling sequences, new recoupling schemes, etc.) will provide an endless source for the material chemist to solve complex structures and elucidate interface interactions.

Acknowledgments

Dr Florence Babonneau and Prof. Dr Christian Bonhomme (LCMCP, Paris, France) are kindly acknowledged for helpful discussions.

References

1. Levitt, M.H. (2001) *Spin Dynamics: Basics of Nuclear Magnetic Resonance*, John Wiley & Sons, Ltd, West Sussex.
2. Duer, M.J. (2004) *Introduction to Solid State NMR Spectroscopy*, Wiley-Blackwell.
3. Schmidt-Rohr, K. and Spiess, H.W. (1994) *Multidimensional Solid State NMR and Polymers*, Academic Press, London.
4. Mehring, M. (1983) *Principles of High Resolution NMR in Solids*, 2nd edn, Springer.
5. Andrew, E.R. and Szczesniak, E. (1995) A historical account of NMR in the solid state. *Prog. Nucl. Magn. Res.*, **28**, 11.
6. Blanc, F., Copéret, C., Lesage, A., and Emsley, L. (2008) High resolution solid state NMR spectroscopy in surface organometallic chemistry: access to molecular understanding of active sites of well-defined heterogeneous catalysts. *Chem. Soc. Rev.*, **37**, 518.
7. Laws, D.D., Bitter, H.-M.L., and Jerschow, A. (2002) Solid-state NMR spectroscopic methods in chemistry. *Angew. Chem. Int. Ed.*, **41**, 3096.
8. Alonso, B. and Massiot, D. (2003) Multi-scale NMR characterisation of mesostructured materials using 1 H → 13 C through-bond polarisation transfer, fast MAS, and 1H spin diffusion. *J. Magn. Reson.*, **163**, 347.
9. Lesage, A. and Emsley, L. (2001) Through-bond heteronuclear single-quantum correlation spectroscopy in solid-state NMR, and comparison to other through-bond and through-space experiments. *J. Magn. Reson.*, **148**, 449.
10. Lesage, A., Sakellariou, D., Steuernagel, S., and Emsley, L. (1998) Carbon-proton chemical shift correlation in solid state NMR by through-bond multiple quantum spectroscopy. *J. Am. Chem. Soc.*, **120**, 13194.
11. Lesage, A., Auger, C., Caldarelli, S., and Emsley, L. (1997) Determination of through-bond carbon-carbon connectivities in solid-state NMR using the INADEQUATE experiment. *J. Am. Chem. Soc.*, **119**, 7867.
12. Brown, S.P. and Spiess, H.W. (2001) Advanced solid-state NMR methods for the elucidation of structure and dynamics of molecular, macromolecular, and supramolecular systems. *Chem. Rev.*, **101**, 4125.
13. Brown, S.P. (2007) Probing proton–proton proximities in the solid state. *Progr.Nucl. Magn. Reson. Spectrosc.*, **50**, 199.
14. Bonhomme, B., Coelho, C., Baccile, N., Gervais, C., Azaïs, T., and Babonneau, F. (2007) Advanced solid state NMR techniques for the characterization of Sol–gel-derived materials. *Acc. Chem. Res.*, **40**, 738.
15. (a) Medek, A., Harwood, J.S., and Frydman, L. (1995) Multiple-quantum magic-angle spinning NMR: a new method for the study of quadrupolar nuclei in solids. *J. Am. Chem. Soc.*, **117**, 12779; (b) Frydman, L. and Harwood, J.S. (1995) Isotropic spectra of half-integer quadrupolar spins from bidimensional magic-angle spinning NMR, *J. Am. Chem. Soc.*, **117**, 5367.
16. (a) Bloch, F. (1956) Dynamical theory of nuclear induction II. *Phys. Rev.*, **102**, 104; (b) Bloch, F. (1958) Theory of line narrowing by double-frequency irradiation. *Phys. Rev.*, **111**, 841.
17. Bennett, A.E., Rienstra, C.M., Auger, M., Lakshmi, K.V., and Griffin, R.G. (1995) Heteronuclear decoupling in rotating solids. *J. Chem. Phys.*, **103**, 6951.
18. Gerstein, B.C., Pembleton, R.G., Wilson, R.C., and Ryan, L.M. (1977) High resolution NMR in randomly oriented solids with homonuclear dipolar broadening: combined multiple pulse NMR and magic angle spinning. *J. Chem. Phys.*, **66**, 361.
19. Lee, M. and Goldburg, W.I. (1965) Nuclear-magnetic-resonance line narrowing by a rotating RF field. *Phys. Rev.*, **140**, A1261.
20. Bielecki, A., Kolbert, A.C., and Levitt, M.H. (1989) Frequency-switched pulse sequences: homonuclear decoupling

and dilute spin NMR in solids. *Chem. Phys. Lett.*, **155**, 341.

21. Vinogradov, E., Madhu, P.K., and Vega, S. (1999) High-resolution proton solid-state NMR spectroscopy by phase-modulated Lee–Goldburg experiment. *Chem. Phys. Lett.*, **314**, 443.

22. (a) Sakellariou, D., Lesage, A., Hodgkinson, P., and Emsley, L. (2000) Homonuclear dipolar decoupling in solid-state NMR using continuous phase modulation. *Chem. Phys. Lett.*, **319**, 253; (b) Lesage, A., Sakellariou, D., Hediger, S., Elena, B., Charmont, P., Steuernagel, S., and Emsley, L. (2003) Experimental aspects of proton NMR spectroscopy in solids using phase-modulated homonuclear dipolar decoupling. *J. Magn. Reson.*, **163**, 105.

23. Pines, A., Gibby, M.G., and Waugh, J.S. (1973) Proton-enhanced NMR of dilute spins in solids. *J. Chem. Phys.*, **59**, 569.

24. Schmidt-Rohr, K., Clauss, J., and Spiess, H.W. (1992) Correlation of structure, mobility, and morphological information in heterogeneous polymer materials by two-dimensional wideline-separation NMR spectroscopy. *Macromolecules*, **25**, 3273.

25. (a) Caravatti, P., Bodenhausen, G., and Ernst, R.R. (1982) Heteronuclear solid-state correlation spectroscopy. *Chem. Phys. Lett.*, **89**, 363; (b) Caravatti, P., Braunschweiler, L., and Ernst, R.R. (1983) Heteronuclear correlation spectroscopy in rotating solids. *Chem. Phys. Lett.*, **100**, 305.

26. Grey, C.P. and Vega, A.J. (1995) Determination of the quadrupole coupling constant of the invisible aluminum spins in zeolite HY with 1H/27Al TRAPDOR NMR. *J. Am. Chem. Soc.*, **117**, 8232.

27. Gullion, T. and Schaefer, J. (1989) Rotational-echo double-resonance NMR. *J. Magn. Reson.*, **81**, 196.

28. Tycko, R. and Dabbagh, G. (1991) Double-quantum filtering in magic-angle-spinning NMR spectroscopy: an approach to spectral simplification and molecular structure determination. *J. Am. Chem. Soc.*, **113**, 9444.

29. Raleigh, D.P., Levitt, M.H., and Griffin, R.G. (1988) Rotational resonance in solid state NMR. *Chem. Phys. Lett.*, **146**, 71.

30. Bennett, A.E., Ok, J.H., Griffin, R.G., and Vega, S. (1992) Chemical shift correlation spectroscopy in rotating solids: Radio frequency-driven dipolar recoupling and longitudinal exchange. *J. Chem. Phys.*, **96**, 8624.

31. Lee, Y.K., Kurur, N.D., Helmle, M., Johannessen, O.G., Nielsen, N.C., and Levitt, M.H. (1995) Efficient dipolar recoupling in the NMR of rotating solids. A sevenfold symmetric radiofrequency pulse sequence. *Chem. Phys. Lett.*, **242**, 304.

32. Brinkmann, A., Edén, M., and Levitt, M.H. (2000) Synchronous helical pulse sequences in magic-angle spinning nuclear magnetic resonance: double quantum recoupling of multiple-spin systems. *J. Chem. Phys.*, **112**, 8539.

33. Feike, M., Demco, D.E., Graf, R., Gottwald, J., Hafner, S., and Spiess, H.W. (1996) Broadband multiple-quantum NMR spectroscopy. *J. Magn. Reson. A*, **122**, 214.

34. Kroto, H.W., Heath, J.R., O'Brien, S.C., Curl, R.F., and Smalley, R.E. (1985) C60: buckminsterfullerene. *Nature*, **318**, 162.

35. Taylor, R., Hare, J.P., Abdul-Sada, A.K., and Kroto, H.W. (1990) Isolation, separation and characterisation of the fullerenes CG0 and CT0: the third form of carbon. *Chem. Commun.*, 1423.

36. Johnson, R.D., Meijer, G., Salem, J.R., and Bethune, D.S. (1991) 2D Nuclear magnetic resonance study of the structure of the fullerene C70. *J. Am. Chem. Soc.*, **113**, 3619.

37. Yannoni, C.S., Bernier, P.P., Bethune, D.S., Meijer, G., and Salem, J.R. (1991) NMR determination of the bond lengths in C60. *J. Am. Chem. Soc.*, **113**, 3190.

38. Fowler, P.W., Lazzeretti, P., Malagoli, M., and Zanasi, R. (1991) Anisotropic nuclear magnetic shielding in C60. *J. Phys. Chem.*, **95**, 6404.

39. Yannoni, C.S., Johnson, R.D., Meijer, G., Bethune, D.S., and Salem, J.R.

(1991) 13C NMR study of the C60 cluster in the solid state: molecular motion and carbon chemical shift anisotropy. *J. Phys. Chem.*, **95**, 9.

40. Piskoti, C., Yarger, J., and Zettl, A. (1998) C36, a new carbon solid. *Nature*, **393**, 771.

41. Tycko, R., Dabbagh, G., Fleming, R.M., Haddon, R.C., Makhija, A.V., and Zahurak, S.M. (1991) Molecular dynamics and the phase transition in solid C60. *Phys. Rev. Lett.*, **67**, 1886.

42. Walton, J.H., Kamasa-Quashie, A.K., Joers, J.M., and Gullion, T. (1993) Spin-rotation relaxation in C60. *Chem. Phys. Lett.*, **203**, 237.

43. Firtej, L., Belahmer, Z., Bernier, P., Zahab, A., Ribet, M., Coustel, N., and Aznar, R. (1993) Molecular motion in solid C70 by 13C high resolution NMR. *Solid State Commun.*, **87**, 669.

44. Waltont, J.H. and Gullion, T. (1994) High-pressure 13C NMR of ca in the solid state. *J. Phys. Chem.*, **98**, 13064.

45. Williams, R.M., Zwier, J.M., and Verhoeven, J.W. (1994) Interactions of fullerenes and calixarenes in the solid state studied with 13C CP-MAS NMR. *J. Am. Chem. Soc.*, **116**, 6965.

46. Kolodziejski, W., Corma, A., Barras, J., and Hinowskis, J. (1995) Detection of fulleroid sites in fullerene-60 by high-resolution solid-state ′H NMR. *J. Phys. Chem.*, **99**, 3365.

47. He, H., Barras, J., Foulkes, J., and Klinowski, J. (1997) Solid-state NMR studies of fullerene C60/benzene solvates. *J. Phys. Chem. B*, **101**, 117.

48. Collins, C., Foulkes, J., Bonda, A.D., and Klinowski, J. (1999) Crystalline C60.2CHBr3 solvate : a solid-state study. *Phys. Chem. Chem. Phys.*, **1**, 5323.

49. Holleman, I., Robyr, P., Kentgens, A.P.M., Meier, B.H., and Meijer, G. (1999) Motion of CO molecules in solid C60 probed by solid-state NMR. *J. Am. Chem. Soc.*, **121**, 199.

50. Li, M. and Chen, Q. (2003) Interactions between fullerene(C60) and poly(ethylene oxide) in their complexes as revealed by high-resolution solid-state 13C NMR spectroscopy. *Polymer*, **44**, 2793.

51. Tomaselli, M. and Meier, B.H. (2001) Rotational-state selective nuclear magnetic resonance spectra of hydrogen in a molecular trap. *J. Chem. Phys.*, **115**, 11017.

52. Carravetta, M., Murata, Y., Murata, M., Heinmaa, I., Stern, R., Tontcheva, A., Samoson, A., Rubin, Y., Komatsu, K., and Levitt, M.H. (2004) Solid-state NMR spectroscopy of molecular hydrogen trapped inside an open-cage fullerene. *J. Am. Chem. Soc.*, **126**, 4092.

53. Orendt, A.M. (2002) Fullerenes and related molecules as studied by solid state NMR. *Encycl. Nucl. Magn. Res.*, **9**, 551.

54. Carravetta, M., Danquigny, A., Mamone, S., Cuda, F., Johannessen, O.G., Heinmaa, I., Panesar, K., Stern, R., Grossel, M.C., Horsewill, A.J., Samoson, A., Murata, M., Murata, Y., Komatsud, K., and Levitt, M.H. (2007) Solid-state NMR of endohedral hydrogen– fullerene complexes. *Phys. Chem. Chem. Phys.*, **9**, 4879.

55. Pennington, C.H. and Stenger, V.A. (1996) Nuclear magnetic resonance of C60 and fulleride superconductors. *Rev. Mod. Phys.*, **68**, 855.

56. Buehl, M. and Hirsch, A. (2001) Spherical aromaticity of fullerenes. *Chem. Rev.*, **101**, 1153.

57. Hebard, A.F., Rosseinsky, M.J., Haddon, R.C., Murphy, D.W., Glarum, S.H., Palstra, T.T.M., Ramirez, P., and Kortan, A.R. (1991) Superconductivity at 18 K in potassium-doped C60. *Nature*, **350**, 600.

58. Carravetta, M., Edén, M., Johannessen, O.G., Luthman, H., Verdegem, P.J.E., Lugtenburg, J., Sebald, A., and Levitt, M.H. (2001) Estimation of carbon-carbon bond lengths and medium-range internuclear distances by solid-state nuclear magnetic resonance. *J. Am. Chem. Soc.*, **123**, 10628.

59. Carravetta, M., Edén, M., Brinkmann, A., Zhao, X., and Levitt, M.H. (2000) Symmetry principles for the design of radiofrequency pulse sequences in the nuclear magnetic resonance of rotating solids. *Chem. Phys. Lett.*, **321**, 205.

60. Tang, X.-P., Kleinhammes, A., Shimoda, H., Fleming, L., Bennoune, K.Y., Sinha, S., Bower, C., Zhou, O., and Wu, Y. (2000) Electronic structures of single-walled carbon nanotubes determined by NMR. *Science*, **288**, 492.
61. Slichter, C.P. (1996) in *Principles of Magnetic Resonance*, Vol. 4 (eds D.M. Grant and R.K. Harris), John Wiley & Sons, Ltd, Chichester, p. 2672.
62. Goze-Bac, C., Latil, S., Lauginie, P., Jourdain, V., Conard, J., Duclaux, L., Rubio, A., and Bernier, P. (2002) Magnetic interactions in carbon nanostructures. *Carbon*, **40**, 1825.
63. Besleya, N.A. and Noble, A. (2008) NMR chemical shifts of molecules encapsulated in single walled carbon nanotubes. *J. Chem. Phys.*, **128**, 101102.
64. Kleinhammes, A., Mao, S.-H., Yang, X.-J., Tang, X.-P., Shimoda, H., Lu, J.P., Zhou, O., and Wu, Y. (2003) Gas adsorption in single-walled carbon nanotubes studied by NMR. *Phys. Rev. B*, **68**, 075418.
65. Goze-Bac, C., Bernier, P., Latil, S., Jourdain, V., Rubio, A., Jhang, S.H., Lee, S.W., Park, Y.W., Holzinger, M., and Hirsch, A. (2001) 13C NMR investigation of carbon nanotubes and derivatives. *Curr. Appl. Phys.*, **1**, 149.
66. Alemany, L.B., Zhang, L., Zeng, L., Edwards, C.L., and Barron, A.R. (2007) Solid-state NMR analysis of fluorinated single-walled carbon nanotubes: assessing the extent of fluorination. *Chem. Mater.*, **19**, 735.
67. Engtrakul, C., Davis, M.F., Gennett, T., Dillon, A.C., Jones, K.M., and Heben, M.J. (2005) Protonation of carbon single-walled nanotubes studied using 13C and 1H-13C cross polarization nuclear magnetic resonance and raman spectroscopies. *J. Am. Chem. Soc.*, **127**, 17548.
68. Cahill, L.S., Yao, Z., Adronov, A., Penner, J., Moonoosawmy, K.R., Kruse, P., and Goward, G.R. (2004) Polymer-functionalized carbon nanotubes investigated by solid-state nuclear magnetic resonance and scanning tunneling microscopy. *J. Phys. Chem. B*, **108**, 11412.
69. Hing, A.W., Vega, S., and Schaefer, J. (1992) Transferred-echo double-resonance NMR. *J. Magn. Reson.*, **96**, 205.
70. Yan, Z., Ma, D., Zhuang, J., Liu, X., Liu, X., Han, X., and Bao, X. (2002) In situ solid state NMR observation of the methanol-to-hydrocarbons (MTH) process over nanosized and microsized HZSM-5 zeolites. *Phys. Chem. Chem. Phys.*, **4**, 4602.
71. Mayer, C. and Lukowski, G. (2000) Solid state NMR investigations on nanosized carrier systems. *Pharm. Res.*, **17**, 486.
72. Zhang, X., Dieu Do, M., Dean, K., Hoobin, P., and Burgar, I.M. (2007) Wheat-gluten-based natural polymer nanoparticle composites. *Biomacromolecules*, **8**, 345.
73. Mayeri, D., Phillips, B.L., Augustine, M.P., and Kauzlarich, S.M. (2001) NMR study of the synthesis of alkyl-terminated silicon nanoparticles from the reaction of SiCl4 with the zintl salt, NaSi. *Chem. Mater.*, **13**, 765.
74. Giuliani, J.R., Harley, S.J., Carter, R.S., Power, P.P., and Augustine, M.P. (2007) Using liquid and solid state NMR and photoluminescence to study the synthesis and solubility properties of amine capped silicon nanoparticles. *Solid State Nucl. Magn. Res.*, **32**, 1.
75. Pery, T., Pelzer, K., Buntkowsky, G., Philippot, K., Limbach, H.-H., and Chaudret, B. (2005) Direct NMR evidence for the presence of mobile surface hydrides on ruthenium nanoparticles. *Chem. Phys. Chem.*, **6**, 605.
76. Zhou, H., Du, F., Li, X., Zhang, B., Li, W., and Yan, B. (2008) Characterization of organic molecules attached to gold nanoparticle surface using high resolution magic angle spinning 1H NMR. *J. Phys. Chem. C*, **112**, 19360.
77. Badia, A., Demers, L., Dickinson, L., Morin, F.G., Lennox, R.B., and Reven, L. (1997) Gold-sulfur interactions in alkylthiol self-assembled monolayers formed on gold nanoparticles studied by solid-state NMR. *J. Am. Chem. Soc.*, **119**, 11104.

78. Bower, P.V., Louie, E.A., Long, J.R., Stayton, P.S., and Drobny, G.P. (2005) Solid-state NMR structural studies of peptides immobilized on gold nanoparticles. *Langmuir*, **21**, 3002.
79. Fiurasek, P. and Reven, L. (2007) Phosphonic and sulfonic acid-functionalized gold nanoparticles: a solid-state NMR study. *Langmuir*, **23**, 2857.
80. García-Antón, J., Axet, M.R., Jansat, S., Philippot, K., Chaudret, B., Tal Pery, T., Buntkowsky, G., and Limbach, H.-H. (2008) Reactions of olefins with ruthenium hydride nanoparticles: NMR characterization, hydride titration, and room-temperature C–C bond activation. *Angew. Chem. Int. Ed.*, **47**, 2074.
81. Nicholas, J.B., Kheir, A.A., Xu, T., Krawietz, T.R., and Haw, J.F. (1998) Theoretical and solid-state NMR study of acetylene adsorption on nano-sized MgO. *J. Am. Chem. Soc.*, **120**, 10471.
82. Reyes-Garcia, E.A., Sun, Y., Reyes-Gil, K., and Raftery, D. (2007) 15N solid state NMR and EPR characterization of N-doped TiO2 photocatalysts. *J. Phys. Chem. C*, **111**, 2738.
83. Gervais, C., Smith, M.E., Pottier, A., Jolivet, J.-P., and Babonneau, F. (2001) Solid-state 47,49Ti NMR determination of the phase distribution of titania nanoparticles. *Chem. Mater.*, **13**, 462.
84. Scolan, E., Magnenet, C., Massiot, D., and Sanchez, C. (1999) Surface and bulk characterisation of titanium-oxo clusters and nanosized titania particles through 17O solid state NMR. *J. Mater. Chem.*, **9**, 2467.
85. Rawal, A., Wei, X., Akinc, M., and Schmidt-Rohr, K. (2008) Dispersion of silicate in tricalcium phosphate elucidated by solid-state NMR. *Chem. Mater.*, **20**, 2583.
86. Pawsey, S., Yach, K., and Reven, L. (2002) Self-assembly of carboxyalkylphosphonic acids on metal oxide powders. *Langmuir*, **18**, 5205.
87. Jaeger, C., Welze, T., Meyer-Zaika, W., and Epple, M. (2006) A solid-state NMR investigation of the structure of nanocrystalline hydroxyapatite. *Magn. Reson. Chem.*, **44**, 573.
88. Lo, A.Y.H., Sudarsan, V., Sivakumar, S., van Veggel, F., and Schurko, R.W. (2007) Multinuclear solid-state NMR spectroscopy of doped lanthanum fluoride nanoparticles. *J. Am. Chem. Soc.*, **129**, 4687.
89. Donnet, J.-B., Fousson, E., Delmotte, L., Samirant, M., Baras, C., Wang, T.K., and Eckhardt, A. (2000) 13C NMR characterization of nanodiamonds. *C. R. Acad. Sci. IIC*, **3**, 831.
90. Thayer, A.M., Steigerwald, M.L., Duncan, T.M., and Douglass, D.C. (1988) NMR study of semiconductor molecular clusters. *Phys. Rev. Lett.*, **60**, 2673.
91. Ladizhansky, V., Hodes, G., and Vega, S. (1998) Surface properties of precipitated CdS nanoparticles studied by NMR. *J. Phys. Chem. B*, **102**, 8505.
92. Tomaselli, M., Yarger, J.L., Bruchez, M., Havlin, R.H., de Graw, D., Pines, A., and Alivisatos, A.P.Jr. (1999) NMR study of InP quantum dots: surface structure and size effects. *J. Chem. Phys.*, **110**, 8861.
93. Ratcliffe, C.I., Yu, K., Ripmeester, J.A., Zaman, M.B., Badarau, C., and Singh, S. (2006) Solid state NMR studies of photoluminescent cadmium chalcogenide nanoparticles. *Phys. Chem. Chem. Phys.*, **8**, 3510.
94. Becerra, L.R., Murray, C.B., Griffin, R.G., and Bawendi, M.G. (1994) Investigation of the surface morphology of capped CdSe nanocrystallites by 31P nuclear magnetic resonance. *J. Chem. Phys.*, **100**, 3297.
95. Pentimalli, M., Antolini, F., Bauer, E.M., Capitani, D., Di Luccio, T., and Viel, S. (2006) A solid state nuclear magnetic resonance study on the thermolytic synthesis of CdS nanoparticles in a polystyrene matrix. *Mater. Lett.*, **60**, 2657.
96. Elbaum, R., Vega, S., and Hodes, G. (2001) Preparation and surface structure of nanocrystalline cadmium sulfide (sulfoselenide) precipitated from dimethyl sulfoxide solutions. *Chem. Mater.*, **13**, 2272.

97. Berrettini, M.G., Braun, G., Hu, J.G., and Strouse, G.F. (2004) NMR analysis of surfaces and interfaces in 2-nm CdSe. *J. Am. Chem. Soc.*, **126**, 7063.
98. Ladizhansky, V., Hodes, G., and Vega, S. (2000) Solid state NMR study of water binding on the surface of CdS nanoparticles. *J. Phys. Chem. B*, **104**, 1939.
99. Damodaran, K., Sanjayan, G.J., Rajamohanan, P.R., Ganapathy, S., and Ganesh, K.N. (2001) Solid state NMR of a molecular self-assembly: multinuclear approach to the cyanuric acid-melamine system. *Org. Lett.*, **3**, 1921.
100. Pham, T.N., Masiero, S., Gottarelli, G., and Brown, S.P. (2005) Identification by 15N refocused INADEQUATE MAS NMR of intermolecular hydrogen bonding that directs the self-assembly of modified DNA bases. *J. Am. Chem. Soc.*, **127**, 16018.
101. Pham, T.N., Griffin, J.M., Masiero, S., Lena, S., Gottarelli, G., Hodgkinson, P., Filipe, C., and Brown, S.P. (2007) Quantifying hydrogen-bonding strength: the measurement of 2hJNN couplings in self-assembled guanosines by solid-state 15N spin-echo MAS NMR. *Phys. Chem. Chem. Phys.*, **9**, 3416.
102. Arrachart, G., Carcel, C., Moreau, J.J.E., Hartmeyer, G., Alonso, B., Massiot, D., Creff, G., Bantignies, J.-L., Dieudonne, P., Wong Chi Man, M., Althoff, G., Babonneau, F., and Bonhomme, C. (2008) Organosilicas based on purine–pyrimidine base pair assemblies: a solid state NMR point of view. *J. Mater. Chem.*, **18**, 392.
103. Badia, A., Lennox, R.B., and Reven, L. (2000) A dynamic view of self-assembled monolayers. *Acc. Chem. Res.*, **33**, 475.
104. Raitza, M., Wegmann, J., Bachmann, S., and Albert, K. (2000) Investigating the surface morphology of triacontyl phases with spin-diffusion solid-state NMR spectroscopy. *Angew. Chem. Int. Ed.*, **39**, 3486.
105. Kresge, C.T., Leonowicz, M.E., Roth, W.J., Vartuli, J.C., and Beck, J.S. (1992) Ordered mesoporous molecular sieves synthesized by a liquid-crystal template mechanism. *Nature*, **359**, 710.
106. Zhao, D., Feng, J., Huo, Q., Melosh, N., Fredrickson, G., Chmelka, B., and Stucky, G.D. (1998) Triblock copolymer syntheses of mesoporous silica with periodic 50 to 300 angstrom pores. *Science*, **279**, 548.
107. Wang, L.-Q., Exarhos, G.J., and Liu, J. (1999) Nuclear magnetic resonance–characterization of self-assembled nanostructured materials. *Adv. Mater.*, **11**, 1331.
108. Epping, J. and Chmelka, B.F. (2006) Nucleation and growth of zeolites and inorganic mesoporous solids: molecular insights from magnetic resonance spectroscopy. *Curr. Opin. Colloid Interface Sci.*, **11**, 81.
109. Geppi, M., Borsacchi, S., Mollica, G., and Veracini, C.A. (2009) Applications of solid state NMR to the study of organic/inorganic multicomponent materials. *Appl. Spectrosc. Rev.*, **44**, 1.
110. Kolodziejski, W., Corma, A., Navarro, M.-T., and Perez-Pariente, J. (1993) Solid-state NMR study of ordered mesoporous aluminosilicate MCM-41 synthesized on a liquid-crystal template. *Solid State Nucl. Magn. Reson.*, **2**, 253.
111. Steel, A., Carr, S.W., and Anderson, M.W. (1996) 29Si solid-state NMR study of mesoporous M41S materials. *Chem. Mater.*, **7**, 1829.
112. Luhmer, M., d'Espinose, J.B., Hommel, H., and Legrand, A.P. (1996) High-resolution 29Si solid-state NMR study of silicon functionality distribution on the surface of silicas. *Magn. Reson. Imaging*, **14**, 911.
113. Liu, S., He, H., Luan, Z., and Klinowski, J. (1996) Solid-state NMR studies of the borosilicate mesoporous molecular sieve MCM-41. *J. Chem. Soc., Faraday Trans.*, **92**, 2011.
114. Khimyak, Y.Z. and Klinowski, J. (2002) Synthesis and characterisation of mesoporous aluminophosphates containing boron. *J. Mater. Chem.*, **12**, 1079.
115. Laha, S.C., Kadgaonkar, M.D., Anuji, A., Ganapathy, S., Amoureux, J.P., and Kumar, R. (2003) Multinuclear solid-state MAS/CP-MAS NMR studies

of promoter (phosphate)-enhanced crystallization of siliceous MCM-41. *J. Phys. Chem. B*, **107**, 14171.

116. Hedin, N., Graf, R., Christiansen, S.C., Gervais, C., Hayward, R.C., Eckert, J., and Chmelka, B.F. (2004) Structure of a surfactant-templated silicate framework in the absence of 3D crystallinity. *J. Am. Chem. Soc.*, **126**, 9425.

117. Huang, Y., Yan, Z., and Richer, R. (2005) Characterization of BAPO- and SAPO-based mesoporous materials by solid-state NMR spectroscopy. *Chem. Mater.*, **17**, 6545.

118. Lin, K.S.K., Tseng, Y.-H., Mou, Y., Hsu, Y.-C., Yang, C.-M., and Chan, J.C.C. (2005) Mechanistic study of apatite formation on bioactive glass surface using 31P solid-state NMR spectroscopy. *Chem. Mater.*, **17**, 4493.

119. Hu, W., Luo, Q., Su, Y., Chen, L., Yue, Y., Ye, C., and Deng, F. (2006) Acid sites in mesoporous Al-SBA-15 material as revealed by solid-state NMR spectroscopy. *Micro. Meso. Mater.*, **92**, 22.

120. Masse, S., Laurent, G., and Babonneau, F. (2007) High temperature behavior of periodic mesoporous ethanesilica glasses prepared from a bridged silsesquioxane and a non-ionic triblock copolymer. *J. Non-Cryst. Solids*, **353**, 1109.

121. Skadtchenko, B.O., Rao, Y., Kemp, T.F., Bhattacharya, P., Thomas, P.A., Trudeau, M., Smith, M.E., and Antonelli, D.M. (2007) A solid-state 17O NMR study of local order and crystallinity in amine-templated mesoporous Nb oxide. *Angew. Chem. Int. Ed.*, **46**, 2635.

122. Kao, H.-M., Chang, P.-C., Liao, Y.-W., Lee, L.-P., and Chien, C.-H. (2008) Solid-state NMR characterization of the acid sites in cubic mesoporous Al-MCM-48 materials using trimethylphosphine oxide as a 31P NMR probe. *Microporous Mesoporous Mater.*, **114**, 352.

123. Rao, Y., Kemp, T.F., Trudeau, M., Smith, M.E., and Antonelli, D.M. (2008) 17O and 15N solid state NMR studies on ligand-assisted templating and oxygen coordination in the walls of mesoporous Nb, Ta and Ti oxides. *J. Am. Chem. Soc.*, 10.1021/ja8056387.

124. Coelho, C., Azais, T., Bonhomme, C., Bonhomme-Coury, L., Boissière, C., Laurent, G., and Massiot, D. (2008) Efficiency of dipolar and J-derived solid-state NMR techniques for a new pair of nuclei 31P,29Si. Towards the characterization of Si-O-P mesoporous materials. *C. R. Chim.*, **11**, 387.

125. Wang, L.-Q., Liu, J., Exarhos, G.J., and Bunker, B.C. (1996) Investigation of the structure and dynamics of surfactant molecules in mesophase silicates using solid-state 13C NMR. *Langmuir*, **12**, 2663.

126. Melosh, N.A., Lipic, P., Bates, F.S., Wudl, F., Stucky, G.D., Fredrickson, G.H., and Chmelka, B.F. (1999) Molecular and mesoscopic structures of transparent block copolymer-silica monoliths. *Macromolecules*, **32**, 4332.

127. De Paul, S.M., Zwanziger, J.W., Ulrich, R., Wiesner, U., and Spiess, H.W. (1999) Structure, mobility, and interface characterization of self-organized organic-inorganic hybrid materials by solid state NMR. *J. Am. Chem. Soc.*, **121**, 5727.

128. Janicke, M.T., Landry, C.C., Christiansen, S.C., Kumar, D., Stucky, G.D., and Chmelka, B.F. (1998) Aluminum incorporation and interfacial structures in MCM-41 mesoporous molecular sieves. *J. Am. Chem. Soc.*, **120**, 6940.

129. Janicke, M.T., Landry, C.C., Christiansen, S.C., Birtalan, S., Stucky, G.D., and Chmelka, B.F. (1999) Low silica MCM-41 composites and mesoporous solids. *Chem. Mater.*, **11**, 1342.

130. Schulz, M., Tiemann, M., Froeba, M., and Jaeger, C. (2000) NMR characterization of mesostructured aluminophosphates. *J. Phys. Chem. B*, **104**, 10473.

131. Christiansen, S.C., Zhao, D., Janicke, M.T., Landry, C.C., Stucky, G.D., and Chmelka, B.F. (2001) Molecularly ordered inorganic framework in layered silicate surfactant mesophases. *J. Am. Chem. Soc.*, **123**, 4519.

132. Khimyak, Y.Z. and Klinowski, J. (2001) Solid-state NMR studies of the organic template in mesostructured aluminophosphates. *Phys. Chem. Chem. Phys.*, **3**, 616.

133. Simonutti, R., Comotti, A., Bracco, S., and Sozzani, P. (2001) Surfactant organization in MCM-41 mesoporous materials as studied by 13C and 29Si solid-state NMR. *Chem. Mater.*, **13**, 771.

134. Jones, M.D., Duer, M.J., Hermans, S., Khimyak, Y.K., Johnson, B.F.G., and Thomas, J.M. (2002) Solid-state NMR studies of MCM-41 supported with a highly catalytically active cluster. *Angew. Chem. Int. Ed.*, **41**, 4726.

135. Sizun, C., Raya, J., Intasiri, A., Boos, A., and Elbayed, K. (2003) Investigation of the surfactants in CTAB-templated mesoporous silica by 1H HRMAS NMR.*Micro. Meso. Mater.*, **66**, 27.

136. Alam, T.M. and Fan, H. (2003) Investigation of templated mesoporous silicate thin films using high speed, solid-state 1H MAS and double quantum NMR spectroscopy. *Macromol. Chem. Phys.*, **204**, 2023.

137. Trébosc, J., Wiench, J.W., Huh, S., Lin, V.S.-Y., and Pruski, M. (2005) Solid-state NMR study of MCM-41-type mesoporous silica nanoparticles. *J. Am. Chem. Soc.*, **127**, 3057.

138. Alonso, B., Douy, A., Véron, E., Perez, J., Rager, M.-N., and Massiot, D. (2004) Morphological and textural control of spray-dried mesoporous silica-based spheres. *J. Mater. Chem.*, **14**, 2006.

139. Egger, C.C., Anderson, M.W., Tiddy, G.J.T., and Casci, J.L. (2005) In situ NMR and XRD studies of the growth mechanism of SBA-1. *Phys. Chem. Chem. Phys.*, **7**, 1845.

140. Boettcher, S.W., Bartl, M.H., Hu, J.G., and Stucky, G.D. (2005) Structural analysis of hybrid titania-based mesostructured composites. *J. Am. Chem. Soc.*, **127**, 9721.

141. Baccile, N., Laurent, G., Bonhomme, C., Innocenzi, P., and Babonneau, F. (2007) Solid-state NMR characterization of the surfactant-silica interface in templated silicas: acidic versus basic conditions. *Chem. Mater.*, **19**, 1343.

142. Han, O.H., Paik, Y., Moon, Y.S., Lee, S.K., Kim, T.Y., Lee, Y.H., and Lee, W.I. (2007) Selective synthesis of lamellar titania with carboxylate precursor and characterization by solid-state NMR. *Chem. Mater.*, **19**, 3615.

143. Cadars, S., Mifsud, N., Lesage, A., Epping, J.D., Hedin, N., Chmelka, B.F., and Emsley, L. (2008) Dynamics and disorder in surfactant-templated silicate layers studied by solid-state NMR dephasing times and correlated line shapes. *J. Phys. Chem. C*, **112**, 9145.

144. Leonova, E., Izquierdo-Barba, I., Arcos, D., Lòpez-Noriega, A., Hedin, N., Vallet-Regì, M., and Edén, M. (2008) Multinuclear solid-state NMR studies of ordered mesoporous bioactive glasses. *J. Phys. Chem. C*, **112**, 5552.

145. Gedat, E., Schreiber, A., Albrecht, J., Emmler, Th., Shenderovich, I., Findenegg, G.H., Limbach, H.-H., and Buntkowsky, G. (2002) 2H-solid-state NMR study of benzene-d6 confined in mesoporous silica SBA-15. *J. Phys. Chem. B*, **106**, 1977.

146. Wasyluk, L., Peplinska, B., Klinowski, J., and Jurga, S. (2002) NMR studies of the molecular dynamics of tert-butyl chloride confined in the mesoporous molecular sieve MCM-41. *Phys. Chem. Chem. Phys.*, **4**, 2392.

147. Shenderovich, I.G., Buntkowsky, G., Schreiber, A., Gedat, E., Sharif, S., Albrecht, J., Golubev, N.S., Findenegg, G.H., and Limbach, H.-H. (2003) Pyridine-15N–a mobile NMR sensor for surface acidity and surface defects of mesoporous silica. *J. Phys. Chem. B*, **107**, 11924.

148. Luo, Q., Deng, F., Yuan, Z., Yang, J., Zhang, M., Yue, Y., and Ye, C. (2003) Using trimethylphosphine as a probe molecule to study the acid sites in Al-MCM-41 materials by solid-state NMR spectroscopy. *J. Phys. Chem. B*, **107**, 2435.

149. Komori, Y. and Hayashi, S. (2004) Dynamics of p-nitroaniline molecules in FSM-type mesoporous silicas studied by solid-state NMR. *Microporous Mesoporous Mater.*, **68**, 111.

150. Masierak, W., Emmler, T., Gedat, E., Schreiber, A., Findenegg, G.H., and

Buntkowsky, G. (2004) Microcrystallization of benzene-d6 in mesoporous silica revealed by 2H solid-state nuclear magnetic resonance. *J. Phys. Chem. B*, **108**, 18890.

151. Gruenberg, B., Emmler, T., Gedat, E., Shenderovich, I., Findenegg, G.H., Limbach, H.-H., and Buntkowsky, G. (2004) Hydrogen bonding of water confined in mesoporous silica MCM-41 and SBA-15 studied by 1H solid-state NMR. *Chem. Eur. J.*, **10**, 5689.

152. Babonneau, F., Yeung, L., Steunou, N., Gervais, C., Ramila, A., and Vallet-Regi, M. (2004) Solid state NMR characterisation of encapsulated molecules in mesoporous silica. *J. Sol-Gel Sci. Technol.*, **31**, 219.

153. Pizzanelli, S., Kababya, S., Frydman, V., Landau, M., and Vega, S. (2005) NMR study of the adsorption-desorption kinetics of dissolved tetraalanine in MCM-41 mesoporous material. *J. Phys. Chem. B*, **109**, 8029.

154. Azaïs, T., Tourné-Péteilh, C., Aussenac, F., Baccile, N., Coelho, C., Devoisselle, J.-M., and Babonneau, F. (2006) Solid-state NMR study of ibuprofen confined in MCM-41 Material. *Chem. Mater.*, **18**, 6382.

155. Vyalikh, A., Emmler, Th., Shenderovich, I., Zeng, Y., Findenegg, G.H., and Buntkowsky, G. (2007) 2H-solid state NMR and DSC study of isobutyric acid in mesoporous silica materials. *Phys. Chem. Chem. Phys.*, **9**, 2249.

156. Buntkowsky, G., Breitzke, H., Adamczyk, A., Roelofs, F., Emmler, T., Gedat, E., Gruenberg, B., Xu, Y., Limbach, H.-H., Shenderovich, I., Vyalikhzb, A., and Findenegg, G. (2007) Structural and dynamical properties of guest molecules confined in mesoporous silica materials revealed by NMR. *Phys. Chem. Chem. Phys.*, **9**, 4843.

157. Shenderovich, I.G., Mauder, D., Akcakayiran, D., Buntkowsky, G., Limbach, H.-H., and Findenegg, G.H. (2007) NMR provides checklist of generic properties for atomic-scale models of periodic mesoporous silicas. *J. Phys. Chem. B*, **111**, 12088.

158. Xu, M., Harris, K.D.M., and Thomas, J.M. (2008) Mapping the evolution of adsorption of water in nanoporous silica by in situ solid-state 1H NMR spectroscopy. *J. Am. Chem. Soc.*, **130**, 5880.

159. Baccile, N. and Babonneau, F. (2008) Organo-modified mesoporous silicas for organic pollutant removal in water: solid-state NMR study of the organic/silica interactions. *Microporous Mesoporous Mater.*, **110**, 534.

160. O'Brien, S., Keates, J.M., Barlow, S., Drewitt, M.J., Payne, B.R., and O'Hare, D. (1998) Synthesis and characterization of ferrocenyl-modified mesoporous silicates. *Chem. Mater.*, **10**, 4088.

161. Babonneau, F., Bonhomme, C., Gervais, C., and Maquet, J. (2004) Advances in characterization methods for sol-gel derived materials: high resolution solid state nuclear magnetic resonance. *J. Sol-Gel. Sci. Tech.*, **31**, 9.

162. Trebosc, J., Wiench, J.W., Huh, S., Lin, V.S.-Y., and Pruski, M. (2005) Studies of organically functionalized mesoporous silicas using heteronuclear solid-state correlation NMR spectroscopy under fast magic angle spinning. *J. Am. Chem. Soc.*, **127**, 7587.

163. Kumar, R., Chen, H.-T., Escoto, J.L.V., Lin, V.S.-Y., and Pruski, M. (2006) Template removal and thermal stability of organically functionalized mesoporous silica nanoparticles. *Chem. Mater.*, **18**, 4319.

164. Kao, H.-M., Chang, P.-C., Wu, J.-D., Chiang, A.S.T., and Lee, C.-H. (2006) Direct synthesis, characterization and solid-state NMR spectroscopy of large-pore vinyl-functionalized cubic mesoporous silica FDU-12. *Microporous Mesoporous Mater.*, **97**, 9.

165. Wiench, J.W., Bronnimann, C.E., Lin, V.S.-Y., and Pruski, M. (2007) Chemical shift correlation NMR spectroscopy with indirect detection in fast rotating solids: studies of organically functionalized mesoporous silicas. *J. Am. Chem. Soc.*, **129**, 12076.

166. Wiench, J.W., Avadhut, Y.S., Maity, N., Bhaduri, S., Lahiri, G.K., Pruski, M., and Ganapathy, S. (2007) Characterization of covalent linkages in organically functionalized MCM-41 mesoporous materials by solid-state NMR and theoretical calculations. *J. Phys. Chem. B*, **111**, 3877.

167. Morales, G., Athens, G., Chmelka, B.F., van Grieken, R., and Melero, J.A. (2008) Aqueous-sensitive reaction sites in sulfonic acid-functionalized mesoporous silicas. *J. Catal.*, **254**, 205.

168. Melnyk, I.V., Zub, Y.L., Véron, E., Massiot, D., Cacciaguerra, T., and Alonso, B. (2008) Spray-dried mesoporous silica microspheres with adjustable texture and pore surfaces homogenously covered by accessible thiol functions. *J. Mater. Chem.*, **18**, 1368.

169. Tsai, H.-H.G., Jheng, G.-L., and Kao, H.-M. (2008) Direct evidence for interactions between acidic functional groups and silanols in cubic mesoporous organosilicas. *J. Am. Chem. Soc.*, **130**, 11566.

170. Kao, H.-M., Liao, C.-H., Hung, T.-T., Pan, Y.-C., and Chiang, A.S.T. (2008) Direct synthesis and solid-state NMR characterization of cubic mesoporous silica SBA-1 functionalized with phenyl groups. *Chem. Mater.*, **20**, 2412.

171. Andersson, J., Johannessen, E., Areva, S., Baccile, N., Azaïs, T., and Lindén, M. Physical properties and in vitro bioactivity of hierarchical porous silica–HAP composites, *J. Mater. Chem.*, **5**, 463.

172. Titirici, M.-M., Antonietti, M., and Baccile, N. (2008) Hydrothermal carbon from biomass: a comparison of the local structure from poly- to monosaccharides and pentoses/hexoses. *Green Chem.*, **10**, 1204.

173. Baccile, N., Laurent, G., Babonneau, F., Fayon, F., Titirici, M.-M., and Antonietti, M. (2009) Structural characterization of hydrothermal carbon spheres by advanced solid-state MAS 13C NMR investigations. *J. Phys. Chem. C*, **113**, 9644.

7
New Tools for Structure Elucidation in the Gas Phase: IR Spectroscopy of Bare and Doped Silicon Nanoparticles

Philipp Gruene, Jonathan T. Lyon, Gerard Meijer, Peter Lievens, and André Fielicke

7.1
Introduction

For a long time, the study of matter focused on systems that are either very small, like atoms and molecules, or so large that they can be treated as infinite. Both of these extreme cases are rather well understood at present. An atom of a certain element is, for example, characterized by its ionization energy (IE), while a well-defined surface in the bulk phase is characterized by its work function. A piece of iron is magnetic, while the electrons in an iron atom have a certain spin. Two atoms are bound together by a specific binding energy, while the heat of vaporization has to be supplied in order to evaporate atoms from the corresponding condensed phase. But how do the properties of single atoms evolve into those of the bulk?

In the early 1980s, new experimental techniques allowed for the production of often elusive particles that contain variable numbers of atoms – between two and several tens or hundreds of thousands. Such aggregates are called *atomic clusters* and bridge the gap between atoms and the bulk. By studying clusters, it can be seen how the properties of the bulk emerge from the properties of the corresponding atoms and molecules [1–3].

Owing to their large fraction of surface atoms, clusters were initially mainly seen as model systems for extended surfaces, on which, for example, catalytic reactions could be studied [4]. However, it was soon recognized that clusters exhibit properties that do not necessarily evolve smoothly with particle size, but rather that there can be a nonscalable regime, in which the cluster may even behave differently from anything known for the atom or for the bulk [5]. This added a third dimension to the periodic table of the elements – the size of the particle. Many unique properties of clusters containing just a few atoms are known at present, for example, the occurrence of ferromagnetism [6] and ferroelectricity [7] in clusters of elements that are nonmagnetic in the bulk [8], or size-dependent changes in melting points [9].

Silicon clusters are among the most studied nanoparticles, which is mainly due to the importance of silicon in the semiconductor industry and other high-level

Ideas in Chemistry and Molecular Sciences: Advances in Nanotechnology, Materials and Devices.
Edited by Bruno Pignataro

ISBN: 978-3-527-32543-6

technological applications. The peculiarity of clusters, namely that the physical and chemical properties vary with size of the particle, brings along opportunities and pitfalls. On one hand, it might be possible to tailor desired properties by carefully controlling the size of the silicon structures. Examples of such devices include three-dimensional photonic silicon crystals [10], silicon-based visible light-emitters [11], and conducting silicon nanowires [12]. On the other hand, a mere downscaling of silicon devices may go hand in hand with changing characteristics of the material and thus may be intrinsically impossible. For example, it is well known that small silicon clusters bear different geometries compared to the bulk material [13, 14]. In contrast to carbon, silicon prefers sp^3 hybridization and thus is not known to form symmetric and compact structures, like fullerenes or nanotubes. Furthermore, the dangling bonds of silicon clusters render them rather reactive and unstable. The opposite would be needed if one thinks of silicon-based building blocks for nanoassembled materials. It has been argued, however, that doping silicon clusters with metal atoms might lead to more stable, symmetric cage structures [15–17].

An intriguing question is thus about how the geometries of silicon clusters change with particle size and how these structures can be modified, controlled, and stabilized upon proper doping with transition-metal atoms. Unfortunately, the determination of the geometric structure at the nanoscale is far from being trivial [18]. A simplification of this problem is to investigate free clusters in the gas phase. In this approach, interactions with the support are absent, and the focus lies on the intrinsic structure of the nanoparticle. Still, experiments that allow for detailed insights into the binding geometries of strongly bound clusters remained elusive for a long time. Only in the last 10 years methods have become available, by either improving existing methods or by developing entirely new ones, that are accurate enough to unravel fascinating structures of very small particles, typically containing between 3 and 30 atoms, in the gas phase.

A short overview of the instrumental methods that have been employed to study the geometries of isolated silicon clusters is given in Section 7.2. Section 7.3 provides an introduction into size-selective vibrational spectroscopy of gas-phase particles. All the approaches presented therein require very intense and tunable infrared (IR) light sources. The Free-Electron Laser for Infrared eXperiment (FELIX) meets these requirements and is briefly described. The results that form the focus of this chapter are obtained with infrared multiple photon dissociation (IR-MPD) spectroscopy, which is explained at the end of this section. In Section 7.4, pure silicon-cluster cations are studied applying IR-MPD. With the exact structure of the pure species known, the influence of dopant atoms can be investigated. Section 7.5 describes a method that can sensitively discriminate between silicon particles, in which the dopant is located on the cluster surface, and particles, in which the dopant is fully surrounded by silicon atoms. Detailed structural insight from vibrational spectroscopy on doped silicon clusters is gained in Section 7.6. The chapter concludes with an outlook on future work on these systems in Section 7.7.

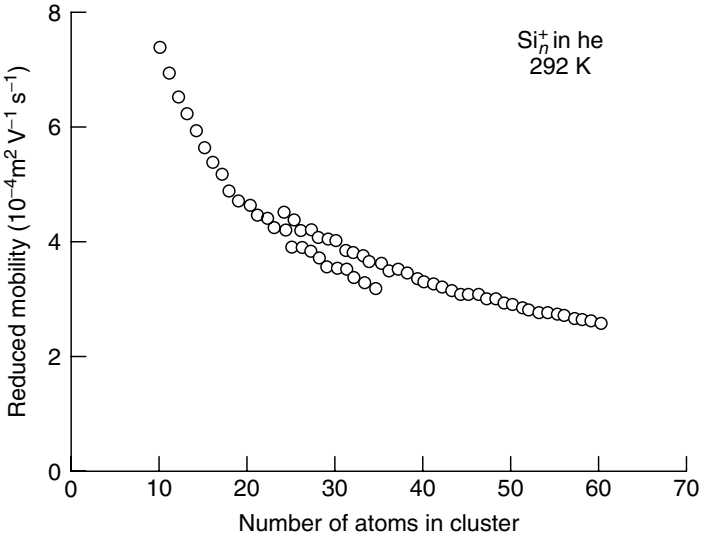

Figure 7.1 The reduced mobility of cationic silicon clusters in helium at 292 K against cluster size. Two structural families are visible, as well as multiple isomers in an intermediate size range. Reprint with permission from *J. Chem. Phys.* 1992, **96**, 9180. Copyright 1992, American Institute of Physics.

7.2
Methods for Structural Investigation of Silicon Clusters

7.2.1
Ion Mobility Measurements

A straightforward way to probe the shape of gas-phase ions is to measure their mobility under the influence of a weak electric field in a drift cell filled with an inert gas [19]. Ions with a large collisional cross section will drift slower than ions with a smaller collisional cross section. If a mass-selected ion is present in two isomeric forms that differ substantially in their shape, they can be resolved in the drift spectrum. Upon comparison with calculated cross sections for various isomers, insight into the shape of the species can be gained. This technique is most valuable for probing size-dependent structural transitions [20–22].

Silicon cluster cations have been among the very first species to be studied by ion-mobility experiments [23, 24]. Two different families of isomers could be resolved due to their different mobilities, as can be seen in Figure 7.1. One family, starting from Si_{10}^+, was identified as prolate or sausage-shaped. From clusters containing 23 or more atoms on, a more spherical oblate-shaped isomer was found. Up to Si_{35}^+ these two structures coexist, while larger clusters prefer the more spherical geometry.

Improvements in the experimental setup [25] led to a much better resolution and for many cluster sizes multiple isomers were found [26]. An unbiased global-search algorithm for the lowest energy isomer based on a genetic algorithm identified a variety of new energetically low-lying geometries. Their collisional cross sections were then compared with the experimental findings. A tri-capped trigonal prism (TTP) was identified as an important building block of cationic silicon clusters containing 12–18 atoms [14].

Obviously, ion mobility is limited to charged particles. Furthermore, it yields only a single experimental value that has to be compared with the outcome of quantum chemical predictions. The information content is thus restricted and different isomers that have similar collisional cross sections but different geometries cannot be distinguished.

7.2.2
Anion Photoelectron Spectroscopy

In anion photoelectron spectroscopy, a cluster anion is excited by means of an UV/vis laser with photon energy $h\nu$. If the photon energy exceeds the binding energy of the electron (electron affinity, *EA*), the electron is detached and any photon energy in excess of that needed for electron detachment is carried by the outgoing electron in the form of kinetic energy E_{kin} according to

$$E_{\mathrm{kin}} = h\nu - EA - E_{\mathrm{exc}}. \tag{7.1}$$

The resulting neutral cluster can either be in the ground state or in a vibronically excited state that lies above the ground state with an energy difference of E_{exc}. The detachment process is fast in comparison to structural rearrangements of the nuclei upon removal of the electron. That is the reason why it is generally stated that photoelectron spectroscopy of cluster anions probes the electronic structure of the neutral cluster in the ground-state geometry of its anion. The kinetic energy of the detached electron depends on the rovibronic states of the anion and the remaining neutral cluster. In addition to the valuable knowledge about electronic states, such spectra can distinguish between structural isomers if the changes in geometry lead to changes in the electronic levels. The electronic structure for various isomers can be predicted by means of quantum mechanical calculations and the results can be compared with the experimental outcome.

Photoelectron spectroscopy has been applied to anionic silicon clusters over a wide range of cluster sizes and detachment laser wavelengths [27–30]. The photoelectron spectra have confirmed the TTP as the dominant building block for clusters containing between 10 and 20 atoms [29]. For smaller clusters Si_{3-7}^-, some vibrational substructure could be resolved [28]. With regard to structural investigations, the resolution of vibrational substructure is highly desirable as molecular vibrations directly reflect the arrangements of atoms in the cluster and the forces acting between them.

7.2.3
Matrix Isolation Vibrational Spectroscopy

The primary technique for the measurement of vibrational spectra is IR absorption spectroscopy. Usually, however, clusters are produced over a broad size distribution and can be handled only in the gas phase. Therefore the achievable densities are low and do not allow for the application of standard spectroscopic techniques. Embedding clusters in an inert host matrix allows for their accumulation without further aggregation, as diffusion and subsequent reactions in the matrix are suppressed and the clusters remain isolated. The matrix usually consists of cryogenically solidified rare gases or chemically inert molecules like N_2. To date, Raman spectroscopy is the preferred technique for the study of the vibrational properties of metal clusters isolated in matrices. By tuning the excitation wavelength in resonance with an electronic transition, the intensity of vibrational transitions can be enhanced by a factor of up to $\sim 10^5$ compared to normal Raman spectra. This resonance-enhanced Raman spectroscopy has been intensively used to study the vibrational modes and force constants of small metal and lanthanide clusters [31].

The vibrational spectra of neutral silicon clusters containing four, six, and seven atoms accumulated in rare-gas matrices have been measured using surface-enhanced Raman spectroscopy (SERS) [13, 32]. In SERS, the electric field surrounding a silver or gold surface increases as the surface plasmons are excited by a laser. As Raman intensities are proportional to the electric field, the signal intensity increases substantially (up to 10^{11}) compared to conventional Raman

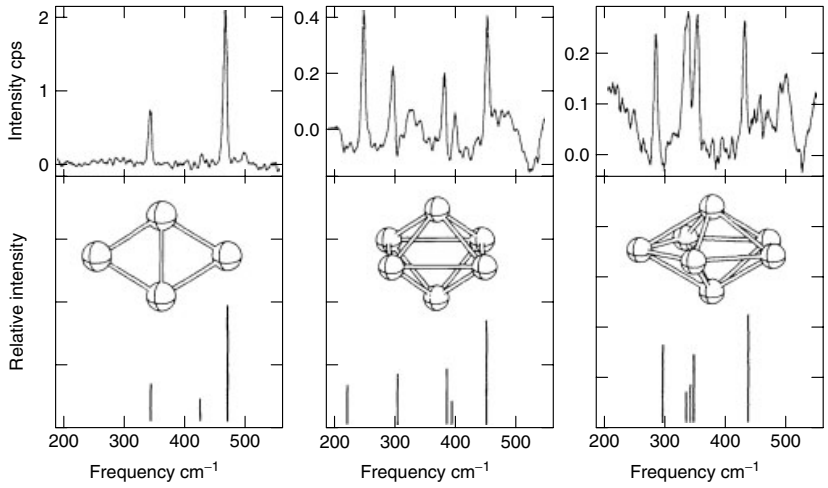

Figure 7.2 Measured Raman spectra of Si_4, Si_6, and Si_7 accumulated in a cryogenic matrix, predicted structures, and predicted spectra. Reprint with permission from *J. Chem. Phys.* 1999, **110**, 12161. Copyright 1999, American Institute of Physics.

spectroscopy. Small silicon clusters have also been detected after deposition into a rare-gas matrix using Fourier transform infrared (FTIR) spectroscopy [33]. On the basis of these studies, sound structural assignments have been made (see Figure 7.2). However, the data is limited to a few cluster sizes.

7.3 Infrared Multiple Photon Dissociation Spectroscopy

7.3.1 Gas Phase Spectroscopy Using Free-Electron Lasers

Besides the accumulation of clusters in a matrix, another way to account for the problem of a low particle density is to use more sensitive particle-detection methods. In particular, ion detection by means of mass spectrometry can have a detection efficiency close to unity and is obviously mass selective.

A suitable method for obtaining vibrational spectra of clusters in the gas phase is infrared multiple photon excitation (IR-MPE) spectroscopy [34]. This approach requires the absorption of many IR photons, until the cluster is excited to internal energies that lie either above its IE, such that ionization can occur, or to energies that lie above its lowest bond-dissociation energy (BDE), such that dissociation of the cluster becomes possible. Both processes can be sensitively detected by means of mass spectrometry but require very intense IR light sources to induce the absorption of the required large number of photons. Further, the light source must be tunable over a broad frequency range in order to cover the whole part of the spectrum, in which vibrational resonances can be expected. Until recently, there were no lasers available that met these requirements. The situation has changed with the development of free-electron lasers (FELs).

7.3.2 Working Principles of an FEL

An FEL is a unique light source, as the lasing medium is a beam of free electrons, whereas in conventional laser systems electrons are bound to atoms, molecules, or crystals. Obviously, the electrons are not completely free, but are under the influence of magnetic forces which cause them to radiate. Figure 7.3 shows the basic ingredients of an FEL. Electrons are accelerated to quasi-relativistic energies and injected into a periodic magnetic field structure referred to as the undulator of period λ_u. Passing through the undulator the electrons experience an oscillating magnetic field and start a wiggling motion. Therefore they spontaneously start emitting light of the wavelength

$$\lambda_0 = \frac{\lambda_u}{2\gamma^2}(1 + K^2) \tag{7.2}$$

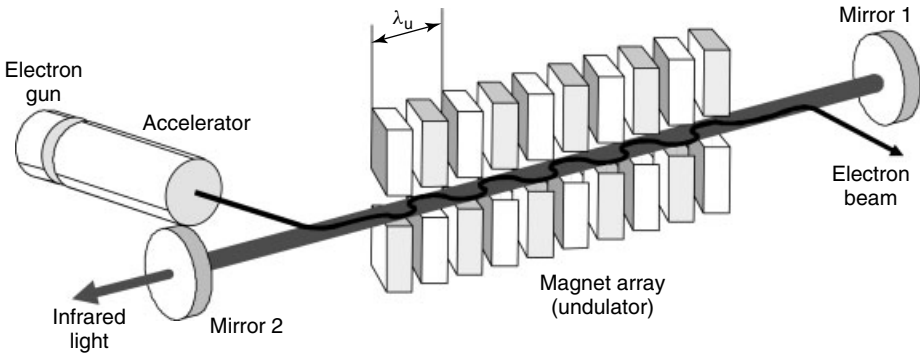

Figure 7.3 Schematic view of a free-electron laser consisting of an electron gun, an accelerator, and an undulator (with period λ_U) placed in a resonator. Electrons oscillate between the undulator magnets and emit radiation, which is stored and amplified in the optical cavity.

where γ is the Lorentz factor and K is a dimensionless parameter that is proportional to the strength of the magnetic field in the undulator.

This spontaneous radiation is usually very weak and incoherent because the electrons are spread over an interval that is much longer than the radiation wavelength. In an oscillator configuration, the spontaneous radiation is trapped between two mirrors of an optical resonator. When new electrons enter the resonator, the stored field leads to the so-called microbunching. Electrons that travel faster than the phase velocity of the field will lose energy to the electromagnetic field while slower electrons will gain energy. In order to have amplification of light, the initial beam energy must be slightly higher than the resonance energy corresponding to the wavelength of the light. The wavelength of the radiation can be changed by varying the strength of the magnetic field and thus the parameter K in Eq. (7.1)

At FELIX, situated at the FOM Institute Rijnhuizen in The Netherlands, this is achieved by changing the gap between the pairs of magnets by means of stepper motors. FELIX is uniquely suited for gas-phase experiments as it is continuously tunable over a range of 4.5–250 μm. Typical output energies of FELIX can be up to 120 mJ in a pulse of ~5 μs duration in the mid-IR and 15–50 mJ/pulse in the far-IR. The bandwidth usually ranges between 0.3 and 1% of the central wavelength.

7.3.3
Infrared Multiple Photon Excitation

It has been realized early on that the IR-MPE induced by FELIX radiation cannot be a purely coherent multiphoton process, given the large amount of photons that need to be absorbed to induce ionization or dissociation [35, 36]. In view of the width of the IR radiation and typical anharmonicities in vibrational potentials, climbing

the vibrational ladder of the excited mode ($\upsilon_i = 0 \rightarrow \upsilon_i = 1 \rightarrow \upsilon_i = 2 \rightarrow \ldots$) is unrealistic due to the anharmonicity bottleneck. The mechanism of IR-MPE is thus better described by two (overlapping) regions, the resonant region and the quasi-continuum region.

In the resonant region, the molecule interacts with the IR radiation and climbs up the discrete energy levels of a vibrational ladder. This resonantly enhanced multiphoton process is governed by the selection rules for direct photoabsorption. With every absorbed photon, the internal energy E_i of the molecule is increased. Since the density of vibrational states $\rho(E_i)$ increases roughly with E_i^N, where N is the number of vibrational degrees of freedom ($3n-6$ for a nonlinear n-atom molecule), even a molecule that contains only few atoms quickly reaches a density of many states per centimeter at an internal energy of $>1000\,\mathrm{cm}^{-1}$, the quasi-continuum. At sufficiently high densities of states, their coupling due to vibrational anharmonicities results in very fast internal vibrational redistribution (IVR), typically on the order of picoseconds, which is short in comparison to the FELIX pulse length. IVR rapidly removes the population from the excited state into the bath of vibrational background states so that the molecule can escape the anharmonicity bottleneck and is ready for the next photon absorption [37].

As a competing process to IR-MPE, the molecule tries to lower its internal energy by either the emission of photons and electrons, or by fragmentation. The rate constants for fragmentation and electron ejection grow exponentially and will thus dominate at high energies. The branching ratio of the two processes depends on the internal energy and the specific properties of the molecule, like its IE (for neutral molecules) and BDE. For all the clusters studied in this chapter the emission of neutral fragments is the faster process, as their BDEs are much lower than their IEs (second IEs in the case of cations).

7.3.4
Dissociation Spectroscopy with the Messenger Technique

The IR spectra discussed in this chapter are obtained via IR-MPD spectroscopy. In dissociation spectroscopy, either the depletion of parent ions or the formation of the photofragments is monitored to probe the absorption process. Probing the fragments relies on an initial mass selection and gives rise to almost background-free spectra [38]. The measurement of depletion has the advantage that all complexes in the molecular beam are probed, and since the detection method is mass-selective, the simultaneous measurement of IR spectra for different cluster sizes is possible [39]. Further, also neutral molecules can be probed with FELIX radiation [40, 41]. A disadvantage of measuring the depletion is that the spectra are not background-free. The mass spectrometric signal of the parent ion is subject to instabilities, mainly due to fluctuations in the cluster intensity produced in the laser-ablation source. Therefore, many mass spectra have to be averaged per FELIX wavelength in order to obtain a good signal-to-noise (S/N) ratio.

Vibrational transitions of silicon clusters lie in the far-infrared (FIR), typically between 150 and $600\,\mathrm{cm}^{-1}$, which corresponds to an energy per photon of only

~20–75 meV. On the other hand, the clusters are rather strongly bound with BDEs around 4 eV [42]. Owing to the nonpolar nature of silicon clusters, the dynamic dipole moments and therefore the IR absorption cross sections are low. Even with the high laser fluence that is provided by FELIX, IR-MPD of such species has not been observed.

This problem can be overcome by using the so-called messenger method, in which a loosely bound ligand that is supposed to have a minor to negligible influence on the structure and vibrational properties is attached to the species that is to be analyzed. It was the messenger technique combined with IR-MPD that facilitated the first FIR spectra of bare metal clusters in the gas phase [43]. All IR spectra discussed below are obtained using either Ar or isotopically enriched ^{129}Xe as the messenger atom.

7.3.5
Experimental Realization

The cluster source consists of a main body with a central channel and sufficient place to mount two targets side by side (see Figure 7.4) [44]. The target holder is pushed against a slit in the source channel. Opposite to the slit there are two entrance channels under an angle of 5°. The second harmonic outputs of two independent Nd YAG laser beams ablate atoms off the targets. The plasmas are quenched by a helium gas pulse delivered from a fast pulsed valve. In the rare-gas pulse, a supersaturated vapor is formed and clustering occurs. The target holder is moved in a rectangular closed-loop pattern by two in-vacuum stepper motors in order to expose a fresh spot of the targets at each laser shot. A laser-ablation source produces neutral as well as cationic and anionic clusters. All species travel down through a temperature-controllable copper channel. When this channel is

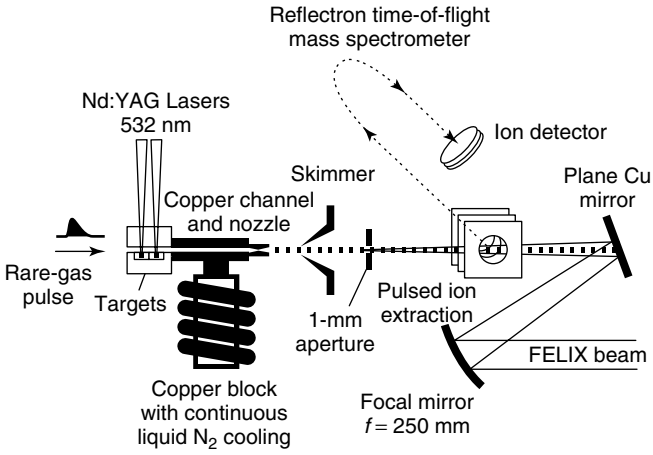

Figure 7.4 Scheme of the molecular-beam setup for the production of silicon-cluster rare-gas complexes.

cooled with a flow of liquid nitrogen and a heavier rare gas like argon or xenon is added to the carrier gas (typically 0.5–1% of the heavier rare gas in helium) also van der Waals complexes of the cluster with the heavy rare gas are formed. Clusters and complexes expand into vacuum and the resulting molecular beam passes through a skimmer and an aperture of 1 mm in diameter. When the clusters arrive in between the acceleration plates an electric field is switched on, which pushes the cationic clusters toward the detector and a time-of-flight mass spectrum is taken (see Figure 7.5a). As can be seen in Figure 7.4, the FELIX beam counterpropagates with respect to the molecular beam and is loosely focused ~30 mm behind the aperture. The aperture ensures that only clusters that have passed the focal region and interacted with FELIX radiation reach the detector, which is crucial for depletion spectroscopy. To correct for intensity fluctuations of the cluster source, the experiments are performed in a toggle mode with the cluster source running at 10 Hz and FELIX at 5 Hz. Using two different channels of a digital storage oscilloscope, mass spectra are recorded and averaged alternatingly with and without FELIX irradiation, and transferred to a computer.

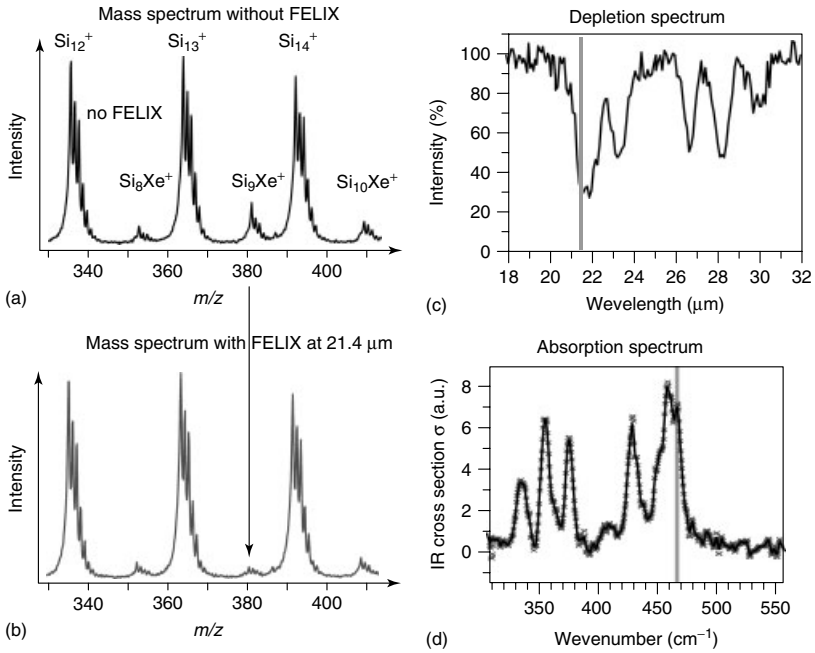

Figure 7.5 (a) Part of the mass distribution of Si_n^+ and Si_n^+Xe complexes without FELIX radiation. (b) Same distribution with FELIX irradiation at 21.4 μm; the mass spectrometric signal of Si_9^+Xe is almost completely depleted as indicated by the arrow. (c) Ratio of the mass spectrometric intensity of Si_9^+Xe with and without FELIX irradiation as a function of FELIX wavelength; note the depletion down to 30% at 21.4 μm as shown by the gray vertical line. (d) After correcting the depletion spectra for the variation of the FELIX pulse energy with wavelength, absorption spectra can be obtained. The absorption at 21.4 μm, corresponding to 467 cm^{-1}, is indicated again by a gray vertical line.

The construction of IR absorption spectra is explained in Figure 7.5. As mentioned above, mass spectra are taken and averaged without (a) and with FELIX radiation (b). The signal intensity with IR radiation, $I(\nu)$, and without, I_0, is integrated for a selected complex. Plotting the ratio $I(\nu)/I_0$ against the FELIX frequency leads to so-called depletion spectra (c). The far-IR absorption spectra are obtained by converting the measured depletion spectra to absorption cross sections $\sigma(\nu)$ and by normalizing for variations of the laser intensity $P(\nu)$ over the tuning range using

$$\sigma(\nu) \sim \frac{1}{p(\nu)} \mathrm{In} \frac{I_0}{I(\nu)} \tag{7.3}$$

This procedure assumes a one-photon absorption process and is justified if the absorption of the first photon is the rate-determining step in the IR-MPD process (see above) [45].

7.4 IR-Spectroscopy on Bare Silicon Cluster Cations

7.4.1 Introduction

There is a long history of experimental studies of silicon clusters. Theoreticians have made many predictions concerning the geometries and properties of neutral silicon clusters, demonstrating that different *ab initio* and density functional theory (DFT) methods predict varied ground-state structures [46–51]. There exist fewer theoretical studies of the geometries of charged silicon clusters [52–56], but different ground-state structures have also been proposed for several ionic clusters. For example, the structure of Si_8^+ has been reported as both a bi-capped octahedron [54, 56] and a face-capped pentagonal bipyramid [55]. Thus, there exists a need for experimental results to validate theoretical predictions.

Some experimental approaches to study silicon clusters have been presented in Section 7.2. It was shown that vibrational spectroscopy in inert matrices led to sound structural assignments for small neutral clusters (Section 7.2.3). Ion mobility proved the existence of multiple isomers for certain cluster sizes and revealed general shape transitions (Section 7.2.1). Photoelectron spectroscopy has added support for the TTP as an important building block in silicon clusters (Section 7.2.2). However, while these experimental techniques give a general idea of cluster structure, they usually cannot distinguish between isomers possessing similar geometries. Indeed, ion-mobility measurements have difficulties distinguishing between different structural isomers for small cationic silicon clusters, Si_n^+ ($n < 13$) [57]. Vibrational spectra of Si_n^+ ($n = 6–23$) have been obtained by IR-MPD spectroscopy of their complexes with xenon ligands. By comparing the observed spectra with those predicted by quantum chemical calculations, precise cluster geometries can be assigned [58].

7.4.2 Results and Discussion

Figure 7.6 shows the vibrational spectrum of Si_6^+ obtained upon IR-MPD of its complex with one xenon atom. Complex formation was promoted by cooling the copper channel to approximately 100 K. The dots represent the raw data while the line interconnects a seven-point binomially weighted average to account for the bandwidth of FELIX. The IR-MPD spectrum shows an intense absorption band at 411 cm^{-1} and a much less intense feature at 441 cm^{-1}. DFT calculations are performed in order to make structural assignments by comparing the predicted IR spectra for multiple isomers with the experimental outcome [58]. The upper panels of Figure 7.6 show the calculated IR spectra of two different isomers **1a** and **1b**. Computed IR frequencies of all calculated isomers in this chapter are scaled

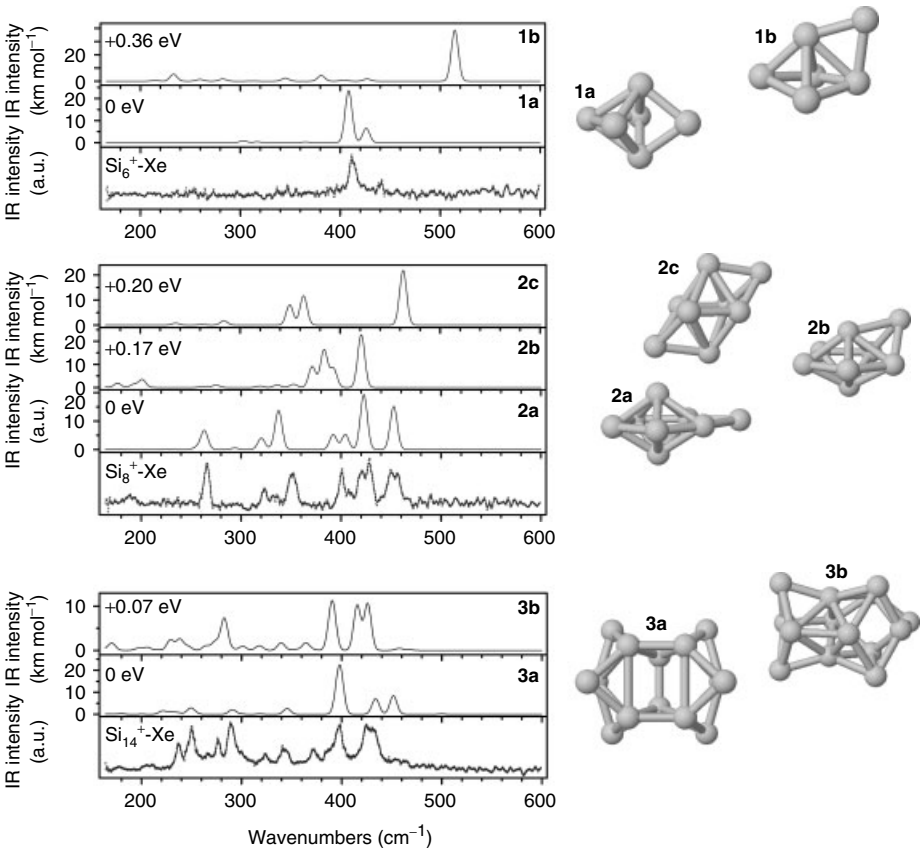

Figure 7.6 IR-MPD spectra of the Si_6^+, Si_8^+, and Si_{14}^+ clusters tagged with a xenon atom compared to the predicted infrared spectra of multiple structural isomers (**1a**–**b**, **2a**–**c**, **3a**–**b**).

by a multiplication factor of 1.03, and are plotted by broadening the predicted frequencies with a Gaussian line shape possessing a full-width at half-maximum of 8 cm^{-1}. There is considerable support in the literature that an edge-capped trigonal bipyramid (which can also be regarded as a distorted octahedron) is the global minimum-energy structure [54, 56, 57]. Also, here, the calculations identify a distorted octahedron **1a** as the lowest energy isomer, well separated from all other calculated structures [58]. Figure 7.6 shows nicely how the vibrational fingerprint can distinguish even between rather similar geometries. **1a** can be viewed as a trigonal bipyramid with an additional atom, which bridges a bond between two equatorial atoms. **1b** is a trigonal bipyramid, in which an atom bridges the bond between an axial and an equatorial atom. Even though the structures are closely related, their IR spectra differ drastically. Comparison with the experimental 1R-MPD spectrum reveals that **1a** is the isomer that is present in the molecular beam.

The importance of experimental verification of quantum chemical predictions is even more evident in the case of Si_8^+. Two geometries have been previously reported as the ground state of Si_8^+, a distorted bi-capped octahedron (isomer **2c** in Figure 7.6) [54, 56] and a face-capped pentagonal bipyramid (isomer **2b**) [55]. However, the calculated IR spectra for these shapes do not reproduce the experimental spectrum. None of these two geometries predict an intense band below 300 cm^{-1}, whereas the experimental IR-MPD spectrum of Si_8^+Xe has a pronounced band at 267 cm^{-1}. In search of additional structural isomers, an edge-capped pentagonal bipyramid structure has been optimized (isomer **2a**). This geometry is computed to be the lowest lying isomer and the predicted IR spectrum matches the experiment well, especially as this computed isomer has an intense absorption band at 264 cm^{-1}. Hence, this edge-capped pentagonal bipyramid geometry is assigned to the Si_8^+ cluster.

Even when the global minimum is found in the quantum mechanical calculations, additional problems can occur. It is not a priori clear that the energetic ordering of the isomers is calculated correctly. Further, in the experiment a structure might be produced, which is kinetically favored in the cluster production process. In that case, the isomer that is responsible for the measured IR-MPD spectrum does not correspond to the global minimum but is metastable. The lowest energy structure found for Si_{14}^+ contains a central trigonal prism building block with eight additional atoms, four on each of the two sides (**3a** in Figure 7.6). However, the predicted IR spectrum for this isomer is dominated by a strong absorption band at 398 cm^{-1}, whereas the experiment reveals a multitude of bands of comparable intensity between 230 and 430 cm^{-1}. A much better fit with the experiment is obtained for the geometry **3b**, which is calculated to be only 0.07 eV higher in energy. In principle, it is possible that both isomers are present in the molecular beam. However, the presence of multiple isomers for Si_{14}^+ was not evident in ion-mobility studies [26] and isomer **3b** can be safely confirmed as the major species present in the experiment.

Unfortunately, there are also sizes for which none of the calculated isomers reproduce the IR-MPD spectra sufficiently, for example, Si_{12}^+[58]. However, for

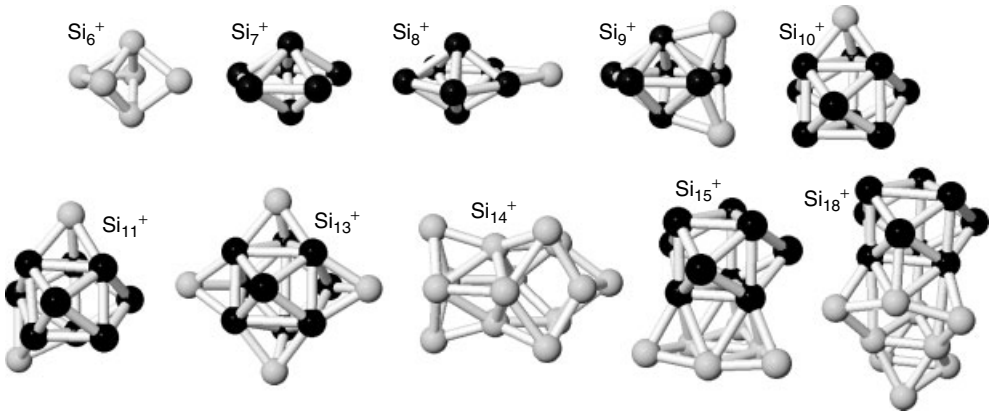

Figure 7.7 Structures of silicon cluster cations identified by vibrational spectroscopy. The pentagonal bipyramid and tri-capped trigonal prism building blocks are shown in dark shade.

many cluster sizes definite structural assignments have been achieved and their geometries are shown in Figure 7.7.

While looking for patterns in the cluster structure as the size increases, some general trends in the growth can be noted. Si_7^+ is a pentagonal bipyramid. Si_8^+ and Si_9^+ retain the pentagonal bipyramid base with additional atoms capping an edge or face. For Si_{10}^+, a new base feature is present, that is, a TTP. It is interesting that Si_9^+ does not have a TTP geometry; this structure is higher in energy. Si_{11}^+ and Si_{13}^+ build upon the TTP base with additional capping of faces. Si_{14}^+ appears to possess a different structure. Although one could argue that this cluster may possess very distorted versions of either building block, they are not assigned here. The TTP reappears in the structures of Si_{15}^+ and Si_{18}^+. Summarizing, TPPs and pentagonal bipyramids are the dominant structural motifs for small silicon-cluster cations.

7.5
Chemical Probe Method for Endo- and Exohedrally Doped Silicon Clusters

7.5.1
Introduction

Elemental silicon clusters are unsuitable as building blocks for future nanomaterials, since their dangling bonds make them chemically reactive [46]. Contrary to carbon fullerenes and nanotubes, sp^2 hybridized silicon clusters are unstable and the formation of a silicon hollow cage or tube is unlikely. It has been argued that proper metal doping can change this behavior [15]. Following up on this idea, many theoretical studies have investigated Si_nM structures for various

dopants from almost every group of the periodic table [17, 59–65]. While it seems that alkaline-doped clusters are always more stable when the dopant is situated on the surface of the cluster [66], transition-metal-doped silicon clusters form cagelike geometries from a certain size onward [65]. It was found that incorporating a single transition-metal atom may dramatically influence the structure and stability of the clusters. For example, doping silicon clusters with Ti results in fullerene-like clusters and Frank–Kasper polyhedra [67]. If, however, the number of Si atoms does not suffice to enclose the dopant atom completely, then basket-like geometries result [67, 68]. It has been suggested that for multiply metal-doped silicon systems, endohedral silicon nanorods can be formed [17, 69–71].

To date, the experimental confirmation of these predictions has been limited to indirect mass spectrometric observations [72–75], photoelectron spectroscopy [76–84], as well as reactivity [76, 78, 80] and fragmentation studies [85]. For the multiply doped analogs there is little gas-phase experimental data available.

One question that immediately arises when adding a dopant atom to a cluster is whether the dopant stays on the surface of the cluster or whether it is fully surrounded by a cage of silicon atoms. Nakajima *et al.* studied the size-dependent reactivity toward H_2O vapor in a flow-tube reactor [76, 78, 80]. The abundance of Si_nTi^+ ($n = 7–11$), for example, decreased upon reaction with H_2O, while the abundance of larger Si_nTi^+ ($n = 13–17$) clusters remained unchanged. It was assumed that an exterior Ti atom is a reactive site for adsorption of H_2O. The low reactivity of larger Si_nTi^+ clusters would then indicate that these clusters have no exterior Ti atom [76, 78, 80]. Complex formation with argon is found to show a very similar behavior [86]. Ar is an ideal probe as it is expected to have a negligible influence on the cluster structure and merely serves as a spectator atom.

7.5.2 Results and Discussion

Figure 7.8a shows the Ar complex formation for mixed Si_nCr^+ clusters obtained at 80 K after adding 1% of Ar to the He carrier gas. The mass spectrum is congested due to the large number of possible compositions and due to the natural isotope distributions of the elements used. The highest ion signals are recorded for bare Si_n^+ and singly doped Si_nCr^+. Also, some doubly doped $Si_nCr_2^+$ clusters and complexes with argon atoms $Si_nCr_{1,2}^+Ar_{1,2}$ are formed, while bare Si_n^+ clusters do not bind any argon at this temperature. Most remarkably, the abundance of the $Si_nCr_{1,2}^+Ar_{1,2}$ complexes is strongly size dependent and collapses after a certain critical number of Si atoms. This is best represented by plotting the fraction of Ar complexes (one or two Ar atoms) as a function of n as shown in Figure 7.8b. Both for singly and doubly doped silicon clusters, critical sizes for argon attachment are observed, which depend on the dopant element [86].

For singly doped silicon clusters, the critical size for Ar attachment changes along the 3d row, that is, $Si_{12}Ti^+$, $Si_{11}V^+$, $Si_{10}Cr^+$, Si_7Co^+, $Si_{11}Cu^+$ are the largest

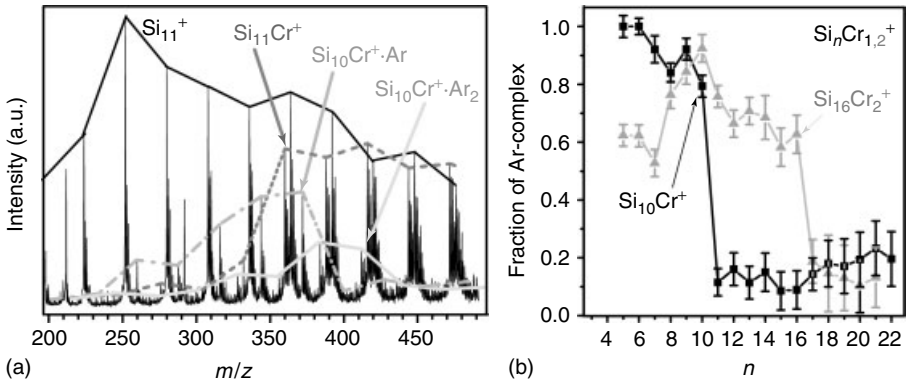

Figure 7.8 (a) Part of the mass spectrum of cationic chromium-doped silicon clusters and their Ar complexes formed at 80 K using He carrier gas containing 1% Ar. Peak maxima of Si_n^+, Si_nCr^+, and $Si_nCr^+Ar_{1,2}$ are connected by solid and dashed lines. (b) Fraction of argon complexes formed for $Si_nCr_{1,2}^+$ as a function of cluster size. A critical size, beyond which the argon complex formation stops, is found for both the singly and doubly doped species.

clusters with pronounced formation of Ar complexes. Knowing that Si_n^+ clusters do not form stable complexes with Ar at 80 K, one can assume that Ar binds to the TM dopant. Binding to the TM atom is only feasible if the dopant is on the surface of the host cluster (exohedral). If the dopant resides in the interior of an Si_n cage (endohedral), the Ar atom can only interact with Si surface atoms, and thus no Ar complexes are formed. Thus, Ar attachment is a probe for an uncompleted caged structure; the disappearance of the Ar complexes marks the formation of endohedral clusters. For doubly doped silicon clusters, the critical size for Ar attachment decreases along the 3d row as well: $Si_{19}Ti_2^+$, $Si_{17}V_2^+$, $Si_{16}Cr_2^+$, $Si_{13}Co_2^+$. It is again reasonable to assume that Ar complex formation is not possible if the dopant atoms are fully surrounded by Si.

In general, the experimental findings of the argon-physisorption method are in excellent agreement with what has been found in the reactivity studies with H_2O vapor [78, 80]. The proposed basket-shaped structures for neutral Si_nTi ($n = 8–12$) and endohedral systems for larger sizes [87] agree nicely with the experiment, though other theoretical studies predict an endohedral structure already for $Si_{12}Ti$ [88]. There had been a discussion in the literature whether $Si_{11}Cr$ [89] or $Si_{12}Cr$ [68] is the smallest endohedral species. Argon-physisorption identifies $Si_{11}Cr^+$ as the smallest cationic cage structure. In case of cobalt as the dopant atom, theory does not reproduce the critical size measured for the cation, as neutral Si_9Co is calculated to be exohedral, while, experimentally, the transition occurs for two silicon atoms less [59]. In the case of copper-doping, the transition for the neutral is in agreement with the experimental finding for the cation to occur between $Si_{10}Cu$ and $Si_{12}Cu$ [90].

7.6
IR-Spectroscopy on Exohedrally Doped Silicon Cluster Cations

7.6.1
Introduction

After knowing the exact geometric structures of bare silicon-cluster cations (Section 7.4), as well as the location of the dopant atom in the silicon cluster (Section 7.5), it is desirable to gain detailed insights into the geometries of doped silicon clusters. While there is no doubt that the structure of silicon clusters can be changed upon appropriate doping, detailed experimental studies on the growth mechanisms of doped silicon clusters are rather scarce. A deep knowledge about the influence of the dopant on the cluster's structure, however, is necessary for the design and production of tailor-made silicon materials. In the following, the vibrational spectra of small cationic copper- and vanadium-doped silicon clusters Si_nCu^+ and Si_nV^+ ($n = 6–8$) are presented. Copper- and vanadium-doped silicon clusters show the same critical size for the transition from exohedral to endohedral structures (Section 7.5). It is thus interesting to address the question of whether doping with these two atoms will generate clusters with the same geometric structure.

7.6.2
Results and Discussion

Figure 7.9 shows the experimental and theoretical vibrational spectra of Si_nCu^+ and Si_nV^+ ($n = 6–8$). Only the theoretical spectrum of the particular isomer that

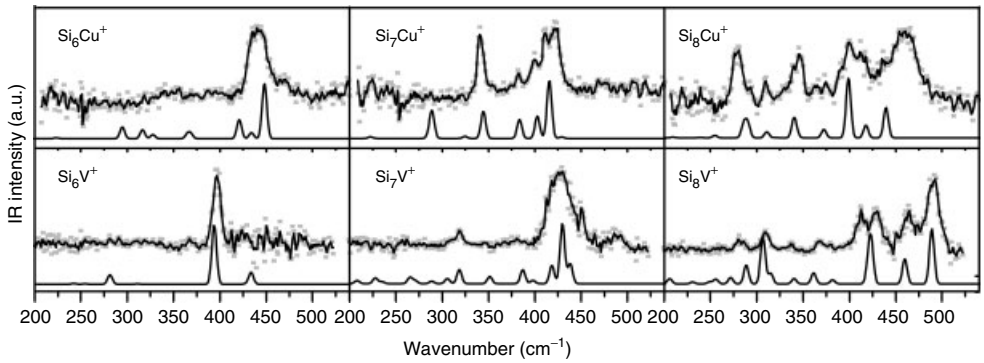

Figure 7.9 Vibrational spectra of Si_nCu^+ (top row) and Si_nV^+ (bottom row) ($n = 6–8$). The upper traces in each panel show the experimental IR-MPD spectra of the corresponding complex with one argon atom. The experimental data points are overlaid with a three-point running average to account for the bandwidth of FELIX. They are compared to the calculated vibrational spectra of the best-fitting isomer. The calculated stick spectra are folded with a Gaussian linewidth function of 5 cm^{-1} full-width at half-maximum for ease of comparison.

best reproduces the experimental spectrum is shown. The number of possible geometrical isomers increases rapidly for increasing cluster size and this holds especially true for binary systems. For example, for Si_8V^+, five structural isomers have been found within 0.14 eV, based on DFT calculations [91]. A structural assignment of the clusters, based only on quantum chemical calculations, is thus not straightforward. For Si_8V^+, most of the experimental spectral features are reproduced in the simulated spectrum of the calculated minimum-energy structure (lower right panel in Figure 7.9). Its structure is that of a bi-capped pentagonal bipyramid with the dopant atom in an axial position (Figure 7.10). The peak positions are in good agreement, although the experimental doublet at ~420 and 430 cm^{-1} is split by three wavenumbers only in calculation and appears as a single line in simulation. The peak intensities deviate between theory and experiment. In particular, the low-energy absorptions around 300 cm^{-1} are less pronounced in the experiment, which could be due to the larger number of photons needed for photodissociation. Furthermore, one has to keep in mind that the IR-MPD spectra do not correspond directly to linear absorption spectra.

In almost all cases, the experimental spectrum is reproduced best by the IR spectrum of the calculated lowest energy structure. For Si_6V^+, theory finds a Si-capped octahedron as the lowest energy structure, while the experiment is reproduced much better by the spectrum of a triplet-state pentagonal bipyramid with vanadium in an equatorial position, which is calculated to be 0.03 eV higher in energy. Interestingly, the experiment does not show any features that would point to the coexistence of a second isomer, although the isomers are calculated to be extremely close in energy.

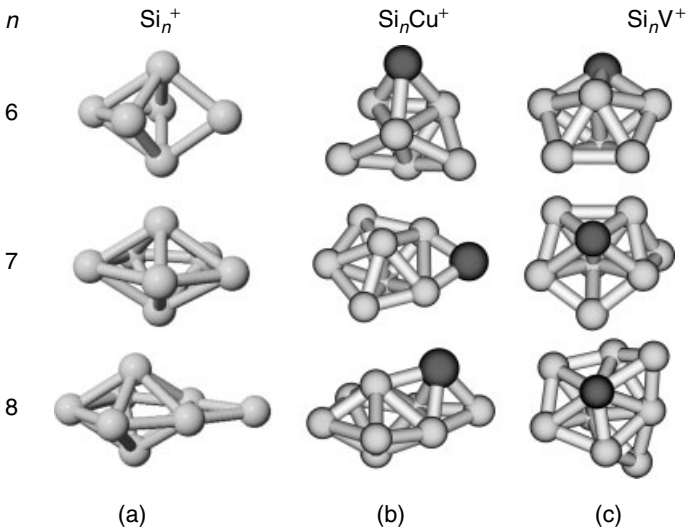

Figure 7.10 Structures of Si_n^+ (a), Si_nCu^+ (b), and Si_nV^+ (c) (n = 6–8) for which the calculated vibrational spectra fit best the experimental findings.

The assigned structures for the copper- and vanadium-doped silicon clusters are shown in Figure 7.10. They can be compared among themselves as well as with the predicted structures of bare cationic silicon clusters in order to elucidate the influence of the dopant. IR-MPD has led to definite assignments for the structures of small cationic silicon clusters (Section 7.4). For Si_6^+, an edge-capped trigonal bipyramid is found to be the lowest energy structure. Si_7^+ is a distorted pentagonal bipyramid, while Si_8^+ is an edge-capped pentagonal bipyramid (Figure 7.10a). In principle, three types of doped silicon structures are possible. The dopant can (i) add to, or (ii) substitute a silicon atom in a bare silicon cluster structure, or it can (iii) induce a complete geometric reconstruction. Si_6V^+ is an example of the second type, in which vanadium adopts the position of a silicon atom in the pentagonal bipyramid structure of Si_7^+. Copper-doping leads instead to the third type, resulting in a new structure that can be described as a distorted bi-capped trigonal bipyramid with copper in an axial position. A very similar structure has been suggested previously [54]. The situation changes for the clusters with one more silicon atom. Now copper leads to a structure that belongs either to the first or to the second type. The copper dopant simply adds to the equatorial edge of a Si_7^+ pentagonal bipyramid. Alternatively, copper substitutes the edge-capping silicon atom in Si_8^+. Vanadium prefers a higher coordination and occupies the axial position of a pentagonal bipyramid, which is face-capped by a silicon atom, thus creating a whole new structure. In Si_8V^+, a silicon atom is added to the face of Si_7V^+, further increasing the coordination of the dopant. The pentagonal bipyramid backbone is also retained in the case of Si_8Cu^+. However, now it consists entirely of silicon atoms and the structure is of type 1 with copper adding to the bare Si_8^+ geometry.

7.7 Summary and Outlook

It has been the scope of this chapter to show the possibility to influence the geometries of silicon-based nanoparticles. The geometries of free nanoparticles in the gas phase can be studied by a variety of experimental methods, but IR spectroscopy is shown to be especially versatile and sensitive to gain detailed structural insights. The vibrational fingerprint of gas-phase clusters is obtained upon IR-MPD spectroscopy of their complexes with loosely bound rare-gas atoms.

This chapter started out with a thorough investigation of the structural properties of bare silicon clusters Si_n^+ ($n = 6–23$). In many cases, excellent agreement between theory and experiment allows for the unambiguous assignment of the cluster structure. On the basis of the detailed knowledge about bare silicon clusters, the structural influence of a dopant was studied next on an atomic level. One way is to dope the cluster with a transition-metal atom. A question that then naturally arises is where the dopant atom is located. A general answer can be found, without any spectroscopy or quantum chemical calculations, by means of a simple

argon-physisorption method. More detailed insight into the geometries of cationic copper- and vanadium-doped silicon clusters containing six to eight silicon atoms was gained again from vibrational spectroscopy. The dopant atom can lead to three different structural motifs. It can substitute a silicon atom in the structure of a bare silicon cluster or it can simply add to it. A third possibility is that it leads to a complete structural rearrangement to produce an entirely new structure. Especially the latter type opens the door for tailoring the properties of doped silicon clusters.

Future work will focus on endohedrally doped silicon clusters. Their vibrational fingerprint can be revealed upon IR-MPD of their complexes with xenon atoms. Neutral particles constitute the next frontier with regard to bare and doped silicon clusters. While a wealth of structural information is available for cationic and anionic silicon clusters, hardly anything is known experimentally for their neutral counterparts. IR-MPD is one of the very few experimental approaches that is not only limited to charged species but can also be applied to neutral clusters [41].

One goal of the gas-phase synthesis of novel materials is their production in macroscopic quantities. C_{60} has been detected first as an enhanced peak in the mass spectrum of carbon clusters and can now be ordered from a standard chemicals catalog. It is interesting to see whether this stabilization can be achieved also for certain silicon nanoparticles.

References

1. Haberland, H. (ed.) (1995) *Clusters of Atoma and Molecules I; Theory, Experiment, and Clusters of Atoms*, Springer, Berlin.
2. Haberland, H. (ed.) (1995) *Clusters of Atoms and Molecules II; Solvation and Chemistry of Free Clusters, and Embedded, Supported and Compressed Clusters*, Springer, Berlin.
3. Johnston, R.L. (ed.) (2002) *Atomic and Molecular Clusters*, Taylor & Francis, London and New York.
4. Dietz, T.G., Duncan, M.A., Powers, D.E., and Smalley, R.E. (1981) Laser production of supersonic metal cluster beams. *J. Chem. Phys.*, **74**, 6511–6512.
5. de Heer, W.A. (1993) The physics of simple metal clusters: experimental aspects and simple models. *Rev. Mod. Phys.*, **65**, 611–676.
6. Billas, I.M.L., Châtelain, A., and de Heer, W.A. (1994) Magnetism from the atom to the bulk in iron, cobalt, and nickel clusters. *Science*, **265**, 1682–1684.
7. Moro, R., Xu, X., Yin, S., and de Heer, W.A. (2003) Ferroelectricity in free niobium clusters. *Science*, **300**, 1265–1269.
8. Cox, A.J., Louderback, J.G., and Bloomfield, L.A. (1993) Experimental observation of magnetism in rhodium clusters. *Phys. Rev. Lett.*, **71**, 923–926.
9. Schmidt, M., Kusche, R., von Issendorff, B., and Haberland, H. (1998) Irregular variations in the melting point of size-selected atomic clusters. *Nature*, **393**, 238–240.
10. Lin, S.Y., Fleming, J.G., Hetherington, D.L., Smith, B.K., Biswas, R., Ho, K.M., Sigalas, M.M., Zubrzycki, W., Kurtz, S.R., and Bur, J. (1998) A three-dimensional photonic crystal operating at infrared wavelengths. *Nature*, **394**, 251–253.
11. Hirschman, K.D., Tsybeskov, L., Duttagupta, S.P., and Fauchet, P.M. (1996) Silicon-based visible light-emitting devices integrated into microelectronic circuits. *Nature*, **384**, 338–341.

12. Landman, U., Barnett, R.N., Scherbakov, A.G., and Avouris, P. (2000) Metal-semiconductor nanocontacts: silicon nanowires. *Phys. Rev. Lett.*, **85**, 1958–1961.
13. Honea, E.C., Ogura, A., Murray, C.A., Raghavachari, K., Sprenger, W.O., Jarrold, M.F., and Brown, W.L. (1993) Raman spectra of size-selected silicon clusters and comparison with calculated structures. *Nature*, **366**, 42–44.
14. Ho, K.-M., Shvartsburg, A.A., Pan, B., Lu, Z.-Y., Wang, C.-Z., Wacker, J.G., Fye, J.L., and Jarrold, M.F. (1998) Structures of medium-sized silicon clusters. *Nature*, **392**, 582–585.
15. Jackson, K. and Nellermoe, B. (1996) $Zr@Si_{20}$: a strongly bound Si endohedral system. *Chem. Phys. Lett.*, **254**, 249–256.
16. Hiura, H., Miyazaki, T., and Kanayama, T. (2001) Formation of metal-encapsulating Si cage clusters. *Phys. Rev. Lett.*, **86**, 1733–1736.
17. Singh, A.K., Kumar, V., and Kawazoe, Y. (2004) Metal encapsulated nanotubes of silicon and germanium. *J. Mater. Chem.*, **14**, 555–563.
18. Billinge, S.J.L. and Levin, I. (2007) The problem with determining atomic structure at the nanoscale. *Science*, **316**, 561–565.
19. Weis, P. (2005) Structure determination of gaseous metal and semi-metal cluster ions by ion mobility spectrometry. *Int. J. Mass Spectrom.*, **245**, 1–13.
20. von Helden, G., Hsu, M.-T., Kemper, P.R., and Bowers, M.T. (1991) Structures of carbon cluster ions from 3 to 60 atoms: linears to rings to fullerenes. *J. Chem. Phys.*, **95**, 3835–3837.
21. von Helden, G., Gotts, N.G., and Bowers, M.T. (1993) Experimental evidence for the formation of fullerenes by collisional heating of carbon rings in the gas phase. *Nature*, **363**, 60–63.
22. Oger, E., Crawford, N.R.M., Kelting, R., Weis, P., Kappes, M.M., and Ahlrichs, R. (2007) Boron cluster cations: transition from planar to cylindrical structures. *Angew. Chem. Int. Ed.*, **46**, 8503–8506.
23. Jarrold, M.F. and Constant, V.A. (1991) Silicon cluster ions: evidence for a structural transition. *Phys. Rev. Lett.*, **67**, 2994–2997.
24. Jarrold, M.F. and Bower, J.E. (1992) Mobilities of silicon cluster ions: the reactivity of silicon sausages and spheres. *J. Chem. Phys.*, **96**, 9180–9190.
25. Dugourd, P., Hudgins, R.R., Clemmer, D.E., and Jarrold, M.F. (1997) High-resolution ion mobility measurements. *Rev. Sci. Instrum.*, **68**, 1122–1129.
26. Hudgins, R.R., Imai, M., Jarrold, M.F., and Dugourd, P. (1999) High-resolution ion mobility measurements for silicon cluster anions and cations. *J. Chem. Phys.*, **111**, 7865–7870.
27. Cheshnovsky, O., Yang, S.H., Pettiette, C.L., Craycraft, M.J., Liu, Y., and Smalley, R.E. (1987) Ultraviolet photoelectron spectroscopy of semiconductor clusters: silicon and germanium. *Chem. Phys. Lett.*, **138**, 119–124.
28. Xu, C., Taylor, T.R., Burton, G.R., and Neumark, D.M. (1998) Vibrationally resolved photoelectron spectroscopy of silicon cluster anions Si_n^- ($n = 3–7$). *J. Chem. Phys.*, **108**, 1395–1406.
29. Müller, J., Liu, B., Shvartsburg, A.A., Ogut, S., Chelikowsky, J.R., Siu, K.W.M., Ho, K.-M., and Gantefor, G. (2000) Spectroscopic evidence for the tricapped trigonal prism structure of semiconductor clusters. *Phys. Rev. Lett.*, **85**, 1666–1669.
30. Hoffmann, M.A., Wrigge, Gv., Issendorff, B.v., Müller, J., Ganteför, G., and Haberland, H. (2001) Ultraviolet photoelectron spectroscopy of Si_4 to Si_{1000} as one expression. *Eur. Phys. J.*, **16**, 9–11.
31. Lombardi, J.R. and Davis, B. (2002) Periodic properties of force constants of small transition-metal and lanthanide clusters. *Chem. Rev.*, **102**, 2431–2460.
32. Honea, E.C., Ogura, A., Peale, D.R., Felix, C., Murray, C.A., Raghavachari, K., Sprenger, W.O., Jarrold, M.F., and Brown, W.L. (1999) Structures and coalescence behavior of size-selected silicon nanoclusters studied by surface-plasmon-polariton enhanced

Raman spectroscopy. *J. Chem. Phys.*, **110**, 12161–12172.

33. Li, S., Van Zee, R.J., Weltner Jr., W., and Raghavachari, K. (1995) Si_3- - Si_7-. Experimental and theoretical infrared spectra. *Chem. Phys. Lett.*, **243**, 275–280.
34. Asmis, K.R., Fielicke, A., von Helden, G., and Meijer, G. (2007) Vibrational spectroscopy of gas-phase clusters and complexes, in *The Chemical Physics of Solid Surfaces*, Atomic Clusters: From Gas Phase to Deposited Atomic Clusters, Vol. 12 (ed. D.P.Woodruff), Elsevier, Amsterdam, pp. 327–375.
35. von Helden, G., Holleman, I., Knippels, G.M.H., van der Meer, A.F.G. and Meijer, G. (1997) Infrared resonance enhanced multiphoton ionization of fullerenes. *Phys. Rev. Lett.*, **79**, 5234.
36. Oomens, J., van Roij, A.A., Meijer, G. and von Helden, G. (2000) Gas phase infrared photodissociation spectroscopy of cationic polyaromatic hydrocarbons. *Astrophys. J.*, **542**, 404–410.
37. Oomens, J., Sartakov, B.G., Meijer, G. and von Helden, G. (2006) Gas-phase infrared multiple photon dissociation spectroscopy of mass-selected molecular ions. *Int. J. Mass Spectrom.*, **254**, 1–19.
38. Asmis, K.R. and Sauer, J. (2007) Mass-selective vibrational spectroscopy of vanadium oxide cluster ions. *Mass Spectrom. Rev.*, **26**, 542–562.
39. Gruene, P., Fielicke, A., and Meijer, G. (2007) Experimental vibrational spectra of gas-phase tantalum cluster cations. *J. Chem. Phys.*, **127**, 234307.1–234307.5.
40. Fielicke, A., Ratsch, C., von Helden, G., and Meijer, G. (2005) Isomer selective infrared spectroscopy of neutral metal clusters. *J. Chem. Phys.*, **122**, 091105.1–091105.4.
41. Gruene, P., Rayner, D.M., Redlich, B., van der Meer, A.F.G., Lyon, J.T., Meijer, G., and Fielicke, A. (2008) Structures of neutral Au_7, Au_{19}, and Au_{20} clusters in the gas phase. *Science*, **321**, 674–676.
42. Jarrold, M.F. (1995) Drift tube studies of atomic clusters. *J. Phys. Chem.*, **99**, 11–21.
43. Fielicke, A., Kirilyuk, A., Ratsch, C., Behler, J., Scheffler, M., von Helden, G., and Meijer, G. (2004) Structure determination of isolated metal clusters via far-infrared spectroscopy. *Phys. Rev. Lett.*, **93**, 023401.1–023401.4.
44. Bouwen, W., Thoen, P., Vanhoutte, F., Bouckaert, S., Despa, F., Weidele, H., Silverans, R.E., and Lievens, P. (2000) Production of bimetallic clusters by a dual-target dual-laser vaporization source. *Rev. Sci. Instrum.*, **71**, 54–58.
45. Fielicke, A., von Helden, G. and Meijer, G. (2005) Far-infrared spectroscopy of isolated transition metal clusters. *Eur. Phys. J.*, **34**, 83–88.
46. Röthlisberger, U., Andreoni, W., and Parrinello, M. (1994) Structure of nanoscale silicon clusters. *Phys. Rev. Lett.*, **72**, 665–668.
47. Zhu, X. and Zeng, X.C. (2003) Structures and stabilities of small silicon clusters: Ab initio molecular-orbital calculations of Si_7 - Si_{11}. *J. Chem. Phys.*, **118**, 3558–3570.
48. Zhu, X.L., Zeng, X.C., Lei, Y.A., and Pan, B. (2004) Structures and stability of medium silicon clusters. II. Ab initio molecular orbital calculations of Si_{12} - Si_{20}. *J. Chem. Phys.*, **120**, 8985–8995.
49. Yoo, S. and Zeng, X.C. (2005) Motif transition in growth patterns of small to medium-sized silicon clusters. *Angew. Chem. Int. Ed.*, **44**, 1491–1494.
50. Yoo, S. and Zeng, X.C. (2005) Structures and stability of medium-sized silicon clusters. III. Reexamination of motif transition in growth pattern from Si_{15} to Si_{20}. *J. Chem. Phys.*, **123**, 164303–164306.
51. Yoo, S. and Zeng, X.C. (2006) Structures and relative stability of medium-sized silicon clusters. IV. Motif-based low-lying clusters Si_{21} - Si_{30}. *J. Chem. Phys.*, **124**, 054304.1–054304.6.
52. Wei, S., Barnett, R.N., and Landman, U. (1997) Energetics and structures of neutral and charged Si_n ($n < 10$) and sodium-doped Si_nNa clusters. *Phys. Rev. B*, **55**, 7935–7944.
53. Kishi, R., Negishi, Y., Kawamata, H., Iwata, S., Nakajima, A., and Kaya, K. (1998) Geometric and electronic structures of fluorine bound silicon clusters. *J. Chem. Phys.*, **108**, 8039–8058.

54. Xiao, C., Hagelberg, F., and Lester Jr., W.A. (2002) Geometric, energetic, and bonding properties of neutral and charged copper-doped silicon clusters. *Phys. Rev. B*, **66**, 075425.1–075425.23.
55. Li, B.-X., Cao, P.-L., and Zhou, X.-Y. (2003) Electronic and geometric structures of Si_n^- and Si_n^+ (n = 2-10) clusters and in comparison with Si_n. *Phys. Status Solidi B*, **238**, 11–19.
56. Nigam, S., Majumder, C., and Kulshreshtha, S.K. (2004) Structural and electronic properties of Si_n, Si_n^+, and $AlSi_{n-1}$ (n = 2-13) clusters: theoretical investigation based on ab initio molecular orbital theory. *J. Chem. Phys.*, **121**, 7756–7763.
57. Liu, B., Lu, Z.-Y., Pan, B., Wang, C.-Z., Ho, K.-M., Shvartsburg, A.A., and Jarrold, M.F. (1998) Ionization of medium-sized silicon clusters and the geometries of the cations. *J. Chem. Phys.*, **109**, 9401–9409.
58. Lyon, J.T., Gruene, P., Fielicke, A., Meijer, G., Janssens, E., Claes, P., and Lievens, P. (2009) Structures of silicon cluster cations in the gas phase. *J. Ame. Chem. Soc.*, **131**, 1115–1121.
59. Lu, J. and Nagase, S. (2003) Structural and electronic properties of metal-encapsulated silicon clusters in a large size range. *Phys. Rev. Lett.*, **90**, 115506.1–115506.4.
60. Sen, P. and Mitas, L. (2003) Electronic structure and ground states of transition metals encapsulated in a Si_{12} hexagonal prism cage. *Phys. Rev. B*, **68**, 155404.1–155404.4.
61. Majumder, C. and Kulshreshtha, S.K. (2004) Impurity-doped Si_{10} cluster: understanding the structural and electronic properties from first-principles calculations. *Phys. Rev. B*, **70**, 245426.1–245426.7.
62. Reveles, J.U. and Khanna, S.N. (2006) Electronic counting rules for the stability of metal-silicon clusters. *Phys. Rev. B*, **74**, 035435.1–035435.6.
63. Gueorguiev, G.K., Pacheco, J.M., Stafstrom, S., and Hultman, L. (2006) Silicon-metal clusters: Nano-templates for cluster assembled materials. *Thin Solid Films*, **515**, 1192–1196.
64. Uchida, N., Miyazaki, T., and Kanayama, T. (2006) Stabilization mechanism of Si_{12} cage clusters by encapsulation of a transition-metal atom: a density-functional theory study. *Phys. Rev.*, **74**, 205427.1–205427.9.
65. Guo, L.-J., Zhao, G.-F., Gu, Y.-Z., Liu, X., and Zeng, Z. (2008) Density-functional investigation of metal-silicon cage clusters MSi_n (M = Sc, Ti, V, Cr, Mn, Fe, Co, Ni, Cu, Zn; n = 8-16). *Phys. Rev.*, **77**, 195417.1–195417.8.
66. Sporea, C. and Rabilloud, F. (2007) Stability of alkali-encapsulating silicon cage clusters. *J. Chem. Phys.*, **127**, 164306.1–164306.7.
67. Kumar, V., Briere, T.M., and Kawazoe, Y. (2003) Ab initio calculations of electronic structures, polarizabilities, Raman and infrared spectra, optical gaps, and absorption spectra of $M@Si_{16}$ (M = Ti and Zr) clusters. *Phys. Rev. B*, **68**, 155412.1–155412.9.
68. Kawamura, H., Kumar, V., and Kawazoe, Y. (2004) Growth, magic behavior, and electronic and vibrational properties of Cr-doped Si clusters. *Phys. Rev. B*, **70**, 245433.
69. Andriotis, A.N., Mpourmpakis, G., Froudakis, G.E., and Menon, M. (2002) Stabilization of Si-based cage clusters and nanotubes by encapsulation of transition metal atoms. *New J. Phys.*, **4**, 78.71–78.14.
70. Menon, M., Andriotis, A.N., and Froudakis, G. (2002) Structure and stability of Ni-encapsulated Si nanotube. *Nano Lett.*, **2**, 301–304.
71. Han, J.G., Zhao, R.N., and Duan, Y. (2007) Geometries, stabilities, and growth patterns of the bimetal Mo_2-doped Si_n (n = 9-16) clusters: a density functional investigation. *J. Phys. Chem. A*, **111**, 2148–2155.
72. Beck, S.M. (1987) Studies of silicon cluster–metal atom compound formation in a supersonic molecular beam. *J. Chem. Phys.*, **87**, 4233–4234.
73. Beck, S.M. (1989) Mixed metal–silicon clusters formed by chemical reaction in a supersonic molecular beam: implications for reactions at the

metal/silicon interface. *J. Chem. Phys.*, **90**, 6306–6312.

74. Neukermans, S., Wang, X., Veldeman, N., Janssens, E., Silverans, R.E., and Lievens, P. (2006) Mass spectrometric stability study of binary MSn clusters (S = Si, Ge, Sn, Pb, and M = Cr, Mn, Cu, Zn). *Int. J. Mass Spectrom.*, **252**, 145–150.
75. Chen, Z., Neukermans, S., Wang, X., Janssens, E., Zhou, Z., Silverans, R.E., King, R.B., von Ragué Schleyer, P., and Lievens, P. (2006) To achieve stable spherical clusters: general principles and experimental confirmations. *J. Am. Chem. Soc.*, **128**, 12829–12834.
76. Ohara, M., Miyajima, K., Pramann, A., Nakajima, A., and Kaya, K. (2002) Geometric and electronic structures of terbium-silicon mixed clusters. *J. Phys. Chem. A*, **106**, 3702–3705.
77. Ohara, M., Miyajima, K., Pramann, A., Nakajima, A., and Kaya, K. (2007) Geometric and electronic structures of terbium-silicon mixed clusters. *J. Phys. Chem. A*. **111**, 10884.
78. Ohara, M., Koyasu, K., Nakajima, A., and Kaya, K. (2003) Geometric and electronic structures of metal (M)-doped silicon clusters (M = Ti, Hf, Mo and W). *Chem. Phys. Lett.*, **371**, 490–497.
79. Koyasu, K., Akutsu, M., Mitsui, M., and Nakajima, A. (2005) Selective formation of MSi_{16} (M = Sc, Ti, and V). *J. Am. Chem. Soc.*, **127**, 4998–4999.
80. Koyasu, K., Atobe, J., Akutsu, M., Mitsui, M., and Nakajima, A. (2007) Electronic and geometric stabilities of clusters with transition metal encapsulated by silicon. *J. Phys. Chem. A*, **111**, 42–49.
81. Akutsu, M., Koyasu, K., Atobe, J., Miyajima, K., Mitsui, M., and Nakajima, A. (2007) Electronic properties of Si and Ge atoms doped in clusters: In*n*Sim and In*n*Gem. *J. Phys. Chem. A*, **111**, 573–577.
82. Furuse, S., Koyasu, K., Atobe, J., and Nakajima, A. (2008) Experimental and theoretical characterization of $MSi_{16^{-1}}$, MGe_{16}-, MSn_{16}-, and MPb_{16}- (*M* = Ti, Zr, and Hf): the role of cage aromaticity. *J. Chem. Phys.*, **129**, 064311.1–064311.6.
83. Zheng, W., Nilles, J.M., Radisic, D., and Bowen Jr., J.K.H. (2005) Photoelectron spectroscopy of chromium-doped silicon cluster anions. *J. Chem. Phys.*, **122**, 071101.1–071101.4.
84. Grubisic, A., Wang, H., Ko, Y.J., and Bowen Jr., K.H. (2008) Photoelectron spectroscopy of europium-silicon cluster anions, $EuSi_n$- ($3 < n < 17$). *J. Chem. Phys.*, **129**, 054302.1–054302.5.
85. Jaeger, J.B., Jaeger, T.D., and Duncan, M.A. (2006) Photodissociation of metal-silicon clusters: encapsulated versus surface-bound metal. *J. Phys. Chem. A*, **110**, 9310–9314.
86. Janssens, E., Gruene, P., Meijer, G., Wöste, L., Lievens, P., and Fielicke, A. (2007) Argon physisorption as structural probe for endohedrally doped silicon clusters. *Phys. Rev. Lett.*, **99**, 063401.1–063401.4.
87. Kawamura, H., Kumar, V., and Kawazoe, Y. (2005) Growth behavior of metal-doped silicon clusters Si_nM (*M* = Ti, Zr, Hf; *n* = 8-16). *Phys. Rev. B: Condens. Matter Mater. Phys.*, **71**, 075423.
88. Guo, L.-J., Liu, X., Zhao, G.-F., and Luo, Y.-H. (2007) Computational investigation of $TiSi_n$ (*n* = 2-15) clusters by the density-functional theory. *J. Chem. Phys.*, **126**, 234704.1–234704.7.
89. Khanna, S.N., Rao, B.K., and Jena, P. (2002) Magic numbers in metallo-inorganic clusters: chromium encapsulated in silicon cages. *Phys. Rev. Lett.*, **89**, 016803.1–016803.6.
90. Hagelberg, F., Xiao, C., William, A., and Lester, J. (2003) Cagelike Si_{12} clusters with endohedral Cu, Mo, and W metal atom impurities. *Phys. Rev. B*, **67**, 035426.1–035426.9.
91. Gruene, P., Fielicke, A., Meijer, G., Janssens, E., Ngan, V.T., Nguyen, M.T., and Lievens, P. (2008) Tuning the geometric structure by doping silicon clusters. *ChemPhysChem*, **9**, 703–706.

8
Direct Observation of Dynamic Solid-State Processes with X-ray Diffraction

Panče Naumov

8.1
Introduction

Ever since the discovery by Röntgen in 1895, the first diffraction pattern of a crystal made by Knipping and von Laue in 1914, and the theory to determine the crystal structure proposed by Bragg in 1915, the utility of X-rays has become and has remained an indispensable tool for structural analysis of materials. The historical developments as well as specific aspects of various analytical techniques based on X-rays, including the X-ray diffraction, have been reviewed extensively, and are not elaborated here. One of the few events in the history of the X-ray diffraction which gave a new impetus to the use of the technique and definitely opened a new era in the structural science – the macromolecular crystallography – is the famous ''Photo 51,'' a single X-ray image of the sodium salt of DNA recorded by Rosalind Franklin in 1952, which enabled Watson and Crick to explain the structure of one of the most important molecules today as early as in 1953. Since those early days, the X-ray diffraction and scattering methods have achieved a tremendous advancement, both in respect to the technical performance and the studied materials. The two main technical components of any method based on X-rays, the source and the detector, have each experienced remarkable improvements: while it was necessary to spend a few months to determine a single crystal structure of a small molecule by using Weissenberg camera, and it would have normally taken several days to complete the task with the later four-circle diffractometers equipped with point detectors, it takes less than only a few hours by using the nowadays widely employed two-dimensional detectors. These requirements are now further being sized down to the second and even millisecond range by the realization of new detectors, which will inevitably shorten the time required for laboratory-scale diffraction experiments for a few orders of magnitude in the very near future. The X-ray sources, on the other hand, have experienced a tremendous increase in their brilliance (a physical quantity which is usually used to characterize one of the properties of radiation) of over 15 orders of magnitude during the recent decades, and pulses in the picosecond time domain are nowadays commonly available with the third-generation synchrotron sources,

Ideas in Chemistry and Molecular Sciences: Advances in Nanotechnology, Materials and Devices.
Edited by Bruno Pignataro

ISBN: 978-3-527-32543-6

in addition to the conventional X-ray tubes which provide timely continuous X-rays [1]. This trend is already at its next step in the recent years, when the fourth generation X-ray sources that provide another four-orders-of-magnitude leap in the average brilliance together with sub-picosecond pulses are becoming available at several light sources around the world, opening the era of femtosecond-scale time-resolved structural science.

Without doubt, the most widespread analytical technique based on utilization of X-rays is the X-ray diffraction method, which employs the interference of X-rays, diffracted from the planes in the crystal, which are composed of the structural building units, to provide quantitative information of the three-dimensional spatial distribution of the atoms – the molecular and crystal structure. Much benefit of the developments in the X-ray diffraction analysis has already gone to the structure analysis field of the materials science, which has evolved in the recent couple of decades as a multidisciplinary, purpose-oriented research, invoked by the needs of the rapidly developing human society. The materials science applications have been boosted by the development of commercially available experimental assemblies for structure determination that usually consist of a diffractometer, a two-dimensional detector, and a low-temperature device. Together with the simultaneous advancement of instrumentation for characterization of optical, mechanical, magnetic, and other properties of the materials, as well as with the advance of the atom-resolution microscopic techniques (SEM, AFM, TEM), these developments have turned the structure determination much into a routine work for rapid identification of bulk organic, metal–organic, organometallic, or inorganic materials, mainly aimed to support the explanation of their physical properties. At the other end of the line stands the macromolecular crystallography, which has seen a tremendous automatization, together with increased resolution and decreased times for data collection by the use of the white-beam techniques at synchrotrons, and is steadily and increasingly contributing to the life sciences with a significant amount of new and important structural information. In such constellation of events, the small molecule crystallography is oftentimes seen as becoming a part of the routine of materials scientists, biochemists, or organic chemists, and the number of both fundamental studies and the researchers who specialize in the field has inevitably increased. The shift of the crystallographers' interests from the intramolecular structure, and the covalent or coordination interactions, to the supramolecular level, related to the hydrogen-bonded and weak intermolecular interactions, and the evolution of the crystal engineering has become one of the expanding research subfields of the structural chemistry, which still has both (X-ray or neutron) diffraction analysis and predictions based on small molecule structures as the main source of information and target of study. In particular, the research interest in polymorphism, cocrystals, and polymeric metal–organic compounds has revived, which added to the increasing number of structures that are being accumulated in the structure databases. A few new, specialized journals also appeared in this field (e.g., Crystal Growth & Design, CrystEngComm, Supramolecular Chemistry, the on-line section E of Acta Crystallographica).

This chapter is devoted to a collection of selected illustrative examples of application of the *X-ray photodiffraction method* (sometimes also referred to as *photocrystallographic method* or *technique*),[1] an important and relatively recently developed research direction in the small molecule crystallography. The subject of the X-ray photodiffraction method are *changes in crystal structures induced by photoexcitation, either during the process of excitation or as a consequence of it*. From this general definition, it follows that this evolving analytical technique combines the photochemistry (or photophysics) with the X-ray diffraction method in order to arrive at precise information about the effects of photoexcitation on the structure. The technique is increasingly being recognized as a very prospective and indispensable tool for direct observation of fundamental processes in the solid state. There are several excellent recent reviews and discussion articles devoted to specific aspects, chemical, physical, or technical, of the X-ray photodiffraction method [2–9]. Rather than being a highly technical or exhaustive report of all reported examples of applications of this technique, the current review text was intended to fit the contents of this monograph by providing its general chemical audience with a brief overview of the main principles behind this important method, together with a selection of examples from our laboratories and some of the leading laboratories in the field, that we considered illustrative of its usefulness and potentials for application to problems in the fundamental and applied chemical sciences. Following the introduction in this section, the basic principles, assets, and pitfalls of the X-ray photodiffraction are briefly discussed in Section 8.2. Selected examples of application of the steady-state and time-resolved photodiffraction, ranging from physical to biological systems, are listed and discussed in Sections 8.3 and 8.4. In Section 8.5, the prospects, potentials, and possible future developments of this and similar methods based on X-ray radiation are briefly described.

8.2
The Basics: Principles, Applications, Advantages and Drawbacks of the X-ray Photodiffraction Method

The usefulness of X-rays for structural studies relies on several important properties inherent to their energy (wavelength), and it is also related to the recent technical advancement of the instrumentation for their generation and detection. One of the reasons behind the preferred choice of light as external stimulus to affect or excite the solid-state structure in the X-ray photodiffraction method, contrary to temperature or pressure, is related to the convenience in terms of the practical realization of such experiments: with the presently commercially available tabletop

1) Both terms *X-ray photodiffraction* and *X-ray photocrystallography* have been used in the literature. The arguments as to the righteousness of their use are similar to those that apply to the differences between the terms *X-ray diffraction* and *X-ray crystallography*. Although more commonly used by chemists and biochemists, the genealogy of the second term implies writing about crystals and is mainly used to refer to *single crystal X-ray diffraction*. As the first term describes the actual physical phenomenon and is more general in meaning (by being used also for powder diffraction methods), "X-ray photodiffraction" is used throughout this chapter.

femtosecond laser sources and the related optics, the light can be very easily produced, energy-tuned, and handled. Furthermore, when using light for excitation, no physical contact with the sample is necessary; this greatly simplifies the X-ray diffraction experiments which ordinarily involve moving instrumental parts. Another, yet probably more important reason, for the use of light for inducing structural changes is related to potential applications, and the fundamental role that light has in the information technology, and the importance that it will probably continue to have for controlling the properties of materials in the future. Holding the absolute speed record in the nature, light will continue to be the fastest medium for control of the properties of materials, and for recording or transfer of information in a variety of applications, starting from photooptical memories and switches, light-coupled spintronics, through applications in the life sciences and medicine, to triggering or switching units coupled to molecular wires within electrical nanocircuits and molecule-sized nanomachines.

The usefulness of the X-ray diffraction technique for structure analysis of the interaction between the light and the bulk matter stems from its very basics: it can provide *direct* and *very precise* information, with atomic-scale resolution, on the geometrical changes that accompany very fundamental processes of structural perturbations induced by excitation, usually with electromagnetic radiation of energies within the ultraviolet or the visible region of the spectrum. The technique provides a tool for structure determination of short-lived, unstable, or metastable species, which are not accessible by other methods [10], and also for real-time *in situ* observation of chemical reactions [11]. This information can be conveniently coupled with details on the reaction energetics, obtained by spectroscopic methods, to provide complete information about the effects on the geometry and the energy, and their relation to the properties of the material.

The solid-state phenomena, which have been studied with the X-ray photodiffraction method or could be considered for future studies, can be provisionally classified as ''chemical'' or ''physical,'' although strictly speaking, there is no strict distinction between these groups. The chemical phenomena (chemical reactions) usually include breaking and/or formation of chemical bonds due to excitation, such as electrocyclizations, cycloadditions, bond isomerizations, dimerizations, transfer of atom groups or hydrogen atoms, polymerizations, bond dissociations, and other reactions. Except for the thoroughly studied [2+2] photodimerizations reactions, which have been a subject of several previous reviews, the most studied chemical reactions have been described in this chapter. The physical phenomena are related to photoexcitation, formation of exciplexes, evolution or progression of phonons and shock waves [12], lattice dynamics [13], laser heating of thin films [14], photomagnetization, spin-related phenomena, displacements or movements of molecules or their parts, charge transfer, phase transitions, and similar processes. The range of systems of interest that could be considered is wide, and extends from crystalline bulk macromolecules, through crystals of small molecules or their assemblies, to single macromolecules [15]. Although there are many ways for practical realization of the X-ray photodiffraction experiments, the most general classification according to the technical background is probably the one based

on whether the method is applied in a *steady-state* or *time-resolved* mode, which depends on whether the structure is analyzed by considering the time as one of the variables. Each of these experiments can be performed either by using single crystals or powders (microcrystals) as sample. In the steady-state version, one can employ *ex situ* or *in situ* excitation of the sample, oftentimes a single crystal, using a continuous wave or a pulsed light source. The time-resolved methods can be further divided by the type of X-ray radiation used, monochromatic or polychromatic (the latter has been used to analyze proteins, but it was recently also applied to small molecules). Both the steady-state and time-resolved photodiffraction can be performed by using pulsed X-rays from a laboratory or synchrotron source.

In the simplest case of a steady-state *ex situ* single-crystal photodiffraction, the crystal is exposed to an appropriately filtered light, until a sufficient amount[2)] of the photoinduced unstable, metastable or stable product has been created. If there are no thermally induced phase transitions, these experiments are usually performed at low (oftentimes cryogenic) temperatures, in order to increase the lifetime of the product (in case it is a metastable phase), and to decrease the thermal effects on electron density that are caused by atomic oscillations at any temperature above the absolute zero and which are additionally enhanced by heating caused by the incident light. The low temperatures are also useful to decrease the possibility of partial melting or the occurrence of fatigue of the sample caused by undesired side reactions. It should be noted, however, that excitation at different temperatures can result in qualitatively and quantitatively different outcome in terms of the structure of the product; the eventual phase transitions of the reactant crystal, the product, thermally induced chemical reactions of the intermediates or the product, and variations in the decay rate or reaction pathways with the temperature, among the other factors, can all affect the result. In addition to low temperatures, some of these practical obstacles can be overcome by using selective and short-term excitation. The thermal effects can be measured either directly (for example, by using the temperature-dependent shifts or intensities of peak(s) originating from the sample itself or that from a purposefully added

2) There are different suggestions about the ''sufficient amount'' of species produced in these experiments which can be considered a low-limit threshold value for reliable detection (the ideal conversion would be 100% which can be realized only in certain cases). The approach ultimately depends on the properties of the particular system; the magnitude of the structural perturbation, the resolution of the data, the diffraction ability of the sample and its (initial and final) quality can be considered as only some of the factors which should be considered in the estimation of the lower observable limit of photoconversion. Conversions above ~10% are usually considered sufficient for organic crystals, whereas yields down to 5% or even <2% are occasionally considered for metal-containing samples. Additional difficulty related to the estimation of this value is the method of its detection: the diffraction methods, as well as the other (e.g., spectroscopic) methods exhibit inherent imperfections in that respect (e.g., related to correlation problems). It should be pointed out that a structure refinement represents a way of fitting a chemical model into an experimental electron density, which ultimately represents an approximation of the real atomic positions. A combined information on the photochemical yield, preferably obtained by a combination of methods based on different properties of the photoinduced species, is probably a more reliable approach to estimate the conversion yield than any of these methods alone.

internal temperature standard, for instance, in powder X-ray photodiffraction, or by direct temperature measurements), or they can be estimated by calculation, considering variables such as the power or the flux of the incident excitation light, the thermal properties of the sample, and the temperature of its environment.

Three of perhaps the most difficult problems, which are related to the solid state of the sample, and have thus far limited, to a significant extent, the widespread utilization of the X-ray photodiffraction technique on a large number of systems, are the limited penetration depth of the excitation light, the preservation of the three-dimensional order of crystals during the photoexcitation and the low diffracting ability of some crystals. The first difficulty is inherent to the significantly different cross-sections (or coefficients) for absorption by the solid-state matter of radiation in the X-ray and the ultraviolet or visible ranges of the electromagnetic radiation spectrum. Various practical methods to overcome this difficulty have been suggested, mainly based on approaches that have been employed since the early days of the electron spectroscopy in solution. These examples include off-maximum selective excitation (''band tail irradiation'') of the absorption transitions that are naturally broadened in the solid state, or multiphoton (usually two-photon) excitation to prevent the light re-absorption by the product and to increase the bulk conversion of the sample. Although very useful, these approaches are of limited applicability due to their dependence on the fortuitous presence in the energy diagram of a certain system of additional (virtual or real) electronic energy levels other than the main absorptions, sufficiently large cross-sections of the nonfundamental transitions and increased thermal effects that can induce additional, thermally induced processes with similar or identical product outcome, when radiation in the near-infrared region is used. The second limitation is related to the decreased crystalline order (sometimes also referred to as increased mosaicisity, although this latter term has alternative interpretations), and light- or heat-induced formation of crystalline domains with similar, but yet slightly differing orientations in the initially uniform single crystals. Although the theory behind this effect is well understood, in practice it is oftentimes difficult to discern clearly and unequivocally the relative importance of the effects of photoexcitation from those related to partial crystal disintegration, especially where minor contribution of each effect may be present in a system which retains its spatial symmetry upon photoexcitation, unless more detailed information is extracted by rigorous mathematical analysis of the information contained in the properties (spatial distribution, shape, intensity) of the diffracted X-ray beam. Some useful insights into the possibility of an occurrence of solid-state chemical reactions or the lack thereof, and the expected preservation of crystallinity during the processes can be obtained by preliminary considerations of the steric requirements based on the well-defined, ordered nature and the rigidity of the crystalline state relative to amorphous or fluid states. These considerations, initially realized for small molecule crystals through the topochemical principle [16, 17], have been developed into the reaction cavity [18] and similar concepts which relate the probability of occurrence of a solid-state processes to the spatial compatibility of the reactive molecule with its surrounding. The third difficulty, the limited diffracting ability which is occasionally caused by large size of the unit cell

or by unavailability of sufficiently large crystalline samples, can be overcome by use of intense X-ray sources of tunable wavelength, which are nowadays available at the synchrotrons.

Particular attention during the course of X-ray photodiffraction analysis should be devoted to the procedure of data processing and structure refinement. The process from the initial recognition of a structural change in the diffraction pattern to the final treatment of the disorder with chemically sensible model requires a substantial amount of time and attention, in addition to the necessary experience. Minute changes of intensities of individual reflections or of the overall diffracting ability, related to changes in the atomic distribution without change of the translational symmetry or gradual decomposition, or appearance/disappearance of reflections caused by changes in the crystal symmetry, can all be very informative about the photoinduced process at the early stages of the experiment. If these effects are successfully resolved from the artifacts due to heating or decreased crystal integrity, they can provide firm evidence of the occurrence (or not) of structural change by photoexcitation. In the later steps of structure determination procedure, reference to any electron density features that could be indicative for presence of additional molecular species in the structure, may be critical to distinguish the photoinduced features. Finally, the refinement of structures where the disorder has been purposefully induced is a nontrivial task that demands a great amount of effort.

8.3
Steady-State X-ray Photodiffraction: Examples

8.3.1
Transfer of Chemical Groups or Atoms, and Electrocyclization/Ring Opening

The earliest reported photoactive solid-state systems are probably the photochromic compounds, because they have in common very long-lived and intensely colored photoproducts (the lifetimes are usually on the order of hours or days), with very different optical properties relative to the reactant. The known families of photochromic compounds and their photochemical reactions are based upon several reaction mechanisms, the most common being the electrocyclic reactions and group or hydrogen transfers. From the latter, the photochromic salicylideneanilines (anils) are particularly suitable for X-ray diffraction studies, because they exhibit significant and easily detectable structural reorganization, due to enol-keto tautomerism combined with cis–trans isomerization. In the simplest version of the reaction mechanism, by intramolecular proton transfer, the enol form is photochemically converted into a cis-keto form, which then occasionally isomerizes to a trans-keto form. The trans-keto form can be detected by X-ray diffraction analysis [19]. In the most recent study by Sekine, Ohashi *et al.* [20], the trans-keto form was produced *in situ* by irradiation with continuous-wave UV light of a single crystal of the enol form in one of the polymorphs of the

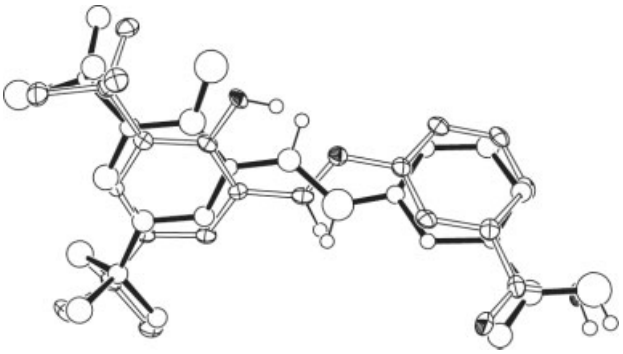

Figure 8.1 Structure of the disordered molecule in the photoirradiated crystal of *N*-3,5-di-*tert*-butylsalicilydiene-3-carboxyaniline (α polymorph), showing the overlapped structures of the enol form (open bonds) and the keto form (filled bonds). Reprinted from Sekine *et al*. (2009) *Bull. Chem. Soc. Jpn*., **82** (1), 50–57. Copyright © 2009, The Chemical Society of Japan.

trimorphic anil *N*-3,5-di-*tert*-butylsalicilydiene-3-carboxyaniline (Figure 8.1). The structure of the photoinduced trans-keto form was clearly detected, and employed for structure-photoactivity correlations with the other polymorphs and similar structures. The result illustrates that, provided that the other conditions required for the reaction are met, the steady-state photodiffraction can be employed with a relatively simple and commonly available experimental setup to obtain useful information on the solid-state photoactivity. In another study, we have provided evidence of the mechanism underlying the photochromism of dinitrobenzylpyridines [21]. These compounds have three groundstates, depending on the position of the proton: CH form, with two benzyl hydrogen atoms, OH form, where one of the benzyl protons is attached to the ortho-nitro group in form of aci-nitro group, and NH form, where the same proton is transferred to the pyridyl nitrogen. By employing the steady-state photodiffraction method with two-photon excitation, similarly to the case of anils [19], we obtained evidence that the blue form corresponds to the NH structure. The photochromic reaction is due to nitro-assisted proton transfer, and its occurrence is possible in the solid state due to the small structural perturbation required by the nitro group to mediate the transfer of the proton as the OH form to the pyridyl nitrogen.

Recently, we obtained the first direct evidence of the photoinduced open-ring structure of a photochromic spiropyran [22]. The spiropyrans and spirooxazines are well-known photochromic compounds, which have already received a variety of photooptical applications. The photochromic activity of these materials in bulk solid state has been described just recently for several salts of cationic spiropyrans and spirooxazines, and it is due to strong stabilization of the open form in the solid state caused by electronic effects. In the photoexcited crystal, the open form exists as zwitterionic resonance structure (Figure 8.2) created by breaking of the spiroconjugation at the C–O bond, with concurrent out-of-plane movement of the

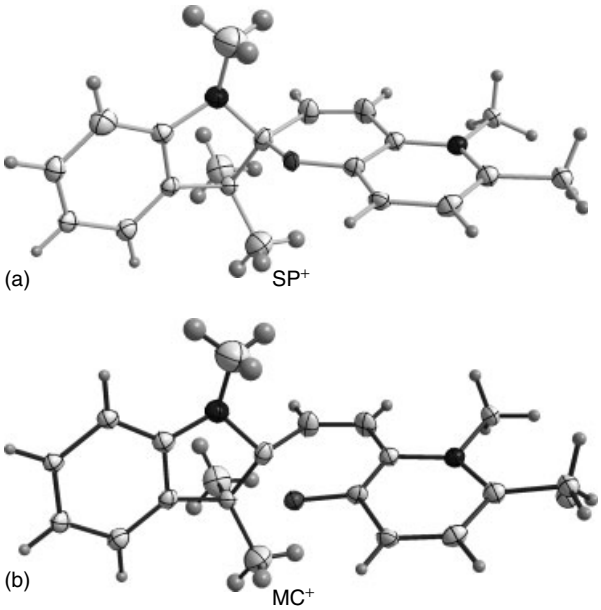

Figure 8.2 ORTEP-style plot of the molecular structure of the disordered cation in UV-irradiated crystal of spiropyran iodide, showing the two components, the reactant spiropyran (SP^+(a)), and the product merocyanine (MC^+(b)).

pyranopyridinium half and in-plane shift of the indoline half, resulting in slight molecular flattening.

One of the early electrocyclic reactions studied by photodiffraction is the photocyclization of *N*-methyl-*N*-{(*E*)-methylmethacrolyl}anilide in a host–guest crystal [23]. Irie *et al*. reported the structure of a photocyclized diarylethene in single-crystalline state [24]. The conclusions about the geometrical changes that accompany this reaction were employed recently to explain the macroscopic morphology changes observed with single crystals of some photochromic diarylethene compounds. An interesting example of the use of neutrons for direct study of solid-state processes is the observation, by neutron diffraction, of the migration of a deuterium atom in the cyclization reaction of formation of chiral thiolactam [25]. Similar neutron diffraction analyses could be combined with X-ray diffraction data in the future to obtain information on the difference electron density redistribution accompanying fundamental chemical reactions.

8.3.2
Bond Isomerizations and Photolytic Reactions

The photodiffraction technique may be also applied in the future to photochemistry of drugs or natural products, an area which has received less attention thus far. A recent example of direct observation of ring-extended intermediate during the

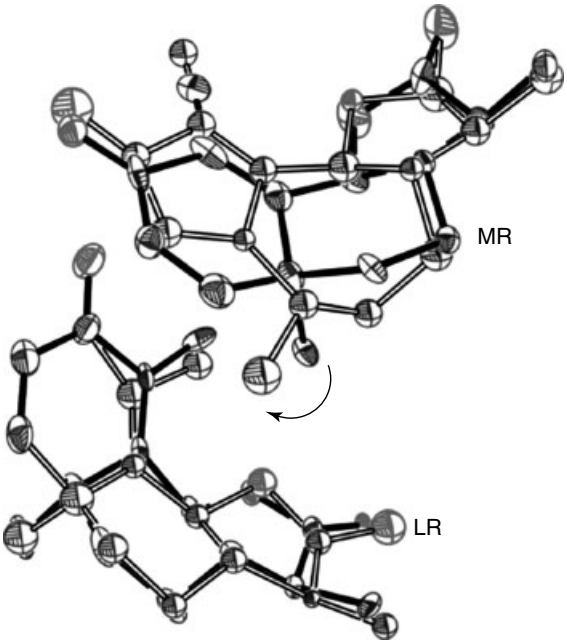

Figure 8.3 ORTEP-style representation of the structure of a 30% converted crystal of α-santonin, showing the original molecules (dark bonds) and the product cyclopentadienone (light bonds). MR and LR denote more and less reactive site, respectively (both molecules at the case of the LR are that of the reactant). Reprinted from Garcia-Garibay *et al.* (2007) *J. Am. Chem. Soc.*, **129**, 9846–9847. Copyright © 2007, The American Chemical Society.

photodimerization of the medicine α-santonin [26] is an excellent illustration of the potentials for such studies. The analysis of the compound helped to unequivocally identify the intermediate species, which is a precursor for the final dimeric product (Figure 8.3). Another example is our report on the study of the intermediate phase during the isomerization of the red mineral realgar to its yellow polymorph pararealgar [27]. The photodiffraction technique provided direct evidence of formation of intermediate phase in which half of the realgar molecule is retained in its envelope-type conformation, while the other half is transformed by effective switching of the positions of one sulfur and one arsenic atom (Figure 8.4).

Owing to the relevance to various processes involving gaseous molecules in biological systems, especially interesting are the photoreactions of linkage isomerization, studied mainly by the group of Coppens. A representative example of successful application of the photodiffraction method to study these systems which have multiple metastable states, is the linkage isomerization of ruthenium sulfur dioxide complexes [28, 29]. Irradiation with 488 nm light of these complexes at low temperature results in re-bonding of the η^1-planar SO_2 molecule, which is initially bound through the sulfur atom, to an η^2-side bound molecule, coordinated through both the sulfur and one oxygen atom (Figure 8.5). Isomerization

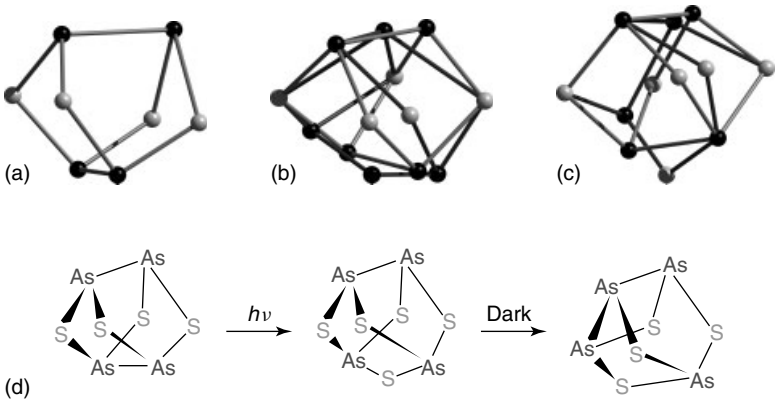

Figure 8.4 Ball-and-stick representation of the structures of the clusters of mineral realgar (α-As_4S_4) before (a), during (b), and after (c) irradiation with visible light. (d): Schematic of the reaction mechanism of photochemical transformation of realgar to pararealgar.

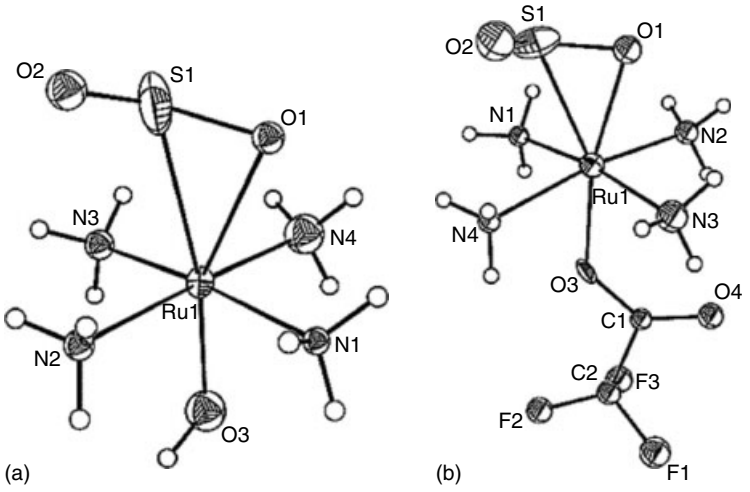

Figure 8.5 Geometry of the cations of *trans*-tetraamineaquo(sulfur dioxide)ruthenium(II) tosylate (a) and *trans*-tetraamine(trifluoroacetate)(sulfur dioxide)ruthenium(II) trifluoroacetate trifluoroacetic acid solvate (1 : 1 : 1) (b) in their metastable state MS2. Reprinted from Coppens *et al*. (2003) *Inorg. Chem*., **42**, 140–147. Copyright © 2003, The American Chemical Society.

of the larger dithionite ion in a binuclear organorhodium complex was reported recently [30].

Another type of chemical reactions that can be studied with X-ray photodiffraction are photolytic reactions of organic molecules, which can provide access to structure elucidation of important reactive intermediates or information of the

respective reaction mechanisms. Although the solid-state photolytic reactions are not uncommon, due to the limited space for separation of the reactive products in the crystal lattice, in many cases the back-reactions of recombination prevent significant amounts of the product to be accumulated. However, in cases where some or all products can be physically or chemically isolated from each other, it is possible to obtain sufficient amount of the unstable product for structure determination. Recently, we have reported the mechanism of a new solid-state reaction of exchange of *N*-chlorine atom and aromatic proton that proceeds selectively and efficiently in single-crystalline state [31]. This reaction can provide green, solventless access to important chloroaromatic compounds which are used as antibiotics and pesticides. By using the *in situ* photodiffraction method we determined the structure of partially reacted crystal, which unraveled that a relatively stable amidyl radical was created (Figure 8.6) in the originally statically disordered crystal. The selectivity of this reaction was explained by the head-to-tail hydrogen bonding arrangement of the reactant molecules, which resulted in reaction between the consecutive molecules within the same hydrogen-bonded chain.

8.3.3
Structures of Species in Excited States, Electron Transfer, and Spin Crossover

One of the most important applications of the X-ray photodiffraction method is the elucidation of structures of molecular species in their excited states. The excited-state structure analysis by steady-state excitation requires, besides the other requirements, systems in which the excited state is sufficiently long-lived, and the structural changes are sufficiently large which will did the distinction from the original structure. One of the first examples, the detailed analysis of the metastable excited state of sodium nitroprusside, $Na_2[Fe(CN)_5NO]\cdot 2H_2O$, was reported by Coppens *et al.* in 1994 [32]. The excitation of the anion to the metastable state I results in elongation of the Fe–N bond by 0.049(8) Å, and decrease of the average angle N–Fe–C around the metal of 0.8(2)°.

Much attention has been devoted to diplatinum paddlewheel complexes which have long-lived luminescent excited states. In the case of the complex of Pt_2 with diphosphine ligand "pop," $[Pt_2(H)_2(pop)_4]^{2-}$, for example, shortening of the Pt–Pt bond was observed by *in situ* steady-state irradiation [33]. The excited-state structures of the ions $[Pt_2(pop)_4]^{4-}$ and $[Pt(pop)_2(popH)_2]^{2-}$ in five complexes with different quaternary ammonium cations were subsequently analyzed in detail in their equilibrium (photosteady) states by using steady-state X-ray diffraction [34]. Significant decrease of the central Pt–Pt and Pt–P distances was observed in the excited states of these compounds. By employing the steady-state method, Ohashi *et al.* have also analyzed the excited-state structure of a three-coordinated complex of gold(I), $[AuCl(PPh_3)_2]\cdot CHCl_3$ [35]. In the excited state, with a lifetime of 4–10 μs, the unit cell decreases due to contraction of the Au–P and Au–Cl bonds. This bond contraction becomes more pronounced at lower temperatures, and it prescribed to excitation from an antibonding to a bonding molecular orbital. Another determination of excited-state structure with laboratory-scale setup was

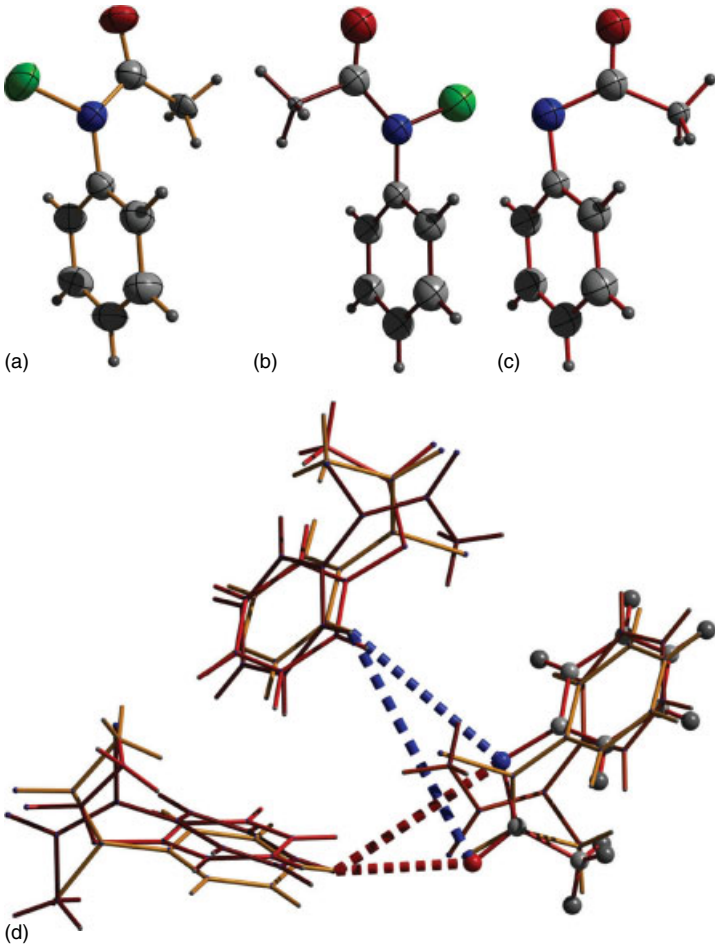

Figure 8.6 (a–c) Molecular structures of the two disordered components of reactant and the radical product molecules, and (d) molecular packing in the disordered crystal of *N*-chloro-*N*-acetylaminobenzene enriched with photoinduced amidyl radical (represented as red ball-and-stick model) by photolysis of the N–Cl bond. The major and minor components of the reactant are presented as ochre and brown stick models, respectively.

recently reported by the same research group for the oxovanadium(IV) cation in its acetylacetonato complex $VO(acac)_2$ (Figure 8.7) [36]. The anisotropies in the thermal and photoexcited lattice changes are different, which provided basis for structure elucidation of the excited state geometry, besides that the lifetime of the excited state is relatively short. Significant extension of the coordination bonds V=O and V–O of the central metal atoms was observed upon d–d* transition.

Owing to the potentials for applications in the spintronics, a lot of attention has been devoted to the study of spin-crossover phenomena, including

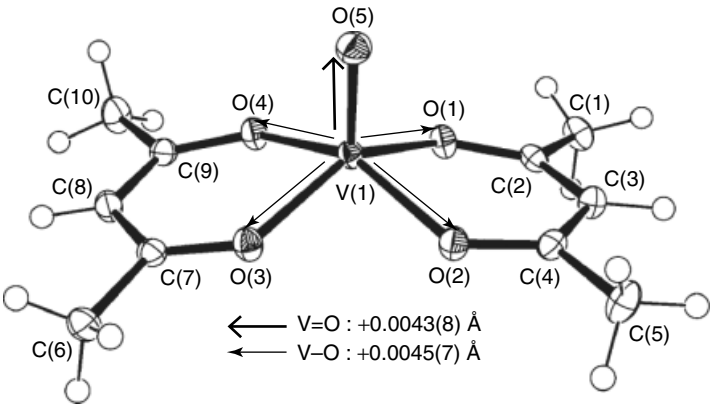

Figure 8.7 Elongation of the V=O and V–O bonds in the excited state of bis(acetylacetonato)oxovanadium(IV). Reprinted from Ohashi *et al.* (2005) *Chem. Lett.*, **34** (9), 1228–1229. Copyright © 2005, The Chemical Society of Japan.

light-induced spin-crossover transitions. An illustrative example is the production of the metastable state of the iron propyltetrazole (ptz) complex $[Fe(ptz)_6](BF_4)_2$ by laser light-induced excited spin-state trapping (LIESST) and its structure elucidation with steady-state photodiffraction [37]. The photoinduced phase transition due to spin crossover in the *tris*(α-picolylamine)iron(II) complex was also studied by steady-state X-ray photodiffraction at cryogenic temperatures [38]. The phase transition is accompanied by a significant increase of the mean Fe–N bonds from 2.011(2) to 2.197(2) Å. The structure of the resulting photoinduced phase produced from the low-temperature phase resembles that of the high-temperature phase.

As mentioned above, among the most serious problems to overcome in the photodiffraction experiments is the decreased crystallinity during the solid-state reactions that are accompanied by large structural reorganization. Some of the possible solutions to this obstacle are preparation of host–guest crystals or cocrystals with suitable secondary molecules, or inclusion of the reactants in the nanospaces of suitable molecular capsules. As representative examples, the incorporation of tiglic [39] or 3-chloroacrylic acids [40] in supramolecular frameworks based on calixarenes provided conditions for complete preservation of crystallinity during the *E*-to-*Z* isomerization, although similar processes are usually destructive to the lattice in crystals of the pure reactants. Another approach is the utilization of powder samples, that is, the powder X-ray photodiffraction method. We have recently demonstrated the usefulness of this method with the photoinduced phase transition in crystals of the free radical 1,3,5-trithia-2,4,6-triazapentalenyl (TTTA) [41]. Around room temperature, this compound undergoes paramagnetic-to-diamagnetic phase transition with exceptionally wide thermal hysteresis. Excitation by pulsed laser light of the low-temperature diamagnetic phase, in which the molecules are dimerized, causes an interdimer electron transfer and local instability within the

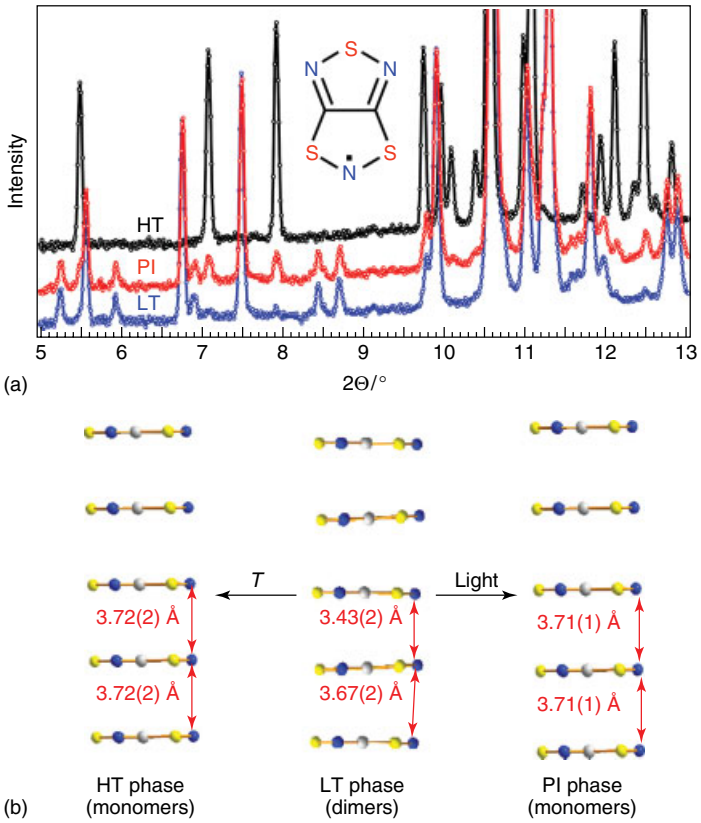

Figure 8.8 (a) Powder diffraction patterns of the 1,3,5-trithia-2,4,6-triazapentalenyl (TTTA) radical in the high-temperature (HT), low-temperature (LT), and photoinduced (PI) phases. (b) Change of the stacking mode and distances accompanying monomer-dimer transitions induced by temperature or light. Adapted from [41]. Copyright © 2007, The American Chemical Society.

stacks. Owing to a cooperative process, this, in turn, triggers separation of the dimers to monomers and results in symmetry changes, which appears as new diffraction peaks corresponding to the structure of the high-temperature phase (Figure 8.8). This result represents the first direct observation of electron transfer between free radical molecules in the solid state.

8.4
Time-Resolved X-ray Photodiffraction: Representative Examples

Relative to the steady-state method, the time-resolved diffraction is technically much more demanding, and therefore, the number of reported examples is still limited. These experiments are related to reversible processes, and they usually

utilize the pump-probe technique, similarly to the time-resolved spectroscopy, but by combining femtosecond laser pulses to initiate the process and short (currently in the picosecond range) X-ray pulses to probe the resulting structure changes. Among the reports that perhaps illustrate the best the application of this method to the study of dynamic physical phenomena is the picosecond-scale observation of paraelectric-to-ferroelectric phase transition in crystals of the organic charge-transfer molecular complex between tetrathiafulvalene and chloranil, reported by Collet, Koshihara *et al.* [42, 43]. Partial charge transfer between the alternating donor and acceptor molecules was photoinduced by femtosecond laser pulses, and the resulting changes in the symmetry of the crystal, caused by the alteration of the intermolecular distances within the molecular stacks, was directly observed by probing the structural change with short X-ray pulses at 100-ps timescale.

The method can be also employed to observe, at ultrashort timescales, laser-pulse-induced atomic movements in the lattice. One of the examples is provided by the elegant study of Sokolowski-Tinten *et al.* [44] who reported observation of phonons at the femtosecond scale by exciting coherent lattice vibrations near to the Lindemann limit of lattice stability. Short X-ray pulses were produced by shining very intense laser pulses on a metal wire, which were used to probe the strong vibrations of the bismuth atoms when the lattice was excited close to the melting point of the material. The results on the frequency of the lattice vibrations correlate well with those obtained using terahertz spectroscopy. Other physical applications of the technique include the observation of melting of semiconductors at a femtosecond scale by Rousse *et al.* [45] and study of the structural changes that accompany solid–solid phase transition of VO_2 at a femtosecond scale by Cavalleri *et al.* [46].

The ultrafast X-ray diffraction has been also employed recently to study the structure and temporal decay of molecules with long-lived excited states (for example, triplet states). These studies give direct insight into the primary processes following photoexcitation, which are determinant to the later stages of the deexcitation process and ultimately decide the distribution and yield of the products. A time-resolved, ''stroboscopic'' experiment, provided direct evidence for the photoexcited state of the paddlewheel ion $[Pt_2(pop)_4]^{4-}$ [47]. Recently, formation of excimer between the neighbor trimers with a lifetime in the microsecond region was detected by time-resolved X-ray photodiffraction study of the trimeric compound $\{[3,5\text{-}(CF_3)_2(\text{pyrazolate})]Cu\}_3$ [48].

Owing to the inherent difficulties related to the large molecular weights, lower accuracy in the determination of the atomic positions, and pronounced instability of the samples in laser beams or at room temperature, perhaps the most challenging goal is the application of the ultrafast X-ray photodiffraction to study time-resolved processes in protein crystals. The result, nevertheless, provides direct insight into very important biological processes, and brings significant advancement in our understanding of the primary processes in biological reaction mechanisms, relative to those that are usually suggested on the basis of the ''still'' structures of the reactants and/or products. As a representative example, the direct observation

of the photolysis of carbon monoxide molecule from a myoglobin active center by Šrajer, Moffat *et al.* [49] should be pointed out. By using the Laue version of the time-resolved X-ray photodiffraction, the processes of relaxation of the protein matrix after the detachment of carbon monoxide ligand and its rebinding to the metal center were studied at a nanosecond timescale. The result provided evidence of the effect of this process on the immediate protein environment. By employing 150-ps time-resolved X-ray diffraction, Schotte *et al.* have observed structural changes which appear in the intermediate stage of the functioning of a myoglobin mutant [50]. In the intermediate stages, they evidenced structural changes which were much more pronounced than the difference between the respective carboxy and the deoxy structures. Much more detailed discussion on the advantages and drawbacks of the biochemical time-resolved crystallography is provided in a review article by Moffat [4].

8.5 Conclusions and Future Outlook

The X-ray photodiffraction technique is a very useful method which can provide invaluable information on dynamic processes in the bulk state of ordered solid materials. This evolving analytical technique, however, is still at its development stages, and the application and suitability to study a particular problem of solid-state reactivity depend on many factors; at present, it still puts a notably large number of requirements both to the technical performance and to the system under investigation, which has ultimately resulted in a limited number of case studies. At the other end, the unavailability of commercial instrumental setup for X-ray photodiffraction hinders analysis of larger number of systems, and in addition, for each particular case, a number of experimental conditions need to be optimized, which is usually a time-consuming process that requires an interdisciplinary experience. Nevertheless, the results obtained by the X-ray photodiffraction method can be conveniently complemented with other, for example, spectroscopic techniques, to obtain chemically important structural information, as well as to shorten the procedure for optimization of the experimental conditions. The advance of the forthcoming X-ray free electron lasers to shorten the timescales is an important direction for further development, both for physics as well as for structural biology [51]. These future applications will also require fast-determining detectors, which are currently a potential bottleneck in the process of squeezing of the timescale. Apparently, the development of new detectors for faster data collection, specialized for time-resolved studies [52] will be an important step forward.

While the importance of the X-ray photodiffraction is being increasingly recognized, other X-ray-based methods to study processes in the time-domain science, in solution as well as in the solid state, have also emerged. As some of the representative examples, the solution-state dynamics of photoexcited iodine was observed with X-ray scattering at a picoseconds scale [53] and solvent reorganization around photo excited species was studied by X-ray absorption spectroscopy [54].

The time-resolved diffraction using neutrons or electrons, for example, for studying phenomena such as those related to the dynamics of electron–phonon relaxation [55] in the femtosecond region is also on the rise, and it will inevitably contribute in the future to deeper understanding of the most fundamental primary processes that occur during the interactions of the matter with light.

Acknowledgments

The author thanks his former advisors, Prof. Yuji Ohashi (Tokyo), Prof. Kenji Sakurai (Tsukuba), Prof. Gligor Jovanovski (Skopje), and Prof. Shunichi Fukuzumi (Osaka) for their support, encouragement, and advice.

References

1. Clegg, W. (2000) Synchrotron chemical crystallography. *J. Chem. Soc., Dalton Trans.*, 3223–3232.
2. Wulff, M., Schotte, F., Naylor, G., Bourgeois, D., Moffat, K., and Mourou, G. (1997) Time-resolved structures of macromolecules at the ESRF: single-pulse Laue diffraction, stroboscopic data collection and femtosecond flash photolysis. *Nucl. Instr. Meth. Phys. Res. A*, **398**, 69–84.
3. Coppens, P. (2002) Time-resolved chemistry at atomic resolution. *Faraday Discuss.*, **122**, 1–11.
4. Moffat, K. (2001) Time-resolved biochemical crystallography: a mechanistic perspective. *Chem. Rev.*, **101**, 1569–1581.
5. Cole, J.M., Raithby, P.R., Wulff, M., Schotte, F., Plech, A., Teat, S.J., and Bushnell-Wye, G. (2002) Nanosecond time-resolved crystallography of photo-induced species: case study and instrument development for high-resolution excited-state single-crystal structure determination. *Faraday Discuss.*, **122**, 119–129.
6. Coppens, P. (2003) What can time-resolved diffraction tell us about transient species?: excited-state structure determination at atomic resolution. *Chem. Commun.*, 1317–1320.
7. Cole, J.M. (2004) Single-crystal X-ray diffraction studies of photo-induced molecular species. *Chem. Soc. Rev.*, **33**, 501–513.
8. Cole, J.M. (2008) X-ray diffraction of photolytically induced molecular species in single crystals, in *Models, Mysteries, and Magic of Molecules* (eds J.C.A. Boeyens and J.F. Ogilvie), Springer, pp. 29–62.
9. Ohashi, Y. (2008) Structural determination of unstable species, in *Models, Mysteries, and Magic of Molecules* (eds J.C.A. Boeyens and J.F. Ogilvie), Springer, pp. 109–135.
10. Schlichting, I. (2000) Crystallographic structure determination of unstable species. *Acc. Chem. Res.*, **33**, 532–538.
11. Ohashi, Y. (1998) Real-time in situ observation of chemical reactions. *Acta Crystallogr.*, **A54**, 842–849.
12. Lindenberg, A.M., Kang, I., Johnson, S.L., Missalla, T., Heimann, P.A., Chang, Z., Larsson, J., Bucksbaum, P.H., Kapteyn, H.C., Padmore, H.A., Lee, R.W., Wark, J.S., and Falcone, R.W. (2000) Time-resolved X-ray diffraction from coherent phonons during a laser-induced phase transition. *Phys. Rev. Lett.*, **84** (1), 111–114.
13. Rose-Petruck, C., Jimenez, R., Guo, T., Cavalleri, A., Siders, C.W., Ráksi, F., Squier, J.A., Walker, B.C., Wilson, K.R., and Barty, C.P.J. (1999) Picosecond-milliångstrom lattice dynamics measured by ultrafast X-ray diffraction. *Nature*, **398** (25), 310–312.

14. Rischel, C., Rousse, A., Uschmann, I., Albouy, P.-A., Geindre, J.-P., Audebert, P., Gauthier, J.-C., Förster, E., Martin, J.-L., and Antonetti, A. (1997) Femtosecond time-resolved X-ray diffraction from laser-hated organic films. *Nature*, **390** (4), 490–492.
15. Neutze, R., Wouts, R., van der Spoel, D., Weckert, E., and Hajdu, J. (2000) Potential for biomolecular imaging with femtosecond X-ray pulses. *Nature*, **406** (17), 752–757.
16. Cohen, M.D. and Schmidt, G.M.J. (1964) Topochemistry. Part I. A survey. *J. Chem. Soc.*, 1996–2000.
17. Schmidt, G.M.J. (1971) Photodimerization in the solid state. *Pure Appl. Chem.*, **27**, 647–678.
18. Ohashi, Y. (1996) Reactivity in molecular crystals. *Curr. Opin. Solid State Mater. Sci.*, **1** (4), 522–532.
19. Harada, J., Uekusa, H., and Ohashi, Y. (1999) X-ray analysis of structural changes in photochromic salicylideneaniline crystals. Solid-state reaction induced by two-photon excitation. *J. Am. Chem. Soc.*, **121**, 5809–5810.
20. Johmoto, K., Sekine, A., Uekusa, H., and Ohashi, Y. (2009) Elongated lifetime of unstable colored species by intermolecular hydrogen bonds formation in photochromic crystals. *Bull. Chem. Soc. Jpn.*, **82** (1), 50–57.
21. Naumov, P., Sekine, A., Uekusa, H., and Ohashi, Y. (2002) Structure of the photocolored 2-(2′,4′-dinitrobenzyl)pyridine crystal: two-photon induced solid-state proton transfer with minor structural perturbation. *J. Am. Chem. Soc.*, **124**, 8540–8541.
22. Naumov, P., Yu, P., and Sakurai, K. (2008) Electronic tera-order stabilization of photoinduced metastable species: Structure of the photochromic product of spiropyran determined with *in situ* single crystal X-ray photodiffraction. *J. Phys. Chem. A*, **112**, 5810–5814.
23. Hosomi, H., Ohba, S., Tanaka, K., and Toda, F. (2000) The first in situ observation of intramolecular rotation and cyclization of anilide by an X-ray study: partial single-crystal to single-crystal photocyclization of *N*-methyl-*N*-{*(E)*-methylmethacrolyl} anilide in inclusion crystals. *J. Am. Chem. Soc.*, **122**, 1818–1819.
24. Kodani, T., Matsuda, K., Yamada, T., Kobatake, S., and Irie, M. (2000) Reversible diastereoselective photocyclization of a diarylethene in a single-crystalline phase. *J. Am. Chem. Soc.*, **122**, 9631–9637.
25. Hosoya, T., Uekusa, H., Ohashi, Y., Ohhara, T., Kimura, H., and Noda, Y. (2003) Deuterium migration mechanism in chiral thiolactam formation by neutron diffraction analysis. *Chem. Lett.*, **32** (8), 742–743.
26. Natarajan, A., Tsai, C.K., Khan, S.I., McCarren, P., Houk, K.N., and Garcia-Garibay, M.A. (2007) The photorearrangement of α-santonin is a single-crystal-to-single-crystal reaction: a long kept secret in solid-state organic chemistry revealed. *J. Am. Chem. Soc.*, **129**, 9846–9847.
27. Naumov, P., Makreski, P., and Jovanovski, G. (2007) Direct atomic scale observation of linkage isomerization of As_4S_4 clusters during the photoinduced transition of realgar to pararealgar. *Inorg. Chem.*, **46**, 10624–10631.
28. Kovalevsky, A.Y., Bagley, K.A., Cole, J.M., and Coppens, P. (2002) The first photocrystallographic evidence for light-induced metastable linkage isomers of ruthenium sulfur dioxide complexes. *J. Am. Chem. Soc.*, **124**, 9241–9248.
29. Kovalevsky, A.Y., Bagley, K.A., Cole, J.M., and Coppens, P. (2003) Light-induced metastable linkage isomers of ruthenium sulfur dioxide complexes. *Inorg. Chem.*, **42**, 140–147.
30. Nakai, H., Mizuno, M., Nishioka, T., Koga, N., Shiomi, K., Miyano, Y., Irie, M., Breedlove, B.K., Kinoshita, I., Hayashi, Y., Ozawa, Y., Yonezawa, T., Toriumi, K., and Isobe, K. (2006) Direct observation of photochromic dynamics in the crystalline state of an organorhodium dithionite complex. *Angew. Chem. Int. Ed.*, **45**, 6473–6476.
31. Naumov, P., Sakurai, K., Tanaka, M., and Hara, H. (2007) Direct observation of aminyl radical intermediate during single-crystal to single-crystal photoinduced Orton rearrangement. *J. Phys. Chem. B*, **111**, 10373–10378.

32. Presseprich, M.R., White, M.A., Vekhter, Y., and Coppens, P. (1994) Analysis of a metastable electronic excited state of sodium nitroprusside by X-ray crystallography. *J. Am. Chem. Soc.*, **116**, 5233–5238.
33. Yasuda, N., Kanazawa, M., Uekusa, H., and Ohashi, Y. (2002) Excited-state structure of a platinum complex by X-ray analysis. *Chem. Lett.*, 1132–1133.
34. Yasuda, N., Uekusa, H., and Ohashi, Y. (2004) X-ray analysis of excited-state structures of the diplatinum complex anions in five crystals with different cations. *Bull. Chem. Soc. Jpn.*, **77**, 933–944.
35. Hoshino, M., Uekusa, H., and Ohashi, Y. (2006) X-ray analysis of excited-state molecular structure of $[AuCl(PPh_3)_2]$. *Bull. Chem. Soc. Jpn.*, **79** (9), 1362–1366.
36. Hoshino, M., Sekine, A., Uekusa, H., and Ohashi, J. (2005) X-ray analysis of bond elongation in $VO(acac)_2$ in the excited state. *Chem. Lett.*, **34** (9), 1228–1229.
37. Kusz, J., Spiering, H., and Gütlich, P. (2000) X-ray study of the light-induced metastable state of a spin-crossover compound. *J. Appl. Crystallogr.*, **33**, 201–205.
38. Huby, N., Guérin, L., Collet, E., Toupet, L., Ameline, J.-C., Cailleau, H., Roisnel, T., Tayagaki, T., and Tanaka, K. (2004) Photoinduced spin transition probed by x-ray diffraction. *Phys. Rev. B*, **69**, 020101.1–0201010.4.
39. Zheng, S.-L., Messerschmidt, M., and Coppens, P. (2007) Single-crystal-to-single-crystal E → Z isomerization of tiglic acid in a supramolecular network. *Acta Crystallogr. B*, **63**, 644–649.
40. Zheng, S.-L., Messerschmidt, M., and Coppens, P. (2007) Single-crystal-to-single-crystal E → Z and E → Z isomerizations of 3-chloroacrylic acid within the nanocavities of a supramolecular framework. *Chem. Commun.*, 2735–2737.
41. Naumov, P., Hill, J.P., Sakurai, K., Tanaka, M., and Ariga, K. (2007) Structural study of the thermally induced and photoinduced phase transitions of the 1,3,5-trithia-2,4,6-triazapentalenyl (TTTA) radical. *J. Phys. Chem. A*, **111**, 6449–6455.
42. Collet, E., Lemée-Cailleau, M.-H., Buron-Le Cointe, M., Cailleau, H., Wulff, M., Luty, T., Koshihara, S., Meyer, M., Toupet, L., Rabiller, P., and Techert, S. (2003) Laser-induced ferroelectric structural order in an organic charge-transfer crystal. *Science*, **300**, 612–615.
43. Guerin, L., Collet, E., Lemée-Cailleau, M.-H., Buron-Le Cointe, M., Cailleau, H., Plech, A., Wulff, M., Koshihara, S., and Luty, T. (2004) Probing photoinduced phase transition in a charge-transfer molecular crystal by 100 picosecond X-ray diffraction. *Chem. Phys.*, **299** (2-3), 163–170.
44. Sokolowski-Tinten, K., Blome, C., Blums, J., Cavalleri, A., Dietrich, C., Tarasevitch, A., Uschmann, I., Förster, E., Kammler, M., Horn-von-Hoegen, M., and von der Linde, D. (2003) Femtosecond X-ray measurement of coherent lattice vibrations near the Lindemann stability unit. *Nature*, **422** (20), 287–289.
45. Rousse, A., Rischel, C., Fourmaux, S., Uschmann, I., Sebban, S., Grillon, G., Balcou, P., Förster, E., Geindre, J.P., Audebert, P., Gauthier, J.C., and Hulin, D. (2001) Non-thermal melting in semiconductors measured at femtosecond resolution. *Nature*, **410** (1), 65–68.
46. Cavalleri, A., Tóth, Cs., Siders, C.W., Squier, J.A., Ráksi, F., Forget, P., and Kieffer, J.C. (2001) Femtosecond structural dynamics in VO_2 during an ultrafast solid-solid phase transition. *Phys. Rev. Lett.*, **87** (23), 237401.1–237401.4.
47. Kim, C.D., Pillet, S., Wu, G., Fullagar, W.K., and Coppens, P. (2002) Excited-state structure by time-resolved X-ray diffraction. *Acta Crystallogr. A*, **58**, 133–137.
48. Vorontsov, I.I., Kovalevsky, A.Y., Chen, Y.-S., Graber, T., Gembicky, M., Novozhilova, I.V., Omary, M.A., and Coppens, P. (2005) Shedding light on the structure of a photoinduced transient excimer by time-resolved

diffraction. *Phys. Rev. Lett.*, **94**, 193003.1–193003.4.

49. Šrajer, V., Teng, T.-Y., Ursby, T., Pradervand, C., Ren, Z., Adachi, S., Schildkamp, W., Bourgeois, D., Wulff, M., and Moffat, K. (1996) Photolysis of the carbon monoxide complex of myoglobin: nanosecond time-resolved crystallography. *Science*, **274**, 1726–1729.

50. Schotte, F., Lim, M., Jackson, T.A., Smirnov, A.V., Soman, J., Olson, J.S., Phillips, G.N., Wulff, M., and Anfinrud, P.A. (2003) Watching a protein as it functions with 150-ps time-resolved X-ray crystallography. *Science*, **300**, 1944–1947.

51. Neutze, R., Huldt, G., Hajdu, J., and van der Spoel, D. (2004) Potential impact of an X-ray free electron laser on structural biology. *Radiat. Phys. Chem.*, **71**, 905–916.

52. Takeda, A., Uekusa, H., Kubo, H., Miuchi, K., Nagayoshi, T., Ohashi, Y., Okada, Y., Orito, R., Takada, A., and Tanimori, T. (2005) Development of μ-PIC as a time-resolved X-ray area detector. *J. Synchrotron Radiat.*, **12**, 820–825.

53. Neutze, R., Wouts, R., Techert, S., Davidsson, J., Kocsis, M., Kirrander, A., Schotte, F., and Wulff, M. (2001) Visualizing photochemical dynamics in solution through picoseconds X-ray scattering. *Phys. Rev. Lett.*, **87** (19), 195508.1–195508.4.

54. Pham, V.-T., Gawelda, W., Zaushitsyn, Y., Kaiser, M., Grolimund, D., Johnson, S.L., Abela, R., Bressler, C., and Chergui, M. (2007) Observation of the solvent shell reorganization around photoexcited atomic solutes by picoseconds X-ray absorption spectroscopy. *J. Am. Chem. Soc.*, **129**, 1530–1531.

55. Harb, M., Ernstorfer, R., Dartigalongue, T., Hebeisen, C.T., Jordan, R.E., and Dwayne Miller, R.J. (2006) Carrier relaxation and lattice heating dynamics in silicon revealed by femtosecond electron diffraction. *J. Phys. Chem. B*, **110**, 25308–25313.

Part III
Understanding of Material Properties and Functions

Ideas in Chemistry and Molecular Sciences: Advances in Nanotechnology, Materials and Devices.
Edited by Bruno Pignataro

ISBN: 978-3-527-32543-6

9
Understanding Transport in MFI-Type Zeolites on a Molecular Basis

Stephan J. Reitmeier, Andreas Jentys, and Johannes A. Lercher

9.1
Introduction

Micro- and mesoporous materials play an important role as catalysts, catalyst supports, or sorbents for catalytic processes in the refining and petrochemical industry. Zeolites, which are the most widespread used group of such materials, are tectosilicates with silicon and aluminum atoms tetrahedrally coordinated to oxygen atoms that bridge these tetrahedra [1]. To balance the charge resulting from the isomorphous substitution of Si^{4+} by Al^{3+} atoms, counterions such as protons or alkaline metal ions are required. The tetrahedral SiO_4 and AlO_4 units can be structurally arranged within 20 topological subunits, which are called *secondary building units* (*SBUs*) [1, 2]. Owing to the unique connection between the tetrahedra, these structures form a void space (channels segments as well as cages, and side pockets) in which guest molecules adsorb and react [3–5]. The periodic lattice is terminated at the outer surface by strained oxygen bridges and terminal hydroxyl groups.

The size of the channels depends on the number of tetrahedral atoms forming the pores, which are typically between 4 and 14 (4–14 membered rings) with some structures having, however, up to 20 membered rings. In Table 9.1, a selection of frequently used zeolites together with a short description of their channel networks is given to emphasize the industrial relevance of zeolite materials. A typical sketch of the zeolite framework of zeolite ZSM5 is exemplified in Figure 9.1 with the tetrahedrally coordinated atoms (T-atoms) highlighted.

The first (natural) zeolite material was identified and reported by Cronstedt [5] in 1757. Almost 200 years later, the first successful synthesis of stable zeolite structures was described by Barrer [6, 7] with first applications of the synthetic zeolites being reported subsequently. The new synthetic porous solids rapidly gained high technical importance in petrochemical industries. Today more than 180 different zeolite structures – 40 natural and over 140 synthetic – are known and distinctly classified using three-letter code classification system, endorsed by the International Union of Pure and Applied Chemistry (IUPAC) [2] and the structure commission of the International Zeolite Association (IZA) [1, 8]. Zeolite-related

Ideas in Chemistry and Molecular Sciences: Advances in Nanotechnology, Materials and Devices.
Edited by Bruno Pignataro

ISBN: 978-3-527-32543-6

Table 9.1 Selection of most commonly used zeolites with characteristic channel systems and pore dimension d_{Pore}.

Zeolite	Code	Number of T-atoms[a]	Channel type		d_{Pore} (nm)
VPI-5	VFI	18	1D	One straight channel	1.27 × 1.27
CIT-5	CFI	14	1D	One straight channel	0.72 × 0.75
Mordenite	MOR	12	1D	Two straight channels	0.70 × 0.65
		8			0.57 × 0.26
ZSM11	MEL	10	2D	Two straight channels	0.54 × 0.53
Zeolite A	LTA	8	3D	Cage structure[b]	0.41 × 0.41
ZSM5	MFI	10	3D	One straight, one sinusoidal channel	0.58 × 0.54 0.56 × 0.53
		10			
Beta	BEA	12	3D	Two straight, one sinusoidal channel	0.77 × 0.66 0.56 × 0.56
		12			
Cloverite	CLO	20	3D	Two straight channels	0.40 × 1.32 0.38 × 0.38
		8			

[a]The number of T-atoms defines the size of the structural units forming the channels.
[b]The cage units within the structure of LTA are ordered in cubic arrays forming the 3D channel system.

materials were, for example, also synthesized by isomorphous substitution of T-atoms or the total replacement of the silicate structure by aluminophosphates (AlPO materials).

Modern hydrocarbon catalysis mainly uses the unique acidic properties of zeolites [9], which can be best described as solid polyacids [10]. Brønsted acidic hydroxyl groups (SiOHAl) are generated, when the net charge within the framework resulting from the substitution of Si^{4+} by Al^{3+} atoms in tetrahedral position, is neutralized by protons, covalently bound to the bridging oxygen atoms of the Si–O–Al linkage. Lewis acid sites are formed by exchanged metal cations, extra-lattice aluminum (EFAl) species, and defect sites within the framework. In an ideal case, the total number of cations divided by their valence or of protons corresponds to the number of AlO_4 units. High-temperature treatment may induce the removal of aluminum from the zeolite structure leading to extra-lattice alumina species residing in the micropores and affecting the catalytic activity [11–14]. The strength of the Brønsted acid sites depends on the chemical composition and the structure of the molecular sieve [15–17]. However, it manifests itself only against the sorbate. The concentration of aluminum atoms influences the acid strength via the formation of Si–O–Al–O–Si–O–Al groups of tetrahedra, which lead to unusually weaker Brønsted acid sites [17]. A more detailed discussion can be found in several reviews [9, 18]. For illustration, a section of the zeolite framework and the corresponding hydroxyls are shown in Figure 9.2.

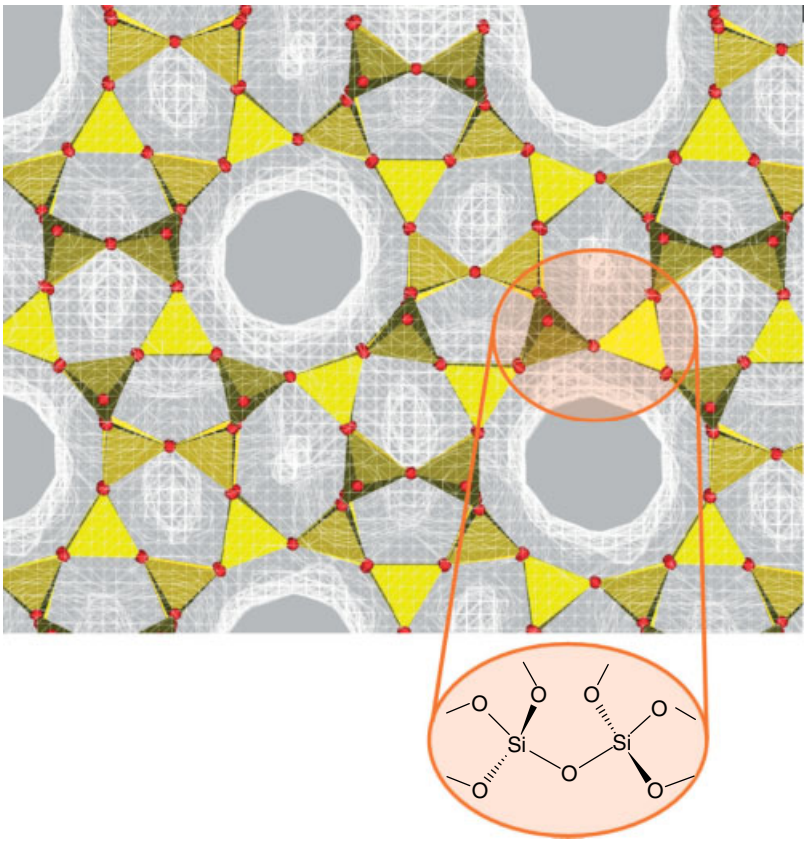

Figure 9.1 Sketch of the framework structure of a ZSM5 zeolite in cross section, shown in direction of and perpendicular to the sinusoidal channel segments. Tetrahedral building units are highlighted in yellow with oxygen bridges in red. The wired mesh indicates the van der Waals surface accessible for sorbate molecules.

The well-defined acid–base properties of zeolites are complemented in importance by the regularity of their pore structure. While being flexible within limits, the uniform pore dimensions similar to the size of small organic molecules induce steric confinements and partially dramatic entropic effects that are only beginning to be explored [19–21]. The effects range from the classic shape selectivity [22–28] over the concept of molecular traffic control (MTC) [29, 30] to the effects of entropy of the adsorbed molecules in the pores on the overall pathways of catalyzed reactions [5, 31, 32].

In the following sections, the description and discussion on transport in zeolites is focused on medium pore zeolites with a strong emphasis on the MFI structure (ZSM5, see Figure 9.1). Its pore structure is composed of straight and sinusoidal intersecting channels. The sinusoidal channels inside the orthorhombic

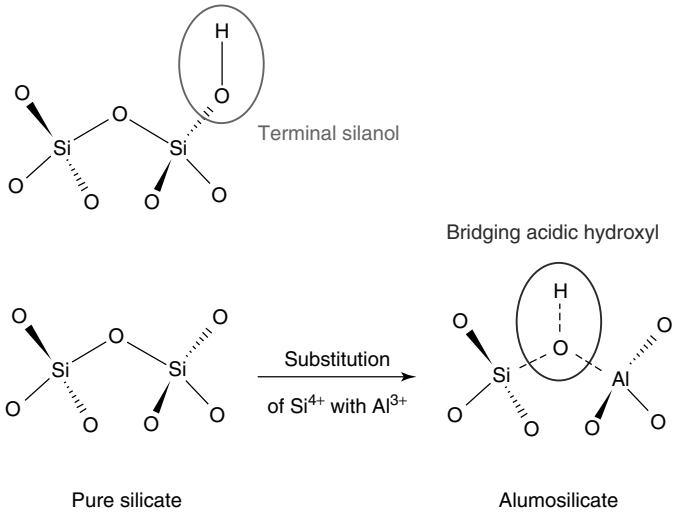

Figure 9.2 Schematic representations of the characteristic terminal and bridging acidic hydroxyl sites of zeolites and silicates.

unit cell of ZSM5 show almost circular cross sections of 0.54–0.56 nm and are oriented perpendicular to the straight channels with elliptical cross sections of 0.53–0.58 nm.

Originating from the analysis of enzyme-catalyzed processes, the concept of shape selectivity was transferred to molecular sieves by Weisz *et al.* [33–37] and further developed by Csicsery [23–26], Derouane [29], and Chen *et al.* [38]. In short, shape selectivity manifests in three ways [39], that is, (i) the exclusion of larger reactants from the catalytically active sites (reactant shape selectivity, RSS), (ii) retention of larger molecules formed inside a catalysts by a slower diffusion rate (product shape selectivity, PSS), and (iii) the hindrance in achieving a transition state because steric constraints do not allow its formation (transition state selectivity, TSS) [40]. A related conceptual idea, MTC, was introduced by Derouane and Gabilica [24, 29] based on independently diffusing streams of reactants that react at the intersections of the channel systems.

Because of the application of H-ZSM5 in large-scale petrochemical processes such as trans-alkylation and isomerization of aromatic molecules [8, 39], shape selectivity has been the subject of various theoretical and experimental studies [20, 21, 41–43]. Moreover, several novel and alternative reactions making use of shape selectivity [19, 20, 43] are currently explored, making the optimization and the development of novel generations of molecular sieves a demanding challenge for modern material research. Especially, materials with predefined activities and selectivities would be desirable, and hierarchically structured, porous materials have been of special interest in this context [44]. The reader interested in this topic is directed to excellent reviews on shape selectivity by Smit [45], Degnan [28], and Marcilly [39].

While these efforts have led to an impressive advancement in understanding and utilizing shape selectivity, the de novo design of processes based on shape selectivity is far from being realizable. The best chances for this are at present related to processes involving the differentiation between molecules via transport, either into or out of the porous system. The present contribution aims, therefore, to summarize the current view on molecular processes during diffusion and adsorption in zeolites from the perspective of our own recent experiments.

Numerous experimental studies have addressed sorption, transport, and diffusion phenomena in zeolites involving aromatic and aliphatic hydrocarbons [30, 46–50]. *In situ* and *ex situ* characterization techniques including IR and Raman spectroscopy [51–55], NMR spectroscopy [56–59], infrared microscopy IFM [60, 61], neutron diffraction [62–64], uptake experiments such as the zero length column method (ZLC) [65, 66], and also the frequency response technique [67–69] have been applied to explore the underlying fundamental principles [70].

The adsorption of molecules inside the zeolite pores was shown not only to be influenced by the strength and concentration of acid–base sites but also by the geometry of the intrazeolite void space [71]. Sorption studies by Mukti *et al.* [72] using thermogravimetry and infrared spectroscopy have described the entropic and enthalpic contributions during sorption of alkyl-substituted aromatic molecules in the pores of MFI zeolites. It is shown that depending on the size of the sorbate molecule, sterically constrained sorption at the bridging hydroxyl groups inside the pores and at the pore openings occurs. At low sorbate coverages, it is concluded that preferential sorption at the acid sites dominates the sorption process [72]. For the intracrystalline transport of aromatic hydrocarbon molecules in MFI zeolites, we have recently shown that the diffusion processes strongly depends on the ability of the molecule to reorient in the channel intersections. If the space requirements do not allow the reorientation and exchange between the channels (such as for *p*-xylene), anisotropic diffusion with two slightly different rates can be observed, while for smaller molecules such as benzene an isotropic diffusion process is observed [73].

The transport of hydrocarbons from the gas phase to the active sites inside the zeolite proceeds via a series of interconnected steps, which are highlighted in Section 9.3.1. The steps of sticking and trapping of the sorbate on the zeolite surface and of entering into the pore network are probably most controversially discussed. Simon *et al.* reported estimated sticking probabilities of approximately one [74, 75] for *n*-butane on silicalite-1 and Kärger *et al.* [76] of around 10^{-4} for benzene in silicalite-1 using PFG-NMR [76, 77]. In contrast, our results on the basis of time-resolved infrared spectroscopy with ZSM5 [78] showed values of around 10^{-7} for benzene, toluene, and xylene.

The process of entering the zeolite pores involves external or internal diffusion barriers [30, 79, 80], the size exclusion during the pore entry [74, 81], and the subtle interplay between entropic and enthalpic effects during sorption within confined spaces [54]. The differentiation between these effects, presumably occurring simultaneously, is challenging. In an interesting experimental approach, Chmelik *et al.* [82, 83] studied isobutane adsorption and desorption on surface-treated silicalite-1

using interference microscopy. Their results indicate that the surface barriers are related to direct to the entrance into the pores and that the extent of modification can induce discretely enhanced barriers, if larger organic modifying agents are used. While this may be the best-defined example, a plethora of methods is reported in the literature [84–87]. These attempts indicate that an exact control of the pore dimensions, of the surface morphology, as well as of the distribution of the acidic sites will allow rational design of catalysts and sorbents [10, 22, 32].

Herein the transport processes occurring on H-ZSM5 materials that have been surface modified via the chemical liquid deposition technique (CLD) with tetraethyl orthosilicate (TEOS) were investigated in detail. A short introduction to the advanced time-resolved rapid scan infrared spectroscopy, the experimental technique applied will be given in Section 9.2.1. Within the Sections 9.3.1 and 9.3.2, we aim to identify the elementary kinetic processes on unmodified zeolite samples and their complex interplay for a series of alkyl-substituted aromatic sorbate molecules. In particular, the underlying principles determining the sticking probabilities for these molecules are further unraveled, providing the basis to investigate the influences of the postsynthetic surface modification of the H-ZSM5 zeolites on the described network of transport steps (Section 9.3.3).

9.2
Experimental Section: Materials and Techniques

9.2.1
Rapid Scan Infrared Spectroscopy

The transport kinetics of benzene, toluene, and *p*- and *o*-xylene to the sorption sites of ZSM5 zeolites, which occur in the timescale of seconds to milliseconds, were studied by rapid scan infrared spectroscopy. Typically, single pressure-step infrared measurements are applied to follow sorption, but require coaddition of interferograms in order to obtain acceptable signal-to-noise ratios. This limits the practical time resolution to 2–10 seconds. Alternatively, adequate time resolution with good signal-to-noise ratio can be realized by using the rapid scan mode for collecting infrared spectra. In this mode a periodic process can be followed by dividing a periodic modulation into short time slots in which a small number of interferograms are collected. The length of these slots determines the time resolution achievable (typically in the range from 100 to 500 microseconds). As this process can be periodically repeated, the number of interferograms necessary for the required signal-to-noise ratio can be collected. The principle of the method is described in Figure 9.3.

The experimental setup according to [55] is schematically depicted in Figure 9.4. A Bruker IFS 66v/S spectrometer is connected to a high-vacuum system, allowing the activation of solid samples and the equilibration with the sorbate gases. Samples are pressed to self-supporting wafers and inserted into the vacuum cell inside the spectrometer. The volume modulation unit, consisting of flexible UHV bellows

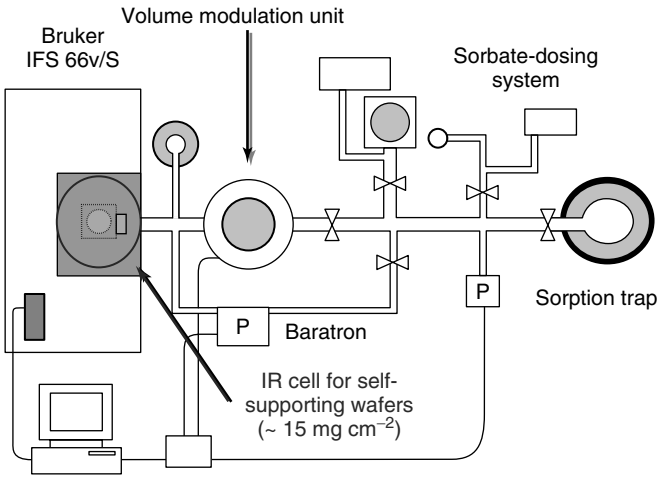

Figure 9.3 Scheme of the combined *in situ* FTIR spectroscopy and frequency response apparatus for transport experiments.

separated by a magnetically driven plate, allows the generation of periodic (square wave) volume perturbations, which results in a perturbation of the sorbate partial pressure over the sample.

By periodically switching between the two partial pressures, the sorption equilibria of the molecules on the active sites of the zeolite are periodically established within each cycle. To minimize adiabatic effects due to the compression of the gas and to exclude local heat effects due to the exothermic sorption process, which would disturb the underlying transport processes, only small volume modulations $\Delta V = \pm 5\%$ were used. For the experiments with aromatic hydrocarbons and H-ZSM5, a cycle time of 60 seconds and a total of 400 modulation cycles were used. The nominal time resolution of 600 milliseconds was appropriate for following the sorption kinetics for all sorbates studied. To highlight the changes of the IR bands, the spectrum before volume modulation was subtracted from the subsequent ones. A series of 100 difference spectra for benzene sorption is shown in Figure 9.5 to demonstrate the quality and information in the IR spectra.

9.2.2
Preparation and Characterization of Zeolite Samples

The measurements were performed on unmodified H-ZSM5 as provided by the Süd-Chemie AG and postsynthetically surface-modified H-ZSM5. The concentrations of terminal and bridging hydroxyl groups determined by ^{1}H/MAS-NMR were 0.27 and 0.21 mmol g^{-1}, respectively. External surface silylation was performed by CLD of TEOS according to the experimental procedure of Zheng *et al.* [51, 88], in order to enhance the shape selectivity by depositing amorphous silica on the outer zeolite surface. Two gradually modified samples with 4 and 12 wt% of silica

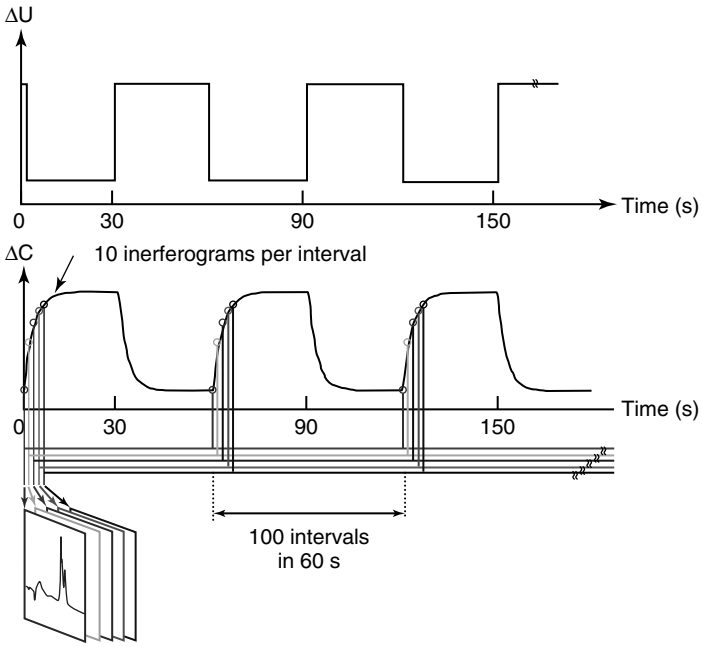

Figure 9.4 Data-acquisition and synchronization scheme for *in situ* FTIR spectroscopy. The full experiment is divided into *n* modulation cycles of equal length of 60 s, each composed of 100 time intervals.

added during the modification process, denoted H-ZSM5-1M and H-ZSM5-3M were investigated. The Si/Al ratio of 45 and the average particles size of 0.5 μm, were obtained by atomic absorption spectroscopy (AAS) and scanning electron microscopy (SEM), respectively. The formation of amorphous deposits was confirmed by X-ray powder diffraction (XRD) and visualized as distinct surface layers of about 3.0 nm by transmission electron microscopy (TEM).

Prior to infrared spectroscopic measurements, all samples were activated for 1 hour under vacuum below 10^{-6} mbar at 823 K with a heating rate of 10 K min^{-1}. The sorbate gases (purity >99.8%) were adsorbed with a partial pressure of 0.06 mbar at 403 K. The series of infrared spectra were normalized to the overtones of lattice vibrations of H-ZSM5 (2105−1740 cm^{-1}) to quantitatively analyze the changes in the surface and active site coverages (see Figure 9.5).

The electron pair donor and electron acceptor interaction (EPD−EPA) of the sorbate molecule with the hydroxyl groups of the zeolite results in a decrease of the characteristic O−H stretching bands and the formation of perturbed O−H bands at lower wavenumbers. The difference in wavenumbers between the perturbed and unperturbed bands is characteristic of the energetic and entropic environment of the sorbate [72]. The coverage of the terminal hydroxyl groups (3745 cm^{-1}) and bridging hydroxyls (3610 cm^{-1}) was directly calculated from the intensity variations of the corresponding bands [55, 89].

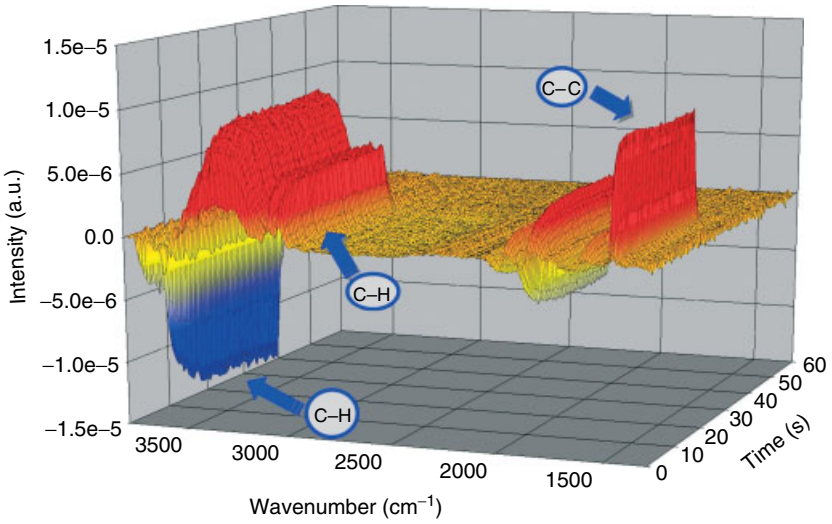

Figure 9.5 Series of difference FTIR spectra for benzene (0.06 mbar) on H-ZSM5 at 403 K. To visualize the subtle changes upon adsorption, the first spectrum of the series was subtracted from the subsequent ones. The O–H, C–C, and C–H vibrational bands used for the data evaluation are marked.

9.2.3
Kinetic Description of the Transport Process

The concentration of adsorbed molecules on the SiOH and SiOHAl groups was calculated from the integral intensity of the hydroxyl bands in the range 3727–3770 cm^{-1} (SiOH groups) and 3577–3640 cm^{-1} (SiOHAl groups). It has been established previously that one molecule is adsorbed per hydroxyl group and the molar extinction coefficients of the OH bands are constant in the pressure range studied. Integration of the series of difference spectra results in characteristic time profiles for the adsorption and desorption steps, illustrated in Figure 9.6. To quantify individual sorption kinetics, the coverage changes $\Delta c_{OH}(t)$ were mathematically described with a first-order kinetic model [55, 90].

$$\text{Adsorption step: } \Delta c_{OH}(t) = \Delta c_{OH,eq}\left(1 - e^{-t/\tau_{ad}}\right) \text{ for } 0 < t \leq t_p/2 \qquad (9.1)$$

$$\text{Desorption step: } \Delta c_{OH}(t) = \Delta c_{OH,eq} e^{-[t-(t_p/2)]/\tau_{de}} \text{ for } t_p/2 < t < t_p \qquad (9.2)$$

$\Delta c_{OH,eq}$ is the difference in the concentration of the sorbate molecules between the two sorption equilibria, τ_{ad} and τ_{de} are the characteristic time constants of the transport steps, which are equivalent to $1/k$. The corresponding initial sorption rates $r_{ini,ad}$(i.e., dc/dt at $t \ll t_p$) for the sorption process at the active site of the catalyst material, following the immediate pressure step can be determined from

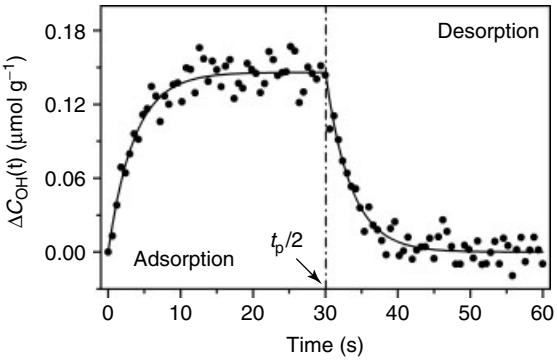

Figure 9.6 Concentration profile during benzene sorption on the internal SiOHAl groups of H-ZSM5 at 403 K and for a pressure modulation around the equilibrium partial pressure of 0.06 mbar.

the initial slope of the concentration profiles [54].

$$r_{\mathrm{ini,ad}} = \frac{\mathrm{d}\left[\Delta c_{\mathrm{OH}}(t)\right]}{\mathrm{d}t} = \frac{1}{\tau_{\mathrm{ad}}} \cdot \Delta c_{\mathrm{OH,eq}} \mathrm{e}^{-t/\tau_{\mathrm{ad}}} \xrightarrow{\text{for } t \ll t_{\mathrm{p}}} r_{\mathrm{ini,ad}} = \frac{\Delta c_{\mathrm{OH,eq}}}{\tau_{\mathrm{ad}}} \tag{9.3}$$

Subsequent comparison of the initial rates on the internal and external hydroxyls for a series of hydrocarbon molecules with increasing size under similar experimental conditions allows to differentiate the transport pathways within the overall transport network [54]. The resulting initial sorption rates were thus divided by the concentration of the respective active sites present within the catalyst material and are tabulated in Table 9.2.

9.3 Surface and Intrapore Transport Studies on Zeolites

9.3.1 Sorption and Transport Model Identified for MFI-type Zeolites

The complex and strongly interconnected network of sequential and parallel steps, determined from rapid scan infrared spectroscopy, is schematically depicted for benzene in Figure 9.7 [54, 55, 90, 91]. The overall sorption process can be subdivided into six consecutive steps. Molecules that freely rotate in the gas phase statistically collide with the surface of the zeolite (Step 1). Only a small fraction of molecules is adsorbed, while the other molecules are directly reflected to the gas phase. We will discuss the probability of the sorbate to be directly trapped on the outer surface in Section 9.3.2 in detail.

Theoretical simulations by Skoulidas and Scholl [92] confirmed that the direct mass transfer of rigid, sphere-shaped particles from the gas phase into the zeolite is impossible for molecules with a size close to the pore apertures. Aromatic

Table 9.2 Initial sorption rates on the SiOH and SiOHAl groups together with the experimental sticking probabilities for a series of aromatic hydrocarbons on H-ZSM5.

Molecule	r_{ini}(SiOH) ($10^{-3}s^{-1}$)	r_{ini}(SiOHAl) ($10^{-3}s^{-1}$)	Sticking probability α (—)
Benzene	0.15	2.34	2.1×10^{-7}
Toluene	0.26	0.96	1.7×10^{-7}
p-Xylene	0.44	0.55	2.2×10^{-7}
o-Xylene	1.25	0.05	2.0×10^{-7}

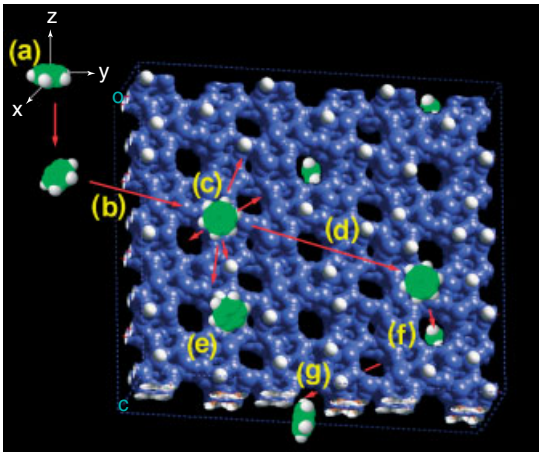

Figure 9.7 Transport steps identified for aromatic gas-phase molecules with free molecular motion (a) impinging on a zeolite surface. (b) The H-ZSM5 lattice is highlighted in blue with terminal hydrogen in white. The physisorbed state (c), parallel transport to pore openings (d) and terminal sites (e), intracrystalline diffusion (f), and sorption to internal sites (g) are included. (Reitmeier *et al.*, Enhancement of sorption processes in zeolite H-ZSM5 by postsynthetic surface modification, *Angew. Chem. Int. Ed.*, 2009, **48**, 533. Copyright Wiley-VCH-Verlag GmbH & Co. KGaA. Reproduced with permission.)

molecules, accessing the inner pore network of ZSM5 need to adsorb first into a weakly bound physisorbed state on the zeolite surface (Step 2), facilitating eventually the accommodation of the kinetic energy. The translational degrees of freedoms (DGFs) are reduced by one degree, but the molecules can still behave thermodynamically comparable to a two-dimensional gas with high mobility on the surface. Additionally, changes within the rotational and vibrational degrees of freedom including hindered rotations and vibrations are most likely. The successfully trapped molecules diffuse on the surface and subsequently populate two parallel transport pathways, the adsorption to the terminal hydroxyls located on the external surface (Step 3) and entering into the pores of the zeolite (Step 4)

followed by consecutive intracrystalline diffusion within the channel network (Step 5). The final step is the sorption on the SiOHAl groups inside the pores (Step 6). Depending on the size of the zeolite crystals, the morphology of the crystal surface, the pore apertures and the sorbate molecules, subtle changes are expected to strongly affect the sorption rates occurring at the internal acidic sites.

Obviously, adjustment or optimization of shape selectivity cannot be achieved by simply changing the catalyst properties without considering the interrelations of the transport steps. Therefore, the prediction of the transport for novel materials requires the profound investigation of the single pathways. First, the interface between the gas phase and the zeolite surface and the probability for impinging molecules to adsorb and consequently enter the zeolite will be addressed.

9.3.2 Initial Collision and Adsorption of Aromatic Molecules – Sticking Probability

9.3.2.1 General Definition and Introduction

The sticking probability describes the probability of gas-phase molecules impinging on metal or oxide particles to be captured on the surface after the collision. Various experimental and molecular simulations studies have described the sticking probabilities for hydrocarbons on zeolite surfaces and reported strongly different values [76, 78]. Our approach is based on the direct infrared spectroscopic investigation of the sorption kinetics. Following the transport model introduced in Section 9.3.1, the collision frequency of a molecule in the gas phase can be related to the experimentally observable sorption rates. The sticking probability α can be expressed as the function of the sorption rate r_{ad} by Equation 9.4 with $\langle u \rangle$ denoting the mean gas velocity and n the number of gas-phase molecules per volume.

$$r_{ad} = \alpha \cdot r_{coll} = \alpha \cdot \frac{\langle u \rangle}{4} \cdot n \tag{9.4}$$

$$\Delta r_{ad} = r_{ad}(p_2) - r_{ad}(p_1) = \alpha \cdot \frac{\langle u \rangle}{4} \cdot \frac{p_2}{R \cdot T} \cdot N_A - \alpha \cdot \frac{\langle u \rangle}{4} \cdot \frac{p_1}{R \cdot T} \cdot N_A \tag{9.5}$$

$$\alpha = \frac{4 \cdot R \cdot T \cdot \Delta r_{ad}}{\langle u \rangle \cdot N_A \cdot (p_2 - p_1)} \tag{9.6}$$

As the changes in the sorption rate Δr_{ad} for each hydroxyl group are experimentally accessible within the pressure limits p_1 and p_2 (i.e., before and after the volume modulation) via the concentration changes at each site, the sticking probabilities on the zeolites can be obtained. Note that microscopic reversibility of the adsorption and desorption steps during each modulation cycle is a prerequisite to be able to record the spectra [90, 93].

9.3.2.2 IR Spectroscopy to Deduce Sticking Probabilities

The initial sorption rates on the SiOH and SiOHAl groups of unmodified H-ZSM5 were determined for benzene, toluene, *p*-xylene, and *o*-xylene from the corresponding sorption time profiles and the experimental sticking probabilities were calculated according to Equation 9.6. The sticking probabilities for all four

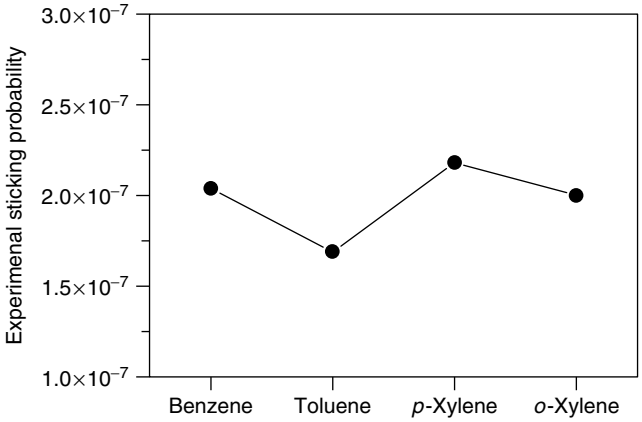

Figure 9.8 Experimental sticking probabilities for benzene, toluene, *p*-, and *o*-xylene on H-ZSM5 determined according to Equation 9.7 at 403 K.

molecules, compiled in Table 9.2 together with the initial sorption rates at the active sites, were in the order of 10^{-7}. The highest sticking probability was found to be that for *p*-xylene, followed by benzene, the smallest molecule, *o*-xylene, and finally toluene, the molecule with the lowest symmetry in the series. The characteristic trend, visualized in Figure 9.8, can be partially explained by the differences within the heats of adsorption in the sequence benzene < toluene < xylene and by the course of the sorbate size determining the space required on the surface for adsorption. Additionally, entropic factors such as the gas-phase symmetry and changes within the translational degrees of freedom during sorption need to be considered to fully account for the observed trends. The detailed discussion of these effects is given in Section 9.3.2.3.

9.3.2.3 Theoretical Sticking Probability – a Statistical Thermodynamics Approach

Following the definition of the sticking probability, the changes within the vibrational, rotational, and translational degrees of freedom between the gas phase and the adsorbed state during the collision, that is, the thermodynamically relevant partition functions for both states, have to be analyzed. The total partition function q of a molecule can be separated into a product of its internal, external, and electronic contributions, for example, translation, vibration, and rotation, respectively.

$$q_{\text{total}} = q_{\text{ext}} \cdot q_{\text{int}} \cdot q_{\text{electronic}} = q_{\text{translation}} \cdot q_{\text{vibration}} \cdot q_{\text{roation}} \cdot q_{\text{electronic}} \tag{9.7}$$

Gas-phase molecules possess in sum $3N$ degrees of rotational, vibrational, and translational freedom with N denoting the number of atoms in the molecule. Trapping of a molecule into the physisorbed state with two-dimensional mobility along the surface is consequently accompanied by the loss of one translational degree of freedom. In addition, partially hindered vibrational and rotational degrees of freedom occur. To reduce the complexity of the partition function analysis and

to give a general estimation rather than a complete thermodynamic description of the sticking probability, we will focus only on the imposed changes in the rotational motion during the sorption process, neglecting interconversions of translational into hindered vibrational and rotational degrees of freedom. Equation 9.8 defines the rotational partition function for the case of free rotational motion around all possible Cartesian principal axes.

$$q_{\mathrm{rot}} = \frac{1}{\sigma}\left(\frac{8\pi^2 k_{\mathrm{B}} T}{h^2}\right)^{\frac{3}{2}} \sqrt{\pi \cdot I_x \cdot I_y \cdot I_z} \tag{9.8}$$

The total symmetry number $\sigma = \sigma_x \cdot \sigma_y \cdot \sigma_z$ of the system, Boltzmann's constant k_{B}, the Planck constant h, and the moments of inertia I_i along the Cartesian coordinates are included. In accordance with statistical thermodynamics and transition state theory for the case of indirect or precursor-mediated adsorption derived by van Santen and Niemantsverdriet [94], a theoretical measure of the sticking probability on an oxide surface was calculated from the quotient of the partition functions in the adsorbed state and in the gas phase. This definition implies that the α directly relates to the decrease of molecular entropy during the sorption process:

$$\alpha^{\#} = \frac{q^{\mathrm{ads}}}{q^{\mathrm{gas}}} = \frac{q^{\mathrm{ads}}_{\mathrm{rotation}} \cdot q^{\mathrm{ads}}_{\mathrm{vibration}} \cdot q^{\mathrm{ads}}_{\mathrm{electronic}}}{q^{\mathrm{gas}}_{\mathrm{rotation}} \cdot q^{\mathrm{gas}}_{\mathrm{vibration}} \cdot q^{\mathrm{gas}}_{\mathrm{electronic}}} \approx \frac{q^{\mathrm{ads}}_{\mathrm{rotation}}}{q^{\mathrm{gas}}_{\mathrm{rotation}}} \tag{9.9}$$

$$\alpha = \chi \,.\, \alpha^{\#} \tag{9.10}$$

Already accounting for the loss of one translational degree of freedom (see Equation 9.9), a limiting value of unity for α is obtained, if the internal degrees of freedom remain unchanged. Somewhat simplistically, it can be concluded that sorption becomes more likely, the more the sorbate molecule is able to retain its entropy in terms of internal degrees of freedom within the physisorbed surface state. For a detailed derivation we refer to [94].

All entropic and enthalpic effects during the sorption process are included in the experimentally determined sticking probability α, which represents the product of the theoretically derived sticking probability $\alpha^{\#}$ and a thermodynamic trapping coefficient χ. This coefficient is related to the ability of the surface to accommodate the energy released during sorption. If both contributions are large, high sticking probabilities are observed, and thus fewer collisions with the external surface are required for successful sorption. The theoretical sticking probabilities and trapping coefficients for the aromatic molecules are summarized in Table 9.3 (Figure 9.9). It may be noted that the theoretical sticking probabilities show a similar trend with respect to the sorbate molecule as the experimental ones, while the absolute values differ approximately by 2 orders of magnitude. Moreover, the symmetry number σ included in the rotational partition functions has a strong influence on the sorption entropy. High symmetry corresponds to a smaller rotational partition function of the gas-phase molecule and thus to a smaller amount of rotational entropy that has to be lost during the adsorption step. Consequently, sticking is favored and higher theoretical sticking probabilities are obtained.

Table 9.3 Rotational partition function, symmetry number, theoretical sticking probability, and trapping coefficient calculated for a series of aromatic molecules.

Molecule	σ	$q_{rot}(10^4)$	$\sigma^{\#}(10^{-5})$	$\chi(10^{-2})$
Benzene	12	1.2	8.70	0.23
Toluene	2	14	0.74	2.28
p-Xylene	4	11	0.91	2.40
o-Xylene	2	22	0.45	4.42

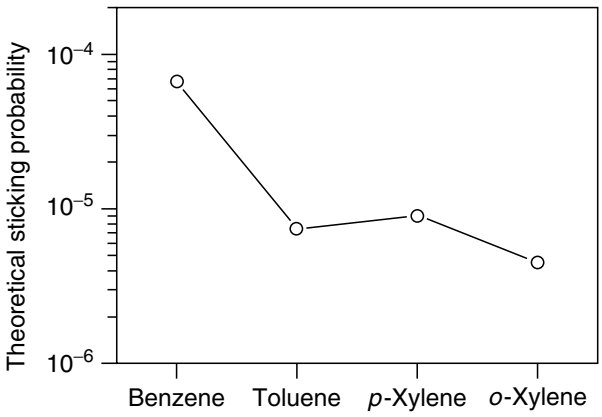

Figure 9.9 Theoretical sticking probabilities $\alpha^{\#}$ for a series of aromatic molecules determined from a statistical thermodynamics approach.

The trapping coefficients χ increase monotonously from benzene to *o*-xylene and represent the enthalpic factors for a sorbate to be successfully trapped after collision with the surface. Conceptually, χ can be related to the properties of the molecules to reside sufficiently long on the surface to accommodate the heat of sorption and also to the space the sorbate occupies in the adsorbed state. Increasing trapping coefficients are, thus, expected for weakly bound molecules with increasing number of atoms and decreasing size dimensions. This is in line with the largest value found for *o*-xylene [90].

Summarizing the role of the entropic and enthalpic effects, the trends in the experimental sticking probabilities can be satisfactorily explained suggesting (i) the existence of a highly mobile, physisorbed state with hindered molecular degrees of freedom; (ii) the symmetry of the sorbate, defining the rotational entropy being lost during sorption; (iii) the heat of adsorption and its accommodation upon sorption; and finally (iv) the sorbate size dimensions. Benzene has by far the highest symmetry ($\sigma = 12$) in the series of molecules studied but, due to its lowest

number of vibrational degrees of freedoms in the series, also the lowest ability to accommodate the sorption enthalpy. Consequently, the low trapping coefficient compensates the theoretically high sticking probability. In contrast, *p*-xylene with a lower symmetry ($\sigma = 4$) strongly benefits from much better trapping, resulting in the highest sticking probability observed. Final support for our concept is given by the lowest sticking probability observed for toluene, which has the lowest symmetry and an intermediate heat of sorption within the series of molecules studied.

9.3.3 External Surface Modification to Influence Transport in Seolites

9.3.3.1 Surface Properties of Postsynthesis Treated ZSM5

Upon postsynthetic surface modification by CLD of TEOS, significant blockage of terminal hydroxyls (3747 cm^{-1}) occurs due to chemisorption and hydrolysis of TEOS. The infrared spectra of the modified H-ZSM5 samples are shown in Figure 9.10. The concentrations of SiOH groups, determined by ^1H/MAS-NMR spectroscopy were 0.18 and 0.12 mmol g^{-1} for H-ZSM5-1M and H-ZSM5-3M, respectively (initial concentration 0.27 mmol g^{-1}). The concentration of bridging hydroxyl groups decreased from 0.18 to 0.16 mmol g^{-1}, that is, to a much lesser extent than the external SiOH groups, because TEOS molecules are too large to enter the pores [51, 54].

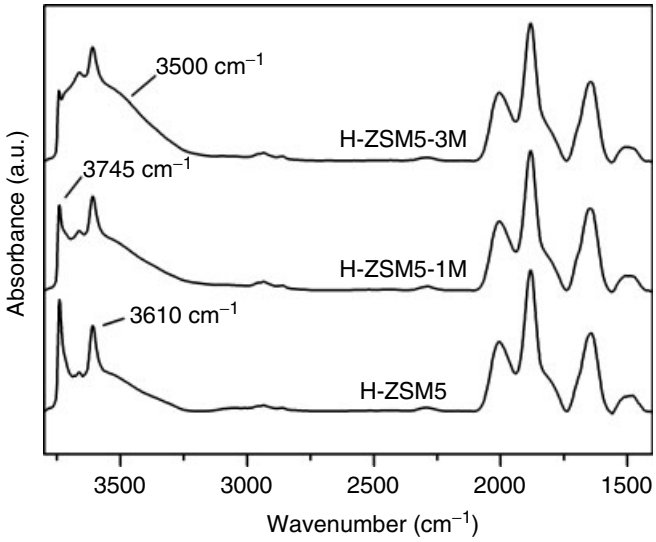

Figure 9.10 IR spectra of the series of activated H-ZSM5 zeolites at 403 K. The spectra were normalized to the lattice and overtone vibrations between 2105 and 1740 cm^{-1}. The stretching vibrational bands for the terminal (3745 cm^{-1}), bridging (3610 cm^{-1}), and perturbed (3500 cm^{-1}) hydroxyl groups are indicated.

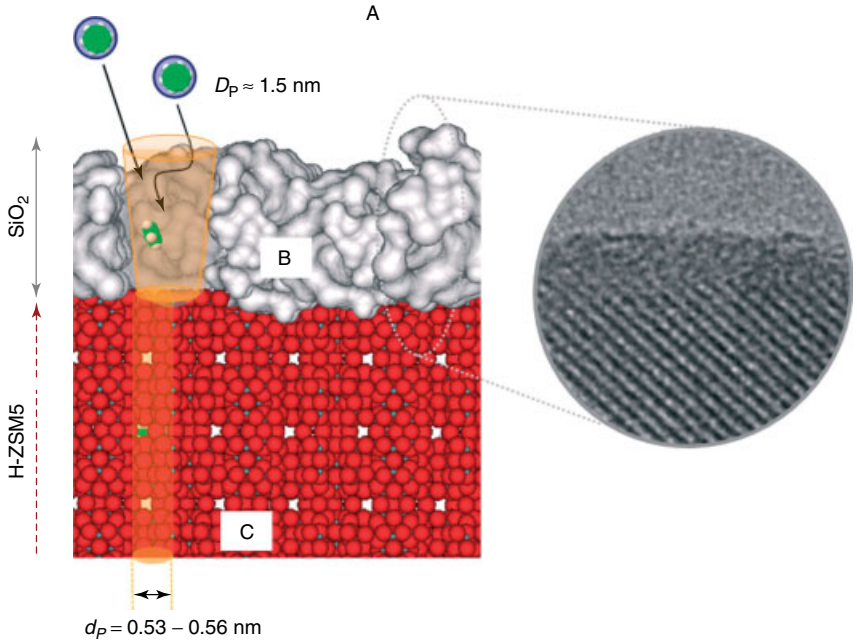

Figure 9.11 H-ZSM5-3M crystal (C) schematically depicted in cross section with gas-phase benzene molecules (A). The TEM inset shows the silica overlayer structure (B) that contains large micropores with diameter D_P, directing the benzene molecules into the zeolite pores of diameter d_p.

TEM images of H-ZSM5-3M showed that the crystalline core of the H-ZSM5 crystal was covered by a thin, untextured region, indicating the formation of a statistically and randomly distributed amorphous SiO_2 layers that significantly roughens the surface. An average thickness for these layers of 2.5–3.0 nm, illustrated in Figure 9.11, was determined by the TEM micrographs [54].

Estimation for the thickness of the layer of around 3.0 nm, based on the size of the unmodified crystals and the total amount of SiO_2 added during the synthesis, is in very good agreement with the TEM experiments. The distinct increase in the mesopore volume of H-ZSM5-3M of 1.4×10^{-2} cm^3 g^{-1} (determined by nitrogen physisorption) [54] indicates that the SiO_2 layers form a characteristic mesoporous structure with an average porosity of 30% and that the silica layer forms a hierarchical network of large micropores with a pore diameter of approximately 1.5 nm. Notably, the pore apertures of the layer surrounding the zeolite core are on one side larger than the critical minimum diameter of 0.58 nm of benzene, but the maximum length of alkyl-substituted derivatives approaches this size. Because of this fact, the overlayer pores can be conceptually compared to a hierarchical funnel-type structure, which is expected to force molecules of appropriate size to enter the underlying zeolite micropores where the active sites are located.

Table 9.4 Initial sorption rates r_{ini} on SiOH and SiOHAl groups and the sticking probabilities α for benzene surface-modified zeolites at 403 K.

Material	r_{ini}(SiOH) (10^{-3} s^{-1})	r_{ini}(SiOHAl) (10^{-3} s^{-1})	Sticking probability α (–)
H-ZSM5	0.15	2.34	2.1×10^{-7}
H-ZSM5-1M	0.16	4.10	2.5×10^{-7}
H-ZSM5-3M	0.16	6.37	3.0×10^{-7}

9.3.3.2 Enhancement of Benzene Sorption on Modified H-ZSM5

The sorption kinetics of benzene on the terminal and acidic bridging hydroxyls of surface- modified H-ZSM5 zeolites were done by infrared spectroscopy. Analysis of the characteristic sorption time profiles (see Table 9.4 and Figure 9.12) yielded strongly decreased initial sorption rates to the terminal hydroxyls and at the same time, a significant increase in the sorption rates to the internal bridging hydroxyl groups.

In analogy to the initial sorption rates, the experimental sticking probabilities at the modified surfaces of H-ZSM-3M showed a marked increase from 2.1×10^{-7} to 3.0×10^{-7} for benzene. Referring to Section 9.3.2, the sticking probabilities of aromatic hydrocarbon molecules are governed by the entropy decrease during the sorption process as a function of the sorbate dimensions and the external surface morphology [54, 95].

The modification of the outer zeolite surface does not change the rate of adsorption of benzene on the external silanol groups. The sum of the initial sorption rates instead increases by a factor of 2.7. This is due to a significantly faster rate of adsorption to the bridging hydroxyl groups for the modified material H-ZSM5-3M. The results reported herein can be explained with the changes of

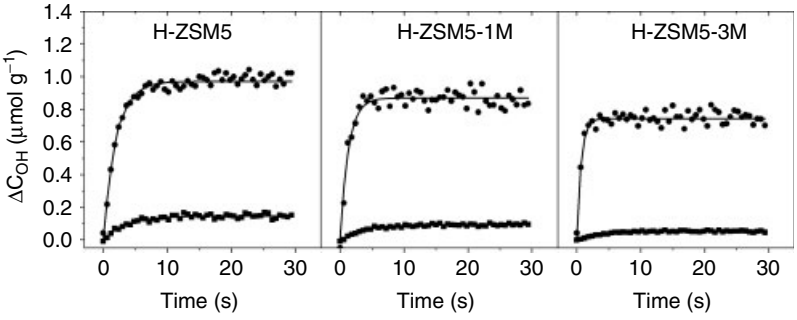

Figure 9.12 Concentration profiles and theoretical functions for benzene sorption on the terminal SiOH (square) and internal SiOHAl (circle) groups of a series of gradually surface-modified H-ZSM5 samples at 403 K.

entropy after sorption (funnel effect), and they revealed for the first time that external surface corrugation can be exploited to further differentiate sorption rates of aromatic hydrocarbons. In contrast to a planar zeolite surface where preorientation of the sorbate is the dominating effect, porous silica layers allow more entropically favorable orientations during collision of the (relatively rigid) molecules with the surface. Furthermore, the micropores on the modified surface enhance the directed mass transfer into zeolite pores, thus increasing the sticking coefficient. For modified surfaces, the probability of the gas-phase molecule to directly enter the silica pores is strongly enhanced and no longer governed by the ability of energy accommodation in the weakly bound physisorbed state. As a direct consequence, the benzene molecules are more likely to be trapped and also preoriented toward the zeolite micropores.

To underline the concept of the enhanced uptake for zeolites with corrugated surfaces and their potential effect for hydrocarbon separation, the changes in the transport diffusivity were studied by pressure-step frequency response experiments. For a detailed description of the mathematical background of the FR technique, we refer the reader to the publications of Yasuda [67, 68]. Similar to the initial sorption rates, the derived transport diffusivities also distinctly increased with modification.

Energetic barriers resulting from strongly narrowed pore apertures are expected to lead significantly higher energies of activation [20, 96], as the molecules need to overcome the barrier. The unchanged energies of activation of around 24 kJ mol^{-1}, however, underline the fact that the modification does not influence the pore cross section. In other words, the pores are either completely blocked or free. In contrast, the preexponential factors on H-ZSM5-3M increased by a factor of 2.7 from 3.0×10^{-11} to 8.0×10^{-11} m^2 s^{-1}. [73], showing that a higher extent of sorption entropy is retained during the sorption in the pores of the silica layer compared to the strongly orientation-dependent sorption on the unmodified surface. The assumption of fully accessible internal sites before and after the silylation was confirmed by comparing the equilibrium coverage changes with thermodynamic sorption isotherms [54]. It is remarkable that the hierarchic silica overlayer, in contrast to other published methods such as precoking, is not accompanied by severe blockage of channels. The enhanced sorption processes, observed for the first time experimentally [54], present a direct proof of our conceptual model to alter the intrapore transport by external modifications and give the first direction to appropriately design surface morphologies and hierarchical overlayer porosities.

9.3.3.3 Tailor-Made Surface Structures, a Novel Concept in Material Optimization

The reported experiments showed that the pores in the silica layer enable the direct entry of the molecules and provide a gradual transition from the gas phase to the highly confined space inside the channels with less hindered molecular motion and subsequently a more gradual entropy loss. The surface morphology and the effective pore dimensions of the silica layer are of crucial importance. The more similar the pore diameter and molecular size, the lower the probability for the direct entry of the molecules into the pores and the larger the pores, the higher this enhancement effect.

Benzene molecules benefit from their ideal relation between the kinetic diameter and the pore apertures of the silica layer. Infrared spectroscopy and diffusivity measurements performed with benzene clearly showed that materials with improved sorption properties can be envisaged by hierarchically structuring the surface of zeolites with mesoporous layers of silica. Contrary to the understanding of shape selectivity in terms of an overall retardation in the entry of the reactant molecules into the pore network based on their kinetic diameters, the enhancement of sorption rates by chemically modifying the outer surface represents a novel concept based on the radius of gyration, which is defined by the length of the sorbate molecule. Sorption and subsequent penetration of molecules into the underlying zeolite pore system are enhanced, if the pore radius is larger than the radius of gyration. In this situation, molecular rotations of the sorbate molecule are not fully suppressed in the pores and the molecules can directly enter the porous overlayer, while the sorption of larger molecules is retarded by the overlayer. The crucial point in this concept is that the separation of molecules is based on the radius of gyration rather than on the kinetic diameter. Defined adjustment of the thickness and porosity of overlayers together with tailoring of the surface roughness is only one option to enlarge the sorption rates of small molecules; however, this concept can be extended to all three dimensionally structured materials with defined pores.

9.4
Future Opportunities for Research and Industrial Application

Surface-modified zeolites with gradually adjusted surface properties represent a promising new class of materials for separation and catalysis. To fully exploit the technological benefit of such materials the impact of surface modification on the intracrystalline diffusion behavior has to be better understood. Pressure frequency response experiments with unmodified H-ZSM5 samples [73] of different crystal sizes have already been performed, which clearly indicate that intracrystalline diffusion of aromatic molecules strongly depends on the ratio between the length of the channel system and the external surface area. For small zeolite crystals ($\sim$ 0.5 μm), the diffusion processes are expected to be rather fast compared to pore entry, therefore, pore entry represent the limiting kinetic step, while for larger zeolite crystals diffusion processes appear to become rate limiting.

The transport model of sequential transport steps allows to describe the contradicting experimental results on sorption and diffusion of aromatic hydrocarbons on zeolites in a coherent manner. Our results intend to close former gaps in the understanding of diffusion and sorption on zeolite materials and also of the molecular origin of shape selectivity. The use of hierarchically structured materials realized via external surface modification of zeolites could potentially enable new processes that allow the reaction of several molecules by combining time and location dependent concentration gradients, leading to new possibilities to exploit the old concept of MTC.

Acknowledgments

The authors gratefully acknowledge the Studienstiftung des Deutschen Volkes for a PhD scholarship and the DFG for financial support under project JE260-7/1. The authors also thank Prof. S. Weinkauf, Dr M. Hanzslik and M. Neukamm for providing SEM and TEM micrographs. The fruitful discussions within the framework of the network of excellence IDECAT, the international graduate school program NanoCat and with Dipl.-Ing. O. Gobin, are further acknowledged.

References

1. Baerlocher, C., Meier, W.M., and Olson, D. (2001) *Atlas of Zeolite Framework Types*, 5th edn, Elsevier, Amsterdam.
2. McNaught, A.D., and Wilkinson, A. Compendium of Chemical Terminology IUPAC Research Triangle Park NC, (1997) 2nd edition.
3. Davis, M.E. (2002) *Nature*, **417**, 813.
4. Pujado, P.R., Rabo, J.A., Antos, G.J., and Gembicki, S.A. (1992) *Catal. Today*, **13**, 113.
5. Chorkendorff, I. and Niemantsverdriet, J.W. (2007) *Concepts of Modern Catalysis and Kinetics*, 2nd edn, Wiley-VCH Verlag GmbH, Weinheim.
6. Barrer, R.M. and Marshall, D.J. (1965) *Am. Mineral.*, **50**, 484.
7. Barrer, R.M. (1949) *Nature*, **164**, 112.
8. Tsai, T.C., Liu, S.B., and Wang, I.K. (1999) *Appl. Catal. A-Gen.*, **181**, 355.
9. Weitkamp, J. (2000) *Solid State Ionics*, **131**, 175.
10. Corma, A. (1997) *Curr. Opin. Solid State Mater. Sci.*, **2**, 63.
11. Zholobenko, V.L., Kustov, L.M., Kazansky, V.B., Löffler, E., Lohse, U., and Oehlmann, G. (1991) *Zeolites*, **11**, 132.
12. Corma, A. and Garcia, H. (2003) *Chem. Rev.*, **103**, 4307.
13. Lischke, G., Schreier, E., Parlitz, B., Pitsch, I., Lohse, U., and Wöttke, M. (1995) *Appl. Catal. A: Gen.*, **129**, 57.
14. Zholobenko, V.L., Kustov, L.M., Borovkov, V.Y., and Kazanskii, V.B. (1987) *Kin. Catal.*, **28**, 847.
15. Kokotailo, G.T., Lawton, S.L., Olson, D.H., and Meier, W.M. (1978) *Nature*, **272**, 437.
16. Jacobs, P.A. (1982) *Catal. Rev.-Sci. Eng.*, **24**, 415.
17. Barthomeuf, D. (1987) *Mater. Chem. Phys.*, **17**, 49.
18. Benesi, H.A. and Winquist, B.H.C. (1978) *Adv. Catal.*, **27**, 97.
19. Smit, B. (2008) *Chem. Rev.*, **108**, 4125.
20. Schenk, M., Calero, S., Maesen, T.L.M., Vlugt, T.J.H., van Benthem, L.L., Verbeek, M.G., Schnell, B., and Smit, B. (2003) *J. Catal.*, **214**, 88.
21. Maesen, T.L.M., Beerdsen, E., Calero, S., Dubbeldam, D., and Smit, B. (2006) *J. Catal.*, **237**, 278.
22. Corma, A. (2004) in *Studies in Surface Science and Catalysis*, Recent Advances in the Science and Technology of Zeolites and Related Materials, Vol. 154 (eds E. van Steen, L.H. Callanan, and M. Claeys), Elsevier B.V., Amsterdam, p. 25.
23. Csicsery, S.M. (1983) *Abstr. Pap. Am. Chem. Soc.*, **185**, 44.
24. Csicsery, S.M. (1984) *Zeolites*, **4**, 202.
25. Csicsery, S.M. (1985) *Chem. Br.*, **21**, 473.
26. Csicsery, S.M. (1986) *Pure Appl. Chem.*, **58**, 841.
27. Csicsery, S.M. (1995) *Catal. Microp. Mat.*, **94**, 1.
28. Degnan, T.F. (2003) *J. Catal.*, **216**, 32.
29. Derouane, E.G. and Gabelica, Z. (1980) *J. Catal.*, **65**, 486.
30. Kärger, J. (2003) *Adsorption*, **9**, 29.
31. Corma, A. (1995) *Chem. Rev.*, **95**, 559.
32. Corma, A. (2003) *J. Catal.*, **216**, 298.
33. Weisz, P.B. (1980) *Pure Appl. Chem.*, **52**, 2091.
34. Weisz, P.B. (1973) *Chemtech*, **3**, 498.
35. Weisz, P.B. (1979) *Chimia*, **33**, 154.

36. Weisz, P.B. (1973) *Science*, **179**, 433.
37. Weisz, P.B., and Frilette, V. (1960) *J. Phys. Chem.*, **64**, 382.
38. Chen, N.Y. and Garwood, W.E. (1986) *Catal. Rev.-Sci. Eng.*, **28**, 185.
39. Marcilly, C.R. (2000) *Top. Catal.*, **13**, 357.
40. Seitz, M., Klemm, E., and Emig, G. (1999) in *Catalyst Deactivation 1999*, vol. **126**, Elsevier Science Publication, Amsterdam, p. 221.
41. Jentys, A., Tanaka, H., and Lercher, J.A. (2004) in *Studies in Surface Science and Catalysis*, Recent Advances in the Science and Technology of Zeolites and Related Materials, Vol. 154 (eds E. van Steen, L.H. Callanan, and M. Claeys), Elsevier B.V., Amsterdam, p. 2041.
42. Khouw, C.B. and Davis, M.E. (1993) *ACS Symp. Ser.*, **517**, 206.
43. Maesen, T.L.M., Krishna, R., van Baten, J.M., Smit, B., Calero, S., and Sanchez, J.M.C. (2008) *J. Catal.*, **256**, 95.
44. Perez-Ramirez, J., Christensen, C.H., Egeblad, K., Christensen, C.H., and Groen, J.C. (2008) *Chem. Soc. Rev.*, **37**, 2530.
45. Smit, B. and Maesen, T.L.M. (2008) *Nature*, **451**, 671.
46. Brandani, S., Ruthven, D.M., and Kärger, J. (1997) *Microporous Mater.*, **8**, 193.
47. Ruthven, D.M. (1995) in *Studies in Surface Science and Catalysis*, Zeolites: A Refined Tool for Designing Catalytic Sites, vol. **97** (eds L.Bonneviot and S. Kaliaguine), Elsevier B.V., Amsterdam, p. 223.
48. Ruthven, D.M. (2007) *Adsorpt. Sci. Technol.*, **13**, 225.
49. Ruthven, D.M. and Eic, M. (1988) *Abstr. Pap. Am. Chem. Soc.*, **195**, 201.
50. Kärger, J. and Ruthven, D.M. (1997) in *Studies in Surface Science and Catalysis*, Progress in Zeolite and Microporous Materials, vol. **105** (eds H. Chon, S.-K.K. Ihm, and Y.S., Uh), Elsevier B.V., Amsterdam, p. 1843.
51. Zheng, S., Heydenrych, H.R., Jentys, A., and Lercher, J.A. (2002) *J. Phys. Chem. B*, **106**, 9552.
52. Trombetta, M., Busca, G., Storaro, L., Lenarda, M., Casagrande, M., and Zambon, A. (2000) *Phys. Chem. Chem. Phys.*, **2**, 3529.
53. Tripathi, A.K., Sahasrabudhe, A., Mitra, S., Mukhopadhyay, R., Gupta, N.M., and Kartha, V.B. (2001) *Phys. Chem. Chem. Phys.*, **3**, 4449.
54. Reitmeier, S.J., Gobin, O.C., Jentys, A., and Lercher, J.A. (2009) *Angew. Chem. Int. Ed.*, **48**, 533.
55. Jentys, A., Tanaka, H. and Lercher, J.A. (2005) *J. Phys. Chem. B*, **109**, 2254.
56. Hong, U., Kärger, J., Pfeifer, H., Muller, U., and Unger, K.K. (1991) *Z. Phys. Chem.*, **173**, 225.
57. Krause, C., Klein, S., Kärger, J., and Maier, W.F. (1996) *Adv. Mater.*, **8**, 912.
58. Vasenkov, S., Bohlmann, W., Galvosas, P., Geier, O., Liu, H., and Kärger, J. (2001) *J. Phys. Chem. B*, **105**, 5922.
59. Kärger, J. and Pfeifer, H. (1991) *J. Chem. Soc. Faraday Trans.*, **87**, 1989.
60. Heinke, L., Chmelik, C., Kortunov, P., Ruthven, D.M., Shah, D.B., Vasenkov, S., and Kärger, J. (2007) *Chem. Eng. Technol.*, **30**, 995.
61. Heinke, L., Chmelik, C., Kortunov, P., Vasenkov, S., Ruthven, D.M., Shah, D.B., and Kärger, J. (2007) *Chem. Ing. Tech.*, **79**, 1195.
62. Jobic, H., Bee, M., Kärger, J., Balzer, C., and Julbe, A. (1995) *Adsorption*, **1**, 197.
63. Jobic, H., Bee, M., and Pouget, S. (2000) *J. Phys. Chem. B*, **104**, 7130.
64. Jobic, H., Fitch, A.N., and Combet, J. (2000) *J. Phys. Chem. B*, **104**, 8491.
65. Brandani, S., Xu, Z., and Ruthven, D. (1996) *Microporous Mater.*, **7**, 323.
66. Hufton, J.R., Brandani, S., and Ruthven, D.M. (1994) in *Studies in Surface Science and Catalysis*, Zeolites and Related Microporous Materials: State of the Art 1994, Vol. 84 (eds E.J.P.Feijen, J.A. Martens, and P.A., Jacobs), Elsevier B.V., Amsterdam, p. 1323.
67. Yasuda, Y. (1994) in *Studies in Surface Science and Catalysis*, Zeolites and Related Microporous Materials: State of the Art 1994, vol. **84** (eds E.J.P.Feijen, J.A. Martens, and P.A. Jacobs), Elsevier B.V., Amsterdam, p. 1331.
68. Yasuda, Y. (1994) *Heterogen. Chem. Rev.*, **1**, 103.

69. Zheng, S.R., Tanaka, H., Jentys, A., and Lercher, J.A. (2004) *J. Phys. Chem. B*, **108**, 1337.
70. Kunieda, T., Kim, J.H., and Niwa, M. (1999) *J. Catal.*, **188**, 431.
71. Eder, F. and Lercher, J.A. (1997) *J. Phys. Chem. B*, **101**, 1273.
72. Mukti, R.R., Jentys, A., and Lercher, J.A. (2007) *J. Phys. Chem. C*, **111**, 3973.
73. Gobin, O.C., Reitmeier, S.J., Jentys, A., and Lercher, J.A. (2009) *Microporous Mesoporous Mater.*, **125**, 3.
74. Simon, J.-M., Bellat, J.-P., Vasenkov, S., and Kärger, J. (2005) *J. Phys. Chem. B*, **109**, 13523.
75. Simon, J.M., Decrette, A., Bellat, J.B., and Salazar, J.M. (2004) *Mol. Simul.*, **30**, 621.
76. Kärger, J. and Vasenkov, S. (2006) *J. Phys. Chem. B*, **110**, 17694.
77. Pieterse, J.A.Z., Veefkind-Reyes, S., Seshan, K., and Lercher, J.A. (2000) *J. Phys. Chem. B*, **104**, 5715.
78. Jentys, A., Mukti, R.R., and Lercher, J.A. (2006) *J. Phys. Chem. B*, **110**, 17691.
79. Kortunov, P., Vasenkov, S., Chmelik, C., Kärger, J., Ruthven, D.M., and Wloch, J. (2004) *Chem. Mater.*, **16**, 3552.
80. Kärger, J. and Ruthven, D.M. (2002) in *Handbook of Porous Solids*, vol. **4** (eds F. Schüth, K.S. Sing, and J. Weitkamp), Wiley-VCH Verlag GmbH, Weinheim, p. 2089.
81. Schüring, A. (2007) *J. Phys. Chem. C*, **111**, 11285.
82. Chmelik, C., Varma, A., Heinke, L., Shah, D.B., Kärger, J., Kremer, F., Wilzok, U., and Schmidt, W. (2007) *Chem. Mater.*, **19**, 6012.
83. Chmelik, C., Kortunov, P., Vasenkov, S., and Kärger, J. (2005) *Adsorpt. Sci. Technol.*, **11**, 455.
84. Weber, R.W., Moller, K.P., and O'Connor, C.T. (2000) *Microporous Mesoporous Mater.*, **35-36**, 533.
85. Wloch, J. (2003) *Microporous Mesoporous Mater.*, **62**, 81.
86. Kim, J.H., Ishida, A., Okajima, M., and Niwa, M. (1996) *J. Catal.*, **161**, 387.
87. Zheng, S., Heydenrych, H.R., Roger, H.P., Jentys, A., and Lercher, J.A. (2003) *Top. Catal.*, **22**, 101.
88. Zheng, S. (2002) PhD thesis, TU München, München Surface Modification of H-ZSM5 zeolites.
89. Armaroli, T., Bevilacqua, M., Trombetta, M., Alejandre, A.G., Ramirez, J., and Busca, G. (2001) *Appl. Catal. A: Gen.*, **220**, 181.
90. Reitmeier, S.J., Mukti, R.R., Jentys, A., and Lercher, J.A. (2008) *J. Phys. Chem. C*, **112**, 2538.
91. Tanaka, H., Zheng, S., Jentys, A., and Lercher, J.A. (2002) in *Studies in Surface Science and Catalysis*, Impact of Zeolites and Other Porous Materials on the New Technologies at the Beginning of the New Millennium, Vol. 142 (eds R. Aiello, F. Testa, and G. Giordano), Elsevier B.V., Amsterdam, p. 1619.
92. Skoulidas, A.I. and Scholl, D.S. (2000) *J. Chem. Phys.*, **113**, 4379.
93. Reshetnikov, S.I., Ilyin, S.B., Ivanov, A.A., and Kharitonov, A.S. (2004) *React. Kinet. Catal. Lett.*, **83**, 157.
94. van Santen, R.A. and Niemantsverdriet, J.W. (1995) *Chemical Kinetics and Catalysis*, Plenum Press, New York.
95. Bhat, Y.S., Das, J., Rao, K.V., and Halgeri, A.B. (1996) *J. Catal.*, **159**, 368.
96. Song, L., Sun, Z.-L., and Rees, L.V.C. (2002) *Microporous Mesoporous Mater.*, **55**, 31.

10
Modeling Layered-Mineral Organic Interactions

Hugh Christopher Greenwell

10.1
Introduction

From the chemistry that produced the first organic molecules to the latest generation of nanomedicines and composite materials, the interaction between organic matter and inorganic minerals has been of fundamental interest as long as mankind first began to experiment with these materials. Over recent years, the power of modern computers has allowed scientists to begin to model mineral–organic systems with ever-increasing accuracy and size, and a diverse range of computational chemistry studies, and associated experiments, have been undertaken to understand the way that minerals and organic matter interact.

The area of research that encompasses the interaction between organic matter and mineral phases, organic geochemistry, can be divided into two main streams; those that address ''organominerals'' and those that address ''biominerals.'' The former are mineral products whose formation is induced by by-products of biological activity, dead and decaying organisms, or nonbiological organic compounds. Organominerals are distinct from biominerals, which are formed by the uptake of elements and their incorporation into mineral structures under direct biological control [1]. This is a particularly useful definition, and this chapter is confined to studying organomineral systems.

Of particular interest is the class of compounds formed when layered minerals interact with organic matter to form layered mineral-organic systems (LMOs). The organic material may be adsorbed on the mineral, intercalated between the layers, or in extremis, and the two-dimensional layers of the mineral may be exfoliated and dispersed within the organic phase. By varying the mineral type and form, the mechanical, electrical, and chemical properties of the individual mineral sheets may be altered.

The use of computational methods for the study of LMOs has become an adjunct to experimental techniques for the analysis of these poorly ordered materials. Although information may be obtained through conventional methods of analysis regarding macroscopic properties of layered minerals, information about the spatial arrangement of individual and collections of molecules within the interlayers is

Ideas in Chemistry and Molecular Sciences: Advances in Nanotechnology, Materials and Devices.
Edited by Bruno Pignataro

ISBN: 978-3-527-32543-6

hard to obtain without the aid of computer simulation. The interpretation of experimental data from techniques such as solid-state nuclear magnetic resonance (NMR) or quasi-elastic neutron scattering (QENS) is considerably assisted by the application of computer simulations. The amount of information that can be gleaned from such simulations continues to grow, and is leading to ever larger scale and hence more realistic classical and quantum mechanical studies, which are beginning to reveal new and unexpected phenomena such as the thermal undulations that have recently been shown to occur in large simulation cells and allow the calculation of materials properties, or the insight into intercalation mechanisms through deformation of the mineral layers during staging in LMOs.

The wide class of compounds known as *layered materials* may be defined as ''crystalline material wherein the atoms in the layers are cross-linked by chemical bonds, while the atoms of adjacent layers interact by physical forces.'' [2] The most common minerals encountered in LMO systems are the clays and related minerals. In general, both the thickness of the clay sheets and interlayer spaces are in the nanometer range. The predominant naturally occurring clay minerals have aluminosilicate sheets that carry a negative charge, which means that the interlayer guest species must be positively charged (giving rise to the description ''cationic clay'') [3]. In anionic clays, the two-dimensional layers are mixed-metal hydroxides that are positively charged; the interlayer guest species carry a negative charge. The term layered double hydroxide (LDH), or hydrotalcite-like (after the natural mineral form) is more frequently applied, and is technically a more correct description, than anionic clays. For the purposes of the present discussion, the terms *cationic clay* and *LDH* will be used.

The existence of a variable interlayer spacing is a common feature of many layered minerals, facilitating intercalation of a wide range of molecules. Owing to the useful properties of natural, modified, and synthetic clays, these materials have found diverse applications in LMOs, some of which are briefly summarized here. Cationic clays are natural Lewis acids, and upon washing with an acid medium become mild Brønsted solid-acid catalysts in organic synthetic chemistry [4]. LDHs exhibit the opposite properties, becoming good solid-base heterogeneous mixed-metal oxide catalysts upon calcination [5]. The catalytic nature of the basic mixed-metal oxide catalysts may further be increased upon rehydration [6], or the parent LDH may become very active when intercalated with anionic bases such as *tert*-butoxide [7]. The catalytic and intercalation properties of these LMOs have resulted in their exploitation as pharmaceutical delivery agents [8], for the protection and production of genetic sequences [9, 10], environmental remediation catalysts [11], radiochemical storage media [12], fillers in polymer composite materials [13], solid-acid or solid-base catalysts for many reactions [14], biomimetic catalysts [15], drilling fluids [16], and sorbents [17]. To increase the thermal stability of the clay system for certain catalyst applications, the clay may be pillared to create a permanent three-dimensional architecture, somewhat similar to the industrially important zeolites, but with the important advantage that the pore size can be tailored by varying the identity of the pillaring species [18].

This chapter seeks to deliver an overview of some of the highlights of recent research by us, and others, into LMOs using a range of computational modeling techniques and to illustrate how simulation can dramatically assist with interpreting the structure and reactivity of these systems. In the next section, computational modeling methods are briefly discussed, before proceeding to a series of case studies where simulation has provided additional insight across a breadth of LMO applications.

10.2
Computer Simulation Techniques

The application and development of simulation techniques represent a huge area, with a diverse range of continually improving methods and techniques, and is dealt with thoroughly in numerous textbooks and monographs [19]. In particular, we have recently reviewed the use of computer simulations for the study of clays at electronic structure level [20], the study of clays in materials chemistry and nanocomposites [21, 22], and in large-scale simulations [23]. In order to familiarize the reader with some of the terminology necessary for the remainder of this chapter, a brief introduction to the topic is given here. Techniques for the simulation of atomistic systems may, in general, be separated according to the accuracy with which they calculate interatomic interactions and the type of structural and statistical data that they provide.

10.2.1
Definition of the Potential Energy Surface

The potential energy surface of a system describes the way in which the energy of the system changes with configuration, and plays an important role in simulation techniques. It is determined from the description of the interactions between individual particles. Broadly speaking, atomic interactions are determined at either the quantum or classical mechanical level, although semiempirical methods, which lie somewhere in between the two levels of accuracy, also exist, but are not discussed here.

Quantum mechanical simulations attempt to solve, to a good approximation, the fundamental equations of quantum mechanics, in order to model the interactions between the electrons and nuclei of a system of atoms. The advantage of quantum mechanical simulations is that they allow the modeling of electron dynamics in a process, for example, bond making and bond breaking, as they have an explicit representation of electrons. In addition, the only input data necessary is the atomic number and initial configuration of the nuclei and total number of electrons. The major disadvantage of the method is the huge associated computational cost as, at present, electronic structure calculations are generally limited to the study of hundreds of atoms, even when using large parallel machines.

Atomistic simulation methods based on classical mechanics consider atoms as a single unit and the forces between them are modeled by potential functions

based on classical physics. In addition to the initial positions of atoms, a set of suitable parameters for the interaction potential functions, known as a *forcefield*, must be provided. Parameters for forcefields are derived from experimental data and/or quantum mechanical calculations on a finite set of systems. The question inevitably arises as to how well a forcefield is able to model the properties of systems dissimilar to those from which it was derived, or one under very different conditions of temperature and pressure. This is an especially pertinent question for modeling interactions in mineral–organic systems such as LMOs, as the potentials required to describe the mineral and the organic molecules are rarely found together and the interaction energy may not be adequately described between the two systems [24]. Classical simulations are well suited to modeling of phenomena predominantly governed by nonbonded interactions. The use of simple interatomic potentials means that it is possible to handle up to millions of atoms and therefore model much larger and realistic systems.

Generally, atomistic forcefield-based simulations can be used to simulate a model LMO system in the order of a nanosecond of time and in the order of tens of nanometers in size, at the very largest. However, the underlying molecular dynamics (MD) methodology can be extended to include longer times and larger systems by introducing further degrees of approximation, for example, coarse-graining the parameter set of the forcefield. In coarse grain simulations, a number of atoms are counted as one bead – the beads are then connected by simple harmonic functions and intermolecular interactions are based on Lennard–Jones-type functions.

10.2.2 Structural and Statistical Data

Having calculated the potential energy surface, there are various means by which it can be traversed and searched, of which we discuss three broad methods: geometry optimization, MD, and Monte Carlo (MC).

The energy of a configuration of atoms may be minimized with respect to geometry (*energy minimization* or *geometry optimization*) by iteratively varying bond parameters, in a systematic way, to follow the curvature of a potential energy well until a minimum is reached. In theory, this should correspond to the expected ''real life'' atomic structure. The method, however, neglects thermal motion and therefore only local minima on the potential energy surface may be searched.

By applying initial velocities to a configuration of atoms and solving Newton's equations of motion, the potential energy surface may be traversed in a deterministic fashion and the evolution of a system followed over a period of time. This is known as *molecular dynamics*. In this technique, thermal energy is included using a thermostat, which allows potential energy barriers to be overcome, in a realistic manner. The main advantage of the method is that the dynamical evolution of a system, with time, may be followed, which allows comparison with additional experimental techniques such as NMR and QENS. It still remains a challenge, however, to follow the evolution of a system beyond the timescale of 1–10 ns, even when using classical mechanics simulations.

MC simulations involve searching the potential energy surface of a system by sampling many different configurations, generated by imposing random changes to a system according to a set of predefined rules. If the potential energy of a configuration is lower than that of the previous one then it is accepted. Those with higher energy are accepted with a Boltzmann factor weighted probability. Properties are calculated as the average of all accepted configurations.

Of the latter two methods, both have advantages depending upon the information desired from the simulation. MD simulation offers the advantage that the dynamical evolution of a system with time may be followed, allowing comparison with time-resolved experimental techniques such as NMR or Fourier transform infrared (FTIR) spectroscopy. MC simulation, by contrast, is very efficient for calculating thermodynamic averages for a system and can rapidly search a set of low-energy configurations and find the global energy minimum in a shorter time than MD for a given set of computational resources, but allows no deterministic pathway to be followed across the potential energy surface. MC simulations can still produce averaged sets of system low-energy configurations that can be compared with QENS or X-ray diffraction (XRD) data from experiments. In general, MC simulations are carried out using rigid clay sheets and fixed interlayer spacing to allow the rapid calculation of the arrangement and loading of interlayer species, whereas MD simulations are carried out increasingly with flexible clay sheets and a variable interlayer spacing to determine the effects that interlayer species have on the interlayer separation.

10.2.3 Statistical Ensembles

The methods of traversing the potential energy surface described above may be carried out with various conditions imposed upon the ensemble of microstates that collectively define the system in a statistical mechanics sense. These conditions include, among others, constant number of atoms (N), pressure (P), and temperature (T) (the isobaric–isothermal NPT ensemble), and constant number of atoms, volume (V) and temperature (the canonical or NVT ensemble). The NPT ensemble most closely represents laboratory conditions in that conditions of constant external pressure and temperature are maintained. In order to simulate processes such as swelling in a stochastic manner, the system must be able to alter its volume, ruling out constant volume ensembles. However, in certain scenarios such as when the clay interlayer molecular loading and arrangement is being calculated for a known d-spacing from XRD studies constant volume ensembles, for example, NVE, may be employed (where E is energy) and the model clay sheets kept locked at the experimentally observed separation. During energy minimization, an NVT ensemble is generally employed to remove unphysical interactions within the initial structures and then the unit cell parameters systematically varied between minimization cycles to attain a lowest energy configuration.

10.2.4
Periodic Systems

In order to model the bulk structure of materials (greater than 10^{23} atoms) using relatively small models (generally less than 10^5 atoms), two approximations are often employed. These are (i) the use of supercells, where the original unit cell, usually derived from a crystal structure, is replicated several times and then redefined as one larger simulation cell and (ii) imposition of periodic boundary conditions on the simulation cell, where the supercell is considered to be replicated infinitely in all three orthogonal space directions. The use of periodic boundary conditions has ramifications from the point of view of calculating long-range electrostatic interactions within the model and that finite size effects may occur, where the property of interest may be affected by the size of the initial simulation cell.

10.2.5
Data Analysis

Computer simulations provide large amounts of information on the electronic, atomic, and molecular structure. Depending on the simulation method employed, further information can be extracted such as self-diffusion coefficients, radial distribution functions (RDFs), principal component analysis (PCA), and atom density plots which show the motion, coordination environment, and distribution of atoms, as well as mechanical properties such as elastic constants. Much of this computed data can be compared more or less directly with experimental measurements.

10.3
Results

Using methods based on those described above, studies of interactions in LMO systems have been carried out for a variety of applications. It is beyond the scope of this text to give an exhaustive overview of research in each of these areas; rather, highlights from our recent work are presented along with relevant studies from the literature. This section starts with a look at some of the research on LMO systems thought to be present at the earliest period of Earth's history and works forward through time to current studies on LMOs in nanocomposite systems and novel catalysts.

10.3.1
Prebiotic Chemistry

The early Earth would have presented a hostile environment for proto-biochemistry with intense volcanic activity, a reducing atmosphere, and intense UV radiation all resulting in degradation, rather than synthesis, of biomolecules. In the Archean oceans, small abiotic organic molecules would have spewed out of hydrothermal vent systems, similar to the black smokers of today's oceans. However, without

means of concentrating the organic molecules, the resulting solution would have been far too dilute to allow molecules to collide and reactions to occur. We have used electronic structure and atomistic computer simulations to illustrate how layered double hydroxide minerals are able to both concentrate and react with organic molecules and protect larger molecules.

In recent large-scale simulation work, we have used MD to examine the stability of deoxyribonucleic acid (DNA) while protected by layered hydroxide minerals. The studies illustrate the protecting nature of the mineral under conditions of elevated temperature and pressure, similar to that of hydrothermal vent systems [25]. In this work, Thyveetil *et al.* also investigated DNA-LDH systems at elevated temperatures and pressures and found that the DNA had enhanced stability when intercalated in the LDH compared to when free in bulk water. These simulations provide some support for the origins-of-life theory that LDHs could have acted as a protective environment for the first nucleic acids in extreme environmental conditions such as those found around deep-ocean hydrothermal vents or seeps [26].

We have also hypothesized that certain LMO systems with ordered mineral charge sites, and disordered guest ions, may have formed proto-genetic systems [27]. Current work examines amino acid uptake, and any chiral selectivity, in layered double hydroxide mineral systems.

10.3.2
Simulating Organomineral Interactions in the Oil and Gas Industry

As first cellular life evolved, countless of these simple organisms died and the detritus was buried under sediments where, over many millennia, organic–mineral interactions converted the material to fossil fuels which were essential to mankind's industrial development in the twentieth century. In its infancy the oil industry was extremely dirty: so-called black gushers spewed oil out onto the surroundings. In modern times, oil exploration has become increasingly cleaner; however, our understanding of the fate of chemicals in the environment has also evolved and legislation has become ever tighter. When drilling for oil offshore, a technical drilling fluid is used, which has to fill several roles including maintaining hydrostatic pressure, transporting cuttings to the surface, lubricating the drill bit and, importantly, stabilizing clay containing shales (prevalent in oil basins) against swelling on contact with water and collapsing the well-bore. Water-soluble oligomers and polymer inhibitors are introduced to control this swelling; a fundamental understanding of the clay-swelling inhibitor interaction is needed to design these inhibitors effectively.

10.3.2.1 Inhibiting Clay Swelling during Drilling Operations

In some instances, the stabilization of oilfield well-bores is required to prevent hydratable clay minerals from swelling upon contact with either the drilling fluid or seawater [28], and it is desirable to produce LMOs through the *in situ* polymerization of small monomer molecules within the clay galleries [29]. In order to rationalize reactivity in these systems it is necessary to understand the interlayer arrangement

of the reactive centers on the oligomers, where present, where polymerization or cross-linking occurs and the nature of the catalytic mechanisms behind *in situ* polymerization.

Experimental work by Coveney *et al.* indicated that when the natural and unmodified clay mineral montmorillonite, typical of the smectite clay minerals found in reactive shales, is treated with a solution of methanal and ethylenediamine under mild conditions, the monomers spontaneously copolymerize to form an intercalated clay–polymer nanocomposite material with desirable properties [28, 29]. This offers a potential route to stabilizing subsea reactive shale formations, which contain large amounts of swelling clays. Stackhouse *et al.* performed electronic structure calculations on a periodic montmorillonite model to investigate the catalytic role played by the clay mineral in the reaction [30]. A variety of possible Brønsted and Lewis acid sites were investigated to understand their role in increasing the susceptibility of the methanal C=O carbonyl toward nucleophilic attack. Initial simulations indicated that methanal could only undergo nucleophilic attack by ethylenediamine when suitably activated by either protonation or coordination to a suitable Lewis acid. These original studies considered only the interlayer species of the natural clay, various cations, and water molecules, and showed that the interlayer cation, when modeled *in vacuo* with the two organic species, could feasibly be sufficiently activating to promote the reaction. Using similar simplistic models, the relative ability of various cations to deprotonate interlayer water was considered. As the deprotonation of water occurred only when Mg^{2+} and Al^{3+} were used rather than the more common naturally occurring interlayer cations Na^{+} and Ca^{2+}, the interlayer cation was deemed to have little role in catalyzing the polymerization reaction. Stackhouse *et al.* subsequently investigated the effects of isomorphous substitution (Al^{3+} by Mg^{2+} or Si^{4+} by Al^{3+}) upon Brønsted acidity of hydroxyl groups located in the octahedral layer, the tetrahedral layer, and at edge sites. Protonation of the methanal molecule was not observed in any of these scenarios, suggesting that the initial step in the *in situ* polymerization reaction was unlikely to be Brønsted acid catalyzed. The Lewis acidity of exposed Al atoms at edge sites on the clay sheets was therefore considered. These were shown to exhibit a catalytic effect, the magnitude of which was found to be strongly dependent upon the degree of substitution of Al^{3+} by Mg^{2+} in the octahedral layer of the clay sheets [30].

Atomistic computer simulations, and coupled experiments, can also be used to understand the very subtle interplay between different organic functional groups, clay types, and hydration state during oil field operations. Forcefield-based simulations have been used to examine issues such as how the nature of the monomer backbone, monomer head-group, and identity of interlayer cations affects the arrangement of intercalated monomers [31, 32]. As in many other studies, this work was carried out in tandem with experiment to ascertain monomer and water loadings in the simulated systems. Early clay-swelling inhibitors included glycol-based systems, which are thought to inhibit swelling of clays through a combination of entropic (as one inhibitor molecule displaces many water molecules from the clay interlayer, each with many degrees of freedom) and enthalpic effects from interactions between the inhibitor and cations in the clay-sheet surface

resulting in the inhibitor preventing hydration shells of water forming around the cations. In more recent years, polyacrylates and polyacrylamides have been used, which additionally polymerize within the interlayer of clays to prevent ingress of water into the stabilized LMO system [16].

In atomistic simulations of polyethylene glycol (PEG) with a variety of cations in clays, no evidence was observed for hydrogen-bond interactions between the protons of the PEG alcohol groups and the tetrahedral oxygen atoms of the clay surface [32]. It seems therefore that, in the presence of water and cations, PEG is unlikely to form strong H-bonds to the clay surface. When functionalized with terminal acrylate or alcohol groups, the polyethylene oxide (PEO) chains tend to orientate with the O atoms toward the midplane for the Na^+ and Li^+ clays, away from the cations that reside at the clay-sheet face. This arrangement, which results in organic monomer C atoms adjacent to the organophilic silica surface, has been reported previously by others [33]. The choice of organic monomer was also found to affect the cation distribution across the composite interlayer. In the PEG composites hydroxyl groups retained some of the cations and associated hydrations shells within the midplane of the interlayer region. The magnitude of this effect was dependent upon the cation present in the simulated clay composite, with the high surface charge density Li^+ more susceptible than Na^+, while the majority of the K^+ ions migrated to the face of the clay sheet. Snapshots of these systems after 1 nanosecond of MD simulation and the derived one-dimensional atom density plots, which show the time averaged atom density for the cations relative to the midplane of the interlayer region, are shown in Figure 10.1. Since the cations are retained in the interlayer region, they are also more closely associated with the monomer backbone O atoms. Therefore, in the RDFs, the order of interaction for both the PEG hydroxyl O atoms and the backbone O atoms with the cations is $Li^+ > Na^+ > K^+$[32]. Conversely, the PEO diacrylate monomers, having no hydroxyl groups, do not retain the cations in the interlayer region, resulting in the vast majority of the Li^+ and Na^+ cations migrating into vacancies on the tetrahedral layer of the clay sheet, with the K^+ cations migrating to the face of the clay sheets. This results in the Li^+ cations, effectively charge-shielded by the O atoms at the clay surface and associated water molecules, from interacting with the monomer oxygen atoms. Comparison of the interaction between the different cations and the PEO diacrylate backbone and endgroup O atoms confirms this, showing preferential interaction with the low surface charge density cations, that is, in the order $K^+ > Na^+ > Li^+$.

In certain instances, low-molecular-weight primary amines are particularly effective at stabilizing clay shales against hydration and subsequent swelling. In experimental studies of polypropylene oxide (PPO) diamine intercalated montmorillonite LMOs, the only interlayer spacing observed corresponds to a monolayer arrangement of organic material while FTIR analysis indicated that increased hydrogen bonding was occurring within the interlayer region, similar to systems where a mixture of ammonium and amine species were co-intercalated [31, 34, 35]. Simulation studies using large-scale MD methods showed that at the experimental organic loadings a monolayer of the PPO diamine monomer forms [35]. If the

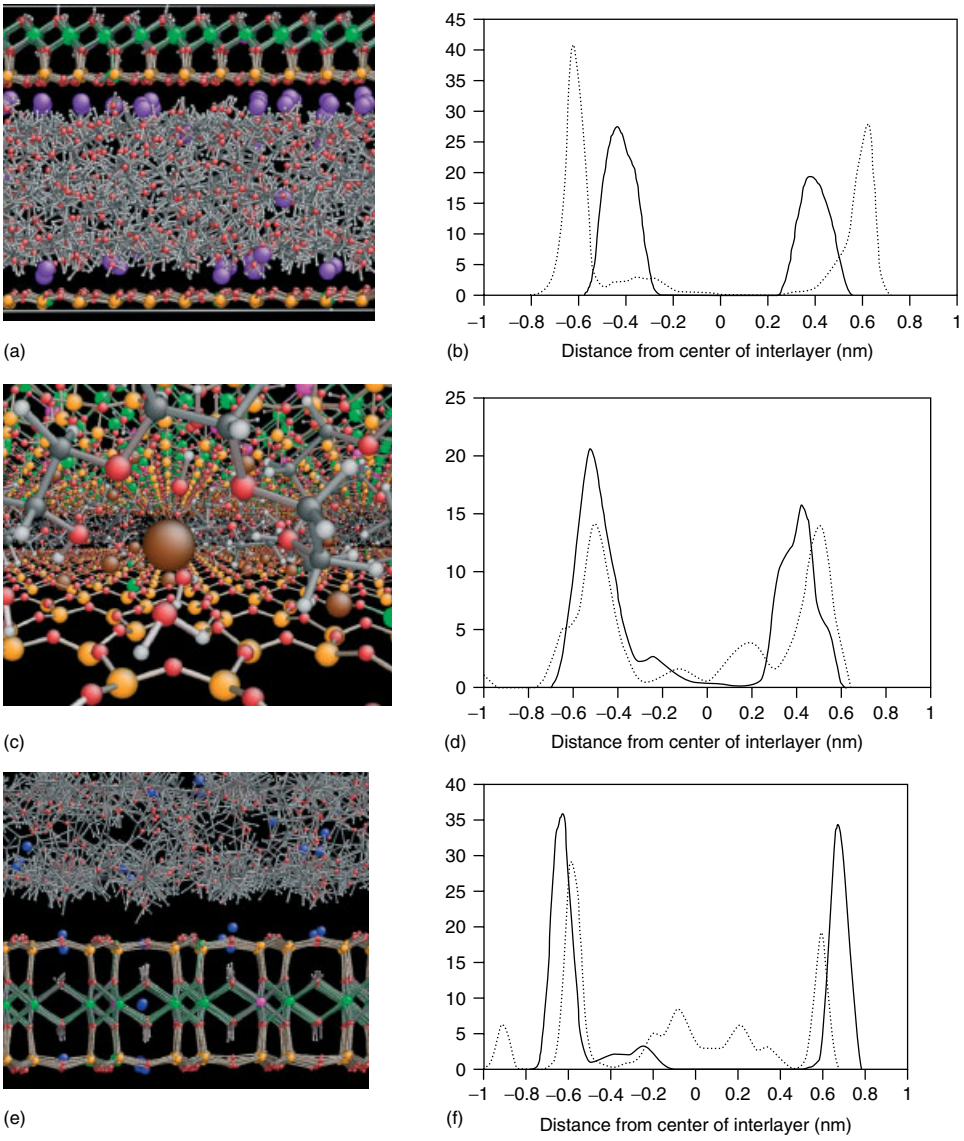

Figure 10.1 Snapshots taken after 1 nanosecond of NPT MD simulation showing the interlayer arrangement in PEG montmorillonite LMOs for where (a) K^+ is the cation; (c) Na^+ is the cation; (e) Li^+ is the cation; (b,d,f) show the time averaged one-dimensional atom density plot across the interlayer region for the respective cations, dashed line is PEG and solid line is PEO diacrylate for comparison. The vertical axes represent relative atom density at any point. (Chen, B., Evans, J.R.G., Greenwell, H.C., Boulet, P., Coveney, P.V., Bowden, A.A., Whiting, A. A critical appraisal of polymer-clay nanocomposites, *Chem. Soc. Rev.*, **37**, 568–594 (2008). Reproduced by permission of The Royal Society of Chemistry.)

amine groups are protonated, that is, to form ammonium groups, a conformational change in the monomers occurs, whereby the ammonium cation strongly coordinates with the surface oxygen atoms of the tetrahedral clay sheet and a slight increase in basal spacing occurs. The similarity between interactions of the ammonium organic cations and Na^+ inorganic cations with the clay sheet are shown in Figure 10.2. In models in which only some of the amine groups are protonated to form the ammonium species, both intra- and intermolecular H-bonds form between amine N atoms and ammonium H atoms, accounting for the increased H-bonding observed in the FTIR spectra and indicating that a mixture of ammonium and amine species was present in the interlayer of the experimental system, as suggested by the experimental evidence.

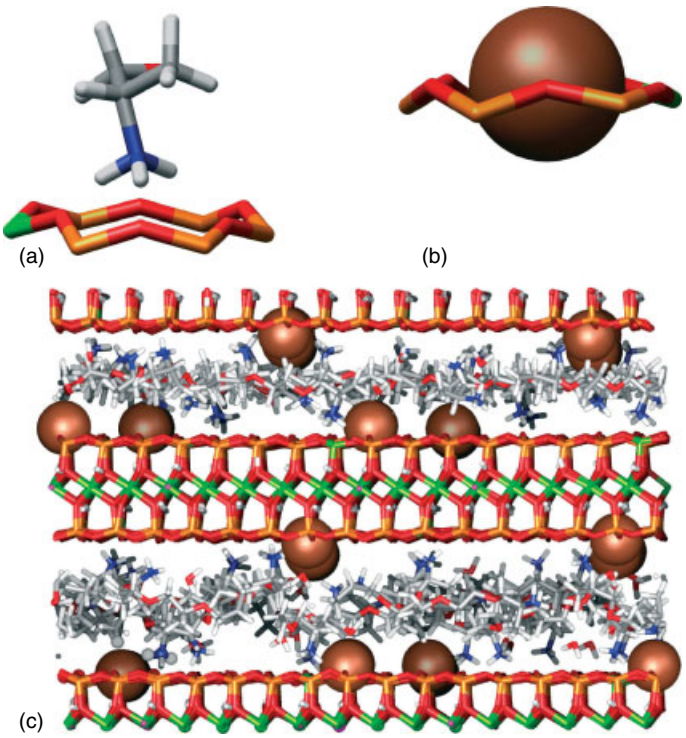

Figure 10.2 Snapshots after 1 nanosecond of MD simulation of PPO-diammonium montmorillonite clay LMOs showing (a) the interlayer arrangement of ammonium cations and adjacent clay-sheet atoms (other atoms omitted for clarity). The ammonium cation is arranged to maximize H-bond and electrostatic interactions. When compared to the Na^+ cation, (b) the ammonium cation is unable to sit closer to the cavities in the tetrahedral layer of the clay sheet due to steric restrictions and strong H-bond interactions with surface O atoms. The full-sized periodic simulation cell is shown in (c). Color indications are as follows: brown is sodium, orange is silicone, red is oxygen, green is aluminum, pink is magnesium, white is hydrogen, blue is nitrogen, and gray is carbon.

10.3.2.2 Understanding Oil Forming Reactions

In early work investigating petroleum formation in source rocks, Almon and Johns used Ca^{2+}-montmorillonite to decarboxylate *n*-docosanoic acid as a representative reaction to understand the conversion of kerogen, from biomass, into fossil fuel oil under reservoir conditions [36]. The ratio of branched alkanes and linear alkanes was 1 : 10 in the presence of water, whereas it was 9 : 2 in the anhydrous system. This reaction was shown to proceed by a free-radical mechanism since it was enhanced in the presence of hydrogen peroxide, a free-radical promoter. The reaction mechanism was suggested to involve the interlayer surface and octahedrally coordinated aluminum ions at the crystallite edges.

In recent years, the conversion of biomass through to hydrocarbons has seen a resurgence in interest owing to the rapid growth in the biofuels sector [37]. The current technology for producing fuels from plant and algae lipids is centered on trans-esterifying the triacylglycerides to form fatty acid methyl esters (FAMEs). However, FAME fuels are only suitable for use when blended at fairly low levels with fossil fuel diesel, so they are not a true replacement fuel. There is increasing interest in looking at the use of catalysts to decarboxylate fatty acids to form a fuel known as *green diesel*, which is a direct carbon neutral replacement for fossil fuel diesel [38].

In order to understand the reaction mechanism of decarboxylation reactions, we have been carrying out electronic structure calculation transition state searches of fatty acids at montmorillonite surfaces. Preliminary results indicate that the charge accepting nature (Lewis acidity) of the surface plays an important role in lowering the activation energy for such processes.

10.3.3 Determining the Material Properties of Nanocomposite Materials

As the twentieth century progressed, mankind's need for lightweight materials rapidly evolved. A driving force has been the birth and evolution of the airplane. From the early canvas and dope fuselages and wings, airframes have driven the evolution of lightweight, high-performance composite materials, which have also increasingly featured in improving the fuel efficiency of other forms of transport. The latest generation of such materials, based on clay fillers entrained in polymers, present significant challenges to the materials scientist as many of the enhanced properties occur at the molecular and atomic level, in the nanometer domain. These materials have been found to have properties similar to conventional composites, but for substantially lower amounts of filler material. Furthermore, the resulting composites can be easily processed to form films with improved barrier properties to gases, and materials with improved fire-retarding ability [13]. Such composites are particularly attractive for improving the properties of more fragile biopolymers for use in, for example, biodegradable packaging applications. Owing to the nanoscale of both the clay platelets and the interlayer spacing between the clay sheets, these compounds became known as *nanocomposites* [39]. In the early work on clay–polymer nanocomposites, cationic clays were investigated [13], but recently there has also been increasing interest in the use of LDHs [40]. In

cationic clay–polymer nanocomposites containing Li^+ cations, the arrangement of the polymer parallel to the clay sheets gives improved ion conduction for potential applications as battery materials [41].

A key performance criterion for a fundamental understanding of LMO nanocomposite materials is to be able to determine the relative reinforcing effect of the inorganic filler on the composite material, something hard to ascertain by virtue of the nanoscopic nature of the filler. It might be expected that two-dimensional sheets will display thermally excited long-range undulations and it is as a consequence of the Mermin–Wagner theorem that long-wavelength fluctuations destroy the long-range order of such crystals [42]. Thermal undulations of aluminosilicate sheets were first reported in the large-scale MD study of PPO-amine intercalated clay–polymer nanocomposites of Greenwell *et al.* [35]. These undulations were not observed in smaller sized models owing to finite size effects, and in many earlier simulations of clay-based LMOs it was assumed that the clay sheets could satisfactorily be treated as rigid bodies. Similar finite size effects have been reported previously in atomistic and mesoscopic simulations of biological and nonbiological membranes [43–45]. The observation of these thermal undulations is of considerable interest as it provides a route to the calculation of materials properties, such as the elastic and bending modulus, required for a theoretical understanding of polymer–clay nanocomposites. This data is exceedingly challenging to obtain by experimental means due to the small size of clay mineral crystals. In ongoing studies, Suter *et al.* have utilized distributed high-performance multiprocessor machines located within Europe and United States (exploiting grid computing techniques) to systematically vary the supercell sizes up to about 10 million atoms to investigate these effects in considerable detail [46]. These studies on montmorillonite clays indicated that thermal fluctuations only become apparent in clay mineral systems above a certain critical system size, that is, finite size effects limit the observation of emergent properties. Direct analysis of the undulations, and coupled stress-strain calculations, allowed the determination of mechanical properties of the montmorillonite model systems, giving a bending modulus of 1.6×10^{-17} J, which corresponds to an in-plane Young's modulus of about 230 GPa. In an analogous series of simulations, Thyveetil *et al.* calculated the previously undetermined materials properties of Mg_2Al-LDHs with charge balancing chloride ions, considering system sizes up to 1 million atoms [47]. The LDHs, having substantially thinner clay sheets, consisting of single mono-octahedral layers, were found to have a bending modulus of about 1.0×10^{-19} J, which corresponds to an in-plane Young's modulus of 135 GPa for the clay sheets, or 63 GPa for the hydrated system. Similarly, these systems exhibited emergent undulatory modes caused by the collective thermal motion of atoms in the LDH layers. However, at length scales larger than 20.7 Å, the thermal undulations caused the LDH sheets to interact and the oscillations were damped.

The materials properties of LDH hybrid biomaterials have been explored by Anderson *et al.* who performed large-scale MD simulations of Mg_2Al-LDHs intercalated with alginate polymers [48]. The effect of two different alginate polymer chain lengths upon the materials properties of these LDH composites was investigated

in model systems containing up to 250 000 atoms. In both cases, the alginate intercalated LDH systems exhibited greater flexibility than both the DNA and Cl^- intercalated Mg_2Al-LDHs investigated by Thyveetil *et al.* [25, 47], although the LDH clay-sheet flexibility was found to be the same as in these systems. The alginate-LDH systems were found to have an in-plane Young's modulus of approximately 135 GPa for the LDH sheets, or 40 GPa for the hydrated systems. Similar to the Cl^- intercalated LDHs, thermal undulations caused the sheets to interact and the thermal undulations were damped at long wavelengths. However, the size and aligned nature of alginate complexes inside the interlayer also affected the undulations; the sheet was found to show undulations related to the size of the alginate molecules. Figure 10.3 shows the fluctuations in height of an LDH sheet, from a 250 000 atom LDH-alginate system.

In a study by Mazo *et al.*, using nonequilibrium molecular dynamics (NEMDs), where shear and tensile deformations are applied to the simulation cell and the stress response is measured, the mechanical behavior of a clay platelet with intercalated PEO was studied [49]. The authors used large-scale MD and evaluated the role of the molecular weight of the polymer on the mechanical properties of the LMO system. The simulation cell investigated contained PEO macromolecules with different degrees of polymerization between 2 and 240 repeat units. The

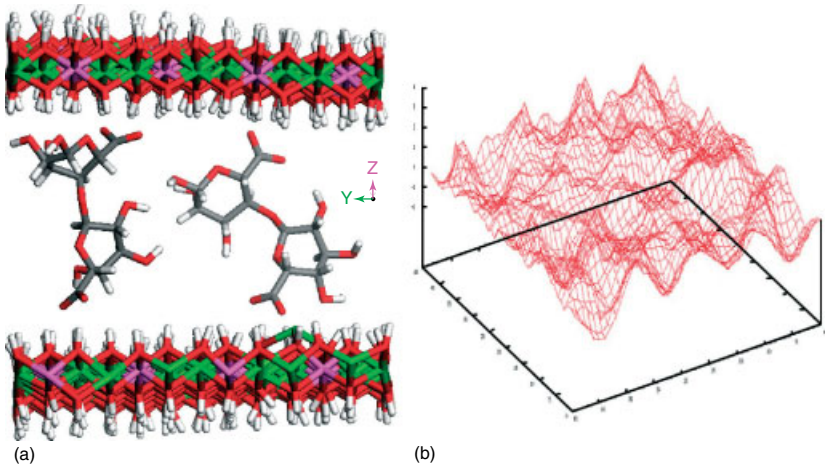

Figure 10.3 (a) Snapshot of a small part of an alginate-LDH LMO system after 1.5 nanosecond of MD simulation showing the orientation of alginate dimer in the interlayer region. The water molecules along with several other dimers have been removed to aid viewing. Color indications are as follows: magnesium is green, aluminum is purple, oxygen is red, carbon is gray, and hydrogen is white. The image (b) shows the height function description of a single LDH clay sheet from the LMO system. The overall size of the simulation cell is approximately 20 nm × 20 nm and the long-wavelength undulatory modes can be clearly seen. (Anderson, R.L., Suter, J.L., Greenwell, H.C., Coveney, P.V., Determining Materials Properties of Biodegradable LDH Biocomposite materials using Molecular Simulation. *J. Mater. Chem.*, Preprint (2009). Reproduced by permission of The Royal Society of Chemistry.)

simulations revealed that the mechanical strength primarily showed a strong dependence on the interlayer spacing, while the degree of polymerization of the PEO intercalates did not affect the mechanical properties. However, the authors reported an increase in shear modulus with increased polymerization.

10.3.4 Characterization and Simulation of Catalysts and Nanoscale Reaction Vessels

Layered double hydroxide minerals have recently seen a resurgence in interest for their application as solid-base catalysts for a range of synthetic procedures [14, 50]. Increasingly, more environmentally friendly catalytic processes are being investigated for catalyst synthesis, many of which use LMO systems as a precursor where the organic molecules are used to direct and control crystal growth of the inorganic catalyst; for example, we have investigated the synthesis of organo-LDH materials by green chemistry methods [51, 52]. In other work, the structure and catalytic reactivity of organo-LDHs has been studied by computational chemistry methods [53, 54].

10.3.4.1 Understanding Photochemistry in Constrained Media: Predicting Reactivity in Cinnamate LDHs

The highly constrained nanoscale environment within LMOs can be used to arrange reactant molecules in specific proximities and orientations, so as to enable otherwise unfavorable reactions to occur, or to selectively favor certain products [55]. Certain reactions between organic guests within anionic clays have been found to be strongly dependent upon the Mg/Al ratio of the clay host. Since the effect of varying the Mg/Al ratio is reflected in the interlayer arrangement of the reacting organic species, simulation can often provide insight into prereaction conditions that may not be accessible by any other method. Valim *et al.* [56], Takagi *et al.* [57], and Shichi *et al.* [58] have experimentally examined the photochemical dimerization of cinnamate anions within the interlayer of MgAl anionic clay systems. The products of these reactions were found to be strongly correlated to the layer charge on the LDH sheet, with different stereochemical dimers being favored at different Mg/Al ratios, suggesting that the constraining nature of the anionic clay host imposed stereo- and regioselectivity upon the reaction.

Though classical, empirical, and forcefield-based simulations cannot be used to directly simulate chemical reactivity, there are methods by which these techniques can be used to give insight into the probable outcome of chemical reactions. We have modeled the interlayer arrangement of cinnamate-LDH LMO systems at various Mg/Al ratios and hydration states, and a ''retrosynthesis'' approach was used to infer the outcome of reactions within the anionic clay interlayer [53]. Dimer precursors, reflecting the prereaction cinnamate monomer positions, were generated on the basis of optimized models of the possible dimer molecule products (Figure 10.4). Independently, close contacts at distances favorable for photodimerization between the reacting double bonds on the cinnamate molecules were monitored in the equilibrated NPT MD simulations at a temperature of

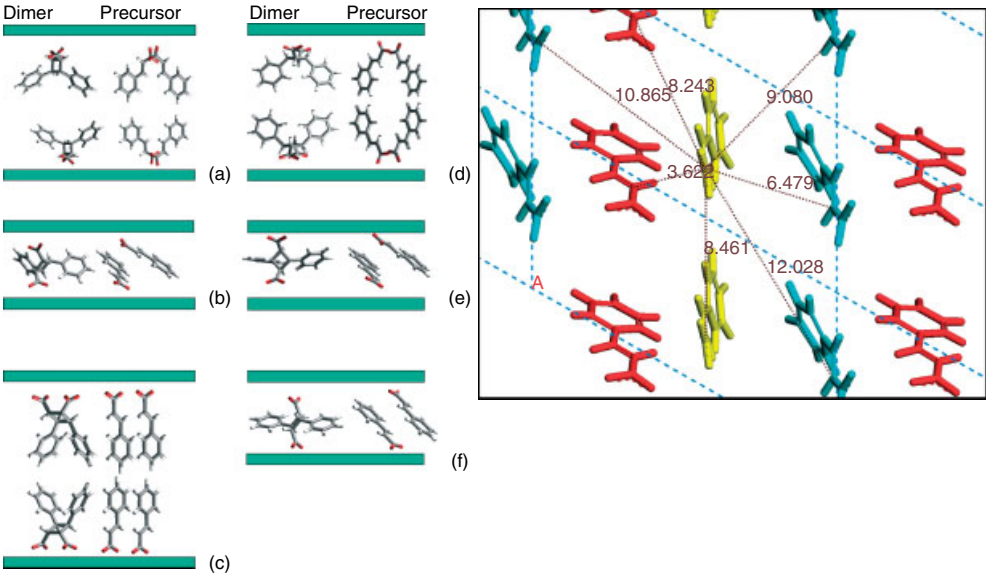

Figure 10.4 The various cinnamate dimers and their prereaction monomer positions are shown in the schematic on the left: (a) *anti*-HH (bilayer), (b) *anti*-HH (monolayer), (c) *syn*-HH (bilayer), (d) *anti*-HT (bilayer), (e) *anti*-HT (monolayer), and (f) *syn*-HT (monolayer). The green rectangles represent the LDH layers. On the right close contacts are shown for cinnamate anions at each face of the hydroxyl sheet where a bilayer existed. To ensure all contacts were included the cell was expanded in the *a* and *b* directions. For each frame of the final 10-picosecond MD simulation the close contacts were monitored (inset). Symmetry-related cinnamate anions are colored identically.

298 K. Where close contacts (as shown in Figure 10.4) occurred, the pair of adjacent cinnamate molecules involved, from the MD simulations, was compared to the various dimer precursor pairs generated previously. The precursor pair, and hence the dimer from which they were derived, most similar to the arrangement of the adjacent cinnamate molecules was deemed to be the most probable outcome of a photochemical reaction.

Within the approximations made in the simulations, reasonable agreement was found with the experimental results. In the experimental work of Shichi *et al.*, it was observed that as the Mg/Al ratio increased, that is, the charge on the clay sheet decreased, the ratio of syn-HH to anti-HH dimer decreased and the proportion of cis-isomer in the product mixture increased. The absence of any significant syn-HT dimer formation at low Mg/Al ratio was taken to confirm that steric control was operating and that a bilayer arrangement of anions perpendicular to the sheets must result in olefin–olefin distances too great for dimer formation [58]. The computational results showed some agreement with the experimental data, the dominant species predicted at low Mg/Al being the syn-HH dimer. For increased Mg/Al ratios and water content the anti-HH dimer is observed to be the likely

product, while at the highest Mg/Al ratio simulated the dominant outcome would appear to be the cis-isomer. The syn-HT dimer is not predicted to form at low Mg/Al ratios: under moderate hydration conditions the lack of a fully interdigitated bilayer arrangement precludes its formation by cinnamate molecules attached to opposite hydroxyl layer faces [53].

In general, it was found that the interlayer arrangement was more dynamic than anticipated and though the cinnamate carboxylate group was invariably oriented toward the MgAl layer the position of the remainder of the anion was quite fluxional. This resulted in pairs of molecules sometimes matching, over the simulation period, the criteria for photodimerization and not at other times.

10.3.4.2 Modeling Catalytic Cycles in Solid-Base Catalysts: t-Butoxide Organo-LDHs

Another class of LMO system of interest for their catalytic properties are the MgAl-*tert*-butoxide LDHs [54]. These materials have been reported in the literature for their ''superbasic'' properties, and they catalyze a range of reactions [7, 59–61]. Plane-wave-based density functional theory electronic structure simulations have been used to investigate possible catalytic pathways in these LMOs; plausible reaction mechanisms have been suggested based upon the products of one such reaction, trans-esterification, and this has been investigated by simulating the steps of the experimentally postulated catalytic cycle [62]. Owing to the extremely high computational cost of such studies, a simple interlayer environment was created, with a fixed interlayer spacing, no explicit solvent, and with just one Al atom per unit cell and an initial interlayer spacing of 16 Å. The trans-esterification of methylacetoacetate with prop-2-en-1-ol was selected as a representative system to simulate [62].

Interactions between the MgAl-*tert*-butoxide LDH and the organic substrate molecules in the LMO system were simulated for each step of the postulated mechanism, which was found to prevent the catalyst regenerating in the simulation work, and an alternative mechanism was proposed consistent with both experiment and simulation. Catalyst regeneration only occurred when interlayer water molecules were present, and the modeling established that the active catalyst was, in fact, most likely a hydroxide-intercalated LDH, with neutral *tert*-butanol molecules associated with the LDH layer. A reduced interlayer spacing of 10.50 Å was also required for the catalyst to regenerate. The regeneration step is illustrated in Figure 10.5. The study of the trans-esterification reaction illustrates the importance of the H-bonding environment within the LDHs. The combination of the variable interlayer spacing of the LDHs, which allows more specificity to substrate molecules, and the amphiphilic nature of the galleries, caused by a hydrophilic layer adjacent to the LDH layer and an organophilic region in the interlayer center (due to the *tert*-butyl groups), is deemed to be responsible for the increased catalytic activity of these materials [54]. Thus organic substrate molecules are more easily adsorbed within the organophilic interlayer region with their polar reactive groups oriented by the LDH layer surface, greatly facilitating subsequent chemical reactions when compared to the organophobic rehydrated hydroxide LDH.

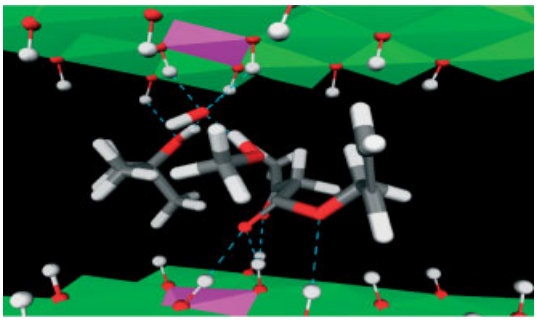

Figure 10.5 Snapshot of an LMO catalyst during an electronic structure simulation of a trans-esterification reaction. The catalyst is based on a *tert*-butoxide intercalated LDH system. Green indicates magnesium, pink is aluminum, gray is carbon, white is hydrogen, and red is oxygen.

10.3.5
Nanomedicine: Drug Delivery and Gene Therapy

Large-scale atomistic MD simulation provides an opportunity to gain insight into the conformations of relatively substantially sized interlayer species. In a recent study, Thyveetil *et al*. performed large-scale MD simulations to investigate the stability and structural changes that occur when double-stranded, linear, and plasmid DNA of up to 480 base pairs in length was intercalated within a magnesium–aluminum LDH (Figure 10.5) [25]. Layered double hydroxides can be used to intercalate drugs or genes and then excalate them where needed, in order to prepare a controlled release formulation for use in drug delivery and gene therapy. Currently, only limited experimental data has been reported for these systems [63–65]. Notwithstanding this, the models were found to be in qualitative agreement with experimental observations, according to which hydration is a crucial factor in determining the structural stability of DNA. The phosphate backbone groups were found to align with aluminum lattice positions, demonstrating the high electrostatic attraction between the clay surface and the charged groups on the DNA molecule. The LDH sheets themselves showed great flexibility; as a consequence, the layers were observed to distort around the large intercalated anions, rendering the concept of a well-defined basal spacing (distance between the clay sheets) somewhat ambiguous.

10.3.6
Formation Mechanisms of LMOs

We have already seen that the intercalation of nucleic acids is now possible through the use of large-scale simulation techniques and studies have been undertaken into the stabilization of nucleic acids by minerals in origin of life scenarios and also the structure of LDH-nucleic acid LMOs used in gene therapy. Though such structures are observed experimentally, it is not immediately intuitive how such

bulky molecules exchange into the mineral host with such high efficiency. A recent study by Thyveetil *et al.* has attempted to address the intercalation behavior and mechanism of bulky molecules in LMOs using large-scale MD [66]. LDHs have been shown to form staged intermediate structures in experimental studies of intercalation, but the mechanism by which staged structures are produced remains undetermined. Staging is a process by means of which layered host materials intercalate guest compounds forming alternate layers periodically occupied by intercalant. While the majority of LDH structures exist with similar interlayers throughout the structure, those with more than one type of interlayer have so-called staged structures [67]. Thyveetil *et al.* explored the role of the LDH flexibility on the possible intermediate structures that may form during intercalation of DNA into MgAl-LDHs [66].

It is generally believed that staged intercalation in LMOs occurs through a Daumas–Hérold (Figure 10.6) or a Rüdorff model [68, 69]. The Rüdorff model involves complete intercalation of alternate interlayers, while the Daumas–Hérold pathway predicts that islands of intercalants are formed, with identical amounts of intercalant in each interlayer. The latter scenario requires a more flexible layer material to distort around the intercalate. The simulations of Thyveetil *et al.* showed greater diffusion coefficients for DNA strands in a Daumas–Hérold configuration compared to a Rüdorff model, providing evidence for the presence of peristaltic modes of motion within Daumas–Hérold configurations [66]. Peristaltic modes are more prominent in the Daumas–Hérold structure compared to the Rüdorff structures and support a mechanism by means of which bulky intercalated molecules such as DNA rapidly diffuse within an LDH interlayer.

In a comprehensive series of coarse-grained studies on LMOs, Farmer and coworkers looked at the behavior of stacks of clay lamellae in both a polymer melt and in a binary fluid (representing a curing agent and a monomer), thereby simulating polymer melt preparation and *in situ* polymerization preparation methods,

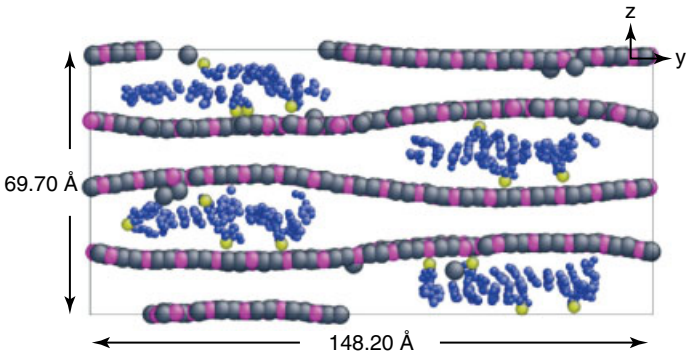

Figure 10.6 A snapshot of a large-scale atomistic simulation showing LDH sheet flexibility (pink and gray spheres) during 12-bp DNA double helices (blue and yellow spheres) intercalation through a Daumas–Hérold mechanism [66].

respectively [70, 71]. Interestingly, the results from the latter intercalation study showed that completely intercalated structures may be formed by simply adjusting the relative concentrations of the binary fluid, or the pressure experienced by the nanocomposite system, with increased swelling observed in some cases, which was suggested by the authors to be indicative of exfoliation [71]. In the simulated polymer melt system, the interaction parameter between the clay sheet and the polymer was adjusted to represent some polymers strongly interacting with the sheet, others having functionalized strongly interacting head groups but weakly attractive (to the clay) polymer segments, and others having no functionality. The studies showed that the strongly interacting polymers ''pinned'' clay sheets together around the anterior, impeding the fraction of intercalated material. Low intercalation density, and decreased interaction between clay sheets, was observed for the end-functionalized polymers. The highest intercalation density was found for simulations containing a blend of end-functionalized and nonfunctionalized polymers [70]. As in large-scale MD studies, significant flexibility of the clay sheets was observed in all these studies.

10.4 Conclusions and Future Work

The recent advances in supercomputing capacity have allowed the simulation of LMO systems to reach unparalleled size and timescales, allowing the observation of previously unseen behavior. Research into LMO systems using electronic structure and large-scale computer simulations have revealed certain interesting properties: (i) the structure of individual mineral sheets with tunable chemical composition may be varied to alter the charge density and impact on the degree of intercalation of guest molecules (ii) the interlayer region between the sheets of LMO materials can have amphiphilic character, modifying the way polar molecules arrange in the LMO – aiding catalyst performance; (iii) the LMO sheet dynamics have been studied, and found to be flexible, which has implications for intercalation mechanisms and catalytic performance as thermal undulations accelerate guest intercalation and the flexible sheets allow better specificity with intercalated substrates; and (iv) by carefully tuning the intercalant during formation of the hybrid system, experiments have shown the crystal morphology may also be systematically varied. Interestingly, phenomena such as emergent thermal undulations and interlayer catalysis are in many ways more reminiscent of biological systems than one would expect from a mineral.

Though research has been predominantly focused on LMO systems where the mineral is a clay, other layered mineral classes such as the manganese oxides (e.g., birnessite) and other layered transition metal systems such as niobates remain to be investigated. Additionally, a diverse range of applications of LMOs has yet to be explored with computer simulation; currently, the carbon capture capacity of soils and the containment of radionuclides by clays and organoclays is of great interest in the drive for cleaner energy supplies and reduction of global carbon dioxide levels.

In our future work on LMOs, we will be using electronic structure calculations to understand decarboxylation reactions in LMO systems, which are important both for understanding petroleum-forming conditions and catalysis in the production of deoxygenated lipids for the next-generation biofuel ''green diesel,'' as well as investigating peptide-forming conditions in the origin of life scenarios. Having developed the very large-scale MD simulations to the level where we can now routinely calculate materials properties of layered systems, even when intercalated with bulky biological molecules and many thousands of water molecules, we are now starting to both apply our techniques in new areas, such as biodegradable packaging design, and also develop the techniques to include edge effects in the clay. The latter research removes some of the artificial nature of periodic supercells, and allows us to examine the interaction of water molecules and organic molecule at the edge of the clay platelets, that is, during the start of intercalation processes, yielding yet more insight into the unseen behavior of chemistry between the sheets.

Acknowledgments

I would like to thank my former supervisors, Prof. Peter V. Coveney and Prof. William Jones for their unstinting enthusiasm and interest in studying layered mineral systems. I also thank Dr James Suter, Dr Richard Anderson, and Dr Mary-Ann Thyveetil for their numerous contributions over the past years. I acknowledge the Addison Wheeler Trust at Durham University for support during the writing of this chapter through the award of the Addison Wheeler Fellowship.

References

1. Perry, R.S., McLoughlin, N., Lynne, B.Y., Sephton, M.A., Oliver, J.D., Perry, C.C., Campbell, K., Engel, M.H., Farmer, J.D., Brasier, M.D., and Staley, J.T. (2007) Defining biominerals and organominerals. *Sediment. Geol.*, **201**, 157–179.
2. Schoonheydt, R.A., Pinnavaia, T.J., Lagaly, G., and Gangas, N. (1999) Pillared clays and pillared layered solids. *Pure Appl. Chem.*, **71**, 2367–2371.
3. Grim, R.E. (1962) *Applied Clay Mineralogy*, Mcgraw-Hill Book Company, New York.
4. Reichle, W.T. (1985) Catalytic reactions by thermally activated, synthetic, anionic clay minerals. *J. Catal.*, **94**, 547–557.
5. Constantino, V.R.L. and Pinnavaia, T.J. (1995) Basic properties of Mg1-X(2+)AlX(3+) layered double hydroxides intercalated by carbonate, hydroxide, chloride and sulfate anions. *Inorg. Chem.*, **34**, 883–892.
6. Rao, K.K., Gravelle, M., Valente, J.S., and Figueras, F. (1998) Activation of Mg-Al hydrotalcite catalysts for aldol condensation reactions. *J. Catal.*, **173**, 115–121.
7. Choudary, B.M., Kantam, M.L., Bharathi, B., and Reddy, C.V. (1998) Superactive Mg-Al-O-t-Bu hydrotalcite for epoxidation of olefins. *Synth. Lett.*, 1203–1204.
8. Tronto, J., Crepaldi, E.L., Pavan, P.C., De Paula, C.C., and Valim, J.B. (2001) Organic anions of pharmaceutical interest intercalated in magnesium aluminum LDHs by two different methods. *Mol. Cryst. Liq. Cryst.*, **356**, 227–237.
9. Choy, J.-H., Kwak, S.Y., Jeong, Y.J., and Park, J.S. (2000) Inorganic layered

double hydroxides as nonviral vectors. *Angew. Chem. Int. Ed.*, **39**, 4042–4045.
10. Choy, J.-H., Oh, J.-M., Park, M., Sohn, K.-M., and Kim, J.-W. (2004) Inorganic-biomolecular hybrid nanomaterials as a genetic molecular code system. *Adv. Mater.*, **16**, 1181–1184.
11. Guo, Y.H., Li, D.F., Hu, C.W., Wang, Y.H., Wang, E.B., Zhou, Y.C., and Feng, S.H. (2001) Photocatalytic degradation of aqueous organochlorine pesticide on the layered double hydroxide pillared by Paratungstate A ion, Mg12Al6(OH)36(W7O24).4H2O. *Appl. Catal., B*, **30**, 337–349.
12. Meunier, A., Velde, B., and Griffault, L. (1998) The reactivity of bentonites: a review. An application to clay barrier stability for nuclear waste storage. *Clay Miner.*, **33**, 187–196.
13. Pinnavaia, T.J. and Beall, G.W. (eds) (2000) *Polymer-clay Nanocomposites*, John Wiley & Sons, Ltd, Chichester.
14. Figueras, F. (2004) Base catalysis in the synthesis of fine chemicals. *Top. Catal.*, **29**, 189–196.
15. Sels, B., De Vos, D., Buntinx, M., Pierard, F., Kirsch-De Mesmaeker, A., and Jacobs, P. (1999) Layered double hydroxides exchanged with tungstate as biomimetic catalysts for mild oxidative bromination. *Nature*, **400**, 855–857.
16. Anderson, R.L., Greenwell, H.C., Suter, J.L., Jarvis, R.M., and Coveney, P.V. (2009) Towards the design of new and improved drilling fluid additives using molecular dynamics simulations. *Ann. Braz. Acad. Sci.*, **82**, Preprint (2010).
17. Li, T.-Q., Häggkvist, M., and Ödberg, L. (1999) The porous structure of paper coatings studied by water diffusion measurements. *Colloids Surf. A*, **159**, 57–63.
18. Cheng, S. (1999) From layer compounds to catalytic materials. *Catal. Today*, **49**, 303–312.
19. Leach, A.R. (2001) *Molecular Modelling, Principles and Applications*, Pearson Education, Ltd, England .
20. Boulet, P., Greenwell, H.C., Stackhouse, S., and Coveney, P.V. (2006) Recent advances in understanding the structure and reactivity of clays using electronic structure calculations. *J. Mol. Struct. Theochem*, **762**, 33–48.
21. Greenwell, H.C., Stackhouse, S., Coveney, P.V., and Jones, W. (2006) On the molecular modelling of the structure and properties of clays: a materials chemistry perspective. *J. Mater. Chem.*, **16**, 708–723.
22. Chen, B., Evans, J.R.G., Greenwell, H.C., Boulet, P., Coveney, P.V., Bowden, A.A., and Whiting, A. (2008) A critical appraisal of polymer-clay nanocomposites. *Chem. Soc. Rev.*, **37**, 568–594.
23. Anderson, R.L., Suter, J.L., Greenwell, H.C., and Coveney, P.V. (2009) Recent advances in large-scale atomistic and coarse-grained molecular dynamics simulation of clay minerals. *J. Mater. Chem.*, doi: /b820455d.
24. Harding, J.H., Duffy, D.M., Sushko, M.L., Rodger, P.M., Quigley, D., and Elliott, J.A. (2008) Computational techniques at the organic/inorganic interface in biomineralization. *Chem. Rev.*, **108**, 4823–4854.
25. Thyveetil, M.-A., Coveney, P.V., Greenwell, H.C., and Suter, J.L. (2008) Computer simulation study of the structural stability and materials properties of DNA-intercalated layered double hydroxides. *J. Am. Chem. Soc.*, **130**, 4742–4756.
26. Martin, W., Baross, J., Kelley, D., and Russell, M.J. (2008) Hydrothermal vents and the origin of life. *Nature Rev. Microbiol.*, **6**, 805–814.
27. Greenwell, H.C. and Coveney, P.V. (2006) Layered double hydroxide minerals as possible prebiotic information storage and transfer compounds. *Orig. Life. Evol. Bio.*, **36**, 13–37.
28. Coveney, P.V., Watkinson, M., Whiting, A., and Boek, E.S., Stabilizing clayey formations. US Patent No. 6,787,507.
29. Coveney, P.V., Griffin, J.L.W., Watkinson, M., Whiting, A., and Boek, E. (2002) Novel non-exfoliated clay-nanocomposite materials by in situ co-polymerisation of intercalated monomers: a combinatorial discovery approach. *Mol. Simul.*, **28**, 295–316.
30. Stackhouse, S., Coveney, P.V., and Sandré, E. (2001) Plane-wave density functional theoretic study of formation

of clay-polymer nanocomposite materials by self-catalyzed in situ intercalative polymerization. *J. Am. Chem. Soc.*, **123**, 11764–11774.

31. Boulet, P., Bowden, A.A., Coveney, P.V., and Whiting, A. (2003) Combined experimental and theoretical investigations of clay polymer nanocomposites: intercalation of single bifunctional organic compounds in Na+-montmorillonite and Na+-hectorite clays for the design of new materials. *J. Mater. Chem.*, **13**, 2540–2550.
32. Bowden, A.A., Boulet, B., Greenwell, H.C., Chen, B., Evans, J.R.G., Coveney, P.V., and Whiting, A. (2006) Intercalation and in situ polymerization of poly(alkylene oxide) derivatives within M+-montmorillonite (M=Li, Na, K). *J. Mater. Chem.*, **16**, 1082–1094.
33. Bujdák, J., Hackett, E., and Giannelis, E.P. (2000) Effect of layer charge on the intercalation of poly(ethylene oxide) in layered silicates: implications on nanocomposite polymer electrolytes. *Chem. Mater.*, **12**, 2168–2174.
34. Lin, J.-J. and Chen, Y.-M. (2004) Amphiphilic properties of poly(oxyalkylene)amine-intercalated smectite aluminosilicates. *Langmuir*, **20**, 4261–4264.
35. Greenwell, H.C., Bowden, A.A., Boulet, P., Harvey, M.J., Coveney, P.V., and Whiting, A. (2005) Interlayer structure and bonding in non-swelling primary amine intercalated clays. *Macromolecules*, **38**, 6189–6200.
36. Almon, W.R. and Johns, W.D. (1975) Advances in Organic Geochemistry, 7th International Meeting, Petroleum forming reactions: the mechanism and rate of clay catalyzed fatty acid decarboxylation. pp. 157–171.
37. Smith, B., Greenwell, H.C., and Whiting, A. (2009) Catalytic upgrading of tri-glycerides and fatty acids to transport biofuels. *Energy Environ. Sci.*, **2**, 262–271.
38. Kalnes, T., Marker, T., and Shonnard, D.R. (2007) Green diesel: a second generation biofuel. *Int. J. Chem. Reactor Eng.*, **5**, A48 .
39. Chen, B. (2004) Polymer-clay nanocomposites: an overview with emphasis on interaction mechanisms. *Br. Ceram. Trans.*, **103**, 241–249.
40. Leroux, F., Aranda, P., Besse, J.P., and Ruiz-Hitzky, E. (2003) Intercalation of poly(ethylene oxide) derivatives into layered double hydroxides. *Eur. J. Inorg. Chem.*, **6**, 1242–1251.
41. Bujdák, J., Hackett, E., and Giannelis, E.P. (2000) Effect of layer charge on the intercalation of poly(ethylene oxide) in layered silicates: implications on nanocomposite polymer electrolytes. *Chem. Mater.*, **12**, 2168–2174.
42. Mermin, N.D. (1968) Crystalline order in two dimensions. *Phys. Rev.*, **176**, 250–254.
43. Marrink, S.J. and Mark, A.E. (2001) Effect of undulations on surface tension in simulated bilayers. *J. Phys. Chem. B*, **105**, 6122–6127.
44. Lindahl, E. and Edholm, O. (2000) Mesoscopic undulations and thickness fluctuations in lipid bilayers from molecular dynamics simulations. *Biophys. J.*, **79**, 426–433.
45. Goetz, R., Gompper, R., and Lipowsky, R. (1999) Mobility and elasticity of self-assembled membranes. *Phys. Rev. Lett.*, **82**, 221–224.
46. Suter, J.L., Coveney, P.V., Greenwell, H.C., and Thyveetil, M.-A. (2007) Large-scale molecular dynamics study of montmorillonite clay: emergence of undulatory fluctuations and determination of material properties. *J. Phys. Chem. C*, **111**, 8248–8259.
47. Thyveetil, M.-A., Coveney, P.V., Suter, J.L., and Greenwell, H.C. (2007) Emergence of undulations and determination of materials properties in large-scale molecular dynamics simulations of layered double hydroxides. *Chem. Mater.*, **19**, 5510–5523.
48. Anderson, R.L., Greenwell, H.C., Thyveetil, M.-A., Coveney, P.V., and Suter, J.L. (2009) Determining materials properties of LDH hybrid biomaterials using molecular simulation, *J. Mater. Chem.*, **19**, 7251–7262.
49. Mazo, M.A., Manevitch, L.I., Gusarova, E.B., Shamaev, M.Yu., Berlin, A.A., Balabaev, N.K., and Rutledge, G.C. (2008) Molecular dynamics simulation of

thermomechanical properties of montmorillonite crystal. 3. Montmorillonite crystals with PEO oligomer intercalates. *J. Phys. Chem. B*, **112**, 3597–3604.

50. Greenwell, H.C., Holliman, P.J., Jones, W., and Vaca Velasco, B. (2006) Studies of the effects of synthetic procedure on base catalysis using hydroxide-intercalated layer double hydroxides. *Catal. Today*, **114**, 397–402.

51. Greenwell, H.C., Marsden, C.C., and Jones, W. (2007) Synthesis of organo-layered double hydroxides by an environmentally friendly co-hydration route. *Green Chem.*, **9**, 1299–1307.

52. Greenwell, H.C., Jones, W., Stamirez, D.N., Brady, M.F., and O'Connor, P. (2006) One step synthesis of acetate intercalated MgAl layered double hydroxides using magnesium acetate. *Green Chem.*, **8**, 1067–1072.

53. Newman, S.P., Greenwell, H.C., Coveney, P.V., and Jones, W. (2003) Computer simulation of interlayer arrangement in cinnamate intercalated layered double hydroxides. *J. Mol. Struct.*, **647**, 75–83.

54. Greenwell, H.C., Stackhouse, S., Coveney, P.V., and Jones, W. (2003) A density functional theory study of catalytic trans-esterification by tert-butoxide MgAl anionic clays. *J. Phys. Chem. B.*, **107**, 3476–3485.

55. Ogawa, M. and Kuroda, K. (1995) Photofunctions of intercalation compounds. *Chem. Rev.*, **95**, 399–438.

56. Valim, J., Kariuki, B.M., King, J., and Jones, W. (1992) Photoactivity of cinnamate-intercalates of layered double hydroxides. *Mol. Cryst. Liquid Cryst.*, **211**, 271–281.

57. Takagi, K., Shichi, T., Usami, H., and Sawaki, Y. (1993) Controlled photocycloaddition of unsaturated carboxylates intercalated in hydrotalcite clay interlayers. *J. Am. Chem. Soc.*, **115**, 4339–4344.

58. Shichi, T., Takagi, K., and Sawaki., Y. (1996) Stereoselectivity control of [2+2] photocycloaddition by changing site distances of hydrotalcite interlayers. *Chem. Commun.*, 2027–2028.

59. Choudary, B.M., Kantam, M.L., Kavita, B., Reddy, C.V., Rao, K.K., and Figueras, F. (1998) Aldol condensations catalysed by novel Mg-Al-O-t-Bu hydrotalcite. *Tetrahedron Lett.*, **39**, 3555–3558.

60. Choudary, B.M., Kantam, M.L., and Kavita, B. (1999) Mg-Al-O-Bu-t-Hydrotalcite: a mild and ecofriendly catalyst for the cyanoethylation of alcohols and thiols. *Green Chem.*, **1**, 289–292.

61. Choudary, B.M., Kantam, M.L., Kavita, B., Reddy, C.V., and Figueras, F. (2000) Catalytic C-C bond formation promoted by Mg-Al-O-t-Bu hydrotalcite. *Tetrahedron*, **56**, 9357–9364.

62. Choudary, B.M., Kantam, M.L., Reddy, C.V., Aranganathan, S., Santhi, P.L., and Figueras, F. (2000) Mg-Al-O-t-Bu hydrotalcite: a new and efficient heterogeneous catalyst for transesterification. *J. Mol. Catal. A: Chem.*, **159**, 411–416.

63. Choy, J.H., Kwak, S.Y., Park, J.S., Jeong, Y.J., and Portier, J. (1999) Intercalative nanohybrids of nucleoside monophosphates and DNA in layered metal hydroxide. *J. Am. Chem. Soc.*, **121**, 1399–1400.

64. Choy, J.H., Kwak, S.Y., Jeong, Y.J., and Park, J.S. (2000) Inorganic layered double hydroxides as nonviral vectors. *Angew. Chem.*, **39**, 4042–4045.

65. Choy, J.H., Kwak, S.Y., Park, J.S., and Jeong, Y.J. (2001) Cellular uptake behavior of [gamma-P-32] labeled ATP-LDH nanohybrids. *J. Mater. Chem.*, **11**, 1671–1674.

66. Thyveetil, M.-A., Coveney, P.V., Greenwell, H.C., and Suter, J.L. (2008) Role of host-layer flexibility in DNA guest intercalation revealed by computer simulation of layered nanomaterials. *J. Am. Chem. Soc.*, **130**, 12485–12495.

67. Fogg, A.M., Dunn, J.S., and O'Hare, D. (1998) Formation of second-stage intermediates in anion-exchange intercalation reactions of the layered double hydroxide [LiAl2(OH)6]Cl.H2O as observed by time-resolved, in situ X-ray diffraction. *Chem. Mater.*, **10**, 356–360.

68. Rudorff, W. (1940) Crystal structure of acid compounds of graphite. *Z. Phys. Chem.*, **45**, 42.

69. Daumas, N. and Herold, A. (1969) Relations between the elementary stage and the reaction mechanisms in graphite

insertion compounds. *Seances Acad. Sci. Ser. C*, **268**, 373.

70. Sinsawat, A., Anderson, K.L., Vaia, R.A., and Farmer, B.L. (2003) Influence of polymer matrix composition and architecture on polymer nanocomposite formation: coarse-grained molecular dynamics simulation. *J. Polym. Sci. B*, **41**, 3272–3284.

71. Anderson, K.L., Sinsawat, A., Vaia, R.A., and Farmer, B.L. (2005) Control of silicate nanocomposite morphology in binary fluids: coarse-grained molecular dynamics simulations. *J. Polym. Sci. B*, **43**, 1014–1024.

Part IV
Materials and Applications in Advanced Devices

Ideas in Chemistry and Molecular Sciences: Advances in Nanotechnology, Materials and Devices.
Edited by Bruno Pignataro

ISBN: 978-3-527-32543-6

11
Status of Technology and Perspectives for Portable Applications of Direct Methanol Fuel Cells

Vincenzo Baglio, Vincenzo Antonucci, and Antonino S. Aricò

11.1
Introduction

Fuel cells, represent an important technology for a large variety of applications including micropower, auxiliary power, transportation, stationary power for buildings and other distributed generation applications, and central power [1]. Several types of fuel cells are in advanced stage of development. They can be classified into different categories, depending on the type of fuel and oxidant, whether the fuel is processed outside (external reforming) or inside (internal reforming) the fuel cell, the type of electrolyte, the temperature of operation, whether the reactants are fed to the cell by internal or external manifolds, and so on. Generally, fuel cells are distinguished on the basis of the electrolyte. If there is an ion exchange membrane, the fuel cell is called *polymer electrolyte fuel cell* (*PEFC*). This technology is now approaching commercialization. The candidate fuel for fuel cells is usually considered hydrogen. However, at present, no suitable large-scale infrastructure exists for hydrogen production, storage, and distribution. Significant efforts have been addressed in the last decades to the direct electrochemical oxidation of alcohol and hydrocarbon fuels [2–5]. Organic liquid fuels are characterized by high-energy density (Table 11.1), whereas, the electromotive force associated to their electrochemical combustion to CO_2 is comparable to that of hydrogen combustion to water. Among the liquid organic fuels, methanol has promising characteristics in terms of reactivity at low temperatures, storage, and handling. Accordingly, a direct methanol proton exchange membrane fuel cell (DMPEMFC) would help to alleviate some of the issues surrounding fuel storage and processing for fuel cells. Technological improvements in direct methanol fuel cells (DMFCs) are thus fueled by their perspectives of applications in portable, transportation, and stationary systems especially with regard to the remote and distributed generation of electrical energy. Methanol is cheap and it can be distributed by using the present infrastructure for liquid fuels. It can be obtained from fossil fuels, such as natural gas or coal, as well as from sustainable sources through fermentation of agricultural products and from biomasses. With respect to ethanol, methanol has the

Ideas in Chemistry and Molecular Sciences: Advances in Nanotechnology, Materials and Devices.
Edited by Bruno Pignataro

ISBN: 978-3-527-32543-6

Table 11.1 Volumetric and gravimetric energy density for various fuels of technical interest for low-temperature fuel cells.

Fuels	Volumetric energy density (kWh l^{-1})	Gravimetric energy density (kWh kg^{-1})
Diluted hydrogen (1.5%)	–	0.49
Hydrogen	0.18 (@ 1000 psi, 25 °C)	–
Methanol	4.82 (100 wt%)	6.1
Ethanol	6.28 (100 wt%)	8
Formic acid	1.75 (88 wt%)	–
Dimethyl ether (DME)	5.61 (in liquid of 100 wt%)	8.4
Ethylene glycol	5.87 (100 wt%)	5.3

significant advantage of high selectivity to CO_2 formation in the electrochemical oxidation process. In general, liquid-fueled fuel cells are a promising alternative to hydrogen-fueled devices as electrochemical power sources in particular, for application in portable technology due to the low power required by these systems.

Portable power is becoming important for many electronic devices, such as notebook computers, personal digital assistants (PDAs), music systems, and cellular telephones. Currently, these devices are powered by primary and secondary batteries. While the power source is often the largest component of the device and, in fact, is the limiting factor in efforts toward miniaturization, the runtime, and functionality of the devices remain limited by the quantity of energy that can be stored and carried within them. Thus, advances in the development of portable fuel cells will have a great impact on the use and development of modern electronic devices. Unlike primary and secondary batteries, where the reactants and products are contained within the battery, fuel cells employ reactants that are continuously supplied to the cell; byproducts also are continuously removed (Figure 11.1). Methanol, which is characterized by low cost, easy storage and handling, and high-energy density, appears well suited for portable fuel cells.

In practice, fuel cells do not operate as single units; rather, they are connected in a series to additively combine the individual cell potentials and achieve a greater, and more useful, potential. A collection of single cells in series is known as a *stack*. For conventional actively driven fuel cells, the most popular means of interconnection are the ''bipolar plates.'' These connect one cathode to the anode of the next cell; furthermore, the bipolar plates serve as a means of feeding oxygen to the cathode and fuel to the anode. The fuel-cell stack consists of a repeated, interleaved structure of membrane electrode assemblies (MEAs), gas-diffusion layers (GDLs), and bipolar plates. All these components are clamped together with significant force to reduce electrical contact resistance. The fuel and oxidant are

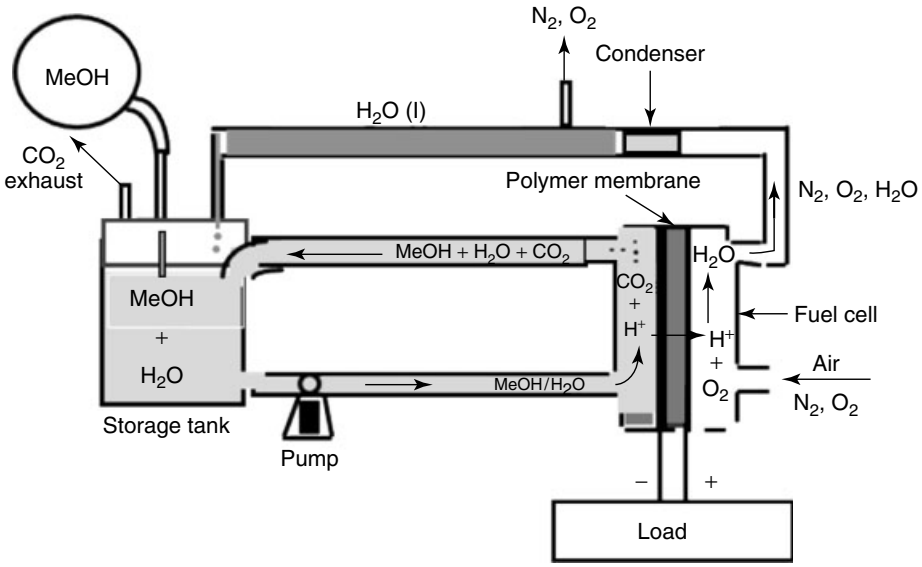

Figure 11.1 Scheme of the DMFC system.

provided with manifolds to the correct electrodes, and cooling is provided either by the reactants or by a cooling medium. Usually, this type of fuel cell works with forced airflow on the cathode side and forced fuel flow on the anode side, requiring various auxiliary components and a rather complicated control system. Such a fuel cell does not fit the requirements for low-power-battery replacement applications. For such applications, the key challenges are to provide acceptable power output and high-energy efficiency under conditions convenient to the user. The desired operating conditions include, for example, an operating temperature near room temperature, no forced airflow, and no recirculation fuel pump. It is well known that a forced air design with an external blower is unattractive for use in small fuel-cell systems, as the parasitic power losses from the blower are estimated at 20–25% of the total power output. To this scope, the concept of passive-feed DMFCs has been the object of significant interest [2]. Under this configuration, DMFCs operate without any external devices for feeding methanol and blowing air into the cells. Oxygen can diffuse into the cathode from the ambient due to an air-breathing action of the cell (partial pressure gradient), whereas methanol can reach the catalytic layer from a reservoir driven by a concentration gradient between the electrode and the reservoir and through capillary force action of electrode pores. The use of low-cost miniaturized ''step-up'' DC/DC converters allows to suitably increase the stack potential with a very small dissipation of power (~90% efficiency). This approach does not require extensive miniaturization of the DMFC stack favoring the development of low-cost DMFC stack architectures with practical electrode area.

11.2
Fundamental Aspects of Direct Methanol Fuel Cells

11.2.1
DMFC Components and Processes

The core of the DMFC is a polymer ion exchange membrane. The electrodes (anode and cathode) are in intimate contact with the membrane faces. The electrodes usually consist of three layers: catalytic layer, diffusion layer, and backing layer, but there are also several different configurations. The catalytic layer is composed of a mixture of catalyst and ionomer and it is characterized by a mixed electronic–ionic conductivity. The catalysts are often based on carbon-supported or unsupported PtRu and Pt materials at the anode and cathode, respectively. The membrane as well as the ionomer consist, in most cases, of a perfluorosulfonic acid polymer. The diffusion layer is usually a mixture of carbon and polytetrafluoroethylene (Teflon). The hydrophobic properties of this layer are fundamental to allow the transport of oxygen molecules to the catalytic sites at the cathode or to favor the escape of CO_2 from the anode. The package formed by electrodes and membrane is called *MEA*.

A scheme of the overall reaction process occurring in a DMFC equipped with a protonic electrolyte is outlined below:

$$CH_3OH + H_2O \longrightarrow CO_2 + 6H^+ + 6e^- (\text{anode}) \tag{11.1}$$

$$3/2O_2 + 6H^+ + 6e^- \longrightarrow 3H_2O (\text{cathode}) \tag{11.2}$$

$$CH_3OH + 3/2O_2 \longrightarrow CO_2 + 2H_2O (\text{overall}) \tag{11.3}$$

The free energy associated with the overall reaction at 25 °C and 1 atm and the electromotive force are $\Delta G = -686$ kJ mol^{-1} CH_3OH; $\Delta E = 1.18$ V [2].

Usually, the *open circuit voltage* (*OCV*) of a polymer electrolyte DMFC is significantly lower than the thermodynamic or reversible potential for the process. This is mainly due to methanol crossover that causes a mixed potential at the cathode and to the irreversible adsorption of intermediate species at electrode potentials close to the thermodynamic values. The coverage of methanolic species is larger at high cell potentials, that is, at low anode potentials. This determines a strong anode activation control that reflects on the overall polarization curve (Figure 11.2). This can be observed in a polarization plot (Figure 11.2) where the terminal voltage of the cell is deconvoluted into the anode and cathode polarizations according to the equation:

$$E_{\text{cell}} = E_{\text{cathode}} - E_{\text{anode}} \tag{11.4}$$

Besides the strong activation control at the anode, the effect of the mixed potential on the cathode polarization curve is clearly observed in Figure 11.2. The onset potential for the oxygen reduction in the presence of methanol crossover is below 0.9 V versus the reversible hydrogen electrode (RHE). This is much lower than the reversible potential for the oxygen reduction in the absence of methanol, that is, 1.23 V versus RHE. As pointed out above, such a result is mainly

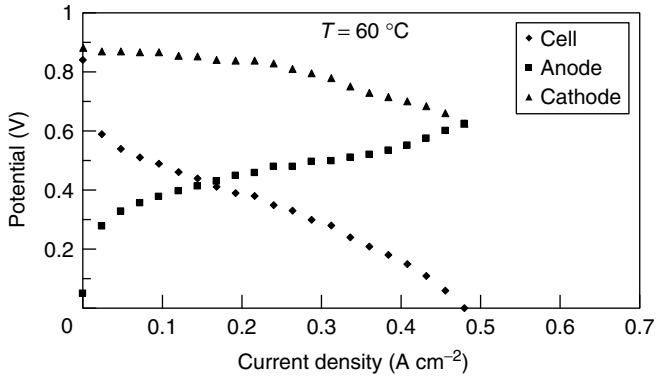

Figure 11.2 Single cell and *in situ* half-cell electrode polarizations for a DMFC operating at 60 °C, ambient pressure with 1 M methanol at the anode air feed at the cathode.

due to the effect of the mixed potential. In addition, the cathode polarization curve in the presence of crossover does not present a clear sigmoidal shape as in hydrogen-fed PEMFCs since the methanol adsorption on the cathode mainly influences the region of activation control for oxygen reduction. In fact, at high cathode potentials, oxygen reduction is slow and oxidation of methanol permeated through the membrane is enhanced by the elevated potential. The two opposite reactions compete with each other and no spontaneous current is registered above 0.9 V (Figure 11.2). At high currents, both anodic and cathodic polarization curves show the onset of mass-transport constraints due to the removal of the CO_2 from the anode and the effect of flooding at the cathode. In the methanol fuel cell, the flooding of the cathode is not only due to the water formed by the electrochemical process but it also especially occurs as a consequence of the fact that a liquid or a vapor (and not a humidified gas) is fed to the anode and this water/methanol mixture permeates through the hydrophilic membrane to the cathode.

In order to be competitive within the portable market, the DMFC must be reasonably cheap and capable of delivering long operation time. At present, there are a few challenging drawbacks in the development of such systems. These mainly consist in finding (i) electrocatalysts which can effectively enhance the electrode-kinetics of methanol oxidation; (ii) electrolyte membranes which have high ionic conductivity and low-methanol crossover; and (iii) methanol-tolerant electrocatalysts with high activity for oxygen reduction.

11.2.2
Methanol Oxidation Electrocatalysts

The state-of-the-art electrocatalysts for the electro-oxidation of methanol in fuel cells are generally based on Pt alloys supported on carbon black [6], even if the

use of high surface area unsupported catalysts has recently gained momentum [7]. The electrocatalytic activity of Pt is known to be promoted by the presence of a second metal, such as Ru or Sn, acting either as an adatom or a bimetal [8–10]. The alloying of Sn and Ru with Pt gives rise to electrocatalysts that strongly promote the oxidation of methanol. Since the complete oxidation of methanol to CO_2 involves the transfer of six electrons to the electrode, the overall reaction mechanism involves several steps including dehydrogenation, chemisorption of methanolic residues, rearrangement of adsorbed residues, chemisorption of oxygenated species (preferentially on the alloying element), and surface reaction between CO and OH to give rise to CO_2. On a pure Pt surface, the dissociative chemisorption of water on Pt is the rate-determining step at potentials below ≈ 0.7 V versus RHE, that is, in the potential region that is of technical interest [11]. It is generally accepted that an active catalyst for methanol oxidation should give rise to water discharging at low potentials and to ''labile'' CO chemisorption. Moreover, a good catalyst for methanol oxidation should also catalyze the oxidation of carbon monoxide. Even if various theories have been put forward to explain the promoting effect of the additional elements [5, 12–14], the subject remains controversial. Transition metal promoters and adatoms are seen as a means to improve the electrocatalytic behavior of electrodes, either by minimizing the poisoning reaction or enhancing the main oxidation reaction. Besides, three main hypotheses have been made. A first hypothesis suggests that the metal promoters and adatoms either alter the electronic properties of the substrate or act as redox intermediates [14–16]. This hypothesis, supported by experimental evidences, also leads to the influence of a possible steric effect on the enhanced oxidation rate [16]. A second hypothesis envisages adatoms as blocking agents for the poison-forming reaction, assumed to occur on a number of sites greater than those required for the main reaction [16]. A third hypothesis based on the bifunctional theory invokes a mechanism by which the oxidation reaction of either the fuel or the poisoning intermediate is enhanced by the adsorption of oxygen or hydroxyl radicals on promoters or adatoms adjacent to the reacting species [5]. Combining the electronic and bifunctional theories, it is derived that the role of the second element is to increase the OH adsorption on the catalyst surface, at lower overpotentials, and to decrease the adsorption strength of the poisoning methanolic residues.

Both Pt–Ru and Pt–Sn systems have been reported to be promising catalysts for electro-oxidation of methanol in DMFCs [17–19]. However, although there is conclusive evidence on catalytic promotion of methanol electro-oxidation on the Pt–Ru system in relation to Pt, contradictory results have been reported in the literature on the promotional effect of Sn for this reaction [12, 20–23]. It is generally accepted that Pt sites in Pt–Ru alloys are especially involved in both the methanol dehydrogenation step and strong chemisorption of methanol residues. At suitable electrode potentials (0.2 V vs RHE), water discharging occurs on Ru sites with formation of Ru-OH groups at the catalyst surface [24]. The final step is the reaction of Ru-OH groups with neighboring methanolic residues adsorbed on Pt to give carbon dioxide.

One of the main requirements for an optimal alloy electrocatalyst, such as Pt–Ru (the most performing at the moment), is its high dispersion. The mass activity (A/g Pt) of the catalyst for methanol electro-oxidation is strictly related to the degree of dispersion, since the reaction rate is generally proportional to its active surface area [25]. For this reason, usually the metal particles are dispersed onto a carbon support in order to avoid the agglomeration of particles and the decrease of surface area. Different carbon blacks are used for this purpose; actually, the most used is Vulcan XC-72 (Brunauer-Emmett-Teller (BET) surface area: 250 $m^2\ g^{-1}$), which appears to be the best compromise with the presence of a small amount of micropores and a reasonable high surface area sufficient to accommodate a high loading of the metal phase.

11.2.3 Oxygen-Reduction Electrocatalysts

Although Pt/C electrocatalysts are, at present, the most widely used materials as cathodes in low-temperature fuel cells, due to their intrinsic activity and stability in acidic solutions, there is still great interest to develop more active, selective, and less-expensive electrocatalysts for oxygen reduction. There are a few directions that can be investigated to reduce the costs and to improve the electrocatalytic activity of Pt, especially in the presence of methanol crossover. One is to increase Pt utilization; this can be achieved either by increasing its dispersion on carbon and the interfacial region with the electrolyte. Another successful approach to enhance the electrocatalysis of O_2 reduction is by alloying Pt with transition metals. This enhancement in electrocatalytic activity has been differently interpreted, and several studies were made to analyze in depth the surface properties of the proposed combinations of alloys [26–36]. Although a comprehensive understanding of the numerous reported evidences has not yet been reached, the observed electrocatalytic effects have been ascribed to several factors (interatomic spacing, preferred orientation, electronic interactions) which play, under fuel-cell conditions, a favorable role in enhancing the oxygen reduction reaction (ORR) rate [16]. A higher activity of Pt–Fe alloy electrocatalysts compared to platinum for oxygen reduction in the presence of methanol was obtained in half-cell and DMFC experiments (Figure 11.3), although a partial Fe dissolution was observed [35].

Alternatively to platinum, organic transition metal complexes are known to be good electrocatalysts for the oxygen-reduction reaction. Transition metals, such as iron or cobalt organic macrocycles from the families of phenylporphyrins, phthalocyanines, and azoannulenes have been tested as O_2-reduction electrocatalysts in fuel cells [37–41]. One major problem with these metal-organic macrocyclics is their chemical stability under fuel-cell operation at high potentials. In many cases, the metal ions are irreversibly dissolved in the acid electrolyte. However, if the metal-organic macrocyclic is supported on a high surface area carbon and treated at high temperatures (from 500 to 800 °C), the residue exhibits electrocatalytic activity comparable to that of Pt without any degradation in performance, from which one may infer the good stability of the metal in the electrocatalyst

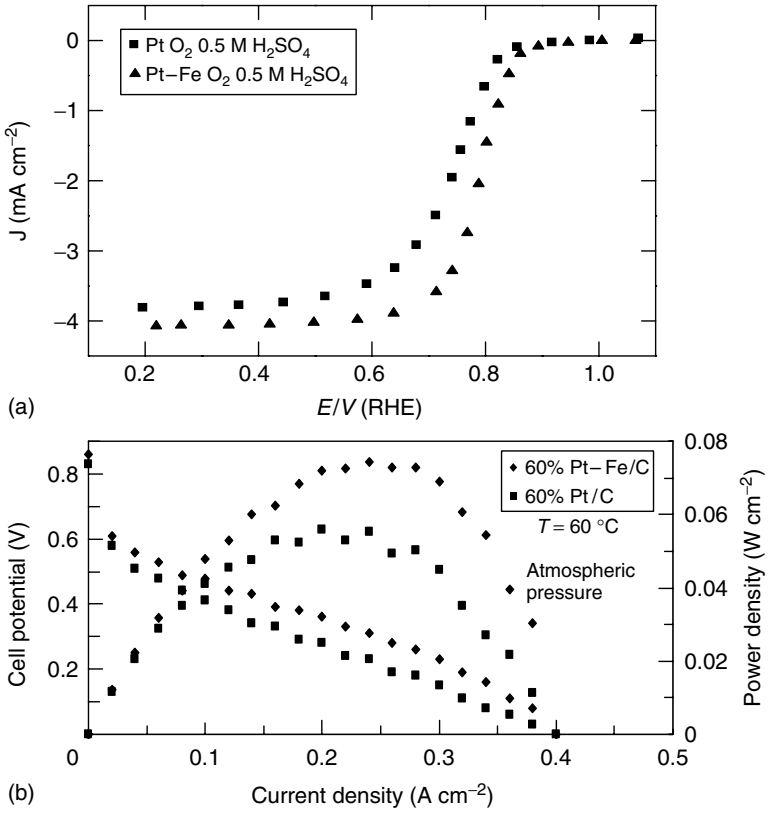

Figure 11.3 Polarization curves for ORR in 0.5 M H_2SO_4(a) and polarization and power density curves in DMFC (b) for Pt/C and Pt—Fe/C cathode catalyzes at 60 °C [34, 35].

[40]. Recently, Savinell and coworkers [40] reported interesting results for the operation of these compounds in solid PEFCs, showing a high selectivity for oxygen.

In some other studies, a few inorganic materials have recently been proposed as suitable substitutes for platinum in methanol fuel cells due to their selectivity for oxygen reduction, even in the presence of methanol. These materials mainly consist of carbon nitrides [42], the Chevrel-phase type ($Mo_4Ru_2Se_8$), transition metal sulfides (Mo_xRu_ySz, $Mo_xRh_yS_z$), or other transition metal chalcogenides ($(Ru_{1-x}Mo_x)SeO_z$) [43, 44]. Some of these possess semiconducting properties; thus, in theory, they could introduce an additional ohmic drop in the electrode. However, their activities for oxygen reduction are significantly lower than Pt [45, 46]. Carbon-supported Ru electrocatalysts are reported to exhibit high selectivity for oxygen reduction in the presence of methanol but their activities are significantly lower [47].

11.2.4
Proton Exchange Membranes

Nafion membranes are currently used as electrolytes in DMFCs; yet, since methanol is rapidly transported across perfluorinated membranes, commonly used in polymer electrolyte membrane fuel cells, and is chemically oxidized to CO_2 and H_2O at the cathode, there is a significant decrease in coulombic efficiency for methanol consumption by as much as 20% under practical operation conditions. Thus, it is very important to modify these membranes by, as example, developing composites [48–50] or finding alternative proton conductors with the capability of inhibiting methanol transport. The polymer electrolyte should have a high ionic conductivity (5×10^{-2} ohm^{-1} cm^{-1}) under working conditions and low permeability to methanol (less than 10^{-6} moles min^{-1} cm^{-2}). Furthermore, it must be chemically and electrochemically stable under operating conditions. These requirements appear to be potentially met by new classes of solid polymer electrolytes that show promising properties even though there has been no clear demonstration of their use in DMFC. Some of the membranes investigated so far are sulfonated poly-ether-ether-ketone [51, 52] and polysulfone [53], polyvinylidene fluoride [54], styrene grafted and sulfonated membranes [55], zeolites gel films (tin mordenite), and/or membranes doped with heteropolyanions [56]. Some recent results obtained from our group using polysulfone membranes are reported in Figure 11.4.

Alternatives to these membranes and Nafion are acid-doped polyacrylamide and polybenzimidazole [57]. The main question about these membranes is the extent of leaching of acids of small molecular weight (H_3PO_4) entrapped in the polymer, during operation of a fuel cell fed with a hot methanol/water mixture as the anode reactant. In fact, these polymers usually swell at high temperature in the presence

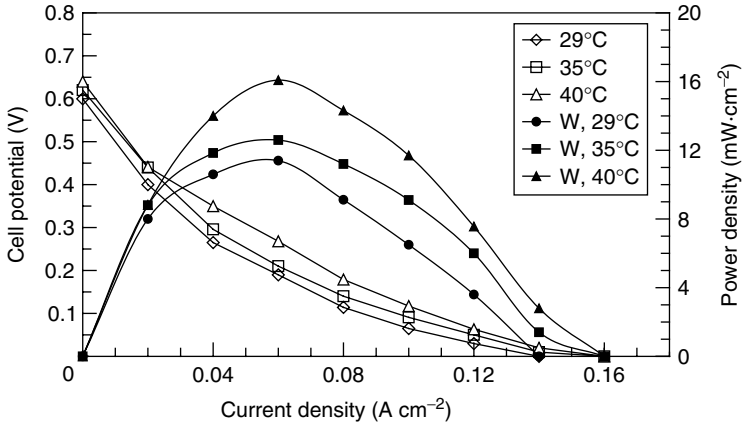

Figure 11.4 Cell potential and power density as a function of current density for the polysulfone (SPSf-70) membrane at ambient temperatures from 29 to 40 °C and at atmospheric pressure [53].

of water and methanol. Probably these problems may be better addressed by using a high molecular weight superacid (such as phosphotungstic acid) that may be physically entrapped in the polymer structure. However, in this case, the uptake of water by the polymer should not be significantly reduced since water is essential for the protonic conduction.

Some investigations have regarded the development of composite membranes [48, 58, 59]. Composite recast Nafion–silica membranes have shown excellent properties in terms of mechanical characteristics, water retention at high temperature, resilience to methanol crossover, and ionic conductivity [59]. These electrolytes allow DMFCs operation at 145 °C with a significant enhancement in methanol oxidation kinetics [59]. The only drawback, at the present time, appears to be the high cost of production, primarily determined by the expensive perfluorinated ionomer necessary for their fabrication. Some variations of this procedure include the use of heteropolyacid-doped silica entrapped into recast Nafion or zirconium phosphate/ extruded Nafion membranes [48, 49]. Recent investigations from our group have shown interesting perspectives for the use of these composite electrolytes in DMFCs [48, 49].

11.2.5 Electrode and MEA Preparation

DMFC electrodes mainly consist of gas-diffusion electrodes similar to those used in H_2-fueled proton exchange membrane fuel cells (polymer electrolyte fuel cell) [7, 60–62]. Typically, such an electrode is made up of a first macroporous layer, which is a carbon cloth or paper. This is the conductive support onto which the microporous GDL and thereafter the catalytic layer are deposited. In most electrode configurations, the GDL is formed by polytetrafluoroethylene (PTFE) and carbon black, whereas the composite catalytic layer consists of carbon-supported Pt or Pt alloy catalysts and Nafion ionomer. The function of PTFE in the diffusion layer is to provide a network for gas transport and to give structural integrity to the layer. The catalytic layer, containing Nafion in an amount ranging between 15 and 33 wt%, is hot pressed or deposited onto the perfluorosulfonic electrolyte membrane [7, 61, 63]. Such an electrode structure was originally developed for operation at 80 °C since the development of DMFC for transportation was historically considered to provide the main perspectives for large-scale application of such devices. In low temperature, liquid-fueled DMFCs finalized to the development of portable systems, this electrode configuration suffers from mass-transport limitations. These constraints mainly occur at the anode due to the low-diffusion coefficient of methanol in water and the release of carbon dioxide gas bubbles [64, 65]. The influence of PTFE content, in the anode diffusion layer, on cell performance was investigated for high-temperature DMFCs. The optimal PTFE amount was found to be between 13 and 20 wt% [66]. Some recent studies have been addressed to replace the carbon cloth or carbon paper support with a titanium net [65] to enhance mass transport. Alternatively, some attempts have been addressed to enhance the morphology of the

conventional electrode structure. As is well known, a correlation between the amount of ionomer, in the catalytic layer, and catalyst porosity exists [63]. The ionomer content influences the hydrophobic and hydrophilic pore distribution in the catalyst layer. Hydrophilicity increases as a function of the Nafion content. DMFCs are generally operated with aqueous methanol solution at different concentrations; therefore, in order to have a better reactant distribution, a good hydrophilicity is important for the anode side. On the other hand, hydrophobic pores have an important role for CO_2 removal from the catalytic layer. The optimization of the structure of the electrode and/or MEA also requires an appropriate investigation of the microstructure of the carbon support, in order to ideally distribute the ionomer on the carbon surface containing Pt or Pt–Ru particles. In this way, Pt loading could be significantly reduced if Pt utilization increased.

The operation of DMFCs with air requires the development of a proper cathode layer. In fact, when air is fed to the cathode side, while oxygen reacts to produce water, the nitrogen contained in the feed stream remains entrapped in the pores of the electrode; the entrapped nitrogen is a diffusion barrier for the incoming oxygen, and results in mass-transport overpotential performance losses even at intermediate current densities. Furthermore, the transport of this gas to the reaction sites is retarded by flooding of the electrocatalyst layer [67]. A few approaches have been proposed to enhance the oxygen transport properties when air is used as the feed stream. Some examples are heat treatments of the recast Nafion gel in the electrocatalytic layer to make it hydrophobic [68] or to use pore formers to increase porosity [69, 70].

11.3
Current Status of DMFC Technology for Portable Power Sources Applications

The potential market for portable fuel-cell systems deals mainly not only with the energy supply for electronic devices but it also includes remote and microdistributed electrical energy generation. Accordingly, DMFC power sources can be used in mobile phones, laptop computers, as well as energy supply systems for weather stations, medical devices, auxiliary power units (APUs), and so on. DMFCs are promising candidates for these applications because of their high-energy density, light weight, compactness, simplicity as well as their easy and fast recharging [71–74]. Theoretically, methanol has a superior specific energy density (6000 $Wh\,kg^{-1}$) in comparison with the best rechargeable battery, lithium polymer and lithium ion polymer (theoretical, 600 $Wh\,kg^{-1}$) systems. This performance advantage translates into more conversation time using cell phones, more time for the use of laptop computers between the replacement of fuel cartridges, and more power available on these devices to support consumer demand. In relation to consumer convenience, another significant advantage of the DMFC over the rechargeable battery is its potential for instantaneous refueling. Unlike rechargeable batteries that require hours for charging a depleted power pack, a

DMFC can have its fuel replaced in minutes. These significant advantages make DMFCs an exciting development in the portable electronic devices market.

Several organizations (Table 11.2) are actively engaged in the development of low-power DMFCs for cellular phone, laptop computer, portable camera, and electronic game applications [72–76]. The primary goal of this research is to develop proof of concept DMFCs capable of replacing high-performance rechargeable batteries in the US$ 6-billion portable electronic devices market.

Motorola Labs – Solid State Research Center, USA [2], in collaboration with Los Alamos National Laboratory (LANL), USA, is actively engaged in the development of low-power DMFCs (greater than 300 mW) for cellular phone applications [77]. Motorola has recently demonstrated a prototype of a miniature DMFC based on an MEA set between ceramic fuel delivery substrates [2]. Motorola utilized their proprietary low-temperature co-fired ceramic (LTCC) technology to create a ceramic structure with embedded microchannels for mixing and delivering methanol/water to the MEA and exhausting the by-product CO_2. The active electrode area for a single cell was approximately 3.5–3.6 cm^2. In the stack assembly, four cells were connected in series in a planar configuration with an MEA area of 13–14 cm^2; the cells exhibited average power densities between 15 and 22 mW cm^{-2}. Four cells (each cell operating at 0.3 V) were required for portable power applications because DC–DC converters typically require 1 V to efficiently step up to the operating voltage for electronic devices. Improved assembly and fabrication methods have led to peak power densities greater than 27 mW cm^{-2}. Motorola is currently improving their ceramic substrate design to include micropumps, methanol concentration sensors, and supporting circuitry for second-generation systems.

Energy Related Devices (ERDs) Inc., USA, is working in alliance with Manhattan Scientific Inc., US) to develop miniature fuel cells for portable electronic applications [72, 78]. A relatively low-cost sputtering method, similar to the one used by the semiconductor industry for the production of microchips, was used for the deposition of electrodes (anode and cathode) on either side of a microporous plastic substrate; the micropores (15 nm to 20 μm) are etched into the substrate using nuclear particle bombardment. Microfuel arrays with external connections in series were fabricated precisely and had a thickness of about a millimeter. The principal advantages of the cell include the high utilization of catalyst, controlled pore geometry, low-cost materials, and minimum cell thickness and weight. A MicroFuel Cell™ was reported to have achieved a specific energy density of 300 Wh kg^{-1} using methanol/water and air as the anodic and cathodic reactants, respectively [2].

The anode design that was developed by MicroFuel Cell™ represents a critical advance in the development of a cost-effective, pore-free electrode that is permeable to only hydrogen ions [2]. This increases the efficiency of a methanol fuel cell because it blocks the deleterious effect of methanol crossover across the membrane. The first layer of the anode electrode formed a plug in the pore of the porous membrane; an example is a 20-nm thick palladium metal film on a nuclepore filter membrane with 15-nm diameter pores. The second layer (platinum) was deposited to mitigate the hydration-induced cracking that occurs on many of these films.

Table 11.2 DMFC power sources for portable applications.

Developer	Number/area of cells	Power density	Temperature (°C)	Oxidant	Methanol concentration (M)	Anode catalyst and loading	Electrolyte	Cathode catalyst and loading
Motorola Labs	Four cells (planar stack)/13–15 cm^2	12–27 mW cm^{-2}	21	Ambient air[a]	1	PtRu alloy, 6–10 mg cm^{-2}	Nafion 117	6–10 mg cm^{-2}
Energy Related Devices	Planar stack	3–5 mW cm^{-2}	25	Ambient air[a]	1	PtRu alloy	Nafion	Pt
Jet Propulsion Lab	Six cells (flat pack)/6–8 cm^2	6–10 mW cm^{-2}	20–25	Ambient air[a]	1	PtRu alloy, 4–6 mg cm^{-2}	Nafion 117	Pt, 4–6 mg cm^{-2}
Los Alamos National Labs	Five cells/45 cm^2	300 W/l	60	Air (three to five times stoichiometry)	0.5	PtRu alloy, 0.8–16.6 mg cm^{-2}	Nafion	Pt, 0.8–16.6 mg cm^{-2}
Forschungszentrum Julich GmbH	40 cells/100 cm^2	45–55 mW cm^{-2}	50–70	O_2 (3 atm)	1	PtRu, 2 mg cm^{-2}	Nafion 115	Pt, 2 mg cm^{-2}
Samsung advanced Institute of Technology	12 cells (monopolar)/2 cm^2	23 mW cm^{-2}	25	Ambient air[a]	5 passive mode	PtRu, 3–8 mg cm^{-2}	Hybrid membrane	Pt, 3–8 mg cm^{-2}
Korea Institute of Energy Research	Six cells (bipolar)/52 cm^2	121–207 mW cm^{-2}	25–50	O_2 (300 ml min^{-1}), ambient pressure	2.5 active mode	PtRu/C	Nafion 115 & 117	Pt-black

(*continued overleaf*)

Table 11.2 *(continued)*

Developer	Number/area of cells	Power density	Temperature (°C)	Oxidant	Methanol concentration (M)	Anode catalyst and loading	Electrolyte	Cathode catalyst and loading
Korea Institute of Science & Technology	Six cells (monopolar)/6 cm^2	40 mW cm^{-2}	25	Ambient air[a]	4 passive mode	PtRu	Nafion 115	Pt
More Energy Ltd.	20 cm^2	60–100 mW cm^{-2}	25	Ambient air[a]	30–5%	PtRu	Liquid electrolyte	Pt
Institute for Fuel Cell Innovation, Canada	Three cells (monopolar)	8.6 mW cm^{-2}	25	Ambient air[a]	2 passive mode	80%PtRu, 4 mg cm^{-2}	Nafion 117	Pt-black, 4 mg cm^{-2}
University of Connecticut, USA	Four cells/18–36 cm^2	30 mW cm^{-2}	25	Ambient air[a]	2–5 passive mode	PtRu alloy, 7 mg cm^{-2}	Nafion 117	Pt, 6.5 mg cm^{-2}
Honk Kong University	Single cell/4 cm^2	28 mW cm^{-2}	22	Ambient air[a]	4 passive mode	PtRu, 4 mg cm^{-2}	Nafion 115	40% Pt/C, 2 mg cm^{-2}
The Pennsylvania State University, USA	Single cell/5 cm^2	93 mW cm^{-2}	85	Air (700 ml min^{-1} and 15 psig)	2 active mode	PtRu, 4 mg cm^{-2}	Nafion 112	40% Pt/C, 1.3 mg cm^{-2}
Harbin Institute of Technology	Single cell	9 mW cm^{-2}	30	Ambient air[a]	2 passive mode	40% PtRu/C, 2 mg cm^{-2}	Nafion 117	40% Pt/C, 2 mg cm^{-2}
Tel-Aviv University, Israel	Flat fuel cell/6 cm^2	12.5 mW cm^{-2}	25	Ambient air[a]	1–6 in H_2SO4 Passive mode	PtRu, 5-7 mg cm^{-2}	NP-PCM	Pt, 4–7 mg cm^{-2}

Tekion Inc., USA	Single cell/5 cm^2	65 mW cm^{-2}	60	Ambient air[a]	2 active mode	PtRu	Nafion	Pt
University of California, USA	μ-Single cell/1.625 cm^2	16–50 mW cm^{-2}	25–60	Air (88 ml min^{-1})	2 active mode	PtRu, 4–6 mg cm^{-2}	Nafion 112	40% Pt/C, 1.3 mg cm^{-2}
Waseda University, Japan	μ-Single cell/0.018 cm^2	0.8 mW cm^{-2}	25	O_2 (10 μl min^{-1}) saturated in H_2SO_4	2	PtRu, 2.85 mg cm^{-2}	Nafion 112	Pt, 2.4 mg cm^{-2}
Institute of Microelectronic of Barcelona-CNM, Spain	μ-Single cell	11 mW cm^{-2}	25	Ambient air[a]	4–5 passive mode	PtRu, 4 mg cm^{-2}	Nafion 117	Pt, 4 mg cm^{-2}
Yonsei University, Korea	Multicell structure (monopolar)	33 mW cm^{-2}	80	O_2 (30 ml min^{-1})	2	60% PtRu/C, 4 mg cm^{-2}	Nafion 117	60% Pt/C, 4 mg cm^{-2}
CNR-ITAE, Italy	Three cells (monopolar)/4 cm^2	20 mW cm^{-2}	21	Ambient aira	5 passive mode	PtRu, 4 mg cm^{-2}	Nafion 117	Pt, 4 mg cm^{-2}

[a]Ambient air usually refers to the air-breathing mode.

The third layer was deposited over the structural metal film and was the most significant layer because it needed to be catalytically active to methanol and capable of accepting hydrogen ions. An alternative method of forming the electrode was to include powder catalyst particles (Pt/Ru on activated carbon) on the surface of the metal films to enhance the catalytic properties of the electrode. Between the anode electrode and the cathode electrode was the electrolyte-filled pore, the cell interconnect, and the cell break. In the pores of the membrane, the electrolyte (Nafion) was immobilized and ERD claims that this collimated structure results in improved protonic conductivity. Each of the cells was electrically separated from the adjacent cells by cell breaks, useless space occupying the central thickness of the etched nuclear particle track plastic membrane. The cathode was formed by sputter depositing a conductive gold film onto the porous substrate first, followed by a platinum catalyst film. The electrode was subsequently coated with a Nafion film. Alternatively, platinum powder catalyst particles were added to the surface of the electrode via an ink slurry of 5% Nafion solution. A hydrophobic coating was then deposited onto this Nafion layer in order to prevent liquid product water from condensing on the surface of the air electrodes. ERD developed a novel configuration to utilize their fuel cell as a simple charger in powering a cellular phone. The fuel cell was configured into a plastic case that was in close proximity to a rechargeable battery. Methanol was delivered to the fuel cell via fuel needle and fuel ports, which allowed methanol to wick or evaporate into the fuel manifold and be delivered to the fuel electrodes.

The Jet Propulsion Laboratory (JPL), USA, has been actively engaged in the development of ''miniature'' DMFCs for cellular phone applications over the last two years [74, 79]. According to their analysis, the power requirement of cellular phones during standby mode is small and steady at 100–150 mW. However, under operating conditions, the power requirement fluctuates between 800 and 1800 mW. In the JPL DMFC, the anode was formed from Pt–Ru alloy particles, either as fine metal powders (unsupported) or dispersed on high surface area carbon. Alternatively, a bimetallic powder made up of submicron platinum and ruthenium particles was reported to give better results than the Pt–Ru alloy. Another method describes the sputter deposition of a Pt–Ru catalyst onto the carbon substrate. The preferred electrolyte was Nafion 117; however, other materials may be used to form proton-conducting membranes. Air was delivered to the cathode by natural convection and the cathode was prepared by applying platinum ink to a carbon substrate. Another component of the cathode was the hydrophobic Teflon polymer utilized to create a three-phase boundary and to achieve efficient removal of water produced by the electroreduction of oxygen. Sputtering techniques can also be used to apply the platinum catalyst to the carbon support. The noble metal loading in both electrodes was 4–6 mg cm^{-2}. The MEA was prepared by pressing the anode, electrolyte, and cathode at 8.62×10^6 Pa and 146 °C. JPL opted for a ''flat pack'' instead of the conventional bipolar plate design, but this resulted in higher ohmic resistance and nonuniform current distribution. In this design, the cells were externally connected in series on the same membrane, with air electrodes on the stack exterior. Two ''flat packs'' were deployed in a back-to-back configuration with a

common methanol feed to form a ''twin pack'' [2]. Three ''twin packs'' in series were needed to power a cellular phone. In the stack assembly, six cells were connected in series in a planar configuration, which exhibited average power densities between 6 and 10 mW cm^{-2}. The fuel cell was typically run at ambient air, 20–25 °C with 1-M methanol. Improvements in the configuration and interconnect design have resulted in improved performance characteristics of the six-cell ''flat-pack'' DMFC. On the basis of the results of current technology, the JPL researchers predict that a 1-W DMFC power source with the desired specifications for weight and volume and an efficiency of 20% for fuel consumption can be developed for a 10-hour operating time, prior to replacement of methanol cartridges.

As stated earlier, LANL has been in collaboration with Motorola Labs – Solid State Research Center to produce a ceramic-based DMFC which provides better than a 10 mW cm^{-2} power density. LANL researchers have also been engaged in a project to develop a portable DMFC power source capable of replacing the ''BA 5590'' primary lithium battery used by the US Army in communication systems [80]. A 30-cell DMFC stack with electrodes with an active area of 45 cm^2 was constructed, an important feature of which was the narrow width (i.e., 2 mm) of each cell. MEAs were made by the decal method, that is, thin-film catalysts bonded to the membrane resulting in superior catalyst utilization and overall cell performance. An anode catalyst loading of Pt between 0.8 and 16.6 mg cm^{-2} in unsupported PtRu and carbon-supported PtRu were used. A highly effective flow field for air made it possible to use a dry air blower to operate the cathode at three to five times stoichiometry. The stack temperature was limited to 60 °C and the air pressure was 0.76 atm, which is the atmospheric pressure at Los Alamos (altitude of 2500 m). To reduce the crossover rate, methanol was fed into the anode chamber at a concentration of 0.5 M. Since water management becomes more difficult at such low methanol concentrations, a proposed solution was to return water from the cathode exhaust to the anode inlet, while using a pure methanol source and a methanol concentration sensor to maintain the low methanol concentration feed to the anode. The peak power attained in the stack near ambient conditions was 80 W at a stack potential of 14 V and approximately 200 W near 90 °C. From this result, it was predicted that this tight-packed stack could have a power density of 300 W l^{-1}. An energy density of 200 Wh kg^{-1} was estimated for a 10-hour operation, assuming that the weight of the auxiliaries is twice the weight of the stack.

Forschungszentrum Julich GmbH (FJG), Germany, has developed and successfully tested a 40-cell 50-W DMFC stack [81]. The FJG system consisted of the cell stack, a water/methanol tank, a pump, and ventilators as auxiliaries. The stack was designed in the traditional bipolar plate configuration, which results in lower ohmic resistance but heavier material requirements. To circumvent the weight limitations, current collectors were manufactured from stainless steel (MEAs were mounted between the current collectors) and inserted into plastic frames to reduce the stack's weight. The 6-mm distance between MEAs (cell pitch) revealed a very tight packaging of the stack design. Each frame carried two DMFC single cells that were connected in series by external wiring [2]. MEAs were constructed in-house with an anode loading of 2 mg cm^{-2} PtRu black, catalyst loading of 2 mg cm^{-2}

Pt-black, and cell area of 100 cm^2 for each of the 40 cells. At the anode, a novel construction allowed the removal of CO_2 by convection forces at individual cell anodes. The conditions for running the stack were 1-M methanol, 60 °C, and 3 bar O_2, which led to peak energy densities of 45–55 mW cm^{-2}. The cathode used air at ambient or elevated pressures; when the stack operated at temperatures above 60 °C, the air was fed into the cathode by convection forces. Recent developments include a three-cell short stack design which has reduced the cell pitch to only 2 mm. The individual cell area of this design is larger, 145 cm^2, than the previous prototype's and although it is not air-breathing, it works with low-air stoichiometric rates (a more efficient cathodic flow distribution structure).

Samsung Advanced Institute of Technology (SAIT), South Korea, has developed a small monopolar DMFC cell pack (2 cm^2, 12 cells, CO_2 removal path, 5–10 M methanol, air breathing, and room temperature) of 600 mW for mobile phone applications [82, 83]. Unsupported PtRu and Pt catalysts were coated onto a diffusion electrode of porous carbon substrate of the anode and cathode, respectively. In order to allow methanol wicking and air breathing, short and capillary paths were designed as the diffusion layer. Catalyst loading was around 3–8 mg cm^{-2}. Ternary alloys with low binding energy for CO adsorption were investigated with the aid of quantum chemical methods. Inorganic-phase-dispersed hybrid membranes based on Nafion or Co-PTFS were prepared and applied to the MEA for attaining high fuel efficiency and preventing a voltage loss on the cathode. A gas chromatography (GC) method was utilized *in situ* during the electrochemical polarization. In this way, the cathode output stream gas was analyzed and it was calculated by the amount of carbon dioxide produced by the permeated methanol, which is consumed at the cathode. A monopolar structure was investigated; 12 cells of 2 cm^2 were connected in series within a flat cell pack. Fuel storage was attached to the cell pack and power characteristics were measured on the free-standing basis without any fuel or air supply systems. A power density of 50 mW cm^{-2} at 0.3 V was achieved in the normal diffusion electrode design. For application in portable electronic devices, methanol wicking and air-breathing electrodes were required; the MEA having this novel diffusion electrode showed 10 mW cm^{-2} at 0.3 V of power density without the aid of any external fueling system. In this MEA, the anode contained a microlayer for the methanol flow field with capillary wicking structure and the cathode contained a microlayer for the air flow field with breathing structure. A hybrid membrane with inorganic phase dispersions was utilized. This was operated as methanol-blocking medium in the hydrophilic channel of the ionomer assisting to reduce the amount of methanol crossover. As measured by GC, the hybrid membrane allowed a 20–40% reduction of methanol permeation, at the nominal potential of 0.3 V, within the various range of methanol concentrations from 1 to 5 M. If a conductivity approaching that of plain Nafion, that is, near 10^{-1} S cm^{-1}, could be achieved with this system, such a process offers the possibility of the development of functional membranes for DMFCs. A monopolar design consisting of 12 cells flat pack was assembled and tested in the severest condition that is methanol wicking and air breathing at room temperature. Each cell had the active area of 2 cm^2 and the pack was equipped with a path of CO_2 removal at the anode.

The maximum power output was 560 mW at 2.8 V, close to that required by the cellular phone. For this cell-pack condition with small active area, the unit cell power density was 23 mW cm^{-2}, which is rather higher than that achieved in the single MEA test (10 mW cm^{-2}). This result could be attributed to the uniform fuel distribution and efficient current collecting design of smaller single cells.

The Korea Institute of Energy Research (KIER, South Korea) has developed a 10-W DMFC stack (bipolar plate, graphite construction) fabricated with six single cells with a 52 cm^2 electrode area [84]. The stack was tested at 25–50 °C using 2.5 M methanol, supplied without a pumping system, O_2 at ambient pressure, and at a flow rate of 300 cc min^{-1}. The maximum power densities obtained in this system were 6.3 W (121 mW cm^{-2}) at 87 mA cm^{-2} at 25 °C and 10.8 W (207 mW cm^{-2}) at 99 mA cm^{-2} at 50 °C. MEAs using Nafion 115 and 117 were formed by hot pressing and the electrodes were produced from carbon-supported Pt–Ru metal powders and Pt-black for anode and cathode electrodes, respectively.

More Energy Ltd. (MEL), ISRAEL, a subsidiary of Medis Technologies Ltd. (MDTL, USA), is developing a direct liquid methanol (DLM) fuel cells (a hybrid PEM/DMFC system) for portable electronic devices [85]. The key features of the DLM fuel cell are as follows: (i) the anode catalyst extracts hydrogen from methanol directly, (ii) the DLM fuel cell uses a proprietary liquid electrolyte that acts as the membrane in place of a solid polymer electrolyte (Nafion), and (iii) novel polymers and electrocatalysts enable the construction of more effective electrodes. The company's fuel-cell module delivers approximately 0.9 V and 0.24 W at 60% of its nominal capacity for 8 hours. This translates into energy densities of approximately 60 mW cm^{-2} with efforts underway to improve that result to 100 mW cm^{-2}. The high power capacity of the cell is attributed to the proprietary electrode ability to efficiently oxidize methanol. In addition, Medis claims the use of high concentrations of methanol (30%) in its fuel stream with plans for increasing that concentration to 45% methanol. The increased concentration of methanol in the feedstock results in concentration gradients that should lead to higher methanol crossover rates. However, this technical concern is not mentioned in the company's literature.

At the Institute for Fuel Cell Innovation in Vancouver, Canada, a passive (air breathing) planar three-cell DMFC stack was designed, fabricated, and tested [86]. In order, to maintain design flexibility, polycarbonate was chosen for the plate material, whereas 304 stainless steel mesh current collectors were used. In order to test the DMFC in different electrical cell configurations (single cell, multiple cells connected in series or in parallel), a stainless threaded rod was attached to each mesh current collector on the anode and cathode side to allow for an external electrical connection. Commercial electrodes from E-TEK were used. The catalyst loading was 4 mg cm^{-2} and consisted of an 80% PtRu alloy on optimized carbon. Unsupported Pt-black with a 4 mg cm^{-2} loading was used for the cathode. A Nafion 117 membrane was utilized as electrolyte. A power density of 8.6 mW cm^{-2} was achieved at ambient temperature and passive operation. Stacks with a parallel connection of the single cells showed a significantly lower performance than in a series configuration. It was also identified that high electrical resistance was the

dominant factor in the low performance as a result of the stainless steel hardware and poor contact between the electrodes and current collectors.

At University of Connecticut, USA, the group of Guo and Faghri developed a design for planar air-breathing DMFC stacks [87]. This design incorporated a window-frame structure that provided a large open area for more efficient mass transfer with modular characteristics, making possible to fabricate components separately. The current collectors had a niobium expanded metal mesh core with a platinum coating. Two four-cell stacks, one with a total active area of 18 cm^2 and the other with 36 cm^2, were fabricated by interconnecting four identical cells in series. These stacks were suitable for portable passive power source application. Peak power outputs of 519 and 870 mW were achieved in the stacks with active areas of 18 and 36 cm^2, respectively. A study of the effects of methanol concentration and fuel-cell self-heating on fuel-cell performance was carried out. The power density reached its highest value in this investigation when 2- and 3-M methanol solutions were used.

At the Honk Kong University of Science and Technology, China, the group of Chen and Zhao [88–91] studied the effect of methanol concentration on the performance of a passive DMFC single cell. They found that the cell performance was improved substantially with an increase in methanol concentration; a maximum of power density of 20 mW cm^{-2} was achieved with 5.0 M methanol solution. The measurements indicated that the better performance with higher methanol concentrations was mainly attributed to the increase in the cell-operating temperature caused by the exothermic reaction between permeated methanol and oxygen on the cathode. This finding was subsequently confirmed by the fact that the cell performance decreased, when the cell running with higher methanol concentrations was cooled down to room temperature. Moreover, they proposed a new MEA, in which the conventional cathode GDL is eliminated while utilizing a porous metal structure, made of metal foam, for transporting oxygen and collecting current. They showed theoretically that the new MEA [90] and the porous current collector enabled a higher mass transfer rate of oxygen and thus better performance. The measured polarization and constant-current discharging behavior showed that the passive DMFC with the new MEA and new current collector yielded better and much more stable performance than did the cell having the conventional MEA and the conventional perforated-plate current collector, in particular with high methanol concentration. The elctrochemical impedance spectroscopy (EIS) spectrum analysis further demonstrated that the improved performance with the new MEA was attributed to the enhanced transport of oxygen as a result of the reduced mass transfer resistance in the fuel-cell system, whereas the improved performance for the porous current collector was attributed to the increased operating temperature as a result of the lower effective thermal conductivity of the porous structure and its fast water removal as a result of the capillary action [91].

Another group at the Honk Kong University, Zhang *et al.* [92], reported on a flexible graphite-based integrated anode plate for DMFCs operating at high methanol feed concentration under active mode. This anode structure, which was made of flexible graphite materials, not only provided a dual role for the liquid

diffusion layer and flow field plate but also served as a methanol blocker by decreasing methanol flux at the interface of catalyst and membrane electrolyte. DMFCs incorporating this new anode structure exhibited a much higher OCV (0.51 V) than that (0.42 V) of a conventional DMFC at 10-M methanol feed. Cell polarization data showed that this new anode structure significantly improved the cell performance at high methanol concentrations (e.g., 12 M or above).

Abdelkareem and Nakagawa from Gunma University, Japan [93], studied the effect of oxygen and methanol supply modes (passive and active supplies of methanol, and air-breathing and flowing supplies of oxygen) on the performance of a DMFC. The experiments were carried out with and without a porous carbon plate (PCP) under ambient conditions using methanol concentrations of 2 M for the MEA without PCP and 16 M for that with PCP. For the conventional MEA, flowing oxygen and methanol were essential to stabilize the cell performance, avoiding flooding at the cathode and depletion of methanol at the anode. As a result of flowing oxygen, methanol, and water fluxes, the conventional MEA performance increased by more than twice as compared to that obtained from the air-breathing cell. For the MEA with a porous plate, MEA/PCP, the flow of oxygen and methanol had no significant effect on the cell performance, where the PCP prevented the cathode from flooding by reducing the mass transport through the MEA. Methanol and water fluxes through the MEA/PCP were not affected by flowing oxygen at $0.1\,l\,min^{-1}$. However, the increase in oxygen flow rate from 0.1 l to $1\,l\,min^{-1}$ had a negative effect on the cell performance either for the conventional MEA or for the MEA/PCP. This was probably due to the cooling effect for conventional MEA and the drying effect for the MEA/PCP. A moderate supply of oxygen to the cathode, like air-breathing, was appropriate for the DMFC with a PCP.

The effect of operating conditions on energy efficiency for a small passive DMFC was analyzed by Chu and Jiang from US Army Research Laboratory, Adelphi, USA [94]. Both faradic and energy conversion efficiencies decreased significantly with increasing methanol concentration and environmental temperature. The faradic conversion efficiency was as high as 94.8%, and the energy conversion efficiency was 23.9% in the presence of an environmental temperature low enough (10 °C) under constant voltage discharge at 0.6 V with 3 M methanol for a DMFC bi-cell using Nafion 117 as electrolyte. Although higher temperature and higher methanol concentration allowed to achieve higher discharge power, they resulted in considerable losses of Faradic and energy conversion efficiencies by using Nafion electrolyte membrane. Their conclusion was that the development of alternative highly conductive membranes with a significantly lower methanol crossover is necessary to avoid loss of faradic conversion efficiency with temperature and with fuel concentration.

Various research groups have focused their attention on the critical aspects, which need to be addressed for the design a high-performance DMFC. These are CO_2 bubble flow at the anode [95] and water flooding at the cathode [96]. Lu and Wang from the Pennsylvania State University, USA [97], developed a $5\,cm^2$ transparent cell to visualize these phenomena *in situ*. Two types of MEA based on Nafion® 112 were used to investigate the effects of backing pore

structure and wettability on cell polarization characteristics and two-phase flow dynamics. One employed carbon paper backing material and the other carbon cloth. Experiments were performed with various methanol feed concentrations. The transparent fuel cell reached a peak power of 93 mW cm^{-2} at 0.3 V, using Toray carbon-paper-based MEA under 2 M methanol solution preheated at 85 °C. For the hydrophobic carbon paper backing, it was observed that CO_2 bubbles nucleated at certain locations and formed large and discrete bubble slugs in the channels. For the hydrophilic carbon cloth backing, the bubbles were produced more uniformly and of smaller size. It was thus shown that the anode-backing layer of uniform pore size and more hydrophilicity was preferable for gas management in the anode. Flow visualization of water flooding on the cathode side of DMFC was also carried out. It was shown that the liquid droplets appeared more easily on the surface of carbon paper due to its reduced hydrophobicity at elevated temperature. For the single-side ELAT carbon cloth, liquid droplets tended to form in the corner between the current collecting rib and GDL since ELAT is highly hydrophobic and the rib (stainless steel) surface is hydrophilic. Even if this study was performed at relatively high temperature (85 °C), such a basic understanding is indispensable for portable DMFC design and optimization.

Lai *et al.* [98] investigated the long-term discharge performance of passive DMFC at different currents with different cell orientations. Water produced in the cathode was observed from the photographs taken by a digital camera. The results revealed that the passive DMFCs with anode facing upward showed the best long-term discharge performance at high current. A few independent water droplets accumulated in cathode when the anode faced upward. Instead, in the passive DMFC with vertical orientation, a large amount of produced water flowed down along the surface of current collector. The passive DMFC with vertical orientation showed relatively good performance at low current. It was concluded that the cathode produced less water in a certain period of time at smaller current. In addition, the rate of methanol crossover in the passive DMFC with anode facing upward was relatively high, which leaded to a more rapid decrease of the methanol concentration in anode. The passive DMFC with anode facing downward resulted in the worst performance because it was very difficult to remove CO_2 bubbles produced in the anode.

Water loss and water recycling in DMFCs are significant issues that affect the complexity, volume, and weight of the system and become of greater concern as the size of the DMFC decreases. A research group at Tel-Aviv University, Israel [99], realized a flat micro DMFC in a plastic housing with a water-management system that controlled the flux of liquid-water through the membrane and the loss of water during operation. These cells contained a nanoporous proton-conducting membrane (NP-PCM). Methanol consumption and water loss were measured during operation in static air at room temperature for up to 900 hours. Water flux through the membrane varied from negative, through zero, to positive values as a function of the thickness and the properties of the water-management system. The loss of water molecules (to the air) per molecule of methanol consumed in the

cell reaction (defined as the *w* factor) varied from 0.5 to 7. When *w* was equal to 2 (water flux through the membrane was equal to zero), there was no need to add water to the DMFC and the cell was operating under water-neutral conditions. On the other hand, when *w* resulted smaller than 2, it was necessary to remove water from the cell and when it was larger than 2, water was added. The cell showed stable operation up to 900 hours and its maximum power was 12.5 mW cm^{-2}.

At the Korea Institute of Science and Technology (KIST), Kim *et al.* [100] developed passive micro-DMFCs with capacities under 5 W to be used as portable power sources. Research activities were focused on the development of MEAs and design of monopolar stacks operating under passive and air-breathing conditions. The passive cells showed many unique features, much different from the active ones. Single cells with active area of 6 cm^2 showed a maximum power density of 40 mW cm^{-2} at 4 M of methanol concentration at room temperature. A six-cell stack having a total active area of 27 cm^2 was constructed in a monopolar configuration and it produced a power output of 1000 mW (37 mW cm^{-2}). Effects of experimental parameters on the performance were also examined to investigate the operation characteristics of single cells and monopolar stacks. Application of micro-DMFCs as portable power sources was demonstrated using small toys and display panels powered by the passive monopolar stacks.

Tekion Inc., Champaign, USA [101], has developed an advanced air-breathing DMFC for portable applications. A novel MEA was fabricated to improve the performance of air-breathing DMFCs. A diffusion barrier on the anode side was designed to control methanol transport to the anode catalyst layer and thus suppressing the methanol crossover. A catalyst-coated membrane with a hydrophobic GDL on the cathode side was employed to improve the oxygen mass transport. The advanced DMFC achieved a maximum power density of 65 mWcm^{-2} at 60 °C with 2 M methanol solution. The value was nearly two times more than that of a commercial MEA. At 40 °C, the power densities operating with 1 and 2 M methanol solutions were over 20 mW cm^{-2} with a cell potential at 0.3 V.

Pennsylvania State University together with University of California at Los Angeles, USA [102], developed a silicon-based micro DMFC for portable applications. Anode and cathode flow fields with channel and rib width of 750 μm and channel depth of 400 μm were fabricated on Si wafers using the microelectromechanical system (MEMS) technology. An MEA was specially fabricated to mitigate methanol crossover. This MEA features a modified anode-backing structure in which a compact microporous layer is added to create an additional barrier to methanol transport, thereby reducing the rate of methanol crossing over the polymer membrane. The cell with the active area of 1.625 cm^2 was assembled by sandwiching the MEA between two microfabricated Si wafers. Extensive cell polarization testing demonstrated a maximum power density of 50 mW cm^{-2} using 2 M methanol feed at 60 °C. When the cell was operated at room temperature, the maximum power density was shown to be about 16 mW cm^{-2} with both 2 and 4 M methanol feed. It was further observed that the present μDMFC still produced reasonable performance under 8-M methanol solution at room temperature.

The Waseda University, Japan, proposed a new concept for μDMFC (0.018 cm^2 active area) based on MEMS technology [103]. The μDMFC was prepared using a series of fabrication steps from micromachined silicon wafer including photolithography, deep reactive ion etching (DRIE), and electron beam deposition. The novelty of this structure is that anodic and cathodic microchannels arranged in plane were fabricated, dissimilar to the conventional bipolar structure. The first objective of the experimental trials was to verify the feasibility of this novel structure on the basis of MEMS technology. The methanol anode and oxidant cathode were prepared by electroplating either Pt–Ru or Pt and Pt, respectively, onto the Ti/Au electrodes. The electroplating solution for Pt was 20 mM $H_2PtCl_6 \cdot 6H_2O$ and 0.5 mM $(CH_3COO)Pb.3H_2O$. The deposition was carried by applying a current density of 30 mA cm^{-2} during 10 minutes. The mass loading of Pt was 2.4 mg cm^{-2}. The Pt–Ru for methanol oxidation was obtained from a solution containing 20 mM $H_2PtCl_6 \cdot xH_2O$ + 20 mM $RuCl_3$ xH_2O. The deposition was performed at −0.15 V versus Ag/AgCl for 5 minutes. The mass loading of Pt–Ru was 2.85 mg cm^{-2}. The electroplating process was carried out at 25 °C for both electrodes. Energy dispersive X-ray (EDX) analysis showed a platinum/ruthenium atomic ratio of 90/10. A Nafion 112 membrane was used as electrolyte. The performance of the μDMFC was assessed at ambient temperature using 2 M CH_3OH/0.5 M H_2SO_4/H_2O as the fuel and O_2-saturated/0.5 M H_2SO_4/H_2O as the oxidant. The O_2-saturated solution was prepared by using oxygen bubbling into 0.5 M H_2SO_4/H_2O solution. The supply of fuel was made by means of a microsyringe pump connected to the fabricated μDMFC unit. The OCV for the Pt cell was 300 mV while it was 400 mV for Pt–Ru cell. The maximum power density was 0.44 mW cm^{-2} at 3 mA cm^{-2} at Pt electrode. While, the maximum power density reached 0.78 mW cm^{-2} at 3.6 mA cm^{-2} for cell with Pt–Ru anode. The reason for this low performance could be due to the nonoptimal composition of Pt–Ru anode catalyst.

The Institute of Microelectronic of Barcelona-CNM (CSIC), Spain, presented a passive and silicon-based micro DMFC [104]. The device was based on a hybrid approach composed of a commercial MEA consisting of a Nafion® 117 membrane with 4.0 mg cm^{-2} Pt–Ru catalyst loading on the anode and 4.0 mg cm^{-2} Pt on the cathode (E-TEK ELAT) sandwiched between two microfabricated silicon current collectors. The silicon plates were provided with an array of vertical squared channels of 300–μm depth that covered an area of 5.0 mm × 5.0 mm. The fabrication process of the silicon plates started with a double-side polished Si wafer 500-mm thick. A first photolithography was done on the front side to define an array of squared windows with 80-mm size. Subsequently, a second photolithography was performed on the backside to define the cavity for the fuel container. Then, a DRIE was realized first on the front side to obtain 200-mm-deep channels, and continued at the back until the wafer was completely perforated. These channels allowed fuel transport to the electrode surface and their dimensions were set to 80 μm × 80 μm in order to ensure the prevalence of the capillary force versus gravity in the anode side regardless of device orientation. In order to provide the current collectors with an appropriate electrical conductivity, a 150-nm

Ti/Ni sputtered layer was deposited covering the front side of the wafer. This conductive layer was used as a seed layer for the 4-mm-thick Ni layer that was electrodeposited afterward. This layer enhanced the electrical conductivity of the current collector; it was then covered by a thin Au layer to prevent oxidation. Finally, the wafer was cut into 10×14 mm chips. In order to guarantee uniform pressure over the active area of the cell, two micromilled methacrylate pieces tightened with four bolts were used as external casing. In addition to provide a mechanical support while testing, the cell was equipped with a 100-ml methanol reservoir. The cell was tested at ambient temperature and different methanol concentrations. It was found that methanol concentration had low impact on the fuel-cell maximum power density, which reached a value around 11 $mW{\cdot}cm^{-2}$ and was comparable to values reported in the literature for larger passive and stainless-steel fuel cells. Temperature measurements were performed; the fuel-cell temperature did not change significantly and was independent from the methanol crossover rate.

A research group of Yonsei University, Korea, realized a DMFC on printed circuit board (PCB) substrates by means of a photolithography process [105]. The effects of channel pattern, channel width, and methanol flow rate on the performance of the fabricated DMFC were evaluated over a range of flow-channel widths from 200 to 400 μm and flow rates of methanol from 2 to 80 ml min^{-1}. A μDMFC with a cross-stripe channel pattern gave superior performance compared with zigzag and serpentine type of pattern. A single cell with a 200−μm-wide channel delivered a maximum power density of 33 mW cm^{-2} when using 2 M methanol feed at 80 °C.

Our group (CNR-ITAE, Messina, Italy) developed passive DMFC mini-stacks for portable applications [106, 107] based on simple designs. Essentially, two designs of flow fields/current collectors for a passive DMFC monopolar three-cell stack were investigated (see Figure 11.5). The first design (a) consisted of two plastic plates (PCBs) covered by thin gold film current collectors with a distribution of holes through which methanol (from a reservoir) and air (from ambient) could diffuse into the electrodes. The second design (b) consisted of thin gold film deposited on the external borders of the fuel and oxidant apertures in the PCBs where the electrodes were placed in contact. A big central hole allowed a direct exposure of electrodes to ambient air (cathodes) and methanol solution (anodes). A methanol reservoir (containing, in total, 21 ml of methanol solution and divided in three compartments), with three small holes in the upper part to fill the containers and to release the produced CO_2, was attached to the anode side (Figure 11.6a). The electrodes were composed of a commercial gas-diffusion layer-coated carbon cloth HT-ELAT and LT-ELAT (E-TEK) at the anode and cathode, respectively. Unsupported Pt–Ru (Johnson–Matthey) and Pt (Johnson–Matthey) catalysts were mixed with 15 wt% Nafion ionomer (ion power, 5 wt% solution) and deposited onto the backing layer for the anode and cathode, respectively. Nafion 117 (ion power) was used as electrolyte. The MEAs for the two stack designs (three cells) were manufactured by assembling simultaneously three sets of anode and cathode pairs onto the membrane (Figure 11.6b), afterward they were sandwiched between

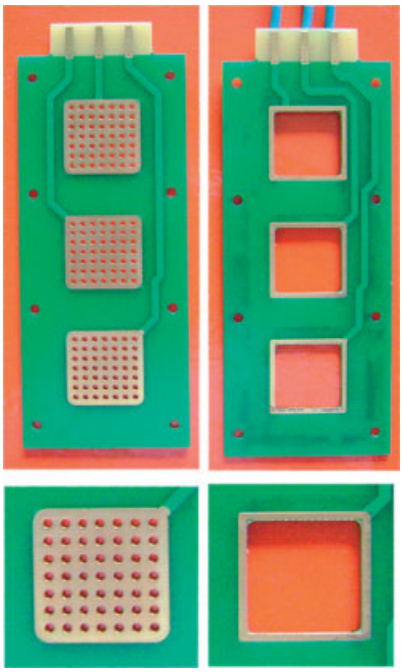

Figure 11.5 Pictures of two different monopolar plates for application in a DMFC three-cell stack operating under passive mode.

two PCBs. The geometrical area of each electrode was 4 cm^2 and the total area of the stack was 12 cm^2. The cells were connected in series externally through the electric circuit. The electrochemical characterization was carried out varying the catalyst loading and methanol concentration. A loading of 4 mg cm^{-2} Pt loading provided the best electrochemical results in the presence of unsupported catalysts. This appeared to be the best compromise between electrode thickness and amount of catalytic sites. Similar performances in terms of maximum power were recorded for the two designs, whereas better mass-transport characteristics were obtained with the design B (Figure 11.7a). On the contrary, OCV and stack voltage at low current were higher for the design A as a consequence of lower methanol crossover. A maximum power of 220–240 mW was obtained at ambient temperature for the three-cell stack with 4 mg cm^{-2} Pt loading on each electrode using both 2 and 5 M methanol concentration at the anode, corresponding to a power density of about 20 mW cm^{-2}. The use of highly concentrated methanol solutions caused a significant decrease of OCV that reflected on the overall polarization curve; however, the activation losses were similar to diluted methanol solutions. A longer discharge time (17 hours) with a unique MeOH charge was recorded with design B (Figure11.7b) at 250 mA compared to design A (5 hours). This was attributed to an easier CO_2 removal from the anode and better mass-transport properties. In fact,

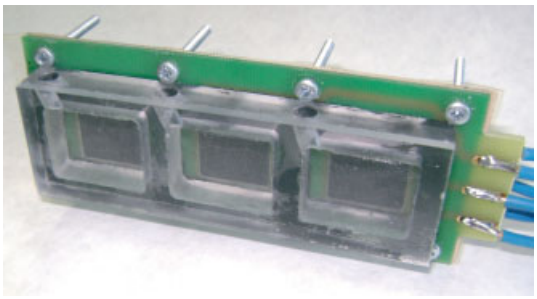

(a)

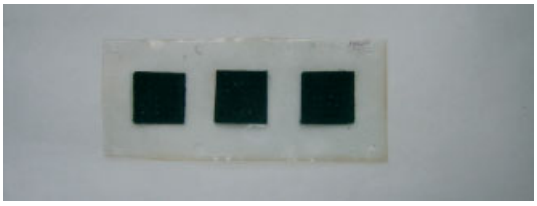

(b)

Figure 11.6 Pictures of the DMFC design B used for a three-cell stack (a) and MEA formed by a single membrane and three couples of electrodes (b).

in design A, CO_2 did not escape easily from the anode hindering the methanol diffusion to the catalytic sites by natural convection. When the small stack based on the A design was mechanically agitated, the effect of this forced convection increased the discharge time.

As mentioned above, the potential market for portable fuel-cell devices not only mainly concerns with small electronic devices, mobile phones, and laptop computers but also includes weather stations, medical devices, signal units, APUs, gas sensors units, and so on. In this regard, a recent European project called *MOREPOWER* was addressing the development of a low-cost, low-temperature (30–60 °C) portable DMFC device of compact construction and modular design in the range of 100-W power. The project was coordinated by GKSS (Germany) and included as partners Solvay, Johnson Matthey, CNR-ITAE, CRF, POLITO, IMM, and NedStack. The electrical characteristics of the device were 40 A, 12.5 V (total power 500 W). The single-cell performance was approaching 0.2 A·cm^{-2} at 0.5 V/cell at 60 °C and atmospheric pressure [108]. Several new membranes were investigated in this project. One of the most promising was a low-cost proton exchange membrane produced by SOLVAY by using a radiochemical grafting technology (Morgane® CRA type membrane), which showed a suitable compromise in terms of reduced methanol crossover and suitable ionic conductivity [109]. Inorganic fillers-modified sulfonated poly-ether-ether-ketone (SPEEK) membranes were also developed in the same project by GKSS (Germany) to reduce the permeability to alcohols while keeping high proton conductivity [109].

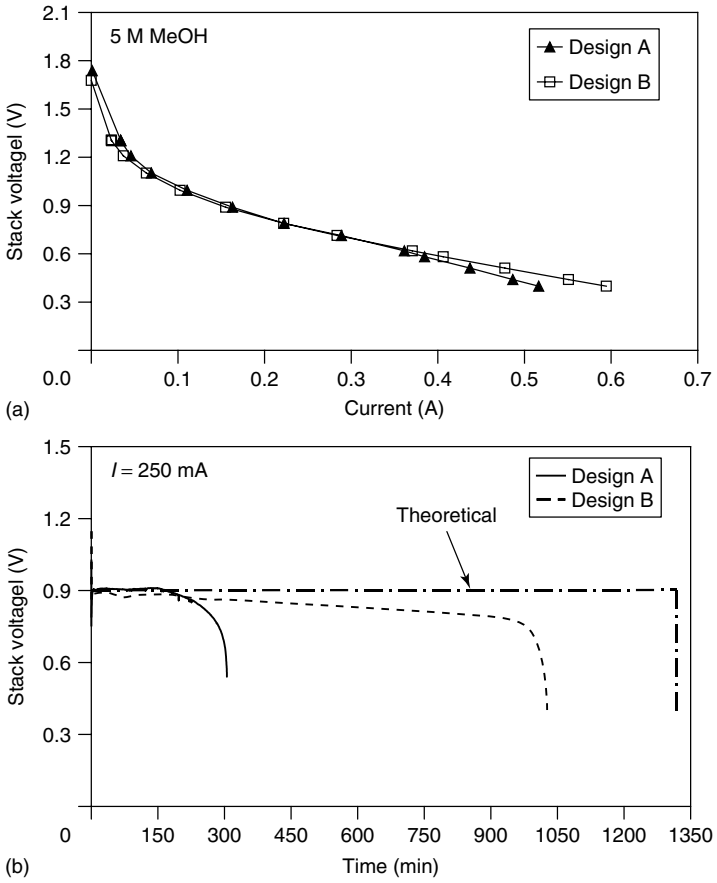

Figure 11.7 Comparison between the polarization curves obtained with the two different designs with a Pt loading of 4 mg cm^{-2} on each electrode and 5 M methanol solution (a), and chrono-potentiometric results at 250 mA obtained with the two designs using a Pt loading of 4 mg cm^{-2} and 5 M methanol solution (b) [107].

11.4 Perspectives and Concluding Remarks

The most challenging problem for the development of DMFCs has been, and still is, a significant enhancement of electrocatalytic activities for the six-electron transfer electro-oxidation of methanol. On the other hand, research in this area has enlightened many scientists and engineers to use highly sophisticated electrochemical surface science and material science techniques for unraveling the mysteries of the reaction path, rate-determining steps, and physicochemical characteristics (electronic and geometric factors, adsorption/desorption energies and

electrocatalyst/support interaction), which influence the activities of the various types of electrocatalysts. The sluggishness of the reaction, especially in the presence of protonic electrolytes, is caused by the very strong chemical adsorption of CO-type species on an electrocatalyst subsequent to the dissociative adsorption of methanol (Pt is the best-known electrocatalyst for this step). A neighboring chemisorbed labile OH species is vital for the electro-oxidation of the strongly adsorbed CO species. To date, a Pt–Ru electrocatalyst has shown the best results. There are some promotional effects by the presence of elements such as Sn, Mo, W, Os, as well as some refractory metal oxides (WO_3). Unfortunately, there has been little success with alternatives to Pt and its alloys in these devices; those tested include transition metal alloys, oxides, and tungsten bronzes (oxide doped with sodium, tungsten carbide). One achievement has been in using carbon-supported electrocatalysts, which has helped to reduce the Pt loading by about a factor of 2–4.

The performance of the oxygen-reduction reaction with a platinum electrocatalyst is affected by the cross over of methanol from the anode to the cathode through the ion exchange membrane. First, the open circuit potential is reduced by about 200 mV and the second effect is due to the competitive adsorption of dissociated methanol and oxygen species. At present, there is a slight catalytic enhancement in oxygen reduction for alloys of Pt with Fe, Cr, Co, and Ni in the presence of methanol crossover. Nonplatinum electrocatalysts, such as heat-treated phthalocyanines and porphyrins, as well as transition metals chalcogenides, have some chance of methanol tolerance but have considerably lower activities than platinum and also raise questions of stability. The near-term prospects of replacing platinum as an electrocatalyst is very slim but a great challenge is to reduce the noble metal loading in both electrodes by a factor of about 10.

The perfluorosulfonic acid polymer electrolyte in the DMFC is an equally expensive material. There has been a lot of research on alternative proton-conducting membranes, which allow CO_2 rejection (sulfonated polyetherketone, polyether sulfone, polysulfone, radiation-grafted polystyrene, zeolites, electrolytes doped with heteropolyacids and sulfonated polybenzimidazole), but, it is still a challenge to attain sufficiently high specific conductivity and stability in the DMFC environment. Nafion-based composite membranes with silicon oxide and zirconium hydrogen phosphate have shown beneficial effects on operation up to about 150 °C with enhanced performance (lower activation and ohmic overpotentials); these can also suitably operate at ambient conditions with reduced crossover due to an increase of the tortuosity factor.

A critical area to improve overall cell performance is the fabrication of MEAs. Progress on preparation of high-performance MEAs has been made by preparing thin electrocatalyst layers (about 10–μm thick) composed of the electrocatalyst and ionomer in the electrode substrate or directly deposited onto the membrane (CCM). Problems caused by barrier layer effects of nitrogen for access of oxygen to the catalytically active sites and electrode flooding need further investigations. Possible solutions to these problems are heat treatments of the recast Nafion gel in the electrocatalytic layer to make it hydrophobic or to use pore formers to increase porosity.

The development of DMFC stacks for portable applications has gained momentum in the last two to three years. The application of DMFC in portable power sources covers the spectrum of cellular phones, personal organizers, laptop computers, military back power packs, and so on. The infusion of semiconductor technology into the development of micro and mini fuel cells by leading organizations such as LANL, JPL, Motorola, has provided an awakening of DMFCs replacing the most advanced type of rechargeable batteries, that is, lithium ion. For several of these applications, a DMFC working at room temperature and ambient pressure with an efficiency of only about 20% may be sufficient to have a strikingly higher performance than the lithium ion batteries, in respect to operating hours between refueling/recharging because of the high-energy density of methanol. Further, the refueling in the case of DMFCs is instantaneous, whereas it requires about 3–5 hours for lithium ion batteries. There is still a challenge in reducing the weight, volume, and costs of the DMFC to a level competitive with lithium ion batteries, as needed for cellular phone and laptop applications. Yet, the Pt loadings are still high in DMFCs (around $4\,mg\,cm^{-2}$). What is most attractive in the portable power applications, as compared with the transportation and stationary applications is that the cost per kilowatt or cost per kilowatt hour could be higher by a factor of 10–100. For this application, there is hardly any competition for lithium ion and DMFCs from any other type of power source. Reducing the loading of noble metals or using cheap nonnoble metal catalysts is actually one of the breakthroughs, which may allow the DMFC to increase its competitiveness on the market of power sources. This field appears the most promising for the near-term and successful utilization of such systems; the progress made in manufacturing DMFCs for portable systems may also stimulate new concepts and designs, which may aid the further development of these systems for electrotraction.

Acknowledgments

We acknowledge the financial support for the DMFC activity from the European Community through the Morepower (EU FP6) project and from Regione Piemonte through the Microcell project. We express our gratitude to our colleagues who have collaborated to the DMFC activity at CNR-ITAE; in particular, A.K. Shukla, H. Kim, S. Srinivasan, C. Yang, R. Dillon, K.M. El-Khatib, Z. Poltarzewski, A.M. Castro Luna, G. Garcia, L.G. Arriaga, I. Nicotera, S. Specchia, G. D'Arrigo, R. Ornelas, F. Lufrano, P. Staiti, and P. L. Antonucci. We are indebted to our collaborators C. D'Urso, A. Stassi, A. Di Blasi, S. Siracusano, T. Denaro, F.V. Matera, E. Modica, G. Monforte, P. Cretì for their invaluable contribution.

References

1. Carrette, L., Friedrich, K.A., and Stimming, U. (2000) *ChemPhysChem*, **1**, 163.
2. Dillon, R., Srinivasan, S., Aricò, A.S., and Antonucci, V. (2004) *J. Power Sources*, **127** (1-2), 112.

3. Lamy, C., Léger, J.-M., and Srinivasan, S. (2000)in *Modern Aspects of Electrochemistry*, vol. 34, Chapter 1 (eds J.O'M., Bockris and B.E., Conway), Plenum Press, New York, p. 53.
4. Shibata, M. and Motoo, S. (1985) *J. Electroanal. Chem.*, **194**, 261.
5. Watanabe, M. and Motoo, S. (1975) *J. Electroanal. Chem.*, **60**, 275.
6. Hamnett, A. (1997) *Catal. Today*, **39**, 445.
7. Ren, X., Wilson, M.S., and Gottesfeld, S. (1996) *J. Electrochem. Soc.*, **143**, L12.
8. Gotz, M. and Wendt, H. (1998) *Electrochim. Acta*, **43**, 3637.
9. Aricò, A.S., Poltarzewski, Z., Kim, H., Morana, A., Giordano, N., and Antonucci, V. (1995) *J. Power Sources*, **55**, 159.
10. Gasteiger, H.A., Markovic, N., Ross, P.N.Jr. and Cairns, E.J. (1994) *J. Electrochem. Soc.*, **141**, 1795.
11. Chandrasekaran, K., Wass, J.C., and Bockris, J.O.M. (1990) *J. Electrochem. Soc.*, **137**, 518.
12. Janssen, M.M.P. and Moolhuysen, J. (1976) *Electrochim. Acta*, **21**, 861.
13. Anderson, A.B., Grantscharova, E., and Seong, S. (1996) *J. Electrochem. Soc.*, **143**, 2075.
14. Mc Breen, J. and Mukerjee, S. (1995) *J. Electrochem. Soc.*, **142**, 3399.
15. Iwasita, T., Nart, F.C., and Vielstich, W. (1990) *Ber. Bunsenges Phys. Chem.*, **94**, 1030.
16. Jalan, V. and Taylor, E.J. (1983) *J. Electrochem. Soc.*, **130**, 2299.
17. Parsons, R. and Van der Noot, T. (1988) *J. Electroanal. Chem.*, **257**, 9.
18. Kita, H., Gao, Y., Nakato, T., and Hattori, H. (1994) *J. Electroanal. Chem.*, **373**, 177.
19. Aricò, A.S., Antonucci, V., Giordano, N., Shukla, A.K., Ravikumar, M.K., Roy, A., Barman, S.R., and Sarma, D.D. (1994) *J. Power Sources*, **50**, 295.
20. Campbell, S.A. and Parsons, R. (1992) *J. Chem. Soc. Faraday Trans.*, **88**, 833.
21. Haner, A.N. and Ross, P.N. (1991) *J. Phys. Chem.*, **95**, 3740.
22. Watanabe, M., Furuuchi, Y., and Motoo, S. (1985) *J. Electroanal. Chem.*, **191**, 367.
23. Wang, K., Gasteiger, H.A., Markovic, N.M., and Ross, P.N.Jr. (1996) *Electrochim. Acta*, **41**, 2587.
24. Ticianelli, E., Berry, J.G., Paffet, M.T., and Gottesfeld, S. (1977) *J. Electroanal. Chem.*, **81**, 229.
25. Giordano, N., Passalacqua, E., Pino, L., Aricò, A.S., Antonucci, V., Vivaldi, M., and Kinoshita, K. (1991) *Electrochim. Acta*, **36**, 1979.
26. Toda, T., Igarashi, H., Uchida, M., and Watanabe, M. (1999) *J. Electrochem. Soc.*, **146**, 3750.
27. Li, W., Zhou, W., Li, H., Zhou, Z., Zhou, B., Sun, G., and Xin, Q. (2004) *Electrochim. Acta*, **49**, 1045.
28. Min, M., Cho, J., Cho, K., and Kim, H. (2000) *Electrochim. Acta*, **45**, 4211.
29. Koffi, R.C., Coutanceau, C., Garnier, E., Leger, J.-M., and Lamy, C. (2005) *Electrochim. Acta*, **50**, 4117.
30. Uchida, H., Ozuka, H., and Watanabe, M. (2002) *Electrochim. Acta*, **47**, 3629.
31. Shukla, A.K. and Raman, R.K. (2004) *Annu. Rev. Mater. Res.*, **33**, 155.
32. Shukla, A.K., Raman, R.K., Choudhury, N.A., Priolkar, K.R., Sarode, P.R., Emura, S., and Kumashiro, R. (2004) *J. Electroanal. Chem.*, **563**, 181.
33. Yang, H., Coutanceau, C., Leger, J.-M., Alonso-Vante, N., and Lamy, C. (2005) *J. Electroanal. Chem.*, **576**, 305.
34. Stassi, A., D'Urso, C., Baglio, V., Di Blasi, A., Antonucci, V., Aricò, A.S., Castro Luna, A.M., Bonesi, A., and Triaca, W.E. (2006) *J. Appl. Electrochem.*, **36**, 1143.
35. Baglio, V., Aricò, A.S., Stassi, A., D'Urso, C., Di Blasi, A., Castro Luna, A.M., and Antonucci, V. (2006) *J. Power Sources*, **159**, 900.
36. Baglio, V., Stassi, A., Di Blasi, A., D'Urso, C., Antonucci, V., and Aricò, A.S. (2007) *Electrochim. Acta*, **53**, 1361.
37. Jasinski, R. (1965) *J. Electrochem. Soc.*, **112**, 526.
38. Franke, R., Ohms, D., and Wiesener, K. (1989) *J. Electroanal. Chem.*, **260**, 63.
39. Faubert, G., Lalande, G., Coté, R., Guay, D., Dodelet, J.P., Weng, L.T., Bertrand, P., and Dénés, G. (1996) *Electrochim. Acta*, **41**, 1689.

40. Sun, G.R., Wang, J.T., and Savinell, R.F. (1998) *J. Appl. Electrochem.*, **28**, 1087.
41. Elzing, A., Van der Putten, A., Visscher, W., and Barendrecht, E. (1987) *J. Electroanal. Chem.*, **233**, 113.
42. Di Noto, V., Negro, E., Gliubizzi, R., Lavina, S., Pace, G., Gross, S., and Maccato, C. (2007) *Adv. Funct. Mater.*, **17**, 3626.
43. Alonso-Vante, N. and Tributsch, H. (1986) *Nature (London)*, **323**, 431.
44. Reeve, R.W., Christensen, P.A., Hamnett, A., Haydock, S.A., and Roy, S.C. (1998) *J. Electrochem. Soc.*, **145**, 3463.
45. Bockris, J.O.M. and Srinivasan, S. (1969) *Fuel Cells: Their Electrochemistry*, McGraw-Hill Book Company, New York.
46. McNicol, B.D., Rand, D.A.J., and Williams, K.R. (1999) *J. Power Sources*, **83**, 15.
47. Schmidt, T.J., Paulus, U.A., Gasteiger, H.A., Alonso-Vante, N., and Behm, R.J. (2000) *J. Electrochem. Soc.*, **147**, 2620.
48. Yang, C., Srinivasan, S., Aricò, A.S., Cretì, P., Baglio, V., and Antonucci, V. (2001) *Electrochem. Solid-State Lett.*, **4**, A31.
49. Aricò, A.S., Baglio, V., Di Blasi, A., Cretì, P., Antonucci, P.L., and Antonucci, V. (2003) *Solid State Ionics*, **161**, 251.
50. Baglio, V., Aricò, A.S., Di Blasi, A., Antonucci, V., Antonucci, P.L., Licoccia, S., Traversa, E., and Serraino Fiory, F. (2005) *Electrochim. Acta*, **50**, 1241.
51. Li, L., Zhang, J., and Wang, Y. (2003) *J. Membrane Sci.*, **226**, 159.
52. Bauer, B., Jones, D.J., Roziere, J., Tchicaya, L., Alberti, G., Casciola, M., Massinelli, L., Peraio, A., Besse, S., and Ramunni, E. (2000) *J. New Mat. Electrochem. Syst.*, **3**, 93.
53. Lufrano, F., Baglio, V., Staiti, P., Aricò, A.S., and Antonucci, V. (2008) *J. Power Sources*, **179**, 34.
54. Peled, E., Duvdevani, T., Aharon, A., and Melman, A. (2000) *Electrochem. Solid-State Lett.*, **3**, 525.
55. Hietala, S., Koel, M., Skou, E., Elomaa, M., and Sundholm, F. (1998) *J. Mater. Chem.*, **8**, 1127.
56. Aricò, A.S., Antonucci, P.L., Giordano, N., and Antonucci, V. (1995) *Mater. Lett.*, **24**, 399.
57. Wang, J., Wasmus, S., and Savinell, R.F. (1995) *J. Electrochem. Soc.*, **142**, 4218.
58. Boysen, D.A., Chisholm, C.R.I., Haile, S.M., and Narayanan, S.R. (2000) *J. Electrochem. Soc.*, **147**, 3610.
59. Aricò, A.S., Creti, P., Antonucci, P.L., and Antonucci, V. (1998) *Electrochem. Solid-State Lett.*, **1**, 66.
60. Okamoto, H., Kawamura, G., Ishikawa, A., and Kudo, T. (1987) *J. Electrochem. Soc.*, **134**, 1645.
61. Hays, C.C., Manoharan, R., and Goodenough, J.B. (1993) *J. Power Sources*, **45**, 291.
62. Antonucci, P.L., Aricò, A.S., Modica, E., and Antonucci, V. (1999) *J. Solid State Electrochem.*, **3**, 205.
63. Thomas, S.C., Ren, X., and Gottesfeld, S. (1999) *J. Electrochem. Soc.*, **146**, 4354.
64. Yang, H., Zhao, T.S., and Ye, Q. (2005) *J. Power Sources*, **139**, 79.
65. Shao, Z.-G., Zhu, F., Lin, W.-F., Christensen, P.A., Zhang, H., and Yi, B. (2006) *J. Electrochem. Soc.*, **153**, A1575.
66. Scott, K., Taama, W.M., and Argyropoulos, P. (1998) *J. Appl. Electrochem.*, **28**, 1389.
67. Srinivasan, S., Mosdale, R., Stevens, P., and Yang, C. (1999) *Annu. Rev. Energy Environ.*, **24**, 281.
68. Aricò, A.S., Creti, P., Giordano, N., Antonucci, V., Antonucci, P.L., and Chuvilin, A. (1996) *J. Appl. Electrochem.*, **26**, 959.
69. Fisher, A., Jindra, J., and Wendt, H. (1998) *J. Appl. Electrochem.*, **28**, 277.
70. Gamburzev, S., Boyer, C., and Appleby, A.J. (1999) *Proton Conducting Membrane Fuel Cells II -Second International Symposium*, Proceedings Volume 98-27, Vol. **23** (eds S.Gottesfeld and T.F. Fuller), The Electrochemical Society, Pennington.

71. Kordesch, K. and Simader, G. (1996) *Fuel Cells and their Applications*, Wiley-VCH Verlag GmbH, Weinheim.
72. Hockaday, R.G., DeJohn, M., Navas, C., Turner, P.S., Vaz, H.L., and Vazul, L.L. (2000)Proceedings of the Fuel Cell Seminar, October 30–November 2, Portland, p. 791.
73. Kelley, S.C., Deluga, G.A., and Smyrl, W.H. (2000) *Electrochem. Solid-State Lett.*, **3** (9), 407.
74. Narayanan, S.R., Valdez, T.I., and Clara, F. (2000)Proceedings of the Fuel Cell Seminar, October 30–November 2, Portland, p. 795.
75. Jung, D.-H., Jo, Y.-H., Jung, J.-H., Cho, S.-Y., Kim, C.-S., and Shin, D.-R. (2000)Proceedings of the Fuel Cell Seminar, October 30–November 2, Portland, p. 420.
76. Ren, X., Zelenay, P., Thomas, S., Davey, J., and Gottesfeld, S. (2000) *J. Power Sources*, **86** (1), 111.
77. Bostaph, J., Koripella, R., Fisher, A., Zindel, D., and Hallmark, J. (2001)Proceedings of the 199th Meeting on Direct Methanol Fuel Cell, Electrochemical Society, March 25–29, Washington, DC.
78. Hockaday, R.G. (1998) US Patent No. 5,759,712.
79. Witham, C.K., Chun, W., Valdez, T.I., and Narayanan, S.R. (2000) *Electrochem. Solid-State Lett.*, **3**, 11, 497.
80. Gottesfeld, S., Ren, X., Zelenay, P., Dinh, H., Guyon, F., and Davey, J. (2000)Proceedings of the Fuel Cell Seminar, October 30–November 2, Portland, p. 799.
81. Dohle, H., Mergel, J., Scharmaan, H., and Schmitz, H. (2001) Proceedings of the 199th Meeting Direct Methanol Fuel Cell Symposium, Electrochemical Society, March 25–29, Washington, DC.
82. Chang, H. (2001) The Knowledge Foundation's Third Annual International Symposium on Small Fuel Cells and Battery Technologies for Portable Power Applications, April 22–24, Washington, DC.
83. Chang, H., Kim, J.R., Cho, J.H., Kim, H.K., and Choi, K.H. (2002) *Solid State Ionics*, **148**, 601.
84. Jung, D.H., Jo, Y.-H. , Jung, J.-H., Cho, S.-H., Kim, C.-S., and Shin, D.-R. (2000) Proceedings Fuel Cell Seminar, October 30–November 2, Portland, p. 420.
85. Lifton, R.F. (2001) The Knowledge Foundation's Third Annual International Symposium on Small Fuel Cells and Battery Technologies for Portable Power Applications, April 22–24, Washington, DC.
86. Martin, J.J., Qian, W., Wang, H., Neburchilov, V., Zhang, J., Wilkinson, D.P., and Chang, Z. (2007) *J. Power Sources*, **164** (1), 287.
87. Guo, Z. and Faghri, H. (2006) *J. Power Sources*, **160**, 1183.
88. Liu, J.G., Zhao, T.S., Chen, R., and Wong, C.W. (2005) *Electrochem. Commun.*, **7**, 288.
89. Chen, R. and Zhao, T.S. (2007) *J. Power Sources*, **167** (2), 455.
90. Chen, R. and Zhao, T.S. (2007) *Electrochem. Commun.*, **9** (4), 718.
91. Chen, R. and Zhao, T.S. (2007) *Electrochim. Acta*, **52** (13), 4317.
92. Zhang, H.F. and Hsing, I.-M. (2007) *J. Power Sources*, **167** (2), 450.
93. Abdelkareem, M.A. and Nakagawa, N. (2007) *J. Power Sources*, **165** (2), 685.
94. Chu, D. and Jiang, R. (2006) *Electrochim. Acta*, **51** (26), 5829.
95. Yang, H., Zhang, T.S., and Ye, Q. (2005) *J. Power Sources*, **139** (1-2), 79.
96. Di Blasi, A., Baglio, V., Denaro, T., Antonucci, E., and Aricò, A.S. (2008) *J. New Mater. Electrochem. Syst.*, **11**, 165.
97. Lu, G.Q. and Wang, C.Y. (2004) *J. Power Sources*, **134** (1), 33.
98. Lai, Q.-Z., Yin, G.-P., Zhang, J., Wang, Z.-B., Cai, K.-D., and Liu, P. (2008) *J. Power Sources*, **175** (1), 458.
99. Blum, A., Duvdevani, T., Philosoph, M., Rudoy, N., and Peled, E. (2003) *J. Power Sources*, **117** (1-2), 22.
100. Kim, D., Cho, E.A., Hong, S.-A., Oh, I.-H., and Ha, H.-Y. (2004) *J. Power Sources*, **130** (1-2), 172.
101. Pan, Y.H. (2006) *J. Power Sources*, **161**, 282–289.
102. Lu, G.Q., Wang, C.Y., Yen, T.J., and Zhang, X. (2004) *Electrochim. Acta*, **49** (5), 82.

103. Motokawa, S., Mohamedi, M., Momma, T., Shoji, S., and Osaka, T. (2004) *Electrochem. Commun.*, **6** (6), 562.
104. Sabate, N., Esquivel, J.P., Santander, J., Torres, N., Gracia, I., Ivanov, P., Fonseca, L., Figueras, E., and Canè, C. (2008) *J. New Mater. Electrochem. Syst.*, **11** (2), 143.
105. Lim, S.W., Kim, S.W., Kim, J., Ahn, J.E., Han, H.S., and Shul, Y.G. (2006) *J. Power Sources*, **161** (1), 27.
106. Baglio, V., Stassi, A., Matera, F.V., Di Blasi, A., Antonucci, V., and Aricò, A.S. (2008) *J. Power Sources*, **180** (2), 797.
107. Baglio, V., Stassi, A., Matera, F.V., Antonucci, V., and Aricò, A.S. (2009) *Electrochim. Acta*, **54**, 2004.
108. Nunes, S.P., EU Funded Project MOREPOWER (compact direct methanol fuel cells for portable applications), project nr. SES6-CT-2003-502652 (2004).
109. Antonucci, V., Aricò, A.S., Baglio, V., Brunea, J., Buder, I., Cabello, N., Hogarth, M., Martin, R., and Nunes, S. (2006) *Desalination*, **200**, 653.

12
Semiconductor Block Copolymers for Photovoltaic Applications

Michael Sommer, Sven Hüttner, and Mukundan Thelakkat

12.1
Introduction and History of Semiconductor Block Copolymers

Ever since the first report of an efficient organic photovoltaic (OPV) device by C. W. Tang in 1986 [1], extensive research activities have created a deeper understanding of the underlying fundamental processes occurring in the active layers of an electron donor (D) and an electron acceptor (A) [2–5]. Vacuum-deposited small molecule solar cells – such as the device made by C. W. Tang – have yielded impressive power conversion efficiencies (PCEs) since then [6, 7]. Polymer blend bulk heterojunction solar cells can be processed on flexible substrates from solution, thus offering large-area production at low cost [8–12]. By extensively optimizing this active layer blend morphology, PCEs between 4 and 6% have been realized [13–16]. In addition, remarkable device performance has been attained with novel materials exhibiting favorable electronic properties [17–19]. Since charge generation and charge recombination in organic bulk heterojunction solar cells occur at the D–A interface, the interfacial size and shape is crucial to the device performance. Even though the morphology can be tuned by accelerating and subsequently freezing in the demixing process of the active layer in bulk heterojunction solar cells [20], a precise arrangement of donor and acceptor units is still a major goal. From a material chemist's point of view, it is therefore essential to develop new materials as well as new concepts that allow improvement of morphology control.

A higher level of morphological control can be achieved by exploiting various interactions between either the same molecules of donor or acceptor, or between the donor and the acceptor molecule. For example, hydrogen bonds between perylene bisimides (PBIs) were introduced as a structure-directing tool. As a result, thin films comprised of a three-dimensional mesoscopic acceptor network could be fabricated. Most strikingly, this acceptor network architecture was maintained even when processing the material together with an amorphous donor polymer, yielding a D–A heterojunction with defined morphology, charge transport pathways, and domain sizes in the range of the exciton diffusion length [21]. This result is encouraging since low molecular weight PBIs tend to form very large one-dimensional stacks or crystals [22, 23], which might have restricted their use in OPV devices [24–27].

Ideas in Chemistry and Molecular Sciences: Advances in Nanotechnology, Materials and Devices.
Edited by Bruno Pignataro

ISBN: 978-3-527-32543-6

Even stronger interactions for interface tuning can be provided by a covalent bond between the donor and the acceptor moiety. Manifold architectures have been designed, for example, D–A dyads [28] or double-cable polymers [29, 30], to name only a few. The motivation for the often challenging synthesis was clearly driven by the advantage of a highly intermixed D–A morphology capable of efficient charge separation. However, once the charges are separated, they have to percolate toward the respective electrodes. This process occurs most efficiently when the transport pathways between the two electrodes are straight and do not exhibit dead ends.

Indeed, the demixing of active layers of D–A bulk heterojunction solar cells is an intricate issue. A phase separation on the nanoscale range is needed for efficient charge transport, yet macrophase-separated polymer blends do not exhibit sufficient interfacial area for charge generation, and recombination of the excitons will occur prior to charge separation [31–33]. In this respect the molecular junction – as realized in molecular assemblies of D–A dyads or in double-cable polymers – enables perfect and stable mixing of donor and acceptor units whereas a polymer blend tends to minimize its interfacial area. Consequently, something in between – a stable morphology with co-continous domains of D and A tens of nanometers thin – is sought to be obtained. The equilibrium microstructures of block copolymers are well-defined and can be tuned in size and shape when the molecular weight and the length of the individual blocks are varied [34]. Therefore, block copolymers with electronic functions are promising materials for OPV devices. Co-continous morphologies suitable for photovoltaic active layers include cylindrical, lamellar, or gyroidal phases. The construction of such microstructures from D–A block copolymers via self-assembly thus addresses the dilemma between the need of having ordered transport pathways and sufficient optical absorption on a length scale that is commensurate to the exciton diffusion length [35]. Furthermore, techniques for preparing ordered microstructures – that is macroscopically aligned domains that are oriented perpendicular to the electrodes – are developed well and have been successfully applied to conventional block copolymers without electronic functions [36–38]. A graphical illustration of various morphological scenarios from active layers from blends and block copolymers is depicted in Scheme 12.1.

While vertical alignment of cylindrical and lamellar block copolymers might be advantageous for improving the device performance, gyroidal films do not require alignment. An elegant example of this has been given recently. Snaith *et al.* used a double sacrificial block copolymer for the preparation of highly ordered gyroidal TiO_2 replicates, and incorporated them into liquid electrolyte dye-sensitized solar cells [39]. However, the direct formation of the gyroid mesophase from fully functionalized D–A block copolymers has not been realized up to now.

Another advantage all-organic D–A block copolymers offer is the covalent connectivity of the two blocks that gives rise to the formation of equilibrium structures. Further crystallization of the two phases, concomitant with an increase in domain size and a decrease in interfacial area, can thereby be excluded. The achievement of stable structures is desired to improve the morphological long-term stability of OPV devices.

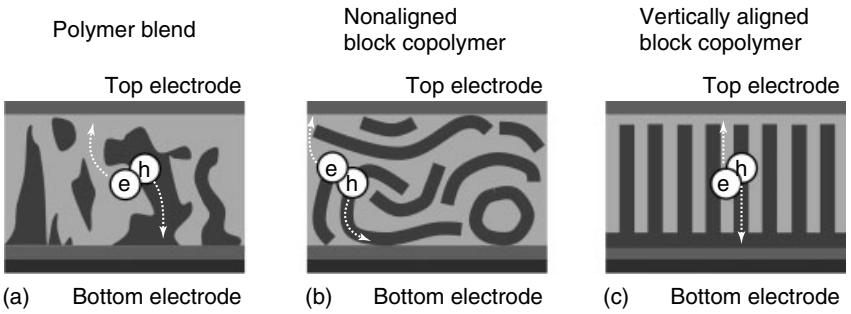

Scheme 12.1 Different donor–acceptor active layer morphologies between the electrodes of the devices: (a) depicts a polymer blend morphology with large, undefined and inhomogeneous domains; (b) depicts schematic morphologies of disordered and (c) vertically aligned microphase separated block copolymer thin films. Dark and light gray domains correspond to the donor and the acceptor phase, respectively.

In contrast to conventional and commercially available block copolymers, block copolymers that carry one or more electronically active blocks are rare and the synthesis is challenging. Very often, multistep organic synthetic procedures have to be combined with one or more polymerization techniques. Further difficulties arise from the limited solubilities and the limited amount of material available from one batch, making the preparation of such materials tedious and time-consuming. Accordingly, only a few examples are known in the literature.

The first D–A block copolymers with suitable electronic properties for charge separation were synthesized by Hadziioannou *et al.*, using a conjugated poly(phenylene vinylene) (PPV) block as macroinitiator for the nitroxide mediated radical polymerization (NMRP) of a second styrenic coil block (Scheme 12.2a). This second segment was converted to the acceptor block by attaching C_{60} molecules [40]. As pointed out by the authors, the strong interactions between the fullerene moieties, either due to partial cross-linking [41] or crystallization [42], possibly accounted for the lack of microdomain formation after functionalization with C_{60}. In another approach, D–A triblock copolymers were prepared from poly(3-hexythiophene) (P3HT) and cyano-substituted PPV via Yamamoto couplings (Scheme 12.2c) [43]. Frechét *et al*. made use of ring-opening metathesis polymerization (ROMP) to subsequently polymerize two macromonomers containing P3HT and fullerene units (Scheme 12.2b). The products found application as compatibilizers in bulk heterojunction solar cells [44]. However, microphase separation was not demonstrated in any of these systems and only in two cases, was a photovoltaic effect with solely the block copolymer as the active layer reported [42, 45]. The molecular structures of these fully functionalized donor–acceptor block copolymers are summarized in Scheme 12.2.

Special attention has to be given to appropriate solubilizing groups when using conjugated polymers and fullerene derivatives as active materials. A low weight fraction of, for example, alkyl chains should render the polymer insoluble whereas

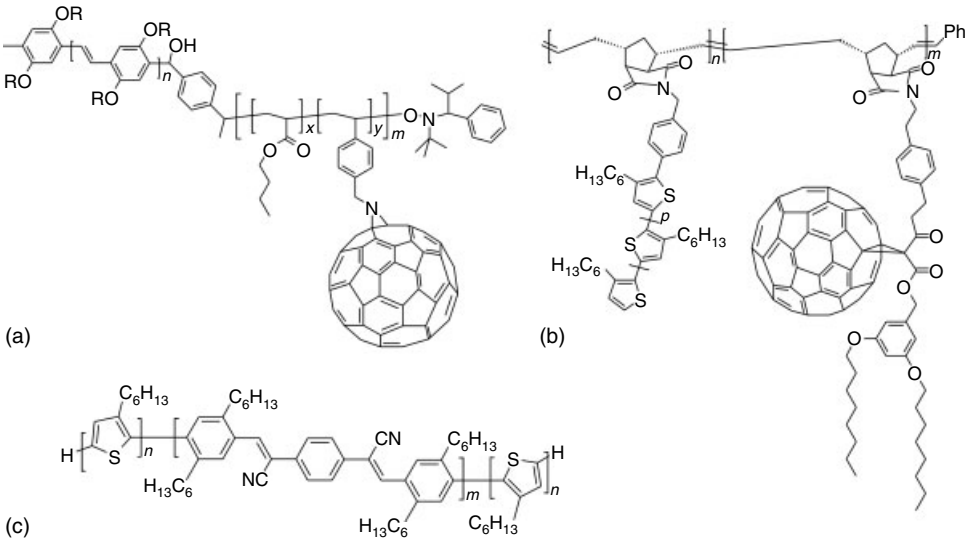

Scheme 12.2 Chemical structures of D–A block copolymers with conjugated polymers and fullerene derivatives. (a) C_{60}-functionalized rod-coil block copolymer proposed by Hadziioannou *et al*. (b) Diblock copolymer with P3HT and a C_{60} derivative in the side chain by Frechet *et al*. (c) All-conjugated triblock copolymer by Scherf *et al*.

a solubilizing group fraction that is too high will lead to poor performance of the device since the amount of active material decreases. This issue of solubility becomes clearly visible in the case of polymers containing fullerene units [46]. PBI as an alternative electron acceptor has been investigated to a lesser extent since the PCEs of solution-processed devices did not reach by far the benchmarks set by conjugated–fullerene solar cellP. The main reason was seen in the uncontrolled crystallization of PBI, giving rise to large crystals concomitant with poor morphological control [24, 25]. Yet, suitable electronic properties and absorption in the visible range make this acceptor compound interesting for light harvesting applications and apparently, interest in PBI for photovoltaic applications is reviving [26, 27, 47]. In addition, the chemical derivatization of the PBI core is feasible since the two distinct imide positions can be substituted independently without altering the electronic properties. Making use of these facts, Thelakkat *et al*. designed a highly soluble and polymerizable PBI derivative with a branched alkyl substituent at one imide position and a linear, acrylate-functionalized alkyl spacer at the other imide position (PerAcr). By incorporating PerAcr into block copolymers with vinyltriphenylamine, highly soluble D–A block copolymers exhibiting all important requirements for photovoltaic applications were obtained [48]. The valuable design and synthesis of this polymerizable electron-conducting monomer marked the beginning of a variety of block copolymers with side chain crystalline PPerAcr blocks and different amorphous poly(triarylamine) polymers. An overview

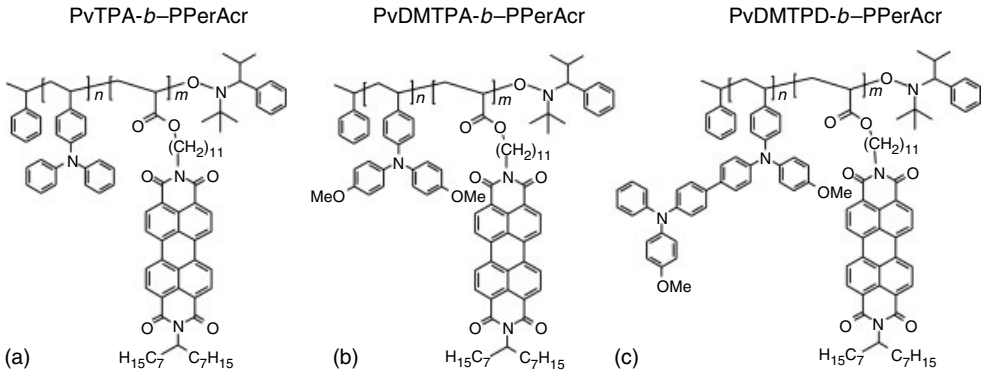

Scheme 12.3 Chemical structures of amorphous–crystalline D–A block copolymers. The block copolymers were prepared by the subsequent polymerization of vinyltriarylamine and perylene bisimide acrylate monomers via nitroxide mediated radical polymerization. PvTPA, poly(vinyl triphenylamine); PvDMTPA, poly[bis(4-methoxyphenyl)-4′-vinylphenylamine]; PvDMTPD, poly[*N*,*N*′-bis(4-methoxyphenyl)-*N*-phenyl-*N*′-4-vinylphenyl-(1,1′biphenyl)-4,4′-diamine]; PPerAcr, poly(perylene bisimide acrylate).

of these amorphous–crystalline block copolymers is given in Scheme 12.3. We have reported extensively on the synthesis [48, 49] morphology [50], and photovoltaic applications [51, 52] of these materials during the last years. In this contribution, very recent work on block copolymers with two crystalline blocks poly(3-hexylthiophene) P3HT and poly(PBI acrylate) PPerAcr is presented. Starting from general remarks and a synthetic perspective, the optical, morphological, and photovoltaic properties are discussed in view of competing crystallization of P3HT and PPerAcr.

12.2
Crystalline–Crystalline D–A Block Copolymers P3HT-b–PPerAcr

Besides the advantage of an improved morphology control, the following considerations prompted us to chose P3HT and PPerAcr as building blocks toward D–A block copolymers for photovoltaic applications: (i) Both materials absorb light in the visible region and thus can contribute to photocurrent generation, (ii) both polymers exhibit high charge carrier mobilities owing to their (semi-) crystalline nature [53, 54], (iii) the energy level offsets are considered to be sufficiently high for efficient electron transfer, (iv) a combination of the chemical methods available should allow for synthesis and derivatization of the single building blocks in such a way that well-defined block copolymers can be obtained. Scheme 12.4 shows the chemical structure of the target block copolymer poly(3-hexylthiophene)-*b*-poly(perylene bisimide acrylate) (P3HT-*b*–PPerAcr).

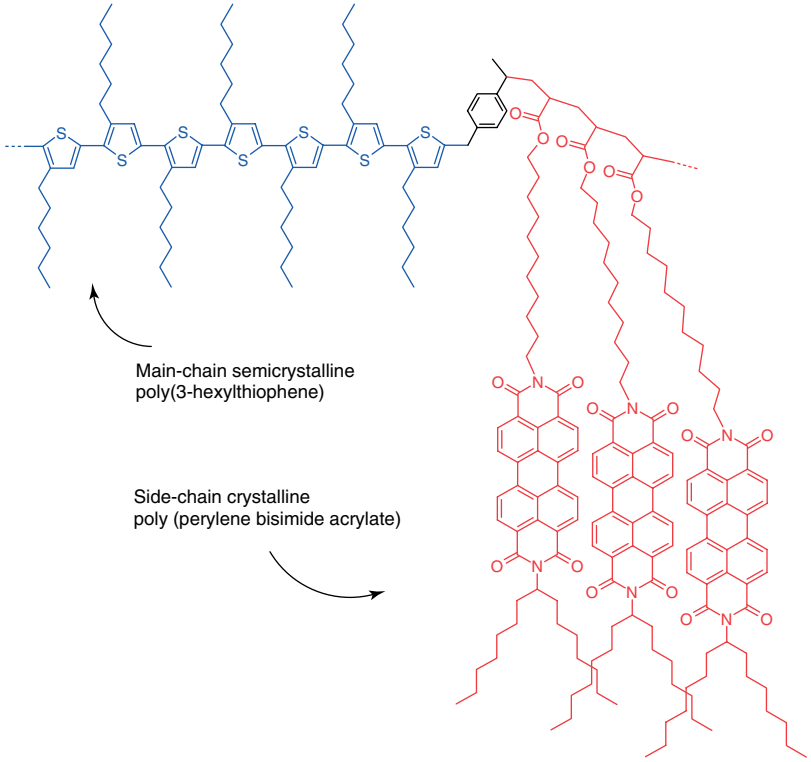

Scheme 12.4 Chemical structure of P3HT-*b*-PPerAcr. P3HT chains are blue and perylene bisimide units red (Reproduced with permission from Wiley-VCH Verlag GmbH & Co. KGaA: M. Sommer, A. Lang, M. Thelakkat, *Angew. Chem. Int. Ed.* 2008, 47, 7901).

12.2.1 Synthesis of P3HT-b–PPerAcr

The objective of synthesizing block copolymers with P3HT and poly(PBI acrylate) PPerAcr involves combination of the two polymerization methods, Grignard Metathesis Polymerization (GRIM) and Nitroxide Mediated Radical Polymerization (NMRP) in a straightforward fashion. Block copolymers with poly(3-alkylthiophenes) prepared via the GRIM method were first reported by McCullough *et al.*, using polymer analogous reactions to generate P3HT macroinitiators for the atom transfer radical polymerization (ATRP) of a second coil block [55, 56]. Later on, this concept was extended to P3HT macroinitiators for NMRP and reversible addition fragmentation termination polymerization (RAFT) [57]. Since the preparation of these P3HT macroinitiators included various polymer analogous reactions of the pristine P3HT, a procedure with less synthetic steps was desirable [57, 58]. Protocols for the *in situ* endcapping of P3HT with

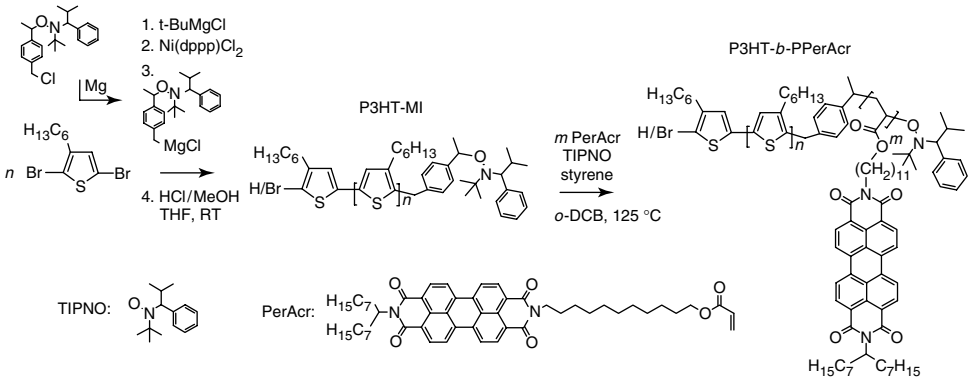

Scheme 12.5 One-pot synthesis of P3HT-macroinitiators (P3HT-MI) for NMRP using GRIM and in-situ encapping with the Grignard derivative of a common alkoxyamine initiator. Starting from P3HT-MI, the acceptor monomer PerAcr is polymerized to give fully functionalized, double-crystalline block copolymers P3HT-*b*-PPerAcr.

different endgroups were readily available from the McCullough group [59], giving an obvious pathway for a straightforward synthetic methodology toward P3HT block copolymers in two steps (Scheme 12.5) [60].

The *in situ* introduction of the NMRP initiator (alkoxyamine) was verified at the end of the P3HT chain (capping efficiencies between 40 and 85%) was verified by ^{1}H-NMR. The degree of endcapping sensitively depended on the fairly complex polymerization conditions. McCullough *et al.* found mixtures of mono- and di-capped P3HT species, depending on the type of Grignard used [59], whereas we could only detect small amounts of dicapped P3HT macroinitiators. A mixture of mono- and di-capped macroinitiators leads to a mixture of diblock and triblock copolymers, which cannot be separated afterwards by simple extraction methods. This complicates characterization and can be disadvantageous regarding the self-assembly of the material. In order to gain insight into the various termination reactions of the GRIM during endcapping with alkoxyamine, the endgroups were analyzed using matrix-assisted laser desorption ionization time-of-flight (MALDI-TOF) as a function of endcapping time. For this purpose, aliquots were withdrawn after adding an 8-fold excess of the alkoxyamine endcapper, quenched with hydrochloric acid, and analyzed by MALDI-TOF [61]. The results are summarized in Figure 12.1 and show the engroups of a P3HT-alkoxyamine macroinitiator after 10 minutes, 1 hour, and 6 hours of endcapping time.

In fact, the alkoxyamine does not survive the MALDI ionization procedure and only P3HT chains carrying the benzylic fragment (Bz) were observed. A quantitative evaluation of the peak heights is critical since the peak intensities do not proportionally represent the amount of the respective species. Qualitatively, P3HTs with hydrogen–hydrogen (H–H), hydrogen–bromine (H–Br), hydrogen–alkoxyamine (H–Bz), and alkoxyamine–alkoxyamine (Bz–Bz) endgroups were found. On

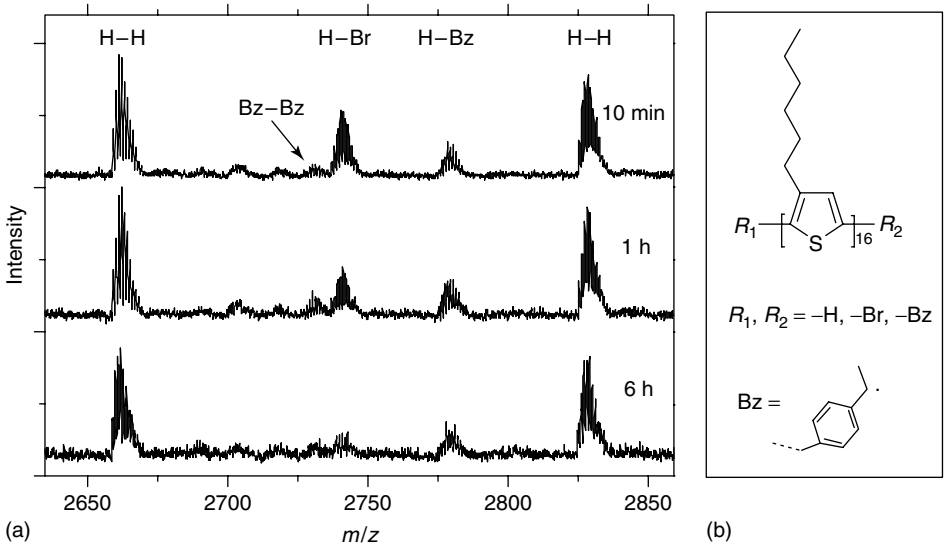

Figure 12.1 (a) Evolution of P3HT endgroups during encapping with the Grignard-functionalized alkoxyamine as revealed by MALDI-TOF. The 16-mer is shown. Most significantly, degradation of H–Br-terminated chains is found. (b) Chemical structures of endgroups found. Bz, benzylic fragment of the alkoxyamine.

comparing the different spectra, most of alkoxyamine endcapping occurred during the first minutes after adding the endcapper and only increased slightly afterwards. The overall degree of alkoxyamine endcapping was small in this case (~40% by ^{1}H-NMR), and despite the presence of further H–Br chain ends, these were not coupled to the initiator. Rather, the H–Br ends degraded (Figure 12.1), concomitant with an increase of the H–H ends. This indicated that despite the presence of Grignard-functionalized alkoxyamine, H–Br-terminated chains underwent a side reaction which converted them into H–H-terminated chains. A general strategy for obtaining higher yields of alkoxyamine-terminated P3HT is therefore to use a larger excess of endcapper. When 15 equiv. of alkoxyamine (with respect to the catalyst) were added, the degree of endcapping increased from 40% to up to 80%. However, a complete endcapping of all P3HT chains with alkoxyamine seemed unlikely as long as degradation of bromine-terminated chains occurred during the GRIM. We believe that the simple and straightforward one-pot procedure compensated for incomplete endcapping. Furthermore, the nonfunctionalized P3HT could be removed afterwards via Soxhlet extraction. More critical is the presence of dicapped macroinitiators leading to triblock copolymers, since the separation of triblock and diblock copolymers is not possible by extraction methods. Using the *in situ* endcapping method presented here, the fraction of P3HT with two alkoxyamine groups was small and as will be shown later, the polydispersities of the resulting block copolymers were sufficiently low (1.2–1.5).

Well-defined P3HT macroinitiator (P3HT-MI) was then used to polymerize PerAcr in a second step (Scheme 12.2). Thereby, the segment length of the PPerAcr could be controlled by the reaction time as well as the ratio of [P3HT-MI] to [PerAcr]. Similar reaction conditions applied earlier to polymerizations of PerAcr were successfully used here [49, 52]. The yield of the polymerization was limited by the viscosity of the reaction mixture; the reaction was typically stopped after 30–40% conversion. Purification of the products was simply achieved by soxhlet extraction, thereby removing nonfunctionalized P3HT and monomer PerAcr. Since the P3HT molecular weight is crucial to the performance of OPV blend devices to a large extent [62], P3HT-MI macroinitiators with different molecular weights were synthesized and incorporated into block copolymers with PPerAcr. Thus, five different block copolymers with different segment lengths of P3HT and PPerAcr, hereafter referred to as *BC 16, 17, 21, 25*, and *30*, were synthesized, with the numbers referring to the overall molecular weights of 16.1, 16.9, 20.6, 24.8, and 29.5 kg mol^{-1}, respectively. Figure 12.2 shows the size exclusion chromatograms (SECs), demonstrating the successful block copolymer synthesis. All important parameters of molecular weight, composition, and polydispersity are collected in Table 12.1.

Low polydispersity indices (PDIs) between 1.15 and 1.31 were obtained, and only for PPerAcr weight fractions as high as 80% (BC 25), the PDI increased to 1.53. For the preparation of active layers in bulk heterojuction solar cells, the donor–acceptor

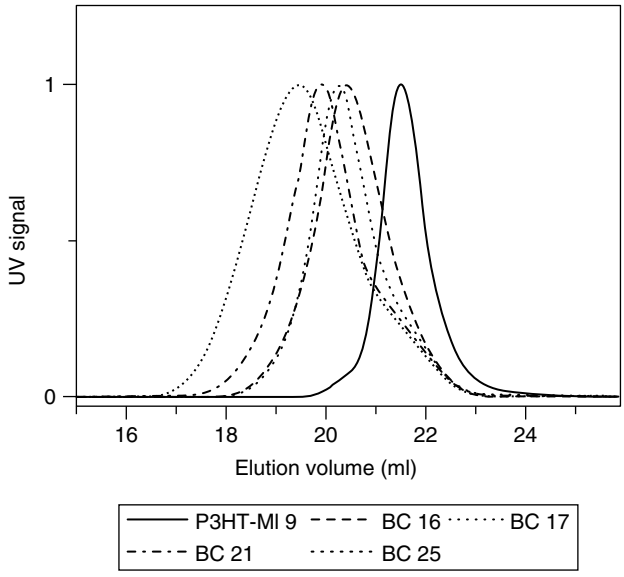

Figure 12.2 Size exclusion chromatography (SEC) of the macroinitiator P3HT-MI 9 and the four block copolymers P3HT-*b*–PPerAcr BC 16, 17, 21, and 25. Curves were measured in THF containing 0.25 wt% tetrabutylammonium bromide (Reproduced with permission from Wiley-VCH Verlag GmbH & Co. KGaA: Sommer, M., Lang, A., and Thelakkat, M. (2008) *Angew. Chem. Int. Ed.*, **47**, 7901.)

Table 12.1 Molecular weights, polydispersity indices, compositions, and thermal properties of homo- and block copolymers.

Polymer	$M_{n,P3HT}$ (kg mol^{-1})	$M_{n,overall}$ (kg mol^{-1})	PDI	PPerAcr (wt%)	T_{m1} (°C)	T_{m2} (°C)	T_{c1} (°C)	T_{c2} (°C)	$\Delta H_{m,P3HT}$ (J g^{-1})
PPerAcr	–	23	1.71	100	191	–	169	–	–
P3HT-MI 9	8.9	–	1.12	0	208	–	180	–	13.1
P3HT-MI 17	17.0	–	1.12	0	223	233	192	–	16.9
BC 16	8.9	16.1	1.25	55.7	190	211	148	162	10.3
BC 17	8.9	16.9	1.24	59.7	191	211	148	163	8.8
BC 21	8.9	20.6	1.31	73.7	202	–	172	–	– [a]
BC 25	8.9	24.8	1.53	81.4	206	–	179	–	– [a]
BC 30	17.0	29.5	1.15	54.9	204	244	178	– [b]	15.4

[a] A single melting peak appeared.
[b] The recrystallization of BC 30 exhibited a peak at 178 °C with a shoulder at ~176 °C.
The molecular weights were determined via SEC using polystyrene calibrations, the compositions via ^{1}H-NMR and the thermal properties were derived from DSC measurements. The melting enthalpies were normalized to their weight fractions.

blend composition commonly lies between 1 : 1 and 1 : 4, depending on the polymer used. The PPerAcr weight fractions in our set of block copolymers exactly matched with these values, spanning the range between ~50 wt% (BC 16, 30) and ~80% (BC 25).

12.2.2 Thermal Properties

The double-crystalline character of P3HT-*b*–PPerAcr was investigated by differential scanning calorimetry (DSC) (Figure 12.3) [60]. P3HT-MI 9 exhibited a melting point (T_m) at 211 °C, whereas the homopolymer PPerAcr melted at 191 °C. In BC 16, the two T_ms observed at 190 and 211 °C were ascribed to melting of PPerAcr and P3HT domains, respectively. The cooling curve of BC 16 showed two exotherms at 162 and 148 °C that are ascribed to the recrystallizations (T_c) of PPerAcr and P3HT, respectively. It is important to note that PPerAcr crystallized prior to P3HT in the series with the lower molecular weight P3HT block P3HT-MI 9. P3HT-MI 17 showed two T_ms at 223 and 233 °C. The observation of a second melting peak probably is due to a smectic liquid-crystalline behavior [63]. BC 30 exhibited two T_ms at 204 and 244 °C in the heating curve, but only one T_c at 178 °C in the cooling curve. This behavior is caused by the higher segment length of P3HT, which shifted the melting and recrystallization temperatures of P3HT toward higher values. As a result, the distance between the two T_ms was larger in BC 30 compared to BC 16, whereas the distance between the two T_cs in BC 16 became smaller with increasing molecular weight of P3HT, and the two peaks

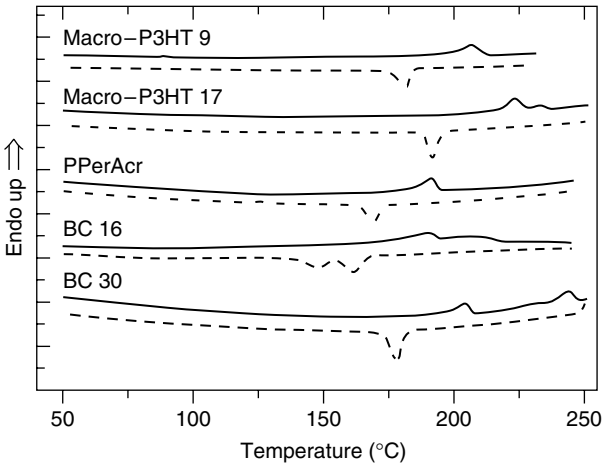

Figure 12.3 Differential scanning calorimetry of P3HT-*b*–PPerAcr, the corresponding PPerAcr homopolymer, and the P3HT-macroinitiators. The second heating (solid line) and the second cooling curve (dashed line) is shown, curves were measured at 10 K min^{-1} under nitrogen, and are offset for clarity.

appeared as one transition in the cooling curve of BC 30. We also note that the degree of P3HT crystallinity was higher in BC 30 compared to BC 16 as indicated by the melting enthalpies ΔH_m of the P3HT melting peak normalized to the weight fraction (Table 12.1). ΔH_m of BC 16 amounted to 10.3 J g^{-1}, whereas 15.4 J g^{-1} were measured in BC 30. This tendency is in line with the melting enthalpy of the P3HT-macroinitiators (ΔH_m macro-P3HT 9 = 13.1 J g^{-1}, ΔH_m macro-P3HT 17 = 16.9 J g^{-1}).

12.2.3 Optical Properties

The solution spectra of PPerAcr exhibited features of aggregated PBI chromophores already in very diluted solutions. This was expected, since the PBI moieties are closely attached in the side chains of a polyacrylate backbone. In tetrahydrofuran (THF) solution, PPerAcr showed three main spectral features at 470, 490, and 525 nm, resulting from the vibronic progressions of Frenkel excitons, but also from intermixed states with charge-transfer excitons (Figure 12.4a). These are a result from the strong operative interactions of the PBI moieties and their coupling of the respective dipole moments. The absorption profile of P3HT in solution is highly dependent on molecular weight, concentration, temperature, and solvent used [64]. Dilute THF solutions of P3HT-MI 9 did not show aggregated species and one broad absorption band peaking at 445 nm was observed. The absorbance spectra of BC 16–25 were a superposition of P3HT and PPerAcr absorption, with

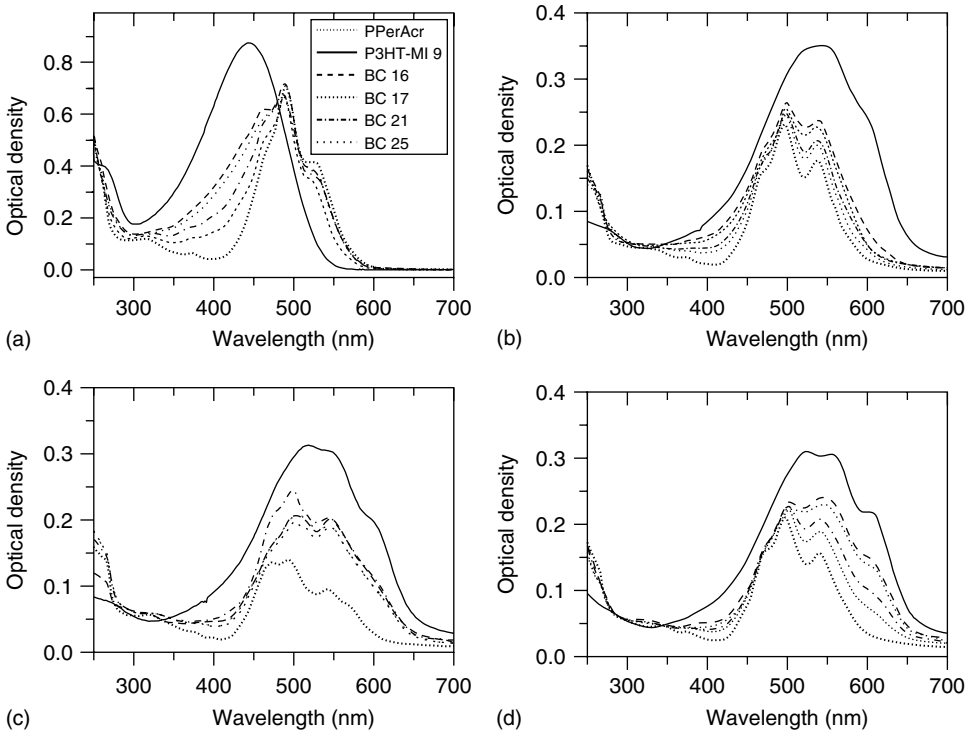

Figure 12.4 Optical densities of homopolymers P3HT-MI 9, PPerAcr, and block copolymers BC 16–25: (a) THF solution (0.02 mg ml^{-1}); (b) films spun from chloroform solutions (~70 nm); (c) films spun from chloroform solutions followed by thermal treatment (30 minutes, 220 °C); (d) films spun from chloroform solutions followed by chloroform vapor annealing. Legend in (a) is same for all plots. Figure 12.4a is reproduced with permission from Wiley-VCH Verlag GmbH & Co. KGaA: Sommer, M., Lang, A., and Thelakkat, M. (2008) *Angew. Chem. Int. Ed.*, **47**, 7901.

contributions of the two segments according to their respective weight fractions [60]. Visually, the color of the solutions shifted from orange to red for increasing degrees of polymerization of PPerAcr (Figure 12.5).

The order of crystallization of P3HT and PPerAcr influenced the optical properties in the solid state. Figure 12.4b displays the absorption profiles of thin films cast from chloroform solutions. The onset of absorption of P3HT-MI 9 redshifted by 100–650 nm. Compared to pristine PPerAcr, the block copolymer absorption was extended into the red as well with increasing P3HT content. The P3HT shoulder at around 600 nm assigned to interchain exciton delocalization [64, 65] was weakly developed in the block copolymer films, indicating low order. The reason for this is that during spin coating the block copolymers from chloroform solution, the P3HT blocks were not given sufficient time to rearrange as the films dry too fast. As reported recently, the intensity of the peak at 600 nm of P3HT films can be correlated to the degree of crystallinity [66].

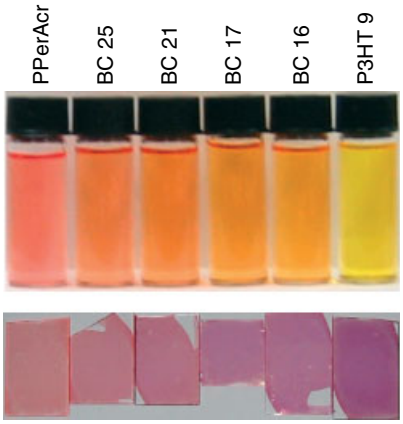

Figure 12.5 Color of homo- and block copolymers. Upper row: Solutions in THF at a concentration of 0.02 mg ml^{-1} (corresponding UV–vis spectra are shown in Figure 12.4a). Lower row: Thin films spun from chloroform and subsequently subjected to chloroform vapor annealing (corresponding UV–vis spectra are shown in Figure 12.4d).

Thermal annealing of the films above the second melting temperature resulted in a small improvement of the vibronic resolution at 600 nm, but these changes were weaker than those after solvent vapor annealing (Figure 12.4c,d). The low degree of P3HT crystallinity in the thermally treated block copolymer films was a logical consequence of the fact that PPerAcr crystallizes first upon cooling. Thus, P3HT has to solidify within the geometric confinement of the already crystallized PPerAcr domain, which typically yields a lower degree of crystallinity compared to the pristine P3HT-MI 9.

The situation changed substantially upon exposing the films to chloroform vapor (Figure 12.4d). In P3HT-MI 9, the shoulder at 600 nm is resolved well (Figure 12.4d) due to rearrangement of P3HT chains during solvent annealing. Rearrangement of P3HT also occurred in all block copolymers, where the absorption profiles now exhibited a clear peak at 600 nm.

In order to investigate the changes in the UV–vis spectra after solvent annealing in more detail, the absorption of pristine P3HT-MI 9 films was tracked *during* the vapor annealing process as a function of chloroform vapor saturation (Figure 12.6a). As the vapor saturation increased, the optical density of the film decreased between 475 and 650 nm, and increased between 300 and 475 nm. The absorption in the high energy region is due to the presence of amorphous or single chains, whereas the absorption in the low energy region arises from aggregate formation. Therefore, with increasing chloroform vapor saturation order and crystallinity decreased for the benefit of the amorphous regions [64]. Quenching the annealing process with nitrogen dried the film, and an enhanced vibronic resolution was observed compared to the film as spun (dotted line in Figure 12.6a).

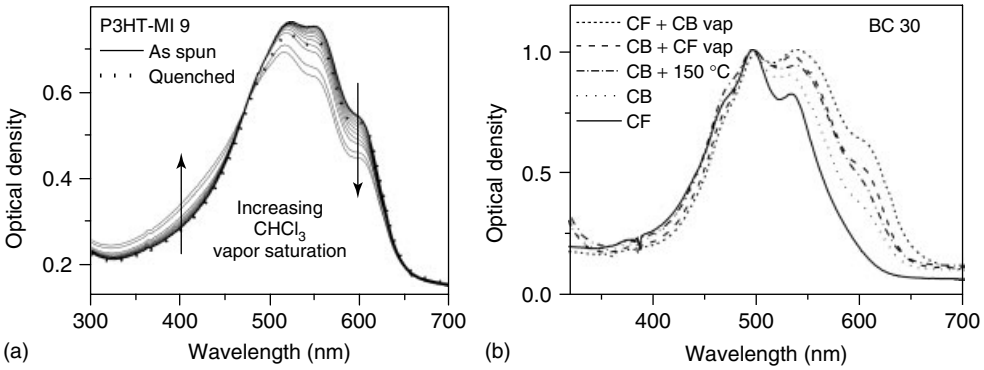

Figure 12.6 (a) Evolution of the absorption profile of P3HT-MI 9 during the chloroform vapor annealing, as a function of vapor saturation. First, P3HT-MI 9 was spun from chloroform (thick solid line). The film was then placed into a chamber and absorption profiles were taken at various chloroform vapor saturations between 10 and 100%. Finally, the chamber was purged with nitrogen (thick dashed line). (b) Optical densities of BC 30 normalized to the peak at 495 nm. The plot showed the effect of the solvent used for spin coating (CF, chloroform; CB, chlorobenzene) and different postannealing treatments on the degree of P3HT crystallinity, as evident from the optical density at 600 nm (150 °C, thermal annealing; CF vap, chloroform vapor annealing; CB vap, chlorobenzene vapor annealing).

We finally investigated the influence of the solvent used for spin coating and different postannealing treatments on the absorption profile of BC 30 (Figure 12.6b). This block copolymer exhibited the same composition as BC 16, but the overall molecular weight was twice as high (Table 12.1). After spin casting BC 30 from chloroform, we found the P3HT crystallinity to be disrupted (solid line). The use of the higher boiling point solvent chlorobenzene (CB) for spin coating–promoted P3HT crystallinity (dotted line), which further increased after thermal annealing the film below the lower T_m (150 °C, 30 minutes, dashed-dotted line). Spin coating from CB followed by chloroform vapor annealing again slightly enhanced the optical density at 610 nm (dashed line). However, the highest degree of P3HT crystallinity of BC 30 among the annealing protocols tested was obtained when treating chloroform cast films with CB vapor (short dashes).

Investigations on the photoluminescence (PL) behavior of P3HT-*b*–PPerAcr is important in order to provide first insights into energy and electron transfer processes. The PL in solution has been investigated in detail [60]. Briefly, the two blocks P3HT and PPerAcr can be excited almost independently at 400 and 530 nm, respectively. Excitation of the block copolymers at 400 nm gave rise to a yellow P3HT fluorescence peaking at 565 nm. Excitation at 530 nm, where P3HT absorbs much weaker than PPerAcr (Figure 12.4a), yielded a red fluorescence of PPerAcr at 622 nm. The PL of PPerAcr in film also occurred at 622 nm and was thus not shifted toward larger wavelengths, as it was observed for low molecular weight PBIs [22]. The PL of all block copolymer films was almost quenched completely,

indicative of electron transfer from P3HT to PPerAcr. Thus, the block copolymers P3HT-*b*–PPerAcr fulfilled another important prerequisite for the application in OPV devices.

12.2.4 Morphology of P3HT-*b*–PPerAcr

Morphological investigations were carried out by scanning electron microscopy (SEM). For a rearrangement of the chains to be induced, the $\pi-\pi$ interactions of both, P3HT as well as PPerAcr need to break up. This can be efficiently done by using chloroform vapor annealing, as deduced from the UV–vis spectra. For these reasons, the samples for morphological investigations were subjected to solvent annealing. Bulk and thin film samples were prepared and imaged using SEM (Figure 12.7). We found excellent contrast between the two blocks, and dark and bright regions are assigned to domains of P3HT and PPerAcr respectively. The same contrast is observed in films of amorphous–crystalline block copolymers comprised of polystyrene and PPerAcr [67]. To illustrate the effect of the covalent attachment of P3HT and PPerAcr on morphology, two SEM images of blend films of P3HT and PBI, are shown in Figure 12.7i,j.

Since the morphologies of thin films and volume samples can differ from each other, they are discussed separately in the following section. The bulk samples (exposed to saturated chloroform vapor during four days) of BC 16 and 17 with PPerAcr weight fractions of 56 and 60 wt%, respectively, (Figure 12.7a,b) show similar micrographs with patterns of mixed bright dots and stripes, reflecting domains of PPerAcr. Most probably, these patterns are due to cylindrical or fiber-like PPerAcr domains in a P3HT matrix, with ~15 nm in diameter and a domain spacing of ~21 nm. The micrographs of BC 21 and 25 with the higher PPerAcr weight fractions of 74 and 81 wt%, respectively, also exhibit bright dots and strips in a darker matrix (Figure 12.7c,d). Again, the bright regions are ascribed to PPerAcr-rich domains. Interestingly, the diameter of the bright, PPerAcr-rich structures remains almost constant compared to Figures 12.7a,b. It is therefore assumed that the dark regions in Figure 12.7c,d are comprised of a mixed phase of P3HT and PPerAcr, in accordance with the results of DSC.

Several annealing procedures were applied to the preparation of the thin film samples. Whereas thermal annealing above the higher T_m of the block copolymers did not produce distinct structural features at the surface, films subjected to chloroform vapor showed good contrast. Longer annealing times led to substantial dewetting of the films. The micrographs of Figures 12.7e–h represent the solvent-annealed films of BC 16–25, respectively. In Figure 12.7e (BC 16), a unique pattern of bright dots in a darker matrix appeared, and BC 17 exhibits dots and elongated structures (Figure 12.7f). This trend continued in Figures 12.7g,h: BC 21 and 25 only showed elongated, fiber-like structures. While there is ambiguity over the extension of these structures into the bulk of the film, we observed a clear correlation between the increasing PPerAcr weight fraction and the decreasing number of dots from Figure 12.7e–h.

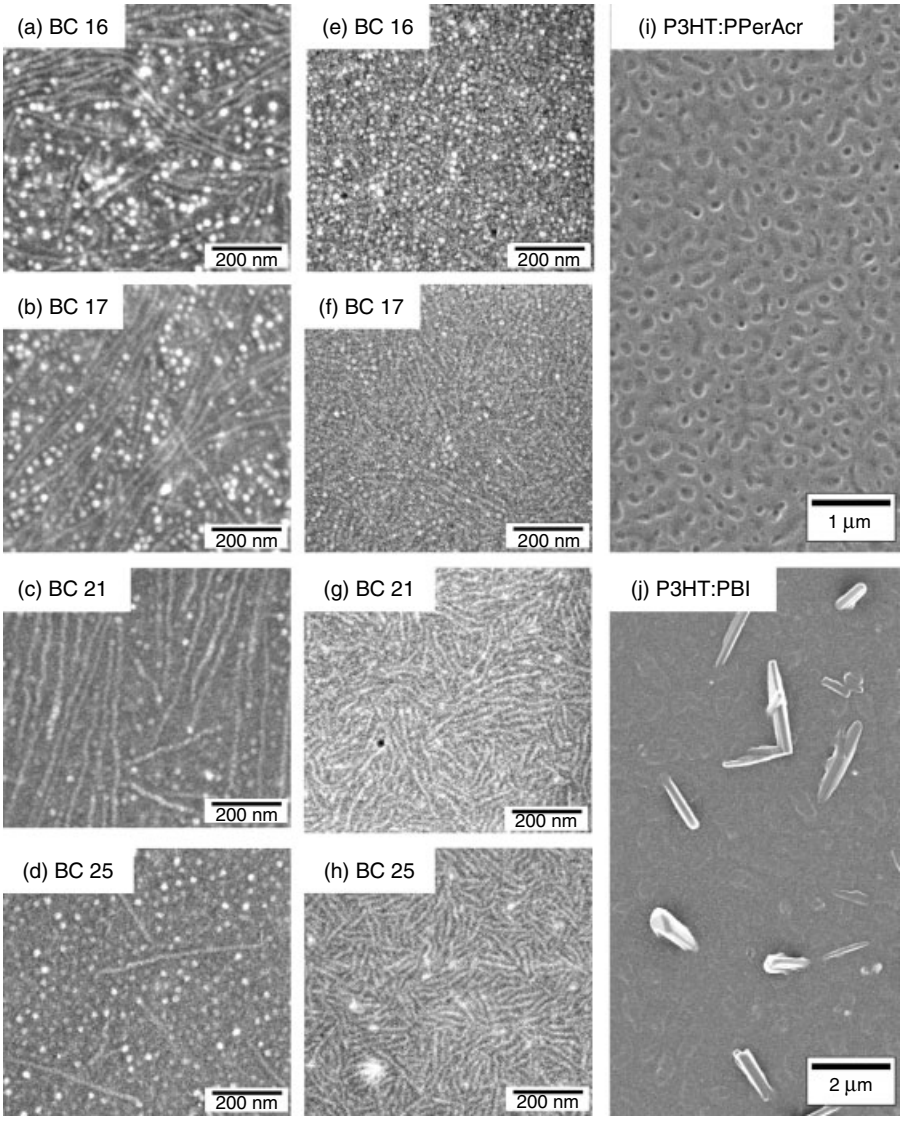

Figure 12.7 Scanning electron micrographs of different P3HT–PBI systems in bulk (drop casting from chlorobenzene) and in film (spin coating from chloroform). Solvent annealing was applied to all samples. (a–d) Bulk samples of BC 16–25, respectively (several microns thick, four days of chloroform vapor annealing). (e–h) Thin films of BC 16–25, respectively (~70 nm, chloroform vapor annealing for 90 minutes). (i) Thin film of a blend P3HT:PPerAcr 40:60 (~150 nm, chloroform vapor annealing for 30 minutes). (j) Thin film of a blend of P3HT and a low molecular weight perylene bisimide (N,N′-di(1-heptyloctyl)perylene-3,4:13,14-tetracarboxdiimide) 50:50 (~150 nm, chloroform vapor annealing for 30 minutes). Note that the scale bars are 200 nm in (a–h), 1 µm in (i), and 2 µm in (j). Bright and dark areas are assigned to perylene bisimide and P3HT, respectively.

These results clearly point out the advantage of the covalent connectivity of P3HT and PPerAcr in terms of a controlled phase separation, since the observed structures are commensurate with the exciton diffusion length. To emphasize this, two polymer blend films comprised of P3HT and PBI were prepared. In Figure 12.7i a polymer–polymer blend consisting of P3HT:PPerAcr 40 : 60 is presented. After solvent annealing for 30 minutes, dark P3HT-rich islands with domain sizes exceeding 100 nm resulted from demixing of the two polymers. Figure 12.7j shows a film comprised of 50% P3HT and 50% of a low molecular weight PBI (N,N′-di(1-heptyloctyl)perylene-3,4 : 13,14-tetracarboxdiimide). Here, diffusion and crystallization of the low molecular weight PBI led to the formation of huge, micrometer long PBI crystals. Both blend film morphologies, the P3HT : PPerAcr blend as well as the P3HT : low molecular weight PBI blend, exhibited features that are too large for photovoltaic applications.

12.2.5
Device Performance of P3HT-*b*–PPerAcr

One major drawback that causes active layer morphologies of blends of donor polymers and PBIs to be ill-defined is the uncontrolled crystallization of PBI and phase separation that has already been mentioned in the last section. Such unfavorable morphologies do not provide sufficient interfacial area of the donor and the acceptor phase which limits charge separation [24, 25]. Consequently, the external quantum efficiencies (EQEs) and device performances are rather low. However, it is not only the uncontrolled crystallization of PBI that leads to poor morphological control and thus limits the device performance. The orientation of the crystals in the film and the relative orientation of PBI moieties toward each other are also very important in order to extract charges efficiently. For example, it has been shown that the angle of the rotational offset of stacked PBIs influences the charge transport properties along the columns [68]. A block copolymer such as P3HT-*b*–PPerAcr addresses these issues since crystallization of PBI can be confined in microdomains. The alignment of the domains might also give rise to alignment of the crystals, and the relative orientation of neighboring chromophores may be tuned by changing the two substituents at the imide positions. Thus, the enhanced morphology control on the one hand, and the advantages of extended absorption and improved hole carrier mobility of P3HT compared to amorphous–crystalline block copolymers on the other hand, render P3HT-*b*–PPerAcr truly promising for the application in photovoltaic devices.

BC 16–25 were tested as active materials in OPV devices using the architecture indium tin-oxide (ITO)/PEDOT : PSS (poly(3,4-ethylenedioxythiophene) poly(styrenesulfonate))/block copolymer/aluminum. The photovoltaic response was investigated by monitoring the EQEs, whereby block copolymers BC 16 and 17 yielded the best device performance. BC 21 and 25 with the higher PPerAcr weight fractions gave lower efficiencies. Therefore, a variety of postannealing procedures was applied to the devices after spin coating BC 16 and 17 from chloroform. As an example, the results of BC 17 are presented in Figure 12.8. The effect of different

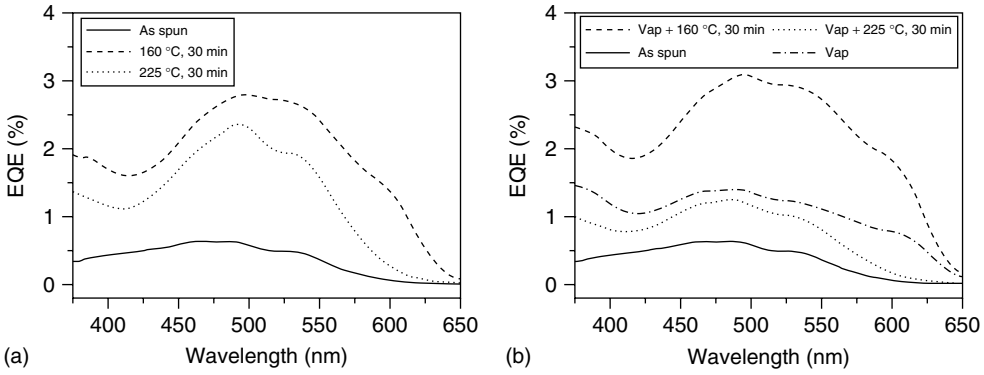

Figure 12.8 External quantum efficiencies of solar cells with BC 17 as the active layer after different annealing conditions. (a) Device performance as spun and after thermal annealing. (b) Device performance as spun and after chloroform vapor annealing (vap) in combination with thermal annealing. Device architecture: ITO/PEDOT:PSS/active layer/aluminum.

thermal treatments on the EQE is presented in Figure 12.8a,b which shows the effect of chloroform vapor annealing with or without additional thermal annealing. The devices were annealed below the lower T_m (160 °C, 30 minutes) and above the higher T_m (225 °C, 30 minutes) (also refer to thermal properties in Figure 12.3a). At 160 °C, the alkyl side chains are in a molten state so that the P3HT backbones can rearrange within the morphology formed after spin coating. At 225 °C, an amorphous melt is present, from which PPerAcr crystallizes first upon cooling.

The maximum EQE value of the device as spun from chloroform is below 1%. Thermal annealing of this device at 160 °C led to a maximum EQE value of 3%. But annealing at a higher temperature of 225 °C decreased this value to 2.5% (Figure 12.8a). Interestingly, the improvement after annealing at 160 °C not only led to higher EQE values, but also extended the spectral response of the block copolymer toward 650 nm. The shape of the EQE spectrum after annealing at 225 °C resembled the PPerAcr homopolymer absorption profile, whereas annealing at 160 °C gave rise to the appearance of the P3HT shoulder at 600 nm. We therefore anticipate that the contribution from P3HT to the photocurrent was low after annealing the device at 225 °C, but much higher after 160 °C. This is consistent with the results obtained from DSC and UV–vis: when the material solidified from its amorphous melt, PPerAcr crystallized first and partially suppressed P3HT aggregate formation, leading to a lower contribution of P3HT to the photocurrent. On the other hand, a postproduction treatment below the melting point of PPerAcr at 160 °C led to a rearrangement of the P3HT chains within the morphology formed after spin coating. As a result, a higher P3HT crystallinity and thus, a higher contribution of P3HT to the photocurrent was observed.

Combining thermal annealing with solvent annealing could further improve the EQE of BC 17 (Figure 12.8b). The direct treatment of the device with chloroform

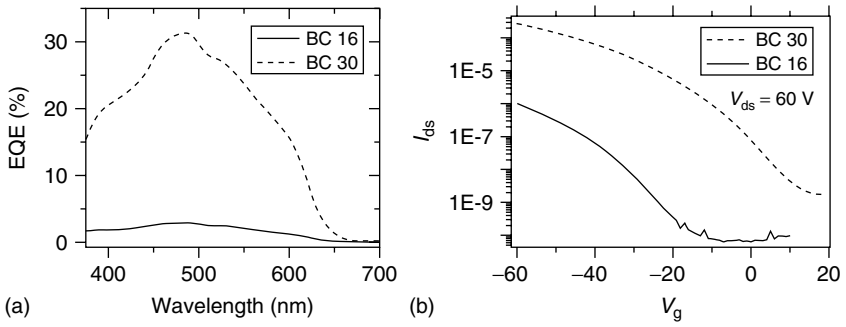

Figure 12.9 (a) External quantum efficiency of BC 16 (solid line) and BC 30 (dashed line). (b) Transfer plots of OFET devices with BC 16 (solid line) and BC 30 (dashed line). The materials were spin coated from chloroform solutions. OFET bottom-gate bottom-contact device architectures were used. (Reprinted with permission from [69]. © (2009), American Institute of Physics).

vapor after spin casting only led to a doubling of the maximum EQE value. Simultaneously, the spectral response was extended to the red, showing increased P3HT contribution to the photocurrent. This was expected since the absorption profile of BC 17 became well-resolved at 600 nm after this type of treatment (refer to Figure 12.4d) and therefore the enhanced absorption of P3HT increased the photocurrent toward 650 nm. Subsequent thermal annealing at 160 °C led to a further doubling of the maximum EQE value to 3% while maintaining the onset of spectral response, whereas subsequent thermal annealing at 225 °C decreased the device performance in terms of the maximum EQE value as well as the onset of the EQE curve. Again, this could be rationalized by the findings from DSC showing that crystallization of PPerAcr led to a reduced P3HT crystallinity.

Note that this argumentation can only qualitatively explain the spectral response from different wavelengths. In general, charge generation and recombination dynamics ultimately determine the device performance. Here, not only crystallinity but also domain size is of importance. Since the domain size is correlated to the segment lengths of the block copolymer, the higher molecular weight of BC 30 should result in larger domains. Figure 12.9 compares the device performance of BC 16 and 30. The D–A composition was equal and their molecular weights were 16.1 and 29.5 kg mol^{-1}, respectively (Table 12.1). The spectral response of BC 16 was similar compared to BC 17. Using CB solutions for active layer preparation led to a similar effect compared to the solvent vapor annealing procedure, including a doubling of the maximum EQE value and extension of the onset to 650 nm. However, spin coating BC 30 from CB led to a maximum EQE value of 31% (Figure 12.9a) [69]. The drastic enhancement is explained by a higher degree of P3HT crystallinity and larger P3HT crystals in BC 30, as indicated by the higher melting enthalpy and higher melting temperature of P3HT (Figure 12.3 and Table 12.1). Since the hole mobility μ_{hole} of P3HT is also a function of its molecular weight [70], one can assume different values of μ in BC 16 and 30. In order to verify this, we measured the charge carrier mobilities of these two block

copolymers in bottom-gate bottom-contact organic field effect transistors (OFETs) (Figure 12.9b). Both block copolymers exhibit p-channel behavior after spin coating from chloroform solutions, and hole carrier mobilities of 10^{-5} and 10^{-3} cm^2 Vs^{-1} were obtained for BC 16 and 30, respectively. Thus, the increase of 2 orders of magnitude in the hole mobility depicted the smaller domain size and the lower degree of P3HT crystallinity in BC 16 compared to BC 30, and was obviously responsible for the huge improvement in device performance. The measured EQEs are the highest reported for block copolymer solar cells [51] and also exceed those reported for blends of P3HT and low molecular weight PBIs showing maximum values of only ~20% [24–27, 47, 71].

While the EQE values of BC 30 are still lower than the ones of state-of-the-art bulk heterojunction blend cells [15], we could show that the morphological issues in blends of donor polymers and low molecular perylene bismides can efficiently be addressed by confining PBI crystallization to microdomains. Further optimization of device production and fine-tuning of the block copolymer molecular weight is under study and is expected to yield higher device efficiencies.

12.3 Conclusions and Perspectives

We have designed, synthesized, and characterized various block copolymers P3HT-*b*–PPerAcr with different compositions and molecular weights for use as active materials in photovoltaic cells. Competing crystallization was elucidated by differential scanning calorimetry, UV–vis spectroscopy, and photocurrent generation. The P3HT crystallinity was found to be hindered with increasing PPerAcr block length, but could be improved when higher molecular weights of P3HT were employed. This improved crystallinity gave rise to higher hole mobilities and high EQEs of 31%. These outstanding results demonstrate that the low device performance of PBI-based solar cells could partially be ascribed to morphological issues, which are efficiently addressed by this block copolymer approach. Further efforts in chemical synthesis and device optimization are needed to improve the overall device performance. In addition, spectroscopic characterization of devices with PBI as the acceptor is essential to characterize fundamental photophysical processes, which are just beginning to be investigated [27].

References

1. Tang, C.W. (1986) *Appl. Phys. Lett.*, **48**, 183.
2. Sariciftci, N.S., Smilowitz, L., Heeger, A.J., and Wudl, F. (1992) *Science*, **258**, 1474.
3. Gregg, B.A. (2003) *J. Phys. Chem. B*, **107**, 4688.
4. Ohkita, H., Cook, S., Astuti, Y., Duffy, W., Tierney, S., Zhang, W., Heeney, M., McCulloch, I., Nelson, J., Bradley, D.D.C., and Durrant, J.R. (2008) *J. Am. Chem. Soc.*, **120**, 3030.
5. Veldman, D., Meskers, S.C.J., and Janssen, R.A.J. (2009) *Adv.*

Funct. Mater. (article ASAP). doi: 10.1002/adfm.200900090.
6. Peumans, P., Uchida, S., and Forrest, S.R. (2003) *Nature*, **425**, 158.
7. Xue, J., Uchida, S., Rand, B.P., and Forrest, S.R. (2005) *Appl. Phys. Lett.*, **86**, 5757.
8. Yu, G., Gao, J., and Hummelen, J.C. (1995) *Science*, **270**, 1789.
9. Shaheen, S.E., Brabec, C.J., Sariciftci, N.S., Padinger, F., Fromherz, T., and Hummelen, J.C. (2001) *Appl. Phys. Lett.*, **78**, 841.
10. Padinger, F., Rittberger, R.S., and Sariciftci, N.S. (2003) *Adv. Funct. Mater.*, **13**, 85.
11. Brabec, C.J., Sariciftci, N.S., and Hummelen, J.C. (2001) *Adv. Funct. Mater.*, **11**, 15.
12. Dennler, G., Scharber, M.C., and Brabec, C.J. (2009) *Adv. Funct. Mater.*, **21**, 1323.
13. Ma, W., Yang, C., Gong, X., Lee, K., and Heeger, A.J. (2005) *Adv. Funct. Mater.*, **15**, 1617.
14. Peet, J., Kim, J.Y., Coates, N.E., Ma, W.L., Moses, D., Heeger, A.J., and Bazan, G.C. (2007) *Nat. Mater.*, **6**, 497.
15. Li, G., Shrotriya, V., Huang, J., Yao, Y., Moriarty, T., Emery, K., and Yang, Y. (2005) *Nat. Mater.*, **4**, 864.
16. Kim, J.-Y., Lee, K., Coates, N.E., Moses, D., Nguyen, T.-Q., Dante, M., and Heeger, A.J. (2007) *Science*, **317**, 222.
17. Wienk, M.M., Turbiez, M., Gilot, J., and Janssen, R.A.J. (2008) *Adv. Mater.*, **20**, 2556.
18. Lenes, M., Wetzelaer, G.-J.A.H., Kooistra, F.B., Veenstra, S.C., Hummelen, J.C., and Blom, P.W.M. (2008) *Adv. Mater.*, **20**, 2116.
19. Ballantyne, A.M., Chen, L., Nelson, J., Bradley, D.D.C., Astuti, Y., Maurano, A., Shuttle, C.G., Durrant, J.R., Heeney, M., Duffy, W., and McCulloch, I. (2007) *Adv. Mater.*, **19**, 4544.
20. Quiles, M.C., Ferenczi, T., Agostinelli, T., Etchegoin, P.G., Kim, Y., Anthopoulos, T.D., Stavrinou, P.N., Bradley, D.D.C., and Nelson, J. (2008) *Nat. Mater.*, **7**, 158.
21. Wicklein, A., Gosh, S., Sommer, M., Würthner, F., and Thelakkat, M. (2009) *ACS Nano*, **3**, 1107.
22. Würthner, F., Chen, Z., Dehm, V., and Stepanenko, V. (2006) *Chem. Commun.*, 1188.
23. Balakrishnan, K., Datar, A., Oitker, R., Chen, H., Zuo, J., and Zang, L. (2005) *J. Am. Chem. Soc.*, **127**, 10496.
24. Dittmer, J.J., Lazzaroni, R., Leclere, P., Moretti, P., Granstrom, M., Petritsch, K., Marseglia, E.A., Friend, R.H., Bredas, J.L., Rost, H., and Holmes, A.B. (2000) *Sol. Energy Mater. Sol. Cells*, **61**, 53.
25. Dittmer, J.J., Marseglia, E.A., and Friend, R.H. (2002) *Adv. Mater.*, **12**, 1270.
26. Shin, W.S., Jeong, H.-H., Kim, M.-K., Jin, S.-H., Kim, M.-R., Lee, J.-K., Lee, J.W., and Gal, Y.-S. (2006) *J. Mater. Chem.*, **16**, 384.
27. Keivanidis, P.E., Howard, I.A., and Friend, R.H. (2008) *Adv. Funct. Mater.*, **18**, 3189.
28. Nishizawa, T., Tajima, K., and Hashimoto, K. (2007) *J. Mater. Chem.*, **17**, 2440.
29. Roncali, J. (2005) *Chem. Soc. Rev.*, **34**, 483.
30. Tan, Z., Hou, J., He, Y., Zhou, E., Yang, C., and Li, Y. (2007) *Macromolecules*, **40**, 1868.
31. Hoppe, H. and Sariciftci, N.S. (2006) *J. Mater. Chem.*, **16**, 45.
32. Campbell, A.R., Hodgkiss, J.M., Westenhoff, S., Howard, I.A., Marsh, R.A., McNeill, C.R., Friend, R.H., and Greenham, N.C. (2008) *Nano Lett.*, **8**, 3942.
33. van Duren, J., Yang, X., Loos, J., Bulle-Lieuwma, C., Sieval, A., Hummelen, J., and Janssen, R. (2004) *Adv. Funct. Mater.*, **14**, 425.
34. Bates, F.S. and Fredrickson, G.H. (1990) *Annu. Rev. Phys. Chem.*, **41**, 525.
35. Buxton, G. and Clarke, N. (2006) *Phys. Rev. B*, **74**, 085207.
36. Kim, S.H., Misner, M.J., and Russell, T.P. (2004) *Adv. Mater*, **16**, 2119.
37. Thurn-Albrecht, T., DeRouchey, J., Russell, T.P., and Jaeger, H.M. (2000) *Macromolecules*, **33**, 3250.
38. Angelescu, D.E., Waller, J.H., Register, R.A., and Chaikin, P.M. (2005) *Adv. Mater.*, **17**, 1878.
39. Crossland, E.J.W., Nedelcu, M., Ducati, C., Ludwigs, S., Hillmyer, M.A.,

Steiner, U., and Snaith, H.J. (2009) *Nano Lett.*, **9**, 2807 (article ASAP). doi: 10.1021/nl800942c

40. Stalmach, U., de Boer, B., Videlot, C., van Hutten, P.F., and Hadziioannou, G. (2000) *J. Am. Chem. Soc.*, **122**, 5464.
41. van der Veen, M.H., de Boer, B., Stalmach, U., van de Wetering, K.I., and Hadziioannou, G. (2004) *Macromolecules*, **37**, 3673.
42. Barrau, S., Heiser, T., Richard, F., Brochon, C., Ngov, C., van de Wetering, K., Hadziioannou, G., Anokhin, D.V., and Ivanov, D.A. (2008) *Macromolecules*, **41**, 2701.
43. Tu, G., Li, H., Forster, M., Heiderhoff, R., Balk, L.J., and Scherf, U. (2006) *Macromolecules*, **39**, 4327.
44. Sivula, K., Ball, Z.T., Watanabe, N., and Frechet, J.M.J. (2006) *Adv. Mater.*, **18**, 206.
45. Sun, S.-S., Zhang, C., Ledbetter, A., Choi, S., Seo, K., Bonner, C.E., Drees, M., and Sariciftci, N.S. (2007) *Appl. Phys. Lett.*, **90**, 043117.
46. Prato, M. (1997) *J. Mater. Chem.*, **7**, 1097.
47. Foster, S., Finlayson, C.E., Keivanidis, P.E., Huang, Y.-S., Hwang, I., Friend, R.H., Otten, M.B.J., Lu, L.-P., Schwartz, E., Nolte, R.J.M., and Rowan, A.E. (2009) *Macromolecules*, **42**, 2023.
48. Lindner, S.M. and Thelakkat, M. (2004) *Macromolecules*, **37**, 8832.
49. Sommer, M. and Thelakkat, M. (2006) *Eur. Phys. J. Appl. Phys.*, **36**, 245.
50. Lindner, S.M., Kaufmann, N., and Thelakkat, M. (2007) *Org. Electron.*, **8**, 69.
51. Lindner, S.M., Hüttner, S., Chiche, A., Thelakkat, M., and Krausch, G. (2006) *Angew. Chem. Int. Ed.*, **45**, 3364.
52. Sommer, M., Lindner, S.M., and Thelakkat, M. (2007) *Adv. Funct. Mater.*, **17**, 1493.
53. Sirringhaus, H., Brown, P.J., Friend, R.H., Nielsen, M.M., Bechgaard, K., Langeveld-Voss, B.M.W., Spiering, A.J.H., Janssen, R.A.J., Meijer, E.W., Herwig, P.T., and de Leeuw, D.M. (1999) *Nature*, **401**, 685.
54. Hüttner, S., Sommer, M., and Thelakkat, M. (2008) *Appl. Phys. Lett.*, **92**, 093302.
55. Liu, J., Sheina, E., Kowalewski, T., and McCullough, R.D. (2002) *Angew. Chem. Int. Ed.*, **41**, 329.
56. Iovu, M.C., Jeffries-EL, M., Sheina, E., Cooper, J.R., and McCullough, R.D. (2005) *Polymer*, **46**, 8582.
57. Iovu, M.C., Craley, C.R., Jeffries-El, M., Krankowski, A.B., Zhang, R., Kowalewski, T., and McCullough, R.D. (2007) *Macromolecules*, **40**, 4733.
58. Zhang, Q., Cirpan, A., Russell, T.P., and Emrick, T. (2009) *Macromolecules*, **42**, 1079.
59. Jeffries-El, M., Sauve, G., and McCullough, R.D. (2004) *Adv. Mater.*, **16**, 1017.
60. Sommer, M., Lang, A., and Thelakkat, M. (2008) *Angew. Chem. Int. Ed.*, **47**, 7901.
61. Liu, J., Loewe, R.S., and McCullough, R.D. (1999) *Macromolecules*, **32**, 5777.
62. Schilinsky, P., Asawapirom, U., Scherf, U., Biele, M., and Brabec, C.J. (2005) *Chem. Mater.*, **17**, 2175.
63. Hugger, S., Thomann, R., Heinzel, T., and Thurn-Albrecht, T. (2004) *Colloid Polym. Sci.*, **282**, 932.
64. Clark, J., Silva, C., Friend, R.H., and Spano, F.C. (2007) *Phys. Rev. Lett.*, **98**, 206406.
65. Österbacka, R., An, C.P., Jiang, X.M., and Vardeny, Z.V. (2000) *Science*, **287**, 839.
66. Zhokhavets, U., Erb, T., Gobsch, G., Al-Ibrahim, M., and Ambacher, O. (2006) *Chem. Phys. Lett.*, **418**, 347.
67. Sommer, M., Hüttner, S., Wunder, S., and Thelakkat, M. (2008) *Adv. Mater.*, **20**, 2523.
68. Marcon, V., Kirkpatrick, J., Pisula, W., and Andrienko, D. (2008) *Phys. Status Solidi B*, **245**, 820.
69. Sommer, M., Hüttner, S., Thelakkat, M. (2009) *Appl. PhyP. Lett.*, **95**, 183308.
70. Kline, R.J., McGehee, M.D., Kadnikova, E.N., Liu, J., Fréchet, J.M.J., and Toney, M.F. (2005) *Macromolecules*, **38**, 3312.
71. Rajaram, S., Armstrong, P.B., Kim, B.J., and Fréchet, J.M.J. (2009) *Chem. Mater.*, **21**, 1775.

13
Switching-on: The Copper Age

Belén Gil and Sylvia M. Draper

13.1
Introduction

At the end of the fifth millennium BC, the climate suddenly cooled and late Neolithic man was forced to find a new raw material for better quality tools. Native copper had been known for the previous 5000 years but its use had been limited to ornaments. It was at this time that the serendipitous smelting of copper ore took place and the production of more effective tools started to transform society. It was the beginning of a new era: the Copper Age.

Presently, mankind finds himself in another period of change. Global warming and the oil-based dependence of society are major issues facing our governments. After more than a century of fossil fuels, the search for new environmentally friendly energy sources has become urgent. Solar energy is one of the more promising options considering the fact that the sun deposits about 120 000 TW of electromagnetic radiation on the surface of the Earth, which is approximately 13 000 times the current total world energy use.

Over the last several decades, chemists and physicists have been working hand-in-hand to provide functional photovoltaic devices. Despite the low efficiency and high cost, these systems seem to offer a real alternative energy source. The main effort has focused on the photochemical and photophysical properties of heavy metal coordination compounds involving Os(II) [1–4], Ir(III) [5], Rh(I) [6–9], or Pt(II) [9–11], because they can act as a chromophore/dye-sensitizer to the semiconductor layer. These materials enable the storage of light and/or electronic information at the molecular level and therefore play a pivotal role in solar-energy conversion.

Polypyridyl ruthenium complexes have received special attention due to their intense luminescence and long-lived electronic excited states [9, 12–18]. However, Ru(II) complexes carry unwanted disadvantages, such as relatively low abundance and high cost, combined with a degree of toxicity. Copper complexes have started to capture the interest of researchers due to their attractive range of properties such as ease of preparation, light absorption in the visible spectrum, intense luminescence, and relatively low cost [19–26]. Just as Neolithic man moved from worked stone to

Ideas in Chemistry and Molecular Sciences: Advances in Nanotechnology, Materials and Devices.
Edited by Bruno Pignataro

ISBN: 978-3-527-32543-6

extracted metal, so has modern man recognized the need to turn from oil and to switch on the Copper Age.

13.2 Optical Properties of Cu(I) Complexes

13.2.1 Overview

The chemical symbol for copper, Cu, originates from the Latin word *cyprium* (later simplified to *cuprum*) meaning ''from the island of Cyprus.'' As one of the few metals to occur naturally as an uncompounded mineral, it was known to some of the oldest civilizations. In its native state, copper is reddish with a bright metallic luster. Together with gold and silver, it is recognized as a coinage metal because of its widespread historical use in stamping coins. Its properties, including high ductility, thermal and electrical conductivity, malleability, and resistance to corrosion, have meant that copper has become a major industrial metal ranking third after iron and aluminum in terms of the quantities consumed.

Copper is a transition metal with a single *4s* electron and a filled *3d* shell. The filled 3*d* shell is much less effective than a noble gas shell in shielding the 4*s* electron from the nuclear charge, so that the first ionization potential of Cu is significant and higher than those of the alkali metal group. Since the 3*d* electrons are also involved in metallic bonding, the heat of sublimation and the melting point of copper are also much higher than those of the alkali metals. These factors are responsible for its noble character [27].

Copper has two active oxidation states Cu(I) and Cu(II). Cu(II) compound with a d^9 electronic configuration have relativity intense colors due to metal-centered (MC) absorption bands. These deactivate via nonradiative pathways and therefore, Cu(II) complexes do not luminesce. Cu(I) complexes with a closed-shell d^{10} configuration do not undergo this deactivation and their optical properties are more interesting. As a consequence, this chapter focuses only on Cu(I) compounds.

Among these Cu(I) compounds, the $[Cu(N^{\wedge}N)_2]^+$ family is the most extensively investigated family, where N^N indicates a chelating diimine ligand (usually phen-based) [19, 25, 26, 28]. In the last years, a number of sophisticated architectures having $[Cu(N^{\wedge}N)_2]^+$ as key building blocks have been prepared, including catenanes [29, 30], rotaxanes [14, 29–35], knots [36, 37], helicates [15, 38], dendrimers [39, 40], racks [13, 41], grids [42], boxes [42], and macrocycles [43]. Some of these exhibit interesting light-induced processes, which are able to trigger motions at the molecular level.

The incorporation of bidentate phosphines in the coordination sphere of these systems has seen heteroleptic complexes $[Cu(N^{\wedge}N)(P^{\wedge}P)]^+$ gain in popularity because of their enhanced optical properties [20, 22–24, 44–66]. More recently, the smart design of new ligands has afforded novel copper-based materials with very promising results. Other Cu(I) compounds such as cuprous halide clusters

[67–77] and polynuclear copper(I) alkynyl clusters [11, 78–83] do not feature in this chapter.

13.2.2
Structural Aspects of the Ground and Excited States

The d^{10} electronic configuration of Cu(I) leads to a symmetric localization of the electronic charge. This situation favors a tetrahedral ligand arrangement in order to locate the coordinative bonds in a manner that minimizes electrostatic repulsions. However, most complexes show distorted tetrahedral geometries due to interactions, such as $\pi \cdots \pi$ stacking [84]. This distortion can be described in terms of *''flattening,'' ''rocking''*, and *''wagging''* and has a major influence on the optical properties of the resulting complex. Kovalevsky and coworkers have demonstrated that, in the solid state, there is a strong dependence of the excited-state lifetimes of $[Cu(N\hat{}N)_2]^+$ complexes on this geometric distortion. Although there are some exceptions, in general, the smaller the distortion from the ideal tetrahedral geometry, the longer the lifetime. Also the emission wavelength of the triplet state tends to red-shift with increasing ground-state distortion [60].

Upon light excitation of copper(I) complexes, the metal-to-ligand charge transfer (MLCT) excited state is populated, and the metal center changes its formal oxidation state from Cu(I) to Cu(II). Structural changes take place, induced as expected, from the structural preferences of Cu(I) (tetrahedral-like) and Cu(II) complexes (square planar-like) in the ground state (see Figure 13.1) [85–89]. In this excited-state with flattened tetrahedral geometry, an additional axial coordination site is exposed for nucleophilic attack (by solvent, counteranion or other Lewis bases present in solution) generating a ''pentacoordinated exciplex'' (see Figure 13.1). In the last decade, much effort has been made to elucidate these processes using a wide range of techniques to aid in understanding and exploiting their potential [60, 90–107]. McMillin and coworkers first reported this type of exciplex quenching [90], and by now, many other studies have confirmed the mechanism for their formation, revealed that they are generated even by very poor donor solvents, such as toluene [91, 92].

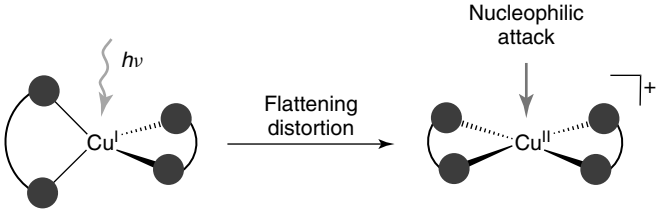

Figure 13.1 Light excitation leads to a flattening distortion of the coordination environment, thus exposing the metal center to nucleophilic attack by external molecules such as solvent or counterions.

The flattening distortion and possible generation of a ''pentacoordinated exciplex'' would seem to make copper complexes unattractive. However, intelligent ligand design limits the formation of exciplexes and increases the luminescence quantum yields and excited lifetime considerably.

13.2.3 Heteroleptic Diimine/Diphosphine $[Cu(N^{\wedge}N)(P^{\wedge}P)]^{+}$ Complexes

One of the biggest family of copper complexes is that of $[Cu(N^{\wedge}N)_2]^{+}$ stoichiometry ($N^{\wedge}N$ = phenanthroline-based ligand system), despite their tendency to display weak emission and short-lived excited states. Some issues have been addressed by the incorporation of bulky substituents into 2 and 9 positions of the phen-based ligands, to preclude the exciplex formation thus, elongating the lifetime of their excited states and increasing their quantum yields [25, 26, 108–113]. However, the most significant impact on the photophysical properties of these $[Cu(N^{\wedge}N)_2]^{+}$ systems was achieved by the inclusion of phosphine ligands by McMillin and coworkers [44, 45]. In these heteroleptic systems $[Cu(N^{\wedge}N)(P^{\wedge}P)]^{+}$, a combination of structural and electronic factors contributes to the remarkable optical properties. They have demonstrated that bulky bidentate phosphines (such as POP = bis[2-(biphenylphosphine)phenyl]ether) inhibit the formation of an exciplex, providing long-lived, and effective green emission compared to the weaker orange emission of the homoleptic complexes [19, 22–26, 46, 51–66]. For example, the compound $[Cu(db\text{-}phen)(dm\text{-}phen)]^{+}$ (db-phen = 2,9-di-tert-butyl-1,10-phenanthroline, dm-phen = 2,9-dimethyl-phenanthroline) presents the highest quantum yield in solution with a relative long lifetime ($\lambda_{em} = 646$ nm, $\phi = 0.01$, $\tau = 730$ ns, oxygen-free CH_2Cl_2) for a Cu-phen-based system, because the bulky *tert*-butyl groups strongly limit the distortion of the excited state [114]. However, the improvement is significant when a diphosphine ligand is included ($[Cu(dp\text{-}phen)(POP)]^{+}$ dp-phen = 2,9-diphenylphenanthroline, $\lambda_{em} = 560$ nm, $\phi = 0.16$, $\tau = 16.1$ μs, oxygen-free CH_2Cl_2, see Table 13.1) [62, 63].

$[Cu(N^{\wedge}N)(P^{\wedge}P)]^{+}$ complexes can absorb throughout the visible region and beyond. The UV portion of the spectra are characterized by the intense ligand-centered (LC) bands typical of the $\pi\pi^*$ transitions of the N-donor and the phosphine ligands [115]. The bands lying in the visible are much weaker than those in the UV and are assigned to MLCT [$Cu \rightarrow \pi^*(N^{\wedge}N)$] transitions [86–89, 108, 116–121]. They occur at relatively low energy because the Cu^{+} ion can be easily oxidized and the diimine ligands possess low-energy empty π^* orbitals [88].

On one hand, the phenanthroline-based ligand play a key role in the absorption of these complexes (also in the luminescence efficiencies and lifetimes), especially the size and electronic character of the substituents in positions 2 and 9 [19, 25].

On the other hand, although not involved in the MLCT transitions ($L = N^{\wedge}N$) the electron withdrawing $P^{\wedge}P$ ligand can serve to shift the MLCT to higher energy than those described for homoleptic analogs [54, 58, 59, 62, 63]. Both steric and electronic properties of the phosphine ligands have and impact on the electronic properties. In the compounds presented in Figure 13.2, the complex with anionic ligand

Table 13.1 Comparative photophysical data of complexes referred to in the text.

			λ_{em} (nm)	τ (μs)
$[Cu(db\text{-}phen)(dm\text{-}phen)]^{+a}$	CH_2Cl_2	298	646 (λ_{exc}450 nm)	0.73
$[Cu(phen')_2]^{+b}$	CH_2Cl_2	298	712	1.20
(Figure 13.3)	MeOH/EtOH	77	692	
$[Cu(pbb)(PPh_3)_2]^{+c}$	DCM	77	553	296(6), 115(5)
(Figure 13.2)	PMMA	298	536	
		77	561	353(1)
$[Cu(pbb)(dppe)]^{+c}$	DCM	77	586	291(8), 106(4)
(Figure 13.2)	PMMA	298	545	
		77	597	503(6), 136(3)
$[Cu(pbb)(POP)]^{+c}$	DCM	77	564	247(6), 106(6)
(Figure 13.2)	PMMA	298	537	
		77	557	322(4), 122(3)
$[Cu(pbb)(DPPMB)]^{c}$	DCM	77	587	315(3), 111(3)
(Figure 13.2)	PMMA	298	593	
		77	603	228.8(7)
$[Cu(db\text{-}phen)(POP)]^{+d}$	Solid	298	554	1.7 (20%), 10.5 (80%)
	CH_2Cl_2	298	554	17.6
		77	510	35.6
$\{Cu(PNP)\}_2^{e}$	Cyclohexane	298	510	10.2
(Figure 13.4a)	THF	298	510	10.9
$[Cu(Bnpa)(PPh_3)_2]^{+f}$	Solid	298	527 (λ_{exc}354 nm)	7.5
(Figure 13.4b)	CH_2Cl_2	298	540 (λ_{exc}354 nm)	8.0
$^{CF3}PNCu(PPh_3)_2{}^{g}$	Solid	298	552, 600 *sh* (λ_{exc}430 nm)	
(Figure 13.4c)		77	505, 550_{max}, 600, 650 *sh* λ_{exc}430 nm)	150
	C_6H_6	298	552 (λ_{exc}444 nm)	

(*continued overleaf*)

Table 13.1 *(continued)*

			λ_{em} (nm)	τ (μs)
$[Cu(dppb)(POP)]^{+}$ [h]	Solid	298	494 (λ_{exc}330 nm)	2.4
	CH_2Cl_2	298	494 (λ_{exc}330 nm)	
		77	454 (λ_{exc}330 nm)	
$[Cu_2(\mu\text{-dppm})_2L_A]^{2+}$	Solid	298	587sh, 635, 660sh (λ_{exc}500 nm)	1.01 (100%) ($\lambda_{exc}460 - \lambda_{em}630$)
		77	670 (λ_{exc}495 nm)	
	CH_2Cl_2	298	670 br (λ_{exc}400 nm)	1.11 (89%), 1.32 (11%)
		77	643, 664_{max} (λ_{exc}500 nm)	($\lambda_{exc}460 - \lambda_{em}630$)
$[Cu_2(\mu\text{-dppm})_2L_B]^{2+}$	Solid	298	642, 666sh (λ_{exc}490 nm)	0.26 (100%) ($\lambda_{exc}460 - \lambda_{em}640$)
		77	681 (λ_{exc}500 nm)	
	CH_2Cl_2	298	675 br (λ_{exc}450 nm)	2.26 (87%), 0.12 (13%)
		77	678 (λ_{exc}450 nm)	($\lambda_{exc}340 - \lambda_{em}400$)
$[Cu_2(\mu\text{-dppm})_2L_C]^{2+}$	Solid	298	676 (λ_{exc}550 nm)	0.61 (100%) ($\lambda_{exc}460 - \lambda_{em}675$)
		77	645 sh, 695 (λ_{exc}495 nm)	
	CH_2Cl_2	298	675_{max} br (λ_{exc}450 nm)	22.83 (85%), 1.01 (15%)
		77	685 (λ_{exc}450 nm)	($\lambda_{exc}460 - \lambda$ em 670)

[a] M. T. Miller, P. K. Gantzel, T. B. Karpishin, *J. Am. Chem. Soc.* 1999, **121**, 4292–4293.
[b] Y. Leydet, D. M. Bassani, G. Jonusauskas, N. D. McClenaghan, *J. Am. Chem. Soc.* 2007, **129**, 8688–8689.
[c] T. McCormick, W.-L. Jia, S. Wang, *Inorg. Chem.*, 2006, **45**, 147–155.
[d] N. Armaroli, G. Accorsi, M. Holler, O. Moudam, J.-F. Nierengarten, Z. Zhou, R. T. Wegh, R. Welter, *Adv. Mater.*, 2006, **18**, 1313–1136.
[e] S. B. Harkins, J. C. Peters, *J. Am. Chem. Soc.*, 2005, **127**, 2030–2031.
[f] S.-B. Zhao, T. McCormick, S. Wang, *Inorg. Chem.*, 2007, **46**, 10965–10967.
[g] A. J. M. Miller, J. L. Dempsey, J. C. Peters, *Inorg. Chem.*, 2007, **46**, 7244–7246.
[h] O. Moudam, A. Kaeser, B. Delavaux-Nicot, C. Duhayon, M. Holler, G. Accorsi, N. Armaroli, I. Séguy, J. Navarro, P. Destruel, J.-F. Nierengarten, *Chem. Commun.*, 2007, 3077–3079.

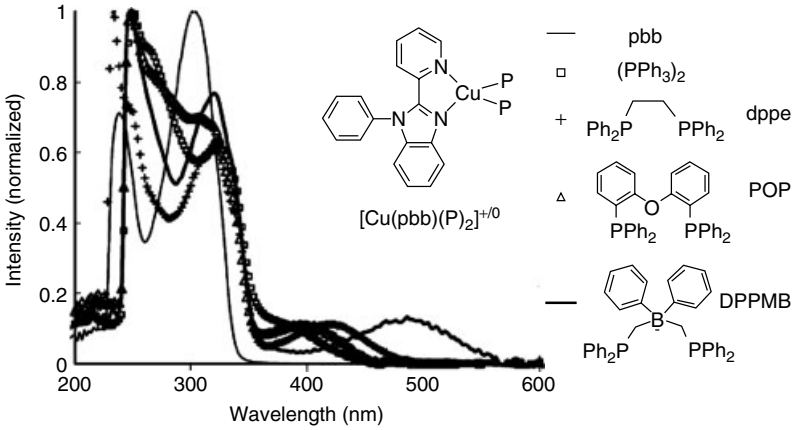

Figure 13.2 Influence of the phosphine ligand in the UV–vis spectra of the compounds $[Cu(pbb)(P)_2]^{+/0}$.

bis(diphenylphosphinomethyl) DPPMB, the strongest electron donor, presents the smallest HOMO-LUMO energy gap. However, for the neutral phosphine ligands (PPh_3, POP, and bis(diphenylphosphino)ethane (dppe)) steric factors are more relevant and the MLCT band shifts to shorter wavelength in the order dppe > POP > PPh_3 (P–Cu–P bond angles 92.02(6)° dppe, 113.35(3)° POP, 124.12(6)° PPh_3).

For these systems, the character of the emissive state as MLCT [Cu → π^*(N^N)] in nature has been established experimentally and theoretically [19, 25, 26, 58, 59, 62, 63]. The luminescence efficiency of the MLCT excited states is clearly solvent and oxygen dependent [45, 95]. The excited-state lifetimes in solution are strongly dependent on the degree of distortion in the excited state and the protection toward exciplex quenching, and this is where these substituents on both, diimines and phosphines play a pivotal role.

Previously reported mixed ligand complexes comprising two triphenylphosphine units gave long-lived luminescence in the solid-state and frozen solution, but showed significant exciplex quenching as room temperature solutions [45, 66, 95]. Diphosphines provide longer lifetimes and higher quantum yields as well as blue-shifted emission compared to phenanthroline-based systems [24, 54, 62].

A significant blue-shift is found on going from room temperature solution samples to a 77-K rigid matrix [54]. This is common behavior for charge transfer emission bands in a rigid medium, but not for $[Cu(N^N)_2]^+$, for which, at 77 K, the emission is red-shifted and less intense in comparison with room temperature. To explain this unusual behavior of the homoleptic systems, McMillin has proposed a ''two-state model,'' where two excited states MLCT, a singlet and a related triplet, are in thermal equilibrium. At room temperature, population of the upper-lying ^{1}MLCT level is achieved to some extent. By temperature decrease, such thermal activation is depressed and only the lowest ^{3}MLCT is significantly populated. The radiative constant of the ^{3}MLCT level is much smaller than the ^{1}MLCT one,

and thus nonradiative processes are comparably more important giving a weaker emission. However, this so-called two-level model does not hold for compounds with phosphine ligands [101, 103].

13.2.4
Alternative N,P-Ligands Types to Enhance Properties Photophysical

Many efforts have been made in this area in recent years with promising results, making these systems potentially attractive for optoelectronic devices such as OLED stacks [22–24, 53], light-emitting electrochemical cell (CELL) [122, 123], or dye-sensitized solar cells [121, 124]. They exhibit good current-to-light efficiency and even color tuning; however, the device lifetime is still an issue. To overcome this problem, careful ligand design has become an essential part of complex formation.

In this line, McClenaghan and coworkers prolonged the lifetimes of copper complexes, using a methodology previously adopted in some ruthenium derivatives, that is, of appending an organic chomophore in the 2,9-phen positions (see Figure 13.3 and Table 13.1) [120]. The double dynamic excited-state equilibration between three different excited states permits the temporary storage of energy on the organic auxiliary before being relayed to the emissive center, extending the lifetime from 70 to 1200 ns, the longest reported to date for Cu-phen-based systems.

In Figure 13.4a, a neutral amido-bridged bimetallic copper system $\{(PNP)Cu\}_2$ ($[PNP]^-$ = bis(2-(diisobutylphosphine)phenyl)amide) is shown [125]. This compound presents a Cu_2N_2 diamond core where the copper centers are in a quite distorted tetrahedral geometry and well protected by the bulky PNP ligand. This, in addition to the absence of a net cationic charge for the complex, renders very interesting optical properties with a high quantum yield, even in polar solvent as THF, and relative long excited-state lifetime ($\lambda_{em} = 510$ nm, $\phi = 0.68$, $\tau = 10.2$ µs, THF, Table 13.1).

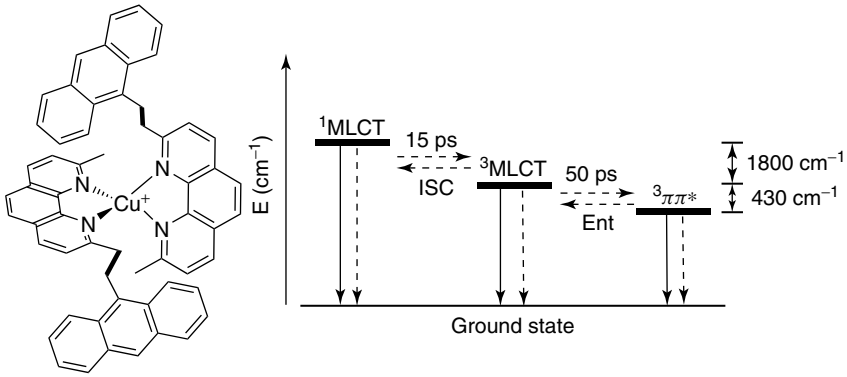

Figure 13.3 Bichromophoric copper(I) complex and its qualitative energy diagram showing pertinent low-lying excited states and notably the interaction of the three lowest lying excited states.

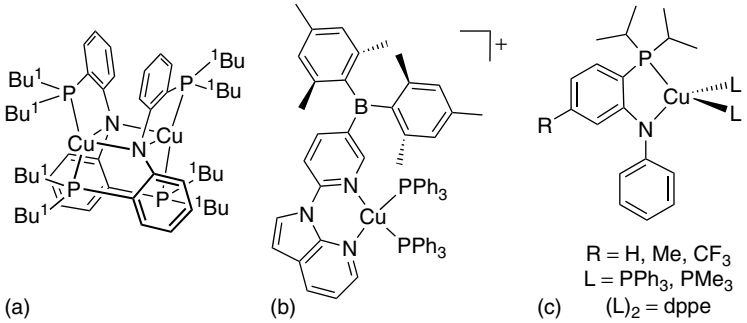

Figure 13.4 Molecular structures of copper complexes $\{(PNP)Cu\}_2$ described by Peters and coworkers [125], $[Cu(Bnpa)(PPh_3)_2]^+$ described by Wang and coworkers [126] and $PNCu(PPh_3)_2$ described by Miller and coworkers [127].

Another very interesting compound is shown in Figure 13.4b, which displays a bright-yellow–green-phosphorescence ($\lambda_{em} = 527$ nm, $\tau = 7.5$ μs, Table 13.1) at room temperature in the solid state with a relatively long lifetime [128]. The most impressive feature is its solid-state quantum yield ($\phi = 0.88$) which is the highest quantum efficiency described for a Cu(I) complex. The group $BMes_2$ seems to play an important role (because of its electron-accepting nature) in lowering the energy of the MLCT state below that of the LC excited state and thus facilitating the MLCT emission.

Miller and coworkers [127] reported a very promising set of neutral amidophosphine complexes of copper (general type $[^{R}PN]Cu(L)_2$ see Figure 13.4c) with very high quantum yields (ranging $0.16 < \phi < 0.70$) and long lifetimes (16−150 μs, see Table 13.1) in solution at room temperature.

Recently, copper complexes containing only phosphine ligands (such as dppb (1,2-bis(diphenylphosphino)benzene) and POP) have been prepared and exhibit bright luminescence in the solid state as well as in dichloromethane solutions, with relatively high intensity and long lifetime emission (for $[Cu(dppb)(POP)]^+$ in CH_2Cl_2 at 298 K, $\lambda_{em} = 494$ nm, $\tau = 2.4$ μs, $\phi = 0.02$ Table 13.1) [129]. These emissions have been tentatively assigned to MLCT and are substantially influenced by conformational changes from the pseudotetrahedral coordination geometry. The complexes have been employed to fabricate devices that exhibit white luminescence. These facts show that there are easy routes to very simple Cu(I) complexes with potential for luminescence-based applications and devices.

13.3
Old Systems for New Challenges

Looking back, it is clear that the nature, bulk, and rigidity of the diimine ligand play an important role in determining the photophysical properties of resultant

Cu(I) complexes [19, 25, 26]. In this context, bipyridyl or phenanthroline-based ligands have been used. Other aromatic diimines have seen application with photoresponsive metal centers [130, 131] and there is scope to rethink and redesign ligand systems that might be appropriate to extending luminescence lifetimes and quantum yields in Cu(I) systems. A synthetic protocol that can be extended to multiple systems is very attractive and new aromatic ligands generated by Diels–Alder cycloaddition have come to the fore in Ru(II) chemistry [132–134].

There is also the option to increase the number of metal centers or to seek cooperative metal centers in a diimine-based system. Only a few examples of binuclear systems are in the diimine complex literature: these use bipyrimidine [65], 2,5-bis(2-pyridyl)pyrazine ligands [56], or others [57]. A downside encountered is that the potential rigidity is reduced, for example, in a transoid disposition. Rigid systems are needed to prevent the distortion and/or exciplet-quenching of the excited state and thus enhance the optical properties. 2,5-Bis(2-pyridyl)tetrazine can favor the cisoid form and presents very interesting properties, even outside of its novel coordination [135–139]. Tetrazines are precursors via inverse electron demand Diels–Alder reactions to pyridazines and this allows a synthetic procedure for the inclusion of new chromophores [140–142]. With this in mind, we have synthesized the ligands: 3,6-di(2-pyridyl)-4,5-diphenylpyridazine L_A, 3,6-di(2-pyridyl)-4,5-di(4-pyridyl)-pyridazine L_B, and 3,6-di(2-pyridyl)-8,9-diazafluoranthene L_C(Scheme 13.1), two of which have been reported elsewhere (L_A [143], L_C[144]).

The treatment of $[Cu(\mu\text{-dppm})(NO_3)]_2$ (dppm, diphenyldiphosphinemethane) with one equivalent of ligand L_A, L_B, or L_C produces a series of air-stable binuclear cationic complexes $[Cu_2(\mu\text{-dppm})_2\mathbf{L}](NO_3)_2$ (Scheme 13.1) whose structures have been verified by single crystal diffraction. The molecular structure of the cation $[Cu_2(\mu\text{-dppm})_2L_B]^{2+}$ is depicted (Figure 13.5a). The two copper atoms are held by three bridging ligands: two dppm ligands bonded through the P atoms and one bipyridylpyridazine ligand (bppn) acting as a tetradentate bridge via the two nitrogen atoms of the pyridazine and the two pyridine groups. The Cu–Cu

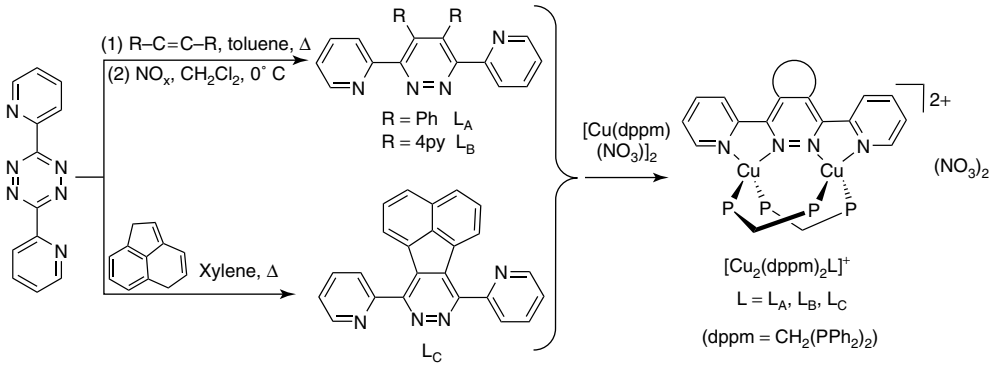

Scheme 13.1

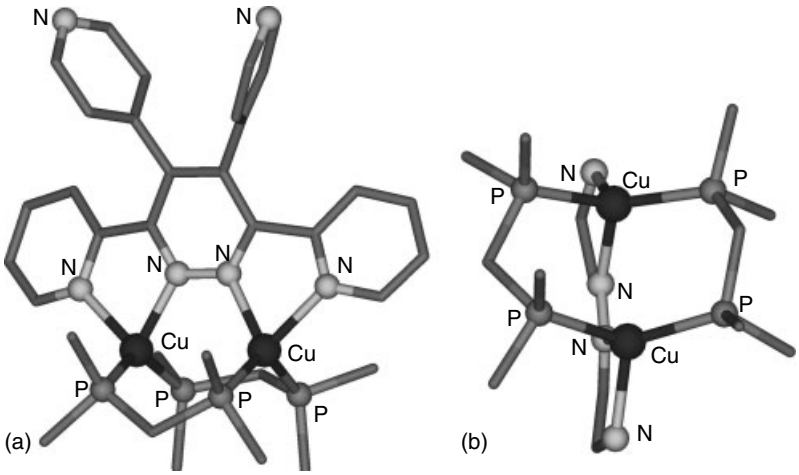

Figure 13.5 (a) View of the structure of $[Cu_2(\mu\text{-dppm})_2L_B]^{2+}$ with the hydrogen atoms and the phenyl rings of the dppm omitted for clarity. (b) The boat-chair conformation of the $[Cu(\mu\text{-dppm})]_2$ ring.

separation (3.404 Å for $[Cu_2(\mu\text{-dppm})_2L_A]^{2+}$, 3.390 Å for $[Cu_2(\mu\text{-dppm})_2L_B]^{2+}$) indicates that the copper atoms are not involved in metal–metal interactions. Both metal atoms are in a distorted tetrahedral arrangement determined by two P and two N atoms (one from the pyridazine, one from a pyridine), with chelating N–Cu–N angles (76.5(2)°, 77.1(2)° for $[Cu_2(\mu\text{-dppm})_2L_A]^{2+}$; 76.75(17)°, 76.19 (17)° for $[Cu_2(\mu\text{-dppm})_2L_B]^{2+}$) that are similar to those found in the literature [138, 139, 145, 146]. The spectroscopic data, NMR and MS spectra, are in agreement with this dinuclear disposition and confirm its presence in solution. The conformation of the two PCuCuP bridges are approximately "eclipsed" (Figure 13.5b), as is shown by $[Cu_2(\mu\text{-dppm})_2(\mu\text{-PPDMe})]^+$ (PPDMe, 3,6-bis(3,5-dimethylpyrazol-1-yl)pyridazine) where the eight-membered $Cu(\mu\text{-dppm})_2Cu$ ring adopts a boat-chair conformation. This eight-membered ring is very rigid and the possible distortion of the copper geometry in the excited state is disabled.

13.3.1 Absorption Spectra

The absorption spectra of the free ligands L_A, L_B, L_C are similar with two absorption bands at 270 and 325 nm, attributed to the $\pi \rightarrow \pi^*$ transition of the bipyridylpyridazine units. In the case of L_C, there is a lower energy band (370 nm) due to the fluoranthene moiety. The absorption spectra of the complexes are similar to those of the ligands but in addition have a weak and broad low-energy shoulder band in the 370–425 nm region (Table 13.2), accounting for the yellow color of the complexes (Figure 13.6). This low-energy transition band is

Table 13.2 Absorption data for the ligands (L_A, L_B, L_C) and the copper complexes ($[Cu_2(\mu\text{-dppm})_2L]^{2+}$) in dichloromethane ($c = 5 \times 10^{-5}$ M).

	$\lambda^a(\varepsilon \times 10^3)^b$
L_A	266 (16.9), 325 (1.2)
L_B	268 (26.9), 329 (0.9)
L_C	271 (28.2), 308 (17.8), 326 (13.2), 370 (13.4)
$[Cu_2(\mu\text{-dppm})_2L_A]^{2+}$	260 (71.6), 328 (21.6), 380 (10.2)
$[Cu_2(\mu\text{-dppm})_2L_B]^{2+}$	274 (76.7), 331 (21.2), 373 (11.7)
$[Cu_2(\mu\text{-dppm})_2L_C]^{2+}$	275 (72.5), 326 (36.0), 374 (32.8), 426 (16.1)

[a] is given in nanometers (nm).
[b] is given in moles per centimeter (M).

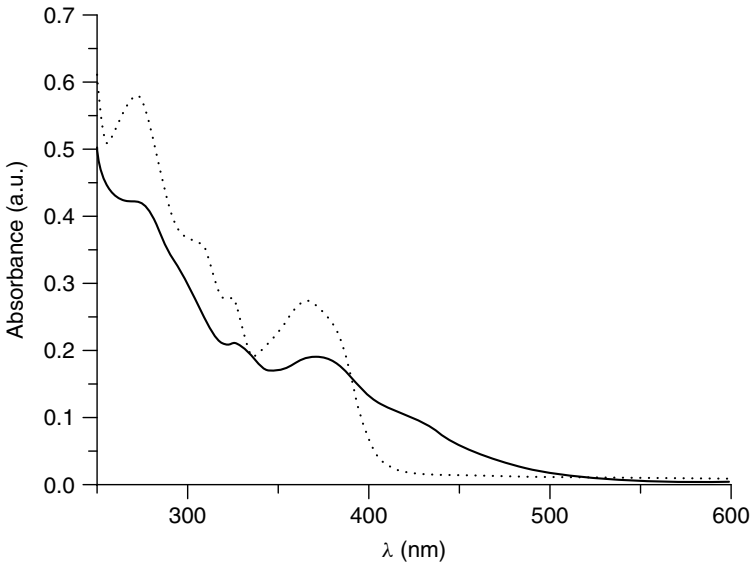

Figure 13.6 UV–vis spectra in dichloromethane of L_C (broken line) and $[Cu_2(\mu\text{-dppm})_2L_C]^{2+}$ (solid line) where the MLCT can be clearly observed.

attributed to MLCT transitions involving the N^N chelate ligand and the Cu(I) ion, although some influence of the phosphine ligand should be considered [19, 26]. In agreement with this MLCT assignment, the low-energy absorption of the $[Cu_2(\mu\text{-dppm})_2L_C]^{2+}$ complex is slightly red-shifted compared to the others, because the diazafluoranthene-containing ligand provides lower energy π^* ligand orbitals.

13.3.2 Luminescence Spectra

These copper complexes are luminescent in the solid state, in solution at room temperature and in frozen solutions at 77 K. Photoluminescence spectra and lifetime data are recorded in Table 13.1.

All the spectra are broad without vibronic progression, suggesting that the emissive excited states have charge transfer character.

In solid state at room temperature, the compounds exhibit a red–orange luminescence, with bands detected in the range 635–676 nm ascribable to deactivations of the MLCT states [19, 23, 25, 26, 44, 45, 61, 66]. In the case of $[Cu_2(\mu\text{-dppm})_2L_A]^{2+}$ ($\lambda_{em} = 635$ nm) and $[Cu_2(\mu\text{-dppm})_2L_B]^{2+}$ ($\lambda_{em} = 642$ nm), the emissions are similar, but for $[Cu_2(\mu\text{-dppm})_2L_C]^{2+}$ ($\lambda_{em} = 676$ nm), the emission is red-shifted due to the presence of the diazafluoranthene, which increases the degree of π-conjugation and thus, stabilizes the π^* of the ligand with concurrent consequences for ^{3}MLCT emissive states.

When cooling the samples ($T = 77$ K), a small red-shift and slightly lower intensity emissions are observed (Table 13.1) in agreement with the presence of a thermal equilibrium between two emissive states ^{1}MLCT and ^{3}MLCT. This behavior concurs with the *odd* trend described previously for very rigid systems, which block the ground-state geometry in a rigid matrix and grant intense red–orange luminescence from the triplet state [19, 101, 103].

For CH_2Cl_2 solutions, the luminescence is quenched almost completely. However, when the samples are thoroughly purged with oxygen through several freeze-thaw-pump cycles under low pressure, an red–orange emission is observed for all the complexes, which is slightly red-shifted with respect to the solid state for $[Cu_2(\mu\text{-dppm})_2L]^{2+}$ (L = L_A, L_B) ($[Cu_2(\mu\text{-dppm})_2L_A]^{2+}$ solid $\lambda_{em} = 635$ nm, CH_2Cl_2 $\lambda_{em} = 670$ nm; $[Cu_2(\mu\text{-dppm})_2L_B]^{2+}$ solid $\lambda_{em} = 642$ nm, CH_2Cl_2 $\lambda_{em} = 675$ nm). These emissions are at similar wavelengths to those found in the literature for related compounds [19, 25, 26].

These complexes show long lifetimes in the microsecond range both in solid state and in solution at room temperature. For $[Cu_2(\mu\text{-dppm})_2\mathbf{L}]^{2+}$ (L = L_A, L_B), the values are very similar being, in both cases, longer in solution than in solid states ($[Cu_2(\mu\text{-dppm})_2L_A]^{2+}$ solid 1.01 μs, CH_2Cl_2 1.11 μs; $[Cu_2(\mu\text{-dppm})_2L_B]^{2+}$ solid 0.26 μs, CH_2Cl_2 2.26 μs). In the solid state, the lifetime of $[Cu_2(\mu\text{-dppm})_2L_C]^{2+}$ is shorter than that observed for the two other compounds (0.61 μs), probably due to the presence of excimers through $\pi \cdots \pi$ interactions of the fluoranthene moieties that could deactivate the excited state. However, in oxygen-free solution, this complex $[Cu_2(\mu\text{-dppm})_2L_C]^{2+}$ has a longer lifetime of 22.83 μs. This value is longer than that previously described by Armaroli for [Cu(POP)(dmdp-phen)]$^+$ (2,9-dimethyl-4,7-diphenylphenanthroline) under the same conditions (17.3 μs in dichloromethane at room temperature) [28, 54] but not as attractive as those of the neutral amidophosphine complexes of copper $[^R$PN]Cu(L)$_2$ reported by Miller and coworkers (16–150 μs) (see Table 13.1) [127].

We believe that the long emission lifetimes of the new $[Cu_2(\mu\text{-dppm})_2\mathbf{L}]^{2+}$ should be attributed to the rigid conformation of the eight-membered ring that precludes the possible distortion of the copper in the excited state and the formation of quenching exciplexes.

13.4 Summary

There are many and multiple diimine-based ligand designs that could be used to improve the current lifetimes, intensities, and emission quantum yields of Cu(I) complexes. The key features to influence are the geometry of the metal center and the inhibition of exciplex formation via ligand topology, bulk, and rigidity. At this stage, significant efforts have focused on establishing, at a molecular level, the parameters that affect the photophysics observed. Despite reports of copper-based devices that have shown promising results, device stability, and light output are still issues that need to be addressed in order to fully exploit these low-cost systems.

References

1. Kumaresan, D., Shankar, K., Vaidya, S., and Schmehl, R.H. (2007) *Top. Curr. Chem.*, **281**, 101–142.
2. Kober, E.M., Caspar, J.V., Lumpkin, R.S., and Meyer, T.J. (1986) *J. Phys. Chem.*, **90**, 3722–3734.
3. Maubert, B., McClenaghan, N.D., Indelli, M.T., and Campagna, S. (2003) *J. Phys. Chem.*, **107**, 447–455.
4. Carlson, B., Phelan, G.D., Kaminsky, W., Dalton, L., Jiang, X., Liu, S., and Jen, A.K.Y. (2002) *J. Am. Chem. Soc.*, **124**, 14162–14172.
5. Flamigni, L., Barbieri, A., Sabatini, C., Ventura, B., and Barigelletti, F. (2007) *Top. Curr. Chem.*, **281**, 143–203.
6. Indelli, M.T., Chiorboli, C., and Scandola, F. (2007) *Top. Curr. Chem.*, **280**, 215–255.
7. Lowry, M.S. and Bernhard, S. (2006) *Chem. Eur. J.*, **12**, 7970–7977.
8. Jiang, C., Yang, W., Peng, J., Xiao, S., and Cao, Y. (2004) *Adv. Mater.*, **16**, 537–541.
9. Chou, P.-T. and Chi, Y. (2007) *Chem. Eur. J.*, **13**, 380–395.
10. Williams, J.A.G. (2007) *Top. Curr. Chem.*, **281**, 205–268.
11. Yam, V.W.-W., Kam-Wing Lo, K., and Man-Chung Wong, K. (1999) *J. Organomet. Chem.*, **578**, 3–30.
12. Bolink, H.J., Cappelli, L., Coronado, E., and Gavina, P. (2005) *Inorg. Chem.*, **44**, 5966–5968.
13. Vos, J.G. and Kelly, J.M. (2006) *Dalton Trans.*, 4869–4883.
14. Bonnet, S., Collin, J.-P., Koizumi, M., Mobian, P., and Sauvage, J.-P. (2006) *Adv. Mater.*, **18**, 1239–1250.
15. Clifford, J.N., Accorsi, G., Cardinali, F., Nierengarten, J.-F., and Armaroli, N. (2006) *C. R. Chim.*, **9**, 1005–1013.
16. Juris, A., Balzani, V., Barigelletti, F., Campagna, S., Belser, P., and Von Zelewsky, A. (1988) *Coord. Chem. Rev.*, **84**, 85–277.
17. Campagna, S., Puntoriero, F., Nastasi, F., Bergamini, G., and Balzani, V. (2007) *Top. Curr. Chem.*, **280**, 117–214.
18. Leydet, Y., Romero-Salguero, F.J., Jimenez-Sanchidrian, C., Bassani, D.M., and McClenaghan, N.D. (2007) *Inorg. Chim. Acta*, **360**, 987–994.
19. Armaroli, N., Accorsi, G., Cardinali, F., and Listorti, A. (2007) *Top. Curr. Chem.*, **280**, 69–115.

20. Xia, H., He, L., Zhang, M., Zeng, M., Wang, X., Lu, D., and Ma, Y. (2007) *Opt. Mater.*, **29**, 667–671.
21. Ma, Y., Zhou, X., Shen, J., Chao, H.-Y., and Che, C.-M. (1999) *Appl. Phys. Lett.*, **74**, 1361–1363.
22. Zhang, Q., Zhou, Q., Cheng, Y., Wang, L., Ma, D., Jing, X., and Wang, F. (2006) *Adv. Funct. Mater.*, **16**, 1203–1208.
23. Zhang, Q., Zhou, Q., Cheng, Y., Wang, L., Ma, D., Jing, X., and Wang, F. (2004) *Adv. Mater.*, **16**, 432–436.
24. Zhang, Q., Ding, J., Cheng, Y., Wang, L., Xie, Z., Jing, X., and Wang, F. (2007) *Adv. Funct. Mater.*, **17**, 2983–2990.
25. Armaroli, N. (2001) *Chem. Soc. Rev.*, **30**, 113–124.
26. Lavie-Cambot, A., Cantuel, M., Leydet, Y., Jonusauskas, G., Bassani, D.M., and McClenaghan, N.D. (2008) *Coord. Chem. Rev.*, **252**, 2572–2584.
27. Cotton, F.A., Wilkinson, G., and Gaus, P.L. (1995) *Basic Inorganic Chemistry*, 3rd edn., John Wiley & Sons.
28. Barbieri, A., Accorsi, G., and Armaroli, N. (2008) *Chem. Commun.*, 2185–2193.
29. Sauvage, J.-P. (2005) *Chem. Commun.*, 1507–1510.
30. Sauvage, J.-P. (1998) *Acc. Chem. Res.*, **31**, 611–619.
31. Flamigni, L., Heitz, V., and Sauvage, J.-P. (2006) *Struct. Bond.*, **121**, 217–261.
32. Kraus, T., Budesinksy, M., Cvacka, J., and Sauvage, J.-P. (2006) *Angew. Chem. Int. Ed.*, **45**, 258–261.
33. Sandanayaka, A.S.D., Watanabe, N., Ikeshita, K.-I., Araki, Y., Kihara, N., Furusho, Y., Ito, O., and Takata, T. (2005) *J. Phys. Chem. B*, **109**, 2516–2525.
34. Li, K., Bracher, P.J., Guldi, D.M., Herranz, M.A., Echegoyen, L., and Schuster, D.I. (2004) *J. Am. Chem. Soc.*, **126**, 9156–9157.
35. Collin, J.-P., Durola, F., Mobian, P., and Sauvage, J.-P. (2007) *Eur. J. Inorg. Chem.*, **17**, 2420–2425.
36. Perret-Aebi, L.-E., von Zelewsky, A., Dietrich-Buchecker, C., and Sauvage, J.-P. (2004) *Angew. Chem. Int. Ed.*, **43**, 4482–4485.
37. Meskers, S.C.J., Dekkers, H.P.J.M., Rapenne, G., and Sauvage, J.-P. (2000) *Chem. Eur. J.*, **6**, 2129–2134.
38. Schultz, D. and Nitschke, J.R. (2006) *J. Am. Chem. Soc.*, **128**, 9887–9892.
39. Gumienna-Kontecka, E., Rio, Y., Bourgogne, C., Elhabiri, M., Louis, R., Albrecht-Gary, A.-M., and Nierengarten, J.-F. (2004) *Inorg. Chem.*, **43**, 3200–3209.
40. Nierengarten, J.-F., Felder, D., Gallani, J.-L., Guillon, D., Nicoud, J.-F., Armaroli, N., Marconi, G., Vicinelli, V., Boudon, C., Gisselbrecht, J.-P., Gross, M., Nierengarten, H., Leize, E., and Van Dorsselaer, A. (2000) *Proc. Electrochem. Soc.*, **2000**, 28–44.
41. Kalsani, V., Bodenstedt, H., Fenske, D., and Schmittel, M. (2005) *Eur. J. Inorg. Chem.*, **10**, 1841–1849.
42. Schmittel, M., Kalsani, V., Fenske, D., and Wiegrefe, A. (2004) *Chem. Commun.*, 490–491.
43. Kalsani, V., Ammon, H., Jaeckel, F., Rabe, J.P., and Schmittel, M. (2004) *Chem. Eur. J.*, **10**, 5481–5492.
44. Buckner, M.T. and McMillin, D.R. (1978) *J. Chem. Soc., Chem. Commun.*, 759–761.
45. Rader, R.A., McMillin, D.R., Buckner, M.T., Matthews, T.G., Casadonte, D.J., Lengel, R.K., Whittaker, S.B., Darmon, L.M., and Lytle, F.E. (1981) *J. Am. Chem. Soc.*, **103**, 5906–5912.
46. Listorti, A., Accorsi, G., Rio, Y., Armaroli, N., Moudam, O., Gégout, A., Delavaux-Nicot, B., Holler, M., and Nierengarten, J.-F. (2008) *Inorg. Chem.*, **47**, 6254–6261.
47. Zhang, J.-F., Fu, W.-F., Gan, X., and Chen, J.-H. (2008) *Dalton Trans.*, 3093–3100.
48. Venkateswaran, R., Balakrishna, M.S., Mobin, S.M., and Tuononen, H.M. (2007) *Inorg. Chem.*, **46**, 6535–6541.
49. Teets, T.S., Partyka, D.V., Esswein, A.J., Updegraff, J.B., Zeller, M., Hunter, A.D., and Gray, T.G. (2007) *Inorg. Chem.*, **46**, 6218–6220.

50. Wei, Y.-Q., Wu, K.-C., Zhuang, B.-T., and Zhou, Z.-F. (2006) *J. Coord. Chem.*, **59**, 713–719.

51. McCormick, T., Jia, W.-L., and Wang, S. (2006) *Inorg. Chem.*, **45**, 147–155.

52. Saito, K., Arai, T., Takahashi, N., Tsukuda, T., and Tsubomura, T. (2006) *Dalton Trans.*, 4444–4448.

53. Che, G., Su, Z., Li, W., Chu, B., Li, M., Hu, Z., and Zhang, Z. (2006) *Appl. Phys. Lett.*, **89**, 103511–103513.

54. Armaroli, N., Accorsi, G., Holler, M., Moudam, O., Nierengarten, J.-F., Zhou, Z., Wegh, R.T., and Welter, R. (2006) *Adv. Mater.*, **18**, 1313–1136.

55. Waterland, M.R., Howell, S.L., Gordon, K.C., and Burrell, A.K. (2005) *J. Phys. Chem. A*, **109**, 8826–8833.

56. Tsubomura, T., Enoto, S., Endo, S., Tamane, T., Matsumoto, K., and Tsukuda, T. (2005) *Inorg. Chem.*, **44**, 6373–6378.

57. Jia, W.L., McCormick, T., Tao, Y., Lu, J.-P., and Wang, S. (2005) *Inorg. Chem.*, **44**, 5706–5712.

58. Yang, L., Feng, J.-K., Ren, A.-M., Zhang, M., Ma, Y.-G., and Liu, X.-D. (2005) *Eur. J. Inorg. Chem.*, **10**, 1867–1879.

59. Howell, S.L. and Gordon, K.C. (2004) *J. Phys. Chem. A*, **108**, 2536–2544.

60. Coppens, P., Vorontsov, I.I., Graber, T., Kovalevsky, A.Y., Chen, Y.-S., Wu, G., Gembicky, M., and Novozhilova, I.V. (2004) *J. Am. Chem. Soc.*, **126**, 5980–5959.

61. Tsubomura, T., Takahashi, N., Saito, K., and Tsukuda, T. (2004) *Chem. Lett.*, **33**, 678–679.

62. Cuttell, D.G., Kuang, S.-M., Fanwick, P.E., McMillin, D.R., and Walton, R.A. (2002) *J. Am. Chem. Soc.*, **124**, 6–7.

63. Kuang, S.-M., Cuttell, D.G., McMillin, D.R., Fanwick, P.E., and Walton, R.A. (2002) *Inorg. Chem.*, **41**, 3313–3322.

64. Schwach, M., Hausen, H.-D., and Kaim, W. (1996) *Chem. Eur. J.*, **2**, 446–451.

65. Vogler, C., Hausen, H.-D., Kaim, W., Kohlmunn, S., Krumer, H.E.A., and Rieker, J. (1989) *Angew. Chem. Int. Ed.*, **28**, 1659–1660.

66. Breddels, P.A., Berdowki, P.A.M., Blasse, G., and McMillin, D.R. (1982) *J. Cherm. Soc., Faraday Trans. 2*, **78**, 595–601.

67. Raston, C.L. and White, A.H. (1976) *J. Chem. Soc., Dalton Trans.*, 2153–2156.

68. Vitale, M. and Ford, P.C. (2001) *Coord. Chem. Rev*, **219-221**, 3–16.

69. Hardt, H.D. and Pierre, A. (1973) *Z. Anorg. Allg. Chem.*, **402**, 107–112.

70. Ford, P.C., Cariati, E., and Bourassa, J. (1999) *Chem. Rev.*, **99**, 3625–3647.

71. Kyle, K.R., Ryu, C.K., Ford, P.C., and DiBenedetto, J.A. (1991) *J. Am. Chem. Soc.*, **113**, 2954–2965.

72. Rath, N.P., Holt, E.M., and Tanimura, K. (1986) *J. Chem. Soc., Dalton Trans.*, 2303–2310.

73. Araki, H., Tsuge, K., Sasaki, Y., Ishizaka, S., and Kitamura, N. (2005) *Inorg. Chem.*, **44**, 9667–9675.

74. Cotton, F.A., Feng, X., and Timmons, D.J. (1998) *Inorg. Chem.*, **37**, 4066–4069.

75. Li, M., Li, Z., and Li, D. (2008) *Chem. Commun.*, 3390–3392.

76. Knorr, M., Guyon, F., Khatyr, A., Däschlein, C., Strohmann, C., Aly, S.M., Abd-El-Aziz, A.S., Fortin, D., and Harvey, P.D. (2009) *Dalton Trans.*, 948–955.

77. Gan, X., Fu, W.-F., Lin, Y.-Y., Yuan, M., Che, C.-M., Chi, S.-M., Li, H.-F.J., Chen, J.-H., Chen, Y., and Zhou, Z.-Y. (2008) *Polyhedron*, **27**, 2202–2208.

78. Yam, V.W.-W. (2002) *Acc. Chem. Res.*, **35**, 555–563.

79. Yam, V.W.-W., Choi, S.W.-K., Chang, C.-L., and Cheung, K.-K. (1996) *Chem. Commun.*, 2067–2068.

80. Dias, H.V.R., Diyabalanage, H.V.K., Eldabaja, M.G., Elbjeirami, O., Rawashdeh-Omary, M.A., and Omary, M.A. (2005) *J. Am. Chem. Soc.*, **127**, 7489–7501.

81. Kharenko, O.A., Kennedy, D.C., Demeler, B., Maroney, M.J., and Ogawa, M.Y. (2005) *J. Am. Chem. Soc.*, **127**, 7678–7679.

82. Wei, Q.-H., Yin, G.-Q., Zhang, L.-Y., Shi, L.-X., Mao, Z.-W., and Chen, Z.-N. (2004) *Inorg. Chem.*, **43**, 3484–3491.

83. Baxter, C.W., Higgs, T.C., Jones, A.C., Parsons, S., Bailey, P.J., and Tasker, P.A. (2002) *J. Chem. Soc., Dalton Trans.*, 4395–4401.

84. Miller, M.T., Gantzel, P.K., and Karpishin, T.B. (1998) *Inorg. Chem.*, **37**, 2285–2290.

85. Miller, M.T., Gantzel, P.K., and Karpishin, T.B. (1998) *Angew. Chem. Int. Ed.*, **37**, 1556–1558.

86. Zgierski, M.Z. (2003) *J. Chem. Phys.*, **118**, 4045–4051.

87. McMillin, D.R., Buckner, M.T., and Ahn, B.T. (1977) *Inorg. Chem.*, **16**, 943–945.

88. Federlin, P., Kern, J.M., Rastegar, A., Dietrich-Buchecker, C., Marnot, P.A., and Sauvage, J.P. (1990) *New J. Chem.*, **14**, 9–12.

89. Gordon, K.C. and McGarvey, J.J. (1991) *Inorg. Chem.*, **30**, 2986–2989.

90. Everly, R.M. and McMillin, D.R. (1989) *Photochem. Photobiol.*, **50**, 711–716.

91. Chen, L.X., Jennings, G., Liu, T., Gosztola, D.J., Hessler, J.P., Scaltrito, D.V., and Meyer, G.J. (2002) *J. Am. Chem. Soc.*, **124**, 10861–10867.

92. Chen, L.X., Shaw, G.B., Novozhilova, I., Liu, T., Jennings, G., Attenkofer, K., Meyer, G.J., and Coppens, P. (2003) *J. Am. Chem. Soc.*, **125**, 7022–7034.

93. Palmer, C.E.A., McMillin, D.R., Kirmaier, C., and Holten, D. (1987) *Inorg. Chem.*, **26**, 3167–3170.

94. Stacy, E.M. and McMillin, D.R. (1990) *Inorg. Chem.*, **29**, 393–396.

95. Palmer, C.E.A. and McMillin, D.R. (1987) *Inorg. Chem.*, **26**, 3837–3840.

96. McMillin, D.R., Kirchhoff, J.R., and Goodwin, K.V. (1985) *Coord. Chem. Rev.*, **64**, 83–92.

97. Chen, L.X. (2005) *Annu. Rev. Phys. Chem.*, **56**, 221–254.

98. Chen, L.X. (2004) *Angew. Chem. Int. Ed.*, **43**, 2886–2905.

99. Coppens, P. (2003) *Chem. Commun.*, 1317–1320.

100. Gunaratne, T., Rodgers, M.A.J., Felder, D., Nierengarten, J.-F., Accorsic, G., and Armaroli, N. (2003) *Chem. Commun.*, 3010–3011.

101. Felder, D., Nierengarten, J.-F., Barigelletti, F., Ventura, B., and Armaroli, N. (2001) *J. Am. Chem. Soc.*, **123**, 6291–6299.

102. Cody, J., Dennisson, J., Gilmore, J., Van Derveer, D.G., Henary, M.M., Gabrielli, A., Sherrill, C.D., Zhang, Y., Pan, C.-P., Burda, C., and Fahrni, C.J. (2003) *Inorg. Chem.*, **42**, 4918–4929.

103. Siddique, Z.A., Yamamoto, Y., Ohno, T., and Nozaki, K. (2003) *Inorg. Chem.*, **42**, 6366–6378.

104. Kirchhoff, J.R., Gamache, R.E. Jr., Blaskie, M.W., Paggio, A.A.D., Lengel, R.K., and McMillin, D.R. (1983) *Inorg. Chem.*, **22**, 2380–2384.

105. Robertazzi, A., Magistrato, A., de Hoog, P., Carloni, P., and Reedijk, J. (2007) *Inorg. Chem.*, **46**, 5873–5881.

106. Shaw, G.B., Grant, C.D., Shirota, H., Castner, E.W.Jr., Meyer, G.J., and Chen, L.X. (2007) *J. Am. Chem. Soc.*, **129**, 2147–2160.

107. Iwamura, M., Takeuchi, S., and Tahara, T. (2007) *J. Am. Chem. Soc.*, **129**, 5248–5256.

108. Ichinaga, A.K., Kirchhoff, J.R., McMillin, D.R., Dietrich-Buchecker, C.O., Marnot, P.A., and Sauvage, J.P. (1987) *Inorg. Chem.*, **26**, 4290–4292.

109. Phifer, C.C. and McMillin, D.R. (1986) *Inorg. Chem.*, **25**, 1329–1333.

110. Everly, R.M. and McMillin, D.R. (1991) *J. Phys. Chem.*, **95**, 9071–9075.

111. Cunningham, C.T., Cunningham, K.L.H., Michalec, J.F., and McMillin, D.R. (1999) *Inorg. Chem.*, **38**, 4388–4392.

112. Miller, M.T. and Karpishin, T.B. (1999) *Inorg. Chem.*, **38**, 5246–5249.

113. Miller, M.T., Gantzel, P.K., and Karpishin, T.B. (1999) *Inorg. Chem.*, **38**, 3414–3422.

114. Miller, M.T., Gantzel, P.K., and Karpishin, T.B. (1999) *J. Am. Chem. Soc.*, **121**, 4292–4293.

115. Armaroli, N., De Cola, L., Balzani, V., Sauvage, J.P., Dietrich-Buchecker, C.O., and Kern, J.M. (1992) *J. Chem. Soc., Faraday Trans.*, **88**, 553–556.

116. Scaltrito, D.V., Thompson, D.W., O'Callaghan, J.A., and Meyer, G.J. (2000) *Coord. Chem. Rev.*, **208**, 243–266.

117. Armaroli, N., Rodgers, M.A.J., Ceroni, P., Balzani, V.,

Dietrich-Buchecker, C.O., Kern, J.-M., Bailal, A., and Sauvage, J.-P. (1995) *Chem. Phys. Lett.*, **241**, 555–558.

118. Samia, A.C.S., Cody, J., Fahrni, C.J., and Burda, C. (2004) *J. Phys. Chem.*, **108**, 563–569.

119. Fu, W.-F., Gan, X., Jiao, J., Chen, Y., Yuan, M., Chi, S.-M., Yu, M.-M., and Xiong, S.-X. (2007) *Inorg. Chim. Acta*, **360**, 2758–2766.

120. Leydet, Y., Bassani, D.M., Jonusauskas, G., and McClenaghan, N.D. (2007) *J. Am. Chem. Soc.*, **129**, 8688–8689.

121. Bessho, T., Constable, E.C., Graetzel, M., Redondo, A.H., Housecroft, C.E., Kylberg, W., Nazeeruddin, M.K., Neuburger, M., and Schaffner, S. (2008) *Chem. Commun.*, 3717–3719.

122. Slinker, J.D., Rivnay, J., Moskowitz, J.S., Parker, J.B., Bernhard, S., Abrunac, H.D., and Malliaras, G.G. (2007) *J. Mater. Chem.*, **17**, 2976–2988.

123. Slinker, J., Bernards, D., Houston, P.L., Abruna, H.D., Bernhard, S., and Malliaras, G.G. (2003) *Chem. Commun.*, 2392–2399.

124. Alonso-Vante, N., Nierengarten, J.-F., and Sauvage, J.-P. (1994) *J. Chem. Soc., Dalton Trans.*, 1649–1654.

125. Harkins, S.B. and Peters, J.C. (2005) *J. Am. Chem. Soc.*, **127**, 2030–2031.

126. Wang, Y., Ding, B., Cheng, P., Liao, D.-Z., and Yan, S.-P. (2007) *Inorg. Chem.*, **46**, 2002–2010.

127. Miller, A.J.M., Dempsey, J.L., and Peters, J.C. (2007) *Inorg. Chem.*, **46**, 7244–7246.

128. Zhao, S.-B., McCormick, T., and Wang, S. (2007) *Inorg. Chem.*, **46**, 10965–10967.

129. Moudam, O., Kaeser, A., Delavaux-Nicot, B., Duhayon, C., Holler, M., Accorsi, G., Armaroli, N., Séguy, I., Navarro, J., Destruel, P., and Nierengarten, J.-F. (2007) *Chem. Commun.*, 3077–3079.

130. Ollagnier, C.M.A., Perera, S.D., Fitchett, C.M., and Draper, S.M. (2008) *Dalton Trans.*, 283–290.

131. Draper, S.M., Gregg, D.J., and Madathil, R. (2002) *J. Am. Chem. Soc.*, **124**, 3486–3487.

132. Gregg, D.J., Fichett, C.M., and Draper, S.M. (2006) *Chem. Commun.*, 3090–3092.

133. Gregg, D.J., Ollagnier, C.M.A., Fitchett, C.M., and Draper, S.M. (2006) *Chem. Eur. J.*, **12**, 3043–3052.

134. Gregg, D.J., Bothe, E., Höfer, P., Passaniti, P., and Draper, S.M. (2005) *Inorg. Chem.*, **44**, 5654–5660.

135. Sleiman, H., Baxter, P.N.W., Lehn, J.-M., Airola, K., and Rissanen, K. (1997) *Inorg. Chem.*, **36**, 4734–4742.

136. Schottel, B.L., Chifotides, H.T., Shatruk, M., Chouai, A., Pérez, L.M., Bacsa, J., and Dunbar, K.R. (2006) *J. Am. Chem. Soc.*, **128**, 5895–5912.

137. Denti, G., Sabatino, L., Rosa, G.D., Bartolotta, A., Marco, G.D., Ricevuto, V., and Campagna, S. (1989) *Inorg. Chem.*, **28**, 3309–3313.

138. Youinou, M.-T., Rahmouni, N., Fischer, J., and Osborn, J.A. (1992) *Angew. Chem. Int. Ed.*, **6**, 733–735.

139. Kaim, W. (2002) *Coord. Chem. Rev*, **230**, 127–139.

140. Xie, H., Zu, L., Oueis, H.R., Li, H., Wang, J., and Wang, W. (2008) *Org. Lett.*, **10**, 1923–1926.

141. Geldard, J.F. and Lions, F. (1965) *J. Am. Chem. Soc.*, **30**, 318–334.

142. Boger, D.L., Coleman, R.S., and Panek, J.S. (1985) *J. Org. Chem.*, **50**, 5377–5379.

143. Constable, E.C., Housecroft, C.E., Neuburger, M., Reymann, S., and Schaffner, S. (2008) *Eur. J. Org. Chem.*, **9**, 1597–1607.

144. Sasaki, T., Kanematsu, K., and Hiramatsu, T. (1974) *J. Chem. Soc., Perkin Trans. 1*, 1213–1215.

145. Weissbuch, I., Baxter, P.N.W., Kuzmenko, I., Cohen, H., Cohen, S., Kjaer, K., Howes, P.B., Als-Nielsen, J., Lehn, J.-M., Leiserowitz, L., and Lahav, M. (2000) *Chem. Eur. J.*, **6**, 725–734.

146. Constable, E.C., Housecroft, C.E., Neuburger, M., Reymann, S., and Schaffner, S. (2004) *Chem. Commun.*, 1056–1057.

14
Understanding Single-Molecule Magnets on Surface

Matteo Mannini

14.1
Introduction

The use of single molecules as active units in functional materials and real devices is one of the most appealing areas of research that motivated the intense activity of many materials scientists, chemists, and physicists. One of the best-suited fields for ''molecular'' technology is electronics. The origin of this idea is hard to define but the role of the seminal paper by A. Aviram and M. A. Ratner in 1974, in which they proposed that molecules can be used as rectifiers [1], cannot be underestimated. Another pioneering work related to the use of molecules for the realization of devices was presented a little later by M. Pomerantz and coworkers, who investigated magnetism of one monolayer of molecules deposed by a Langmuir–Blodgett film technique [2]. This was the first attempt to explore one of the limits of magnetic data-storage devices controlling the thickness of the active material down to the molecular scale [3]. The next milestone was the implementation of innovative techniques like scanning tunneling microscopy [4, 5] and single-molecule junction techniques [6] that permit to address directly the single nano-object and to read out its properties. Reading the magnetism of single molecules is still far from a fulfilment, but scanning probe microscopy-related techniques are providing exciting solutions [7–9].

In a more recent paper, Aviram, again, described several classes of molecular candidates for molecular circuitry purposes [10] and with regard to memory units he suggested the use of a specific class of molecules, the single-molecule magnets (SMMs), discovered in Florence 10 years earlier by R. Sessoli and D. Gatteschi. These molecules are characterized by an intrinsic magnetic hysteresis and hence, in principle, can be used to store information [11]. Other exciting features of SMMs are the possibility to exploit their sizable quantum effects [12] in quantum-logic computation [13] and for spin-transport purposes [14]. For these reasons, the discovery of SMMs has been considered a milestone for the physics of the spin [15].

As already suggested by Pomerantz, the organization of molecules in a monolayer can make the addressing of a single-molecular unit feasible, for instance, by

Ideas in Chemistry and Molecular Sciences: Advances in Nanotechnology, Materials and Devices.
Edited by Bruno Pignataro

ISBN: 978-3-527-32543-6

exploiting the outstanding lateral resolution of scanning probe techniques. This chapter describes the efforts that have been made to approach these technological goals by combining surface science and molecular magnetism. In particular, the deposition of molecular nanomagnets is dealt with, and the chemical tools that can be exploited to graft SMM to the substrate are described. The chapter focuses on an advanced synchrotron-based technique, the X-ray magnetic circular dichroism (XMCD), which allows the magnetic characterization of these nanostructured surfaces, determining the cases in which the peculiar magnetic properties of SMMs are preserved and, in principle, exploitable for technological purposes.

14.2 SMM for Dummies

SMMs are among the smallest magnetic structures that can be conceived as they comprise a few magnetic centers, usually coordination compounds of *d*-block transition-metal or rare-earth ions. These molecules are characterized by a large spin ground state and a strong easy axis of magnetic anisotropy. These characteristics determine the occurrence of slow relaxation of the magnetization, and of magnetic hysteresis at low temperature, attributable to molecular properties [16]. In fact, the hysteresis loop recalls the magnetic behavior of bulk ferromagnetic materials, but this is not due to long-range cooperative phenomena, the organic ligands around the core of each molecule efficiently shielding the single units. The coupling between the individual spins in a molecule gives rise to a big resulting spin S, which is split in zero field by crystal-field effects. To observe SMM behavior, the $M_S = \pm S$ levels of the S multiplet must lie lowest, M being the projection of the spin along the anisotropy axis. Each molecule can be represented with a double-well potential scheme, as sketched in Figure 14.1, and magnetization reversal can occur through thermal activation. In addition to this, the discrete spin levels allow also the magnetization to relax by quantum tunneling [17], which enlarges the perspective of technological applicability of SMM to the quantum-logic calculation purposes.

The basic physics of the SMM is bound to the energy barrier related to the double well, which must be as high as possible to observe the magnetic hysteresis at temperatures high enough to be compatible with technological applications. In summary, the recipe for SMM is, in principle, simple: a high-spin ground state of the system (or, more generally, an elevated total magnetic moment) and a strong easy axis magnetic anisotropy.

The archetypal SMM, the Mn12 molecule, fully possesses these features. On the one hand, the ground state is characterized by an $S = 10$ obtained by the coupling of 8 Mn^{III} ions ($S = 2$) with 4 Mn^{IV} ions ($S = 3/2$) via a superexchange interaction transmitted by the bridging oxide ligands (see Figure 14.2a). On the other hand, the axial anisotropy is provided by the Jahn–Teller elongation of the octahedra around Mn^{III} ions, which are essentially collinear in Mn12.

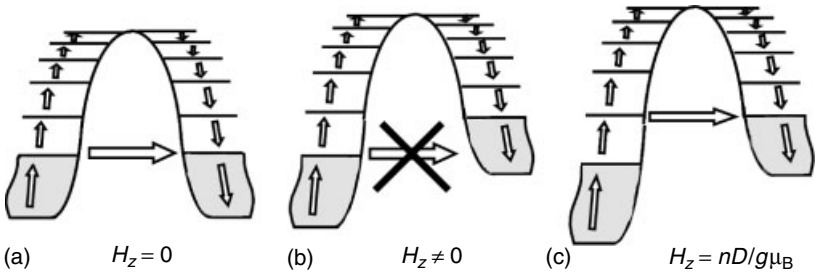

Figure 14.1 Double-well potential model of an SMM. In zero field, states corresponding to opposite projection of the spin along the anisotropy axis, *z*, are degenerate but on opposite sides of the barrier. Magnetization reversal can occur both through climbing the barrier (*thermal activation*) and short cutting it via *quantum tunneling* (a). The latter is efficient between degenerate levels. The application of a longitudinal magnetic field, H_z, removes the degeneracy of the levels in opposite wells thus suppressing the mechanism of resonant quantum tunneling (b), which is, however, reestablished for discrete values of H_z (c).

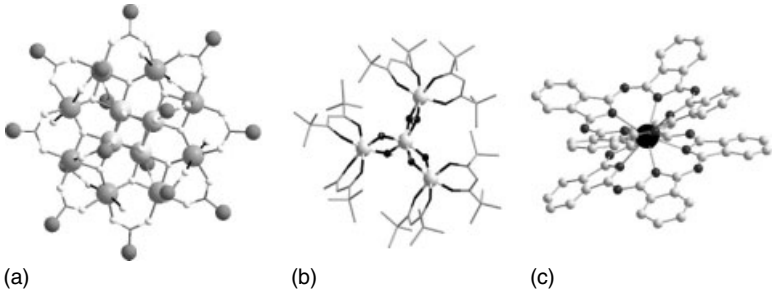

Figure 14.2 Molecular structure of some SMMs: (a) the dodecamanganese(III,IV), Mn12 cluster, intermediate gray spheres indicate functionalizable units while black bonds indicate Jahn–Teller distortion axes; (b) the tetrairon(III), Fe4 cluster, black spheres indicate oxygen atoms of methoxo bridges, linking sites for tripodal ligands replacements; and (c) the lanthanide(III)-based double-decker Ln-DD system.

This "molecular cluster" has been investigated with almost all the accessible experimental techniques of condensed matter physics library and has been used as a playground for the development of a rich chemistry capable of handling and functionalizing these compounds to prepare innovative SMM-based materials [18].

Properties of SMM can be tuned following several different strategies: (i) by building complex structures with a larger number of metal ions to achieve very large spin multiplicity; (ii) by modifying the chemical structure and interactions among metal ions in an existing SMM to magnify the magnetic anisotropy (increasing the zero field splitting); and (iii) by using anisotropic building blocks to take advantage not only of transition-metal but also of rare-earth ions [19, 20].

Following the second strategy, it was possible to improve the magnetic properties of a simpler SMM, the tetrairon(III) Fe4 cluster (Figure 14.2b), in which a high-spin iron(III) is connected to three others joined together by methoxo

bridges that transmit an antiferromagnetic coupling between the inner atom and the external ones (this determines the high-spin ground state $S = 7$) [21]. The improvement in the behavior of this molecule was carried out through the replacement of the methoxo bridges with two tripodal ligands, forcing the molecular core into a more rigid and axially elongated structure that enhances the magnetic anisotropy [22]. The additional advantage of these ligands is their potentiality in introducing further functional groups that are well-suited for direct surface grafting [23].

A parallel development has been followed for Ln-based double-decker compounds (Ln-DD, Figure 14.2c), first of all by demonstrating that SMM behavior can be achieved in a monometallic (Tb^{III}, Dy^{III}, and Ho^{III}) system [24], then demonstrating step by step, how it is possible to enhance their magnetic properties by playing with the oxidation state the two phthalocyanines [25, 26]. This transformation leads to a contraction of the distance within the two phthalocyanines affecting the crystal field parameter of the central rare-earth core. Through these redox modifications it is possible to increase the blocking temperature of the SMM (still to cryogenic temperatures). Ln-DD and multi-center Ln-based SMM are major candidates for the further development of SMM concepts toward higher temperature regimes.

Crucial points currently strongly investigated are also the structural and magnetic stability of the SMMs units as well as their versatility in terms of structural functionalization of the magnetic centers toward the creation of oriented arrays of SMMs acting as molecular memory banks.

14.3
The "Self-Assembling" Concept

The control of molecular organization in regular arrays is not a dream. Several techniques allow the organization of molecules on surfaces exploiting chemical and physical properties of the molecules. The basis of this strategy is the *self-assembly,* a spontaneous process in which components form ordered aggregates without direct human intervention. In a nutshell, this is the extension of the chemical synthesis to a mesoscopic scale and is the domain of weak interactions [27, 28]. *Complementarities in shape or in chemical functionalities* promote the organization determining the structure of the assembly. In addition to this, a key role is played by the intermolecular interactions; these are typically noncovalent, and they allow a *reversibility (or adjustability)* of the assembling process. Self-assembled molecular structures are usually in equilibrium states (or at least in metastable states) thus permitting the self-correction processes that guarantee the long-range ordering of these objects. Energy and boundary conditions required for this self-correction process are provided by the last "ingredient" for the self-assembling, the *environment* through the thermal agitation as well as through the characteristics of the solvent or vacuum (pressure) employed during the process.

Almost all techniques employed to deposit molecules on surfaces follow these general rules. Similar parameters affecting the deposition characteristics can be defined from the ''molecule side'' like the stability in the selected environment (solution, high vacuum, high temperature), the affinity between molecules and with the substrate, and the shape of molecules. On the other hand, from the ''surface side'' important parameters contributing to the organization of molecules are the cleanness of the substrate, its roughness and, related to this, the atomic orientation of the surface that can promote a *templating effect*. Additional important aspects are related to the hydrophobicity of the surface and the temperature at which the deposition is carried out, both capable of promoting specific interaction or hampering good assembling.

In a simplified picture, the different techniques can be classified as *physisorption process,* in which the adsorbate preserves its electronic structure, and *chemisorption process*, in which some modification of electronic levels of the adsorbate occur due to a strong interaction with the surface [29]. This interaction is usually imposed by a specific functionalization of the molecules and is at the basis of the different assembling approaches. Selective interactions between molecules (or molecule functionalizations) and a specific surface are exploited in the *self-assembling of monolayers* (SAMs) approach to grow bidimensional molecular lattices on surfaces from a solution [30]. The introduction of amphiphilic units allows the use of the *Langmuir–Blodgett* approach to grow controlled multilayered structures [31], while by introducing long aliphatic chains, it is possible to promote the ordering of molecules deposited by *drop casting* onto a surface [32]. The fluorination of molecular systems enhances their evaporability, while the contemporaneous evaporation of chemically complementary units allows the *surface-assisted coordination chemistry* [33].

The SAM technique is a ''wet-chemistry'' approach that consists in the exploitation of reversible chemical reaction at the interphase between the solid and solution; it is based on the presence of specific reactants suitable to form covalent bonds within the functional molecule and the surface. The reversibility of the molecule–surface interaction promotes the self-correction that reduces the number of defects. The structure of the employed molecule (see Figure 14.3) is at the basis of this process: the spontaneously occurring interaction between the surface and a *linker* (chemical functionality with a strong affinity for a specific substrate) is strong enough to form either polar covalent or ionic bonds with the surface, while lateral interactions (obtained by a *spacer*) between adjacent molecules permit, if steric hindrance is absent, a real assembly of these molecules in a bidimensional structure. The terminal functional group (*head group*) of a SAMs is generally the active functional part of the nanostructure but also plays a critical role in the assembling and the interfacial properties of the surface. Self-assembly is one of the most versatile approaches allowing also multistep preparations of complex architectures: it permits the stable anchoring of bunglesome molecules as well as the growth of 3D structures.

To conclude, it is then possible to select a specific molecule characterized by a functional property and develop these self-assembling strategies to ''transmit'' this

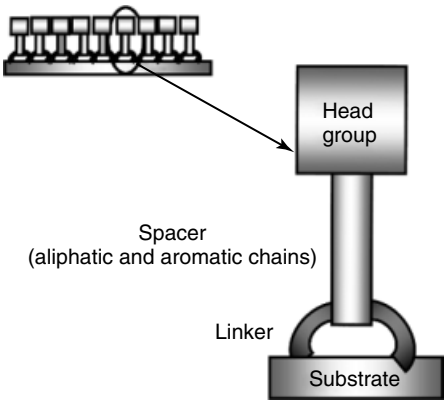

Linker	*Substrate*
–SH –RS–SR –Sac –RSR′ –SCN	Au, Cu, Ag
–OH –NH_2	Pt
–COOH –OPO_3H_2	Al_2O_3 TiO_2 (....)
–$SiCl_3$	SiO_2
–CH_2=CH	Si(–H)

Figure 14.3 (a) Typical scheme of molecules for SAMs. Characteristic components of molecules suitable for self-assembling from solution. (b) The table shows the most typical combinations between linkers and surfaces.

functionality to a nanostructured material. This function can be, for instance, the magnetic bistability of a SMM.

14.4 Deposition of Magnetic Molecules

The deposition of monolayers of magnetic molecules has been performed following several different approaches related directly or indirectly to the SAM method: (i) direct deposition of pristine molecules on native surfaces, taking advantage of unspecific molecule–surface interactions (exploiting both wet approaches as well as ultrahigh vaccum (UHV)-compatible approaches); (ii) direct deposition of derivatized molecules on native surfaces through specific molecule–surface interactions; (iii) surface prefunctionalization with chemical groups that provide specific docking sites for pristine molecules; and (iv) derivatization of both molecules and surface with complementary groups ensuring an efficient grafting via either covalent or noncovalent interactions. These strategies are summarized in Figure 14.4. The first method has been widely employed for structurally simple molecules such as monometallic systems [34]. Wet deposition is carried out either by simply drop casting a very dilute solution on the substrate (followed by solvent evaporation) by dipping the substrate in a dilute solution (followed by careful cleaning with fresh solvent and drying). Slight alterations of molecular structure may allow a better assembling on the surface, like in the case of Cu^{II} phthalocyanines [35] and lanthanides-based double-decker complexes [36] substituted with alkyl chains that promote a bidimensional ordering.

In some cases, similar results are achievable by also exploiting a vacuum sublimation processes, preferable for high-purity material production. This last

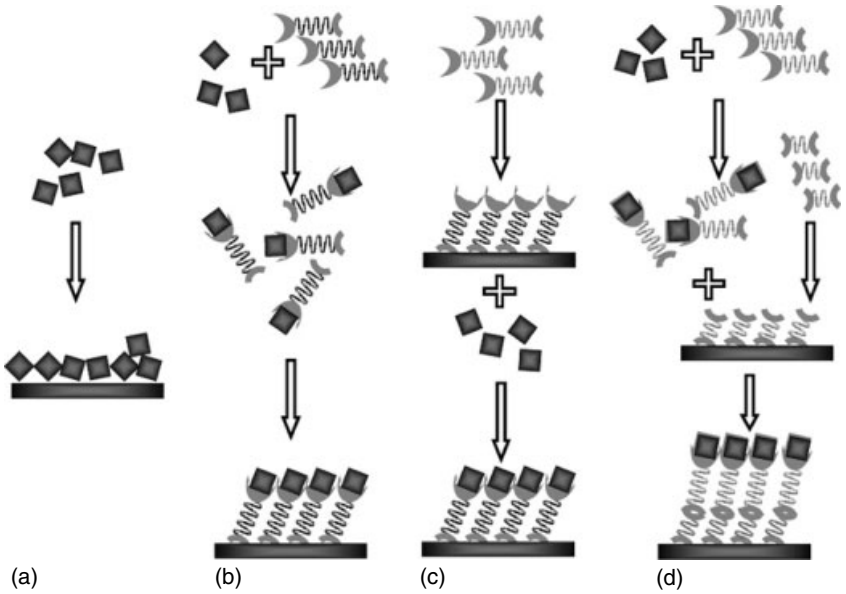

Figure 14.4 Self-assembling approaches for deposition of magnetic molecules: direct deposition of (a) pristine molecules; (b) derivatized molecules; (c) surface prefunctionalization with docking group for molecules; and (d) complementary derivatization of molecules and surface.

approach was considered limited to simple systems, but the horizon was widened with the introduction of the concept of ''surface-assisted coordination chemistry'' [37] (relating to assembling complex molecular structures by starting from the evaporation of their molecular components) and with the evidence that complex magnetic molecules can be also evaporated [38].

On the other hand, wet approaches (b,c,d) consisting of the chemical functionalization of molecules and/or surfaces with specific binding groups have been demonstrated to be better suited for the assembling on surfaces of SMMs. This molecular magnetism itinerary in surface science started with the functionalization of Mn12 molecules with sulfur-based *n*-alkyl ligands that allowed the direct formation of homogeneous layer deposits on top of a gold surface [39] and anticipated by similar attempts carried out exploiting electrostatic interactions as well as the Langmuir–Blodgett approach [40]. These first attempts promoted the deposition of Mn12 on surfaces different from gold, for example, silicon [41]. In fact, while gold surface is preferred both for its physical properties (i.e., the high conductivity) and its chemical advantages (the extreme stability and the easily preparation flat surfaces), silicon is the typical host for microelectronics, thus represents the ideal link between the ''old'' technology and molecular electronics. The use of alternative grafting approaches, including the use of prefunctionalized surfaces, and the subsequent grafting of Mn12 molecules, has been proposed [42, 43] and peculiar

influence of the solvent [44] used in deposition as well as the variation of the grafting group [45, 46] have been explored.

The strategies developed for Mn12 clusters, have been rapidly transferred to other SMMs, for instance [47, 48] the Fe4 SMM previously introduced. Despite its lower blocking temperature, this SMM appears to be better suited for applications associated with organization on surfaces. To reach this conclusion, the following paragraphs explain how the selection of optimal SMMs has been made exploiting the unique capabilities of unconventional chemical and magnetic characterization of monolayers of these magnetic molecules.

14.5
Assessing the Integrity of SMM on Surface

The complexity of molecular magnets is a crucial factor that requires extreme care during the preparation as well as in the identification of specific tools suitable to characterize the functionalized surfaces from both chemical and magnetic points of view. The use of surface techniques is of fundamental importance to confirm, first of all, the presence of objects compatible with the starting bulk material, exploiting, for instance, surface sensitivity of X-ray photoelectron spectroscopy [44, 49, 50] and time-of-flight secondary ion mass spectrometry [51, 52]. These techniques can confirm the presence of intact molecules on surface, but they are limited to the chemical aspects.

Tentatively, the use also of local probes to evidence the intactness of SMMs assembled on surface has been proposed, for instance, by exploiting the spectroscopic capabilities of STM techniques [53]. Nevertheless, these techniques now seem inappropriate to verify the stability of the molecules and to guarantee a high reproducibility of these depositions, mainly because of the absence in the literature of a solid support coming from systematic investigations. In the long term, the local nature of these approaches, coupled to significant improvements in addressing the magnetism of the single objects, will provide a unique tool for addressing magnetic molecules but more fundamental work must be done.

Obviously, the most direct confirmation of the presence of intact magnetic molecules might come from classical magnetic measurements but, except in rare cases as in organic radicals [54], the limited sensitivity of traditional magnetic techniques hampers the detection of the small signals coming from a monolayer of magnetic molecules. Specific powerful tools like a ''nano-SQUID'' a superconducting quantum interference device, based on carbon nanotubes [55], have been recently developed but are not yet operative.

Magneto-optical techniques are known to be very sensitive. They exploit the Faraday rotation of electromagnetic radiation induced by a magnetic field. MCD (visible light-based magnetic circular dichroism) measurements evidenced how magnetic molecules are influenced by the environment in nanostructured phases [56]. A higher sensitivity can be obtained using polarized X-rays: the presence of SMM behavior in molecules grafted to a surface has been demonstrated exploiting

the capabilities of X-ray light available at third-generation synchrotrons [57, 58] and taking advantage of X-ray Absorption Spectroscopy (XAS) and of XMCD [59, 60]. In the following sections we will focus our attention on these techniques.

14.6 X-ray Absorption and Magnetic Dichroism for SMM

The great advance in the use of the XAS technique for SMMs investigation lies, first of all, in the atomic-species selectivity of this technique. Moreover, it provides direct information on the oxidation state of the investigated element, which is useful to confirm the presence of intact species in the same electronic states at surfaces. In addition, the use of a polarized X-ray light by extracting the dichroic contribution allows to gather information on the coupling between spins in molecular systems. This, associated with the element and valence sensitivity of XAS, provides a very useful fingerprint for magnetic materials. Moreover, the dependence of the dichroic signals in soft X-rays on the externally applied magnetic field reflects the magnetic behavior of the molecular compound containing the probed 3D-metal and can be used as a conclusive confirmation of the preservation of the magnetic behavior in materials of very low concentration (as also nanostructured ones).

The X-ray absorption originates from the excitation of electrons from core levels of a selected atom by the absorption of a photon. This absorption probes the electronic structure of the absorber at the orbital levels reached by the excited electron [61]. If circularly polarized X-rays are used in presence of a magnetic field the absorption process depends on the relative orientation of the magnetization of the sample with respect to the propagation vector, **k**, of photons. Considering an electric dipolar approximation, in fact, in the absence of a net magnetic momentum ($M = 0$) in the sample, the absorbance of a polarized light in one helicity (i.e., left-circular light, with a polarization vector $\boldsymbol{\varepsilon}$) and the opposite one (right-circular light, with a polarization vector $\boldsymbol{\varepsilon}^*$) are identical: $\boldsymbol{\sigma}(\boldsymbol{\varepsilon}) = \boldsymbol{\sigma}(\boldsymbol{\varepsilon}^*)$. On the other hand, if a net magnetic moment is present in the investigated sample ($M \neq 0$) the invariance respect to time is lost, then $\boldsymbol{\sigma}(\boldsymbol{\varepsilon}) \neq \boldsymbol{\sigma}(\boldsymbol{\varepsilon}^*)$, and the difference corresponds to the dichroic component of the spectra: $\boldsymbol{\sigma}_{\mathrm{XMCD}} = \boldsymbol{\sigma}(\boldsymbol{\varepsilon}) - \boldsymbol{\sigma}(\boldsymbol{\varepsilon}^*)$. This phenomenon follows an electric dipolar selection rule: $\Delta\ell = \pm 1$; $\Delta s = 0$; $\Delta m_\ell = +1$ (for left-circular light) and $\Delta m_\ell = -1$ (for right-circular light), where ℓ is the orbital kinetic momentum, s is the spin kinetic momentum while m_ℓ is the orbital quantum number. Since σ_{XMCD} is a magnetic signal and the absorption mainly deals with electric dipole transition (where the spin contribution appears) it is not surprising that Thole [62] found that the integral of σ_{XMCD} is proportional to the *orbital magnetic moment*.

In the particular case of transition from 2p ($L_{2,3}$ edges) or 3 d ($M_{4,5}$ edges) core levels, where a strong spin–orbit coupling is present, the dichroism contains also indirect information about the *spin magnetic moment* [63]. In this specific case, that is, the case of a most of SMM (where, in particular, the orbital magnetic moment is close to zero), information about the total magnetic moment can be recovered

from an XMCD set of data, defining also the contribution of orbital and spin moments. This information can be extracted, depending on the case, by exploiting a simple model, that is, the sum rules [62, 63] or by a more complex analysis [64].

The first investigations of an SMM with this technique was performed on bulk Mn12-acetate, recording XAS and XMCD spectra at Mn $L_{2,3}$ edge [65, 66]. Obtained results, supported by crystal-field multiplet calculations [64, 65], confirmed the expected proportions of Mn^{III} and Mn^{IV} ions and, exploiting the XMCD capability, evidenced the ferrimagnetic structure of the molecule in agreement with the expectations [67].

An analogous investigation has been carried out more recently on Mn12-functionalized molecules suitable to be grafted on surfaces. This functionalization consists in the replacement of the external shell of organic ligands of the Mn12 cluster, constituted by acetate anions, with specific carboxylic acids bringing connected sulfur-based anchoring groups suitable for grafting to gold surfaces. Either aliphatic [39] or aromatic functionalities [51] can be added without affecting magnetic properties of the SMM as demonstrated by the XAS and XMCD analysis [68]. This is clearly evident in the case of the results obtained by investigating a drop-cast sample (a thick-film deposit from a solution) of $[Mn_{12}O_{12}(O_2CC_6H_4SCH_3)_{16}(H_2O)_4]$ (see Figure 14.5a).

Following a fingerprint approach, it is possible to demonstrate the presence of the expected relative amount of manganese ions in the two oxidation states with an empirical treatment. It is possible to reproduce the experimental spectra as the linear combination of the XAS and XMCD spectra corresponding to compounds containing Mn ions in the different oxidation states in similar chemical environment. This analysis [68] of the contribution of each species gives the percentage $(\%)^{\alpha}$ of ions in different oxidation states following the general expressions

$$I(E) = \sum_{\alpha} C_{\alpha} I_{\alpha}(E) \text{ and } (\%)^{\alpha} = 100c^{\alpha} / \left(\sum_{i} C_i \right) \tag{14.1}$$

where $I(E)$ is the energy dependent intensity of the experimental XAS spectrum, $I_{\alpha}(E)$, the intensity of each reference compounds containing the Mn ion in the α oxidation state and c_{α} are the normalized coefficients of the linear combination.

It is also possible to treat XMCD spectra following a similar semiquantitative approach. The crucial point is that the experimental spectra will be directly dependent on the percentage of species in different oxidation states but will reflect also the average polarization of the local magnetic moment of each species induced by the applied field. To take into account this factor convolution of XMCD, spectra will be evaluated as

$$S(E) = \sum_{\alpha} c_{\alpha} \delta_{\alpha} S_{\alpha} \tag{14.2}$$

where $S(E)$ is the intensity of the experimental XMCD spectrum, $S_{\alpha}(E)$, the intensity of each reference compound and δ_{α} is a sort of ''magnetic polarization'' (positive if parallel to the field), a qualitative estimation of the relative magnetic alignment of each component.

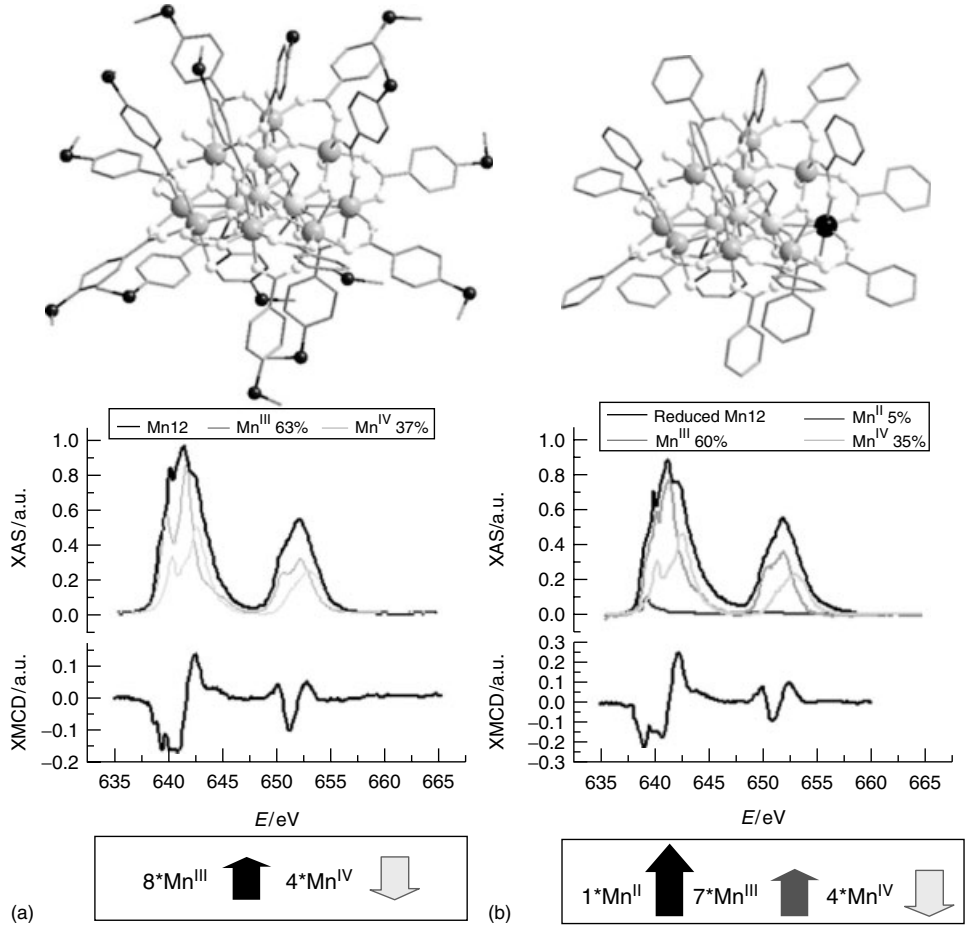

Figure 14.5 Molecular structures and bulk XAS and XMCD investigations of (a) $[Mn_{12}O_{12}(O_2C_6C_4HSCH_3)_{16}(H_2O)_4]$ a sulfur-functionalized Mn12 and (b) $(PPh_4)[Mn_{12}O_{12}(O_2CPh)_{16}(H_2O)_4]$ of a chemically monoreduced Mn12 systems. Partially reproduced with permission from [68]. Copyright 2008 Wiley-VCH.

The expected values for the typical ferrimagnetic structure of Mn12 are completely reproduced by this analysis (at least in a semiqualitative limit imposed by the experimental error limitations). Moreover, the power of this method can be easily verified by synthesizing an analogous of Mn12 partially reduced, presenting one of the eight Mn^{III} ions replaced by a Mn^{II} ion (see Figure 14.5b). In this specific case, the cluster $(PPh_4)[Mn_{12}O_{12}(O_2CPh)_{16}(H_2O)_4]$ was prepared according to the literature [69] and the analysis of the XAS spectra demonstrated the capability of this technique in detecting such small variations; in fact, the ratios Mn^{II} : Mn^{III} : Mn^{IV} (5 : 60 : 35) obtained by deconvolution of the spectra compared quite well

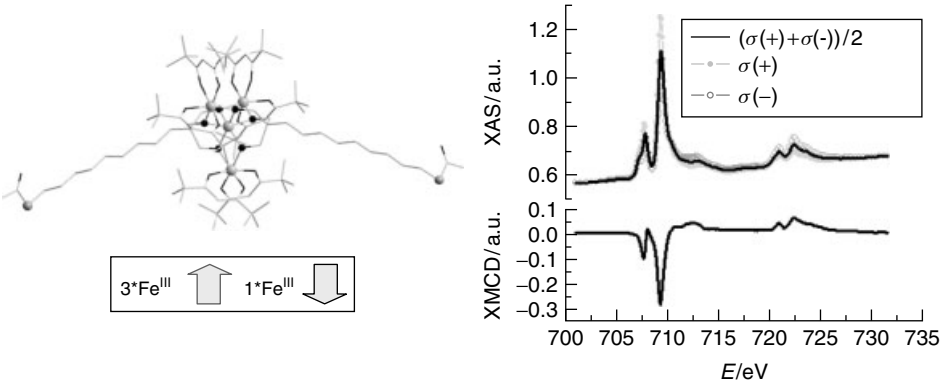

Figure 14.6 Molecular structure and bulk XAS and XMCD investigation of $[Fe_4(L)_2(dpm)_6]$ with H_3L = 11-(acetylthio)-2,2-bis(hydroxymethyl)undecan-1-ol and H*dpm* = dipivaloylmethane. Partially reproduced with permission from [70]. Copyright 2009 Wiley-VCH.

with the expectation (8 : 58 : 33). Also XMCD spectra analysis supported the validity of this method confirming the presence of Mn^{II} ions ferromagnetically coupled with Mn^{III} ions [69].

XAS and XMCD analysis can be carried out also on ''simpler'' systems like the Fe4 cluster. This cluster is formed by four iron(III) ions arranged in a propeller-like structure constituted by a central Fe ion antiferromagnetically coupled with the three external ones. The presence of a unique oxidation state hampers the association of the orientation of the magnetic moment with a specific metal site as in the case of Mn12. In that case, the use of simulation tools becomes necessary to confirm the magnetic structure of the cluster as well as to reproduce, with confidence, fine-structure features in XAS and XMCD spectra. This can be done taking into account the chemical environment of each metallic ion and their coordination geometry [47]. In Figure 14.6, XAS and XMCD investigations are reported for a derivative of Fe4 system suitable for grafting on gold surface [23, 70]. Thanks to the analysis of the dichroic component, it was possible to have a sound confirmation of the expected ferrimagnetic structure of the cluster, as well as to have a well-established fingerprint of the intact cluster for this newer system.

14.7 Electronic Characterization of Monolayer of SMMs

Besides the highly selective information, the uniqueness of XAS/XMCD tools in the investigation of SMM lies in the extreme sensitivity of this technique [71]. In particular, this has been made possible by exploiting the detection mode used in these experiments carried out at very low temperature, namely, the total electron yield mode (TEY) [72, 73], which is sensitive to the first few of nanometers of

a conductive sample. This sensitivity fills the gap between the single-molecule properties of SMMs and the problem of detection of magnetism in small amounts of materials. XAS and XMCD, moreover, can draw a clear picture of the health of the molecules by verifying both their electronic and magnetic state down to the submonolayer level.

The first complete demonstration of these capabilities relative to SMMs has been done by investigating monolayers and submonolayers of Mn12 deposited on gold surfaces exploiting the wet-chemistry approach based on sulfur-functionalized systems [68].

The outcome of this comprehensive characterization vanished, at least partially, the hope of using Mn12 molecules as building blocks of nanostructured arrays on surfaces. In fact, XAS spectra recorded on depositing of the system $[Mn_{12}O_{12}(O_2CC_6H_4SCH_3)_{16}(H_2O)_4]$ (see Figure 14.5) both from tetrahydrofurane (THF) and dichloromethane (CH_2Cl_2) millimolar solutions evidence a strong modification of the average electronic structure of the clusters at the surface. Despite STM images [44, 45] of these deposits (top of Figure 14.7), showing in the direct topography objects with size corresponding to the dimension of Mn12 clusters, an analysis of the XAS spectra carried out following the previously introduced method demonstrates the appearance of a strong contribution from Mn^{II} species [68]. Thanks to experimental conditions used for this investigation, where the photon flux is on purpose reduced hundreds of times compared to the usual conditions, it has been possible to rule out the possibility that these contributions comes from photoreduction processes induced by the X-ray photon flux, as confirmed by verifying that the spectra are not time dependent. In both samples, the Mn^{II} content corresponds to the 20–30% range, suggesting that the underlying redox process is not comparable to the one involved in the formation of the monoreduced Mn12 cluster.

The contradiction between the morphological results and these spectroscopic evidences can be fixed by assuming that the process of assembling to the gold surface affects the electronic structure of the Mn12 but keeps almost intact the molecular structure of the system. A similar reduction process has also been suggested from independent theoretical calculations [74].

However, the efforts made introducing the XAS and XMCD characterization for monolayer and submonolayer deposits on surfaces do not correspond to a complete failure of the connection between surface science and molecular magnetism. In fact, these techniques recently permitted to demonstrate that another class of SMMs are more stable with respect to these kinds of nanostructuration processes.

The Fe4 cluster can be functionalized with sulphur based tripodal ligands [23] acting as alligator clips on gold through thioacetic/thiolate linker groups. These ligands allow the assembling of a disordered monolayer on the surface (Figure 14.8) STN, XAS, and XMCD characterizations are fully compatible with the conclusion that this SMM remains intact when chemically anchored to the surface [47]. In particular, reduction phenomena are absent and the ferrimagnetic structure of the cluster is conserved. In fact, the XMCD/XAS intensities ratio is the same as in the bulk sample and is characteristic of having three spins parallel to the applied field

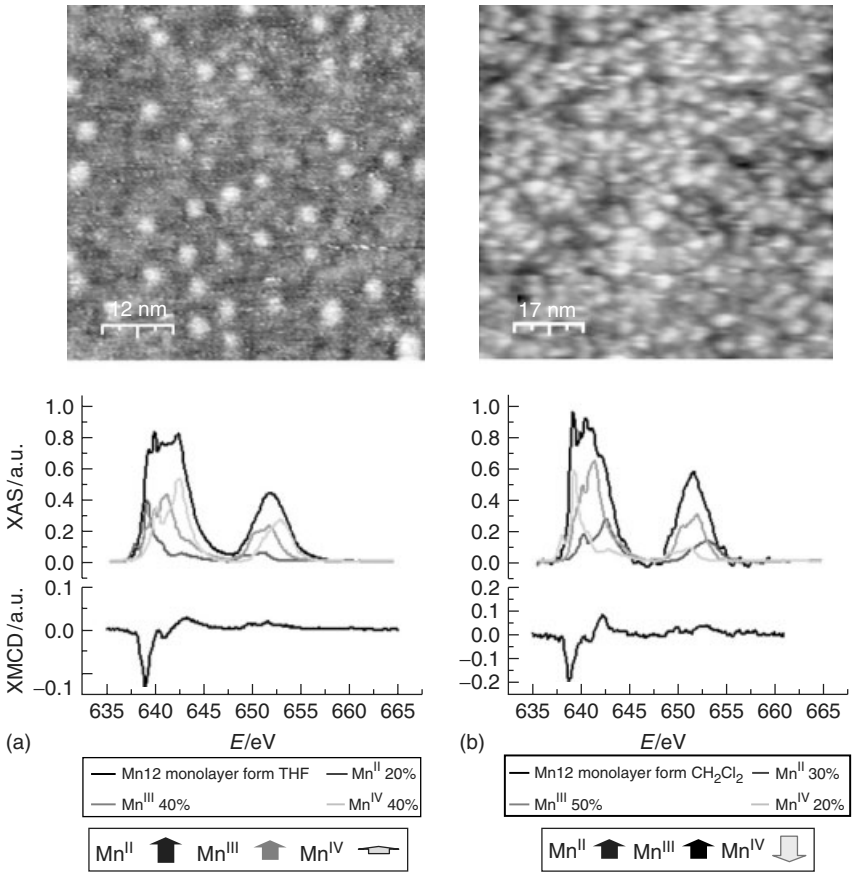

Figure 14.7 STM and XAS/XMCD characterization of monolayers of $[Mn_{12}O_{12}(O_2CPhSCH_3)_{16}(H_2O)_4]$ deposited on gold surface from THF (a) and CH_2Cl_2 (b0. Partially reproduced with permission from [68]. Copyright 2008 Wiley-VCH.

and one antiparallel to it. A damage of the cluster would likely result in a significant change of this ratio [47].

14.8 Magnetism of SMMs Using XMCD

The capability of this technique is not limited to spectroscopic information. In fact, by monitoring the field dependence of the dichroic signal is possible to extract information that is directly related to the magnetization state of the molecule.

When a thick deposit of SMM is investigated exploiting the TEY detection mode, the probed sample is constituted by the first layers on top of this deposit. This

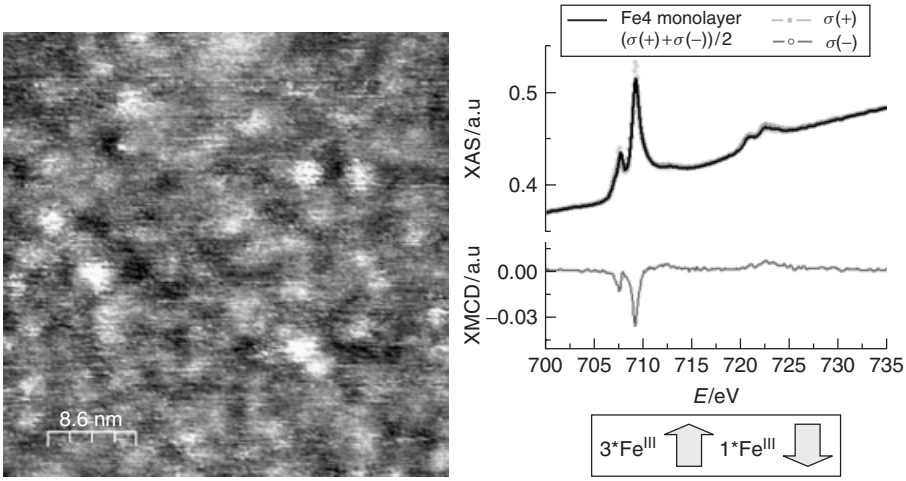

Figure 14.8 STM and XAS/XMCD characterization of monolayers of $[Fe_4(L)_2(dpm)_6]$ deposited on gold surface from CH_2Cl_2. Partially reproduced with permission from [47]. Copyright 2009 Nature Publishing Group.

emulates the confinement of SMM on surface excluding the additional spare contribution of the substrate and of the substrate-SMM film interphase. This kind of characterization has been recently carried out on thick deposits of both Mn12 and Fe4 [70], demonstrating that even if degradation processes are absent, Mn12 clusters lose their peculiar magnetic properties, and contrary to expectation, it is impossible to observe the opening of a hysteresis loop (see Figure 14.9a). These measurements have been carried out by monitoring the field dependence of the signal at the energy corresponding to one of the maxima in the XMCD spectrum and have provided direct evidence of the disappearance of the slow relaxation in the magnetization characteristic of SMM.

On the contrary, an analogous measurement on Fe4 system has demonstrated the permanence of the expected features. For instance, by monitoring the variation of the negative peak of the dichroic signal with the magnetic field at two temperatures above the blocking temperature of the cluster, it has been possible to build up the analogs of isothermal magnetization curves which, when plotted versus the reduced variable H/T, shows the typical behavior of anisotropic systems with a noncoincidence of the curves recorded at different temperatures (Figure 14.9b). Moreover, the XMCD data are fully in agreement with the expected ones assuming that the magnetic anisotropy of the topmost layers is the same as in the bulk, in contrast to what happen in the case of Mn12, as shown in Figure 14.9a.

On decreasing the temperature below 1 K, the blocking temperature of Fe4, it has been possible to observe the opening of the hysteresis loop. XAS/XMCD investigations have thus been demonstrated to be very powerful tools in the selection of the SMMs that are best suited to retain their peculiar behavior once they are grafted on a surface.

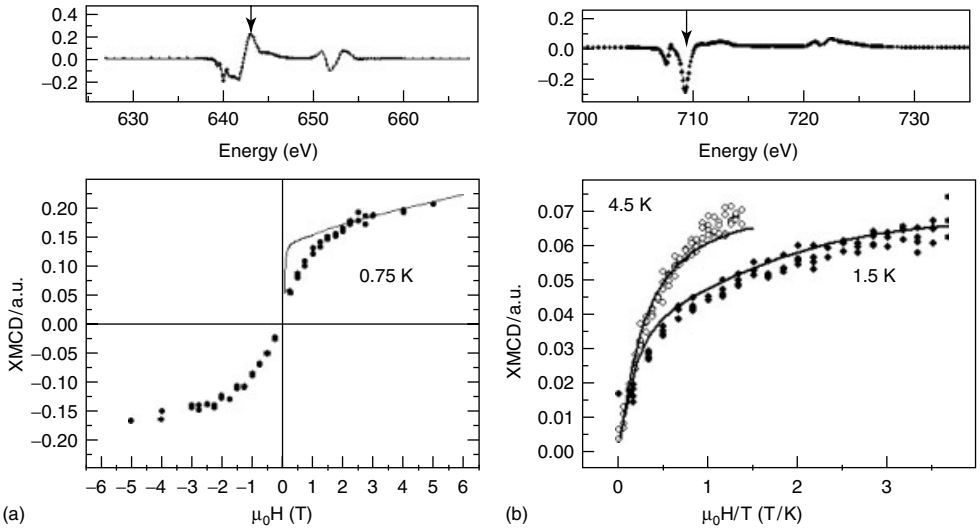

Figure 14.9 (a) Dependence of the XMCD signal at the maximum of the dichroic signal (indicated by the arrow in the upper plot) for $[Mn_{12}O_{12}(O_2CPhSCH_3)_{16}(H_2O)_4]$ respect to the magnetic field and (b) isothermal XMCD-detected magnetization curve (evaluated in the negative peak of dichroism indicated by the arrow in the upper plot) for $[Fe_4(L)_2(dpm)_6]$, in bulk drop-cast samples. Partially reproduced with permission from [70]. Copyright 2009 Wiley-VCH.

The next step, that is, the investigation of the magnetism of a monolayer of SMM, has been achieved by exploiting to the maximum the capabilities of one of the most stable synchrotron light sources [75] as well as the extreme condition of low temperatures and high magnetic field available in one of the best-performing XMCD end station, the TBT (*très basse température*) setup developed by Dr Philippe Sainctavit and Dr Jean Paul Kappler [76, 77]. This setup was previously used also to investigate another SMM, the Fe8 cluster [77] in bulk deposit and the results suggested the feasibility to observe a magnetic remanence from an XMCD characterization. The investigation on the Fe4 thick-film deposit [70] also revealed that the sensitivity of the setup is able to reach the detection of a monolayer of Fe4 SMM. Figure 14.10, in fact, shows that the ''magnetic memory effect'' associated with the magnetic hysteresis of SMM can be observed also in the monolayer deposit [47].

The butterfly-like shape of this hysteresis is fully in agreement with the observed one for this cluster in bulk samples [70] and is justified by the presence of a strong tunneling of the magnetization at zero field. This fact, coupled with the very low temperature constraints, hampered the resolution of better defined features.

To circumvent these limitations, our team introduced an alternative method to observe the slow relaxation of the magnetization by monitoring the time variation of the dichroic signal at a low field (in the regime of slow relaxation but far from zero) after having magnetized the sample with an opposite strong magnetic field.

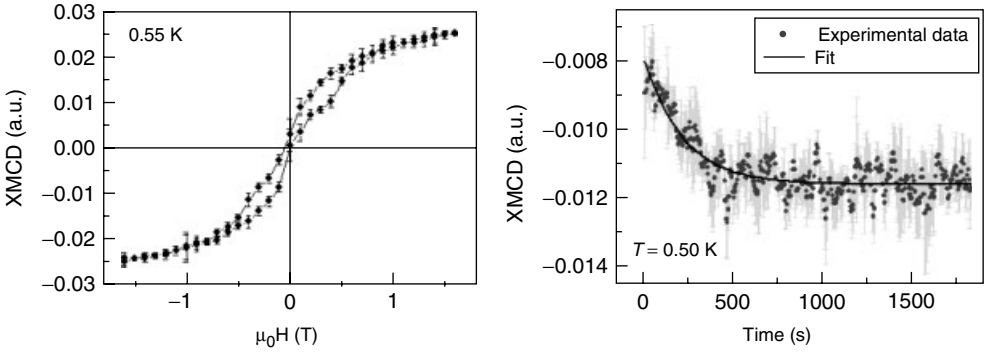

Figure 14.10 (a) Magnetic hysteresis for the $[Fe_4(L)_2(dpm)_6]$ monolayer, monitored through the XMCD intensity (multiplied by −1) at the negative peak of dichroism. (b) Time dependence of the dichroic signal for the same sample previously magnetized with a strong positive magnetic field (+2.0 T), then the field was rapidly ramped to a moderate negative value (−0.25 T) where the time dependence is measured. Reproduced with permission from [47]. Copyright 2009 Nature Publishing Group.

From a single exponential fit of the time decay of the dichroic signal, it has been possible to extract the characteristic time of this relaxation process.

The observation of the magnetism of a monolayer of SMM is in line with recent results obtained by several groups working on simpler molecular systems like Fe-porphyrin units [78] and terephtalate -coordinated Fe-systems [79]. The peculiarity of Fe4 originates from the attractive magnetic features that were demonstrated to survive when molecules are wired to a surface. This effect is intrinsically related to the bistable nature of this molecule and to the complexity of the involved phenomena. These promising aspects indicate that SMMs will soon play a major role in the field of surface science. This research represents only the tip of the iceberg of unexplored magnetic systems ready to be investigated with this technique and then used in innovative devices.

14.9 Perspectives

The successful deposition of intact molecules as single layers is mandatory for their use as magnetic memory cells or as novel elements in molecular spintronics, but other important requisites must be fulfilled. To fully exploit the storage capability of SMM, the periodic structure of the layer and, more importantly, the molecular orientation at the surface must be controlled. The molecules must be anchored with their unique molecular axes perpendicular to the surface to ensure iso-orientation within the layer. Both direct assembling of rationalized structures as well as supramolecular approaches seem to suggest promising solutions to this problem.

In this direction, the contribution of XMCD is far from being exhausted. For instance, angular dependence of the dichroic signal to detect the real orientation

of the molecular clusters seems fully exploitable. Moreover, a deeper analysis of the element-specific magnetism typical of this technique can be used to fully understand the origin of molecular magnetism, thus helping in the development of newer class of SMM.

Even though the first step toward the realization of SMM-based nanodevices has been taken by demonstrating that isolated and addressable molecules maintain their peculiar ''memory effect,'' strong efforts must be made to increase their blocking temperature before they can be put to practical use. This challenge can be tackled following a rational approach and by controlling, down to the monolayer level, the factors that generate the SMM behavior.

Acknowledgments

I am fully indebted to all the people working with me in the field of surface deposition of SMMs and their investigation using XMCD. First of all, I thank my two mentors and supervisors Prof. Dante Gatteschi and Prof. Roberta Sessoli who guided my research along the years, directly participating in the research activities. I would like to mention also the fundamental scientific support and contribution of Prof. Andrea Cornia (University of Modena and Reggio Emilia, Italy) in the design and characterization of graftable SMM as well as of Dr. Philippe Sainctavit (University of Pierre et Marie Curie, Paris, France) in the introduction to the ''world'' of the synchrotron light source-based techniques. I also acknowledge Dr. Laura Zobbi, Dr. Daniele Bonacchi, Dr. Christophe Cartier dit Moulin, Dr. Francesco Pineider, Dr. Chiara Danieli, and Dr. Marie-Anne Arrio as well as all the staff of LAMM and at SLS and BESSY for their friendship and scientific contribution to this research.

References

1. Aviram, A. and Ratner, M.A. (1974) *Chem. Phys. Lett.*, **29**, 277.
2. Pomerantz, M. and Pollak, R.A. (1975) *Chem. Phys. Lett.*, **31**, 602.
3. Talham, D.R. (2004) *Chem. Rev.*, **104**, 5479.
4. Binning, G. and Rohrer, H. (1982) *Helv. Phys. Acta*, **55**, 726.
5. Zhao, A., Li, Q., Chen, L., Xiag, H., Pan, S., Wang, B., Xiao, X., Yang, J., Hou, J.G., and Zhu, Q. (2005) *Science*, **309**, 1542.
6. Multani, D.S., Briggs, S.P., Chamberlin, M.A., Blakeslee, J.J., Murphy, A.S., and Johal, G.S. (2003) *Science*, **302** (81), 5.
7. Bode, M., Kubetzka, A., Pietzsch, O., Nie, X., Blugel, S., and Wiesendanger, R. (2000) *Science*, **288**, 1805.
8. Rugar, D., Budakian, R., Mamin, H.J., and Chui, B.W. (2004) *Nature*, **430**, 329.
9. Manassen, Y., Hamers, R.J., Demuth, J.E., and Castellano, A.J. Jr. (1989) *Phys. Rev. Lett.*, **62**, 2531.
10. Joachim, C., Gimzewski, J.K., and Aviram, A. (2000) *Nature*, **408**, 541–548.
11. Sessoli, R., Gatteschi, D., Caneschi, A., and Novak, M.A. (1993) *Nature*, **365**, 141.
12. Thomas, L., Lionti, F., Ballou, R., Gatteschi, D., Sessoli, R., and Barbara, B. (1996) *Nature*, **383**, 145.

13. Leuenberger, M.N. and Loss, D. (2001) *Nature*, **410**, 789.
14. Rocha, A.R., Garcia-Suarez, V.M., Bailey, S.W., Lambert, C.J., Ferrer, J., and Sanvito, S. (2005) *Nature Mater.*, **4**, 335.
15. Ziemelis, K. (1996) Nat. Milestones, Spin, Milestone 22: (Mesoscopic tunnelling of magnetization, doi: 10.1038/nphys877).
16. Gatteschi, D., Sessoli, R., and Villain, J. (2006) *Molecular Nanomagnets*, Oxford University Press, Oxford.
17. Sangregorio, C., Ohm, T., Paulsen, C., Sessoli, R., and Gatteschi, D. (1997) *Phys. Rev. Lett.*, **78**, 4645.
18. Cornia, A., Fabretti Costantino, A., Zobbi, L., Caneschi, A., Gatteschi, D., Mannini, M., and Sessoli, R. (2006) *Struct. Bonding (Berlin)*, **122**, 133.
19. Sessoli, R. and Powell, A.K. (2009) *Coord. Chem. Rev.*, **253**, 2328.
20. Ishikawa, N. (2007) *Polyhedron*, **26**, 2147.
21. Barra, A.L., Caneschi, A., Cornia, A., Fabrizi de Biani, F., Gatteschi, D., Sangregorio, C., Sessoli, R., and Sorace, L. (1999) *J. Am. Chem Soc.*, **121**, 5302.
22. Cornia, A., Faretti, A.C., Garrisi, P., Mortalò, C., Bonacchi, D., Gatteschi, D., Sessoli, R., Sorace, L., Wernsdorfer, W., and Barra, A.-L. (2004) *Angew. Chem. Int. Ed.*, **43**, 1136.
23. Barra, A.L., Bianchi, F., Caneschi, A., Cornia, A., Gatteschi, D., Gorini, L., Gregoli, L., Maffini, M., Parenti, F., Sessoli, R., Sorace, L., and Talarico, A.M. (2007) *Eur. J. Inorg. Chem.*, 4145.
24. Ishikawa, N., Sugita, M., Ishikawa, T., Koshihara, S., and KaizuIshikawa, Y. (2003) *J. Am. Chem Soc.*, **125**, 8694.
25. Takamatsu, S., Ishikawa, T., Koshihara, S., and Ishikawa, N. (2007) *Inorg. Chem.*, **46**, 7250.
26. Ishikawa, N., Mizuno, Y., Takamatsu, S., Ishikawa, T., and Koshihara, S. (2008) *Inorg. Chem.*, **47**, 10217.
27. Whitesides, G.M. and Boncheva, M. (2002) *Proc. Natl. Acad. Sci. U.S.A.*, **99**, 4769.
28. Whitesides, G.M. and Grzyboski, B. (2002) *Science*, **295**, 2418.
29. Zangwill, A. (1988) *Physics at Surfaces*, Cambridge University Press, Cambridge.
30. Ulman, A. (1996) *Chem. Rev.*, **96**, 1533–1554.
31. Roberts, G. (1990) *Langmuir-Blodgedtt Films*, Plenum Press, New York.
32. Qiu, X.H., Wang, C., Yin, S.X., Zeng, Q.D., Xu, B., and Bai, C.L. (2000) *J. Phys. Chem. B*, **104**, 3570.
33. Ruben, M. (2005) *Angew. Chem. Int. Ed.*, **44**, 1594.
34. Jung, T.A., Schlittler, R.R., Gimzewski, J.K., Tang, H., and Joachim, C. (1996) *Science*, **271**, 181–184.
35. Qiu, X.H., Wang, C., Yin, S.X., Zeng, Q.D., Xu, B., and Bai, C.L. (2000) *J. Phys. Chem. B*, **104**, 3570.
36. Gomez-Segura, J., Diez-Perez, I., Ishikawa, N., Nakano, M., Veciana, J., and Ruiz-Molina, D. (2006) *Chem. Commun.*, 2866.
37. Ruben, M., Ziener, U., Lehn, J.M., Ksenofontov, V., Gutlich, P., and Vaughan, G.B.M. (2004) *Chem. Eur. J.*, **11**, 94.
38. Margheriti, L., Mannini, M., Sorace, L., Gorini, L., Gatteschi, D., Caneschi, A., Chiappe, D., Moroni, R., Buatier de Mongeot, F., Cornia, A., Piras, F.M., Magnani, A., and Sessoli, R. (2009) *Small*, **5**, 1460.
39. Cornia, A., Fabretti, A.C., Pacchioni, M., Zobbi, L., Bonacchi, D., Caneschi, A., Gatteschi, D., Biagi, R., Del Pennino, U., De Renzi, V., Gurevich, L., and Van Der Zant, H.S.J. (2003) *Angew. Chem. Int. Ed.*, **42**, 1645.
40. Clemente-Leon, M., Soyer, H., Coronado, E., Mingotaud, C., Gomez-Garcia, C.J., and Delhaes, P. (1998) *Angew. Chem. Int. Ed. Engl.*, **37**, 2842.
41. Condorelli, G.G., Motta, A., Fragala, I.L., Giannazzo, F., Raineri, V., Caneschi, A., and Gatteschi, D. (2004) *Angew. Chem. Int. Ed.*, **43**, 4081.
42. Nait Abdi, A., Bucher, J.P., Gerbier, P., Rabu, P., and Drillon, M. (2005) *Adv. Mater.*, **17**, 1612.
43. Voss, S., Fonin, M., Rudiger, U., Burgert, M., and Groth, U. (2007) *Appl. Phys. Lett.*, **90**, 133104.
44. Pineider, F., Mannini, M., Sessoli, R., Caneschi, A., Barreca, D., Armelao, L., Cornia, A., Tondello, E., and Gatteschit, D. (2007) *Langmuir*, **23**, 11836.

45. Zobbi, L., Mannini, M., Pacchioni, M., Chastanet, G., Bonacchi, D., Zanardi, C., Biagi, R., Del Pennino, U., Gatteschi, D., Cornia, A., and Sessoli, R. (2005) *Chem. Commun.*, 1640.
46. Phark, S., Khim, Z.G., Kim, B.J., Suh, B.J., Yoon, S., Kim, J., Lim, J.M., and Do, Y. (2004) *Jpn. J. Appl. Phys.*, **43**, 8273.
47. Mannini, M., Pineider, F., Sainctavit, Ph., Danieli, C., Otero, E., Sciancalepore, C., Malarico, A.M., Arrio, M.-A., Cornia, A., Gatteschi, D., and Sessoli, R. (2009) *Nature Mater.*, **8**, 194.
48. Condorelli, G.G., Motta, A., Pellegrino, G., Cornia, A., Gorini, L., Fragalà, I.L., Sangregorio, C., and Sorace, L. (2008) *Chem. Mater.*, **20**, 2405.
49. Condorelli, G.G., Motta, A., Favazza, M., Nativo, P., Fragala, I.L., and Gatteschi, D. (2006) *Chem. Eur. J.*, **12**, 3558.
50. Di Bella, S., Condorelli, G.G., and Motta, A. (2006) *Langmuir*, **22**, 7952.
51. Zobbi, L., Mannini, M., Pacchioni, M., Chastanet, G., Bonacchi, D., Zanardi, C., Biagi, R., Del Pennino, U., Gatteschi, D., Cornia, A., and Sessoli, R. (2005) *Chem. Commun.*, 1640.
52. Mannini, M., Bonacchi, D., Zobbi, L., Piras, F.M., Speets, E.A., Caneschi, A., Cornia, A., Magnani, A., Ravoo, B.J., Reinhoudt, D.N., Sessoli, R., and Gatteschi, D. (2005) *Nano Lett.*, **5**, 1435.
53. Fonin, M. (2008) Polyhedron, doi: 10.1016/j.poly.2008.11.028.
54. Mannini, M., Sorace, L., Gorini, L., Piras, F.M., Caneschi, A., Magnani, A., Menichetti, S., and Gatteschi, D. (2007) *Langmuir*, **23**, 2389.
55. Cleuziou, J.-P., Wernsdorfer, W., Bouchiat, V., Ondarçuhu, T., and Monthioux, M. (2006) *Nat. Nanotech.*, **1**, 53.
56. Bogani, L., Cavigli, L., Gurioli, M., Novak, R.L., Mannini, M., Caneschi, A., Pineider, F., Sessoli, R., Clemente-León, M., Coronado, E., Cornia, A., and Gatteschi, D. (2007) *Adv. Mater.*, **19**, 3906.
57. *http://www.lightsources.org.*
58. Stöhr, J. (1994) *New Directions in Research with Third-generation Soft X-ray Synchrotron Radiation Sources*, Kluwer, Amsterdam, p. 221.
59. de Groot, F. and Kotani, A. (2008) *Core Level Spectroscopy of Solids*, CRC Press.
60. Stöhr, J. (1999) *J. Magn. Magn. Mater.*, **200**, 470.
61. Koninsberger, D.C. and Prins, R. (1988) X-ray absorption, *Principles and Applications: Techniques of EXAFS, SEXAFS and XANES Chemical Analysis, 92*, John Wiley & Sons, Inc.
62. Thole, B.T., Carra, P., Sette, F., and van der Laan, G. (1992) *Phys. Rev. Lett.*, **68**, 1943.
63. Carra, C.P., Thole, B.T., Altarelli, M., and Wang, X. (1993) *Phys. Rev. Lett.*, **70**, 694.
64. Thole, B.T., van der Laan, G., and Sawatzky, G.A. (1985) *Phys. Rev. Lett.*, **55**, 2086.
65. Ghigna, P., Campana, A., Lascialfari, A., Caneschi, A., Gatteschi, D., Tagliaferri, A., and Bor-gatti, F. (2001) *Phys. Rev. B*, **64**, 132413.
66. Moroni, R., Moulin, C.C.D., Champion, G., Arrio, M.A., Sainctavit, P., Verdaguer, M., and Gatteschi, D. (2003) *Phys. Rev. B*, **68**, 064407.
67. Robinson, R.A., Brown, P.J., Argyriou, D.N., Hendrickson, D.N., and Aubin, S.M.J. (2000) *J. Phys.: Condens. Matter*, **12**, 2805.
68. Mannini, M., Sainctavit, Ph., Sessoli, R., Cartier dit Moulin, Ch., Pineider, F., Arrio, M.A., Cornia, A., and Gatteschi, D. (2008) *Chem. Eur. J.*, **14**, 7530.
69. Eppley, H.J., Tsai, H.-L., de Vries, N., Folting, K., Christou, G., and Hendrickson, D.N. (1995) *J. Am. Chem. Soc.*, **117**, 301.
70. Mannini, M., Pineider, F., Sainctavit, Ph., Joly, L., Fraile-Rodrìguez, A., Arrio, M.-A., Cartier dit Moulin, Ch., Wernsdorfer, W., Cornia, A., Gatteschi, D., and Sessoli, R. (2009) *Adv. Mater.*, **20**, 167.
71. Gambardella, P., Dhesi, S.S., Gardonio, S., Grazioli, C., Ohresser, P., and Carbone, C. (2002) *Phys. Rev. Lett.*, **88**, 047202.
72. Nakajima, R., Stöhr, J., and Idzerda, Y.U. (1999) *Phys. Rev. B*, **59**, 6421.
73. Ufuktepe, Y., Akgülb, G., and Lüning, J. (2005) *Alloys Compd.*, **401**, 193.

74. Barraza-Lopez, S., Avery, M.C., and Park, K. (2007) *Phys. Rev. B*, **76**, 224413.

75. *http://sls.web.psi.ch*.

76. Sainctavit, Ph. and Kappler, J.-P. (2001) in *X-ray Magnetic Circular Dichroism at Low Temperature in Magnetism and Synchrotron Radiation* (eds E. Beaurepaire, F. Scheurer, G. Krill, and J.-P. Kappler), Springer, pp. 135–153.

77. Letard, I., Sainctavit, Ph., Cartier dit Moulin, Ch., Kappler, J.-P., Ghigna, P., Gatteschi, D., and Doddi, B. (2007) *J. Appl. Phys.*, **101**, 113920.

78. Wende, H., Bernien, M., Luo, J., Sorg, C., Ponpandian, N., Kurde, J., Miguel, J., Piantek, M., Xu, X., Eckhold, Ph., Kuch, W., Baberschke, K., Panchmatia, P.M., Sanyal, B., Oppeneer, P.M., and Eriksson, O. (2007) *Nat. Mater.*, **6**, 516.

79. Gambardella, P., Stepanow, S., Dmitriev, A., Honolka, J., de Groot, F.M.F., Lingenfelder, M., Gupta, S.S., Sarma, D.D., Bencok, P., Stanescu, S., Clair, S., Pons, S., Lin, N., Seitsonen, A.P., Brune, H., Barth, J.V., and Kern, K. (2009) *Nat. Mater.*, **8**, 189.

15
Sculpting Nanometric Patterns: The Top-Down Approach

Rui M. D. Nunes

15.1
Introduction

The production of nanostructures with increasingly higher resolution has been the focus of the electronics industry, causing paradigmatic changes in Materials Science. This ''quiet revolution'' is being followed closely by society and economy, since the decreasing size of patterns has caused an increase in the quality of life. The effect this technology induces is obvious when comparing the size and capacity of a computer in the 1980s with a modern-day cell phone. The decrease in size of the components of an integrated circuit (IC) results in larger processing capabilities, more memory, and so on. This also dramatically reduces the production cost.

Why does this technology have the potential to create such a huge social and economic impact? Nanotechnology is a designer science capable of creating new tools to alter matter on a molecular level. This capability, though it has yet to be fully developed, is changing our society. The path to achieve such impact has its difficulties. The laboratory feasibility of basic concepts does not guarantee a straightforward production implementation, that is, how the nanostructures will be manufactured in volume is a key issue. It is therefore essential to develop nanotechnologies that can be produced in a scalable, cost-effective, reproducible, and reliable manner. The IC industry is committed to exploring such technologies because there are benefits to using smaller components: performance gains, power consumption, reliability – but none has been as important as the reduction in cost per transistor or bit. The reason for the cost per transistor reduction is dimensional scaling, that is, to have more components in each IC. Reducing the size of the components to the nanoscale brings about other particular issues. For example, the forces that we normally consider and use, such as gravity, become less important in comparison to other forces, such as superficial tension or hydrogen bonding. Consequently, nanostructures are best described with statistical mechanics and quantum size effects.

The demonstration of such scaling effects can be found in the field of electronics with the discovery of the giant magnetoresistance effect. Albert Fert and Peter

Ideas in Chemistry and Molecular Sciences: Advances in Nanotechnology, Materials and Devices.
Edited by Bruno Pignataro

ISBN: 978-3-527-32543-6

Grunberg were awarded the Physics Nobel Prize in 2007 for the discovery of the effect and its applications. In 2000, another Nobel Prize in Physics was awarded to Jack Kilby for his part in invention of the IC. The reduction of the components of the ICs brings the classical transistor close to its physical limit. Presently, to activate a single transistor, 1000 electrons are required while projections show that in 2010, it will require 10 electrons and in 2020, the one-electron limit will be reached [1]. This will be the frontier of the current transistor design.

15.2 Production of Micro and Sub-Micro Patterns

There are two opposing approaches for the construction of nanopatterns: the bottom-up approach, where smaller and simpler components are combined to form a complex system; and the top-down approach, where large systems are used to create nanostructures. The bottom-up approach uses the kinetic and thermodynamic properties of molecules to control the formation of highly ordered structures. This technique has the power of parallel production, but the structures are not fabricated as much as they are grown. This means that the size and shape of the structures are determined by the chemical and physical forces that direct the formation rather than by the requirements of its end application [2]. This greatly restricts the broad utility of this approach.

Ultimate control is achieved when a structure is assembled atom by atom, the proposition behind the top-down approach. Demonstration has been performed using atom manipulation with the tip of a scanning tunneling microscope [3]. This method is specific to few substances and substrates and, because each structure is built atom by atom or molecule by molecule, has a very low throughput. Another technique associated with the top-down approach is optical lithography.

Optical microlithographic techniques aim to obtain very small patterning using light. The critical dimension (CD) is the absolute size of a minimum feature in an IC (linewidth/spacing/contact dimension). The overall resolution of a process describes the consistent ability to point a minimum size image, a CD under conditions of reasonable manufacturing variation. The resolution R of optical lithography, defined as the half pitch of a dense lines and spaces pattern, is determined by Abbe's equation [4, 5] (Eq. 15.1)

$$R = k_1 \frac{\lambda}{\mathrm{NA}} \tag{15.1}$$

where λ is the wavelength of exposure, NA is the numerical aperture of the optical system used, and k_1 is an image-enhancing parameter. Equation (15.1) reveals that feature size reductions can be accomplished by reducing the exposure wavelength, increasing the numerical aperture of the optical system, or by reducing the k_1 factor. The improvement of resolution has been accomplished mainly by reducing the wavelength of the exposure radiation, using, at present, 193-nm radiation. Decreasing k_1 is possible through the incorporation of resolution-enhancement techniques but has the significant drawback of decreasing the throughput. *Throughput* is the

number of wafers that can be exposed per hour for a given mask level. The NA is proportional to the refractive index of the imaging medium and, at a fixed focal length, can be related to the size of the lens apparatus. Readers interested in this subject, outside the scope of this work, are directed to reference works [4, 6]. Increasing the size of the projection lens has become unfeasible, so the refractive index has been altered using different media than air. By using water, the refraction index increases from 1.00 to 1.43, attaining a better resolution of the printed features [7]. Increasing the NA also causes a reduction of the depth of focus (DOF) [4, 7] (Eq. 15.2), a drawback for 2D and 3D patterning because the possible height of the patterns is reduced.

$$\mathrm{DOF} = k_2 \frac{\lambda}{\mathrm{NA}^2} \tag{15.2}$$

The microlithographic process involves the application of a photoresist onto a substrate. A photoresist is a mixture of components, some of which are photoactive, that is used to transfer the desired pattern to the substrate, also called *hard mask*. After application, the photoresist is soft baked to remove casting solvent and subsequently exposed to patterned UV light. Depending on the photochemistry of the resist, the exposed areas either become more soluble (positive tone) or less soluble (negative tone) in the developer. The resulting chemical changes produce differences in dissolution rates in a developer solution, used to wash off the undesired areas of the resist film. Consequently, selective dissolution of either the exposed or unexposed areas of the resist film affords positive- or negative-mode relief images [8], shown in Figure 15.1. The resulting patterned polymer is used as a protective template for subsequent etch. After etching, the resist is thoroughly removed from the substrate surface.

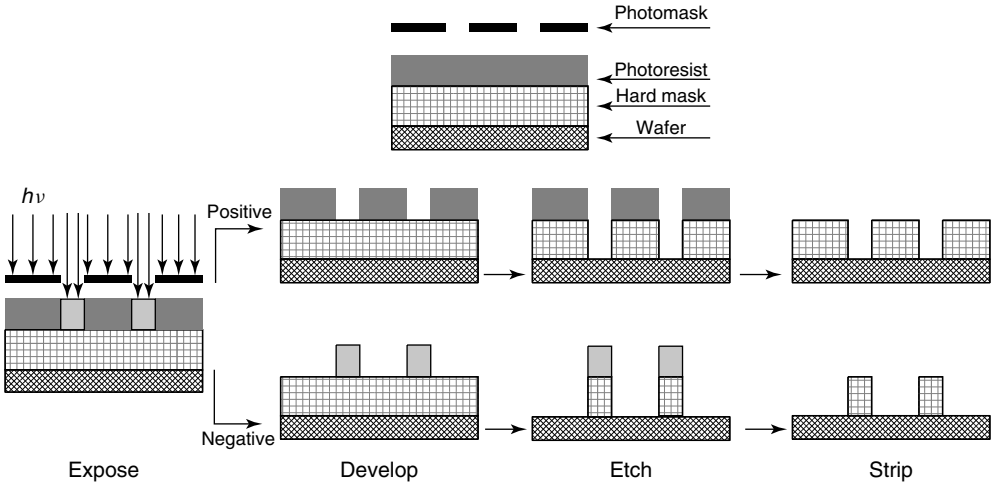

Figure 15.1 Schematic representation of conventional lithographic process.

15.2.1
Resist History

The first commercial microlithographic system [9], bisarylazide-rubber, used from 1954 to 1972, was a negative tone resist composed of two components: the photoactive compound bisarylazide and a resin made of rubber. The photoactive bisarylazide provided the resist with imaging and sensitivity requirements while the rubber provided the film-forming properties and resistance to etch. Upon exposure to radiation, nitrogen was evolved from the azide to form a reactive nitrene that could add to double bonds to give aziridines. Each bisarylazide had two reactive groups that could be formed, not necessarily in one step, and cross-link the rubber monomers (Figure 15.2).

The bisarylazide-rubber system became obsolete when it reached the maximum possible resolution and was replaced by a positive tone DNQ–novolac photoresist system. Diazonaphthoquinone (DNQ) derivatives were synthesized around 1940 by Oskar Sues [10, 11] and the first DNQ–novolac system was introduced in a printing plate around 1950 [12], becoming the ''workhorse'' resist of optical lithography. This system provided resolutions down to 350 nm and greater chemical etch resistance than the bisarylazide system. Chemically, the resist is composed of the photoactive DNQ dispersed in phenol–formaldehyde resin matrix, commonly called *novolac*. The DNQ is a dissolution inhibitor that retards the dissolution of the weak acidic resin, shown in Figure 15.3, in the aqueous alkaline developer solution. Irradiation of the hydrophobic DNQ yields the aqueous soluble indenecarboxilic acid, through a Wolff rearrangement with a quantum yield of 0.1–0.3 [12] (Figure 15.4).

The photosensitive DNQ exhibits a much higher sensitivity to ultraviolet radiation than the bisarylazide resist, allowing higher throughput and producing high-resolution patterns upon exposure to 436-nm (g-line) and 365-nm (i-line) radiation, with excellent etch resistance and no swelling in an aqueous base developer. In the mid-1990s, the industry was moving toward 250-nm features. It became necessary to use even lower wavelength-processing radiation known as the *deep*

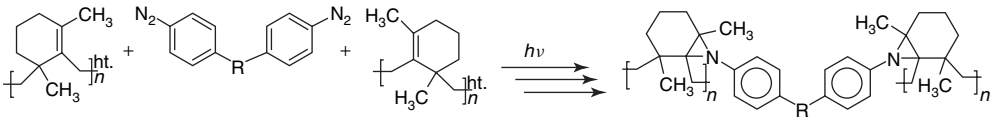

Figure 15.2 Reaction of bisarylazide with rubber resin.

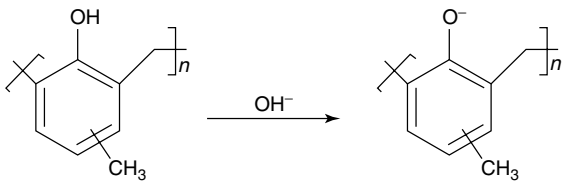

Figure 15.3 Soluble form of novolac resin.

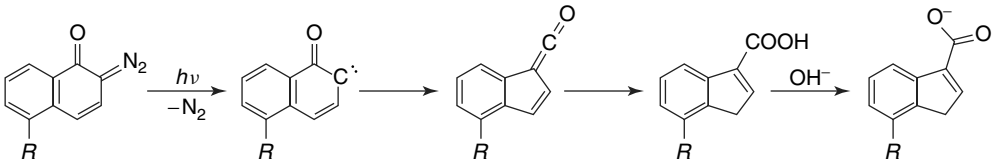

Figure 15.4 Diazonaphthoquinone Wolff photorearrangement and subsequent aqueous soluble form.

ultraviolet (*DUV*). The DNQ–novolac resist had several drawbacks for wavelengths below 300 nm since the novolac resin had a strong absorbance in this spectral region and low sensitivity to DUV. The absorption by the resin prevented light from penetrating through the entire thickness of the resist, making it impossible to create a relief image in it. There were attempts to use more transparent matrix polymers (e.g., poly(hydroxystyrene)) and alternative diazoketone-based dissolution inhibitors [13] but these modified materials did not meet the requirements for volume manufacturing.

To achieve higher sensitivity and resolution, the next evolutionary step was the introduction of the chemical amplification concept. Because of the mechanism by which chemically amplified resists act, the sensitivities achieved can be up to two orders of magnitude [14] greater than that of conventional DNQ–novolac resists. A chemical amplification reaction in photoresists is an acid-catalyzed reaction promoted by Brønsted or Lewis acids photogenerated from a photoreactive acid generator (PAG). The first photochemical event in these systems is the dissociation of the excited-state PAG, forming the reactive acid species. A single molecule of the photogenerated acid is involved in a cascade of bond-making or bond-breaking reactions.

Photoresist systems used at present are a mixture of several components: a polymer, a PAG, and other additives. In this approach, the PAG excited by light reacts to form a low concentration of a strong Brønsted acid, becoming an acid catalyst formed *in situ*. The subsequent acidic thermolysis of the polymer, the major component in weight, achieves the formation of patterns. Additives, such as the base quencher used to limit the diffusivity of the acid catalyst, may be used to improve the resolution of the patterns formed. Table 15.1 is a summary of the CDs obtained with different wavelengths and resist technology.

The first application of a chemically amplified photoresist was the cationic ring-opening polymerization of epoxides using aryldiazonium salts as photoinitiators, reported by Sheldon Schlesinger, a chemist at the American Can Company in 1974 [15, 16]. The reaction sequence is shown in Figure 15.5. Despite the promise of this photochemistry, aryldiazonium salts did not succeed as photoinitiators due to their thermal instability. In addition, the production of N_2 gas during the photolysis led to pinholes in the final polymer film.

Crivello synthesized a series of cationic photoinitiators, called *onium salts*, which generate Brønsted acids after irradiation and are used as PAGs for cationic polymerization of epoxy and vinyl ether monomers [17–23]. These salts were

Table 15.1 Critical dimension obtained with different incident light wavelength for different lithography technology generations

Year	Critical dimension (nm)	Exposure wavelength (nm)	Resist chemistry	Light source
Until 1972	>2000	–	Cross-linking to inhibit dissolution	High-pressure mercury arc lamp
1972–1988	1200–800	436 (g-line)	Selective dissolution using diazonaphthoquinone-based resists	–
1988–1995	800–350	365 (i-line)	–	–
1995–2003	248	248	Chemically amplified acid-catalyzed photoresist	KrF excimer laser
Since 2003	90–60	193	–	ArF excimer laser

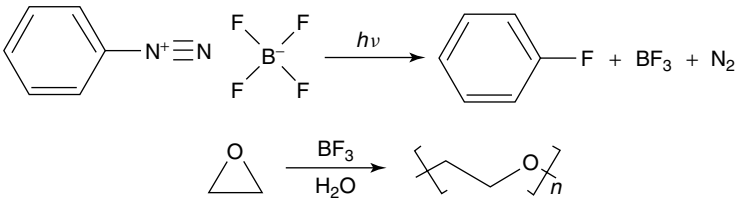

Figure 15.5 Cationic ring-opening polymerization of epoxides photoinitiated with aryldiazonium salts.

studied and the photolysis mechanism determined [24–28] and found to be very efficient, for example, diaryliodonium salts have quantum yields of 0.7–0.9. The history of the creation of these molecules and several uses has been reported in great detail by Crivello in a comprehensive review [29].

An example of a chemically amplified resist system used for creating positive toned images is shown in Figure 15.6 [30]. Fluoroantimonic acid is created upon exposure to ultraviolet light of the triarylsulfonium salt. This acid catalyzes the hydrolysis of the tertiary-butoxycarbonyl protected poly(vinylphenol) resin. The *tert*-butyl cation, which is a product of this hydrolysis, rearranges to regenerate acid in the matrix. This regenerated acid catalyzes another chemical event. Because of this regeneration, one photochemical event can catalyze up to 1 million hydrolysis reactions in the resist. This means that the photochemical processes that induce changes have effective quantum efficiencies that are higher than one.

Iodonium and sulfonium salts are thermally very stable (<200 °C) and with a low vapor pressure, thus less dangerous, thus also diminishing the possibility to damage the optical system by deposition of volatile substances. In addition, these molecules have high molar extinction coefficients in the deep UV and good solubilities in

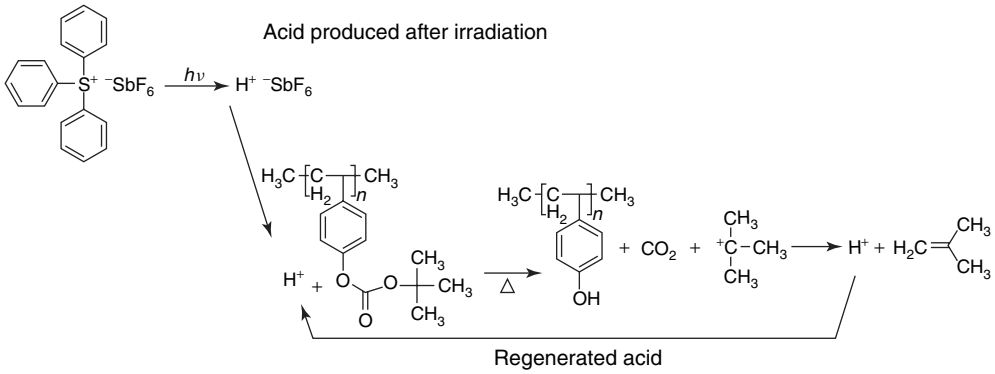

Figure 15.6 Process of creating positive toned features in a sulfonium salt chemically amplified resist.

Table 15.2 Relation between the moieties and the photochemical and reactivity properties of an onium salt photoinitiator

Cation	Anion
Determines photochemistry	Determines polymer chemistry
λ_{max}	Acid strength
Molar absorption coefficient	Nucleophilicity (ion pairing)
Quantum yield	Anion stability
Photosensitization	Initiation efficiency
Thermal stability	Propagation rate constants

resist films. These are the first known photochemical source of organic super acids [31], such as triflic acid. Many of the photochemical and reactivity properties can be adjusted by varying the cation or the anion moieties. Thus, it is possible to have different acidity, volatility, and size of the photogenerated acid by changing the relevant moiety. The properties are identified in Table 15.2.

There are several other examples of compounds that, after irradiation, form a Brønsted acid. The most familiar are the nitrobenzyl esters, which undergo a photochemical-induced rearrangement producing nitrosobenzaldehyde and an organic acid. Derivatives of these esters have been synthesized and used as PAGs in nanolithography [32]. These materials are useful in photoresist applications, with some having thermal stability up to 250 °C and forming strong acids as 2,2,2-trifluoroethanesulfonic acid (tresic acid) or pentafluorobenzenesulfonic acid. The *o*-nitrobenzyl esters also show good absorption properties in the 150-nm UV region and the measured quantum yield of the photolysis in polymer matrix ranges from 0.07 to 0.16. The photoactivation and subsequent chemistry of an *o*-nitrobenzyl ester is depicted in Figure 15.7.

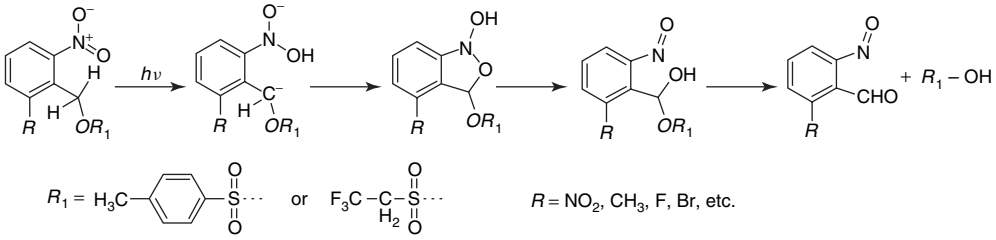

Figure 15.7 *o*-Nitrobenzyl photoactivation yielding an acid.

A more complete and thorough review of the use of photoacid generators for chemical amplification and its applications can be found in reviews of the subject [33–37].

15.2.2
The Present Day in Nanolithography

The semiconductor industry releases a roadmap to find potential near-term and long-term solutions to obey Moore's Law [38, 39]. In 2001, 193-nm lithography was successfully used for the production of the 130- and 90-nm node. As previously discussed, the minimum resolution in nanolithography improves with a decrease in the wavelength of the irradiating light. Owing to the slow progress for next generation lithographic technologies, it was suggested that 157-nm exposure would extend optical lithography past the 65-nm node, where "dry" 193-nm lithography could not succeed. Photoresist systems that exhibited higher sensitivity and comprised a binder transparent to the high-energy radiation were developed and exposure technology had to be reformulated. The new material for lenses should be metal fluorides, such as CaF_2, but unfortunately these materials exhibited severe drawbacks [40, 41]. During the production stage, a thin membrane was used to keep contaminants off the photomask during multiple exposures, increasing the lifetime of the photomask material. The membrane materials developed for the 157-nm exposure did not meet the expected lifetime requirements due to discoloration and transparency loss after several exposures to 157-nm irradiation light. Another major problem with high-energy exposure technology was the formation of volatile gases. A 157-nm laser generates about 7.9 eV, which is much higher than the energy necessary for bond breaking in organic compounds, (4–5 eV) [42, 43]. Bond dissociations can create volatile gases, which evaporate through the resist into the air between the substrate and the projection lens system. When evaporating, these molecules can create small holes in the projected film and can disrupt the aerial image while passing through the chamber, increasing the optical loss.

These were the obstacles to surmount until 2001, when it was expected that the next evolution in the production process was the usage of a 157-nm light source. However, these issues became insurmountable and, in 2003, Intel announced that the company production roadmap did not include 157-nm exposure production. Also, due to the high development costs associated with bringing the 193-nm

lithography to production, it was desired to keep as much continuity with the current process as possible.

The issues above were the driving force to implement immersion lithography. Immersion fluids have been used in optics for over a century, especially in the area of immersion microscopy. When light passes from a material of one refractive index to material of another, as from glass to air, it bends. Light of different wavelengths bends at different angles, so that when objects are magnified the images become less distinct. Placing a drop of a fluid with the same refractive index as glass between the sample and objective lens eliminates two refractive surfaces, increasing the NA so that higher magnifications can be achieved while still preserving good resolution, see Eq. (15.1) [41]. The viability of immersion lithography was first determined in 1994 [44] using immersion microscopy as a model for improved resolution and DOF.

The proposed fluid for 193-nm immersion lithography is water because of its high transmittance at 193 nm, the availability of high-purity water, and the transport properties needed for the supply and recovery system. This technology inherits much from ''dry'' projection lithography and the photoresists used in 193-nm projection lithography are viable for immersion lithography. Also, the development of full-field projection optics with high numerical apertures [45, 46] shows great promise for future uses in the 32-nm node and lower.

There are still limitations being addressed. Variations in temperature cause variations in the refractive index and therefore image distortion [47, 48]. It is therefore necessary to maintain temperature uniformity with a rapidly moving stage and a pulsed laser is passing through the fluid. Contamination of the immersion liquid by the photoresist will also lead to image degradation and possible degradation of the lens. Two methods to prevent this from happening are being studied. One is the use of a top-coating insoluble layer to prevent the leaching of resist components into the fluid while allowing water penetration into the resist film [49]. The second one is a presoaking step of the photoresist where most of the leachable resist components are removed from the photoresist film before immersion exposure [47, 50]. Another serious problem for immersion lithography is the formation and adhesion of bubbles, responsible for various exposure failures by reducing the resolution and control of CDs of lithographic features [50]. It has been found that using degassed water with a maximum velocity of $14\,\mathrm{m\,s^{-1}}$ significantly reduces the amount of bubbles formed in the immersion fluid. Also, the contamination of the lenses by organic byproducts of the photoresist increases the formation and adhesion of microbubbles onto the lenses surface. Keeping the lens surface clean is necessary in order to prevent microbubble adhesion [50].

15.2.3
The Future for Nanolithography

It is increasingly difficult to obtain higher resolution unless one resorts to multiple exposures or multiple patterning. In principle, better resolution could always be resolved by multiplicity, if cost were not an issue – unfortunately, cost is indeed an

issue. Cost dictates whether the product is marketable compared with the previous generation. Cost-effective solutions have to be found either by limiting the number of imaging layers that require multiple patterning or by finding a less-expensive successor to ArF water-immersion lithography. Some of the new technologies can be used without a mask but with an increasing complexity and time needed for the pattern to be formed. Other technologies can forgo the photoacid generator for amplification due to the higher energy used, but until now the amplification concept has proved useful by increasing sensitivity and thus throughput.

There are several leading candidates that have shown promise toward solving the problem. Extreme ultraviolet lithography (EUVL) is the apparent successor [51] for the sub 22-nm node. With the use of a 13.5-nm irradiation source, as in the past, the reduction of irradiation wavelength leads to the reduction of the CDs achieved. The 13.5-nm radiation is generated by a plasma source with the entire optic system under vacuum. The wafer throughput of an EUVL exposure tool is a critical metric for manufacturing capacity. Because of the high vacuum required, the throughput is limited by the transfer of wafers in and out of the vacuum chamber, to only a few wafers per hour [52]. Owing to the extremely high energy used by EUV sources, all the optical elements, including the photomasks, must be completely different from the commercially available projection optics used with 193-nm photolithography. The optics system used, like Mo/Si multilayers used to reflect light by means of interlayer interference, absorb much of the available EUV light. As a result, the EUV source will need to be sufficiently bright. Recently, the EUV source power has been increased by more than an order of magnitude, raising productivity to more than two wafers per hour [53], but such improvements are still not enough. The Mo/Si mirror is directly exposed to the plasma and is therefore vulnerable to damage from the high-energy radiation [54] and other debris [50, 55]. Also, during the high-energy exposure, carbon byproducts are produced and build up in the lenses system [41, 56]. Because of these obstacles, EUV lithography implementation has been postponed.

The resolution obtained using the EUV exposure technology is not limited by the exposure wavelength but because of the photoelectrons and secondary electrons generated by ionization [57]. These secondary electrons have energies of tens of electronvolts and diffuse tens of nanometers inside the photoresist before initiating any chemical reactions, particularly exciting the PAG. This rather large diffusion distance is due to the significant amount of free volume in polymers [58]. These electrons increase the resist exposed volume due to a secondary random electron pattern, shown in Figure 15.8, which is superimposed on the projected image, increasing the CD obtained. In addition, there are statistical factors effects for areas under 1500 nm^2 such as shot noise. The results of resolution limit trial exposure experiments demonstrate that the small field exposure can delineate lines and spaces with half pitches ranging from 45 to 25 nm [59].

Although it was planned that EUV lithography would be implemented in 2012 for the 22-nm node [51], Intel has announced it will postpone the implementation [60, 61] and will instead extend 193-nm lithography using double-patterning methods. Although there are variations, the double-patterning techniques are

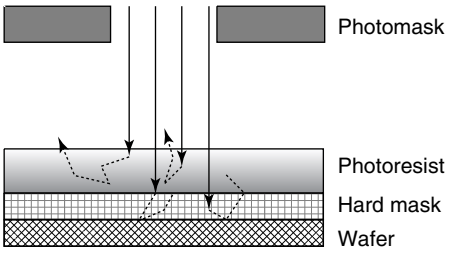

Figure 15.8 Image formation mechanism in EUV lithography. Top: EUV mask pattern for imaging a line. Bottom: EUV radiation (→) is absorbed in the resist and substrate hard mask, producing photoelectrons and secondary electrons (⇢).

considered to be spacer, double patterning (litho–etch–litho–etch), and double exposure (litho–litho–etch) [62]. Double-patterning or exposure techniques have the ability to use existing exposure tools to print technology nodes below the NA limit for single exposure processes. This means lower costs to implement these techniques because, in principle, they can be used without expensive new technology development. However, the two exposure stages require doubling the number of masks, that is, reducing the throughput due to increased processing time.

The double-patterning method is the most simple and uses materials that are readily available. This consists of a sequence of two separate exposures of the same photoresist. A double-patterning scheme is shown in Figure 15.9a. The first exposure prints the features of the photomask that are transferred onto a second layer. Using a second photomask, which can be different from the first one or identical to the first one, only shifted, there is a second exposure and transfer. The image-transfer step is essential. Since each exposure produces a sinusoidal modulation, the final effect of an out-of-phase double patterning without image transfer would be like adding two out-of-phase sinusoidal functions. In addition, the removal of the wafer from the wafer chuck between exposures poses severe overlay issues that may be difficult to overcome, especially at the CDs where this technology will be implemented.

The double-patterning method has problems producing more complex patterns due to the critical realignment step. Also, because of the number of steps required, the process has a low throughput, increasing the cost per wafer. A simplification is the litho–litho–etch double exposure concept [63, 64], which only introduces an additional exposure pass in comparison to the single-exposure patterning, and since the wafer is not removed from the imaging tool between exposures, the overlay issues are moderate. The process is depicted in Figure 15.9b. The double-exposure (litho–litho–etch) process means that the entire lithographic patterns are completed before pattern transfer, so that only a single etching step is needed and higher throughput can be expected [65]. However, there is the possibility that the second lithographic process damages the first lithographic

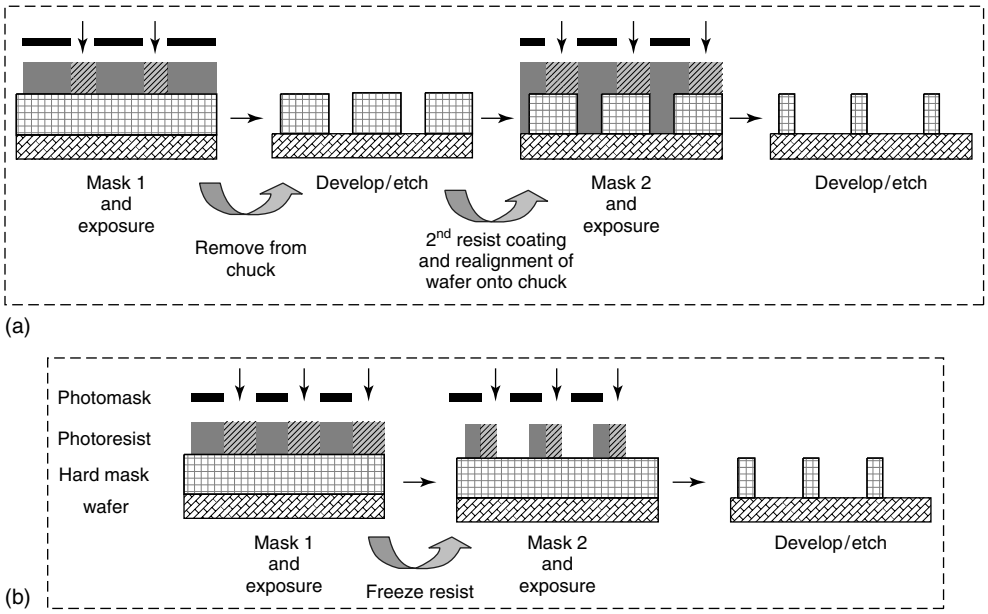

Figure 15.9 Schematic procedure for (a) double patterning and (b) double-exposure lithography.

pattern. For a successful patterning, the photoresist must have sufficient contrast to support a double exposure or two different resists have to be used. To coat a second resist on top of a patterned first resist, a step to prevent intermixing of these two resists is required. The typical step reported is to UV-cure the first resist [66] and then coat the second resist. Other approaches are being developed. One approach "freezes" the first resist [65] before the coating of a second resist; another approach is the use of a contrast-enhancing layer that will act as a mask, becoming transparent in highly irradiated regions and reversing to opaque before the second exposure [67], or the pack–unpack technique [68]. The double-exposure approach has put pressure in developing new photoresist chemistry in order to achieve its full potential.

The previous double-patterning options have critical overlay issues. The spacer double patterning avoids the overlay problems through self-alignment, but requires more complex processing. In this approach, normal lithography is used to create a feature in the photoresist. A spacer is formed by deposition or reaction of a film on the previous pattern, followed by etching to remove all the film material on the horizontal surfaces, leaving only the material on the sidewalls. Removing the original patterned feature, only the spacer is left (Figure 15.10). However, since there are two spacers for every feature, the line density is doubled [69–71]. There are concerns if the spacers can stay in place after the patterned resist to which they are attached is removed, whether the spacer profile is acceptable and whether the underlying hard mask is attacked by the step to remove the resist attached to the

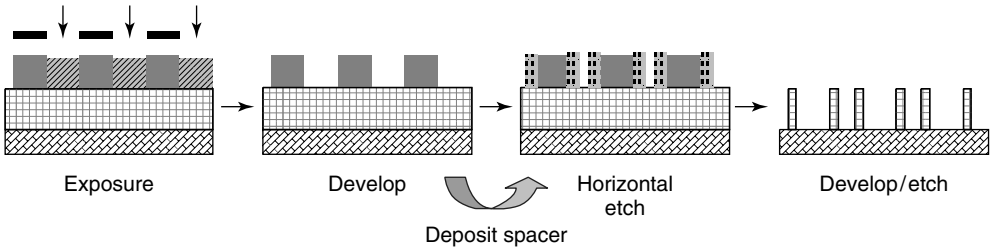

Figure 15.10 Scheme for the spacer double-patterning lithography.

spacer. Pattern transfer is complicated when the removal of the resist adjacent to the spacers also removes a little of the underlying hard mask, resulting in different heights of the patterned features throughout the exposed area.

Another approach, still using 193-nm single exposure, is the development of high refractive index liquids and lens materials to achieve NA higher than the theoretical limit of 1.44. The development of a working system is dependent not as much in the liquid but more in the lenses because the use of quartz concave lenses is not possible [51], limiting the practical design of the optical system to flat lenses. New high-index material for the lenses has been proposed, such as ceramic spinel and LuAG (lutetium aluminium garnet), but the implementation of this approach is still much in the future [72].

Another technique that uses a smaller wavelength source is electron beam or ion beam lithography. Electron beam lithography is a well known and mature solution, already used to provide advanced patterning for research and development. The first electron beam lithography systems were based on the scanning electron microscope (SEM) and were developed in the late 1960s. The simplest version relies on the SEM scanning circuitry with a stationary work piece and a computer pattern generator to blank the beam in the appropriate intervals. More sophisticated systems use an interferometer to continuously monitor the position of the stage, being able to write while the stage is in motion. However, right from the start, its low throughput hindered this as a credible option for manufacturing purposes [73]. The problem is the individualism of e-beams compared with the mass parallelism of photon beams [74]. Various attempts were made to correct it but it has not yet been proven practical. Multi-e-beam maskless lithography is gaining some momentum but is still not ready for commercial application [75]. To produce massively parallel e-beams inexpensively is now also a computational problem, with the obstacles being the cost, size, and thermal management of the substantial data handling needed. The control of the data rate, data integrity, electromagnetic interference shielding, and beam consistency are other important issues which must be taken into account.

One scenario that is gaining popularity is the implementation of a hybrid process [75]. Electron beam lithography is used to pattern the high-resolution features while optical projection lithography is used for the remainder. In this way, only a small fraction of the wafer is patterned with electron beam, saving time, and reducing costs.

There are also nonradiation-based patterning techniques that have already proven themselves capable of producing high-resolution patterns. Nonradiation-based patterning techniques are very simple and inexpensive methods to replicate a master pattern in large scale. These methods do not change the chemical nature of the resist material using properties like self-assembly, in soft lithography, or mechanical deformation, in nanoimprinting, for the creation of very small structures.

Soft lithography [76–81] uses elastomeric stamps and moulds, made with polydimethylsiloxane (PDMS) for example, created from a master pattern of the structures to be produced. Liquid PDMS is spread on the master pattern and is cured. This forms a rubberlike solid that can be peeled off the master pattern, and the mold formed can be attached to a stamp. The stamp is then coated with a solution of the ''ink,'' for example, thiol molecules that will self-assemble upon contact with a gold or silver thin film that has been deposited onto a silicon substrate. There are several techniques developed for this purpose: microcontact printing (μCP) with a minimum feature size of 35 nm (Figure 15.11a), replica moulding (REM) with a minimum feature size of 30 nm (Figure 15.11b), microtransfer moulding (μTM) with a minimum feature size of 500 nm (Figure 15.11c), micromoulding in capillaries with a minimum feature size of 350 nm and solvent-assisted microcontact moulding (minimum feature size of 60 nm), among others [82, 83]. Soft lithography has several strong points in comparison to optical projection lithography: lower cost than traditional photolithography in mass production; easily patterned nonplanar surfaces; several options for patterning methods and ''inks''; the lack of need for a reactive surface to create a nanostructure; the avoidance of the diffraction limit, since it is not an optical procedure; fast production (e.g., with μCP,

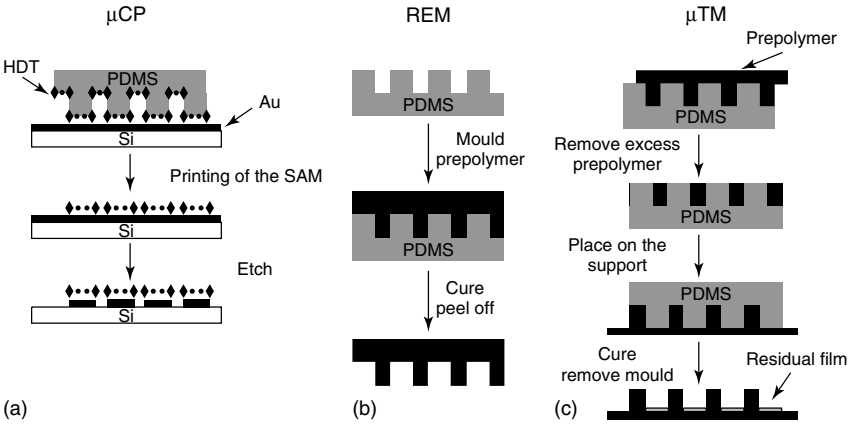

Figure 15.11 The simplest soft-lithography procedures for nanopatterning; (a) microcontact printing (μCP) of hexadecanethiol (HDT) forming a self assembled monolayer (SAM); (b) replica moulding (REM); and (c) microtransfer moulding (μTM).

a contact time of less than 30 ms is required to deposit molecules onto the surface of the substrate). There are also some drawbacks associated with this technique already identified by Xia and Whitesides [84]. The PDMS stamp shrinks by 1% upon curing and the cured PDMS can be swelled by a number of nonpolar organic solvents; the elasticity and thermal expansion of PDMS make it difficult to achieve high accuracy in registration across a large area; and the softness of an elastomer limits the aspect ratio of nanostructures in PDMS, because of the deformation of the patterns by pairing or by sagging. Recent reviews on this technique are available [85–87].

Nanoimprint lithography, also a lensless replication technique, causes a physical deformation of the support material with a rigid mould [75]. The technique offers a very easy and cheap way to achieve high-resolution patterns, with CDs as low as 5 nm [88]. There are various forms to transfer the pattern: thermal nanoimprint lithography, photo nanoimprint lithography, and electrochemical nanoimprint; and several schemes to achieve large- or small-area patterning: Step-and-flash imprint, roller nanoimprint, transfer nanoimprint, and casting nanoimprint. The first step, and common step to all nanoimprint technology, is to imprint the pattern, and this relies on physically deforming a thin resist film using the rigid mould. The mould is removed and the pattern is etched either by thermal etching, photo etching, or electrochemical etching. The procedure is not without problems. Contact printing is always vulnerable to defects, either due to particles that adhere to the mould from one imprint to the next, or from the lift procedure. The mould may have a shorter life span than optical masks, due to physical pressure against a surface. These problems have been addressed by Chou *et al.* [89, 90] and others [91–93]. Another feature of nanoimprint molding is the bubble defect. This happens because air bubbles are trapped when the mould is being pressed. The problem is greatly reduced by using vacuum systems and by a pacing step to allow the bubbles to dissolve. There are also proximity effects that arise from polymer displacement, which could lead to long distance effects. When a dense array of protrusions in the mould press into the resist thin film, because it is viscous, the excess polymer can migrate to the outer edges of the mould, forming different resist thickness in some areas or holes in unprinted areas [94]. Several recent reviews on nanoimprinting are available [95–98].

15.2.3.1 Optical Lithography beyond the Diffraction Limit

Optical projection nanolithography is, so far, limited by the diffraction limit imposed by the exposure radiation wavelength. This is a consequence of the wave nature of light that prevents imaging and defining spatial dimensions much smaller than the radiation wavelength. Diffraction of visible light prevents the imaging of live cells at the nanoscale and prevents the downsizing of features in data storage and lithography. To advance biological imaging, concepts have been introduced that overcome the diffraction barrier in far-field fluorescence microscopy in a fundamental way [99–102]. The first concept of this kind was stimulated emission depletion (STED) microscopy [99], with which a new far-field spatial resolution benchmark of 26 nm has been achieved [103]. In these concepts, the breaking of

the diffraction barrier is based on the idea of saturating a molecular transition that inhibits fluorescence. In STED microscopy, a second laser beam is used to saturate the quenching of the fluorescent state through stimulated emission. To gain a subdiffraction-sized focal spot, the STED beam has a light distribution of zero intensity in the center and nonzero intensity around. In this way, the focal point is squeezed to the zero-intensity region of the STED beam.

The conventional resolution limits of image projection lithography are well known, as are the variety of resolution-enhancement techniques that are being developed to go beyond those limits for certain categories of patterns – a subject for the next chapter. The use of reversible saturable transitions was put forward as a promising step to overcome the diffraction limit for optical lithography [104–106]. The application of such concept has only been achieved using the absorbance-modulation technique [107, 108], where a photochromic material is placed on top of a photoresist film. These photochromic molecules reversibly change their absorbance upon exposure to light, that is, illumination switches the molecule from an opaque configuration to a transparent one and vice versa. A dual illumination of the photochromic material, with a focused spot of the bleaching wavelength and a ring-shaped spot of the reversible bleaching wavelength, causes the dynamic competition between the two photoreactions, and creates a subwavelength transparent aperture. This technique is limited by the photochromic materials developed, especially for UV radiation and also the time needed to achieve the required transparency.

Reversible photoacids with the ability to change the acidity of an aqueous solution within the time of a short laser pulse and use the resulting low pH to drive acid-catalyzed reactions in the irradiated volume opens new perspectives for the spatial and temporal control of the optical projection lithographic process. So far, using reversible photoacids have been hindered by the limited diffusion of the proton before recombination with the conjugate base. In a very simple description, the proton can only diffuse away during the excited-state lifetime of the anion [109, 110] and this is the available time to be involved in a catalytic reaction. Using a STED-like irradiation procedure with a photoacid that produces a time-extended and reversible acidification of an aqueous solution will accomplish this feat. This new class of molecules [111] combines the fast photoacid properties of an aromatic alcohol with the slow proton transfer rates of a stabilized carbanion [112]. The concept of reversible photoacids capable of rapidly acidifying an aqueous solution and slowly returning to neutrality has its roots in the interacting-state model (ISM) [113–115] and in enzyme catalysis [116]. Figure 15.12 shows the rates of the proton transfer cycle calculated [117] with ISM based on known pk_a values of analogous compounds [109, 118]. ISM predicts that intramolecular quenching of the electronically excited naphtholate ion by an acidic proton of a nitroalkane moiety is competitive with its nanosecond lifetime.

Steady-state absorption and fluorescence emission of 1-(2-nitroethyl)-2-naphthol in water solution at different pH values, depicted in Figure 15.13, show the expected acid–base equilibrium for an aromatic alcohol. The p$k_a = 9.7$ and p$k_a^* = 1.9$ values were determined.

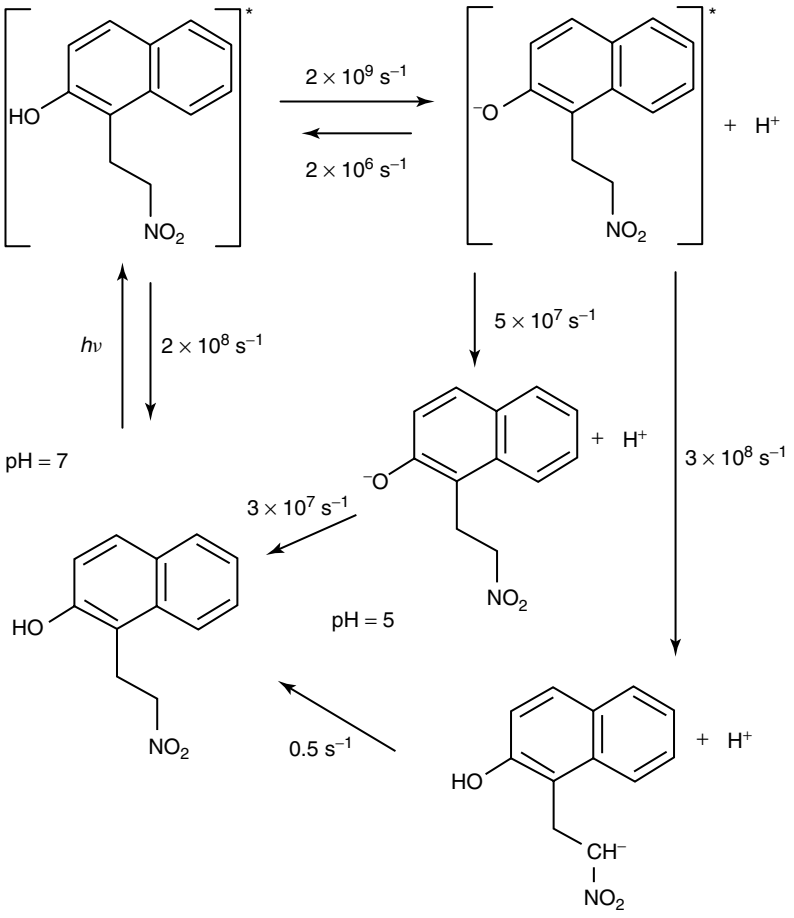

Figure 15.12 First-order rate constants calculated with the ISM free web tool [64] using pk_a(2-naphthol) = 9.4 [65], pk_a*(2-naphthol) = 1, and pk_a(2-phenyl-1-nitroethane) = 9 [66] for the given pH values.

The relative quantum yield for the excited-state dissociation of the naphthol moiety is about 0.48 and photoinduced proton release quantum yield is estimated to reach 0.3. Final evidence for the proposed mechanism is the photolysis in 2% MeOD : D_2O, leading to the incorporation of deuterium in the alkyl side chain, as determined by ^1H NMR spectroscopy.

The color change of pH indicators is a very convenient tool to assess the amplitude of the pH jump and the availability of the excess protons to participate in chemical reactions. We employed bromocresol green ($pk_a = 4.9$) and observed the bleaching and recovery of its basic form at 616 nm, Figure 15.14. The absorbance change produced after a 3-mJ laser pulse with 2-mm optical path in a 2% MeOH : H_2O solution shows the pH changes to 6.3.

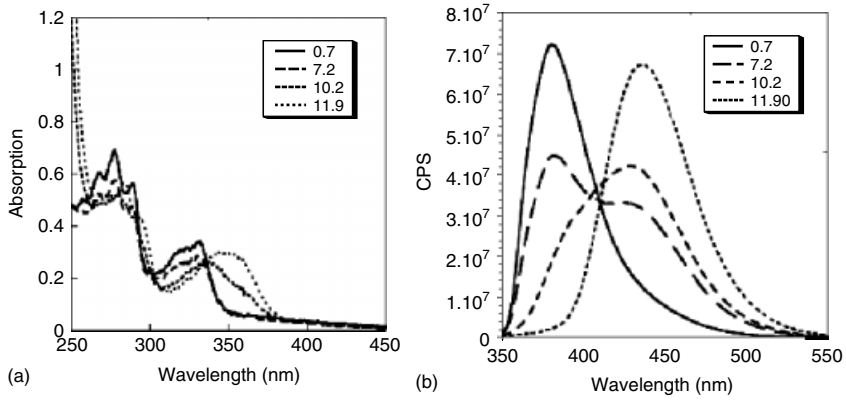

Figure 15.13 Steady-state (a) absorption and (b) fluorescence emission of 1-(2-nitroethyl)-2-naphthol in 2% methanol in water solution.

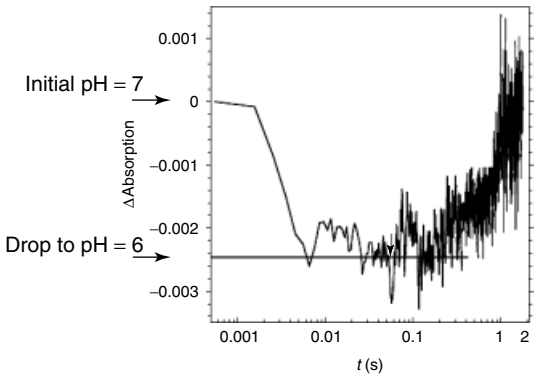

Figure 15.14 Transient bleaching and recovery of bromocresol green absorption at 616 nm following flash photolysis of [1-(2-nitroethyl)-2-naphthol] $= 2 \times 10^{-4}$ M in 2% MeOH : H_2O.

More importantly is the fact that the magnitude of the pH jump is directly proportional to the laser energy. With intense laser pulses, the proton concentration should approach the solubility limit of 1-(2-nitroethyl)-2-naphthol.

Because of the reversible nature of the acidification mechanism, it is possible to use a second red-shifted wavelength STED beam, with a light distribution of zero intensity in the center and nonzero intensity around, in order to achieve a subdiffraction acidification of the photoresist. Also, the need to use base additives to achieve greater resolution and linewidth roughness is diminished, if not eliminated. The coupled acid diffusion of an iodonium PAG in polymer matrix has been determined to have a diffusion length of 5 nm for a postexposure bake at 100 °C for

2 minutes [119]. This is probably the major problem for a STED optical projection lithography proposal that can have a regular focal spot of 20–30 nm [120].

15.3 Conclusions and Outlook

What is going to be the technology to take lithography beyond the 22-nm node is still unknown but there are several promising candidates. The development of new materials with tailored properties, either new resists or lenses and mask, is required. New approaches with multiple masking also need new robust and fast algorithms for mask image decomposition to be an option.

The use of reversible switching molecules can perhaps take nanophotolithography beyond the diffraction limit, taking the theoretical attainable resolution to the molecular level maintaining much of the lithography technology used at present.

Acknowledgments

The author deeply appreciates the supervision and guidance of Prof. Luis Arnaut, with whom part of this work was done. The author acknowledges Prof. Luis Arnaut, Drs. Marta Piñeiro, and Raquel Rondão, University of Coimbra, and Dr. David Noga and Prof. Laren Tolbert, Georgia Institute of Technology, for fruitful discussion and reviewing. Marvin was used for drawing, displaying and characterizing chemical structures, substructures and reactions, Marvin 5.1.4, 2008, ChemAxon (*http://www.chemaxon.com*). Funding from Fundação para a Ciência e Tecnologia (SFRH/BD/24005/2005) and project POCI/QUI/55505/2004.

References

1. Kilby, J.S.C. (2001) *ChemPhysChem*, **2** (8-9), 482.
2. Wallraff, G.M. and Hinsberg, W.D. (1999) *Chem. Rev.*, **99**, 1801.
3. Avouris, P. (1995) *Acc. Chem. Res.*, **28** (3), 95.
4. Campbell, S.A. (2001) *The Science and Engineering of Microelectronic Fabrication*, Oxford University Press, New York.
5. Hofmann, M., Eggeling, C., Jakobs, S., and Hell, S.W. (2005) *Proc. Natl. Acad. Sci*, **102** (49), 17565.
6. Bouhelier, A., Hartschuh, A., and Novotny, L. (2005) Scanning near-field optical microscopy in nanosciences, in *Handbook of Microscopy for Nanotechnology* (eds N. Yao and Z.L. Wang), Kluwer Academic Publishers, Boston, p. 25.
7. Lin, B.J. (2002) *J. Microlith. Microfab. Microsyst.*, **1** (1), 7.
8. Reiser, A. (1989) *Photoreactive Polymers, the Science and Technology of Resists*, Wiley-VCH Verlag GmbH, New York.
9. Hephner, M. and Wagner, H.M. (1954) Patent BP762.985.
10. Sues, O. (1944) *Annalen*, **556**, 65.
11. Sues, O. (1947) *Annalen*, **557**, 237.
12. Dammel, R. (1993) *Diazonaphthoquinone-based Resists*, SPIE, Bellingham.

13. Leeson, M.J., Pawloski, A.R., Levering, V., Yueh, W., and Willson, C.G. (1997) *Proc. SPIE*, **3049**, 861.
14. Willson, C.G. (1994) Organic resist materials in introduction to microlithography, in *Introduction to Microlithography* (eds L.F. Thompson, C.G. Willson, and M.J. Bowden), American Chemical Society, Washington, DC, p. 139.
15. Schlesinger, S.I. (1974) *Polym. Eng. Sci.*, **14** (7), 513.
16. Schlesinger, S.I. (1974) *Photogr. Sci. Eng.*, **18** (4), 387.
17. Crivello, J.V. and Lam, J.H.W. (1977) *Macromolecules*, **10** (6), 1307.
18. Crivello, J.V. and Lam, J.H.W. (1979) *J. Polym. Sci. A: Polym. Chem.*, **17**, 977.
19. Crivello, J.V. and Lam, J.H.W. (1979) *J. Polym. Sci. A: Polym. Chem.*, **17**, 3845.
20. Crivello, J.V. and Conlon, D.A. (1983) *J. Polym. Sci. A: Polym. Chem.*, **21**, 1785.
21. Crivello, J.V., Lee, J.L., and Conlon, D.A. (1983) *J. Radiat. Curing*, **10** (1), 6.
22. Crivello, J.V. and Conlon, D.A. (1984) *J. Polym. Sci. A: Polym. Chem.*, **22**, 2105.
23. Rajaraman, S.K., Mowers, W.A., and Crivello, J.V. (1999) *Macromolecules*, **10** (6), 1307.
24. Dektar, J.L. and Hacker, N.P. (1990) *J. Org. Chem.*, **55**, 639.
25. Dektar, J.L. and Hacker, N.P. (1991) *J. Org. Chem.*, **56**, 1838.
26. Hacker, N.P., Leff, D.V., and Dektar, J.L. (1991) *J. Org. Chem.*, **56**, 2280.
27. Dektar, J.L. and Hacker, N.P. (1987) *J. Chem. Soc. Chem. Commun.*, **20**, 1591.
28. Dektar, J.L. and Hacker, N.P. (1990) *J. Am. Chem. Soc.*, **112**, 6004.
29. Crivello, J.V. (1999) *J. Polym. Sci. A: Polym. Chem.*, **37**, 4241.
30. Allen, R.D., Conley, W.E., and Kunz, R.R. (1997) Deep-UV resist technology, in *Handbook of Microlithography, Micromaching, and Microfabrication*, Microlithography, Vol. **1** (ed. P. Rai Choudhury), SPIE Optical Engineering Press, Bellingham, p. 321.
31. Castellanos, F., Fouassier, J.P., Priou, C., and Cavezzan, J. (1996) *J. Appl. Polym. Sci.*, **60** (5), 705.
32. Mulkens, J., Fahey, T.J., McClay, J.A., Stoeldraijer, J.M.D., Wong, P., Brunotte, M., and Mecking, B. (2002) *Proc. SPIE*, **4691**, 613.
33. Macdonald, S.A., Willson, C.G., and Frechet, J.M.J. (1994) *Acc. Chem. Res.*, **27** (6), 151.
34. Shirai, M. and Tsunooka, M. (1996) *Prog. Polym. Sci.*, **21** (1), 1.
35. Hinsberg, W.D., Houle, F.A., Sanchez, M.I., and Wallraff, G.M. (2001) *IBM J. Res. Dev.*, **45** (5), 667.
36. Ito, H. (2005) *Microlith.: Mol. Imprint.*, **172**, 37.
37. Moon, S.Y. and Kim, J.M. (2007) *J. Photochem. Photobiol., C*, **8** (4), 157.
38. Moore, G.E. (1965) Cramming more componants onto integrated circuits, *Electronics*, **38** (8), 114–117.
39. Hien, S. *et al.* (2001) *Proc. SPIE*, **4345**, 439.
40. Martin, L.C. and Johnson, B.K. (1958) *Practical Microscopy*, Blackie and Son, Ltd, London.
41. Mulkens, J., Flagello, D.G., Streefkerk, B., and Graeupner, P. (2004) *J. Microlithogr. Microfabr. Microsyst.*, **3** (1), 104.
42. Switkes, M., Kunz, R.R., Rothschild, M., Sinta, R.F., Yeung, M., and Baek, S.-Y. (2003) *J. Vac. Sci. Technol., B*, **21** (6), 2794.
43. Switkes, M., Kunz, R.R., Sinta, R.F., Rothschild, M., Gallagher-Wetmore, P.M., Krukonis, V.J., and Williams, K. (2003) *Proc. SPIE*, **5040**, 690.
44. Slezak, M., Liu, Z., and Hung, R. (2004) *Solid State Technol.*, **47** (7), 91.
45. Ichimura, I., Hayashi, S., and Kino, G.S. (1997) *Appl. Opt.*, **36** (19), 4339.
46. Taylor, J.C., Chambers, C.R., Deschner, R., LeSuer, R.J., Conley, W.E., Burns, S.D., and Willson, C.G. (2004) *Proc. SPIE*, **5376**, 34.
47. Smith, B.W., Bourov, A., Kang, H.Y., Cropanese, F., Fan, Y.F., Lafferty, N., and Zavyalova, L. (2004) *J. Microlithogr. Microfabr. Microsyst.*, **3** (1), 44.
48. Wei, A., Abdo, A., Nellis, G., Engelstad, R.L., Chang, J., Lovell, E.G., and

Beckman, W. (2004) *Microelectron. Eng.*, **73-74**, 29.
49. Sewell, H., Graeupner, P., McCafferty, D., Markoya, L., Samarakone, N., van Wijnen, P., Mulkens, J., and Benschop, J. (2008) *J. Photopolym. Sci. Technol.*, **21** (5), 613.
50. Kawai, A. and Tanaka, D. (2008) *J. Photopolym. Sci. Technol.*, **21** (6), 727.
51. Benschop, J.P.H. (2007) 32 nm: lithography at a crossroad, in *Future Trends in Microelectronics – Up the Nano Creek* (eds S. Luryi, J. Xu, and A. Zaslavsky), John Wiley & Sons, Inc., Hoboken, p. 167.
52. Brunton, A. *et al.* (2004) *Proc. SPIE*, **5448**, 681.
53. Benschop, J., Banine, V., Lok, S., and Loopstra, E. (2008) *J. Vac. Sci. Technol., B*, **26** (6), 2204.
54. Komori, H., Soumagne, G., Hoshino, H., Abe, T., Suganuma, T., Imai, Y., Endo, A., and Toyoda, K. (2004) *Proc. SPIE*, **5374**, 839.
55. Srivastava, S.N., Thompson, K.C., Antonsen, E.L., Qiu, H., Spencer, J.B., Papke, D., and Ruzic, D.N. (2007) *J. Appl. Phys.*, **102** (2), 023301.
56. Owa, S. and Nagasaka, H. (2004) *J. Microlithogr. Microfabr. Microsyst.*, **3** (1), 97.
57. Henke, B.L., Smith, J.A., and Attwood, D.T. (1977) *J. Appl. Phys.*, **48** (5), 1852.
58. Alegaonkar, P.S. and Bhoraskar, V.N. (2004) *Radiat. Eff. Defects Solids*, **159** (8/9), 511.
59. Tawarayama, K., Magoshi, S., Tanaka, Y., Shirai, S., and Tanaka, H. (2008) *Jap. J. Appl. Phys.*, **47** (6), 4866.
60. Mutschler, A.S. (2007) Survey: No EUV Until 2015 or Later, Electronics Design, Strategy, News.
61. Lammers, D. (2008) Intel: 'EUV Facts Don't Add Up' for 22 nm in 2011, Semiconductor International.
62. Hand, A. (2008) Double Patterning Battles Cost, Complexity, Semiconductor International.
63. Saul, L., Jeffrey, B., Kane, J., Paul, Z., Bryan, R., Nicholas, J.T., and Willson, C.G. (2008) *Proc. SPIE*, **6924**, 69242A.
64. Chen, K.-J.R., Huang, W.-S., Li, W.-K., and Varanasi, P.R. (2008) *Proc. SPIE*, **6923**, 69230G.
65. Hori, M. *et al.* (2008) *Proc. SPIE*, **6923**, 69230H.
66. Kuang-Jung Rex, C., Wu-Song, H., Wai-Kin, L., and Varanasi, P.R. (2008) *Proc. SPIE*, **6923**, 69230G.
67. Kim, R.H. and Levinson, H.J. (2007) *J. Vac. Sci. Technol., B*, **25** (6), 2466.
68. Owe-Yang, D.-C., Yu, S.S., Chen, H., Chang, C.Y., Ho, B.-C., Lin, J.C., and Lin, B.J. (2005) *Proc. SPIE*, **5753**, 171.
69. Choi, Y.K., King, T.J., and Hu, C.M. (2002) *Solid-State Electron.*, **46** (10), 1595.
70. Choi, Y.K., King, T.J., and Hu, C.M. (2002) *IEEE Trans. Electron Devices*, **49** (3), 436.
71. Choi, Y.K., King, T.J., and Hu, C.M. (2002) *IEEE Electron Device Lett.*, **23** (1), 25.
72. Lin, B.J. (2006) *C. R. Phys.*, **7** (8), 858.
73. Pain, L., Tedesco, S., and Constancias, C. (2006) *C. R. Phys.*, **7** (8), 910.
74. Chang, T.H.P. *et al.* (1996) *J. Vac. Sci. Technol., B*, **14** (6), 3774.
75. Pease, R.F. and Chou, S.Y. (2008) *Proc. IEEE*, **96** (2), 248.
76. Kim, E., Xia, Y.N., and Whitesides, G.M. (1995) *Nature*, **376** (6541), 581.
77. Xia, Y.N. and Whitesides, G.M. (1998) *Angew. Chem. Int. Ed.*, **37** (5), 551.
78. Xia, Y.N., Mrksich, M., Kim, E., and Whitesides, G.M. (1995) *J. Am. Chem. Soc.*, **117** (37), 9576.
79. Kim, E., Xia, Y.N., and Whitesides, G.M. (1996) *J. Am. Chem. Soc.*, **118** (24), 5722.
80. Beh, W.S., Kim, I.T., Qin, D., Xia, Y.N., and Whitesides, G.M. (1999) *Adv. Mater.*, **11** (12), 1038.
81. Xia, Y.N., Rogers, J.A., Paul, K.E., and Whitesides, G.M. (1999) *Chem. Rev.*, **99** (7), 1823.
82. Jackson, M.J. (2006) The future of micro-and nanomanufacturing, in *Microfabrication and Nanomanufacturing* (ed. M.J. Jackson), CRC Press, Taylor & Francis Group, Boca Raton, p. 367.
83. Steed, J.W., Turner, D.R., and Wallace, K.J. (2007) Nanochemistry, in *Core Concepts in Supramolecular Chemistry and Nanochemistry* (eds J.W. Steed, D.R. Turner, and K.J. Wallace), John Wiley & Sons, Ltd, Chichester, p. 229.

84. Xia, Y.N. and Whitesides, G.M. (1998) *Annu. Rev. Mater. Sci.*, **28**, 153.
85. Kim, P., Kwon, K.W., Park, M.C., Lee, S.H., Kim, S.M., and Suh, K.Y. (2008) *BioChip J.*, **2** (1), 1.
86. Ruiz, S.A. and Chen, C.S. (2007) *Soft Matter*, **3** (2), 168.
87. Innocenzi, P., Kidchob, T., Falcaro, P., and Takahashi, M. (2008) *Chem. Mater.*, **20** (3), 607.
88. Austin, M.D., Ge, H.X., Wu, W., Li, M.T., Yu, Z.N., Wasserman, D., Lyon, S.A., and Chou, S.Y. (2004) *Appl. Phys. Lett.*, **84** (26), 5299.
89. Chou, S.Y., Krauss, P.R., and Renstrom, P.J. (1996) *J. Vac. Sci. Technol., B*, **14** (6), 4129.
90. Chou, S.Y. and Xia, Q.F. (2008) *Nat. Nanotech.*, **3** (5), 295.
91. Houle, F.A., Miller, D.C., Fornof, A., Truong, H., Raoux, S., Sooriyakumaran, R., Ito, H., and Hart, M. (2008) *J. Photopolym. Sci. Technol.*, **21** (4), 563.
92. Lin, M.W. *et al.* (2008) *J. Micro-Nanolithogr. MEMS MOEMS*, **7** (3), 8.
93. McMackin, I., Martin, W., Perez, J., Selinidis, K., Maltabes, J., Xu, F., Resnick, D., and Sreenivasan, S.V. (2008) *J. Vac. Sci. Technol., B*, **26** (1), 151.
94. Landis, S., Chaix, N., Gourgon, C., Perret, C., and Leveder, T. (2006) *Nanotechnology*, **17** (10), 2701.
95. He, Q.H. and Chen, S.A. (2008) *Prog. Chem.*, **20** (12), 2061.
96. Ali, M., Wagner, T., Shakoor, M., and Molian, P.A. (2008) *J. Las. Appl.*, **20** (3), 169.
97. Sreenivasan, S.V. (2008) *MRS Bull.*, **33** (9), 854.
98. Schift, H. (2008) *J. Vac. Sci. Technol., B*, **26** (2), 458.
99. Hell, S.W. and Wichmann, J. (1994) *Opt. Lett.*, **19** (11), 780.
100. Hell, S.W., Hanninen, P.E., Schrader, M., Wilson, T., and Soini, E. (1995) *Zool. Stud.*, **34**, 70.
101. Klar, T.A., Engel, E., and Hell, S.W. (2001) *Phys. Rev. E*, **64** (6), 066613.
102. Hell, S.W. (2009) *Nat. Met.*, **6** (1), 24.
103. Westphal, V. and Hell, S.W. (2005) *Phys. Rev. Lett.*, **94** (14), 143903.
104. Hell, S.W., Jakobs, S., and Kastrup, L. (2003) *Appl. Phys. A*, **77** (7), 859.
105. Hell, S.W. (2004) *Phys. Lett. A*, **326** (1-2), 140.
106. Menon, R. and Smith, H.I. (2006) *J. Opt. Soc. Am. A: Opt. Im. Sci. Vis.*, **23** (9), 2290.
107. Menon, R., Tsai, H.Y., and Thomas, S.W. (2007) *Phys. Rev. Lett.*, **98** (4), 043905.
108. Tsai, H.Y., Wallraff, G.M., and Menon, R. (2007) *Appl. Phys. Lett.*, **91** (9), 3.
109. Tolbert, L.M. and Haubrich, J.E. (1994) *J. Am. Chem. Soc.*, **116** (23), 10593.
110. Tolbert, L.M. and Solntsev, K.M. (2002) *Acc. Chem. Res.*, **35**, 19.
111. Nunes, R.M.D., Piñeiro, M., Gonsalves, A.Md.A.R., and Arnaut, L.G. (2008) Submitted.
112. Nunes, R.M.D., Piñeiro, M., and Arnaut, L.G. (2009) *J. Am. Chem. Soc.*, **131** (26), 9456. doi: 10.1021/ja901930c.
113. Arnaut, L.G. and Formosinho, S.J. (2008) *Chem. Eur. J.*, **14** (22), 6578.
114. Arnaut, L.G., Pais, A.A.C.C., Formosinho, S.J., and Barroso, M. (2003) *J. Am. Chem. Soc.*, **125** (17), 5236.
115. Barroso, M., Arnaut, L.G., and Formosinho, S.J. (2007) *J. Phys. Chem. A*, **111** (4), 591.
116. Barroso, M., Arnaut, L.G., and Formosinho, S.J. (2008) *J. Phys. Org. Chem.*, **21** (7-8), 659.
117. Oliveira, D., Barroso, M., and Arnaut, L.G. (2006) Intersecting/ Interacting State Model, *http://www.ism.qui.uc.pt:8180/ism/* (accessed 1 March 2009).
118. Bordwell, F.G. and Bartmess, J.E. (1978) *J. Org. Chem.*, **43** (16), 3101.
119. Houle, F.A., Hinsberg, W.D., Morrison, M., Sanchez, M.I., Wallraff, G., Larson, C., and Hoffnagle, J. (2000) *J. Vac. Sci. Technol., B*, **18** (4), 1874.
120. Hell, S.W. (2007) *Science*, **316** (5828), 1153.

Index

Ideas in Chemistry and Molecular Sciences: Advances in Nanotechnology, Materials and Devices.
Edited by Bruno Pignataro

ISBN: 978-3-527-32543-6